DOE/ER-0313/6

Fusion Reactor Materials

Semiannual Progress Report
for Period Ending
March 31, 1989

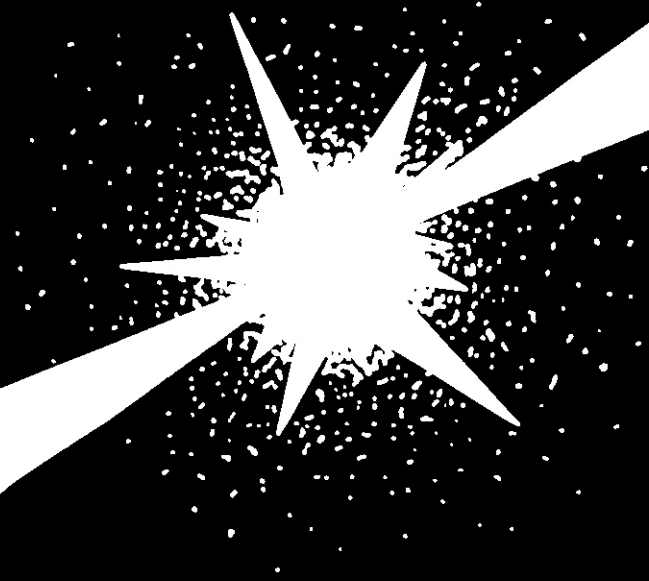

U. S. Department of Energy
Office of Fusion Energy

This report has been reproduced directly from the best available copy.

Available to DOE and DOE contractors from the Office of Scientific and Technical Information, P.O. Box 82. Oak Ridge, TN 37631; prices available from (615) 576-8401. FTS 828-8401.

Available to the public from the National Technical Information Service. U.S Department of Commerce. 5285 Port Royal Rd., Springfield. VA 22181.

NTIS price codes—Printed Copy: A19 Microfiche A01

This report was prepared as an account of work sponsored by an agency of the United States Government. Neither the United States Government nor any agency thereof. nor any of their employees, makes any warranty, express or implied. or assumes any legal liability or responsibility for the accuracy, corn pleteness, or usefulness of any information, apparatus. product, or process disclosed. or represents that its use would not infringe privately owned rights. Reference herein to any specific commercial product, process, or service by trade name, trademark, manufacturer. or otherwise. does not necessarily constitute or imply its endorsement, recommendation, or favoring by the United States Government or any agency thereof. The views and opinions of authors expressed herein do not necessarily state or reflect those of the United States Government or any agency thereof.

DOE/ER-0313/6
Distribution
categories
UC-423, -424

FUSION REACTOR MATERIALS SEMIANNUAL PROGRESS REPORT FOR THE PERIOD ENDING MARCH 31, 1989

Date Published:

Prepared for
WE Office of Fusion Energy
(AT 15 02 03 A)

Prepared by
OAK RIDGE NATIONAL LABORATORY
Oak Ridge, Tennessee 37831
operated by
MARTIN MARIETTA ENERGY SYSTEMS, INC.
for the
U.S. DEPARTMENT OF ENERGY
under Contract DE-AC05-84OR21400

Reports previously listed in this series are as follows:

DOE/ER-0313/1	Period Ending September 30, 1986
DOE/ER-0313/2	Period Ending March 31, 1987
DOE/ER-0313/3	Period Ending September 30, 1987
DOE/ER-0313/4	Period Ending March 31, 1988
DOE/ER-0313/5	Period Ending September 30, 1988

FOREWORD

This is the sixth in a series of semiannual technical progress reports on fusion reactor materials. This report combines research and development activities which were previously reported separately in the following technical progress reports:

- Alloy Development for Irradiation Performance
- Damage Analysis and Fundamental Studies
- Special Purpose Materials

These activities are concerned principally with the effects of the neutronic and chemical environment on the properties and performance of reactor materials; together they form one element of the overall materials program being conducted in support of the Magnetic Fusion Energy Program of the U.S. Department of Energy. The other major element of the program is concerned with the interactions between reactor materials and the plasma and is reported separately.

The Fusion Reactor Materials Program is a national effort involving several national laboratories, universities, and industries. The purpose of this series of reports is to provide a working technical record for the use of the program participants, and to provide a means of communicating the efforts of materials scientists to the rest of the fusion community. both nationally and worldwide.

This report has been compiled and edited under the guidance of A. F. Rowcliffe, Oak Ridge National Laboratory, and D. G. Doran, Battelle-Pacific Northwest Laboratory. Their efforts, and the efforts of the many persons who made technical contributions, are gratefully acknowledged. T. C. Reuther, Reactor Technologies Branch, has responsibility within DOE for the programs reported on in this document.

R. Price, Chief
Reactor Technologies Branch
Office of Fusion Energy

TABLE OF CONTENTS

FOREWORD .....

1. IRRADIATION FACILITIES, TEST MATRICES, AND EXPERIMENTAL METHODS 1

1.1 Design and Fabrication of HFIR-MFE RB* Spectrally Tailored Irradiation Capsules — A. W. Longest (Oak Ridge National Laboratory), J. E. Corum (Midwest Technical, Inc.), and D. W. Heatherly (Oak Ridge National Laboratory) 3

Design and fabrication of four HFIR-MFE RB* capsules (60, 200, 330. and 400°C) to accommodate MFE specimens preirradiated in spectrally tailored experiments in the ORR (and associated facility preparations) are proceeding satisfactorily. These capsule designs incorporate provisions for removal, examination, and re-encapsulation of the MFE specimens at intermediate exposure levels en route to a target exposure level of 24 (formerly 30) displacements per atom (dpa). With the exception of the 6J/C capsule, which, the test specimens will be in direct contact with the reactor cooling water, the specimen temperatures (monitored by 21 thermocouples) will be controlled by varying the thermal conductance of a small gap region between the specimen holder and the containment tube. Hafnium liners will be used to tailor the neutron spectrum to closely match the helium production-to-atom displacement ratio (14 appm/dpa) expected in a fusion reactor first wall.

Assembly of the 60 and 330°C capsules is complete and irradiation of both will begin when the HFIR returns to full-power operation. Design of the remaining two (200 and 400°C) capsules is complete, and issue of fabrication drawings is near. Fabrication of parts and assembly of the 200 and 400°C capsules is scheduled for completion by the end of FY 1990; operation of these two capsules will follow the first two (60 and 330°C).

1.2 Image Calculation of Tilted Contamination Deposit for the Thickness Measurement of specimen Foil — T. Sawai [Japan Atomic Energy Research Institute (JAERI), assigned to ORNL] and M. Suzuki, JAERI 7

A new imaging model has been proposed to explain some features of the image (formed by tilted contamination cones) that is used to determine the specimen thickness in a transmission electron microscope (TEM). The calculation assumes the lines with clear contrast in the image appear when the surface of tilted combination cones is parallel to the imaging electron beam. The calculated result explains some features of the actual image rather well. Also, the calculation shows the image shift, which leads to an overestimation of the parallax between two contamination cones, which leads to the overestimation of the foil thickness.

1.3 Small-Scale Bending Fatigue specimen Development — 6. A. Chin, G. R. Roa (Auburn University), and E. H. Lee (Oak Ridge National Laboratwy) 13

Two small-scale bending fatigue teat specimens were developed. The first specimen, termed the "rectangular" specimn, has overall dimensions of 30.1625 x 4.7625 x 0.762 mm, with e gauge length of 6.35 mm. The unirradiated rectangular specimens were tasted at both room temperature and at 600°C.

The second specimen is a "miniature-disc" specimen with outer dimensions of a 3-mm diameter Transmission Elecwon Microscope specimen and a reduced gauge section formed by two circular radii of 1.6 mm. The thickness is 0.264 mm. The miniature specimens w e fabricated using three different techniques: (1) punching followed by electropolishing, (2) electrical discharge machining, and (3) punching followed by annealing. The three sets of miniature-disc specimens were tasted separately at room temperature.

Tests were performed using annealed type 316 stainless steel (Reference Heat 6092297). The results were found to conform to the Coffin-Manson relationship, where the value of the exponent was found to lie between 0.1 and 0.25. There was some degradation in fatigue life for the rectangular specimen at 600°C compared with the room-temperature fatigue data. The miniature-disc specimens gave higher than expected values of fatigue endurance for all three sets of specimens. Both specimen designs appear to be suitable for scoping irradiated specimens for bending fatigue properties.

2. DOSIMETRY. DAMAGE PARAMETERS, AND ACTIVATION CALCULATIONS 21

2.1 Neutron Dosimetry and Damage Calculations for the ORR-MFE 7J Experiment — L. R. Greenwood (Argonne National Laboratory) 23

Neutron measurements and damage calculations have been completed for the joint U.S.-Japanese 7J experiment in the Oak Ridge Research Reactor. Tensile and TEM specimens were irradiated from June 28, 1983, to March 26, 1967 1475 full-power days) in position C3 at temperatures between 300-400°C. The maximum fast neutron fluence was 9.5 x 10^{21} n/cm^2, which produced 7.4 dpa and 102 appm helium in 316 stainless steel.

2.2 Production of ^{49}V, ^{93}Mo, and ^{93m}Nb near 14.7 MeV — L. R. Greenwood. D. L. Bowers, and A. Intasorn (Argonne National Laboratory) 27

Results are presented for the production of ^{49}V (331 d), ^{93}Mo (3500 y), and ^{93m}Nb (16 y) by 74 MeV neutrons. Samples ware *irradiated at RTNS II.* Chemical separations *were performed* to remove *impurities* and to *separate the Mo-Nb* fractions. Thin *samples* were then X-ray *counted. Results* predict that we *will produce* 28 *mCi/cc* of ^{49}V in vanadium and 2.8 *mCi/cc* of ^{93}Mo and *106 mCi/cc* of ^{93m}Nb *in molybdenum* in a *fusion first-wall, assuming the STARFIRE reactor design.*

2.3 Dosimetry and Damage Calculations for the ORR-MFE 4A/4B Spectral Tailoring Experiments — L. R. Greenwood (Argonne National Laboratory) 29

Results are presented for me *MFE 4A/4B spectral tailoring experiments in* me *Oak Ridge Research Reactor. These experiments started* with *an aluminum core piece filled* with *water, switched to a solid aluminum core piece, and finally added hafnium liners* to suppress the *thermal neutron flux. The maximum exposure* for *MFE 4A at 107.0 FPO 1223.1 FPD under HF)* was *4.2* x 10^{22} *n/cm^2, resulting* in *13.1 dpa and 243 appm helium* for *316 stainless steel. Corresponding values for MFE 4B at 995.5 FPD (121.8 FPD under HF) were 4.0* x 10^{22} *n/cm^2, resulting in 12.0 dpa and 216 appm helium* for *3 16 stainless steel.*

2.4 Neutron Spectral Calculations for the REAL88 Exercise—L. R. Greenwood and A. Intasorn (Argonne National Laboratory) 37

Neutron spectral analyses and damage calculations have been completed for *six reference data* sets *distributed by the IAEA in Vienna. This interlaboratory intercomparison* is *designed to standardize dosimetry techniques and damage estimates for various spectra including fusion reactor simulations, pressure vessel surveillance,* ^{235}U fission. *and fast fission reactors. The data will be reviewed at a meeting in ECN Petten, The Netherlands, in October 1988.*

3. MATERIALS ENGINEERING AND DESIGN REQUIREMENTS 39

4. FUNDAMENTAL MECHANICAL BEHAVIOR 41

4.1 Grain Size Effect *on* Radiation Hardening in Neutron-Irradiated Polycrystalline Copper—S. Kqima, S. J. Zinkle (Oak Ridge National Laboratory). and H. L. Heinisch (Pacific Northwest Laboratory) 43

Microstructural changes in 14 MeV neutron-irradiated polycrystalline copper were observed by transmission electron microscopy and correlated with me *variation* of *yield stress. Conventional theory* of *radiation hardening was found to be not directly applicable to polycrystals. Radiation-induced point defect clusters are considered to become obstacles not only to* me *motion of dislocations on the piling-up side of a grain, but also to the generation of dislocations on the next grain. Generally, applicable simplified equations* for *polycrystals are proposed. By applying the equations to the published tensile test results,* the *contribution* of *matrix hardening was found to be fairly low.*

4.2 Correlation of Mechanical Property Changes in Neutron-Irradiated Pressure Vessel Steels *on* the Basis of Spectral Effects — H. L. Heinisch (Pacific Northwest laboratory) 51

Defect production functions derived from atomistic modeling were evaluated for *use* in *correlating yield stress changes of A2 128 and A3028 pressure vessel steels irradiated in a wide variety* of *neutron spectra at low temperatures (40-90°C) and* low *doses (<0.1 dpa). The irradiations were performed* in *RTNS-II,* O M , *ORR, and* the *HFIR pressure vessel surveillance positions. The data from RTNS-II,* O M , *and ORR are correlated fairly well on the basis of dpa, but the* data *from HFIR show that only one tenth as m y dpa are needed to produce* the *same radiation-induced yield stress changes as in the other neutron spectra. About 96% of the neutrons* in the *HFIR surveillance position are thermal neutrons, and a significant fraction of the displacements is produced by recoils from thermal neutron captures. The best correlation* of *all* the *data is achieved when the property changes are compared on the basis* of *the production* of *freely migrating self-interstitial* defats, which *better represents the defects participating in the radiation-strengthening process.*

5. RADIATION EFFECTS MECHANISTIC STUDIES, THEORY, MODELING 57

5.1 Tensile Behavior and Swelling *of* Ternary Austenitic Alloys Irradiated in Different Neutron Spectra— M. L. Hamilton (Pacific Northwest Laboratory.) A. Okada (Hokkaido University), and F. A. Garner (Pacific Northwest Laboratory) 59

Two nominally identical experiments designed to study the effects of *nickel level, chromium level, and helium generation* rate *on* the *microstructural development and tensile properties* of *Fe-Cr-Ni alloys are currently undergoing examination. One* of *these, conducted in the ORR at a higher He/dpa rate and a lower displacement rate compared* with *the other*

experiment in EBR-II, show substantially more strengthening and a different temperature range of swelling. The effects of irradiation temperature, neutron flux, and neutron spectra appear to be larger than those of the compositional variations studied. Transmission electron microscopy (TEM) examination is in progress to determine the origin of the observed changes.

5.2 Radiation-Induced Spinodal-Like Decomposition of Fe-Cr-Ni Alloy and Its Influence on Electropolishing of Microscopy Disks—J. M. McCarthy and F. A. Garner (Pacific Northwest Laboratory) **73**

Scanning electron microscopy was used as a tool to investigate the dependence on nickel content of radiation-induced spinodal-like decomposition in Fe-15Cr-XNi alloys. It appears that the relative resistance to swelling observed in the Invar compositional regime at 510°C is concurrent with spinodal-like decomposition. The influence of this phenomenon in prolonging the loop-dominated phase of dislocation evolution and also suppressing the onset of accelerated void growth has not yet been determined.

5.3 Microstructural Examination of a Reactor-Irradiated Dilute Copper-Boron Alloy—S. J. Zinkle (Oak Ridge National Laboratory) 77

An initial microstructural examination has been performed on copper specimens containing ~20 wt ppm B that were irradiated with fission neutrons to ~1.2 dpa at a damage rate of 2 x 10^{-7} dpa/s. A bimodal size distribution of cavities was observed for the irradiation temperatures of 182 through 500°C as a result of the generation of 100 appm He during the irradiation. Stacking fault tetrahedra were also observed at all irradiation temperatures. Comparison with pure copper specimens irradiated in the same capsule revealed several interesting differences in the microstructure—namely, a slight enhancement in the SFT density at all temperatures and the presence of voids at 182°C in the copper-boron specimens.

5.4 Radiation Damage in Binary Ceramic Oxides: A Preliminary Model—Roger E. Stoller (Oak Ridge National Laboratory) **85**

A preliminary model of radiation damage in binary ceramic oxides has been developed. The model described here accounts in an approximate way for some of the major differences between metallic alloys and ceramics that are believed to be responsible for the fact that ceramic materials are observed to behave differently than metallic alloys when exposed to displacive irradiation. The model considers the influence of the existence of a second lattice and the additional constraint of stoichiometric point defect absorption by dislocation loops on the concentrations of point defects that would be observed at steady-state in an irradiated ceramic. These point defect concentrations are then used to compute various measures of the sensitivity of these materials to the type of microstructural evolution that is observed in irradiated metals. Initial results obtained with the present model indicate that both the lattice and stoichiometry effects can help to mitigate radiation damage in ceramics. However, the effect is not necessarily large; in agreement with recent data, the results indicate that at least some ceramic oxides may exhibit a sensitivity to displacement damage that is similar to metals.

5.5 Microstructural Evolution of Neutron-Irradiated Fe-Cr-Ni Alloy at 495% in Response to Changes in He/dpa Ratio—J. F. Stubbins and J. E. Nevling (University of Illinois). F. A. Garner (Pacific Northwest Laboratory). and R. L. Simons Westinghouse Hanford Company) **93**

A series of three Fe-15Cr-XNi alloys in both annealed and cold-worked conditions was irradiated in the Fast Flux Text Facility at 495°C to 14 dpa. The experiment was developed to determine the separate and synergistic effects of nickel and phosphorus content, cold-work, and helium/dpa ratio. This experiment was conducted without introducing variations in displacement rate, a variable known to strongly influence microstructural evolution. Each alloy condition was irradiated in two variants, one with natural nickel and one enhanced with the ^{59}Ni isotope. The latter variant produces helium/dpa ratios typical of fusion reactor spectra, while the former yields a much lower level of helium. The results show that helium alters the microstructural evolution somewhat at 495°C, but its effect is relatively small compared with the influences of the other variables studied. Increases in starting dislocation density, nickel content, or phosphorus level all retard swelling temporarily, while higher rates of helium generation, usually, but not always, accelerate swelling. Phosphorus addition of 0.04 wt % not only decreased swelling but lead to refinement of dislocation loop microstructure and stabilization of dislocation networks created by cold working. Phosphide precipitates did not form at this temperature and dose level.

5.6 Precipitation at Grain Boundaries in Irradiated Austenitic Fe-Cr-Mn Alloys—J. M. McCarthy (Pacific Northwest Laboratory) 103

In previous work, the phase stability of Fe-Cr-Mn alloys during irradiation was investigated in a study that included simple binaries, simple ternaries, and commercially produced alloys. These low-activation alloys are being considered for fusion reactor service in the first wall and in other structural applications subject to high neutron doses. In addition to phase instabilities observed within the grains, grain boundaries were susceptible to varying levels of precipitation dependent upon alloy composition, displacement dose, and irradiation temperature. This report describes the grain boundary microstructures that developed in these Fe-Cr-Mn alloys during irradiation.

5.7 The Effect of Phosphorus on Microstructures of Fe-15Cr-25Ni Alloys Irradiated with Fast Neutrons—T. Muroga (Kyushu University). F. A. Garner, and J. M. McCarthy (Pacific Northwest Laboratory) .. 110

Fe-15Cr-25Ni austenitic alloys with *various phosphorus contents were irradiated* with *fast neutrons in the EBR-II reactor at temperatures ranging from 399 to 649°C and between 8.2 and 14.3 dpa. Observations of* and *microchemical analyses were carried out to determine the various roles of phosphorus. At low irradiation temperatures and lower phosphorus contents, where no precipitate formation was observed, phosphorus remained in solution and had a strong but variable influence on swelling* and *void density. However,* the *results suggest that more than one mechanism involving phosphorus-point defect interaction* was *operating and that the net effect was a result of the competition of several mechanisms. Phosphide precipitates were observed to form at higher irradiation temperatures and phosphorus levels. The formation of* these *precipitates then exerted a further influence on void density and distribution.*

6. DEVELOPMENT OF STRUCTURAL ALLOYS 123

6.1 Ferritic Steels 125

6.1.1 Void Formation and Helium Effects in 9Cr-1MoVNb and 12Cr-1MoVW Steels Irradiated in HFIR and FFTF at 400°C—P. J. Maziasz and R. L. Klueh (Oak Ridge National Laboratory) 127

Martensitic/ferritic 9Cr-1MoVNb and *12Cr-1MoVW steels doped* with *up to 2 wt % Ni have up to 450 appm He after HFIR irradiation to ~38 dpa, but only 6 appm* He *after 47 dpa* in *FFTF.* No *fine helium bubbles and few or no larger voids were observable in any of these steels after FFTF irradiation at 407°C. By contrast, many voids* were *found in the undoped steels (30-90 appm* He) *irradiated in HFIR at 400°C, while* voids *plus many more fine helium bubbles were found in the nickel-doped steels (400-450 appm He). Irradiation in both reactors at ~ W produced significant changes in the as-tempered lath/subgrain boundary, dislocation, and precipitation structures that were sensitive to alloy composition, including doping* with *nickel. However, for each specific alloy the irradiation-produced changes* were *exactly the same, comparing samples irradiated in FFTF and HFIR, particularly in nickel-doped steels. Therefore,* the *increased* void *formation appears solely due to the increased helium generation found in HFIR. While* the *levels of* voids *are relatively low after 37 to 39 dpa in HFIR (0.1-0.4%), details* of the *microstructural evolution suggest that* void *nucleation* is *still progressing, and swelling could increase* with dose. *The effect of helium on* voids *remains a valid concern* for *fusion application that requires higher-dose experiments.*

6.1.2 Tensile Properties of 9Cr-1MoVNb and 12Cr-1MoVW Steels Irradiated to 23 dpa at 390 to 550°C—R. L. Klueh (Oak Ridge National Laboratory) 145

Normalized-and-tempered 9Cr-1MoVNb and *12Cr-1MoVW steels were irradiated in* the *Experimental Breeder Reactor II (EBR-II) at 390, 450, 500,* and *550°C to displacement damage levels of up to 25 dpa. Tensile tests* were *made at the irradiation temperatures on three types of specimens: irradiated specimens, normalized-and-tempered specimens,* and *specimens thermally aged 10,000 h at the irradiation temperatures. Observations from these tests were compared* with *results on these same materials irradiated in EBR-II at the same temperatures up 13 dpa* and *thermally aged 5000 h. Results were interpreted in terms of the precipitate and dislocation microstructures developed during heat treatment, thermal aging,* and *irradiation.*

6.1.3 Impact Behavior of 9Cr-1MoVNb and 12Cr-1MoVW Steels Irradiated in HFIR—R. L. Klueh and D. J. Alexander (Oak Ridge National Laboratory) 155

Impact specimens of 9Cr-1MoVNb and 12Cr-1MoVW steals were irradiated in the *High Flux Isotope Reactor (HFIR) at 300 and 400°C to as high* as *42 dpa. Irradiation caused large increases in* the *ductile-brittle transition temperature (DBTT) of* both *steels,* with *the increase being greater at 400°C than at 300°C. At 400°C, shifts in DBTT of 204* and *242°C were observed for the 9Cr-1MoVNb and 12Cr-1MoVW Steals, respectively. These* are the *largest shifts* ever *observed for these* steels and are *attributed to the higher helium concentration generated during irradiation in HFIR.*

6.1.4 The Fracture Toughness Data Base for HT9 and Modified 9Cr-1Mo Irradiated in Several Reactors up to ~100 dpa—F. H. Huang (Westinghouse Hanfwd Company). and M. L. Hamilton (Pacific Northwest Laboratory) 161

A summary is presented of the entire fracture toughness database for HT9 and 9Cr-1Mo generated at Hanford. Fracture toughness tests were recently performed on miniature specimens of HT9 and modified 9Cr-1Mo irradiated in FFTF to exposures ranging from 35 to about 100 dpa. At test temperatures ranging from 20 to 430°C, values of toughness and tearing modulus at 35 to 100 dpa were no lower than those obtained

previously in tests conducted on specimens irradiated in EBR-II, despite differences in orientation between the EBR-II and FFTF specimens.

6.1.5 Effect of Specimen Size on the Upper Shelf Energy of Ferritic Steels—A. S. Kumar (University of Missouri-Rolla) and F. A. Garner and M. L. Hamilton (Pacific Northwest Laboratory) 177

A previous effort led to the development of size effect correlations for the ductile-brittle transition temperature (DBTT) and upper shelf energy (USE) of ferritic steels. An improved methodology is proposed that can be used to better predict the USE based on subsize specimen data. The proposed methodology utilizes the partitioning of the USE to energies required for crack initiation and crack propagation. Notched-only Charpy specimens are used in conjunction with precracked specimens to separate the two components. An unirradiated ferritic steel, HT-9, was used to demonstrate the validity of the methodology. Unlike previous correlations that were limited in their applicability to either highly ductile or brittle material, the proposed methodology is expected to be applicable over a wide range of ductility and to be particularly useful for materials which harden significantly during irradiation.

6.1.6 Processing of Two Iron-Chromium Oxide Dispersion Strengthened Steels by Mechanical Alloying—A. N. Niemi, M. G. McKimpson (Michigan Technology Institute). and D. S. Gelles (Pacific Northwest Laboratory) 187

Two low-activation ferritic ODS alloys haw been manufactured, using mechanical alloying procedures, into extruded bar. The alloy compositions in weight percent are: Fe-14Cr-1.0Ti-0.5W-0.25Y_2O_3 and Fe-9Cr-2.0W-0.3V-0.08C-0.25Y_2O_3. Dispersoid phase instability is indicated in the Fe-9Cr carbon-containing alloy, but the 14Cr alloy appears to offer a novel material which m y be suitable for first wall applications and warrants further study.

6.1.7 Microstructural Examination of HT-9 Irradiated in the FFTF/MOTA to 110 dpa—D. S. Gelles (Pacific Northwest Laboratory) and Akira Kohyama (University of Tokyo) 193

HT-9 in two heat treatment conditions has been examined following irradiation at 420°C to 114 dpa. The irradiations were performed in the Fast Flux Test Facility Materials Open Test Assembly (FFTF/MOTA). Void swelling is found in both conditions, with swelling values as high as 0.9% in isolated regions. Voids show a wide range of truncation between cubic and octahedral shapes. Void swelling appears to vary as a function of preirradiation heat treatment, whereas the dislocation structure and precipitation thet developed during irradiation is unaffected. Quantitative microstructural measurements are in good agreement with results on similar simple alloys.

6.1.8 Irradiation Creep of Ferritic (and other BCC) Alloys—R. J. Puigh (Westinghouse Hanford Company) and D. S. Gelles (Pacific Northwest Laboratory) 201

Ferritic/martensitic alloys are now being used as structural materials in several reactor systems and are being considered as structural materials for future fusion reactors. The irradiation creep response of body centered cubic (BCC) alloys has been studied for over 20 years; however, only in the last 10 years has the effort narrowed to concentrate on the irradiation creep behavior of ferritic/martensitic alloys. This paper reviews our current understanding of irradiation creep behavior in ferritic alloys by reviewing the literature and reporting new data on the topic.

6.2 Austenitic Stainless Steels 226

6.2.1 The Development of Austenitic Stainless Steels for Fast Induced-Radioactivity Decay—R. L. Klueh and P. J. Maziasz (Oak Riie National Laboratory) 227

A program is under way to develop a nickel-free austenitic stainless steel for fusion-reactor applications. Previous work has shown thet an austenite-stable alloy should be possible with a base composition of Fe-20Mn-12Cr-0.25C. Tensile properties for this base composition were comparable to those of type 316 stainless steel. To improve strength and irradiation resistance, closely controlled quantities of W, Ti, V, C, B, and P were added to this base. Such additions resulted in improved tensile properties over those for type 318 stainless steel in both the solution-annealed and 20% cold-worked conditions.

6.2.2 Development of Tensile Property Relations for ITER Data Base—M. L. Grossbeck (Oak Ridge National Laboratory) 243

Tensile data from the Oak Ridge Matrix (Fusion Implementing Agreement Annex II), the U.S. Japan collaboration, and the available literature were reviewed. Type 316 stainless steel, in both cold-worked and annealed

conditions and PCA (both U.S. and Japanese heats) were included. Equations were developed for yield strength, uniform elongation, and total elongation. In many cases, one expression could be used for alloys and conditions; in others, separate equations had to be used. In all cases an attempt was made to provide a conservative expression rather than to have the best fit to the data. Especially in the case of strength, the value was rather insensitive to alloy composition.

6.2.3 Tensile Properties of Austenitic Stainless Steels Irradiated in the ORR Spectral Tailoring Experiment ORR-MFE-6J and -7J—M. L. Grossbeck (Oak Ridge National Laboratory). T. Sawai. S. Jitsukawa (Japan Atomic Energy Research Institute, assigned to ORNL), and L. T. Gibson (Oak Ridge National Laboratory) 259

Tensile properties were found to be consistent with those of previous irradiations in mixed-spectrum reactors. The yield strength at 60°C was found to be less than that at 330°C, but this can be understood in terms of hardening by dislocation loops. The properties of welds were found to resemble those of annealed base metal whether or not the weld was made in annealed or cold-worked material.

6.2.4 Development of Low Activation Fe-Mn and Fe-Mn-Cr Alloys for Fusion Service—L. D. Thompson (San Diego State University) and T. Lechtenberg (General Atomics) 269

Recent attention in the fusion materials research community has been focused on attempting to define compositional requirements for low-activation stainless steel alloys for first wall and blanket structures of future fusion reactors. Alloy design efforts have been initiated by the NIM, as well as in other fusion materials programs, to develop materials and microstructures inherently resistant to neutron damage. More recently, to address the concern about expected post-service neutron activation characteristics, the baseline programs focused primarily on developing neutron damage resistant materials have expanded to include the investigation and development of low-activation structural steels containing manganese (Refs. 1-5). Iron alloys containing 25-50% Mn and ternary alloys containing 10-20% Mn with 5-20% Cr are included in the alloy classes being studied.

The former U.S. Energy Research and Development Administration (ERDA), and now the Department of Energy (DOE), was interested in developing alternative austenitic stainless steels which would rely less on strategic and expensive alloying elements for their properties. They sponsored a substantial alloy design effort during the 1970s directed at investigating the properties of Fe-Mn and Fe-Mn-Cr alloy compositions for cryogenic applications (such as liquid natural gas containment structures) which were similar to those of interest in the fusion materials program. While the database for the Fe-Mn and Fe-Mn-Cr systems is limited, the data obtained in these earlier studies are useful in understanding the alloy design capabilities of this system and for providing guidance to the current program. Many of the compositions previously investigated complement those in the NIM program and the data we will report will help establish trends in behavior. Mechanical properties and microstructural characterization data and their correlations are presented for those alloy systems of general interest to the present NIM program and ITER alloy development efforts.

6.2.5 Effects of Low-Temperature Neutron Irradiation on the Properties of 300 Series Stainless Steels—G. R. Odette and G. E. Lucas (University of California. Santa Barbara) 313

Neutron irradiation of austenitic stainless steels can result in significant property changes. Property degradation appears to be greatest for irradiation temperatures (and comparable mi temperatures) near 300°C. Here, hardening and loss of ductility may reduce fracture toughness values to as low as 45 MPa$\sqrt{m}$ by exposure levels of 6 dpa. These data suggest an experimental test program designed to evaluate critical microstructural and mechanical property changes in austenitic stainless steels at low irradiation temperatures.

6.3 Vanadium Alloys 337

6.3.1 Swelling of Neutron-Irradiated Vanadium Alloys— B. A. Loomis and D. L. Smith (Argonne National Laboratory) and F. A. Garner (Pacific Northwest Laboratory) 339

The swelling of V-10.0Cr-0.1Al, V-14.1Cr-0.3Al, V-3.1Ti-0.3Si, V-4.9Ti, V-9.8Ti, V-14.4Ti, V-17.7Ti, V-20.0Ti, V-14.4Cr-0.3Ti-0.3Al, V-14.1Cr-1.0Ti-0.3Al, V-13.7Cr-4.8Ti, V-9.0Cr-3.3Fe-1.2Zr (Vanstar-7), V-14.5Ti-7.2Cr, V-8.6W, V-4.0Mo, and V-12.3Ni alloys and unalloyed V was determined after neutron irradiation at 420°C and 600°C to irradiation damage levels ranging from 17 to 77 dpa in the FFTF-MOTA reactor facility. The swelling of these alloys was obtained from a determination of the density for the unirradiated and irradiated alloys on immersion in CCl_4. The swelling of unalloyed V at 600°C was substantially increased by the addition of Cr. The addition of either Ni, W, or Mo to V had a relatively minor effect on the swelling of V. The

swelling of the V-Cr-Ti alloys was strongly dependent on the Ti concentration. The swelling of the V-3.1Ti-0.3Si and V-14.4Ti alloys at 600°C was greater than that exhibited by the other binary V-Ti alloys. The Vanstar-7 alloy underwent larger swelling than the V-Ti and V-Cr-Ti alloys. For the binary V-Ti alloys and the ternary V-Cr-Ti alloys, the dependence of swelling on the amount of irradiation damage was <0.1% swelling per dpa.

6.3.2 Literature Review of Research on Vanadium and Vanadium Base Alloys for Use in Fusion Reactor First Wall/Blanket Applications—C. A. Marsh and A. B. Hull (Argonne National Laboratory) 347

The literature was reviewed for research on the fabrication of vanadium base alloys and the effects of chemical environment, helium implantation, and neutron irradiation on the mechanical properties, microstructure, and corrosion behavior of vanadium and vanadium boas alloys. The relevant material was compiled into an annotated bibliography of more than 100 representative references. These references address the topics highlighted in this report.

6.4 Copper Alloys 349

6.4.1 Overview of Copper Irradiation Programs—F. A. Garner, M. L. Hamilton (Pacific Northwest Laboratory), K. R. Anderson, J. F. Stubbins (University of Illinois). B. N. Singh. A. Horsewell (RISO National Laboratory), and W. F. Sommer (Los Alamos National Laboratory) 351

Researchers (Pacific Northwest Laboratory) are collaborating with scientists from RISO National Laboratory, Los Alamos National Laboratory, and the University of Illinois to generate data on the response to radiation of copper alloys intended for use in ITER, NET. and long-term fusion devices. An overview of these experiments is presented.

6.4.2 Electrical Resistivity Changes Induced in Copper Alloys by Fast Neutron Irradiation—K. R. Anderson (NORCUS Program, University of Illinois), F. A. Garner, M. L. Hamilton (Pacific Northwest Laboratory), and J. F. Stubbins (University of Illinois) 357

Thirteen copper-base alloys were irradiated in FFTF/MOTA to determine the response of various alloy classes to neutron irradiation. This effort is directed towards the selection of copper alloys to serve as high heat flux components in both near-term and long-term fusion devices. Post-irradiation measurements s h o d that a wide variety of responses was observed in the neutron-induced changes in electrical resistivity. Tensile tests are in progress, and microscopy examination will be initiated soon.

6.5 Environmental Effects on Structural Alloys 371

6.5.1 Design of an Electrochemical Testing System to Evaluate Sensitization of Austenitic Stainless Steels Using Miniaturized Specimens—T. Inazumi [Japan Atomic Energy Research Institute (JAERI). assigned to ORNL] and G.E.C. Bell (Oak Ridge Associated Universities) 373

An electrochemical testing system was developed to evaluate the sensitization of austenitic stainless steels using miniaturized disk-type specimens, 3 mm diam by 0.26 mm thick. The specimens are also suitable for examination using transmission electron microscopy (TEM) after electrochemical testing. The apparatus consists of a specimen holder in which a miniaturized specimen is mounted as the working electrode, a test cell designed to handle radioactive materials and waste, and a potentiostat/galvanostat. Sensitization of thermally aged austenitic stainless steal specimens was successfully detected by the single-loop electrochemical potentiokinetic reactivation (SL-EPR) method.

6.5.2 Aqueous Stress Corrosion of Austenitic Steels—H. Khalak, A. B. Hull, and T. F. Kassner (Argonne National Laboratory) 379

Stress corrosion cracking (SCC) of austenitic stainless steal in water is considered a key unresolved issue for the U.S. ITER shield and blanket design activities. A computer code has been developed to determine the concentration of radiolytic species produced in the aqueous environment in various subsystems of a fusion reactor in order to estimate the subsequent likelihood of stress corrosion cracking. This code also serves as a valuable precursor to slow-strain-rate tests to determine the SCC susceptibility of austenitic stainless steels. The code is being benchmarked with the concentrations of radiolytic molecular species in boiling water reactors. Samples of candidate steels, primarily Type 316 NGSS, are being prepared to initiate low-strain-rate tests.

6.5.3 Corrosion and Compatibility Studies in Flowing Lithium Environments—A. E. Hull and O. K. Chopra (Argonne National Laboratory) 385

The Argonne Lithium Corrosion Experiment (ALICE), a high-flow-velocity ferritic steel forced circulation mi facility, is now fully operational and is being used io address the effects of fluid flow velocity and nonmetallic elements on corrosion, mass transfer, and deposition in liquid metal systems. Hydrogen distribution data were obtained from the austenitic steel Fatigue and Failure Testing in Lithium (FFTL-3) facility in which the b w circulation velocity provided only for impurity control of the liquid metal; analysis of these data indicates that hydrogen fractionates between lithium and vanadium alloys in accordance with the thermodynamic distribution coefficients.

6.5.4 Assessment of Stress-Corrosion Cracking in a Water-Cooled ITER—R. H. Jones and S. M. Bruemmer (Pacific Northwest Laboratory) 389

Water-cooled, near-term reactors will operate under conditions ai which SCC is possible; however, control of material purity and processing and coolant chemistry can either eliminate a- greatly reduce the probability of this type of structural failure. This evaluation has focused on an assessment of water impurity effects on SCC of austenitic stainless steel ai temperatures below 100°C and on the conditions controlling sensitization in the fusion heat of Tvpe 316 SS and the fusion materials heat of modified Tvpe 316 SS designated as PCA. This assessment identifies the dominant effect of small concentrations of impurities in high-purity water on SCC such that crack growth ram ai 25-75°C in water with as little as 6-16 ppm Cl^- are equal to the crack growth rates at 200-300°C in high-purity water. These effects are primarily for sensitized Tvpe 304 SS, so analysis of sensitization behavior of fusion austenitic alloys was also undertaken. An SSDOS model developed ai PNL was used io make these assessments, and correlation to experimental results for Tvpe 316 SS was very good. Both the fusion heat of Tvpe 316 SS and PCA can be severely sensitized, but with proper thermal treatment, it should be possible io avoid sensitization.

7. SOLID BREEDING MATERIALS 397

7.1 A Fast Neutron, In Situ Tritium Recovery Experiment on Soli Breeder Materials—G. W. Hollenberg (Pacific Northwest Laboratory). T. Kurasawa and H. Watanabe (Japan Atomic Energy Research Institute) S. E. Berk (U.S. DOE/OFE), Institute), I. J. Hastings and J. Miller (Atomic Energy of Canada Research Company), D. E. Baker. R. E. Eauer. and R. J. Puigh (Westinghouse Hanford Company) 399

An in situ tritium recovery experiment has bean designed and is being fabricated for the irradiation of Li_2O in the Fast Flux Test Facility (FFTF). Two in situ tritium recovery canisters will be irradiated wirh lithium atom burnups to 4%. One canism will provide fundamental data on tritium release as a function of temperature, gas composition, and flow rate. The other canister will contain solid pellet specimens with large (430°C) radial temperature gradients in order to provide integrated performance data.

7.2 Interfacial Roughness and the Thermal Conductivity of a Sphere-Pac Bed—S. W. Tam and C. E. Johnson (Argonne National Laboratory) 407

Various configurations for the solid breeder (e.g., Li_2O) plus neutron multiplier (i.e., Be) component has ban considered for blanket application in fusion reactor technology. One possible option is the sphere-pac configuration. This consists of the solid component in the form of small particles (ideally as spheres) put together in a bed in a close-packed manner. In order io achieve high packing density, particles of several different sizes need to be used. The interstitial spaces between particles of a given size are packed with particles of the next smaller size and so on in a heirachical manner. The packing process can be achieved by vibratory compaction. Much experience has ban gained on this configuration in fission reactor related technology. In particular extensive data has been gathered via fission-related research m well as from high thermal insulation technology work on the thermal conductivities K_{sp} of such systems. The heat conduction properties of systems possess unusual characteristics dun to the convoluted interweaving bicontinuous nature of the solid component and the porosity phase. For example, when sphere-pac beds are immersed in a gas (e.g., He, Ar), the thermal conductivities K_{sp} are found to be dependnet on the gas pressure P. Typically, K_{sp} increases rapidly by 50-100%, when P is raised by as little as a MPa and then changes much more slowly thereafter (see Fig. 1 and discussion in the following section). It m y bs thought that such subtle behavior m y be exploited io the advantage of blanket technology if a sphere pac configuration is utilized in the breeder-plus-multiplier component. However, straightforward extrapolation from fission and thermal and insulation technological experience to a fusion blanket environment should be treated with care since quite different materials characteristics are involved. It turns out that a careful analysis of the physics of the situation reveals that a gas pressure-

sensitive thermal conductivity is a much less prominent effect than would have been suggested from other technology experiences alone. In order to understand this, one needs to first appreciate the reasons why such pressure effects are so dramatic in fission and thermal insulation materials.

7.3 Tritium Transport Modeling—J. P. Kopasz and C. E. Johnson (Argonne National Laboratory) 411

The modeling effort for this period was focused on the desorption process. The desorption process consists of a surface reaction and desorption of surface-bound tritium in the form of HTO, T_2O, HT, or T_2. Of concern are the order of the surface reaction and the energetics of the surface reaction and desorption step. In most of our previous work, desorption of tritium was considered to be first order in tritium due to the expected excess of hydrogen in the system. Equations for desorption which are second order in tritium were derived for situations where the hydrogen concentration on the breeder surface would be low and comparable to the expected tritium concentration. Expressions for tritium inventory were derived and calculations were performed to determine the grain radius regimes where desorption would be expected to be the rem controlling release process. In our previous work we have found evidence that the desorption energetics change as a function of surface coverage. We believe that this is due to the presence of multiple sites for desorption of tritium from the ceramic. To support this view we haw analyzed constant-rem heating tritium release experiments from the literature to determine the number or desorption sites and to obtain estimates or the desorption activation energies. Estimates of activation energies for desorption or tritium from Y O and Li_4SiO_4 were obtained.

7.4 Adsorption, Dissolution, and Desorption Characteristics of the $LiAlO_2$-$H_2O(g)$ System—Albert K. Fischer and Carl E. Johnson (Argonne National Laboratory) 419

Adsorption of $H_2O(g)$, dissolution of OH^-, and rates of evolution of $H_2O(g)$ ara being measured for the $LiAlO_2$-$H_2O(g)$ system. These thermodynamic and kinetic data for these processes relate to the issues of tritium retention and release, and, hence, to concerns about tritium inventory in ceramic tritium breeder materials. The information will enable (1) comparison of candidate breeder materials. (2) calculation of operating conditions, and (3) elucidation of the principles underlying the behavior of tritium in breeder materials.

8. CERAMICS 423

1. IRRADIATION FACILITIES, TEST MATRICES, AND EXPERIMENTAL METHODS

DESIGN AND FABRICATION OF HFIR-MFE RB* SPECTRALLY TAILORED IRRADIATION CAPSULES — A. W. Longest (Oak Ridge National Laboratory), J. E. Corum (Midwest Technical, Inc.), and O. W. Heatherly (Oak Ridge National Laboratory)

OBJECTIVE

The objective of this work is to design and fabricate irradiation capsules for testing magnetic fusion energy (MFE) first-wall materials in the High Flux Isotope Reactor (HFIR) removable beryllium (RB*) positions. Japanese and U.S. MFE specimens are being transferred to RB* positions following irradiation to 7.5 dpa at temperatures of 60, 200, 330, and 400°C in Oak Ridge Research Reactor (ORR) experiments ORR-MFE-6J and -7J.

SUMMARY

Oesign and fabrication of four HFIR-MFE RB* capsules (60, 200, 330, and 400°C) to accommodate MFE specimens preirradiated in spectrally tailored experiments in the ORR (and associated facility preparations) are proceeding satisfactorily. These capsule designs incorporate provisions for removal, examination, and re-encapsulation of the MFE specimens at intermediate exposure levels en route to a target exposure level of 24 (formerly 30) displacements per atom (dpa). With the exception of the 60°C capsule, where the test specimens will be in direct contact with the reactor cooling water, the specimen temperatures (monitored by 21 thermocouples) will be controlled by varying the thermal conductance of a small gap region between the specimen holder and the containment tube. Hafnium liners will be used to tailor-the neutron spectrum to closely match the helium production-to-atom displacement ratio (14 appm/dpa) expected in a fusion reactor first wall.

Assembly of the 60 and 330°C capsules is complete and irradiation of both will begin when the HFIR returns to full power operation. Design of the remaining two (200 and 400°C) capsules is complete and issue of fabrication drawings is near. Fabrication of parts and assembly of the 200 and 400°C capsules is scheduled for completion by the end of FY 1990; operation of these two capsules will follow the first two (60 and 330°C).

PROGRESS AND STATUS

Introduction

A series of spectrally tailored irradiation capsules are being designed and fabricated as part of the U.S./Japan collaborative program for testing MFE first-wall materials in mixed-spectrum fission reactors. The test specimens will be irradiated in the new RB* facility' of the HFIR.

The first four HFIR-MFE RB* capsules are designed to accommodate Japanese and U.S. MFE specimens preirradiated to 7.5 dpa at temperatures of 60, 200, 330, and 400°C in the ORR in spectrally tailored experiments ORR-MFE-6J and -7J. Details of these ORR experiments, including descriptions of the test matrix, mechanical property specimens, and techniques of spectral tailoring, have been reported elsewhere.[2,3]

Spectral tailoring of the neutron flux to simulate in austenitic stainless steels the expected helium production-to-atom displacement ratio of 14 appm/dpa in the fusion reactor first wall is accomplished by varying the amount of neutron moderator and thermal neutron absorber materials surrounding the capsule. This controls the two-step ^{58}Ni thermal neutron reaction producing helium, while fast neutrons are simultaneously producing atomic displacements. In general, the neutron energy spectrum must be hardened as the irradiation progresses; this requires ongoing neutronics analysis support as provided for the ORR experiments.[4]

The HFIR-MFE RB* capsules are designed for insertion into any of the eight large-diameter holes (46 mm) of the HFIR RB* facility. Damage rates will increase from about 4 dpa/year in the ORR experiments to 7.4 dpa/year in the HFIR RB* facility (based on 85 MW HFIR power).

Test specimen nominal loadings for the first four capsules are given in Table 1. Beginning with return of the HFIR to full power in FY 1989, these capsules will be irradiated in pairs (first the 60 and 330°C capsules, then the 200 and 400°C capsules) to a damage level of 16 dpa. After these four irradiations, the test specimens will be removed, examined, and approximately one-half of them re-encapsulated for irradiation to 24 dpa. Target exposure levels were formerly 20 and 30 dpa; however, because of the unexpected length of the HFIR shutdown, it was decided to decrease the exposure levels to stay close to the original schedule for these experiments.

Table 1. Test specimen nominal loadings for the HFIR-MFE RB* capsules

Specimen Type	Number of specimens in capsule			
	60°C	200°C	330°C	400°C
Pressurized tube	39	26	45	39
Tube blank	9	9	9	9
Transmission electron microscopy tube				
Length (mm)				
16.5	2	2	0	0
19.1	0	0	4	4
25.4	5	7	6	6
SS-I tensile	90	83	16	64
SS-3 tensile	54	54	15	15
Grodzinski fatigue	56	24	56	40
Crack growth	30	30	10	10
Rod tensile	0	0	4	0
Hourglass fatigue	0	0	0	4

60°C Capsule — The 60°C capsule, designated HFIR-MFE-60J-1, is an uninstrumented capsule with the test specimens in contact with the reactor coolant water. Predicted specimen temperatures are within ±10°C of 60°C.

Assembly of the 60°C capsule and details of the specimen loading were described previously.[5] This capsule is in dry storage at the HFIR where it will remain until the reactor returns to full power.

330°C Capsule — The 330°C capsule, designated HFIR-MFE-330J-1. is an instrumented and singly contained capsule where the specimen temperatures will be monitored by 21 thermocouples and controlled by adjusting the thermal conductance of a small gas gap region between the specimen holder outer sleeve and the containment tube. This capsule will be cooled with 49°C reactor coolant water flowing downward over the containment tube surface. Calculated temperature distributions indicate that specimen temperatures will be within ±25°C of 330°C, which satisfies the temperature criterion for these experiments. The 330°C capsule design was described in detail previously.[6]

Assembly of the 330°C capsule and details *of* the specimen loading were described in the preceding progress report.' This capsule is in the HFIR pool where it will remain until the reactor returns to full power.

200 and 400°C Capsules — The 200 and 400°C capsule designs are basically the same as that of the 330°C capsule described previously." The main differences in the three capsule designs are associated with (1) the number and spacing of the specimen holder slots and holes to accommodate the different specimen loadings, (2) the width of the temperature control gas gap region between the specimen holder outer sleeve and containment tube to obtain the desired specimen temperatures, and (3) the test piece included in the aluminum plug and holder above the test specimen holder to obtain extra information.

Vertical sections through the 200 and 400°C capsules, designated HFIR-MFE-200J-1 and HFIR-MFE-400J-1, are shown in Figs. 1 and 2, respectively. In addition to accommodating the planned test specimen loadings, a simulated packet of transmission electron microscopy (TEM) specimens in the 200°C capsule and a simulated hourglass fatigue specimen in the 400°C capsule are located in the aluminum plug and holder above the test specimen holder and instrumented with three thermocouples to obtain temperature rise data for these respective specimen-specimen holder configurations.

Issue of fabrication drawings for both capsules is near. Fabrication of parts and assembly of the capsules are scheduled for completion by the end of FY 1990. Operation of these two capsules will follow the first two (60 and 330°C).

HFIR-MFE RB* FACILITIES (MIF-3 AND MIF-4)

Facility preparations required for operation of the HFIR-MFE RB* capsules are in various stages of completion. Preparations completed include issue of instrument application and wiring diagrams for Materials Irradiation Facility No. 3 (MIF-3) and MIF-4, which are to be used for the HFIR-MFE RB* capsules; installation of remaining MIF-3 and MIF-4 components; assembly of the in-pool flexible hose section for connection of the instrumented 300°C capsule to MIF-3; preparation of detailed installation and operating procedures; and preparation of an experiment information and safety analysis document for the 60 and 330°C capsules, which was submitted with a request for approval to operate these capsules in the HFIR. Preparations in progress include installation of a storage rack for HFIR RB* capsules at the west end of the HFIR pool and checkout of the MIF-3 and MIF-4 facilities.

FUTURE WORK

Installation of the MIF-3 in-pool flexible hose section, connection of the HFIR-MFE-330-J-I capsules tc the flexible hose assembly, and final preparations for start-up of the 60 and 330°C capsules will be completed during the next report period.

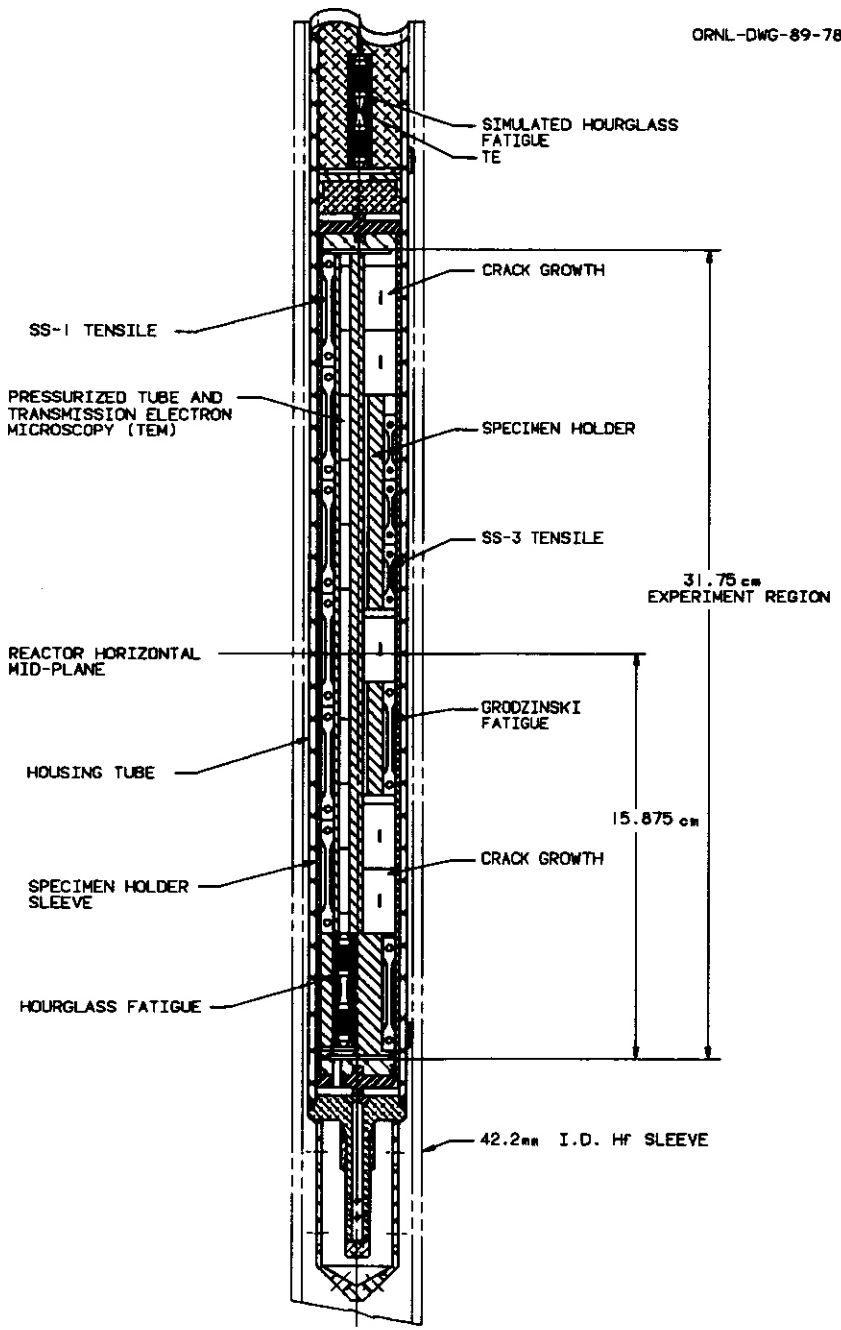

Fig. 1. Vertical section through HFIR-MFE 200J-1 capsule.

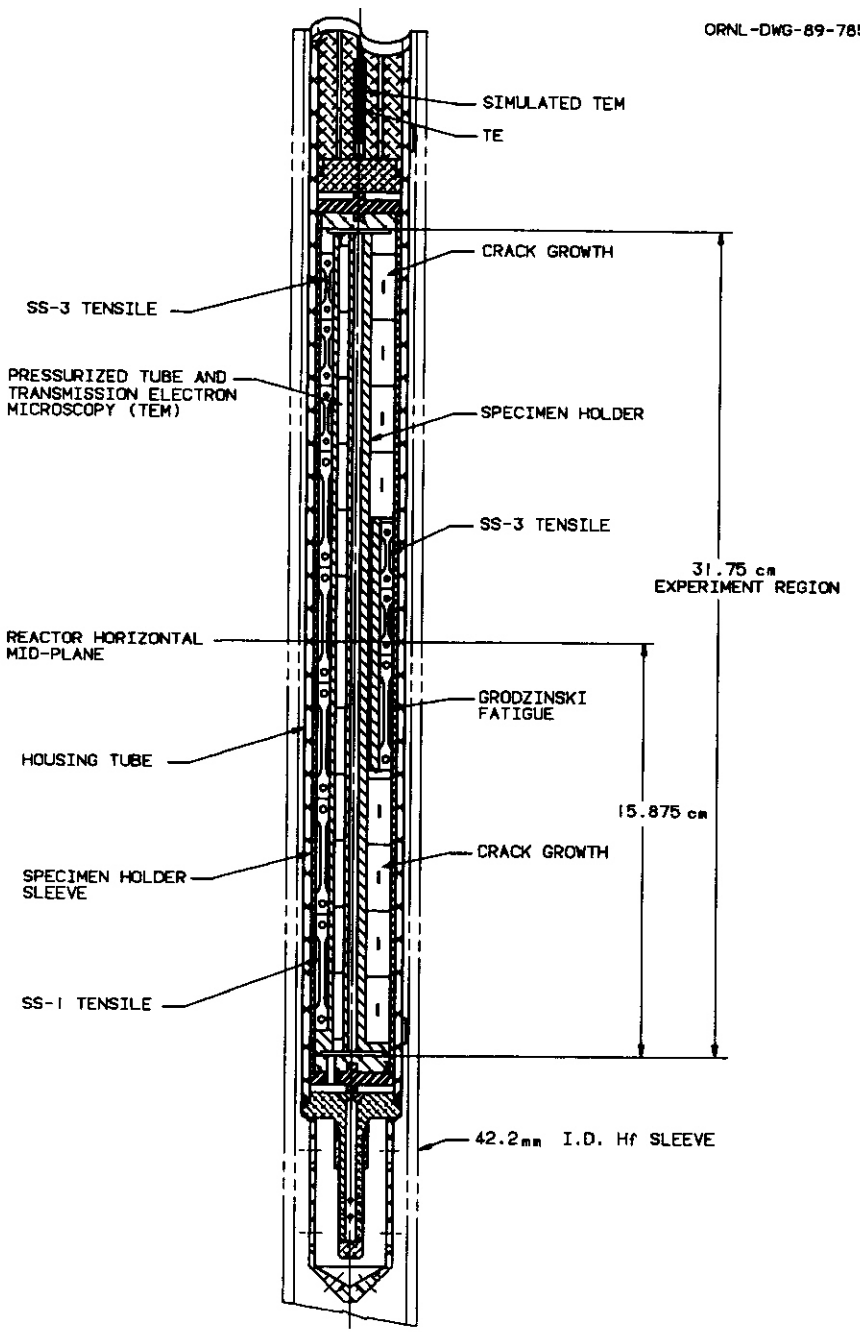

Fig. 2. Vertical section through HFIR MFE 400J-1 capsule.

Fabrication of parts and assembly of the 200 and 400°C capsules will continue into FY 1990. Capsule design and preparation of fabrication drawings for re-encapsulation of the MFE specimens after 16 dpa are scheduled to be completed in FY 1990.

REFERENCES

1. K. R. Thoms et al., "HFIR Irradiation Facilities Improvements – Completion of the HIFI Project," J. Nucl. Mater. 155-157 (1988) 1340–45.

2. J. L. Scott et al., pp. 12–20 in ADIP Semiann. Prog. Rep., March 31, 1985, DOE/ER-0045/14, U.S. DOE, Office of Fusion Energy.

3. J. L. Scott et al., Second Annual Prog. Rep. on United States-Japan Collaborative Testing in the High Flux Isotope Reactor and the Oak Ridge Research Reactor, Sept. 30, 1985, ORNL/TM-10102.

4. R. A. Lillie, pp. 36–38 in Fusion Reactor Materials Semiann. Prog. Rep., Sept. 30, 1986, DOE/ER-0313/1, U.S. DOE, Office of Fusion Energy.

5. A. W. Longest et al., "Design and Fabrication of HFIR-MFE RB* Spectrally Tailored Irradiation Capsules," in Fusion Reactor Materials Semiann. Prog. Rep., March 31, 1988, DOE/ER-0313/4, U.S. DOE, Office of Fusion Energy.

6. A. W. Longest et al., "Design and Fabrication of HFIR-MFE RB* Spectrally Tailored Irradiation Capsules," in Fusion Reactor Materials Semiann. Prog. Rep., Sept. 30, 1987, DOE/ER-0313/3, U.S. DOE, Office of Fusion Energy.

7. A. W. Longest et al., "Design and Fabrication of HFIR-MFE RB* Spectrally Tailored Irradiation Capsules," in Fusion Reactor Materials Semiann. Prog. Rep., Sept. 30, 1988, DOE/ER-0313/5, U.S. DOE, Office of Fusion Energy.

IMAGE CALCULATION OF TILTED CONTAMINATION DEPOSIT FOR THE THICKNESS MEASUREMENT OF TEM SPECIMEN FOIL – T. Sawai [Japan Atomic Energy Research Institute (JAERI), assigned to ORNL] and M. Suzuki, JAERI

OBJECTIVE

The objective of this work is to re-evaluate the methods used to determine foil thicknesses using transmission electron microscopy.

SUMMARY

A new imaging model has been proposed to explain some features of the image formed by tilted contamination cones which is used to determine the specimen thickness in a transmission electron microscope (TEM). The calculation assumes the lines with clear contrast in the image appear where the surface of tilted contamination deposits is parallel to the imaging electron beam. The calculated result explains some features of the actual image rather well. Also, the calculation shows the image shift, which leads to an overestimation of the parallax between two contamination cones, which leads to the overestimation of the foil thickness.

PROGRESS AND STATUS

Introduction

The accurate measurement of specimen thickness is of great concern in two areas of quantitative electron microscopy: (1) determination of the concentration of defects and precipitates from micrographs, and (2) chemical analysis using characteristic X rays where the spatial resolution of analysis and appropriate X-ray absorption and fluorescence corrections reflect specimen thickness.

The ability of analytical electron microscopy to focus its electron beam on the specimen has also provided one method to measure the specimen thickness. The irradiation of the specimen by a highly focused beam results in a pair of contamination deposits both on the top and bottom surfaces of the specimen, whose parallax after tilting the specimen can be used to calculate the specimen thickness.[1,2] This is called the contamination spot separation (CSS) method. This method has been favored especially for specimens that have been highly irradiated in a nuclear reactor3 since no thickness fringes appear due to the high density of radiation-introduced defects. However, the accuracy of this method was examined[4-6] and an appreciable error (overestimation) has been reported. Rae et al.[5] have proposed a "witch's hat" model to explain the observed overestimation. This model assumes that both of the contamination spots deposited on the upper and lower surfaces of the specimen, have spread bases under sharp cones (Fig. 1). Lorimer[7] explained this spread base by the spreading of the' electron beam due to the condenser aberration in early analytical electron microscopes.

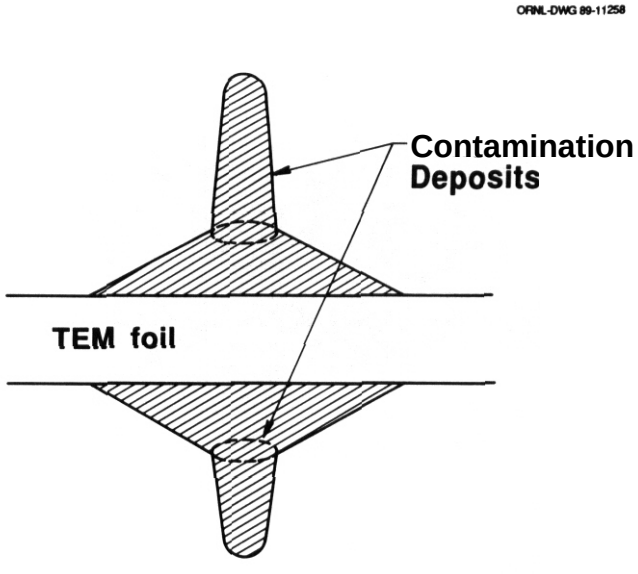

Fig. 1. Schematic diagram of "witch's hat" model of contamination proposed by Rae et al.[5] which assumes spread bases under sharp cones.

An example of a TEM image of contamination deposits formed with the specimen perpendicular to the beam and then tilted is shown in Fig. 2(a). The image has two marked lines of high contrast each for the upper and lower deposits. They are the line representing the shape of the deposited contamination (hereafter, outer line) and the line appearing inside of it (hereafter, inner line). Figure 2(b) is a schematic diagram of the image to aid in explanation. The inner line [P′,S′,Q′ in Fig. 2(b)] has been considered to be formed by the intersection of the sharp cone with the specimen surface or with a plane parallel to the surface, even in the "witch's hat" model. But one question still remains to be answered – why this oval disappears imnediately upon touching the outer line.

To explain both the above features of the image made by tilted contamination deposits, a new imaging model is presented, as shown in Fig. 3. This model assumes a tailing profile for the

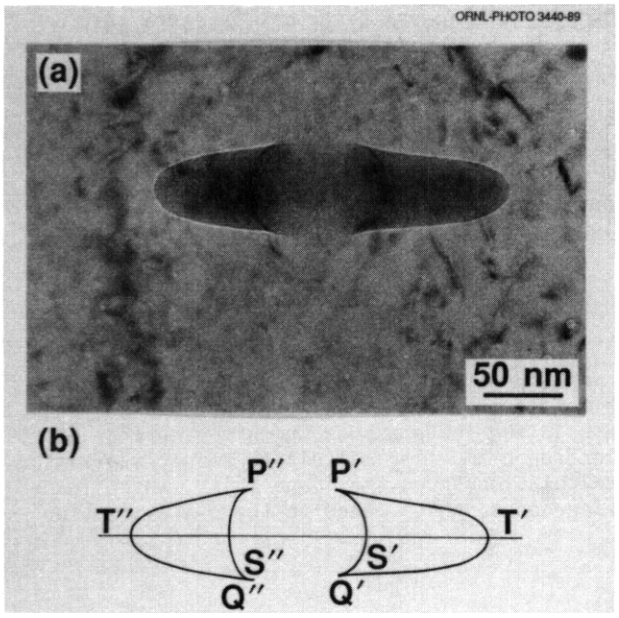

Fig. 2. (a) Typical electron micrograph of tilted contamination deposit and (b) schematic drawing of this image for explanation (see text).

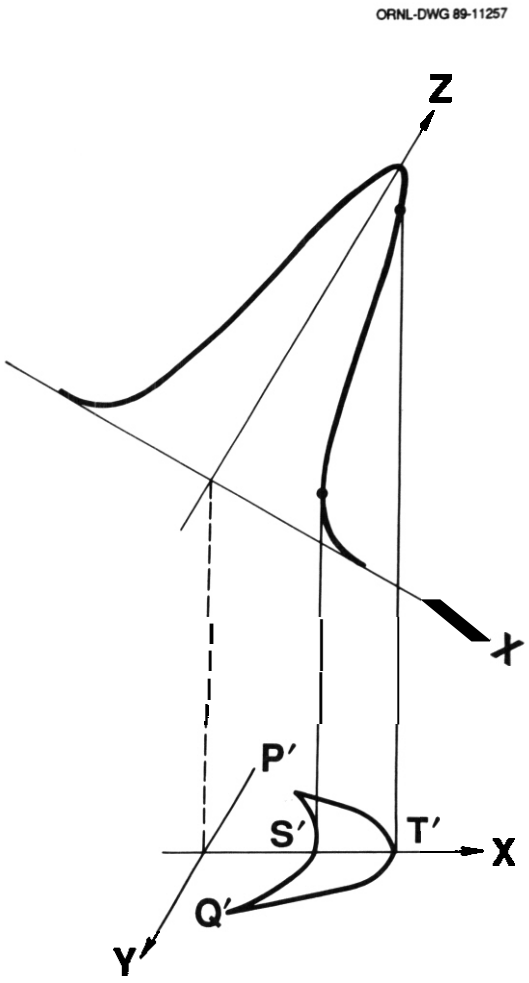

Fig. 3. Schematic diagram of presented imaging model. Lines appearing in the image are made by the contamination surface where the imaging electron beam is parallel to the contamination surface.

contamination deposit instead of a sharp cone. It is also assumed that the line, which was considered to be due to the edge of the deposit in the old model, is made by the surface of the contamination deposit at the point of tangency with the imaging electron beam. The subject of this paper is to describe this new imaging model and to examine the feasibility of this model by comparing the calculated result and the actual image.

Theoretical Model

The profile of the contamination deposit, which appears as a bump on the specimen surface, was approximated by a Gaussian surface of revolution:

$$z(x,y) = a \exp\{-b\,(x^2 + y^2)\}\ , \tag{1}$$

where a and b are constants. For simplicity of numerical analysis, the y-axis is taken as the tilting axis. On the plane $y = y_0$ which is perpendicular to the y-axis, the cross section of the deposited contamination is also Gaussian and is described as follows:

$$z = a \exp\{-b\,(x^2 + y_0^2)\}\ . \tag{2}$$

The point (x_0, y_0, z_0) on this line where the surface of the contamination deposit is tangent to the incident beam should satisfy both Eq. (2) and the following:

$$\frac{dz}{dx}(x_0,y_0) = -\cot\theta\ , \tag{3}$$

where θ is the tilting angle of the specimen and also is equal to the deflecting angle of the electron beam measured from the z-axis. Equations (2) and (3) were solved numerically for each given value of y_0 and the locus of points obtained (x_0, y_0, z_0) was projected onto the film plane $(x'\text{-}y')$.

The coordinates of the tips of cusps in the image — points P'and Q' in Fig. 2(b), which are important points in the actual measurement of parallax — can also be obtained by an analytical solution. Usually two tangents are possible to the Gaussian curve for a given value of θ which is sufficiently large. Two tangent points, one on the curve where it is concave downward and the other where it is concave upward, project onto the image plane and form the outer line and the inner line, respectively. The points on the contamination surface which make the tips of cusps in the projected image are the inflection points of the Gaussian curve represented by Eq. (2) where the gradient of the curve is $-\cot\theta$ [i.e., the coordinate of the points should satisfy Eqs. (2) and (3) and following Eq. (4)].

$$\frac{d^2z}{dx^2}(x_0,y_0) = 0 \quad . \tag{4}$$

And the solution is:

$$x_p = \sqrt{1/2\,b} \quad ; \tag{5.1}$$

$$y_p = \pm\sqrt{\frac{1}{b}\left\{\ln\left(\frac{a\sqrt{2b}}{\cot\theta}\right) - \frac{1}{2}\right\}} \quad ; \tag{5.2}$$

$$z_p = z(x_p,y_p) \quad . \tag{5.3}$$

An example of a calculated image is shown in Fig. 4, with the parameters used in the calculation. The height parameter A and tilting angle correspond to the constants a in Eq. (1) and θ in Eq. (3). The width parameter B is used instead of the constant b in Eq. (1) for easier understanding of contamination width, where

$$b = 1/B^2 \quad . \tag{6}$$

The x'-y' plane shown in Fig. 4 is the projection of the x-y plane of the specimen surface on the film plane, and the origin of the coordinate x'-y' (point O') corresponds to the center of the contamination deposit.

A side view of the contamination deposit shown in Fig. 4 is shown in Fig. 5, and the curve where the surface of contamination is tangent to the incident beam is included. This line makes inner and outer lines in the image after projection.

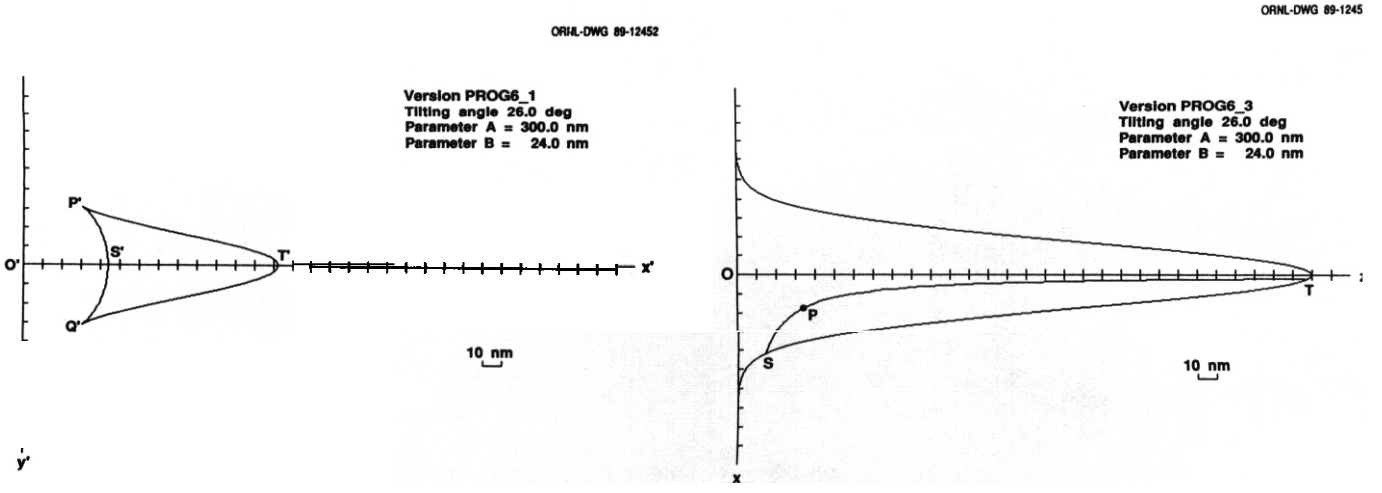

Fig. 4. Calculated contrast lines in the image of a tilted contamination cone (on upper side surface of specimen). Coordinate axes x' and y' are on the film plane and projections of specimen surface coordinate axes x and y.

Fig. 5. Side view of the contamination deposit used in the calculation. This diagram also includes the line which forms high contrast lines in the image, where the surface of the tilted contamination deposit is tangent to the imaging beam. The point marked P is the point which makes a tip of the cusps in the image.

DISCUSSION

It is apparent that the calculated image (Fig. 4) yell-resembles the actual image [Fig. 2(a)]. A portion of the inner oval line appears in Fig. 4 (P′, S′, Q′). Strictly speaking, there is no reason that the curve P′S′Q′ in Fig. 4 should be a portion of a true ellipse, although it is well approximated by the ellipse with a ratio of major and minor axes of cos θ, where θ is the angle of specimen tilt.

The whole image of the contamination deposit appears far off the ideal projected center, O. It is clear that a significant overestimation of parallax and thus foil thickness will occur if the parallax is measured between the tips of cusps in this image. The true parallax should be measured between the projected centers of both contamination deposits, which are hard to locate in the image.

Point P in Fig. 5 is the point on the surface of the contamination deposit which corresponds to the tips of cusps in the projection. This point is located at a rather high position (large value of the z coordinate), still higher than the point S where the gradient of the Guassian curve is $-\cot\theta$. Point P is located off the y-z plane (i.e., its x coordinate is greater than 0). This is the reason that the tips of cusps P′ and Q′ in Fig. 4 appear well off-center after projection.

This imaging model explains the experienced overestimation of the specimen thickness. It assumes a smooth profile of the deposited contamination rather than a two-stepped witch's hat profile, whose sharp step seems to be less likely if beam spreading and the drift of the beam and/or the specimen are considered.

Although the calculation assumes a Gaussian profile of deposit with infinite tailing, the outer line (P′T′Q′ in Fig. 4) in the image, which represents the shape of the contamination, looks as if the contamination deposit stands steeply on the specimen surface with little tailing. This feature is often observed in an actual TEM image. Because of the high position of point P in Fig. 5, the line on the contamination surface which makes the outer line in the projected image exists only on the upper portion of the contamination deposit where the spread of the Gaussian curve is relatively small. This observation is also an important result of this calculation along with the appreciable image shift already mentioned. This misleading feature may have led many microscopists, who have observed this image, to assume that this image can result only from a very steep profile of contamination with little tailing. A steep image does not always mean a steep contamination deposit.

If the curved line P′T′Q′ in Fig. 4 were approximated with an ellipse with the ratio of axes equal to cos θ, although P′T′Q′ is not an arc of a true ellipse, then the assumed ellipse intersects the extension of an outer line, as is also often the case with the actual image. This feature of the image is difficult to explain from the old model that assumes the inner line is formed by the edge of the base of the deposited contamination. In Fig. 6, an actual image is superimposed with an ellipse which is tangent to the outer line at the cusps and has an axes ratio of cos θ. It is clear that a larger ellipse which intersects the outer line or an ellipse with a different axes ratio is necesfary to approximate the actual inner line. In some explanations,[4-6] the tips of the cusps [points P and Q′ in Fig. 2(b)] are implicitly considered to represent the longer axis of the ellipse which is made by the projection of the circular base plane. The assumed ellipses usually had axes ratios different from cos θ; usually more elongated ellipses were assumed. These assumptions have less physical bases than the present assumption of a Gaussian-shaped deposit.

ORNL-PHOTO 4239-89

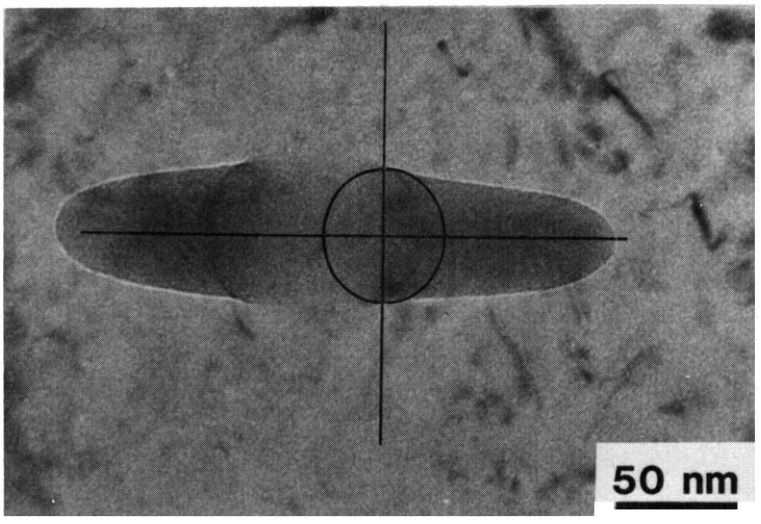

Fig. 6. Typical electron micrograph of tilted contamination deposit superimposed with an ellipse tangent to the outer line at the points where the inner line intersects and also has the axes ratio of cos θ, where θ is the angle of specimen tilt. In this case, θ is 26 deg.

Nevertheless, the calculated image does not perfectly approximate the features of the actual image. The shape of the outer line is not a good approximation to the observed image. The calculated shadow of contamination has too sharp a top and the basic shape of the outer line is accordingly different. This discrepancy can be corrected by correcting the profile of the deposit without changing the basic imaging principle. A profile which has a tailing like a Gaussian curve but has a more fattened top will have a projection that will better approximate the actual image.

CONCLUSIONS

A new image interpretation of tilted contamination deposits is presented. It assumes that the lines in the image are made by the projection of the tangent points on a smooth and tailing profile of the contamination deposit. This model has sufficient advantages over the conventional imaging model to make a significant correction to specimen thickness measurement. The inevitable overestimation in thickness measurement using the contamination spot separation method is also demonstrated with this model.

REFERENCES

1. G. W. Lorimer, G. Cliff, and J. N. Clark, Developments in Electron Microscopy and Analysis, (ed., J. A. Venables), Academic Press, London, 1976.

2. W. A. Knox, Ultramicroscopy 1 (1976) 175.

3. A. Hishinuma and S. Jitsukawa, to be published in Journal of Nuclear Materials.

4. N. Stenton, M. R. Notis, J. I. Goldstein, and D. B. Williams, Quantitative Microanalysis with High Spacial Resolution, (eds., G. W. Lorimer, M. H. Jacobs, and P. Doig), The Metal Society, London, 1981.

5. D. A. Rae, V. D. Scott, and G. Love, ibid., p. 57.

6. Z. Horita, K. Ichitani, T. Sano, and M. Nemoto, Scripta Met. **20** (1986) 381.

7. G. W. Lorimer, Electron Microscopy and Analysis 1981, London: Istitute of Physics, 1982, p. 147.

SMALL-SCALE BENDING FATIGUE SPECIMEN DEVELOPMENT - B. A. Chin. G. R. Rao (Auburn University) and E. H. Lee (ORNL)

OBJECTIVES

The objective of this study is to develop and evaluate small-scale fatigue specimen designs for testing irradiated specimens. The immediate objective is to test and compare results obtained using unirradiated specimens.

SUMMARY

Two small-scale bending fatigue test specimens were developed. The first specimen, termed the "rectangular" specimen, has overall dimensions of 30.1625 x 4.1625 x 0.762 mm with a gauge length of 6.35 mm. The unirradiated rectangular specimens were tested at both room temperature as well as at 600°C.

The second specimen is a "miniature-disc'' specimen with Outer dimensions of a 3 mm diameter Transmission Electron Microscope specimen and a reduced guage section formed by two circular radii of 1.5 mm. The thickness is *0.254* mm. The miniature specimens were fabricated using three different techniques: (1) Punching followed by electropolishing, (2) electrical discharge machining and (3) punching fallowed by annealing. The three sets of miniature-disc specimens were tested separately at room temperature.

Tests were performed using annealed type 316 stainless steel (Reference Heat 8092297). The results were found to conform to the Coffin-Manson relationship where the value of the exponent was found to lie between 0.1 and 0.25. There was some degradation in fatigue life for the rectangular specimen at 600°C as compared to the room temperature fatigue data. The miniature-disc specimens gave higher than expected values of fatigue endurance for all three sets of specimens. Both specimen designs appear to be suitable for scoping irradiated specimens for bending fatigue properties.

PROGRESS AND STATUS

Introduction

Small-scale specimens have received considerable attention for extraction of mechanical properties of irradiated materials. Size constraints within the reactor is one reason for the development of miniaturized specimens. Apart from that, considerable savings in irradiation time and cost due to smaller volume, the availability of a greater number of samples far testing and temperature control Considerations have spurred the development of miniaturized specimens. Minimal irradiation hazard to personnel during handling of the specimens is also an important consideration.

This report describes the investigation of fatigue properties of metals using two small-scale specimen designs. *The* two non-standard fatigue specimen designs have been tested and results using these Specimens are reported. One specimen design is for a subsized-rectangular specimen. The other design is for a miniature-disc specimen with dimensions of a transmission electron microscope specimen. The rectangular specimens were tested at room temperature as well as at 600°C while the miniature-disc specimens were tested only at room temperature. The results obtained using both specimens are compared and feasibility of further development of the miniature-disc specimen is discussed.

Specimens

The specimens were made from type 316 stainless steel (Reference Heat 8092297). The composition is given in table 1.

The rectangular specimen is shown in figure 1. The specimens were fabricated by cutting rectangular pieces of material from the parent sheet metal. These were then milled to the dimensions of the specimen. The reduced gauge section was also formed by milling. The specimens were hand polished using polishing papers of different grades in sequence. *The* final step involved electropolishing using a 90% ethanol - 10% perchloric acid electrolyte far a minute at -2.5°C to +2.5°C.

Table 1. Chemical Composition of Reference Heat 8092297 of type 316 stainless steel

Element	Composition (wt%)	Element	Composition (wt%)
Fe	Bal	CO	0.02
C	0.057	cu	0.10
Mn	1.86	N	0.03
P	0.024	B	0.0005
S	0.019	Ti	0.02
Si	0.58	Pb	0.034
Ni	13.48	Sn	0.004
Cr	17.25	Mo	2.34

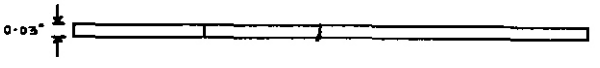

Figure 1. The Rectangular Specimen

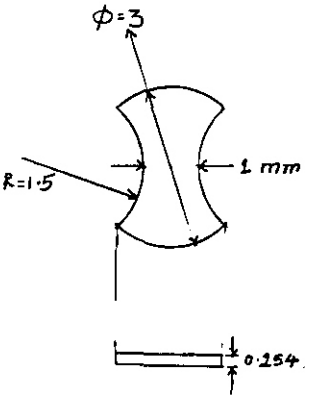

Figure 2. The Miniature-Disc Specimen

The miniature-disc specimen is shown in figure 2. The miniature-disc specimens were fabricated using three different techniques: (1) The specimens were punched and then electropolished, (2) the specimens were spark cut using an electrical discharge machining equipment and (3) the specimens were punched and then annealed at 1050°C for one hour in vacuum. The specimens obtained using the three methods were tested separately and the results were compared.

Experimental Procedure

The specimens were tested using a bending fatigue machine. The machine tests sheet type specimens in pure bending. The specimens are positioned as a cantilever beam. The load is applied at the free end of the specimen through a connecting arm.

The connecting arm is attached to an eccentric cam which is at one end of the motor shaft. The eccentricity is adjustable to increase or decrease the deflection and is calibrated as a function of a circular scale. The motor is a variable speed A. C. motor connected to a speed control circuit. The experimental set-up is shown schematically in figure 3.

The load cell consists of four strain gauges in a Wheatstone bridge network. The null position can be adjusted on the shutdown control box. The shutdown control box is the control unit for the set-up and is used to set the value of load at which the specimen is defined to have failed. Once this threshold value is set, the test can be started. When the load decays to this threshold value, the machine is tripped off. The number of reversals is noted with the help of a mechanical counter.

The rectangular specimen was also tested at 600°C. The elevated temperature test fixture consists of a furnace with the heating element connected to a temperature controller. The actual temperature is measured with the help of a thermocouple and this information is fed back to the controller which maintains the required temperature. The furnace is held by two supports and is attached to metal bellows to allow the furnace to move along with the specimen during the test. Argon is pumped into the furnace to maintain an inert gas atmosphere within the furnace.

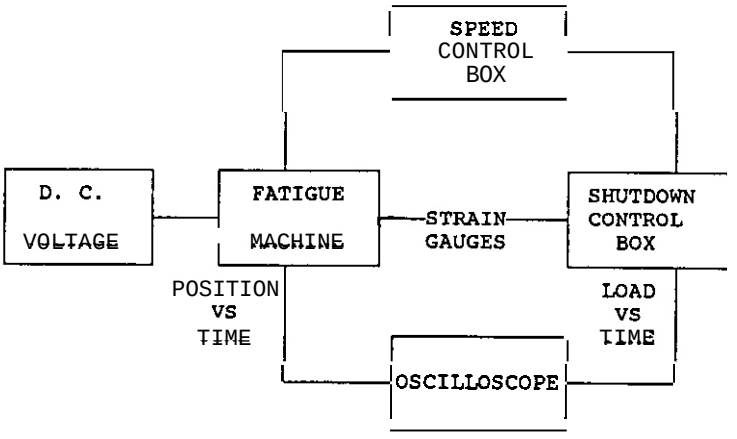

Figure 3. A Schematic of the Experimental Set-Up

Once the specimen is positioned. the motor is started and motor speed is adjusted to 600 rpm. The peak signal is adjusted to 100% and the signal amplitude on the oscilloscope is measured. This value gives the load acting on the specimen. This information is used in a computer program which gives stress and strain values along the specimen.

Results

The results were found to conform to the Coffin-Manson equation which relates the plastic strain range to the failure cycles through a power law:

$$\epsilon N^m = C$$

where ϵ = plastic strain range
N = cycles to failure
m = exponent
C = constant

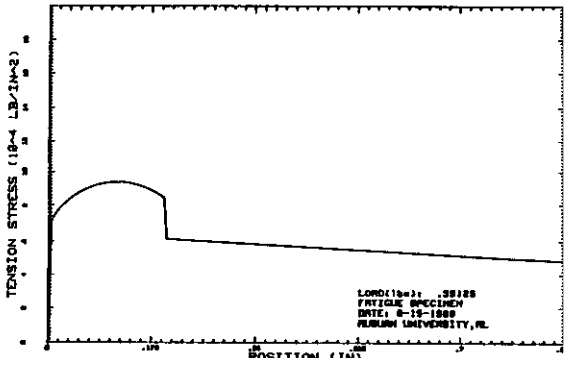

Figure 4. Tension Stress vs Position Plot for the Rectangular Specimen

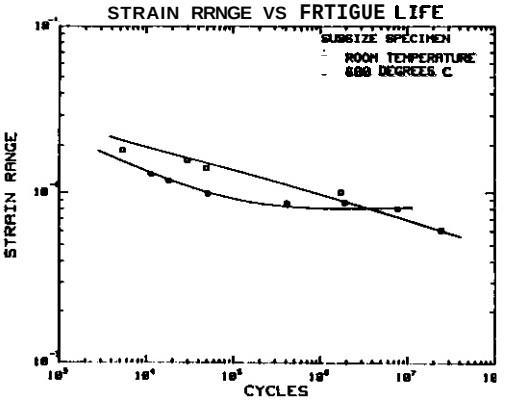

Figure 5. Fatigue Test Results at room Temperature and at 600°C for the Rectangular Specimen

Figure 4 shows the tension stress plotted as a function of position along the specimen for the rectangular specimen. The tests showed that the fatigue crack formed at this position of maximum stress without exception. Figure 5 shows the room temperature and the 600°C results far the subsize specimen. The results are plotted using strain range as a function of the number of cycles on logarithmic axes. The Coffin-Manson constants are given in table 2.

Table 2. Coffin-Manson constants for the rectangular specimen

Temperature	m	C
Room	-0.1306	0.059
600°C	-0.118	0.0696

The tension stress vs position plot is shown in figure 6 for the miniature-disc specimen. Figure 7 shows the fatigue data obtained for the specimen. The data is separated according to the technique of fabrication. The Coffin - Manson constants are given in table 3.

Table 3. Coffin - Manson constants for the miniature-disc specimen

Fabrication Technique	m	C
Punched/electropolished	-0.195	4.9545
EDM	-0.1806	1.6282
Punched/Annealed	-0.1995	2.9791

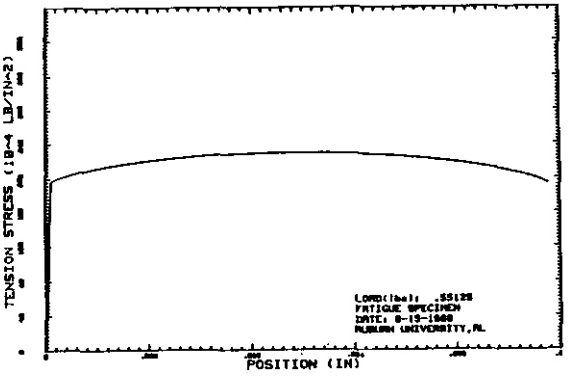

Figure 6. Tension Stress vs Position Plot for the Miniature-disc Specimen

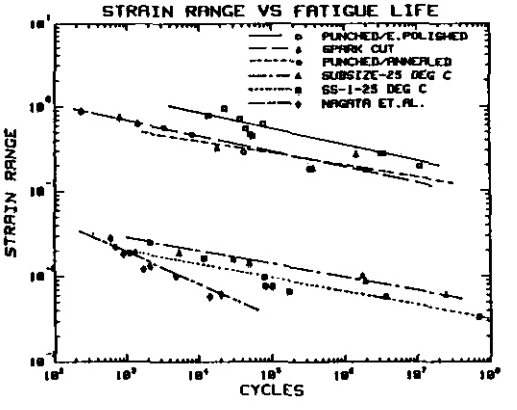

Figure 7. Room Temperature Results for the Miniature-Disc Specimen

Discussion

The room temperature data for the rectangular specimen is compared with fatigue data for 316 stainless steel obtained by Nagata et.al.[1], from Boller et.al.[2] (Figure 8) and using the SS-1 specimen[3]. The Coffin - Manson constants are compared in table 4. The room temperature results compare well with that of other investigations. The variations may be explained by the fact that there were small differences in the compositions and microstructures of the type 316 stainless steel tested. In these studies, different reference heats were used. However, all of them were candidates for fusion reactor blanket structural material.

The same annealed material was used in this study for the rectangular and miniature-disc specimens. Nagata et.al. used solution annealed and water quenched material and conducted strain controlled axial fatigue tests on hourglass specimens. They used a triangular waveform with a longitudinal strain rate of 5×10^{-3} sec^{-1}. The SS-1 specimens were tested using the experimental set-up described in this study.

Table 4. Comparison of Coffin - Manson constants for the rectangular specimen at room temperature

Specimen	m	C
Rectangular	-0.1306	0.059
Nagata et.al.[1]	-0.40	0.30
Boller et.al.[2]	-0.3476	0.1183
SS-1[3]	-0.1811	0.0763

There is some degradation in the fatigue life for the rectangular specimen at 600°C as cornpared to the room temperature results (Figure 5). The 600°C data is also compared with other elevated temperature data (Figure 9). The Coffin-Manson constants *are* compared in table 5.

Table 5. Comparison of Coffin-Manson constants for the rectangular specimen at elevated temperatures

Specimen	Temperature	m	C
Rectangular	600' C	-0.18	0.0696
SS-l	600°C	-0.268	0.139
Grossbeck/Liu[4]	430°C	-0.218	0.0796
Grossbeck/Liu[5]	550°C	-0.2046	0.0809
Grossbeck/Liu[6]	650°C	-0.2052	0.0695
Conway et. al.	430°C	-0.34	0.218

There is a fairly good correlation of data although there is a greater deviation at low strain ranges. Nagata et.al., report no reduction in the fatigue life at elevated temperatures when tested in vacuum[1]. Similarly, Cheng et.al., also found no temperature effect on the endurance of 316 stainless steel as long as there was no tension hold time[7]. Coffin performed axial push-pull fatigue tests on various metals at high temperatures and in a vacuum[9]. His results showed no temperature effect either, on the fatigue life of metals.

In contrast. the results of this study do indicate a detrimental effect on the fatigue life of 316 stainless steel due to elevated temperature. However, tests in this study were performed under an inert gas atmosphere of Argon, which was continually pumped into the furnace chamber. It is hypothesized that there is an effect of the external atmosphere on the specimen material being tested. Comparisons of specimens tested at 600°C in air and in other inert atmospheres are under way.

The results indicate that all the studies show a good correlation of fatigue properties of 316 stainless steel tested in the vicinity of 600°C. The observed variations may be caused by small differences in composition, microstructure, specimen size and environment. The inert gas atmosphere used in this study may have had a greater degrading effect as compared to the vacuum environments used in the other studies.

Moreover, this study used strain rates ranging from $1x10^{-3}$ to $1x10^{-2}$ sec^{-1}, which were higher than the strain rates used by Grossbeck and Liu. Grossbeck and Liu used a strain rate of $4x10^{-3}$ sec^{-1} for the 430°C and 550°C tests and a strain rate of $4x10^{-4}$ sec^{-1} for the 650°C tests. In general, increasing the strain rate appears to reduce the value of the Coffin-Manson exponent m.

The results for the rectangular specimen indicate that the specimen design can be used for comparing the fatigue life of different materials as well as for studying the effect of different variables on the fatigue life of a particular material.

The minizture-disc specimen results are compared with the rectangular specimen results as well as with other results (Fig.7). The Coffin-Manson constants are given in Table 6. The results indicate a fair correlation of the exponents. However. the data points consistently lie at higher strain range values as compared to the other results. There is a difference of about an order in strain range magnitudes.

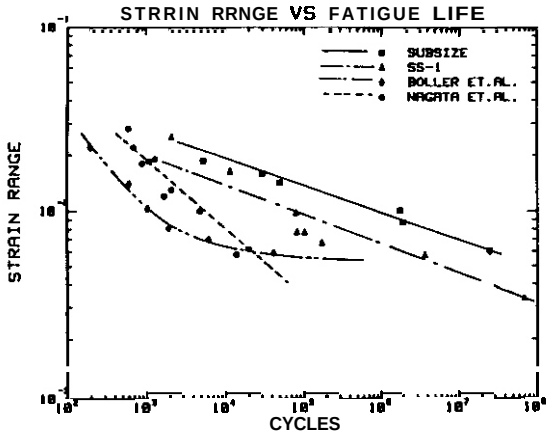

Figure 8. Comparison of Rectangular Specimen Results with Other Results (Room Temperature)

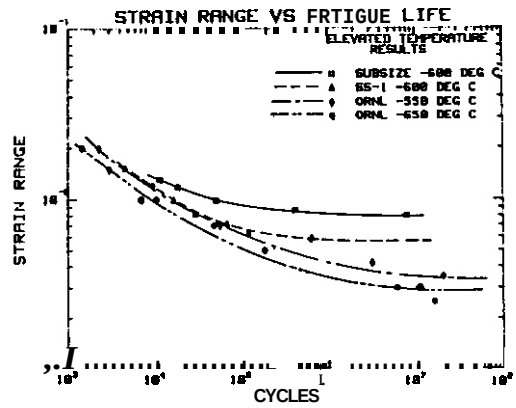

Figure 9. Comparison of Rectangular Specimen Results with Other Results (Elevated Temperatures)

The higher strain range values could be due to the following three major causes:
(a) Specimen Load - The fatigue machine essentially tests sheet type specimens in a cantilever beam arrangement. However, the design of the specimen holder for the miniature specimen is such that some axial loading is induced. This would give a higher apparent value of the bending load acting on the specimen which would then give values of strain ranges higher than the true values.

(b) Sample Preparation - As described earlier, the miniature-disc specimens were obtained by three methods, punching followed by electropolishing, spark cutting using the EDM (electrical discharge machining) equipment and punching followed by annealing. In the first method, the punching must have induced a cold worked region on the surface.
This damage was not completely removed by electropolishing which removes only *a* few microns of material from the surface.

Table 6. Comparison of Coffin-Manson constants for room temperature results for type 316 stainless steel for the miniature-disc specimen

Specimen	m	C
Miniature I[a]	-0.195	4.9545
Miniature II[b]	-0.2078	3.1012
Miniature III[c]	-0.1995	2.6797
Rectangular	-0.1306	0.059
SS-1 (20% CW)	-0.1811	0.0763
Nagata et.al.[1]	*-0.40*	0.30

a Annealed, punched and electropolished
b Annealed and spark cut
c Punched and annealed

In the second case, where the specimens were obtained using the EDM equipment, the cutting action is obtained by an electric spark discharge which is maintained between the specimen and tool electrode. There will always be surface damage when spark cutting is used. Even though surface damage can be reduced by employing slow cutting rates, it is never negligible. Also, sparking can occur between the tool and sides of the cut region in the specimen resulting in a tapered cut. There is also the possibility of bending of thin slices towards the tool as the cut nears completion due to electrostatic attraction. The depth of damage could range from a few um up to *40* um[10].

To avoid inducing significant damage to the surface. a very precise tool could be used with a very slow cutting rate (on the order of 0.004 mm/min). A more preferable method would be to use the so called "travelling wire EDM" method. A 3 mm diameter rod is used as the starting material. The grooves can be machined onto the rods. A very fine wire, 0.002 to 0.004 inches in diameter can then be used in conjunction with the EDM equipment. The wire is continuously unreeled and drawn over the specimen. Once the disk specimen is obtained, it would then be precision lapped to obtain the final thickness.

(c) Strain Rate · Strain rates may influence the fatigue properties of miniature-disc specimens. In this study very high strain rates were used, ranging from $5x10^{-1}$ to 5 sec^{-1}. This is high compared to strain rates of $1x10^{-3}$ to $1x10^{-2}$ sec^{-1} for the rectangular specimens and $4x10^{-3}$ to $4x10^{-4}$ sec^{-1} for the axial specimens used by Grossbeck and Liu. The high strain rates may be partially responsible for the higher load values and the low Coffin-Manson exponents obtained for the miniature-disc specimens.

CONCLUSIONS

The results obtained using the rectangular specimen design conform to the Coffin-Manson relationship. The value of the exponent was found to lie between -0.1 and -0.2. The repeatability of the position of crack formation was found to agree with that predicted by theoretical calculations. The results indicate that the specimen design can be used to study the effects of irradiation on the fatigue properties of alloys. The 600°C tests indicate some amount of degradation in the fatigue life at elevated temperatures.

The miniature-disc specimen results also conform to the Coffin-Manson relationship with the exponent having values ranging from -0.19 to -0.21. The values of the exponent compare favorably with other results but overall strain range values are about an order higher than results obtained by other investigators. This could be due to a combination of factors including specimen preparation techniques and the specimen not being subjected purely to bending loads. The results, however, do indicate that the miniature-disc specimen can be used to test irradiated specimens with some improvements.

FUTURE WORK

The specimen holding fixture for the miniature-disc specimen will be modified so that the specimen is a true cantilever beam. Finite element analysis will be used to improve theoretical calculations. Further comparison tests with other size specimens will be conducted after modification has been completed.

REFERENCES

1. N.Nagata, K. Furuya and R. Watanabe, " Low cycle fatigue behavior of blanket structural materials', J. of Nuclear Materials, 85 & 86, pp.839-843, (1981).
2. C. Boller and T. Seeger, Materials data for cyclic loading, Part C: High alloy steels, Materials science monographs, 42C. Elsevier publishers, p.155, 1987.
3. R. H. Wong, Metal fatigue for fusion applications, M. s. Thesis. Auburn University, (1986).
4. M. L. Grossbeck and K. C. Liu, "Low-cycle fatigue behavior of 20% cold worked type 316 stainless steel after irradiation in the HFIR", ORNL Report, pp.42-47, (1979).
5. M. L. Grossbeck and K. C. Liu, "High temperature fatigue life of 316 stainless steel containing irradiation induced helium", J. of Nuclear Materials. 103 & 104, pp.853-858, (1981).
6. M. L. Grossbeck and K. C. Liu, "Fatigue life at 650°C of 20% cold worked type 316 stainless steel irradiated in the HFIR at 550°C", ORNL Report, pp.136-140, (1982).
7. V. B. Conway, R. H. Stentz and J. T. Berling, "Fatigue, tensile and relaxation behavior of stainless steels", TID-26135. p.39, (1975).
8. C. F. Cheng. C. Y. Cheng, D. R. Diercks and R. W. Weeks, "Low cycle fatigue behavior of 304 and 316 s.s. at LMFBR Operating temperatures", Fatigue at Elevated Temperatures, ASTM STP 520, (1973).
9. L. F. Coffin,"High temperature fatigue life of 316 stainless steel containing Irradiation Induced Helium", Metallurgical Transactions, 3 , pp.1777-1788, (1972).
10. A. Szirmae and R. M. Fisher,"Specimen damage during cutting and grinding", Electron microscopy, diffraction and microprobe analysis, pp.3-9.

2. DOSIMETRY, DAMAGE PARAMETERS, AND ACTIVATION CALCULATIONS

NEUTRON DOSIMETRY AND DAMAGE CALCULATIONS FOR THE ORR-MFE 7J EXPERIMENT - L. R. Greenwood (Argonne National Laboratory)

OBJECTIVE

To provide dosimetry and damage analysis for fusion reactor materials irradiation experiments.

SUMMARY

Neutron measurements and damage calculations have been completed for the joint U.S.-Japanese 7J experiment in the Oak Ridge Research Reactor. Tensile and TEM specimens were irradiated from June 28, 1983 to March 26, 1987 (475 full power days) in position C3 at temperatures between 300-400°C. The maximum fast neutron fluence was 9.5×10^{21} n/cm^2 which producmed 7.4 dpa and 102 appm helium in 316 stainless steel.

PROGRESS AND STATUS

Neutron fluence and energy spectral measurements and damage calculations have been completed for the MFE-7J experiment in the Oak Ridge Research Reactor at Oak Ridge National Laboratory. This experiment was conducted jointly with Japanese experimenters and contained a variety of tensile and TEM specimens.[1] The experiment was irradiated at temperatures between 300-400°C in core position C3 from June 28, 1983, to March 26, 1987. The total exposure was 341,806 MWH or 475 full power days at 30 MW. Twelve dosimetry capsules were placed throughout the sample area. Four capsules measuring 7 cm in length were placed in level 1 and two capsules measuring 4.5 cm were placed in level 3 for each temperature region. Each capsule measured 1.6 mm OD and contained wires of Fe, Ti, and 0.1% Co-Al. Due to required cooling times and shipping delays, the samples were not received for analysis until September 1988.

Each capsule was opened in a hot cell at Argonne and individual wires were segmented, weighed, and mounted for gama spectroscopy. Due to the long decay time, we were only able to analyze ^{46}Sc, ^{54}Mn, and ^{60}Co. The measured activation rates are listed in Table 1. The activities were corrected for burnup of target and product activity, decay during and after irradiation, and gama self-absorption. The values in the table represent averages of several different samples at each level. In all cases, these radial flux gradients were less than 5%. A more detailed radial flux map was not determined since all measured values deviated by less than 3% from the averages in Table 1. All of the data are well fit by the equation $A(x) = A(0)(1+bx+cx^2)$, where A is the activity at height x. The average values of the parameters b and c for the three different reactions are $b = -1.015 \times 10^{-2}$ and $c = -7.614 \times 10^{-4}$. The maximum activity position was determined to be at about -6.7 cm below midplane.

The maximum activities were used as input to the STAY'SL computer code to adjust the flux spectrum. The input spectrum was taken from previous spectral measurements in ORR.[2] The resultant neutron fluence integrals are listed in Table 2. Damage parameters were than calculated with the SPECTER3 computer code and resultant dpa and helium values are listed for various elements in Table 3. The values in Tables 2 and 3 are given at the maximum flux position. To obtain values at other heights, simply use the equation given above. The only exception to this prescription is for nickel or 316SS where the thermal effect in nickel depends non-linearly on the thermal neutron fluence.[4] Consequently, helium and dpa values for 316SS are listed as a function of height in Table 4.

FUTURE WORK

The MFE-6J experiment was run at the same time as the 7J experiment. Dosimetry samples were received from the 60°C part of this run and they are now being analyzed. Dosimeters from the 200°C region are expected shortly. These experiments were the final runs in ORR since this reactor has now been decommissioned.

REFERENCES

1. Description of the U.S.-Japanese Spectral-Tailoring Experiment in ORR, J. L. Scott, L. K. Mansur, M. L. Grossbeck, E. H. Lee, K. Farell, L. L. Horton, A. F. Rowcliffe, M. P. Tanaka, and H. Hishinama, Alloy Development for Irradiation Performance, Semiannual Progress Report, DOE/ER-0045/15, pp. 22-40, Sept. 1985.

2. L. R. Greenwood, Alloy Development for Irradiation Performance, Semiannual Progress Report, DOE/ER-0045/15, pp. 4-14. Sept. 1985.

3. L. R. Greenwood and R. K. Smither, ANL/FPP/TM-197, SPECTER: Neutron Damage Calculations for Materials Irradiations, January 1985.

4. L. R. Greenwood, D. W. Kneff, and R. P. Skowronski, Journ. of Nucl. Mater. 122, pp. 1002-1010 (1984).

Table 1. Measured Activation Rates for ORR-MFE 7J
(Values normalized to 30 MW; accuracy ±2%)

Heiaht, cm	Activation Rate (atom/atom-s)[a] $^{59}Co(n,\gamma)^{60}Co$ ($\times 10^{-9}$)	$^{54}Fe(n,p)^{54}Mn$ ($\times 10^{-11}$)	$^{46}Ti(n,p)^{46}Sc$ ($\times 10^{-12}$)
2.3	6.38	-	-
0.4	6.77	1.30	1.70
-0.8	7.07	1.30	1.72
-1.0	6.87	1.31	1.73
-1.5	-		1.74
-3.2	6.87	1.33	1.73
-5.5	6.87	1.35	1.73
-9.5	6.94	1.36	1.76
-11.8	6.62	1.33	1.74
-14.0	6.52	1.29	1.70
-18.8	6.12	1.22	1.61
-21.6	5.51	1.15	1.50

[a]Values represent averages of radial flux monitors; radial gradients <5%.

Table 2. Neutron Fluences for ORR-MFE 7J
(Maximum values at -6.7 cm below midplane)

Energy	Fluence ($\times 10^{21}$ n/cm^2)	Uncertainty (%)
Total	27.0	7.
Thermal (<.5 eV)	8.07	7.
0.5 eV - 0.1 MeV	9.46	12.
>0.1 MeV	9.47	10.
>1 MeV	5.14	12.

Table 3. Damage Parameters for ORR-MFE 7J
(Maximum values at -6.7 cm: Use gradient equation elsewhere)

Element		DPA	He, appm
Al		12.6	5.7
Ti		8.0	4.3
V		8.9	0.21
Cr		8.0	1.4
Mn		8.5	1.2
Fe		7.1	2.4
co		8.1	1.2
	Fast	7.5	34.
Ni	Thermal	1.3	736.
	Total	8.8	770.
Cu		6.8	2.1
Nb		6.8	0.45
Mo		5.0	-
316SS[a]		7.4	102.

a316 SS: Fe(.645), Ni(.13), Co(.18), Mn(.019), Mo(.026)

Table 4. Damage Parameter Gradients for 316 SS ORR-MFE7J

Heiaht, cm	DPA	He, appm
0	7.19	97.
-4	7.40	101.
-8	7.43	102.
-12	7.28	99.
-16	6.95	91.
-20	6.45	80.
-24	5.77	66.

PRODUCTION OF ^{49}V, ^{93}Mo, and ^{93m}Nb NEAR 14.7 MeV - L. R. Greenwood, O. L. Bowers, and A. Intasorn (Argonne National Laboratory)

OBJECTIVE

To measure the production of long-lived isotopes in fusion reactor materials for activation and waste disposal applications.

SUMMARY

Results are presented for the production of ^{49}V (331 d), ^{93}Mo (3500 y), and ^{93m}Nb (16 y) by 14 MeV neutrons. Samples were irradiated at RTNS II. Chemical separations were performed to remove impurities and to separate the Mo-Nb fractions. Thin samples were then x-ray counted. Results predict that we will produce 28 mCi/cc of ^{49}V in vanadium and 2.8 mCi/cc of ^{93}Mo and 106 mCi/cc of ^{93m}Nb in molybdenm in a fusion first-wall assuming the STARFIRE reactor design.

PROGRESS AND STATUS

Measurements have been completed for the production of several long-lived isotopes at neutron energies near 14 MeV. Such data is needed to predict the activation of fusion reactor materials, especially for waste material applications. Similar experiments have been reported previously.[1-3] The samples were irradiated at the Rotating Target Neutron Source II at Lawrence Livermore National Laboratory. Details of the neutron flux and energy distributions have been published.[1] The metallic samples of V, natural Mo, and ^{94}Mo enriched Mo were pressed into discs measuring 3 mm od by 1 mm thick. The samples were irradiated over many months to fluences as high as 10^{18} n/cm^2. We have already published results for the production of ^{91m}Nb (650 y) and ^{94}Nb (20,300 y).[1]

Following the irradiation, samples have been analyzed for the presence of long-lived activities using a combination of chemical separations, x-ray counting, and liquid scintillation counting. O. Bowers (ACL) performed ion-exchange separations of Mo and Nb and Mn and V. Thin samples were then deposited for x-ray counting relative to ^{55}Fe and ^{93m}Nb standards.

Table 1 lists the results for ^{49}V (331 d), ^{93m}Nb (16 y), and ^{93}Mo (3500 y). The measured cross sections of 258 mb for ^{49}V, 550 mb for ^{93}Mo, and 0.75 mb for ^{93m}Nb were then used to calculate the production of these radioisotopes in a fusion first-wall material using the STARFIRE reactor design. The results show that we will produce about *2.8* mCi/cc of ^{49}V in vanadium, and *28* mCi/cc of ^{93}Mo and 106 mCi/cc of ^{93m}Nb in molybdenum. None of these reactions have been measured previously: hence, our data are the only reliable determination of these activities in fusion materials. Table 1 also summarizes our work on other long-lived isotooes.

FUTURE WORK

A paper is now being written to publish these results. Work is also continuing on the production of other long-lived isotopes such as ^{14}C (5730 y), ^{93}Zr (1,500,000 y), and ^{92}Nb (3,700,000 y).

A joint project has been initiated with Don Smith (EP), Bob Haight (LANL), and Y. Ikeda (JAERI) to measure the production of long-lived isotopes in the rare-earth materials Tb, Hf, and Eu. Four identical packets of material have been assembled, each measuring 1" OD x about 5/8" thick. Each packet contains plastic containers of HfO_2, Tb_4O_7, and Eu_2O_3 as well as Ag and Ni, Cu, Fe, and Ti dosimetry foils.

Two packets have already been irradiated at accelerator neutron sources, one in broad-spectrum Be(d,n) field at Argonne and the other in a 10 MeV H(p,n) neutron field at Los Alamos. The other packets have been sent to Japan for irradiation in the 14 MeV T(d,n) field at the FNS facility at JAERI. All of the samples will then be gama counted at Argonne, with a duplicate count in Japan.

The long-lived activities which we plan to measure include ^{108m}Ag(127 y) from Ag: $^{178m2}Hf$(31 y) from Hf; ^{150m}Eu(36 y), ^{152}Eu(13.3 y), and ^{154}Eu(8.8 y) from Eu; and ^{158}Tb(150 y) from Tb. We can also measure ^{63}Ni(100 y) from Cu. The dosimetry foils will be used to determine the neutron fluence and energy spectra from the $^{54}Fe(n,p)^{54}Mn$, $^{54}Fe(n,\alpha)^{51}Cr$, $^{63}Cu(n,\alpha)^{60}Co$, $^{58}Ni(n,p)^{58}Co$, $^{58}Ni(n,pn)^{57}Co$, $^{58}Ni(n,2n)^{59}Ni$, $^{46}Ti(n,p)^{46}Sc$, $^{47}Ti(n,p)^{47}Sc$, and $^{48}Ti(n,p)^{48}Sc$ reactions.

For the two irradiations at ANL and LANL, we have already measured the long-lived reactions on Eu. In all of the other cases, we must wait at least six months for shorter-lived activities to decay prior to looking for the longer-lived isotopes of interest.

References

1. L. R. Greenwood, ASTM-STP956, pp. 743-749 (1988).

2. L. R. Greenwood and D. L. Bowers, Measurement of Long-Lived Radionuclides in Fusion Materials, ASTM-STP1001, pp. 508-514 (1989).

3. L. R. Greenwood, D. G. Doran, and H. L. Heinisch, Phys. Rev. 35C, 76-80 (1987).

Table 1. Production of Long-Lived Isotopes Near 14 MeV

Reaction	σ,mb	$T_{1/2}$,y	Activity,mCi/cc[a]
$^{50}V(n,2n)^{49}V$	258±39	0.90	2.8
$^{56}Fe(n,2n)^{55}Fe$	454±35	2.7	25,000.
$^{63}Cu(n,p)^{63}Ni$	54±4	100.	1795.
$^{64}Ni(n,2n)^{63}Ni$	958±64	100.	227.
$^{60}Ni(n,2n)^{59}Ni$	104±25	$7.5x10^4$	1.0
$^{94}Mo(n,p)^{94}Nb$	55±6	$2.0x10^4$	–
$^{Nat}Mo(n,x)^{94}Nb$	7.8It0.8	$2.0x10^4$	0.77
$^{92}Mo(n,2n)^{91}Nb$	603±119	350.1	243.
$^{94}Mo(n,2n)^{93}Mo$	550±136	3500.	28.
$^{94}Mo(n,x)^{93m}Nb$	5.71t0.9	16.1	–
$^{95}Mo(n,x)^{93m}Nb$	1.36±0.27	16.1	–
$^{Nat}Mo(n,x)^{93m}Nb$	0.75It0.11	16.1	106.

"STARFIRE reactor; first wall spectrum; 21.6 MW-y/m^2; 3000 day cooling; production from natural element

Dosimetry and Damage Calculations for the ORR-MFE 4A/4B Spectral Tailoring Experiments - L. R. Greenwood (Argonne National Laboratory)

OBJECTIVE

To provide neutron dosimetry and damage calculations for fusion reactor materials irradiation experiments.

SUMMARY

Results are presented for the MFE 4A/4B spectral tailoring experiments in the Oak Ridge Research Reactor. These experiments started with an aluminum core piece filled with water, switched to a solid aluminum core piece, and finally added hafnium liners to suppress the thermal neutron flux. The maximum exposure for MFE 4A at 1077.0 FPD (223.1 FPO under HF) was 4.2×10^{22} n/cm^2 resulting in 13.1 dpa and 243 appm helium for 316 stainless steel. Corresponding values for MFE 48 at 995.5 FPD (121.8 FPD under HF) were 4.0×10^{22} n/cm^2, resulting in 12.0 dpa and 216 appm helium for 316 stainless steel.

PROGRESS AND STATUS

The MFE 4A and 4B experiments in the Oak Ridge Research reactor used spectral-tailoring techniques to obtain a desired fusion reactor-like helium-to-dpa ratio in stainless steel. Initially the experiments produced helium via the two-stage thermal neutron reactions on nickel. After a lengthy exposure, the samples were placed in a hafnium core piece. This had the effect of reducing the thermal neutron flux by about 50%. thereby limiting further production of helium while permitting continued displacement damage. A brief summary of the exposure histories are as follows:

MFE-4A			MFE-4B		
Dates	Exposure MWD	Core Piece	Dates	Exposure MWD	Core Piece
6/12/80-4/26/82	12,189	Al, H_2O	4/22/81-10/20/82	12,720	A, H_2O
9123182-12/7/82	1,866	Al, H_2O	7/29/83-12/31-84	13,492	Al, Solid
12/8/82-5/1/84	11,562	Al, Solid	2/5/85-6/26/85	3,654	Hf Sleeve
5/1/84-1/20/85	6,693	Hf Sleeve	Total	29,866	
Total	32,310		Full Power Days	995.5	
Full Power Days	1,077.0				

The 4A experiment was in the E3 position while 48 was is E7. The complete, more detailed irradiation histories were used to correct for decay of activities during irradiation and to determine helium production. Some of the dosimeters were removed from the 4A experiment in January 1981 after 5471 MWD and in April 1982 at 12,189 MWD. Some of the dosimeters in 4B were removed in October 1982 at 12,720 MWD. These results were all reported previously.[1,2,3] As each dosimeter was removed. a new one was inserted to take its place. For both experiments, some of the dosimeters remained with the samples for the entire exposure history.

Each dosimeter consisted of a stainless steel tube 1/16" x 2.75" long and contained small samples of Fe, Ni, Co-Al, Ti. Nb. Cu. 80% Mn-Cu, and helium monitors from Rockwell International. All of the samples were gamma counted and the corrected activation rates are shown in Table 1. Dosimeters were located on both the upper and lower levels and inside and outside of a stainless steel annulus surrounding the NaK and experimental samples. Exact locations are given for each sample in Table 1. Some of the dosimetry wires were lost due to the fact that some of the stainless dosimetry tubes burst or the welds failed, thereby allowing extreme oxidation of some materials. In particular, many of the Co-Al alloy, Ti, and Mn-Cu alloy wires were lost. Nevertheless, we were able to analyze adequate samples from all of the runs to determine the required activation rates for spectral analysis.

In order to determine the effect of hafnium on the activities, a special experiment was run at lower power on February 25-26, 1984, and the results were published previously.4 In that experiment, the Co and Fe captive gama reactions were about 56% lower when covered with 0.040' of hafnium. Assuming a similar reduction in the present experiment, irradiation history corrections were generated for all reactions. The results, as listed in Table 1, are in good agreement with previous experiments[1-3] indicating that the corrections are appropriate.

There are two other conclusions which can be made comparing the nmdified (solid Al and Hf) portion of the run. In the hafnium experiment we observed a reduction of 5-10% in the fast reaction rates which is not evident in the present data. This may be due to the fact that the reactor may have operated at higher flux to offset the hafnium effect in order to maintain a 30 MW power level. Secondly, although part of the modified runs were conducted using a solid aluminum core piece, this seems to have had little effect on the activities inside the assembly, although a small effect (5-10%) is apparent in the outer dosimeters.

The activities given in Table 1 can all be fit by a polynomial, as follows:

$$f(Z) = f(max)\ [1 + C\ (X-Xo)^2] \qquad (1)$$

where Xo is the position of the flux maximum (-3" below midplane), f(max) is the maximum activity, and C is a constant. For the present results Xo = -2.3", C = -5.40 x 10^{-3} for MFE 4A and Xo = -3.1", C = -1.4 x 10^{-2} for MFE 48. This equation can be used in general to describe fluence and damage rates within the assembly. The inner rates are of most interest since they represent the materials locations.

The neutron spectrum was determined at the maximum flux location (-3") using the STAY'SL least-squares adjustment code. The adjustments to the Table 1 spectrum were generally small (<20%) and the results are in good agreement with previous measurements.[1-4] The initial spectra were calculated by R. A. Lillie (ORNL.[5] The adjusted fluences are listed in Table 2. Damage calculations were performed for the net exposure in both the 4A and 48 irradiations and the results are given in Table 3. Since the hafnium liner appears to have had little effect on the fast neutron flux, the damage rates (dpa and helium) were nearly constant throughout the entire irradiation histories. However, the helium accumulation rate in nickel was reduced by about a factor of 0.2 during the hafnium-covered exposure. This assumes the hafnium effect which we measured,[4] as discussed previously. Helium in nickel was thus computed assuming a reduced net thermal fluence. Although there is some uncertainty in this procedure, our results are not very sensitive to the exact hafnium reduction factor. This is true because most of the helium was generated during the uncovered exposure. Hence, we estimate that the helium rates in nickel are accurate to about ±10%. Of course, helium data will be available later from Rockwell International. We should also mention that previous calculations for nickel agreed very well with the helium measurements.[1,2] The helium and dpa gradients for 316 stainless steel are listed in Table 4.

FUTURE WORK

Samples have been received from the 60°C region of the ORR-MFE7J experiment and analysis is in progress. Samples from the 200°C region should be received shortly. We are also expecting samples from the CTR49-56 experiments In HFIR.

REFERENCES

1. L. R. Greenwood, Alloy Development for Irradiation Performance, Semiannual Progress Report, DOE/ER-004517, pp. 15-19, Sept. 1981.

2. L. R. Greenwood, ibid., DOE/ER-0045/9, pp. 6-16, Sept. 1982.

3. L. R. Greenwood, ibid., DOE/ER-0045/12, pp. 17-21, March 1984.

4. L. R. Greenwood, ibid., DOE/ER-0045/12, pp. 13-17, March 1984.

5. R. A. Lillie, ibid., DOE/ER-0045/15, pp. 45-46, Sept. 1985.

Table 1A. Activation Rates - ORR - MFE 4A3
1078 FPD (entire run), 30 MW

Reaction	Ht, in.	Activity, at/ats	
		Inner	Outer
$^{58}Fe(n,\alpha)^{59}Fe$	-0.63	1.74^{-10}	1.90^{-10}
	-2.53	1.76^{-10}	1.76^{-10}
	-3.69		1.82^{-10}
	-3.94	1.65^{-10}	
	-5.84	1.57^{-10}	1.67^{-10}
$^{59}Co(n,\gamma)^{60}Co$	-4.25		4.41-9
$^{93}Nb(n,\gamma)^{94}Nb$	-1.00	3.08^{-10}	
	-1.81	2.96^{-10}	2.74^{-10}
	-4.44		3.03^{-10}
	-5.13	2.73^{-10}	2.85^{-10}
$^{54}Fe(n,p)^{54}Mn$	-0.63	1.10^{-11}	1.18^{-11}
	-2.53	1.11^{-11}	1.14^{-11}
	-3.69		1.21^{-11}
	-3.94	1.09^{-11}	
	-5.84	1.01^{-11}	1.15^{-11}
$^{46}Ti(n,p)^{46}Sc$	-1.59	1.58^{-12}	1.67^{-12}
	-4.91	1.46^{-12}	1.64^{-12}
$^{63}Cu(n,\alpha)^{60}Cu$	-2.06	7.29^{-14}	7.21^{-14}
	-4.06		9.02-14
	-5.38	6.85^{-14}	7.33-14
$^{55}Mn(n,2n)^{54}Mn$	-0.81	3.32-14	3.61^{-14}
	-3.88		4.66
	-4.13	3.21-14	

Table 18. Activation Rates - ORR - 4A - Mod
672 FPD (9/23/82 to 1/21/85), 30 MW

Reaction	Ht, in.	Activity, at/ats Inner	Outer
$^{58}Fe(n,\gamma)^{59}Fe$	-0.53	1.75^{-10}	1.87^{-10}
	-2.56	1.80^{-10}	
	-3.84	1.76^{-10}	
	-5.88	1.47^{-10}	
$^{59}Co(n,\gamma)^{60}CO$	-0.69	4.07^{-9}	4.34^{-9}
$^{93}Nb(n,\gamma)^{94}Nb$	-2.19	2.86^{-10}	2.99^{-10}
	-5.28	2.74^{-10}	
$^{54}Fe(n,p)^{54}Mn$	-0.53	1.09^{-11}	1.17^{-11}
	-2.56	1.09^{-11}	
	-3.84	1.06^{-11}	
	-5.88	0.97^{-11}	
$^{46}Ti(n,p)^{46}Sc$	-2.06		1.65^{-12}
$^{63}Cu(n,\alpha)^{60}Co$	-2.31		8.20^{-14}

Table 1C. Activation Rates - ORR - MFE 4B/2
Entire Run 996 FPD, 30 MW

Reaction	Ht, in.	Activity, atlats Inner	Outer
$^{58}Fe(n,\gamma)^{59}Fe$	-0.72		1.66^{-10}
	-2.41		1.75^{-10}
	-4.03	1.74^{-10}	1.84^{-10}
	-5.72	1.63^{-10}	1.65^{-10}
$^{59}Co(n,\gamma)^{60}Co$	-4.20	4.31^{-9}	4.42^{-9}
$^{93}Nb(n,\gamma)^{94}Nb$	-5.37	2.96^{-10}	
	-4.88	2.74^{-10}	2.79^{-10}
$^{54}Fe(n,p)^{54}Mn$	-0.72		1.16^{-11}
	-2.41		1.24^{-11}
	-4.03	1.11^{-11}	1.25^{-11}
	-5.72	1.05^{-11}	1.16^{-11}
$^{46}Ti(n,p)^{46}Sc$	-4.63	1.48^{-12}	1.67^{-12}
$^{63}Cu(n,\alpha)^{60}Co$	-5.38	7.11^{-14}	7.82^{-14}
$^{55}Mn(n,2n)^{54}Mn$	-1.81	3.06^{-14}	
	-5.13	3.17^{-14}	3.54^{-14}

Table 10. Activation Rates - ORR - MFE 4B/Mod
572 FPD (7/29/83 to 6/26/85), 30 MW

Reaction	Ht, in.	Activity, at/ats	
		Inner	Outer
$^{58}Fe(n,\gamma)^{59}Fe$	-0.53	1.87^{-10}	1.83^{-10}
	-2.63	1.89^{-10}	1.83^{-10}
	-3.84	1.76^{-10}	1.95^{-10}
	-4.94	1.79^{-10}	
	-5.94	1.56^{-10}	1.73^{-10}
$^{59}Co(n,\gamma)^{60}Co$	-4.00	3.94-9	4.27-9
$^{93}Nb(n,\gamma)^{94}Nb$	-2.19	2.95^{-10}	3.04^{-10}
	-2.88	2.75^{-10}	
	-4.19	2.70^{-10}	3.08^{-10}
	-5.50	2.72^{-10}	3.01^{-10}
$^{54}Fe(n,p)^{54}Mn$	-0.53	1.09^{-11}	1.15^{-11}
	-2.63	1.09^{-11}	1.14^{-11}
	-3.84	1.09^{-11}	1.20^{-11}
	-4.94	1.07^{-11}	
	-5.94	1.00^{-11}	1.10^{-11}
$^{46}Ti(n,p)^{46}Sc$	-2.06	1.48^{-12}	1.56^{-12}
	-4.44	1.41^{-12}	
	-5.38	1.39^{-12}	1.56^{-12}
$^{63}Cu(n,\alpha)^{60}Co$	-2.31	7.21^{-14}	7.79-14
	-4.69	6.95^{-14}	
	-5.63	6.92^{-14}	8.12^{-14}

Table 2. Neutron Fluences for ORR - MFR 4A/4B
Values inside the assembly at maximum flux
Fluence x 10^{22} n/cm^2

Energy	MFE 4A[a]	MFE 4B[a]
Exposure (FPD)	1078.4	995.5
Total	4.23	3.96
Thermal (<.5 eV)	1.28	1.24
0.5 eV-0.11 MeV	1.33	1.26
>0.11 MeV	1.62	1.46
>1 MeV	0.91	0.83

[a]Values assume 223.1 FPD under Hf for 4A and 121.8 FPD for 4B.

Table 3. Damage Parameters for ORR - MFE 4A/4B
Values at maximum flux location, -2.3" for A, -3.1" for B

Element		MFE 4A He, appm	MFE 4A DPA	MFE 4B He, appm	MFE 4B DPA
Al		9.95	21.80	8.84	19.90
Ti		7.75	14.00	7.06	12.82
V		0.35	15.50	9.31	14.17
Cr		2.49	13.94	2.23	12.76
Mn[a]		2.07	14.79	1.84	13.53
Fe		4.34	12.40	3.88	11.34
Co[a]		2.06	14.01	1.83	12.81
Ni	Fast	63.03	13.01	56.84	11.89
	^{59}Ni	1781	3.14	1580	2.79
	Total	1844	16.15	1637	14.68
cu	Fast	3.04	11.92	2.81,	10.89
	^{65}Zn	0.49	--	0.46	--
	Total	3.53	11.92	3.27	10.89
Zr		0.38	12.85	0.33	11.73
Nb		0.82	11.85	0.73	10.82
Mo		--	8.69	--	7.93
la		--	5.99	--	5.48
316SS[b]		243	13.12	216	12.00
	He/DPA	18.5		18.0	

[a]Thermal neutron self-shielding may reduce damage (dpa).

[b]316SS: Fe(0.645), Ni(0.13), Cr(0.18), Mn(0.019), Mo(0.026).

Table 4. Helium and DPA Gradients in 316SS - ORR - MFE 4A/4B

Height, in.	MFE 4A		MFE 4B	
	He, appm	DPA	He, appm	DPA
0	232	12.7	170	10.3
-1	235	13.0	194	11.2
-2	243	13.1	210	11.8
-3	242	13.1	216	12.0
-4	237	12.9	212	11.8
-5	228	12.6	198	11.4
-6	214	12.1	176	10.5

NEUTRON SPECTRAL CALCULATIONS FOR THE REAL88 EXERCISE - L. R. Greenwood and A. Intasorn (Argonne National Laboratory)

OBJECTIVE

To standardize nuclear data and techniques used to measure neutron flux spectra and to calculate radiation damage in materials.

SUMMARY

Neutron spectral analyses and damage calculations have been completed for six reference data sets distributed by the IAEA in Vienna. This interlaboratory intercomparison is designed to standardize dosimetry techniques and damage estimates for various spectra including fusion reactor simulations, pressure vessel surveillance, ^{235}U fission, and fast fission reactors. The data will be reviewed at a meeting in ECN Petten, The Netherlands, in October, 1988.

PROGRESS AND STATUS

We are participating in a project to compare neutron spectral adjustment codes and damage predictions sponsored by the International Atomic Energy Agency in Vienna, Austria. Neutron activation data were collected and distributed by the IAEA for six distinctly different neutron spectra including a pressure vessel surveillance capsule from the Arkansas Nuclear One power reactor, two pressure vessel simulator experiments in the Oak Ridge Research Reactor, a ^{235}U fission spectrum, the Coupled Fast Reactivity Measurement Facility at Idaho Nuclear Engineering Laboratory, and a fusion-simulation spectrum measured at RTNS II (provided by the author).

The REAL88 exercise followed the previous REAL801 and REAL842 exercises. Each successive exercise has placed tighter restrictions on the quality of the input data, knowledge of covariance information, nuclear data, and types of computer codes which are allowed. The goal is to standardize procedures and to establish reference data sets.

Over fifteen different laboratories are expected to participate in eight different countries. We have submitted our results to the ECN laboratory in Petten, The Netherlands, where all results will be compared.

FUTURE WORK

A meeting will then be held in Petten in late October, 1988, to assess the preliminary results of the comparison and to plan future work. The exercise is scheduled to be completed in time to issue a final report at the Seventh ASTM-Euratom Symposium on Reactor Dosimetry in August 1990 in Strasbourg, France.

REFERENCES

1. W. L. Zijp, E. M. Zsolnay, H. J. Nolthenius, E. J. Szondi, G. C. Verhaag, O. E. Cullen, and C. Ertek. Final Report on the REAL-80 Exercise. INDCCNED)-7, 1983.

2. E. M. Zsolnay, H. J. Nolthenius, and W. L. Zijp, Fifth Progress Report on the REAL84 Exercise, ECN-87-045, April 1987.

3. MATERIALS ENGINEERING AND DESIGN REQUIREMENTS

No contributions.

4. *FUNDAMENTAL MECHANICAL BEHAVIOR*

GRAIN SIZE EFFECT ON RADIATION HARDENING IN NEUTRON-IRRADIATED POLYCRYSTALLINE COPPER — S. Kojima, S. J. Zinkle (Oak Ridge National Laboratory) and H. L. Heinisch (Pacific Northwest Laboratory)

OBJECTIVE

The objective of this study is to obtain fundamental knowledge of the correlation between microstructural change and the variation of yield stress in neutron-irradiated metals.

SUMMARY

Microstructural changes in 14 MeV neutron-irradiated polycrystalline copper were observed by transmission electron microscopy and correlated with the variation of yield stress. Conventional theory of radiation hardening was found to be not directly applicable to polycrystals. Radiation-induced point defect clusters are considered to become obstacles not only to the motion of dislocations on the piling-up side of a grain, but also to the generation of dislocations on the next grain. Generally, applicable simplified equations for polycrystals are proposed. By applying the equations to the published tensile test results, the contribution of matrix hardening was found to be fairly low.

PROGRESS AND STATUS

Introduction

The study of neutron irradiation damage at a very low fluence reveals the characteristics of individual cascade damage since little interaction exists between other cascade damages. The gradual increase of the neutron fluence makes it possible to feature the interaction between cascades which plays an important role in high fluence irradiation. One of the fruitful results obtained from earlier studies of RTNS-II irradiation using electron microscopy is the observation that the number density of point defect clusters varies from a linear dependence on neutron fluence to a one-half power dependence as the fluence increases.[1-3] This change of fluence dependence is an indication of the interaction of freely migrating point defects with irradiation-produced defect clusters. The switch from linear to square root dependence does not occur until a certain amount of defect clusters comparable to the permanent sink concentration are accumulated.

The present study investigates the variation of the yield stress change at low fluences in 14 MeV neutron-irradiated copper. Like the interaction between point defects and defect clusters, the interaction between dislocations and defect clusters is also expected to be observed starting from very low fluences where only a few defect clusters exist. Mitchell[8] has shown a result that the yield stress change in 14 MeV neutron-irradiated copper abruptly increases at about 3×10^{20} n/m^2. This implies that a certain abrupt change has occurred in the microstructure and/or the interaction between dislocations and defect clusters at this fluence. A previous report[9] suggested the possibility that the barrier strength of defects may be fluence dependent. This possibility was obtained from a comparison of electron microscopy and electrical resitivity measurements[9] with Mitchell's results. However, the comparison suffered a serious drawback in that different heats of copper were used in the two studies. In the present experiment, microstructural observation by electron microscopy has been performed on specimens prepared and irradiated at the same time as the specimens used for tensile tests[10,11] to avoid the ambiguity arising from specimen differences.

The conclusion of the present study is that the abrupt increase of yield stress is due to the participation of "source hardening" in addition to the initial "lattice hardening."[12] The relation between the distance between radiation-induced defect clusters and the size of Frank-Read-type source is considered to be controlling this phenomenon. The large contribution of the "source hardening" is thought to be a serious problem from a practical viewpoint since it means most of the stress is concentrated at the head of piled-up dislocations (i.e., grain boundaries). We propose a simplified equation which expresses this contribution of "source hardening" according to the variation of grain size.

Experimental Procedure

Miniature sheet-type tensile specimens were prepared from pure (Marz grade) copper. The specimens were punched from 0.25 mm sheet stock, de-burred, laser engraved, then annealed at 723 K for 15 min in argon. The resultant grain size was ASTM 7 which corresponds to a diameter of about 36 μm. The specimens were irradiated with 14 MeV neutrons at 363 K in the RTNS-II facility to fluences of 0.62 to 20.0 $\times 10^{21}$ n/m^2.

Tensile tests were performed at room temperature with a strain rate of 4.9×10^{-4}/s. Electron microscope specimens for microstructural observation were prepared from several tensile specimens which had not been used for the tensile tests. They were examined in a JEOL 2000FX electron microscope.

Weak beam dark field conditions were used for the observation of microstructure of radiation-induced defects. The observing beam direction was [110] using the 200 reflection to obtain the triangle shape of stacking fault tetrahedra (SFT) for their identification. The areal number density of defects was measured from several areas of foil thickness of 0 to about 100 nm which was determined from thickness fringes. The volume number density was determined from the slope of the line through plotted data points of areal number density vs. foil thickness. This method is considered to be the best way to eliminate the error in measuring the volume number density.[13] The print magnification was 500,000× for number density measurements and 1,000,000× for size measurements. No correction has been made for invisible small defects which have the same image intensity as the background.[14]

Results

Electron Microscopy — The defects observed were SFT and dislocation loops. Figure 1 shows the typical microstructure of a specimen irradiated to a fluence of 1×10^{21} n/m^2. They were distributed homogeneously in the matrix. In this specimen, 70% of the defects were SFT and the rest were dislocation loops. SFT are vacancy-type[15] point defect clusters formed directly in subcascades. The majority of the dislocation loops are believed to be interstitial-type, presumably formed from the clustering of free interstitial atoms released from each subcascade. Figure 2 plots the total number density of defect clusters against the neutron fluence. Although only three different fluences were available for microstructural observation in the present study, Fig. 2 suggests that the increase in the number density of defect clusters is linear with the neutron fluence up to approximately 2×10^{21} n/m^2 and then changes to a square root dependence on fluence. This relation between the number density and fluence is in agreement with previous results on the room temperature irradiation of copper with 14 MeV neutrons.[1,3,16]

J-15336

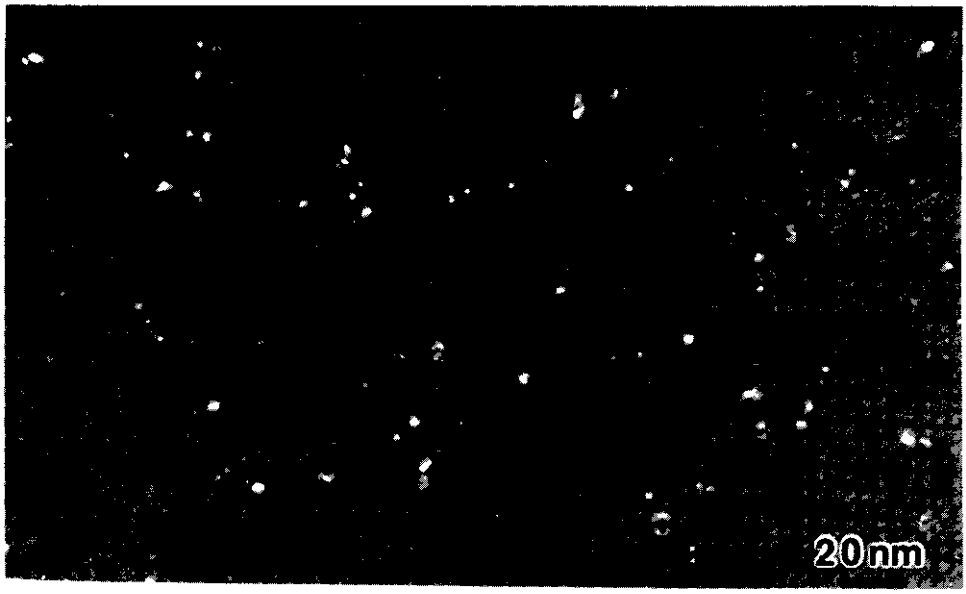

Fig. 1. Defect structures developed in 14 MeV neutron irradiated copper. 1×10^{21} n/m^2 at 363 K. Weak beam dark field condition (g,6g), g = 200.

Figure 3 shows the size distribution of defect clusters for three observed fluences. The mean size of the defect clusters was approximately the same for the three fluences, ranging from 2.4 to 2.7 nm. Values of the measured results of number density and mean size of defect clusters are listed in Table 1. The slight decrease of the mean size of defect clusters with increasing neutron fluence is attributed to the absorption of interstitial atoms at SFT.

Tensile testing — The measured increases in the 0.2% offset yield stress are listed in Table 2. The unirradiated yield stress was 49 MPa. Figure 4 shows the variation of yield stress change with neutron fluence. There was little scatter among the data points and a smooth curve could be drawn through the data points. The slope of the log-log curve drawn through the two lowest fluence data points was about 0.75, which is shown as tan θ in the figure. The yield stress of the specimens used for electron microscopy was determined from Fig. 4. They are listed in Table 3.

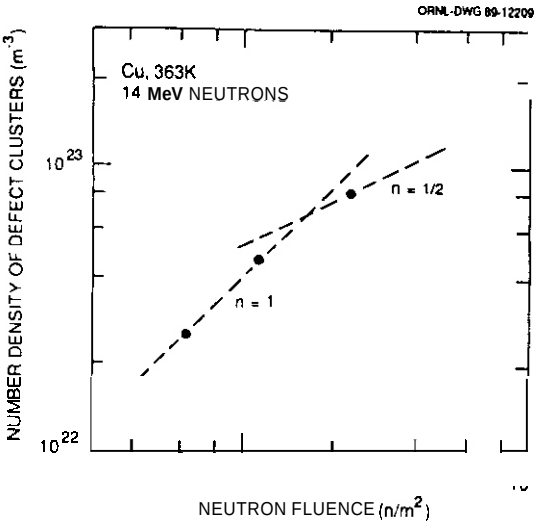

Fig. 2. Variation of the number density of defect clusters with neutron fluence irradiated at 363 K.

Table 1. Number density and mean size of defect clusters

Fluence	Number density	Mean Diameter (nm)
0.62 × 10^{21} n/m^2	2.5 × 10^{22}/m^3	2.7
1.21	4.7	2.5
2.36	8.1	2.4

Table 2. Yield stress changes in RTNS-II irradiated copper

Fluence	Change in Yield stress (MPa)	Fluence	Chanoe in Yield-stress (MPa)
0.617 × 10^{21} n/m^2	45	4.35 × 10^{21} n/m^2	128
0.627	41	8.99	150
		9.21	154
		11.2	152
2.23	91	13.6	174
2.35	90	15.6	183
3.98	114	20.4	185
4.30	113		

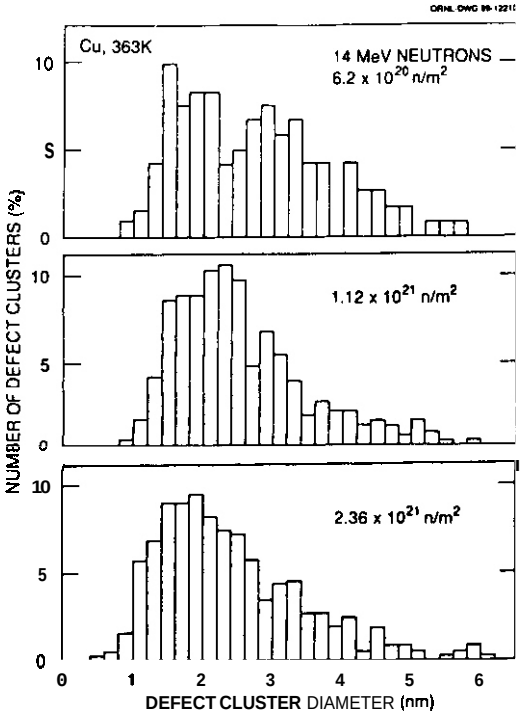

Fig. 3. Size distribution of defect clusters at three different neutron fluences.

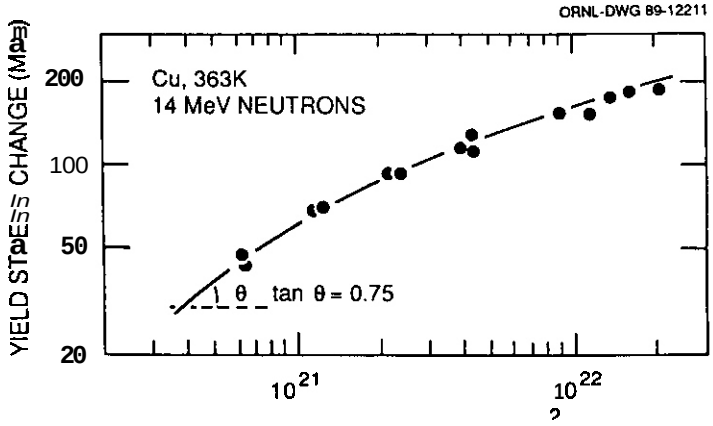

Fig. 4. Variation of the yield stress change with neutron fluence. The slope of the curve at the two lowest fluence data points is about 0.75.

Table 3. Estimated yield stress change for TEM specimens

Fluence	Change in Yield stress (MPa)
0.62 × 10^{21} n/m^2	45
1.21	67
2.36	91

Using the values in Tables 1 and 3, a correlation between the yield stress change and the number density of defect clusters can be determined. Figure 5 shows a plot of the yield stress change vs. the square root of the product of number density and mean size of defect clusters. This plot can be used to examine the validity of the following equation" for the yield stress change — thatis:

$$\Delta\sigma = \alpha G b (Nd)^{1/2} \quad , \qquad (1)$$

where α is the hardening coefficient indicating the barrier strength of defect clusters against dislocations, G is the rigidity modulus, b is the Burgers vector, N is the number density of defect clusters, and d is the size of defect clusters. The three data points indicate that a linearity exists between the yield stress change and $(Nd)^{-1/2}$. However, the line connecting the points did not intersect the origin of the coordinates but shows a negative value of yield stress change, -22 MPa, at $(Nd)^{1/2} = 0$.

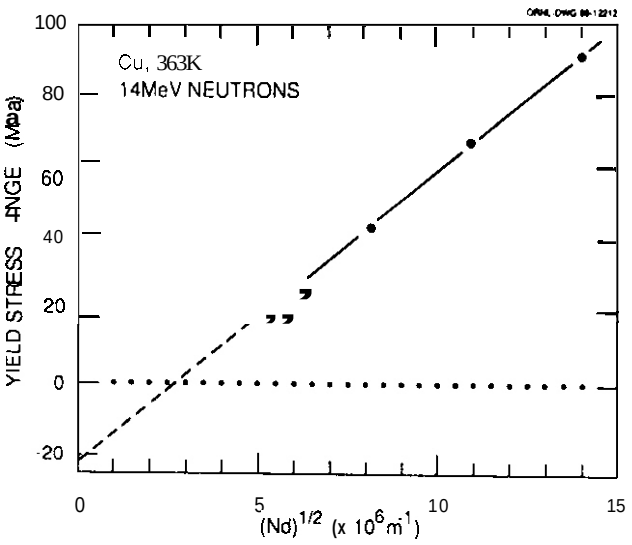

Fig. 5. Relation between the yield stress change and the inverse of mean distance between defect clusters.

Discussion

Two surprising results were observed in this study. Firstly, the slope of the lower fluence hardening data in Fig. 4 was 0.75. The expected slope from Eq. (1) was 0.5 since the relation between the number density of defect clusters and the neutron fluence was linear in this dose regime and the mean size of defects was almost constant as shown in Figs. 2 and 3. Secondly, the extrapolated line in Fig. 5 from the data points to $(Nd)^{1/2} = 0$ showed a negative value of yield stress change (-22 MPa) instead of zero. The good linearity of the data in Fig. 5 suggests it is unlikely that the value of α in Eq. (1) is changing over this fluence range. Instead, it would be better to assume an additional term in Eq. (1) — thatis:

$$\Delta\sigma = \alpha G b (Nd)^{1/2} - X \quad , \qquad (2)$$

where X is equal to 22 MPa in the present case. Hence by taking a logarithm

$$\log Aa = \log\{\alpha G b (Nd)^{1/2} - X\} \quad , \qquad (3)$$

it can be seen that the slope of this relation is higher at low fluences than at high fluences. This may explain why the initial slope in Fig. 4 was 0.75 instead of the expected value of 0.5. By transposing the extra term X to the left side of Eq. (2) and taking a logarithm, the following equation is obtained:

$$\log(\Delta\sigma + X) = \log \alpha G b (Nd)^{1/2} \quad . \qquad (4)$$

Figure 6 is the replotted version of Fig. 4 which simply adds 22 MPa to the yield stress change listed in Table 2. It clearly shows the expected tendency of the radiation hardening from a one-half power dependence of neutron fluence to a one-fourth power dependence. The fluence corresponding to the change in slope is around 2×10^{21} n/m^2, which is close to the fluence where the TEM data (Fig. 2) indicates a slope change.

The obvious question is: What is the physical origin of the extra term X? The easiest solution might be to attribute it to the error in measuring the yield stress of the unirradiated specimens — namely, $\sigma_{unirrad.}$ = 49 MPa - 22 MPa = 27 MPa. However, the error in the unirradiated measurement is no more than 5% and an error of 22 MPa is hardly possible. Since the irradiated samples were polycrystals, it is worthwhile exploring the possibility that the extra 22 MPa is related to a grain boundary effect. Eased on this assumption, we would like to review the result of Makin[18] who has extensively studied the grain size dependence of the lower yield stress of fission neutron-irradiated copper.

The result of Makin given in ref. (18) is shown in Fig. 7. The irradiation temperature was 353 K and the lower yield stress was measured at 78 K. The fluence shown is for epithermal neutrons, and the fast neutron fluence was reported to be approximately 10%of these values. Figure 7 shows that the relation between the yield stress σ and the grain size D is described by the Hall-Petch relation:

$$\sigma = \sigma_i + kD^{-1/2} \quad . \qquad (5)$$

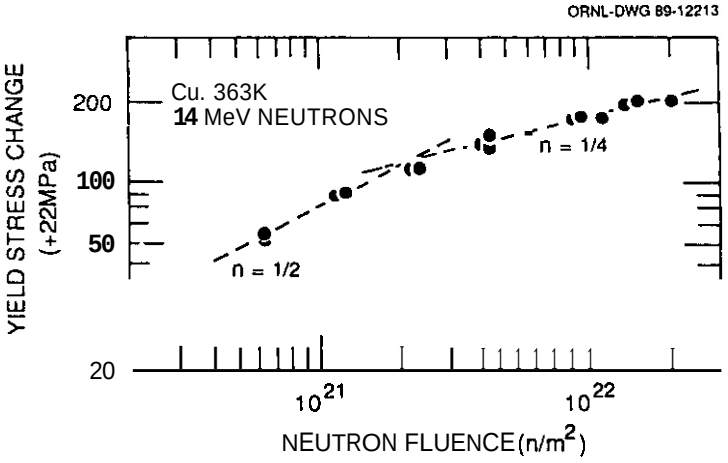

Fig. 6. Replotted version of Fig. 4. 22 MPa was added to the yield stress of each fluence. Note the variation from one-half power dependence to one-fourth dependence with with increasing fluence.

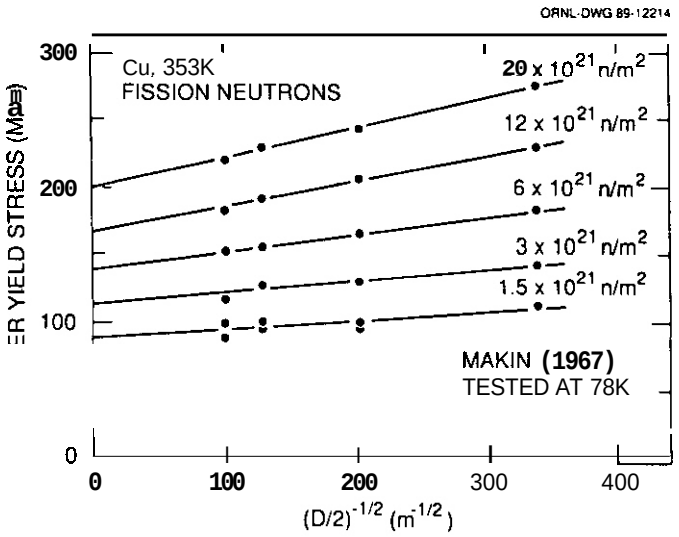

'Fig. 7. Grain size dependence of the lower yield stress of fission neutron-irradiated copper. The fluence shown is for epithermal neutrons. From Makin.[18]

An important feature to be noticed is that not only σ_i but also k, the Hall-Petch "constant," is increasing with fluence.

In order to examine the fluence dependence of the yield stress, Fig. 7 was replotted with coordinates that have the square root of neutron fluence as the abscissa (Fig. 8). The bottom curve is the extrapolated value to an infinite grain size $D^{-1/2} = 0$. This curve is considered to be equivalent to the contribution of the matrix. The fluence dependence of the yield stress of the matrix is seen to be proportional to the square root of the epithermal neutron fluence up to 3×10^{21} n/m^2; thereafter it shows a weaker dependence on fluence (perhaps one-fourth power dependence).

An especially important result obtained from Fig. 8 is that the extrapolation of the yield stress data for all five grain sizes from 3×10^{21} n/m^2 to zero fluence meet at a unique value σ_0. Since the real values for zero fluence (unfortunately, no data is available in Makin[18]) should be distributed according to the "unirradiated Hall-Petch relation," Fig. 8 implies that the "irradiated Hall-Petch relation" is strictly controlled by the existence of defects formed by neutron irradiation.

Theoretical Model

Here, we propose simplified equations for the "irradiated Hall-Petch relation" by referring to the equations used to derive the unirradiated Hall-Petch relation based on a dislocation pileup model.[19]

When the motion of a dislocation is stopped at a grain boundary, dislocations on the same slip plane start to pile up and a large stress concentrates at the head of the piled-up dislocations. The concentrated stress induces the generation of dislocations in the next grain. This generation of dislocations is taken as the yield of fcc polycrystals. Therefore, in explaining the mechanism of radiation hardening in polycrystals, it would be also necessary to take this dislocation generation into consideration. The existence of radiation-induced point defect clusters is considered to impede not only the motion of dislocations in the piling-up side of the grain boundary but also the generation of dislocations in the next grain. If the working dislocation source is a Frank-Read-type source, generation of dislocations would be unaffected until the mean distance between defects in the slip plane $(Nd)^{-1/2}$ becomes comparable to the size of the Frank-Read-type source s. At high fluence, the stress required to generate dislocations would become proportional to the ratio of s and $(Nd)^{-1/2}$. Using β as the proportionality constant between s and $(Nd)^{-1/2}$, τ as the applied shear stress, where $\tau = m\sigma$ (m: Schmid factor), τ_0 as the frictional stress, τ_d as the stress required to generate dislocations from Frank-Read-type source, D as the grain size, and r as the distance between the head of piling-up and Frank-Read-type source, equations are given as follows:

(a) Unirradiated specimen[19]

$$(\tau - \tau_0)(D/r)^{1/2} = \tau_d \; ; \tag{6}$$

hence

$$\tau_{unirrad} = \tau_0 \; t \; (r/D)^{-1/2} \; \tau_d \; = \tau_0 + kD^{-1/2} \tag{7}$$

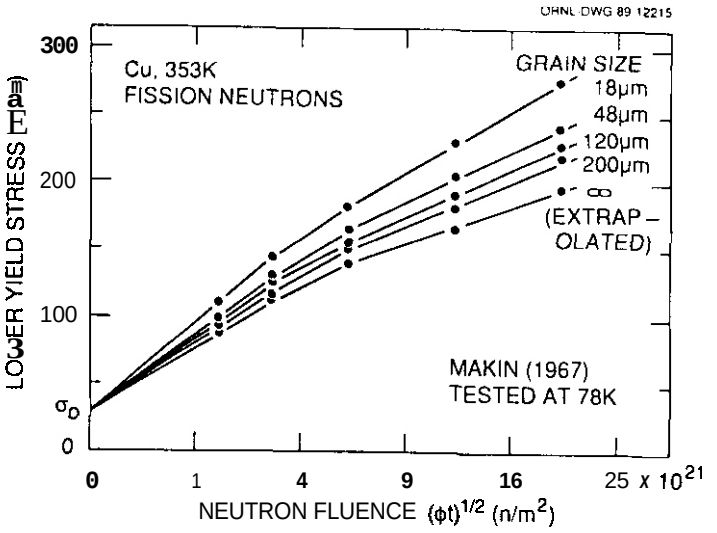

Fig. 8. Replotted version of Fig. 7. Square root of neutron fluence is taken as the abscissa.

(b) $s < (Nd)^{-1/2}$

$$[\tau - \{\tau_0 + \alpha Gb(Nd)^{1/2}\}](D/r)^{1/2} = \tau_d \ ; \tag{8}$$

$$\tau = \tau_0 + \alpha Gb(Nd)^{1/2} + kD^{-1/2} \ ; \tag{9}$$

$$\Delta\tau = \tau - \tau_{unirrad} = \alpha Gb(Nd)^{1/2} \ . \tag{10}$$

(c) $s > (Nd)^{-1/2}$

$$[\tau - \{\tau_0 + \alpha Gb(Nd)^{1/2}\}](D/r)^{1/2} = \beta\tau_d \, s/(Nd)^{-1/2} \ ; \tag{11}$$

$$\tau = \tau_0 + \alpha Gb(Nd)^{1/2} + \beta s(Nd)^{1/2}kD^{-1/2} \ . \tag{12}$$

$$\Delta\tau = (\alpha Gb + \beta skD^{-1/2})(Nd)^{1/2} - kD^{-1/2} \ . \tag{13}$$

Equation (12) clearly describes the feature of Fig. 8, and Eq. (13) successfully demonstrates the appearance of the extra term X in Eq. (2) — namely,

$$X = kD^{-1/2} \tag{14}$$

Equations (8)–(13) may be used to analyze yield stress measurements on 14 MeV neutron-irradiated copper reported by Mitchell.[8] Figure 9 plots Mitchell's results by taking the yield stress change as the ordinate and the square root of neutron fluence as the abscissa. It shows that the yield stress changes at low fluences (up to 3×10^{20} n/m^2) exhibit a square root dependence on neutron fluence as predicted by Eq. (10). The slope of the radiation hardening curve increases for fluences above 3×10^{20} n/m^2. According to Eq. (13), this is an indication that the defect cluster spacing is less than the size of the Frank-Read dislocation source. The mean distance between defect clusters in copper at 3×10^{20} n/m^2 is $(Nd)^{-1/2} \simeq 0.2$ μm, which is a physically reasonable value for the size of Frank-Read-type sources. The simplified Eqs. (8)–(13) are thus well supported by the experimental results.

It is considered that Eq. (10) and the second term of Eq. (12) correspond to so-called "lattice hardening" and the third term of (12) is the "source hardening."[12] The slope at very low fluences in Fig. 9 indicates that the contribution of "lattice hardening" is fairly low. Recent results by Okada[20] using RTNS-II irradiated copper specimens of large grain size comparable to the specimen thickness also supports this low slope "lattice hardening." Another factor to consider is that the "lattice hardening" is temperature sensitive, whereas the "source hardening" is temperature insensitive."

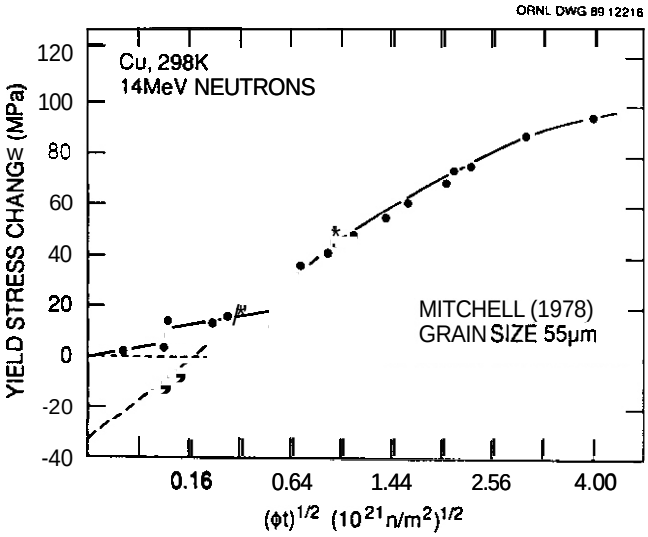

Fig. 9. Variation of the yield stress "source change" with the square root of neutron fluence. Tensile data from Mitchell.

CONCLUSIONS

The proposed simplified equations for neutron-irradiated polycrystals are considered to give a satisfactory explanation of the observed variation of yield stress with neutron fluence.

FUTURE WORK

The present equations assume that the point defect clusters are uniformly distributed throughout the specimen. However, it is often the case that the number density of defect clusters is increased or decreased in the vicinity of sinks such as grain boundaries. Consequently, if the source of dislocation-generation exists in these region, $(Nd)^{1/2}$ on the right side of Eq. (11) should be modified. Application of modified versions of Eqs. (8)–(13) to various experimental situations will be investigated.

ACNOWLEDGEMENTS

The authors would like to thank N. H. Rouse and E. L. Ryan for their help in the experiments and Frances Scarboro for manuscript arrangement.

REFERENCES

1. N. Yoshida, Y. Akashi, K. Kitajima and M. Kiritani, J. Nucl. Mater. 133&134 (1985) 405.
2. M. Kiritani, T. Yoshiie and S. Kojima, J. Nucl. Mater. 141-143 (1986) 625.
3. S. J. Zinkle, J. Nucl. Mater. 150 (1987) 140.
4. L. Thompson, G. Youngblood and A. Sosin, Rad. Effects 20 (1973) 111.
5. S. J. Zinkle, J. Nucl. Mater. 155-157 (1988) 1201.
6. M. Kiritani, Materials Science Forum 15-18 (1987) 1023.
7. S. Kojima, Y. Satoh, T. Yoshiie and M. Kiritani, to be submitted to ICFRM-4, Kyoto, 1989.
8. J. B. Mitchell, Lawrence Livermore Laboratory Report, UCRL-52388 (January 1978); also J. 8. Mitchell et al., p. 172 in Radiation Effects and Tritium Technology for Fusion Reactors, Vol. II, eds., J. S. Watson and F. W. Wiffen, Gatlinburg, TN (1975).
9. S. J. Zinkle, Fusion Reactor Materials Semiann. Prog. Rep. March 31, 1987, DOE/ER-0313/2 (1987) 99.
10. H. L. Heinisch, S. 0. Atkin and C. Martinez, J. Nucl. Mater. 141-143 (1986) 807.
11. H. L. Heinisch and C. Martinez, J. Nucl. Mater. 141-143 (1986) 883.
12. M. A. Adams and P. R. B. Higgins, Philos. Mag. 4 (1959) 777.
13. N. Yoshida, M. Kiritani and F. E. Fujita, J. Phys. Soc. Japan, 39 (1975) 170.
14. Y. Satoh, Ph.D. thesis, Hokkaido University (1989).
15. S. Kojima, Y. Satoh, H. Taoka, I. Ishida, T. Yoshiie and M. Kiritani, Philos. Mag. A59 (1989) 519.
16. Y. Satoh, I. Ishida, T. Yoshiie and M. Kiritani, J. Nucl. Mater. 155-157 (1988) 443.
17. A. L. Bement, Jr., in: 2nd Int. Conf. on Strength of Metals and Alloys, (ASM, 1970) p. 693.
18. M. J. Makin, in: Radiation Effects, Ed. W. F. Sheely (Gordon and Breach, New York, 1967) p. 627.
19. G. E. Dieter, Mechanical Metallurgy, (McGraw-Hill, 1976).
20. A. Okada, unpublished.

CORRELATION OF MECHANICAL PROPERTY CHANGES IN NEUTRON IRRADIATED PRESSURE VESSEL STEELS ON THE BASIS OF SPECTRAL EFFECTS - H. L. Heinisch, (Pacific Northwest Laboratory)[a]

OBJECTIVE

To investigate the effects of the neutron spectrum on mechanical property changes in metals.

SUMMARY

Defect production functions derived from atanistic modeling were evaluated for use in correlating yield stress changes of A2126 and A3026 pressure vessel steels irradiated in a wide variety of neutron spectra at low temperatures (40-90°C) and low doses (< 0.1 dpa). The irradiations were performed in RTNS-II, OWR, ORR and the HFIR pressure vessel surveillance positions. The data from RTNS-II, OWR and ORR are correlated fairly well on the basis of dpa, but the data from HFIR show that only one tenth as many dpa are needed to produce the same radiation-induced yield stress changes as in the other neutron spectra. About 96% of the neutrons in the HFIR surveillance position are thermal neutrons. and a significant fraction of the displacements is produced by recoils from thermal neutron captures. The best correlation of all the data is achieved when the property changes are compared on the basis of the production of freely migrating self-interstitial defects, which better represents the defects participating in the radiation strengthening process.

PROGRESS AND STATUS

Introduction

The effects of the neutron spectrum on tensile property changes of metals at relatively low doses (< 0.1 dpa) and irradiation temperatures from 25 - 450°C have been studied in an ongoing series of experiments that includes A302B pressure vessel Steel'. Irradiations were performed with 14 MeV neutrons at the Rotating Target Neutron Source (RTNS-II) and with pool type reactor neutrons at the Omega West Reactor (OWR). A212B pressure vessel steel was later included[2] in OWR irradiations to extend the data base for the pressure vessel steel of the High Flux Isotope Reactor (HFIR), which had been observed to undergo embrittlement much sooner than original projections had predicted[3].

A2126 and A3026 have very similar compositions. especially with respect to the elements suspected of affecting embrittlement. A2126 and A3028 steels displayed the same irradiation hardening when irradiated in OWR[2], and it is reasonable to assume they will harden the same in any neutron spectrum. This assumption effectively broadens the data base for low-dose radiation-induced yield stress changes of A302B and A2128 to include four very different neutron spectra. Tensile data have been obtained for A2128 irradiated at 50°C in the HFIR pressure vessel surveillance positions and in the Oak Ridge Reactor (ORR)[3], for A2126 at 90°C in OWR[2] and for A302B at 90°C in OWR and RTNS-II[1].

In this report the radiation-induced changes in yield stress occurring in all four neutron spectra will be compared on the basis of several damage parameters. including defect production functions derived from atanistic modeling results. In making these comparisons it is assumed that A3028 and A2126 behave similarly in low-dose. low-temperature irradiations and that any differences in behavior due to the differences in irradiation temperatures (90°C and 50°C) are small.

The Neutron Spectra

Characteristics of the four neutron spectra used in the computations are listed in Table 1. The HFIR and ORR spectra were supplied by K. Farrell of Oak Ridge National Laboratory (ORNL). The HFIR spectrum is a calculated spectrum. The ORR spectrum is a modification of that for position A9 within the core. where A2126 Charpy specimens were irradiated. The tensile specimens were irradiated outside the core at P8, where the neutron spectrum is similar at high energies, but has about 70% more thermal neutrons. An additional thermal neutron contribution was added to the A9 spectrum. which was then used in the computations. The RTNS-II and OWR spectra were supplied by L. R. Greenwood of Argonne National Laboratory (ANL). The variation in neutron spectra is quite extreme: the HFIR pressure vessel surveillance flux is dominated by thermal neutrons, while the RTNS-II flux consists entirely of 14 MeV neutrons. In RTNS-II the magnitude of the neutron flux decreases with distance from the source. so doses varying by about a factor of 100 were achieved by placing specimens at increasing distances from the source during the same run. Damage rates in RTNS-II varied from 3×10^{-11} to 3×10^{-9} dpa/s, placing the damage rate of RTNS-II between that of HFIR and the other reactors.

(a) Operated for the U.S. Department of Energy by Battelle Memorial Institute under Contract DE-AC06-76RLO 1830.

TABLE 1
Characteristics of Neutron Spectra

	HFIR[a]	ORR[b]	OWR[c]	RTNS-II[d]
Total Flux (n/cm2/s)	1.2e+10[f]	1.8e+14	1.9e+14	1.0e+12
Thermal Flux Fraction	0.96	0.56	0.42	0.0
Flux Fraction (E > 0.1 MeV)	0.022	0.15	0.32	1.0
Flux Fraction (E > 1.0 MeV)	0.015	0.072	0.17	1.0
Damage Rate in Iron (dpa/s)	3.9e-13	1.9e-8	5.7e-8	3.0e-9 to 3.0e-11

a surveillance position, key 7, location 7, at pressure vessel
b location P8, outside core (based on in-core spectrum at A9)
c in core
d peak flux; fluxes in RTNS-II vary with distance from the source
f "e+10" should be read "x 10^{10}"

Damage Correlation Par ters

Meaningful comparison of mechanical property changes of materials irradiated in different neutron environments requires a damage correlation parameter that accounts for the effects of the spectrum of neutron energies in the materials. Comparing property changes on the basis of the measured fast neutron fluence (e.g. E > 1 MeV) is one attempt at incorporating spectral sensitivity, recognizing that more defects per neutron are produced by higher energy neutrons. How well this works depends on the neutron spectra involved. Clearly, damage in a largely thermal neutron spectrum, which can produce recoil atoms through thermal neutron-gamma capture reactions, is poorly represented by the fast neutron flux.

Opa is in wide use as an exposure index and as a correlation parameter. It is a measure of the average number of times an atom of the material can be displaced to a stable defect position during an irradiation, and it takes into account the energy lost to inelastic processes that cannot produce displacement damage. The displacement cross section or displacement energy cross section is calculated for the given neutron spectrum and material[4]. Calculation of dpa requires a neutron spectrum, a set of neutron reaction cross sections, a model of the kinematics of the reactions that produce primary atanic recoils. a model for the dissipation of the primary recoil energy as electronic excitation and damage energy, and a model for the conversion of damage energy into dpa.

Opa is a measure of the potential to create point defects. It is not necessarily equal to, or even proportional to, the actual number of residual point defects. The actual number of point defects present in a material at any time depends on the temperature and the material's history. including the neutron fluence. It also depends on the number of defects produced during primary damage production in the recoil events. which is dependent on the recoil energy[5].

Within a collision cascade created by a high-energy recoil, a significant fraction of the hundreds of initially produced point defect pairs (Frenkel pairs of vacant sites and self-interstitial atoms, referred to here as "vacancies" and "interstitials") will recombine as the locally high energy density in the cascade region dissipates. Of the ranaining defects, most form into clusters (the stability of which depends on the crystal temperature), while a small fraction escapes the cascade region, becoming freely migrating defects. The fractions of initially produced defects that recombine or become freely migrating defects are constant above a minimum recoil energy (on the order of 10-100 keV). At the other end of the energy scale, low-energy recoils that can create only a few isolated defect pairs do not have high enough energy density to drive significant correlated recombination or clustering; nearly all the defects produced become freely migrating defects. Thus, the efficiency of defect production relative to calculated dpa values is a function of recoil energy, becoming constant at higher energies.

Dpa can be an effective damage correlation parameter for irradiation in different neutron environments only if the property change of interest is influenced by a quantity that is proportional to dpa. Proportionality of the damage to dpa can be influenced by the rate of damage production as well as the spectrum. Since environments with different neutron spectra usually have different damage rates, failure to correlate data on the basis of dpa has often been attributed to rate effects.

For example, initial comparison[3] of HFIR pressure vessel surveillance Charpy data with reference data at higher damage rates was made on the basis of fast neutron fluence. The order-of-magnitude "accelerated

embrittlement" of the HFIR pressure vessel steel was attributed to unspecified rate effects. Comparison of the HFIR data with recent low-fluence tests by Nanstad et al. in ORR[6] showed the same accelerated embrittlement in both tensile and Charpy tests when canpared on the basis of fast fluence (and dpa obtained from the fast fluence). They concluded that the results could be explained by either rate effects or spectral effects, but not unambiguously, since the effects are concurrent and inseparable in this case.

Failure of data to correlate on the basis of dpa can be due to the importance of the more detailed spectral effects. Property changes are likely to be sensitive to the number of residual point defects. the numbers of freely migrating defects. or the numbers of defect clusters contained in collapsed displacement cascades. All of these quantities vary with the recoil spectrum and are proportional to dpa only at high recoil energies.

The existence of tensile data for these pressure vessel steels over a wide range of neutron spectra and damage rates. from RTNS-II to HFIR. provides an opportunity to investigate other spectrally sensitive quantities as correlation parameters. In an earlier consideration of these data with respect to damage rate[2], it was found that there was no apparent effect of damage rate for the CWR, ORR and RTNS-II irradiated material. Furthermore. if the "accelerated embrittlement" of the HFIR surveillance material is due to a rate effect, then this effect would be important only below a very low flux. We will examine here possible spectral effects on these steels. based on damage production functions derived from atanistic modeling results for freely migrating vacancies. freely migrating interstitials, and total residual point defect pairs.

Computations

Greenwood's SPECTER computer code[7] was used to generate the primary recoil spectra for iron into which the damage correlation functions were folded. Sane issues with regard to using this code should be discussed. The SPECTER code is not particularly well suited to cases where thermal neutrons play a large role in the damage process. For most cases for which the code was developed, thermal neutrons have been thought to have little effect. Thus. in calculating some quantities. including the recoil spectra. the code omits the contributions due to thermal neutron captures. They can easily be added manually. at least to the level of precision necessary for the present investigation. Another more serious difficulty in the computations is that the integration schemes for obtaining and utilizing the recoil spectra lead to errors on the order of 20-30% in calculating the quantities from which they were derived. The effect of this for our application is that the criteria for "correlation" must be somewhat looser than if these quantities could be calculated exactly. Nevertheless. the extreme cases of neutron spectra are so different that the effects are large, and the main points of this report are well-established.

The damage correlation functions reported in reference 8 were used. although they were originally derived fran simulations of cascades in copper. Parameter values in the expression for residual defects were modified according to Simons' prescription[5] to reflect more appropriate values for iron. The recoil energy-dependent damage functions that describe the partitioning of the residual defects into freely migrating defects and clusters were taken to be the same for iron as for copper. While the magnitudes are expected to be somewhat different for copper and iron. the recoil energy dependence of these functions should be qualitatively the same for both metals.

Results

Irradiation tenperatures for HFIR and ORR were 49°C and 43°C, respectively. while the RTNS-II and CWR irradiations were at 90°C. All the tensile tests were done on miniature tensile specimens. Those used at ORNL for HFIR and ORR were about four times larger in cross-sectional area than those for the RTNS-II and CWR tests done at PNL.

In Fig. 1 the radiation-induced yield stress changes at roan temperature in *A3028* and A2128 pressure vessel steels are plotted as a function of fast neutron fluence (E > 1 MeV) in the various irradiation environments. Each point is the result of an individual test. The hand-drawn curve is simply to aid visual organization. It is reproduced in the same position relative to the CWR data in each figure.

(At the highest dose in ORR the yield stress changes are significantly smaller than in CWR. It is possible that this difference may be due to the irradiation environment. The ORR specimens were irradiated in contact with the reactor coolant water, and it was found[3] that, despite being anodized to reduce rusting, those specimens irradiated for more than a few days displayed considerable rusting. The CWR specimens were irradiated in helium-filled capsules. However. in several of the earlier CWR runs the capsules developed leaks. and the specimens were exposed to reactor coolant water for several days or more, becoming rusty. The irradiations were redone, and both the clean and rusty specimens were tested. The rusty specimens at three fluences uniformly yielded at 70-80 MPa less than the clean specimens. No further tests have been done to determine the cause of these differences. Assuming the differences are related to the specimen surface, one expects the smaller CWR specimens to be more affected than the ORR specimens. Nevertheless. the ORR results with rusty specimens may result in somewhat lower values than expected for clean specimens.)

While the general trend of radiation hardening is observed in the data for all spectra in Fig. 1, the data can hardly be said to be well-correlated. In particular, in HFIR the fast fluence necessary to produce a yield stress change of 50 MPa is less by an order of magnitude than that in the other spectra.

In Fig. 2 the data are replotted as a function of calculated dpa. For all but HFIR, the data grouping is much tighter, being within a factor of 2 in dpa.

Fig. 3 shows the yield stress data replotted as a function of freely migrating interstitials per atom (fmipa). The number of fmipa needed to produce a yield stress change of 50 MPa in HFIR is within a factor of two of that needed in OWR, ORR and RTNS-II. Relative to their separation in the dpa plot, Fig. 2, the HFIR data have been shifted toward the WR data by a factor of 4.4.

In Fig. 4 the yield stress data are plotted as a function of freely migrating vacancies per atom (fmvpa). Relative to the dpa plot, the HFIR data are shifted toward the WR data by a factor of 14.2, which places them at a higher fmvpa level than OWR for the production of the same yield stress change.

Compared on the basis of total residual defect pairs (not shown), the tensile data for HFIR shift toward the data for the other spectra by a factor of 1.5 compared to the dpa plot.

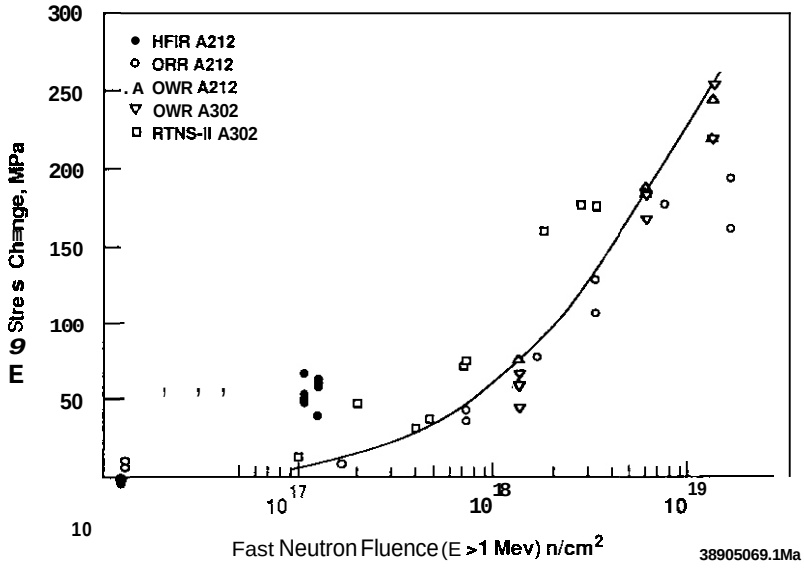

Figure 1. Change in 0.2% offset yield stress of A302B and A212B pressure vessel steels as a function of fast neutron fluence (E > 1 MeV). The hand-drawn curve is simply to aid visual organization. It is reproduced in the same position relative to the OWR data in each figure.

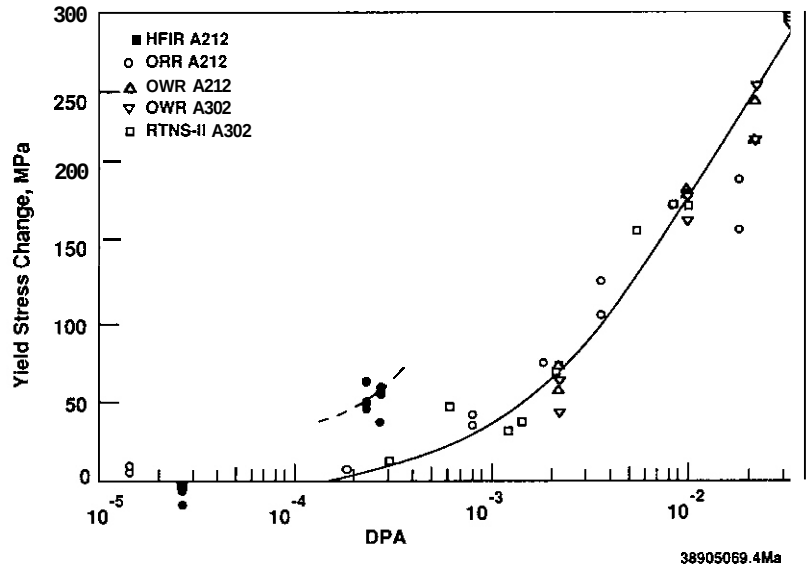

Figure 2. Change in 0.2% offset yield stress of A302B and A2128 pressure vessel steels as a function of dpa.

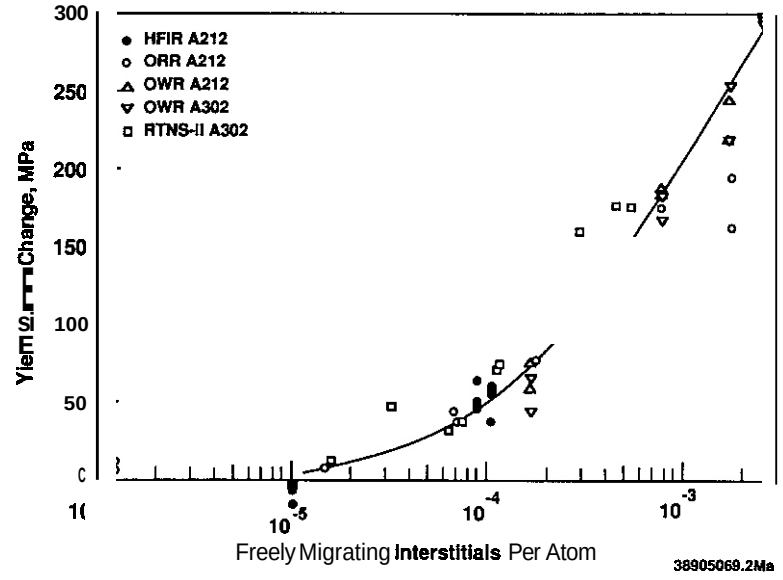

Figure 3. Change in 0.2% offset yield stress of A3026 and A2126 pressure vessel steels as a function of freely migrating interstitials per atom (fmipa).

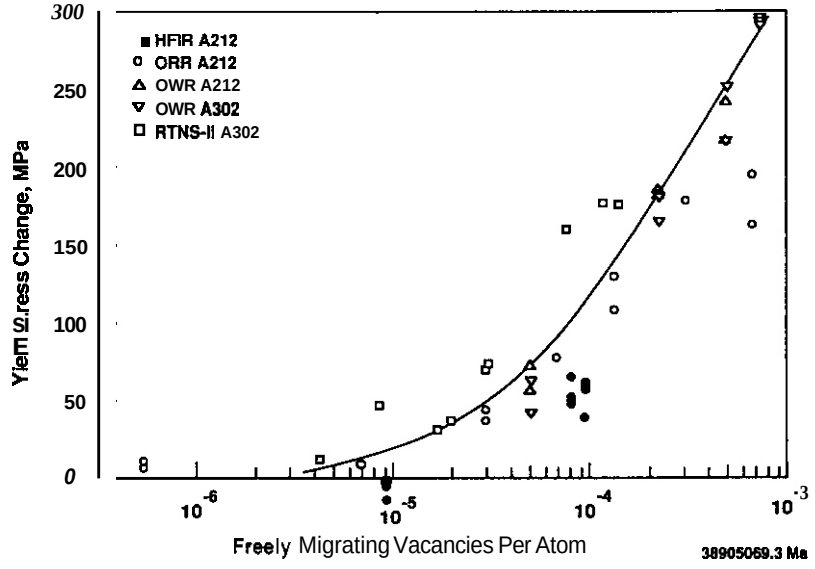

Figure 4. Change in 0.2% offset yield stress of A3028 and A212B pressure vessel steels as a function of freely migrating vacancies per atom (fmvpa).

Discussion

The best correlation of the yield stress changes of A212B and A302B pressure vessel steels irradiated in different neutron facilities is obtained when the data are compared on the basis of fmipa. Since the Charpy test data and tensile test data exhibit the same dependence on fluence^3, the same correlation will occur for mbrittlment when fmipa is used as a damage parameter.

The HFIR results show a dramatic difference relative to the results in the other spectra when fmipa or fmvpa are used as damage parameters instead of dpa. This is the result of the 96% thermal neutron spectrum at the HFIR surveillance positions, combined with the increased efficiency of freely migrating defects per dpa at low energies. Thermal neutron captures in iron produce recoils with an average energy of 395 eV, enough to make about 4 displacements per recoil. Of the displaced atoms, an average of 2.4 displaced atoms per recoil become freely migrating interstitials (according to the model used here). In contrast. a 200 keV recoil produces on average about 1100 displacements and 63 freely migrating interstitials.

The defect production functions used in these calculations were derived from binary collision simulations of collision cascades and random jump simulations of short-term annealing In copper. Parameters in the semi-Empirical annealing simulation were adjusted such that the fractions of freely migrating defects inferred from experiments were reproduced for non-interacting higher energy cascades (where they are independent of recoil energy). The energy dependence of freely migrating defect production was determined by modeling the annealing of thousands of cascades over a wide range of energy. Thus, the shapes of the defect production curves are a consequence of the Initial spatial distributions of the defects. Cascades In Iron have a slightly more diffuse character compared to cascades In copper because of the relatively more open bcc crystal structure. The efficiency of producing residual defects is higher in iron than copper (40% vs 30%). However, the two metals should exhibit the same relative energy dependence of free defect production because increased efficiency at lower energies is due more to the small number of defects produced than the details of the energy density.

Yarious types of microscopic analyses provide good evidence that the increases in yield stress and Embrittlement of A2128 irradiated in HFIR and ORR are due to irradiation hardening Involving hardening centers too small to be imaged by transmission electron microscopy[3]. Post-irradiation annealing studies on A2128[3] showed no significant annealing below 300°C. Thus, at irradiation temperatures below 100°C small clusters are expected to be relatively stable.

Hardening centers can consist of defect clusters formed both immediately within cascades and by diffusion of the freely migrating defects. The freely migrating defects can recombine, go to existing sinks, form clusters or form complexes with Interstitial impurities. Effectiveness of pure vacancy or interstitial clusters as hardening centers depends on the size of the clusters, although observations show that no clusters are very large. If pure interstitial or vacancy clusters are the primary source of hardening, then the data should correlate well on the basis of total residual point defects (especially if cluster sire distributions are about the same). but they do not. Impurity complexes may be the most effective hardening Centers. This is consistent with the successful correlation of the tensile data on the basis of freely migrating defects.

Since pure vacancy and interstitial clusters probably contribute to the hardness, the best damage correlation parameter would be a properly weighted canbination of freely migrating interstitials and clusters produced directly In cascades. Additional experimental information or more extensive modeling will be necessary to determine the optimum combination for use as a damage function.

The above arguments suppose the effects of damage rate are not important. Indeed, there is no evidence of damage rate effects In tensile data in the range from 3×10^{-11} to 2×10^{-8} dpa/s[2]. A damage rate effect would have to be significant only at a threshold rate somewhat less than 10^{-11} dpa/s. Irradiations of these pressure vessel steels to low doses in a very high flux of thermal neutrons would help determine whether spectral or rate effects are responsible for the behavior observed in the HFIR surveillance specimens.

REFERENCES

1. H. L. Heinisch. "Effects of the Neutron Spectrum on Mechanical Property Changes in Low Dose Irradiations," J. Nuc. Mater. 155-157, 121 (1988).

2. M. L. Hamilton and H. L. Heinisch, "Tensile Properties of Neutron Irradiated A212B Pressure Vessel Steel." Proceedings of the 14th ASTM International Symposium on Radiation Effects in Metals, Andover, MA, June 27-29, 1988.

3. "Evaluation of HFIR Pressurevessel Integrity Considering Radiation Embrittlement." R. D. Cheverton, J. G. Merkle and R. K. Nanstad. eds.. ORNL/TM-10444 (1987).

4. D. G. Doran and N. J. Graves. "Displacement Cross-sections and PKA Spectra: Tables and Applications." HEDL-TME 76-70 (1976).

5. R. L. Simons, "Evaluation of Defect Production Cross Sections and Calculated Fission-fusion Neutron Spectrum Sensitivity." J. Nuc. Mater. 141-143, 665 (1986).

6. R. K. Nanstad, K. Farrell, D. N. Braski and W. R. Corwin, "Accelerated Neutron Embrittlement of Ferritic Steels at Low Fluence: Flux and Spectrum Effects," J. Nuc. Mater. 158, 1 (1988).

7. L. R. Greenwood and R. K. Smither, "SPECTER: Neutron Damage Calculations for Materials Irradiations." ANL/FPP/TM-197 (1985).

8. H. L. Heinisch and F. M. Mann, "Neutron Cross Sections for Defect Production by High Energy Displacement Cascades in Copper." J. Nuc. Mater. 122-123, 1023 (1984).

5. RADIATION EFFECTS: MECHANISTIC STUDIES, THEORY, AND MODELING

TENSILE BEHAVIOR AND SWELLING OF TERNARY AUSTENITIC ALLOYS IRRADIATED IN DIFFERENT NEUTRON SPECTRA,
M. L. Hamilton (Pacific Northwest Laboratory), A. Okada (Hokkaido University), and F. A. Garner (Pacific Northwest Laboratory)

OBJECTIVE

The objective of this effort is to explore the influence of composition, irradiation environment and neutron energy spectra on radiation-induced microstructural evolution and associated changes in tensile properties.

SUMMARY

Two nominally identical experiments designed to study the effects of nickel level, chromium level and helium generation rate on the microstructural development and tensile properties of Fe-Cr-Ni alloys are currently undergoing examination. One of these, conducted in DRR at a higher He/dpa rate and a lower displacement rate compared to the other experiment in EBR-II, shows substantially more strengthening and a different temperature range of swelling. The effects of irradiation temperature, neutron flux and neutron spectra appear to be larger than those of the compositional variations studied. Transmission electron microscopy (TEM) examination is in progress to determine the origin of the observed changes.

PROGRESS AND STATUS

Introduction

In the early stages of the U.S. Fusion Materials Program, a number of irradiation tests designed for high exposures were inserted into three U.S. reactors, the Experimental Breeder Reactor II (EBR-II), the Oak Ridge Research Reactor (ORR) and the High Flux Isotope Reactor (HFIR). While most of the current fusion-relevant irradiations are being conducted in the Fast Flux Test Facility (FFTF), some of these earlier experiments continue to be examined.

Of current interest are two experiments which were designed to be comparable and which explored the influence of composition (primarily the nickel level) and helium on radiation-induced changes in tensile behavior of Fe-Cr-Ni ternary alloys. One experiment, designated AD-1,[1] was irradiated in EBR-II and produced relatively low He/dpa levels while the other, designated MFE-4,[2] was irradiated in ORR, yielding much higher levels of helium.

Whereas at first glance it appears that the primary variation between the two experiments was in the helium/dpa ratio, further examination reveals that the EBR-II test was conducted at a displacement rate that was almost an order of magnitude higher than that in ORR. It has recently been recognized that differences in displacement rate can have a strong influence on the evolution of radiation-induced microstructure in general and the incubation period of swelling in particular. Void swelling is in turn a major contributor to changes in tensile properties.

Since these experiments were designed, other insights have been gained that add to the complexity of the interpretation of these two experiments. While it was recognized that nickel variations would lead to differences in helium generation rate, particularly in mixed spectrum reactors such as ORR, it was not known at that time that the recoil of the ^{56}Fe atom from the ^{59}Ni (n,α) reaction could lead to substantial increases in displacement rate.[3] Thus the displacement levels attained in ORR are not only larger than was anticipated when the experiment was designed, but vary as a function of nickel content, the major variable in the experiment. In addition, it appears that displacements associated with (n,γ) events may also influence damage production disproportionately.[4] Thus, the "effective" displacement dose in the ORR experiment may be larger than anticipated.

AD-1 Experiment

This test utilized only subsize flat tensile specimens, 0.76 mm (0.030 in.) thick with a gauge width and length of 1.52 and 20.3 mm (0.060 in. and 0.80 in.), respectively. The specimens were in the annealed condition (954°C/15min/AC). Five alloys were irradiated which form a compositional 'crossroads" with Fe-34.5Ni-15.1Cr (weight percent) at the center; the nickel varies from 24.4 to 45.3 weight percent about the center and the chromium content from 7.5 to 21.7 weight percent (see Table 1).

Three groups of thirty tensile specimens (six identical specimens for each of the five compositions) were irradiated in each of three pins, designated 8284, 8285 and 8286. Pin 8284, designed to run at 394°C, spent the latter portion of its residence in EBR-II in row 5 after beginning irradiation in row 2, while the other two pins, 8285 (450°C) and 8286 (550°C), spent all of their residence in row 2. The fluence accumulated by 8284 is therefore somewhat less than that accumulated by the other two pins. The subcapsules containing the tensile specimens were located in level 0 of the pin, the center of which was 19.8 cm (7.8 in.) above the core midplane. Thus the specimens straddled the core upper boundary and resided in a region where the flux

TABLE 1

Alloys Used in AD-1 and MFE-4 Experiments(a)

Alloy	Composition, wt%	AD-1 Tensile	MFE-4 TEM Disk	MFE-4
E19	Fe-19.7Ni-14.7Cr	--	SA	--
E20	Fe-24.4Ni-14.9Cr	SA	SA,CW	SA
E21	Fe-30.1Ni-15.1Cr	--	SA	--
E22	Fe-34.5Ni-15.1Cr	SA	SA,CW	SA
E23	Fe-45.3Ni-15.0Cr	SA	SA	SA
E37	Fe-35.5Ni-7.5Cr	SA	SA	--
E38	Fe-35.1Ni-21.7Cr	SA	SA	SA

(a) SA - solution annealed.
CW - 30% cold worked.

gradient was rather steep. The fluence level at the center of the gauge length of the specimens at 395°C was 2.1 x 10^{22} n cm^{-2} and was 2.5 x 10^{22} n cm^{-2} at the other two temperatures. This corresponds to 9.5 and 11.3 dpa, respectively.

The centers of the gauge lengths of some of the tensile specimens were used to prepare microscopy specimens which will be examined later, while other identical specimens were used to measure changes in density, the latter being an average of the density changes over the entire length of the specimen. Selected specimens were also used for tensile tests. In an earlier publication[5] the results of tensile tests were presented for specimens irradiated and tested at 450°C. In the subsequent study reported here, tests on identically irradiated companion specimens were conducted at room temperature, and identical room temperature tests were performed on specimens irradiated at 395 and 550°C. All tensile tests were conducted at a strain rate of 4 x 10^{-4} sec^{-1}. Yield strengths were calculated at 0.2% offset.

MFE-4 Exoeriment

This test utilized both TEM disks and subsize tensile specimens, although the dimensions of the latter were somewhat different from those of the AD-1 experiment. They were SS-2 specimens, with a 12.7 mm (0.5 in.) and 1.0 mm (0.040 in.) gauge length and width, respectively, and a thickness of 0.25 mm (0.010 in.). The TEM disks were in a condition consisting of 30% cold work followed by an anneal at 950°C/15m/AC. Two additional alloys, E19 (20% Ni, 15% Cr) and E21 (30% Ni, 15%Cr), were also included in the TEM matrix and two alloys, E20 (25% Ni, 15% Cr) and E22 (35% Ni, 15%Cr), were also included in the 30% cold worked condition. The tensile specimen matrix in the MFE-4 test contained one less alloy than the AD-1 experiment, with E37 (7.5% Cr, 35% Ni) missing. The tensile specimens were given the same annealing treatment as the disks after having been 40% cold worked.

Specimens were irradiated at four temperatures (330, 400, 500, and 600°C) in the ORR MFE-4A/4B spectral tailoring experiments. The two lowest temperatures were reached in the 4A experiment in ORR position E3 and the two highest temperatures were attained in the 4B experiment in position E7. Initially the experiments produced helium via the two-step thermal neutron reactions involving ^{58}Ni and ^{59}Ni. After a lengthy exposure the experimental canisters were placed into a hafnium core piece to reduce thermal neutron flux by about 50%, thereby reducing the helium production rate while permitting continued displacement damage. This procedure allowed the damage rate and helium generation rate to be nearly constant throughout the entire experiment. Depending on the nickel levels of the alloys, the displacement levels ranged from 13.4 to 14.3 dpa in the 330 and 400°C canisters and 12.2 to 13.1 dpa in the 500 and 600°C canisters. The displacement and helium levels are given in Table 2. Since earlier studies showed that the threshold for steady state swelling is about 10 dpa,[7] relatively large differences in swelling may occur for small changes in displacement levels close to 10 dpa. To emphasize these differences, the calculated dpa levels, which would ordinarily be listed with only two significant figures, have been given to three significant figures.

TEM disks were used for both density measurements and electron microscopy, the latter of which is currently ongoing. Tensile tests were conducted on the tensile specimens under the same conditions as the tests performed on the AD-1 soecimens.

TABLE 2

Displacement and Helium[a] Levels in the MFE-4 Experiment

Alloy	330 & 400°C dpa	330 & 400°C He, appm	500 & 600°C dpa	500 & 600°C He, appm
E19	13.4	371	12.2	332
E20	13.6	463	12.4	414
E21	13.8	555	12.6	495
E22	14.0	647	12.7	513
E23	14.3	832	13.1	740

(a) Calculated using elemental contributions tabulated in Reference 6.

Results

Density Chanaes. The swelling results from the two experiments are compared in Figures 1 and 2. The average swelling at 395 and 450°C along the length of the AD-1 tensile specimens exhibits the trends observed in other EBR-II irradiations,[7,8] decreasing with increasing nickel or temperature and increasing with increasing chromium. Due to the displacement gradient and the threshold for swelling mentioned earlier, it is expected that the swelling in the gauge region is lower than the average. At 550°C the 11.3 dpa level achieved does not exceed the incubation fluence at that temperature and therefore no measurable swelling was observed.

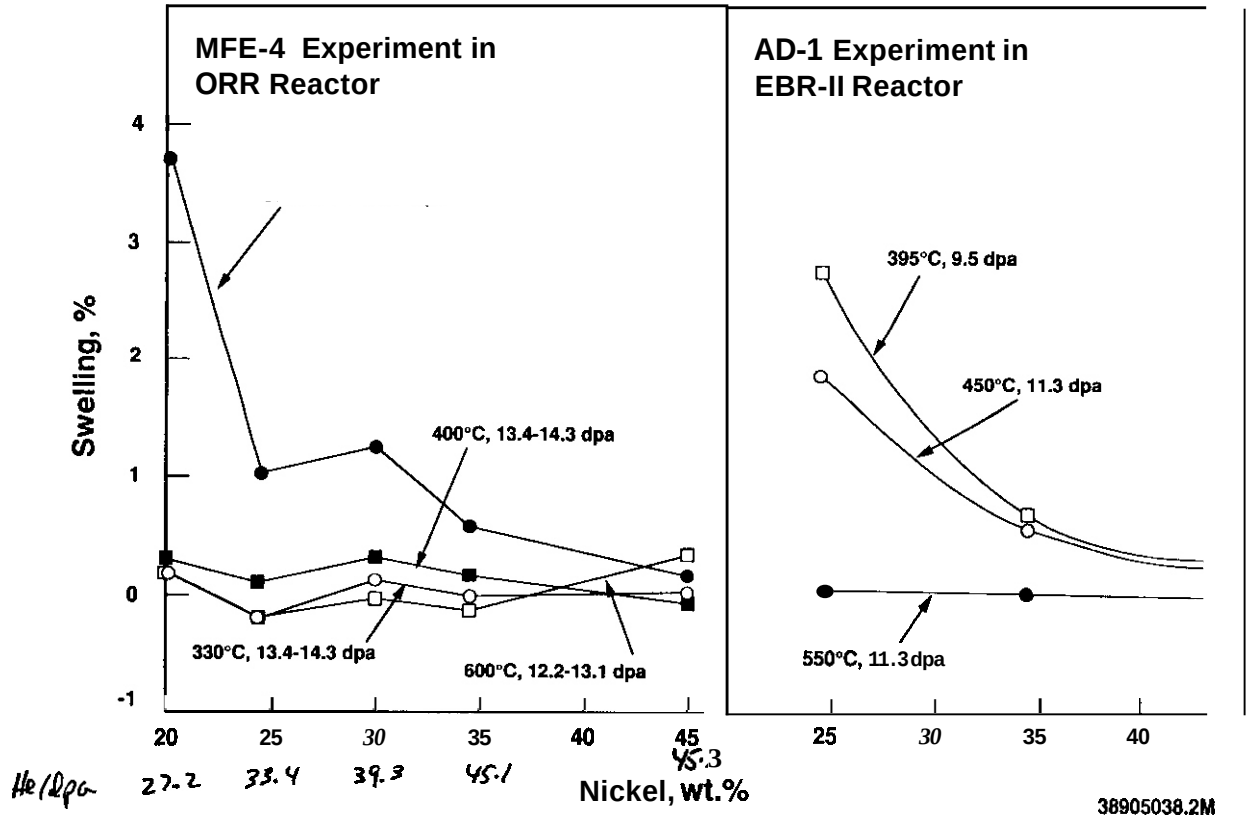

Figure 1. Comparison as a function of nickel content of the swelling of Fe-Cr-Ni alloys in the MFE-4 and AD-I experiments

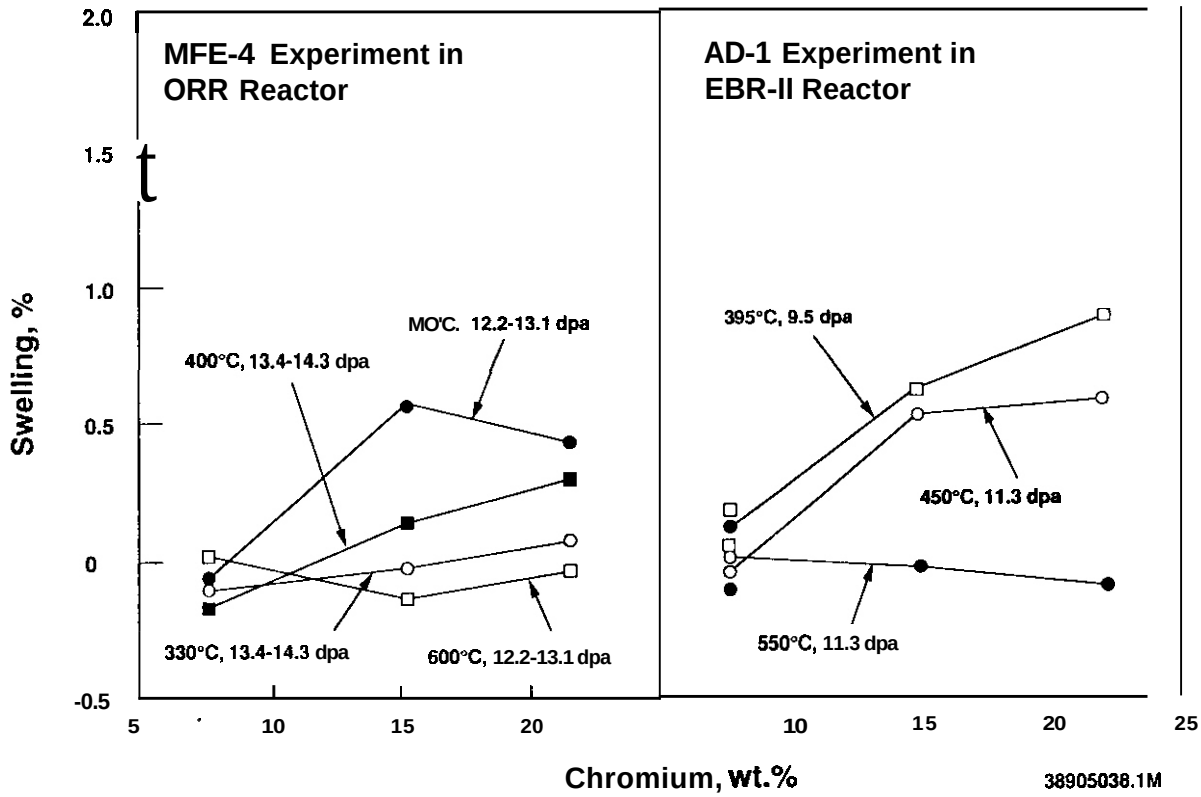

Figure 2. Comparison as a function of chromium content of the swelling of Fe-Cr-Ni alloys in the MFE-4 and AD-1 experiments

The MFE-4 results are somewhat different, however. Significant swelling was found only at 500°C and was suppressed for both higher and lower temoeratures. At 500°C the swelliny in general decreased as expected with nickel. An unanticipated non-monotonic response was observed around 30% nickel at all four temperatures and is therefore probably not an artifact, reflecting possibly some differences in chromium level or in minor solutes

The data given in Table 3 show the influence of cold work on swelling. At 500°C, where swelling is very clearly occurring, cold work reduced swelling in Fe-15Cr-25Ni from 1.04 to 0.21% and in Fe-15Cr-35Ni from 0.55 to -0.11%. At the other temperatures, where the swelling is low and near the resolution limit (±0.16%), the effect of cold work is not well defined. Negative values of density change, particularly for the Fe-15Cr-35Ni alloy, may reflect densification associated with spinodal-like decomposition rather than measurement uncertainty.[9]

Tensile Properties. The tensile data from the two experiments are given in Tables 4 and 5. The strength and ductility data are shown as a function of composition in Figures 3 and 4 for both the AD-1 and MFE-4 experiments. Each plot shows the response to both nickel and chromium variations. The effect of nickel and chromium are also shown separately in subsequent comparisons of the MFE-4 and AD-1 data.

The strength of these alloys (Figure 3) in the unirradiated condition increases slightly with both increasing nickel and chromium. This trend is reproduced with only two exceptions in the irradiated condition in the AD-1 specimens: 1) at the lowest chromium level and an irradiation temperature of 550°C the yield (but not the ultimate) strength is somewhat higher than what would be expected from the trends exhibited by the rest of the data, and 2) the yield strength trend is actually reversed as a function of nickel for irradiation at 394°C. Such a reversal is more frequently observed in the strength data from the MFE-4 experiment, where it appears in both the yield and ultimate strengths for all except the highest irradiation temperature. The strength data exhibit a "knee" in the vicinity of the 35Ni level, where something is apparently changing in the response of these alloys to increased nickel content during irradiation in ORR. The ductility data (Figure 4) also exhibit a "knee" at the intermediate nickel level, at all irradiation temperatures in MFE-4 and in both the irradiated and unirradiated conditions in AD-l.

TABLE 3

Density Data from the MFE-4 Experiment

	Swelling, %			
	Fe-25Ni-15Cr		Fe-35Ni-15Cr	
Temperature, °C	SA	CW	SA	CW
330	0.21	0.15	-0.05	-0.10
400	0.04	0.04	0.14	-0.06
500	1.04	0.29	0.55	-0.11
600	-0.21	0.16	-0.14	-0.07

The ductility of the specimens irradiated in the AD-1 experiment (Figure 4) remained relatively high after irradiation, the only exception being for irradiation at the lowest temperature, 394°C. Conversely, in the MFE-4 experiment, only specimens irradiated at the highest temperature (600°C) retained significant ductility after irradiation. Almost every irradiation condition in MFE-4 at temperatures below 600°C produced close to a total loss in ductility. Only the 45Ni level at 500°C exhibited more than about 5% ductility.

The difference between uniform and total elongation appears to be a fairly constant value, roughly 5%, for all specimens irradiated in the AD-1 experiment, regardless of composition and irradiation temperature. In contrast, the difference between the uniform and total elongation values in the specimens irradiated in MFE-4 is generally smaller, varying from values approaching zero to only as much as 2 or 3%. Similar behavior is observed in the data obtained on unirradiated specimens tested as controls for each experiment.

Since the only difference in the control data between the two experiments is the specimen geometry, particularly the specimen thickness, the ductility data raise a question about the validity of the thinner specimens used in the MFE-4 experiment. Figure 5, however, demonstrates that both the uniform and total elongations obtained from the two types of control specimens are roughly equal, suggesting that the ductility data from the MFE-4 specimens are indeed valid, at least where relatively large levels of ductility are involved. It is nonetheless possible that for low levels of ductility, for example following irradiation under conditions which induce significant microstructural hardening, that the geometry of the MFE-4 specimens predisposes early failures due to the sensitivity of brittle materials to any type of stress concentration.

The irradiation-induced increase in yield strength is shown in Figure 6 as a function of nickel and chromium levels for both the MFE-4 and the AD-1 experiments. Increases in the chromium level generally produce increases in the change in yield strength, particularly with decreased irradiation temperature, in both experiments, while the effect of nickel is just the opposite.

The yield strength changes observed in AD-1 at 394 and 550°C are almost identical to those produced at 500 and 600°C in MFE-4 (Figure 7), suggesting that significantly more strengthening is produced during irradiation in ORR than in EBR-II. This is shown more definitively in Figure 8, where changes in yield strength are shown to be linear as a function of irradiation temperature in AD-1 and strongly nonlinear in MFE-4.

Discussion

It appears that irradiation variables such as temperature, neutron flux and spectra lead to larger variations in alloy response than do the compositional variables in these two experiments. It is difficult at this time to determine the reasons for either these differences or the additional strengthening observed in the MFE-4 experiment relative to the AD-1 experiment. While the MFE-4 experiment reached slightly higher displacement levels, its swelling levels are not larger. Void swelling, known to be a major contributor to radiation-induced strengthening, cannot therefore be solely responsible for the differences.[10] The dislocation microstructure is known to saturate relatively quickly at ~500°C[11] and one would not expect large differences in dislocation density in the 11 to 14 dpa range. While the higher helium levels of the MFE-4 experiment may contribute to a refinement of the void and Frank loop microstructures, thereby causing more strengthening, the lower displacement rate of MFE-4 would tend to produce less refinement. The possibility may exist that the additional strengthening arises from some previously unforeseen aspect of the damage created by (n,α) recoil events. These and other issues can only be addressed after electron microscopy examinations are performed.

TABLE 4

Tensile Data from the MFE-4 Experiment

$\dot{\varepsilon} = 4 \times 10^{-4}\ sec^{-1}$

Specimen ID	Irradiation Temp (°C)	Test Temp (°C)		YS (MPa)	UTS (MPa)	True UTS (MPa)	UE (%)	TE (%)	Average ΔYS (MPa)
25Ni - 15Cr									
JL28	--	RT		125	422	623	47.5	49.0	
JL29	--	RT		147	448	661	47.5	48.5	--
			Ave:	136	435	642	47.5	48.8	
JL00	330	RT		776	777	780	0.4	2.0	
JL03	330	RT		776	811	814	0.4	2.2	640
			Ave:	776	794	797	0.4	2.1	
JL06	400	RT		690	715	718	0.4	2.2	
JL10	400	RT		716	750	753	0.4	2.4	567
			Ave:	703	733	736	0.4	2.3	
JL13	500	RT		612	655	672	2.6	3.0	
JL15	500	RT		604	673	689	2.4	3.2	472
			Ave:	608	664	681	2.5	3.1	
JL19	600	RT		241	451	632	40.0	42.0	
JL21	600	RT		243	479	646	35.0	37.5	106
			Ave:	242	465	639	37.5	39.8	
35Ni - 15Cr									
JN25	--	RT		142	461	676	46.5	46.5	
JN28	--	RT		142	457	663	45.0	48.0	--
			Ave:	142	459	668	45.7	47.2	
JN00	330	RT		759	776	778	0.3	2.2	
JN04	330	RT		759	773	776	0.4	2.4	617
			Ave:	759	774	777	0.4	2.3	
JN06	400	RT		690	715	718	0.4	2.4	
JN09	400	RT		724	750	753	0.4	2.2	565
			Ave:	707	733	736	0.4	2.3	
JN13	500	RT		629	683	701	2.6	3.6	
JN15	500	RT		604	663	690	4.0	6.0	475
			Ave:	617	673	696	3.3	4.8	
JN19	600	RT		237	439	525	19.5	20.0	
JN20	600	RT		250	487	666	36.8	37.5	
JN22[a]	600	RT		--	--	--	--	--	102
			Ave:	244	463	596	28.6	28.8	
45Ni - 15Cr									
JP16	--	RT		151	479	682	42.5	46.0	
JP18	--	RT		155	457	651	42.5	45.0	
JP27	--	RT		147	461		4 .0	45.5	--
			Ave:	151	466	664	42.7	45.5	
JP01	330	RT		750	793	796	0.4	3.0	599

(a) Test invalid.

TABLE 4

(continued)

Specimen ID	Irradiation Temp (°C)	Test Temp (°C)		YS (MPa)	UTS (MPa)	True UTS (MPa)	UE (%)	TE (%)	Average ΔYS (MPa)
45Ni-15Cr, (continued)									
JP04	400	RT		669	697	757	8.6	9.0	
JP06	400	RT		672	707	728	3.0	4.4	520
			Ave:	671	702	743	5.8	6.7	
JP09	500	RT		586	656	708	8.0	9.6	
JP10	500	RT		552	638	702	10.0	12.8	418
			Ave:	569	647	705	9.0	11.2	
JP13	600	RT		248	474	607	28.0	29.0	
JP15	600	RT		259	502	648	29.0	29.5	103
			Ave:	254	488	628	29.0	29.3	
35Ni - 20Cr									
JR25	--	RT		181	535	762	42.5	43.5	
JR29	--	RT		185	535	759	42.0	43.0	--
			Ave:	183	535	760	42.3	43.3	
JR00	330	RT		931	965	969	0.4	2.2	748
JR07	400	RT		862	863	866	0.4	2.0	
JR10	400	RT		897	896	900	0.4	2.0	697
			Ave:	880	880	883	0.4	2.0	
JR13	500	RT		724	785	813	3.6	5.2	
JR14	500	RT		698	768	806	5.0	6.2	528
			Ave:	711	777	810	4.3	5.7	
JR19	600	RT		322	591	783	32.5	33.5	
JR21	600	RT		323	560	668	19.3	19.5	140
			Ave:	323	576	726	25.9	26.5	

TABLE 5

Tensile Data from the AD-1 Experiment

$\dot{\varepsilon} \sim 4 \times 10^{-4}\ sec^{-1}$

Specimen ID	Irradiation Temp (°C)	Test Temp (°C)		YS (MPa)	UTS (MPa)	True UTS (MPa)	UE (%)	TE (%)	Average ΔYS (MPa)
25Ni - 15Cr									
X06	--	RT		138	441	636	44.3	48.7	
X12	--	RT		134	450	665	47.7	52.7	
			Ave:	136	446	651	46.0	50.7	
X50	394	RT		619	627	630	0.5	5.2	483
X13	550	RT		212	453	611	34.9	38.7	76
X14	--	450		96	319	421	31.9	36.0	--
X25	450	450		373	373	374	0.3	4.2	277
35Ni - 15Cr									
AA15	--	RT		140	449	631	40.6	44.6	
AA11	--	RT		139	445	643	44.5	47.4	
			Ave:	140	447	637	42.6	46.0	
AA47	394	RT		607	634	675	6.2	10.3	467
AA27	450	RT		457	547	632	15.6	20.0	317
AA02	550	RT		226	472	636	34.9	38.1	86
AA12	--	450		90	375	509	35.8	38.5	--
AA24	450	450		384	422	426	1.0	1.7	294
45Ni - 15Cr									
AB02	--	RT		190[a]	473	675	42.7	46.8	
AB05	--	RT		153	474	675	42.4	46.2	--
			Ave:	153	474	675	42.6	46.5	
AB21	394	RT		584	670	733	9.4	13.5	431
AB03	550	RT		238	500	686	37.1	41.2	85
AB15	--	450		103	374	497	32.8	36.3	
AB16	--	450		102	397	528	33.0	35.8	--
			Ave:	103	386	513	32.9	36.1	
AB30	450	450		413	486	526	8.3	11.4	310
35Ni - 20Cr									
AN09	--	RT		177	491	699	42.4	45.9	
AN15	--	RT		182	506	708	39.9	43.7	--
			Ave:	180	499	705	41.2	44.8	
AN35	394	RT		670	737	783	6.2	10.2	490

(a) YS value probably invalid.

TABLE 5

(continued)

Specimen ID	Irradiation Temp (°C)	Test Temp (°C)		YS (MPa)	UTS (MPa)	True UTS (MPa)	UE (%)	TE (%)	Average ΔYS (MPa)
AN54	450	RT		509	614	728	18.6	23.1	329
AN28	550	RT		292	546	723	32.5	36.8	112
AN06	--	450		129	412	556	35.0	37.5	
AN17	--	450		132	420	560	33.4	36.5	--
			Ave:	131	416	558	34.2	37.0	
AN61	450	450		418	473	508	7.5	9.8	287
35Ni - 7Cr									
AE16	--	RT		142(a)	408	574	40.6	45.5	
AE21	--	RT		126	407	576	41.5	46.5	--
			Ave:	126	408	575	41.1	46.0	
AE34	394	RT		540	598	636	6.4	10.2	414
AE26	550	RT		244	430	540	25.6	29.3	118
AE09	--	450		62	303	387	27.7	30.6	--
AE60	450	450		350	512	525	2.5	5.9	288

(a) YS value probably invalid

CONCLUSIONS

Two nominally similar experiments directed toward assessing the effects of composition and helium were irradiated in reactors which possessed different neutron spectra and displacement rates. Differences attributable to the reactor environment were seen in both the bulk swelling and the tensile properties. The effects of irradiation temperature, neutron flux and neutron spectra appear to be larger than those of the compositional variations studied. The most surprising result is that a significantly higher level of radiation-induced strengthening was found in the ORR experiment. The explanation for such behavior is not obvious and awaits examination of the microstructure.

FUTURE WORK

Comparison will be made between the tensile and disk bulge tests conducted on the MFE-4 specimens. Microscopy on both the AD-1 and MFE-4 specimens will be completed.

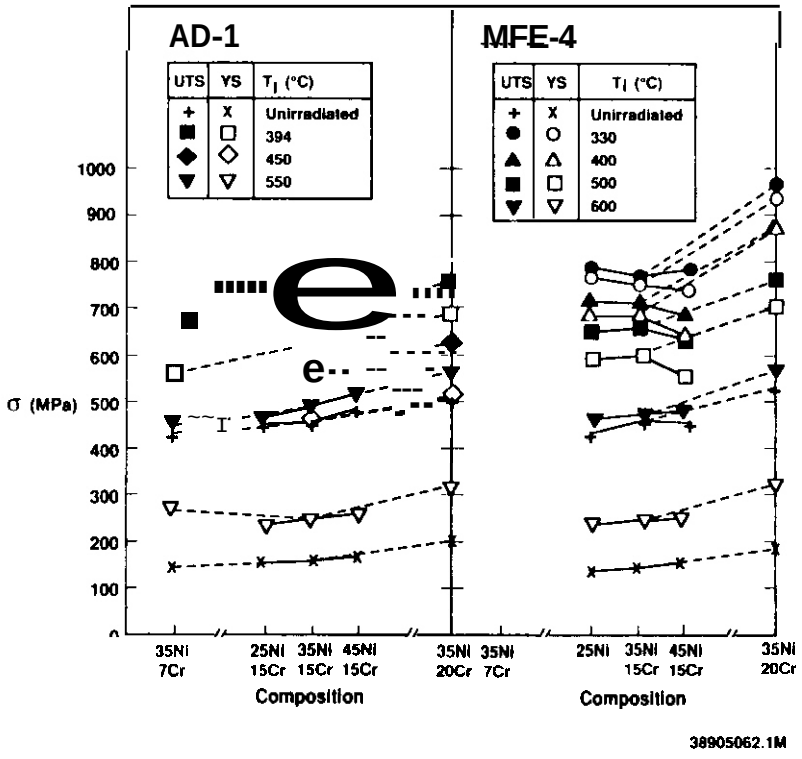

Figure 3. Tensile strength of ternary alloys irradiated in the MFE-4 and AD-1 experiments (solid line denotes nickel variations, dotted 1ine denotes chromium variations)

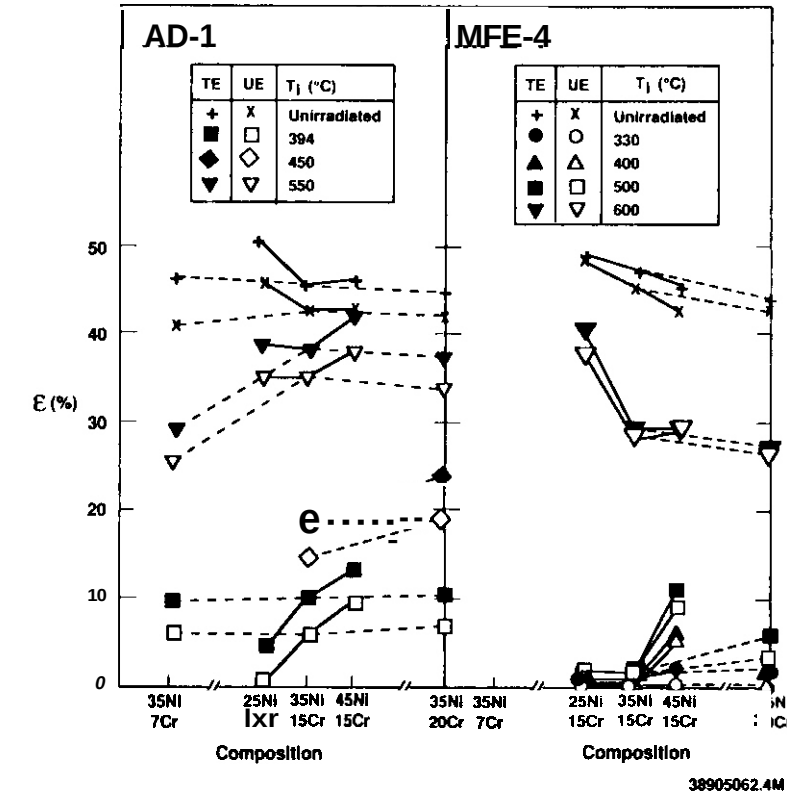

Figure 4. Ductility of ternary alloys irradiated in the MFE-4 and AD-1 experiments

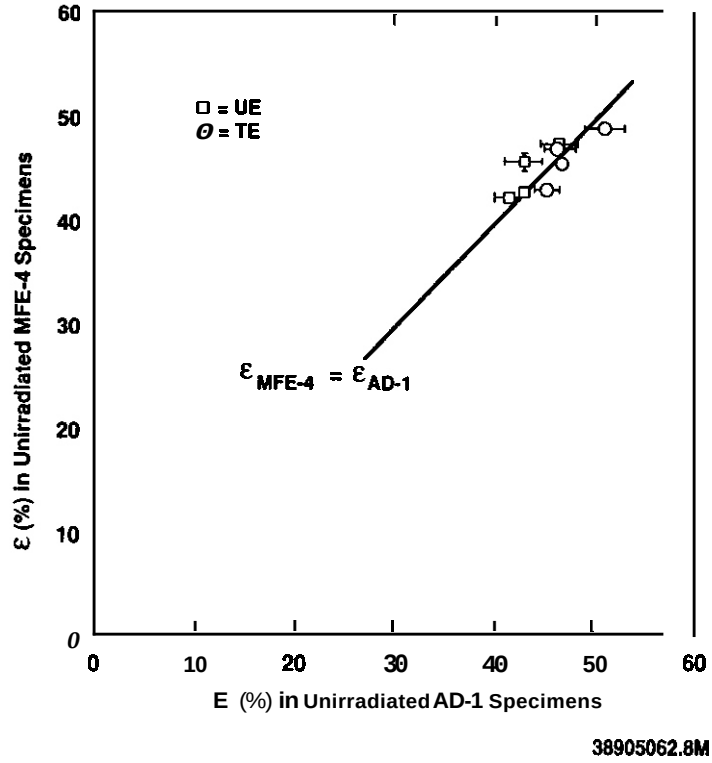

Figure 5. Comparison of strains obtained on unirradiated specimens in the MFE-4 and AD-1 specimen geometries (error bars omitted when the width of the bar is smaller than the data point itself)

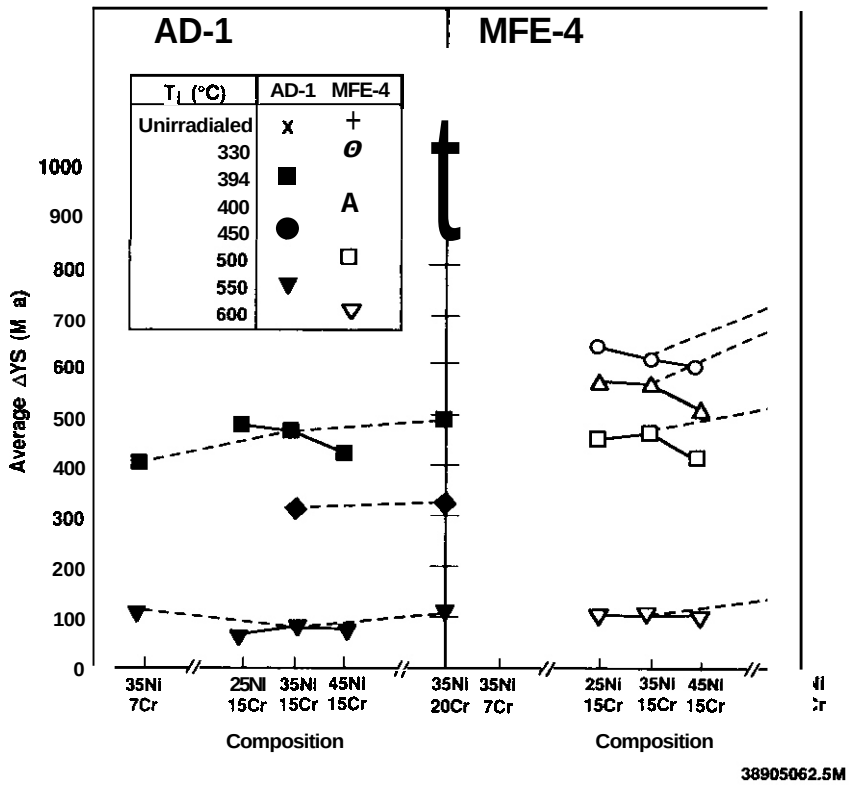

Figure 6. Yield strength changes observed in MFE-4 and AD-l

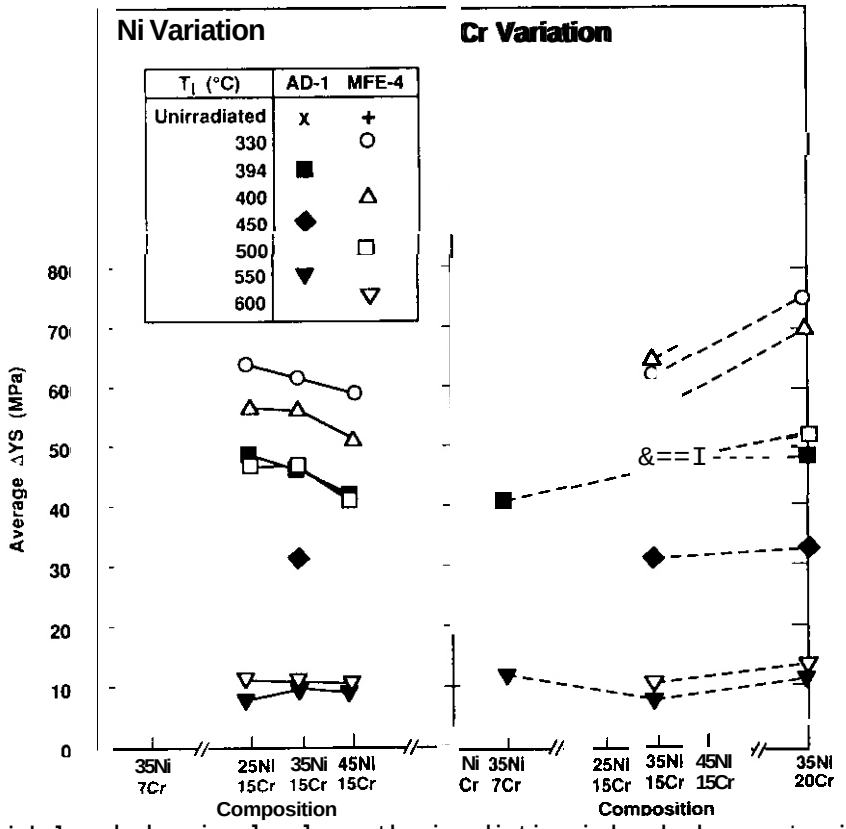

Figure 7. Effect of nickel and chromium levels on the irradiation-induced changes in yield strength in MFE-4 and AD-I

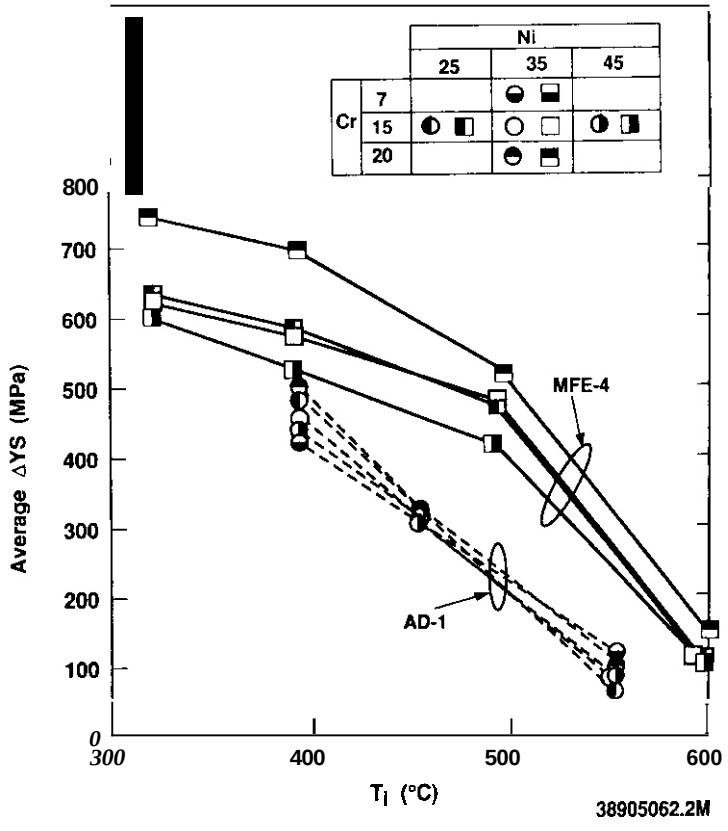

Figure 8. Change in yield strength as a function of irradiation temperature for MFE-4 and AD-I

References

1. O. T. Peterson and J. A. Sprague, "Status of the AD-1 Irradiation Test," Damage Analysis and Fundamental Studies Quarterly Progress Report, January-March 1980, DOE/ER-0046/1, pp. 238-241.

2. D. T. Peterson and R. W. Powell, "DAFS Specimen Matrix for the ORR MFE-IV Test," ibid, pp. 242-245.

3. L. R. Greenwood, J. Nucl. Mater., 115 (1983) pp. 137-142.

4. F. A. Garner, H. L. Heinisch, R. L. Simons and F. M. Mann, "Implications of Neutron Spectrum and Flux Differences in Fission and Fusion Correlations at High Neutron Fluence," PNL-SA-15704A, presented at a Workshop on Effects of Recoil Spectrum and Nuclear Transmutations on the Evolution of Microstructure, Lugano, Switzerland, March 24-29, 1988.

5. H. R. Brager, F. A. Garner, and M. L. Hamilton, J. Nucl. Mater., 133 & 134 (1985). pp. 594-598.

6. Letter report, "Displacement and Helium Levels for ORR-MFE-4A/4B," from L. R. Greenwood to M. Grossbeck dated July 8, 1987.

7. F. A. Garner and H. R. Brager, in Effects of Radiation on Materials: Twelfth International Symposium, ASTM STP 870, F. A. Garner and J. S. Perrin, Eds., American Society for Testings and Materials, Philadelphia, 1985, pp. 187-201.

8. F. A. Garner and A. S. Kumar, in Radiation-Induced Changes in Microstructure: 13th International Symposium (Part 1), ASTM STP 955, F. A. Garner, N. H. Packan and A. S. Kumar, Eds., American Society for Testing and Materials, Philadelphia, 1987, pp. 289-314.

9. F. A. Garner, H. R. Brager, and J. M. McCarthy in Ref. 8, pp. 775-787.

10. F. A. Garner, M. L. Hamilton, N. F. Panayotou and G. D. Johnson, J. Nucl. Mater., 103 & 104 (1981), pp. 803-808.

11. T. Muroga, F. A. Garner and S. Ohnuki, "Microstructural Investigation of the Mechanism of Swelling Dependence on Nickel Content in Fast Neutron-Irradiated Fe-Cr-Ni Austenitic Ternaries," Annual Progress Report for Fusion Year 1988, Monbush-DOE Collaboration in Fundamental Studies of Irradiation Effects in Fusion Materials Utilizing Fission Reactors, in press.

RADIATION-INDUCED SPINODAL-LIKE DECOMPOSITION OF Fe-Cr-Ni ALLOYS AND ITS INFLUENCE ON ELECTROPOLISHING OF MICROSCOPY DISKS - J. M. McCarthy and F. A. Garner, Pacific Northwest Laboratory

OBJECTIVE

The object of this effort is to provide an understanding of the factors which control the radiation-induced evolution of microstructure in structural alloys.

SUMMARY

Scanning electron microscopy was used as a tool to investigate the dependence on nickel content of radiation-induced spinodal-like decomposition in Fe-15Cr-XNi alloys. It appears that the relative resistance to swelling observed in the Invar compositional regime at 510°C is concurrent with spinodal-like decomposition. The influence of this phenomenon in prolonging the loop-dominated phase of dislocation evolution and also suppressing the onset of accelerated void growth has not yet been determined.

PROGRESS AND STATUS

Introduction

In an earlier report Muroga, Garner and Ohnuki discussed the influence of nickel content on the radiation-induced microstructural evolution of Fe-15Cr-XNi alloys in EBR-II.[1] Their results showed that void nucleation at 510°C, as evidenced by its saturation density, was influenced strongly by nickel content but that the saturation void number density at any given nickel level was reached well before 10 dpa was attained. Whereas earlier charged particle irradiation studies at higher temperatures showed that the end of the transient regime of swelling was related to the attainment of the saturation void density,[2] the results at 510°C in EBR-II showed that the duration of the transient regime was not only sensitive to nickel content but in general was much longer than 10 dpa. Microstructural analysis showed that the duration of the transient regime appeared to be related not to void nucleation but to void growth, apparently restrained during the transient regime by the relative persistence of the loop-dominated phase of dislocation evolution. This persistence seemed most strong in the 30-35 wt% nickel range.

To describe the compositional dependence of loop evolution, one must consider all of the factors which govern loop nucleation and growth, loop unfaulting and subsequent dislocation-loop interactions. Such a description will involve the compositional dependence of many physical properties such as stacking fault energy, shear modulus and diffusivity, as well as the compositional dependence of radiation-induced processes such as segregation and atomic ordering, both of which are known to occur on the surfaces of Frank loops in neutron-irradiated Fe-Ni alloys.[3,4]

There is one other phenomenon known to influence the behavior of these alloys; namely, radiation-induced spinodal-like decomposition.[5,6,7] This process leads to large three-dimensional oscillations in composition on a microscopic scale, with nickel acting as one species and iron and chromium acting as another. The consequences of this phenomenon on diffusivity, physical properties and loop growth and stability have yet to be fully explored.

The spinodal-like decomposition appears to occur in the Invar compositional range (30-37 wt% nickel) and was first discovered at relatively high irradiation temperatures (600 to 750°C).[5] More recently, however, such decomposition has been observed in Fe-35.5Ni-7.5Cr irradiated to 12 dpa at 550°C in EBR-II and in Fe-35Ni-0Cr irradiated to 14 dpa at 520°C in *FFTF*.[7] This suggests that decomposition may also have occurred in the 510°C study of Muroga and coworkers.[1] Since the wavelength of the decomposition decreases as the irradiation temperature decreases, it is difficult to determine the presence of such micro-oscillations using X-ray dispersive energy analysis (EDS). It was shown in an earlier report,[7] however, that one consequence of such decomposition is a selective electropolishing in which the low-nickel areas are preferentially attacked. To investigate this possibility, scanning electron microscopy was used to observe the surfaces of the electropolished microscopy disks examined by Muroga and his coworkers.

Results and Discussion

At 510°C and 2.0 x 10^{22} n cm^{-2} (E >0.1 MeV) or ~10 dpa the surfaces of Fe-15Cr-XNi (X ≅ 15, 19, 21, 30, 35, 45, 75) were observed. All specimens were polished using the same procedure. As shown in Figure 1, only the Fe-34.5Ni-15Cr alloy displays the surface irregularity associated with spinodal-like decomposition. Figure 2 shows micrographs of this alloy at higher magnification. Note in Figure 2 that grain boundaries, which tend to segregate nickel at the expense of the adjacent regions, tend to be preferentially attacked. The attack actually proceeds in the nickel-depleted regions on each side of the boundary rather than directly on the boundary.

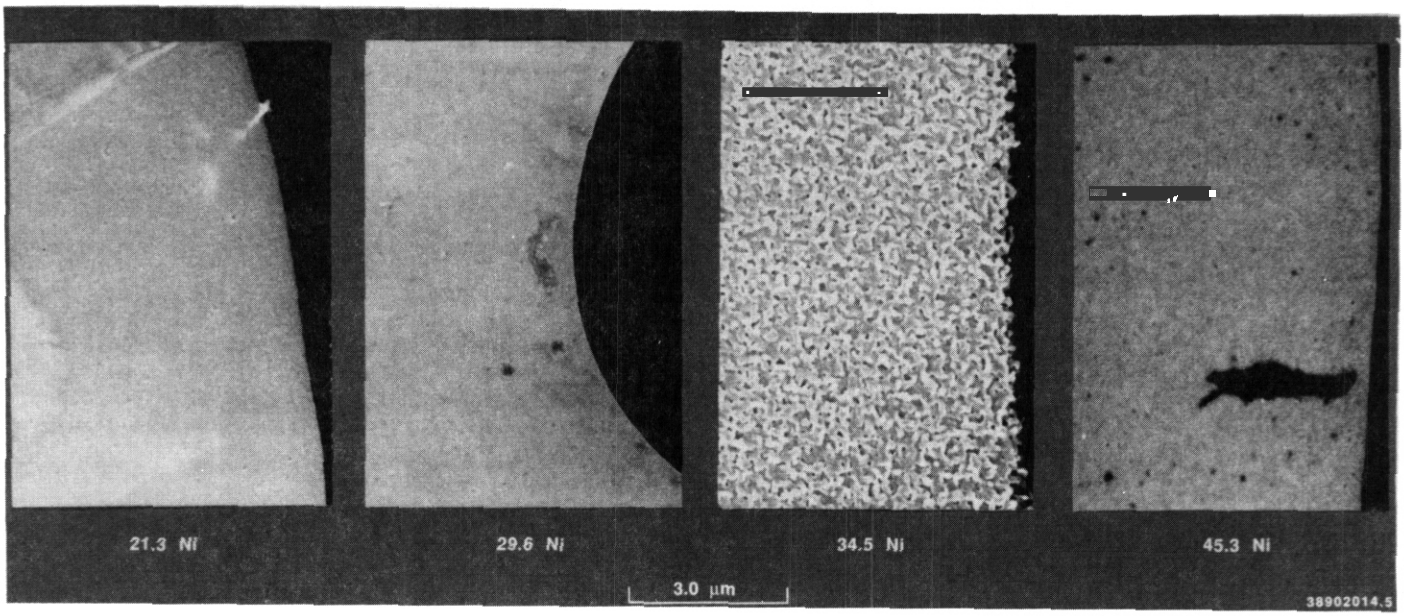

Figure 1. Influence of Nickel Content on Electropolished Surfaces of Fe-15Cr-XNi Alloys Irradiated to ~10 dpa in EBR-II at 510°C

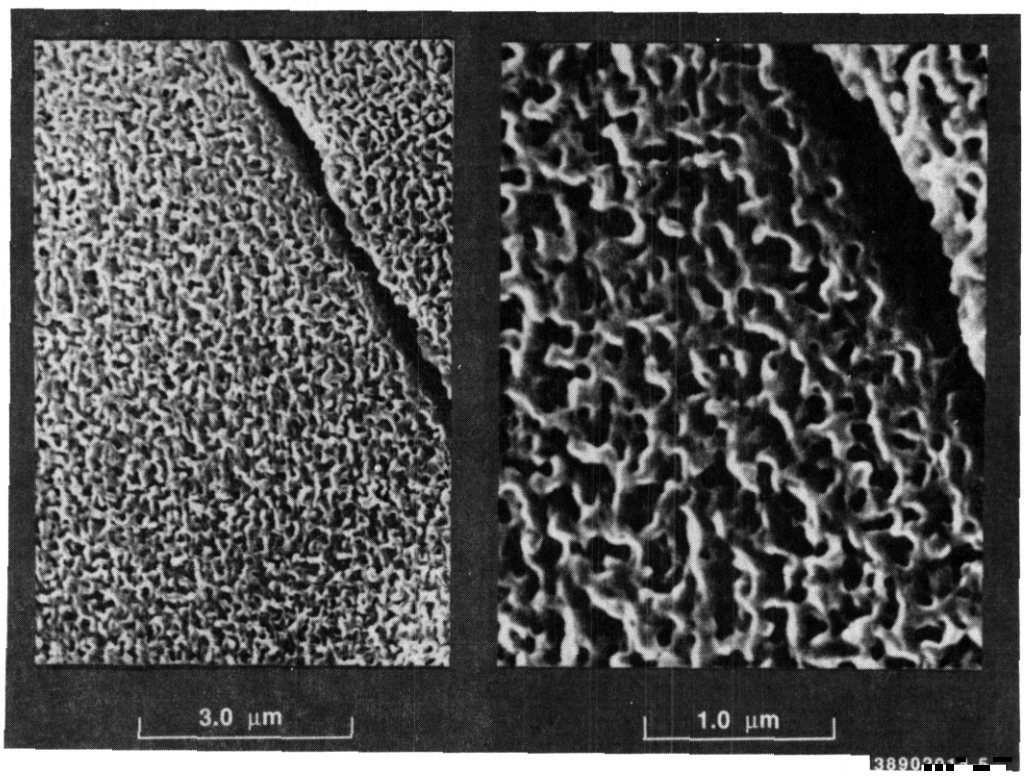

Figure 2. Irregular Electropolishing of Irradiated Fe-15Cr-34.5Ni. Severe attack has occurred on the grain boundary in the upper right corner, causing a canyon to form.

At 510°C and higher fluences, 5.3 and 7.3 x 10^{22} n cm^{-2} (E >0.1 MeV), preferential polishing was not observed in the Fe-34.5Ni-15Cr alloy, however, suggesting that either the selective electropolishing phenomenon is sensitive to some currently uncontrolled variable or that the micro-oscillations subside when swelling begins. As shown in Figure 3, the surfaces of the polished foils at three higher exposure levels are relatively flat. Swelling increases from essentially zero at 2 x 10^{22} n cm^{-2} to 0.2% and 1.8% at 5.3 and 7.3 x 10^{22} n cm^{-2}, with the near-surface voids visible under the scanning conditions employed, as also shown in Figure 3.

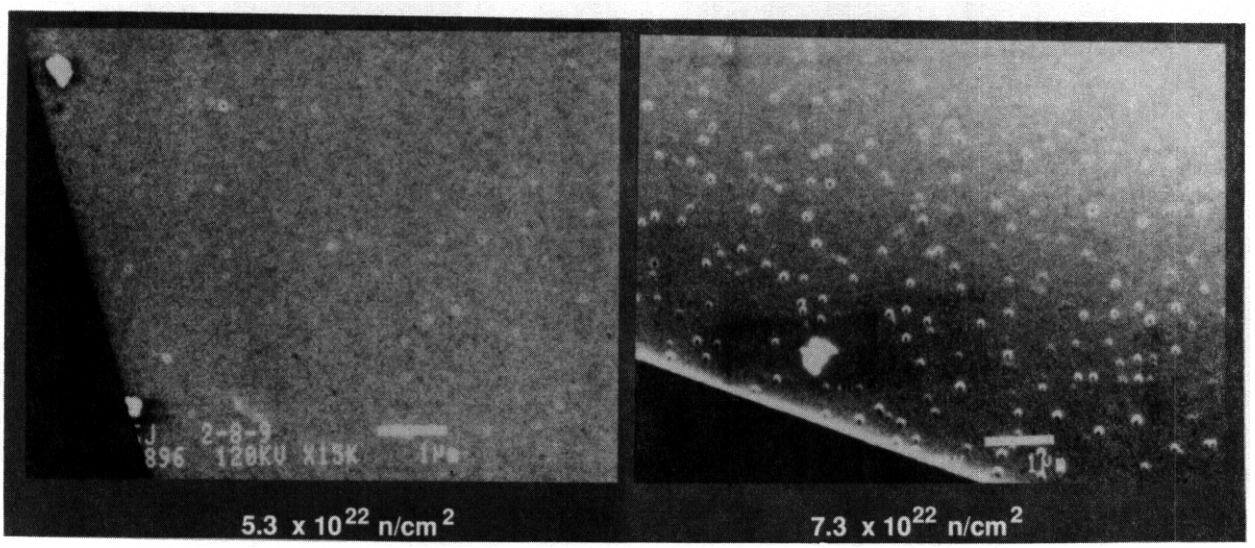

Figure 3. SEM Micrographs of Fe-15Cr-34.5Ni Irradiated at 510°C to Higher Fluence Levels

Observation of the surfaces of the Fe-15Cr-45Ni alloy were also performed at 5.3 and 7.3 X 10^{22} n cm^{-2} at 510°C, 4.1 x 10^{22} n cm^{-2} at 482°C and 5.4 X 10^{22} n cm^{-2} at 649°C. No preferential polishing was observed in any of these specimens.

CONCLUSIONS

Spinodal-like decomposition was observed to occur in Fe-34.5Ni-15Cr alloy under the one exposure condition where void swelling was restrained. It was not observed at other exposure levels or compositions.

Although the role played by the spinodal-like decomposition of Invar alloys is as yet unidentified, the possibility exists that it affects the void evolution and the related relative persistence of loop microstructure. At this time it can only be said that the two phenomena occur concurrently.

FUTURE WORK

This study will continue, utilizing specimens irradiated in FFTF.

References

1. T. Muroga, F. A. Garner, and S. Ohnuki, "Microstructural Investigation of Swelling Dependence on Nickel Content in Neutron-Irradiated Fe-Cr-Ni Austenitic Ternaries" in Annual Progress Report for Fusion Year 1988, Monbusho-DOE Collaboration in Fundamental Studies of Irradiation Effects in Fusion Materials Utilizing Fissfon Reactors, in press.

2. W. A. Coghlan and F. A. Garner in Radiation-Induced Chanses in Microstructure: 13th International Symposium (Part 1) ASTM STP 955, F. A. Garner, N. H. Packan and A. S. Kumar, Eds.; American Society for Testing and Materials, Philadelphia, 1987, pp. 315-329.

3. J. Pauleve, A. Chamberod, K. Krebs, and A. Marchand, IEEE Trans. Vol. MAG-2, No. 3 (1966) p. 475.

4. G. Silvestre, A. Silvent, C. Regnard and G. Sainfort, J. Nucl. Mater., 57 (1975) p. 125.

5. F. A. Garner, H. R. Brager, R. A. Dodd and T. Lauritzen, Nucl. Inst. Meth. 816 (1986) pp. 244-250.

6. R. A. Dodd, F. A. Garner, J.-J. Kai, T. Lauritzen, and W. G. Johnston, in ref. 2, pp. 758-784.

7. F. A. Garner, H. R. Brager, and J. M. McCarthy, in ref. 2, pp. 775-787.

MICROSTRUCTURAL EXAMINATION OF A REACTOR-IRRADIATED DILUTE COPPER-BORON ALLOY — S. J. Zinkle (Oak Ridge National Laboratory)

OBJECTIVE

To compare the microstructural response of a dilute copper-boron alloy and pure copper subjected to fission neutron irradiation over an extended temperature range. The high levels of helium generated in the copper-boron alloy during irradiation can be used to study a number of interesting phenomena important for radiation effects modeling.

SUMMARY

An initial microstructural examination has been performed on copper specimens containing ~20 wt ppm B that were irradiated with fission neutrons to ~1.2 dpa at a damage rate of 2×10^{-7} dpa/s. A bimodal size distribution of cavities was observed for the irradiation temperatures of 182 through 500°C as a result of the generation of 100 appm He during the irradiation. Stacking fault tetrahedra were also observed at all irradiation temperatures. Comparison with pure copper specimens irradiated in the same capsule revealed several interesting differences in the microstructure — namely, a slight enhancement in the cavity and SFT density at all temperatures, and the presence of voids at 182°C in the copper-boron specimens.

PROGRESS AND STATUS

Introduction

Copper has been the subject of numerous radiation effects studies.[1] A recent series of high-dose experiments[2-4] have provfded valuable information about the electrical and mechanical properties and the microstructural development in copper and its alloys at neutron irradiation temperatures of 385 to 450°C. Several lower dose experiments (1 to 5 dpa) have examined the microstructure[5] and tensile properties[6] of copper following neutron irradiation at temperatures of 182 to 500°C.

The effect of helium on the microstructural development of irradiated copper is deserving of further study. Single ion irradiation experiments[7] have determined that low-oxygen, high-purity copper does not exhibit resolvable void formation for irradiation temperatures of 100 to 500°C, whereas substantial void swelling occurs when helium is coimplanted during irradiation.[8] Several researchers have investigated neutron-irradiated copper-boron alloys as a means to study helium effects.[9-14] Both helium and lithium are produced in boron-bearing alloys during neutron irradiation due to the thermal neutron reaction $^{10}B(n,\alpha)^{7}Li$. According to the published[15] phase diagram for Cu-Li, the solid solution solubility limit for Li in copper is >10 at. % for temperatures of 200 to 800°C. The previous copper-boron neutron irradiation experiment~~were conducted at reactor ambient temperatures (60 to 100°C) with irradiation doses <0.1 dpa. Postirradiation annealing at temperatures of 400 to 1000°C was employed to produce resolvable helium bubbles. This sequence of experimental conditions is not particularly relevant for a detailed study of helium effects under fusion reactor conditions. The present study examines the microstructure of a copper-boron alloy irradiated at doses of ~1.2 dpa at temperatures of 182 to 500°C, where ~100 appm He was generated during the irradiation.

Experimental Procedure

Pure copper was arc melted in an argon atmosphere with B_4C powder (—325 mesh size) enriched with 92% ^{10}B. The copper-boron alloy was turned and remelted several times to ensure homogeneity, then cold pressed and cold rolled with intermediate vacuum anneals to a foil thickness of 0.5 mn. Transmission electron microscopy (TEM) of the as-fabricated alloy did not reveal the presence of any second-phase particles. The chemical analysis of the alloy is given in Table 1. The chemical analysis indicated that only a small amount of the B_4C powder was incorporated into the alloy during the melting. Disks of dimensions 3.2 mn diam by 0.28 mm thick were annealed in vacuum for 1 h at 550°C prior to the irradiation. The disks were irradiated along with pure copper specimens[5] in nine separate helium-filled, temperature-controlled capsules in the B8 site of the Oak Ridge Research (ORR) reactor for a period of 14 weeks. The nine irradiation temperatures varied from 182 to 500°C. Details of the neutron fluence and temperature measurements are given elsewhere.[5] The damage rate was ~2×10^{-7} dpajs. The respective total, thermal, and fast neutron fluences were ~3.7, 1.2. and 1.2 $\times 10^{25}$ n/m^2. This produced a calculated damage level of ~1.2 dpa in all of the specimens. The helium concentration in the disks following irradiation was measured[16] to be 107 ± 5 appm. According to neutron activation analysis techniques, this helium concentration is also equal to the initial concentration of ^{10}B in the alloy since >99% of the ^{10}B isotope would have transmuted to helium in a thermal fluence of 1.2×10^{25} n/m^2. The total boron content in the as-fabricated alloy was therefore 116 appm (18 wt ppm) since the ^{10}B enrichment level was 92%. The microstructure of the irradiated specimens was examined with TEM. Foil thicknesses were determined from stereo-pair and thickness fringe measurements.

Table 1. Chemical analysis of copper-boron alloy

Impurity	(wt ppm)	Impurity	(wt ppm)
Ag	20	Mo	<1
Al	3	Na	1
B	<900[a]	Ni	10
C	320	P	<1
Ca	3	S	1
Cl	1	Si	1
Co	<1	Sn	<3
Cr	3		
Fe	20	V	1
K	1	Zn	<1
Mg	1	Zr	<1
Mn	1	O	48
		N	6

[a]The boron content was measured to be 18 wt ppm by neutron activation analysis techniques (see text).

Results

Cavity formation was observed at all of the irradiation temperatures (182 to 500°C) employed in this study. All of the observable radiation-induced defects (cavities, SFT. etc.) were homogeneously distributed throughout the foil. There was no evidence of any "damage halos" that have been observed in other studies[14,17,18] of neutron-irradiated metals containing boron particles. The absence of observable boron particles and damage halos indicates that the boron contained in the copper alloy was either in solution or else contained in sub-microscopic precipitates. Figure 1 shows an example of void formation in a copper-boron specimen irradiated at 182°C. The presence of cavities in this specimen may be contrasted with the result of no observable void formation in pure copper specimens irradiated at 182°C in the same irradiation capsule.[5]

The cavities exhibited a bimodal size distribution at all irradiation temperatures. According to the established theory on helium-assisted cavity swelling,[19] the maximum radius of the smaller size group is an approximate measure of the critical radius for the conversion of helium bubbles to bias-driven cavity growth. Figure 2 shows the distinct bimodal cavity microstructure of a copper-boron specimen irradiated at 350°C.

OWL-PHOTO-0626-88

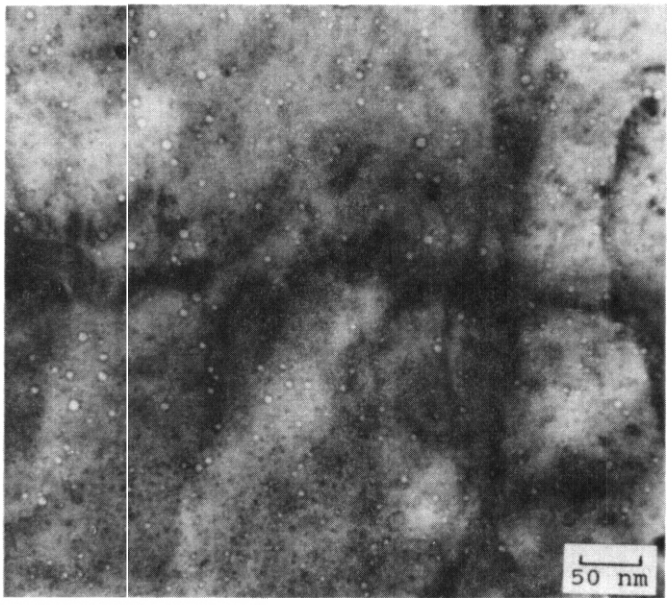

Fig. 1. Void formation in a copper-boron specimen irradiated at 182°C.

ORNL-PHOTO-4851-89

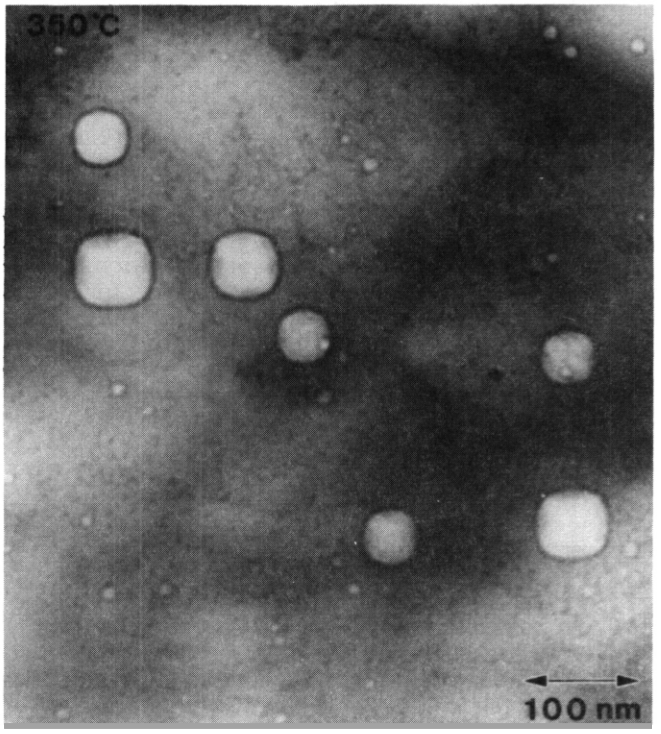

Fig. 2. Bimodal distribution of cavities observed in a Cu-B specimen irradiated at 350°C.

Table 2 lists the measured void and helium bubble parameters for specimens irradiated at temperatures between 182 and 500°C. Microstructural analysis of copper-boron specimens irradiated at 275 and 300°C is still in progress and further analyses are being performed at all temperatures. The critical radius was estimated to be equal to the maximum size observed in the smaller size portion of the bimodal cavity distribution. The void density in the copper-boron specimens was greater than that observed in the pure copper specimens[5] at all irradiation temperatures. The measured cavity parameters obtained from the study of the pure copper specimens are listed in Table 3 for comparison. The void density decreased rapidly with increasing irradiation temperature for temperatures above 400°C, in agreement with the pure copper result.

Table 2. Void and helium bubble parameters for irradiated copper-boron specimens

Temperature (°C)	Void Density (m^{-3})	Void Diameter (nm)	Bubble Density (m^{-3})	Bubble Diameter (nm)	Critical Radius (nm)
182	1.0×10^{22}	3.2	?	<3	1
220	2.5×10^{21}	9.2	?	<4	1.2
250	7.3×10^{20}	16	?	<4	2.5
350	7×10^{19}	70	6×10^{20}	6	>5
400	2×10^{18}	130	1×10^{21}	6	>5
450	$<3 \times 10^{14}$	?	4×10^{20}	3.2	>10
500	$<1 \times 10^{14}$	~4000	3×10^{20}	9.5	>10

Table 3. Void parameters for irradiated copper (from ref. 5)

Temperature (°C)	Density (10^{18}/m)	Mean Diameter (nm)	TEM ΔV/V (%)	Density Change (%)
182	-	-	0	-0.05
220	146	19	0.06	0.08
250	155	28	0.23	0.34
275	66	46	0.38	0.56
300	65	45	0.37	0.49
350	38	49	0.35	0.55
400	1.8	140	0.26	0.26
450	0.1	400	0.2	0.18
500	<0.01	-	-	0.00

The decrease in the helium bubble density was less pronounced over this temperature range and was accompanied by a gradual increase in the mean bubble size.

The regions near grain and twin boundaries were observed to be devoid of cavities. Figure 3 shows the void microstructure near several twin boundaries in a copper-boron specimen irradiated at 250°C. The width of the void-denuded zone (measured from the grain or twin boundary) varied from <0.1 μm at 182°C to ~2 μm at 400°C. These denuded zone widths are in good agreement with the values measured in the companion pure copper specimen.[5] Helium bubble formation was also found to be suppressed in the near vicinity of grain and twin boundaries. However, the effective denuded zone width for helium bubbles was typically about 20% of the corresponding void-denuded zone width. Table 4 sumarizes the temperature-dependent denuded zone width measurements obtained for voids and helium bubbles in the irradiated copper-boron alloys. Figure 4 shows the bubble and void microstructure near a grain boundary in a copper-boron specimen irradiated at 400°C. Figure 5 shows the measured size and density of helium bubbles as a function of distance from grain boundaries for a specimen irradiated at 350°C. Bubbles lying on the grain boundary were larger than bubbles in the grain interior, whereas the occasional bubbles lying in the low-density denuded zone near the grain boundary were smaller than matrix bubbles.

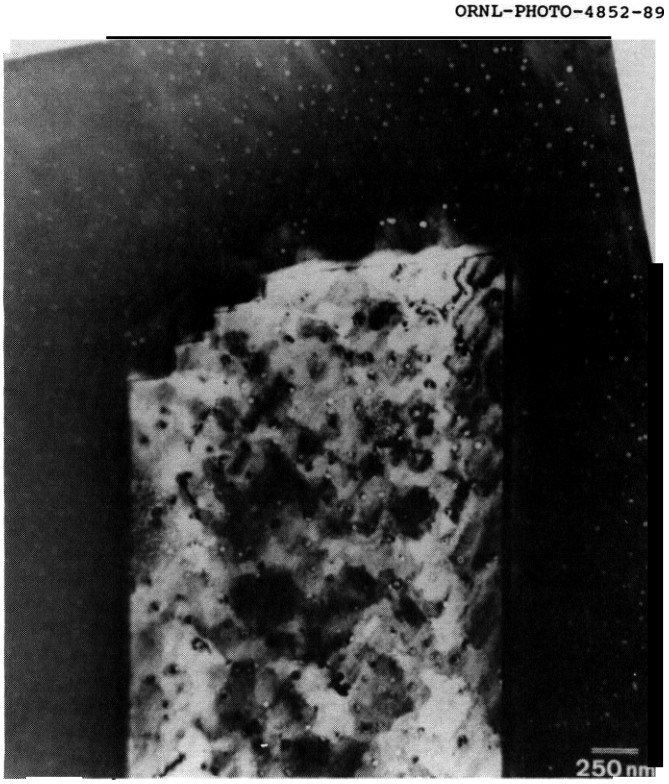

Fig. 3. Void microstructure adjacent to a twinned region in Cu-B irradiated at 250°C.

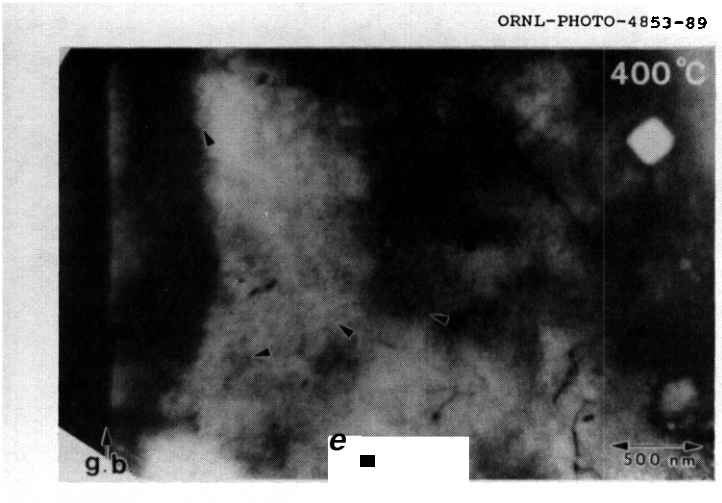

Fig. 4. Helium bubble and void denuded region adjacent to a grain boundary in a Cu-B specimen irradiated at 400°C.

Table 4. Measured widths of cavity and SFT-denuded zones near grain and twin boundaries in irradiated copper-boron specimens

Temperature (°C)	Denuded zone width, nm		
	Void	Bubble	SFT
182	< 100	--	<lo
250	120	-20	~20
350	1200	200	--
400	2000	400	600
500	--	700	700

Stacking fault tetrahedra (SFT) and dislocation loops were observed at all irradiation temperatures along with the cavities. Figure 6 shows the defect microstructure in a specimen irradiated at 182°C under diffraction contrast (left) and absorption (right) conditions A high density of SFT was present in the Cu-B alloy irradiated at 182°C; despite the high density of cavities that are

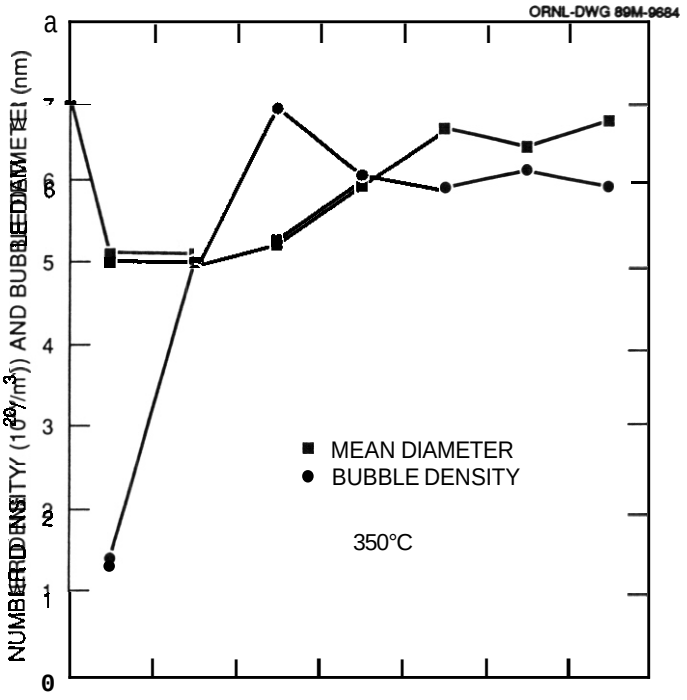

ORNL-PHOTO-0627-88

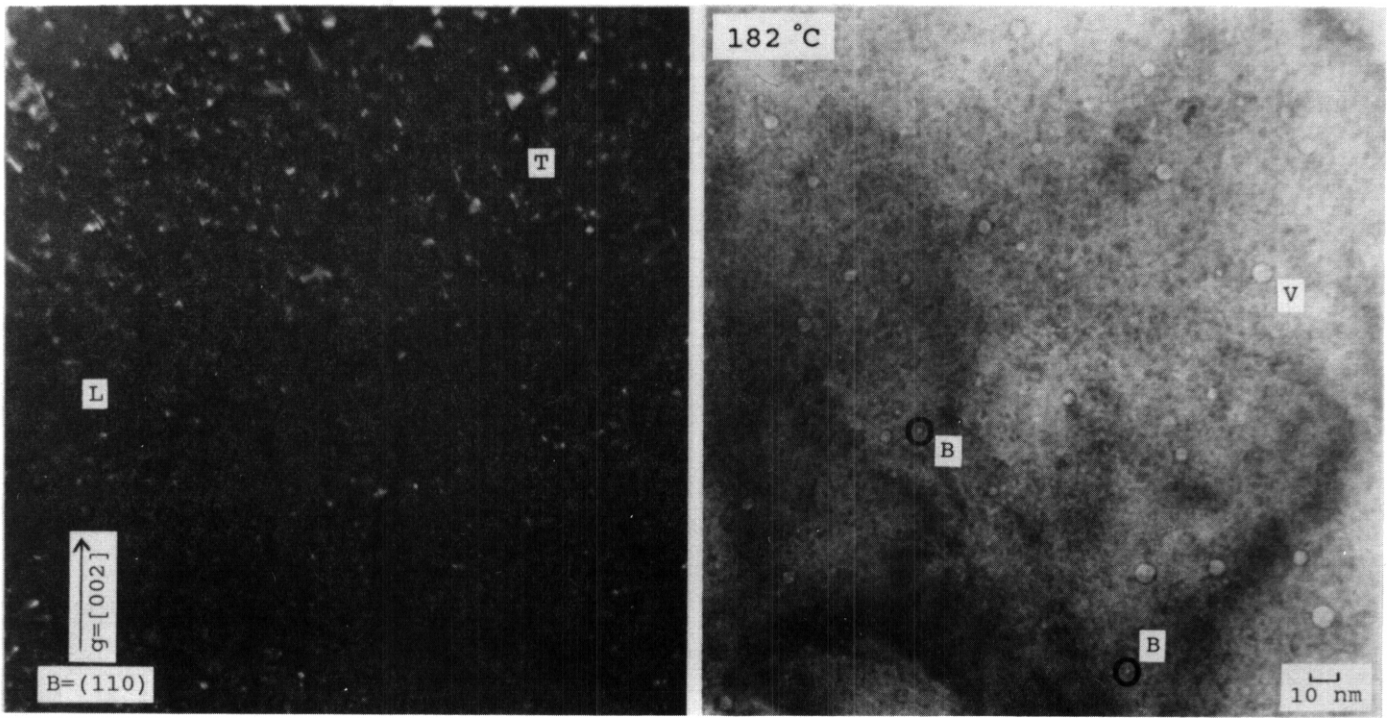

Fig. 6. Micrographs illustrating the simultaneous presence of high densities of SFT and cavities in a Cu-B specimen.

Table 5. Planar defect cluster parameters of irradiated copper-boron specimens[a]

Temperature (°C)	Total Cluster Mean Diameter (nm)	N_{TOT} (m^{-3})	$\frac{n_{SFT} + n_{TL}}{n_{TOT}}$
182	2.5	~2.0 × 10^{23}	>0.55
220	--	6.2 × 10^{22}	>0.4
250	--	2.9 × 10^{22}	~0.5
350	3.2	6 × 10^{20}	~1.0
400	3.2	~4 × 10^{20}	~1.0
A50	3.5	<1 × 10^{20}	~1.0
500	3.2	<1 × 10^{20}	~1.0

[a]The total cluster density is given by N_{TOT}, whereas SFT and TL refer to stacking fault tetrahedra and triangular-shaped dislocation loops, respectively.

The SFT density was decreased in the region very near to grain and twin boundaries compared to the grain interior. The width of the denuded zone was comparable to that measured for the bubbles in the Cu-B specimens. The results of some measurements are given in Table 4. The accuracy of the measurement is poor at high temperatures due to the low density of SFT in the matrix, which made it difficult to statistically determine the extent of the denuded zone.

A moderate density of triangular shaped dislocation loops were observed in the irradiated copper-boron specimens. Figure 7 shows two large triangular loops that were observed in a specimen irradiated at 350°C. These loops lie on {111} close-packed planes and are faulted as evident by the fringed stacking fault contrast in Fig. 7. A preliminary determination of the loop nature indicates that these loops are vacancy type. The size of these triangular loops was generally much larger than SFT (arrowed in Fig. 7). An accurate differentiation between triangle loops and SFT required micrographs taken with beam directions of <110> and <001>. The four types of observed vacancy clusters (bubble, void, SFT. and triangle loop) appeared to be homogeneously distributed throughout the grain interiors of the irradiated foils. Figure 8 shows an example of these four types of clusters occurring in close vicinity of each other in a specimen irradiated at 350°C.

ORNL-PHOTO-0762-88

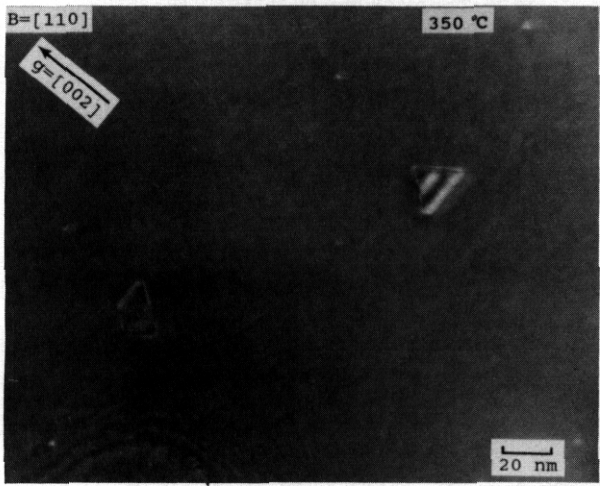

Fig. 7. Triangular-shaped dislocation loops and SFT in irradiated copper-boron.

Discussion

A comparison of the copper-boron and pure copper[5] results reveals several significant differences in their irradiated behavior. The two most striking effects in the Cu-B alloy that were not observed in pure copper are the formation of cavities at 182°C and the existence of a bimodal cavity distribution at all irradiation temperatures (182 to 500°C). It seems appropriate to ascribe these differences to helium effects, although the effects of other impurities (including lithium and oxygen) should also be considered.

The present copper-boron results are not directly applicable to predict the behavior of copper in a fusion reactor environment due to the high helium production rate (>10 times the fusion rate of ~7 appm He/dpa) and the fact that most of the helium was produced during the early stages of the irradiation. (The initial helium generation rate was ~500 appm/dpa.) In this latter respect it is somewhat analogous to the case of helium preimplantation in ion bombardment studies, where an excess nucleation of cavities is known to occur under these conditions.[21] This is borne out by the higher cavity densities in the copper-boron specimens compared to pure copper.

Keeping in mind the limitations introduced by the helium generation details, several interesting observations may be made regarding the effects of helium on cavity and SFT formation in copper. The SFT density was high even in the presence of high cavity densities. In particular, the measured SFT density at 182°C was ~30% higher in the copper-boron specimens (where cavities were present) compared to the pure copper case (where no cavities were observed). This may be considered somewhat surprising since both SFT and cavities are vacancy clusters. The mean SFT size exhibited a slight increase with increasing temperature, due to a preferential loss of small SFT in the size distribution at elevated temperatures. The SFT size in the copper and copper-boron specimens was comparable for a given irradiation temperature.

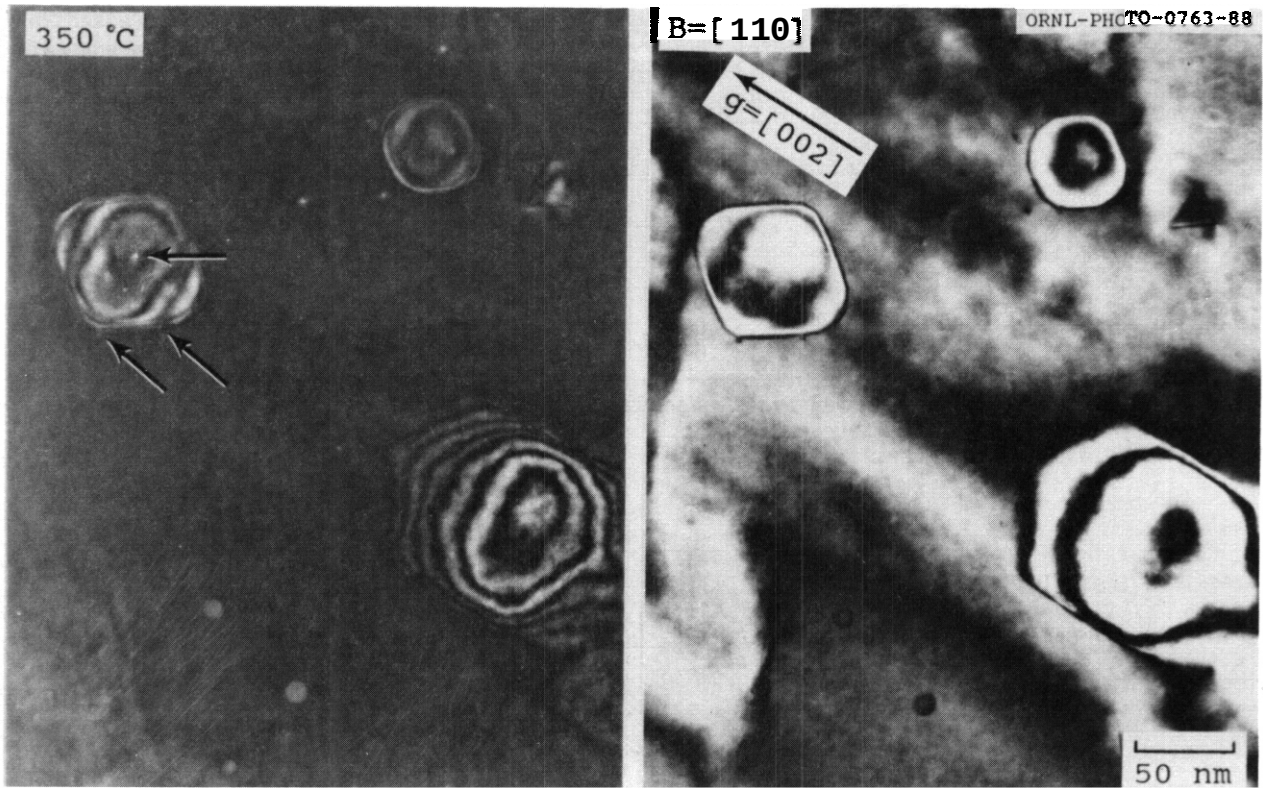

Fig. 8. Micrographs illustrating the four types of defect clusters observed in irradiated copper-boron.

Some SFT formation was observed at all irradiation tenperatures, including 500°C. It is possible that the SFT observed in the specimens irradiated at high temperatures are due to inadvertent irradiation with stray neutrons as the capsule was cooling down at the end of the irradiation. However, if this were the case, then the SFT density should be independent of the irradiation temperature in all of the high-temperature specimens. Since a steady decrease in SFT density was observed with increasing irradiation temperature (Table 5), it is more likely an SFT thermal stability effect. The lifetime of a SFT is short at elevated temperatures, so only these SFT created near the conclusion of the irradiation should survive. In this case, the results can be analyzed using a thermal stability model analogous to that of English et al.[22,23]

The shrinkage and collapse of SFT may be attributed to thermal emission of vacancies (important at high temperatures) and to absorption of freely migrating interstitials (FMI). An increase in the density of point defect sinks in the matrix (such as cavities) would promote the annihilation of FMI and thereby lower the fraction of FMI that would be absorbed at SFT. This interpretation is consistent with the observation of a slightly higher SFT density in the cavity-containing Cu-B specimens compared to pure copper. Similar results regarding sink density effects on SFT concentration have been observed in 14-MeV neutron-irradiated fcc metals.[24,25]

The following physical model is proposed to interpret the observed behavior of SFT and cavities in the irradiated copper and copper-boron specimens. The weak dependence of SFT size and density on helium content suggests that SFT formation in copper occurs in the vacancy-rich core of the displacement cascade. Independent evidence for this hypothesis has been found in numerous studies of 14-MeV neutron-irradiated metals[25] and in helium ion irradiation studies.[26,27] As noted by Singh and Foreman,[28] physically realistic helium concentrations have an insignificant effect on the stabilization of in-cascade vacancy clusters produced during neutron irradiation. The enhanced nucleation of cavities (bubbles plus voids) in the Cu-B specimens compared to copper may be evidence that cavity nucleation is due to freely migrating vacancies that nucleate heterogeneously on helium atoms.

The spatial distribution of cavities. dislocation loops, and SFT was homogeneous throughout the matrix (except for small denuded regions near grain boundaries). This is in contrast to a heterogeneous or segregated behavior of loops/SFT and cavities observed in previous low-dose studies of neutron-irradiated copper.[29,30]

The amount of cavity swelling in the copper-boron specimens was larger at all irradiation temperatures than that observed in the pure copper specimens. Cavity formation was observed in the helium-containing Cu-B specimens at both 182 and 500°C. The observation of cavities at 182°C in the high-helium Cu-B specimens is in agreement with the predictions of a cavity stability model.[31] According to the

model, copper irradiated at 182°C at a damage rate of 2×10^{-7} dpa/s requires a helium concentration greater than ~0.2 appm to stabilize the nucleated cavities. This may explain the absence of observable cavities at 182°C in copper (0.2 appm He) and the presence of cavities in copper-boron (100 appm He). On the other hand, the effects of other solute atoms must also be considered.

Some cavity formation was observed in the copper-boron specimens irradiated at 500°C, but the calculated amount of swelling ($\Delta V/V$ ~0.02%) was insignificant for the 1.2 dpa irradiation dose. It is uncertain whether appreciable amounts of cavity swelling could occur in specimens irradiated to higher doses. A series of high-dose irradiation experiments at temperatures of 373 to 529°C utilizing the FFTF reactor are currently in progress.[32] These studies should establish the upper temperature limit for void formation in copper.

CONCLUSIONS

Cavity and SFT formation was observed in the copper-boron alloy at all irradiation temperatures of 182 to 500°C. A bimodal size distribution was observed for the cavities, presumably due to the generation of ~100 appm He during the irradiation. Regions imnediately adjacent to grain and twin boundaries were denuded of voids, helium bubbles, and SFT. Void formation was enhanced at all temperatures compared to the case of pure copper. The results suggest that helium accelerates the development of cavities in copper, in particular at the low-temperature limit of the void swelling regime. The present results are not directly applicable to the fusion reactor environment due to the high amounts of generated helium. The density of SFT at 182°C was slightly enhanced in the cavity-containing copper-boron alloy compared to pure copper. This observation may be used to obtain fundamental information about the relative roles of freely migrating point defects and clusters produced in the displacement cascade.

FUTURE WORK

The microstructure of copper-boron specimens irradiated at 275 and 300°C will be examined and density changes will be measured for all irradiation temperatures. A detailed comparison of the microstructures in the irradiated copper and copper-boron specimens will be made at all irradiation temperatures.

ACKNOWLEDGMENTS

The author would like to acknowledge K. Farrell for supplying the irradiated specimens, N. H. Rouse, L. T. Gibson and E. L. Ryan for experimental assistance, and Frances Scarboro for manuscript preparation.

REFERENCES

1. S. J. Zinkle and R. W. Knoll, A Literature Review of Radiation Damage Data for Copper and Copper Alloys, University of Wisconsin Fusion Technology Institute Report UWFDM-578, 1984.

2. R. J. Livak, T. G. Zocco, and L. W. Hobbs, J. Nucl. Mater. 144 (1987) 121.

3. O. K. Harling et al., J. Mater. Res. 2 (1987) 568.

4. H. R. Brager and F. A. Garner, p. 254 in Fusion Reactor Materials Semiannu. Prog. Rep. Sept. 30, 1987, DOE-ER-031313, U.S. DOE, Office of Fusion Energy.

5. S. J. Zinkle and K. Farrell, J. Nucl. Mater., 1989, in press; also see Fusion Reactor Materials Semiannu. Prog. Rep. Sept. 30, 1987, DOE-ER-031313, p. 90.

6. W. Vandermeulen et al., 14th Symp. on Fusion Technology, September 1986, Avignon, France, Comn. Eur. Communities, Pergamon Press, 1986, p. 1031.

7. S. J. Zinkle, G. L. Kulcinski, and R. W. Knoll, J. Nucl. Mater. 138 (1986) 46.

8. S. J. Zinkle, p. 86 in Fusion Reactor Materials Semiannu. Prog. Rep. Sept. 30, 1987, DOE-ER-031313, U.S. DOE, Office of Fusion Energy.

9. P. Vela and E. Russell, J. Nucl. Mater. 19 (1966) 312.

10. P. Vela and E. Russell, J. Nucl. Mater. 19 (1966) 327.

11. G.J.C. Carpenter and R. B. Nicholson, p. 383 in Radiation Damage in Reactor Materials, Vol. 2, IAEA, Vienna, 1966.

12. G.J.C. Carpenter and R. B. Nicholson, Report AECL-3331, Chalk River, Ontario, 1969.

13. D. E. Barry and B. L. Eyre, Phil. Mag. 22 (1970) 717.

14. D. E. Barry, Phil. Mag. 23 (1971) 495.

15. M. L. Mendelsohn, D. M. Green, and A. R. Krauss, J. Nucl. Mater. 141–143 (1986) 184.

16. B. M. Oliver, Rockwell International, Canoga Park, CA, 1988, personal communication.

17. D. A. Woodford, J. P. Smith, and J. Moteff, J. Iron & Steel Inst. (1969) 70.

18. R. C. Lau and R. L. Ladd, J. Appl. Phys. 40 (1969) 2899.

19. L. K. Mansur, J. Nucl. Mater. 150 (1987) 105.

20. S. J. Zinkle and R. L. Sindelar, J. Nucl. Mater. 155–157 (1988) 1196.

21. K. Farrell, Rad. Effects 53 (1980) 175.

22. C. A. English, B. L. Eyre, and J. Summers, Phil. Mag. 34 (1976) 603.

23. J. W. Muncie, B. L. Eyre, and C. A. English, Phil. Mag. A 52 (1985) 309.

24. N. Yoshida, Y. Akashi, K. Kitajima, and M. Kiritani, J. Nucl. Mater. 133&134 (1985) 405.

25. M. Kiritani. T. Yoshiie, and S. Kojima, J. Nucl. Mater. 141-143 (1986) 625.

26. A. A. Gadalla, W. Jäger, and P. Ehrhart. J. Nucl. Mater. 137 (1985) 73.

27. P. Ehrhart, A. A. Gadalla, W. Jager, and N. Tsukuda, Acta Metall. 35 (1987) 1929.

28. B. N. Singh and A.J.E. Foreman, J. Nucl. Mater. 155157 (1988) 1258.

29. C. A. English, J. Nucl. Mater. 108&109 (1982) 104.

30. B. N. Singh, T. Leffers, and A. Horsewell, Phil. Mag. A 53 (1986) 233.

31. S. J. Zinkle, W. G. Wolfer, G. L. Kulcinski, and L. E. Seitzman, Phil. Mag. A 55 (1987) 127.

32. K. R. Anderson, F. A. Garner, M. L. Hamilton, and J. F. Stubbins, this volume (DOE/ER-0313/6).

RADIATION DAMAGE IN BINARY CERAMIC OXIDES: A PRELIMINARY MODEL — Roger E. Stoller (Oak Ridge National Laboratory)

OBJECTIVE

To develop a physically based, theoretical model of point defect and extended defect behavior in ceramic materials and to use this model to improve our understanding of the response of these materials to disolacive irradiation.

SUMMARY

A preliminary model of radiation damage in binary ceramic oxides has been developed. The model described here accounts in an approximate way for some of the major differences between metallic alloys and ceramics that are believed to be responsible for the fact that ceramic materials are observed to behave differently than metallic alloys when exposed to displacive irradiation. The model considers the influence of the existence of a second lattice and the additional constraint of stoichiometric point defect absorption by dislocation loops on the concentrations of point defects that would be observed at steady-state in an irradiated ceramic. These point defect concentrations are then used to compute various measures of the sensitivity of these materials to the the type of microstructural evolution that is observed in irradiated metals. Initial results obtained with the present model indicate that both the lattice and stoichiometry effects can help to mitigate radiation damage in ceramics. However, the effect is not necessarily large; in agreement with recent data, the results indicate that at least some ceramic oxides may exhibit a sensitivity to displacement damage that is similar to metals.

PROGRESS AND STATUS

Introduction

The use of ceramic materials in fusion reactor components has been discussed for some time.[1-4] The primary applications proposed for these materials include: as electrical insulators in rf heaters and neutral beam injectors, as rf windows, and in the first wall that provides a vacuum barrier for the plasma. Both structural and protective functions are proposed in the first wall applications. The ceramics most frequently discussed in the context of fusion reactor designs are magnesia (MgO), alumina (Al_2O_3), spinel ($MgAl_2O_4$), silicon carbide (SiC) and silicon nitride (Si_3N_4), lithium oxide (Li_2O) and graphite (C). References 1 to 8 provide a good overview of some of the materials and their applications.

In the presence of displacive neutron or charged particle irradiation, ceramic materials display a sequence of microstructural evolution that is similar to that observed in irradiated metals.[9-13] Unfortunately, the straightforward application of the theory developed to describe radiation damage in metallic alloys is precluded by several substantial differences between these two types of materials. The major differences are due to the fact that ceramics exhibit chemical (both ionic and covalent) rather than metallic bonding. As a result, a theory of radiation damage in ceramics must be concerned with the preservation of stoichiometry, multiple (anion and cation) lattices, and the charge state of the various point defects that can exist. In addition, atomic displacements will not occur in a stoichiometric ratio in materials in which the atomic mass and the displacement energy is different for one chemical species than for the other(s). Atomic displacements can also be generated in some compound materials due to radiolysis,[8] although this mechanism is thought to be negligible in most of the materials mentioned above.[8,9]

The work described here represents a first step in the development of a model of radiation damage in ceramics. The rate theory description that has been successfully applied to a range of problems in metals[14,15] provides the starting point for the present work. Because of the complexities of the physical system mentioned above, the model involves many approximations. Therefore, the results should be viewed as being preliminary in nature. The calculations provide some illustrations of the possible behavior of irradiated ceramics and some comparisons with irradiated metals.

Model Description

A general equation for the point defect concentrations of a multicomponent ceramic would be of the form:

$$\frac{dC^L_{i,v}}{dt} = G^L_{i,v} - C^L_{i,v} \sum_{k=1}^{L} \alpha_{Lk,kL}\, C^L_{v,i} - D^L_{i,v} C^L_{i,v} \sum_k S^L_{i,v}(k) , \qquad (1)$$

where the subscripts i and v denote interstitials and vacancies, and the superscript L indicates each atomic species in the material. Since parameters such as the migration energy can be influenced by the charge state of the various defects,[8] the family of equations represented by the superscript L in Eq. (1) should also reflect this dependence. The first term on the right-hand side of Eq. (1) is the total generation rate of each defect type, the second term represents all possible recombination reactions between the types of vacancies and interstitials present, and the last term is the loss of each defect type by absorption at extended defects of type k. This latter term reflects the possibility that the sink strengths of the various extended defects may be different for different types of defects. The dose dependence of the extended defects should also be explicitly modeled, and the microstructural evolution of the irradiated ceramic could in principle be obtained by the simultaneous solution of the family of Eqs. (1) and the sink evolution equations. Such a solution has been obtained for the primary defects that are observed in austenitic stainless steels.[15]

The general case is certainly more complicated than can be dealt with reasonably at this time. As a first step, the mdel has been formulated to deal with a binary ceramic, with a composition A_aB_b. This approach could be applied to a simple ternary as well if one can consider the metal atoms in a material like spinel to be roughly equivalent. In this case, Eq. (1) can be written for the two constituents as:

$$\frac{dC_i^A}{dt} = G_i^A - \alpha_{AA} C_i^A C_v^A - \alpha_{AB} C_i^A C_v^B - D_i^A C_i^A (Z_i^{cA} S_c + Z_i^{nA} S_n + Z_i^{\ell A} S_\ell) \; ; \tag{2a}$$

$$\frac{dC_v^A}{dt} = G_v^A - \alpha_{AA} C_i^A C_v^A - \alpha_{BA} C_i^B C_v^A - D_v^A C_v^A (Z_v^{cA} S_c + Z_v^{nA} S_n + Z_v^{\ell A} S_\ell) \; ; \tag{2b}$$

$$\frac{dC_i^B}{dt} = G_i^B - \alpha_{BA} C_i^B C_v^A - \alpha_{BB} C_i^B C_v^B - D_i^B C_i^B (Z_i^{cB} S_c + Z_i^{nB} S_n + Z_i^{\ell B} S_\ell) \; ; \tag{2c}$$

$$\frac{dC_v^B}{dt} = G_v^B - \alpha_{AB} C_i^A C_v^B - \alpha_{BB} C_i^B C_v^B - D_v^B C_v^B (Z_v^{cB} S_c + Z_v^{nB} S_n + Z_v^{\ell B} S_\ell) \; ; \tag{2d}$$

where the α_{jk} are the recombination rate coefficients for reactions between type-j interstitials and type-k vacancies.

$$\alpha_{jk} = \frac{4\pi}{\Omega} (r_v^{kj} D_i^j + r_i^{jk} D_v^k) \quad , \tag{3}$$

where $r_{i,v}^{jk}$ is the recombination radius for interstitials (vacancies) of type j with vacancies (interstitials) of type k. For a material with only one lattice, Eq. (3) reduces to the familiar result for metals.[14] The average atomic volume (Ω) appears in Eq. (3) when the defect concentrations are given in units of number per atom, as they are here.

The sink strengtns in Eq. (2) are: S_c, the cavity sink strength; S_n, the dislocation network sink strength; and S_ℓ, the dislocation loop sink strength. The need to prevent ionic charge imbalance may require that all extended defects in a ceramic absorb point defects in a stoichiometric ratio. However, in this initial study this constraint has only been applied to the dislocation loops.[9,12] The influence of requiring stoichiometric defect absorption by other sinks will be explored as the model is developed further. Presently, the point defect sink strengths of cavities and dislocations are calculated in the same way as has been done for metals,[14,15] and the sink capture efficiencies are given in the next section. For the dislocation loops. the requirement for net point defect absorption from both lattices to occur in a stoichiometric ratio can be expressed as:

$$\underbrace{Z_i^{\ell A} D_i^A C_i^A - Z_v^{\ell A} D_v^A (C_v^A - C_v^{\ell A})}_{a} = \underbrace{Z_i^{\ell B} D_i^B C_i^B - Z_v^{D\ell B} D_v^B (C_v^B - C_v^{\ell B})}_{b} \; . \tag{4}$$

The $Z_{i,v}^{\ell L}$ in Eq. (4) are the loop capture efficiencies for interstitials and vacancies and the $C_v^{\ell L}$ are the vacancy concentrations in equilibrium with the loop on each lattice. As a result of the constraint imposed by Eq. (4), at least one of the capture efficiencies must be dependent on the other three. For example,

$$Z_i^{\ell B} = \frac{\frac{b}{a}\left[Z_i^{\ell A} D_i^A C_i^A - Z_v^{\ell A} D_v^A (C_v^A - C_v^{\ell A})\right] + Z_v^{\ell B} D_v^B (C_v^B - C_v^{\ell B})}{D_i^B C_i^B} \quad (5)$$

If one invokes the steady-state assumption,[14,15] Eqs. (2) and (5) can be solved simultaneously to obtain the point defect concentrations and $Z_i^{\ell B}$.

The choice of which of the four possible loop capture efficiencies to calculate using an equation like Eq. (5) is arbitrary at this point. However, the choice does affect the results that are obtained from the model. The model dependence on this choice is simply due to the fact that the system bias is determined by the various capture efficiencies. For example, considering the simple case of an irradiated metal with network dislocations and cavities as the only sinks, the bias can be defined as:[14]

$$2 = Z_i^n Z_v^c - Z_v^n Z_i^c \quad . \quad (6)$$

Any variation in the individual extended defect capture efficiencies is therefore reflected in the bias. The expression for the bias is similar, but more complicated, with the present model. Using the nominal values listed in Table 1 for any three of the loop capture efficiencies and the other material parameters given there as well, the calculated results for the fourth is:

$$Z_i^{\ell A} = 1.41; \; Z_i^{\ell B} = 1.17; \; Z_v^{\ell A} = 0.88; \text{ or } Z_v^{\ell B} = 1.07.$$

As discussed in the next section, there must be at least one parameter difference between the two lattices in order for the calculated capture efficiency to be different from the corresponding one on the other lattice. The results just given were calculated with the displacement rate equal to 2.0×10^{-6} on the B lattice and 1.0×10^{-6} on the A lattice. Examples of the influence of this model dependence on the capture efficiencies will be discussed below.

Although the dose dependence of the extended defects is certainly an important aspect of models such as these,[15] this dependence is presently being neglected in these calculations. A proper treatment of the dose dependence would require the formulation of a more complex defect nucleation model. The present knowledge of material parameters and defect kinetics in ceramics do not justify such a treatment in this initial work. Even the use of the present model is hampered by the need for material parameters that are not well known. This is discussed further in the next section.

Table 1. Parameters for 'metal-like' binary compound

	Both lattices	
Damage rate, dpa/s	1.0×10^{-6}	
Energy, eV		
Vacancy migration	1.4	
Vacancy formation	1.6	
Interstitial migration	0.85	
Recombination radii, all (nm)	1.0	
Sink strength		
Cavity	1.0×10^9	
Network dislocation	5.0×10^{10}	
Dislocation loop	5.0×10^{10}	
Capture efficiencies for:	Interstitials	Vacancies
Cavities	1.0	1.0
Network Dislocations	1.1	1.0
Dislocation loops	1.25	1.0

Model Parameters and Calculations

Even a cursory survey of the literature shows that there is no well established value for many of the material parameters required by even a simple model. In particular, the values quoted for activation energies for point defect migration and formation lead to diffusivities that vary by as much as three or four orders of magnitude in some cases.[16-19] There seems to be some systematic variation of these parameters with measurement technique (i.e., whether the method used is tracer diffusion, electrical conductivity, sintering, ...),[16] and some of the variation is also related to impurity concentrations.[18,19] Atomic displacement rates for various irradiation environments are also not well known since the study of primary damage formation in compound materials is presently relatively new.[20-23] Displacement thresholds are known to vary between the anion and cation lattices[21,24] and the kinetics of intracascade annealing and defect clustering have not been studied in detail.

Because of these uncertainties, the strategy followed here was to first analyze the effect of a second lattice and that of stoichiometric loops while using a set of "metal-like" parameters as summarized in Table 1. Then, some of the parameters were changed in order to simulate MgO as shown in Table 2. In addition, some of the parameters listed in the tables were varied to determine their influence on the calculations. This will be discussed further below. The diffusion parameters listed in Table 2 for MgO were taken from refs. 16, 25 and 26. The vacancy formation energies in the two lattices were taken as one-half of the calculated formation energy of the Schottky defect.[26] Similar displacement thresholds of 60 to 65 eV have been measured for both Mg and O in MgO[27,28] and for such a case, Parkin and Coulter[21] have indicated that the stoichiometry of the displacement cascade is within several percent of the material stoichiometry. This conclusion is generally consistent with the total displacement cross sections calculated by Sharp and Rumsby[27] for MgO; therefore. the calculations conducted for this material used the same damage rate on both lattices.

Table 2. Parameters for MgO

	Mg	O
Vacancy migration energy, eV	2.0	2.1
Vacancy formation energy, eV	3.8	3.8
Interstitial migration energy, eV	0.05	0.05
Lattice parameter, nm	0.4213	
Density, g/cm^3	3.58	

In order to provide one basis for the comparisons discussed below, it is useful to define a quantity that will be referred to as the effective vacancy supersaturation,

$$S^L = \frac{Z_v^{CLLL} D_v^{CLLL} C_v^{CLLL} - Z_i^{CLLL} D_i^{CLLL} C_i^{CLLL}}{D_v^L C_v^{eL}} \qquad (7)$$

where $_v$ is the thermal equilibrium concentration in the L lattice. This quantity provides a measure of the material's deviation from thermal equilibrium. In particular, it is a direct measure of the susceptibility of a material to void swelling since the critical number of gas atoms for void formation is inversely proportional to $\ell n^2(S)$.[29] However, when comparing values of S for metals and ceramics, it is important to note that for a given difference

$$Z_v^{CL} D_v^L C_v^L - Z_i D_i^L C_i^L,$$

S^L will be much greater for the metal than for the ceramic since $D_v C_v^e$(metal) >> $D_v^e C_v$(ceramic), as shown by the activation energies in Tables 1 and 2. A second useful quantity to evaluate is the fraction of radiation-produced defects that recombine since in the limit of 100% recombination no effect of irradiation should be observed.

The first calculations were done using the parameters in Table 1 on both lattices of an imaginary binary material with composition A_aB_b irradiated at 500°C to explore the influence of the second lattice and of stoichiometry. Assuming a stoichiometry ratio (a/b) of 1.0 and that all four recombination radii are equal, the influence including the second lattice is equivalent to simply doubling bulk recombination coefficient in the simple metal lattice. This leads to a modest decrease in the vacancy supersaturation from 64.5 for a metal with the same parameters to 62.8 for the compound. The small reduction in the supersaturation is a reflection of the fact that for the sink parameters listed in Table 1, a relatively small fraction of the point defects are lost to recombination in the matrix; most recombine at sinks. However, it is unlikely that the probability of mixed (cation and anion) recombination is as high as self-recombination due to charge effects and the ionic radii of the two species. Figure 1 shows the effect of various assumed recombination radii and the stoichiometric ratio on the effective vacancy supersaturation on the A (Fig. la) and B (Fig. 1b) lattices. The supersaturations have been normalized to that for a metal lattice with the same parameters.

Figure 1 indicates that the influence of the various assumed recombination coefficients and of the stoichiometry ratio is greater on the B lattice than on the A lattice. This is a result of the fact that the calculations assume that vacancies on the B lattice are responsible for balancing the stoichiometry, [i.e., Eq. (5) was solved for $Z_v^{\ell B}$ in the iterative solution of the point defect concentrations]. The dependence of $Z_v^{\ell B}$ (with $Z_v^{\ell A}$ = 1.0) on the stoichiometry ratio is shown in Fig. 2. It is difficult to draw any general conclusion from Figs. 1 and 2 since assumptions about recombination that lead to an increase in the supersaturation on the A lattice lead to a decrease on the B lattice. The trend is for the supersaturations to increase as the stoichiometric ratio deviates from 1.0. In principle, this means the compound materials should become somewhat less resistant to cavity formation. The calculated growth rate of a 10 nm test cavity also increases. On the other hand, the calculated growth rates of dislocation loops decreases slightly as a/b decreases from 1.0 to 0.5. For example, using the case where the probabilities of all possible recombination reactions are equal, the loop growth rate for a/b = 1 is 1.71 × 10^{-4} nm/s and the cavity growth rate is 2.76 × 10^{-4} nm/s. For a/b = 0.5, the loop growth rate reduces to 1.66 × 10^{-4} nm/s and the cavity growth rate increases to 3.31 × 10^{-4} nm/s.

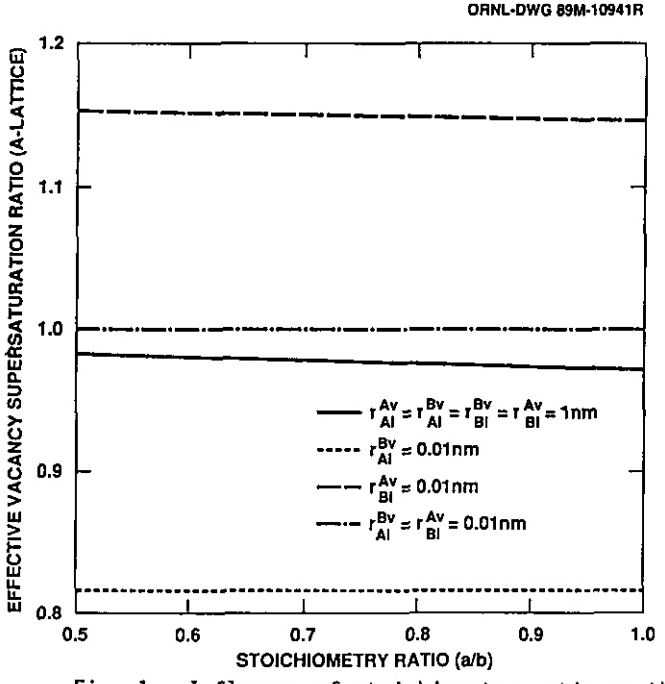

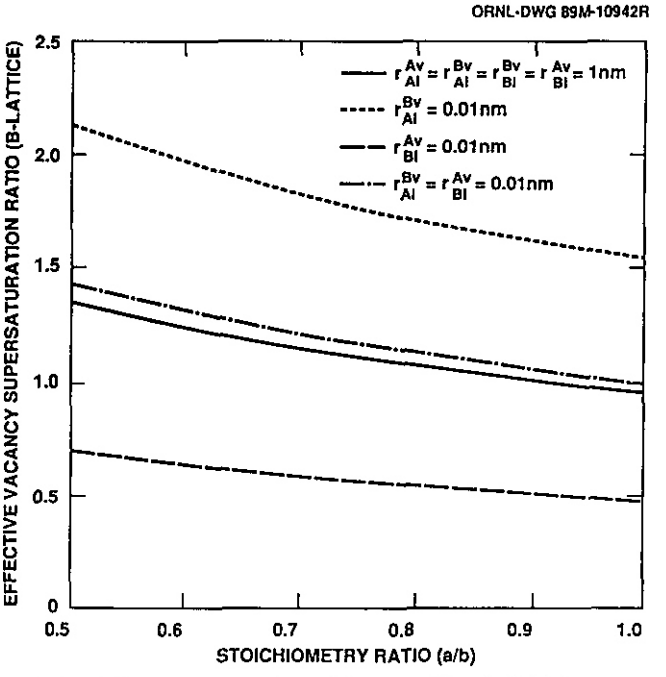

Fig. 1. Influence of stoichiometry ratio on the effective vacancy supersaturation on the A lattice (a) and B lattice (b). Results are shown for four different cases of recombination.

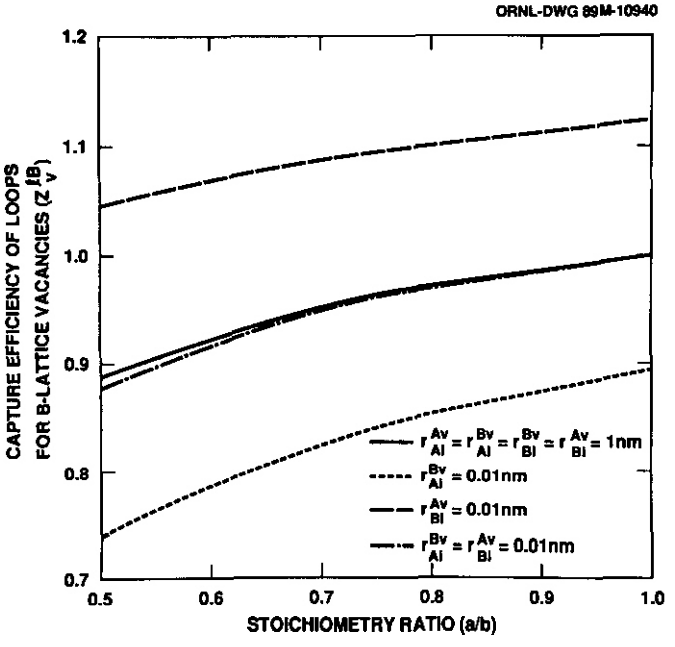

Fig. 2. Influence of stoichiometric ratio on the loop capture efficiency for B-lattice vacancies. Results are shown for four different cases of recombination.

This observation that some parameter changes can lead to a reduction in the loop growth rate while increasing the cavity growth rate as a function of the stoichiometry ratio is dependent on which of the loop capture efficiencies is assumed to be dependent in the model. For the case just mentioned. if either $Z_i^{\ell B}$ or $Z_v^{\ell B}$ are calculated, the observation holds. But if $Z_i^{\ell A}$ or $Z_v^{\ell A}$ are calculated, both the loop and cavity growth rates are reduced. This is a result of the influence of the various capture efficiencies on the point defect calculations. When either $Z_i^{\ell B}$ or $Z_v^{\ell B}$ are calculated, the effect of moving from a/b = 1.0 to a/b < 1.0 is to decrease C_i^A and increase C_v^A; however, when $Z_i^{\ell A}$ or $Z_v^{\ell A}$ are calculated, C_i^A increases and C_v^A decreases. The changes in the cavity growth rate simply follow from these changes in the paint defect concentrations. If vacancy emission is neglected, the cavity growth rate is proportional to the differences of the point defect fluxes[14,15] as given in the numerator of Eq. (7). The case for loops is more complex because one of the capture efficiencies is a function of the point defect concentrations due to the stoichiometric constraint given by Eq. *(5)*. The loop growth rate is proportional to the numerators given in Eq. (4). Inspection of this equation shows even with an increase in C_i^A and a decrease in C_v^A, the loop growth rate can be reduced if $Z_i^{\ell A}$ is reduced or $Z_v^{\ell A}$ is increased to compensate for the change. This is indeed what happens. For a/b = 2/3, the calculated $Z_i^{\ell A}$ is 1.222 instead of 1.25 and $Z_v^{\ell A}$ is 1.024 instead of 1.00. Any physical significance of these results is not yet clear, but they do illustrate the potential level of complexity introduced by coupling the equations describing the two 1attices.

Using the parameters from Table 2 as approximately appropriate for a binary ceramic like MgO, a number of calculations were then performed. Some of these results are summarized in Tables 3 and 4 and in Fig. 3. These results were also calculated using equal probabilities for each of the possible recombination reactions. Because of the uncertainties mentioned above regarding diffusion parameters in MgO (and other ceramics), the influence of varying the vacancy migration energy was examined. Using the calculated values of the loop growth rate and the loop capture efficiency for oxygen vacancies as metrics, Table 3 shows that the sensitivity to the assumed diffusion parameters is very high, with the loop growth rate varying from fairly large positive to negative values. The loop capture efficiency for oxygen vacancies changes by a factor of about 350 in order to balance stoichiometry.

It is not clear which type of point defect is responsible for maintaining the loop stoichiometry. Table 4 summarizes the range of growth rates that were obtained when each of the four possible capture efficiencies were calculated. The results for the capture efficiencies are not symmetrical between the two lattices because of the use of unequal vacancy migration energies.

Table 3. Dependence of loop growth rate and calculated loop capture efficiency for oxygen vacancies on the vacancy migration energies

Vacancy migration energy (eV)		$Z_v^{\ell O}$	$\frac{dr_\ell}{dt}$ (nm/s)
Mg	O	--	---
2.1	1.9	0.055	2.21×10^{-4}
2.1	2.0	0.23	7.72×10^{-5}
2.1	2.1	1.00	7.10×10^{-6}
2.0	2.1	4.37	-3.57×10^{-5}
1.9	2.1	18.78	-9.99×10^{-5}

Table 4. Dependence of loop growth rate on calculated loop capture efficiency[a]

Calculated capture efficiency	$\frac{dr^\ell}{dt}$ (nm/s)
$Z_i^{\ell Mg} = 3.42$	7.64×10^{-5}
$Z_i^{\ell O} = 0.13$	-3.64×10^{-5}
$Z_v^{\ell Mg} = 0.23$	7.72×10^{-5}
$Z_v^{\ell O} = 4.37$	-3.57×10^{-5}

[a] $E_m^v(Mg) = 2.0$; $E_m^v(O) = 2.1$ eV.

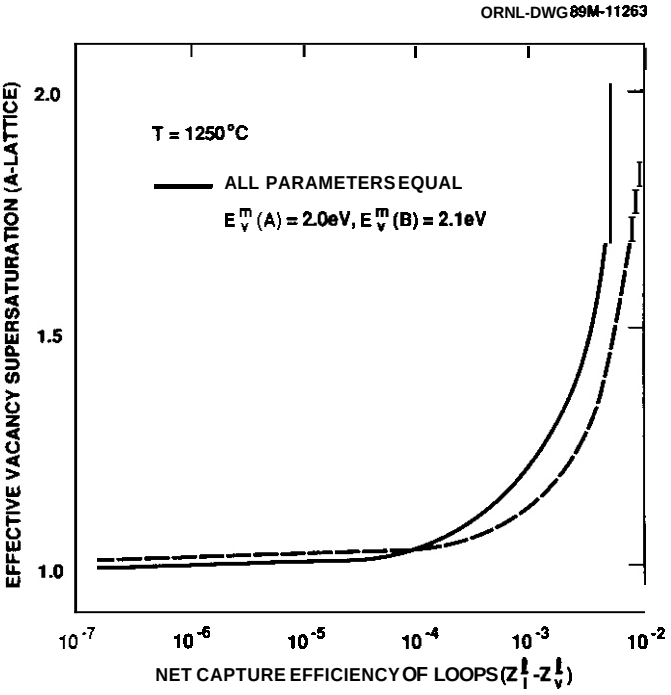

Fig. 3. Effective vacancy supersaturation on the A lattice as a function of the net capture efficiency of loops.

The fact that material parameters are not equal on the two lattices leads to one significant difference between the compound material and a metal. For a metal, the effective vacancy supersaturation approaches 1.0 as the system bias approaches 0. This is a result of the fact that in the absence of any bias to drive differential partitioning of point defects, all sinks will absorb and emit defects at equal rates. This is similarly true of a compound material if each parameter has an equal value on both lattices. However, parametrical asymmetries give rise to what could be termed an effective low "bias," even in the absence of sink biases. This is shown in Fig. 3. The calculations shown here were done for a 1250°C irradiation temperature so that the nominal supersaturation would be fairly low. All sinks except the loops were assumed to have capture efficiencies of unity for both vacancies and interstitials, and the loop capture efficiency was varied as shown. The solid curve in Fig. 3 corresponds to the case in which all parameters on the Mg and O lattices are equal, and the dashed curve is for the case in which the vacancy migration energy on the Mg lattice is 0.1 eV lower than on the O lattice. A small vacancy supersaturation persists on the Mg lattice even

when the net loop capture efficiency (and hence the system bias) approaches zero. Although it is not shown in Fig. 3, a comparable subsaturation ($S_v^0 < 1$) of vacancies exists on the 0 lattice.

DISCUSSION AND SUMMARY

A simple, first mdel of radiation damage in ceramics has been developed and some preliminary calculations have been completed. The results obtained for a "metal-like" binary compound indicate that the presence of multiple lattices will lead to somewhat greater bulk recombination than in metals. This effect will be small if mixed (anion-cation) recombination does not occur at an appreciable rate. The influence of stoichiometry was included in the mdel by calculating one of the four possible loop capture efficiencies in terms of the other three in order to maintain a net stoichiometric absorption of point defects by the loops. This constraint acts to reduce the loop growth rate when the stoichiometry ratio deviates from 1.0. This same deviation can lead to either an increase or a decrease in the cavity growth rate, depending on which three of the four loop capture efficiencies are fixed and which one is calculated to maintain stoichiometry. In general, the parameter sensitivity of the results increases for smaller values of the stoichiometry ratio. Although this effect of stoichiometry is physically reasonable, it is not possible to make direct comparisons with real ceramics (e.g., MgO vs Al_2O_3), since other material parameters also vary.

Using material parameters that are reasonable for MgO, the influence of asymmetry in material parameters was examined. The results were quite sensitive to variations in diffusion parameters and to which type of defect was assumed to be responsible for balancing the stoichiometry of the loop. A persistent effect of parameter asymmetry was an effective "bias" of the material as evidenced by the vacancy supersaturation remaining greater than 1.0 even when the conventional, sink-based bias approached 0. This "bias" was the only observation in the work to date that indicated some inherent difference in behavior between compound materials and metals. The major inference that can be drawn from these calculations is that that as more data is obtained from experiments at higher doses, ceramic materials are likely to exhibit behavior similar to metals. This points out the importance of further irradiation experiments and of other experiments to obtain better measurements of key material parameters.

FUTURE WORK

Further work with the model described above will include a test of the validity of the steady-state approximation by explicitly integrating the point defect equations [Eq. 2(a)-2(d)]. Additional parametric studies will be conducted and direct comparisons with data will be made where possible.

REFERENCES

1. D. Steiner, Nucl. Sci. and Engr. 58 (1975) 107-165.
2. G. L. Kulcinski, "Radiation Damage: The Second Most Serious Obstacle to Commercialization of Fusion Power," in Radiation Effects and Tritium Technology for Fusion Reactors, CONF-750989-1, U.S. ERDA, 1976, pp. 17-72.
3. F. W. Clinard, G. F. Hurley and R. W. Klaffky, Res Mech. 8 (1983) 207-234.
4. G. P. Pells, J. Nucl. Mater. 122 & 123 (1984) 1338-1351.
5. N. Itoh and K. Morita, J. Nucl. Mater. 155-157 (1988) 58-66.
6. G. P. Pells, J. Nucl. Mater. 155-157 (1988) 67-76.
7. C. E. Johnson, K. R. Kummerer and E. Roth, J. Nucl. Mater. 155-157 (1988) 188-201.
8. F. W. Clinard and L. W. Hobbs, "Radiation Effects in Non-Metals," in Physics of Radiation Effects in Crystals, R. A. Johnson and A. N. Orlov, Eds., Elsevier Science Publishers, 1986, pp. 387-471.
9. F. W. Clinard, G. F. Hurley and L. W. Hobbs, J. Nucl. Mater. 108 & 109 (1982) 655-670.
10. M. D. Rechtin, Rad. Eff. 42 (1979) 129-144.
11. C. Kinoshita, K. Hayashi and S. Kitajima, Nucl. Instr. and Meth. in Phys. Res. B1 (1984) 209-218.
12. A. Y. Stathopoulos and G. P. Pells, Phil. Mag. A 47 (1983) 381-394.

13. S. J. Zinkle, "Ion Irradiation Studies of Oxide Ceramics," in Structure Property Relationships in Surface Modified Ceramics, C. J. McHargue, et al., Eds., Kluwer Academic Publishers, Dordrecht, Netherlands, 1989, pp. 215-225.

14. L. K. Mansur, "Mechanisms and Kinetics of Radiation Effects in Metals and Alloys," in Kinetics of Nonhomogeneous Processes, G. F. Freeman, ed., Wiley and Sons, New York, 1987.

15. R. E. Stoller and G. R. Odette, "A Composite Model of Microstructural Evolution in Austenitic Stainless Steel Under Fast Neutron Irradiation," in Radiation Induced Changes in Microstructure, ASTM STP 955, F. A. Garner, N. H. Packan and A. S. Kumar, Eds., ASTM, Philadelphia, 1987, pp. 371-392.

16. J. M. Vieira and B. J. Brook, "Lattice-, Grain-Boundary-, Surface-, and Gas-Diffusion Constants in Magnesium Oxide," in Structure and Properties of MgO and Al_2O_3 Ceramics, W. D. Kingery, Ed., American Ceramic Society, Columbus, 1984, pp. 438-463.

17. F. A. Kroger, "Experimental and Calculated Values of Defect Parameters and the Defect Structure of α-Al_2O_3, in Structure and Properties of MgO and Al_2O_3 Ceramics, W. D. Kingery, Ed., American Ceramic Society, Columbus, 1984, pp. 100-118.

18. B. J. Wuensch, "On the Interpretation of Lattice Oiffusion in Magnesium Oxide," in Mass Transport Phenomena in Ceramics, A. R. Cooper and A. H. Heuer, Eds., Plenum Press, New York, 1975, pp. 211-231.

19. Y. Oishi and K. Ando, "Oxygen Diffusion in MgO and Al_2O_3," in Structure and Properties of MgO and Al_2O_3 Ceramics, W. D. Kingery, Ed., American Ceramic Society, Columbus, 1984, pp. 379-393.

20. M. T. Robinson, Phys. Rev. B 27 (1983) 5347-5359.

21. D. M. Parkin and C. A. Coulter, J. Nucl. Mater. 117 (1983) 340-344.

22. L. R. Greenwood, "Radiation Damage Calculations for Compound Materials." in Effects of Radiation on Materials, ASTM STP 1046, N. H. Packan, R. E. Stoller and A. S. Kumar, Eds., ASTM, Philadelphia, 1989 (in press).

23. N. M. Ghoniem and S. P. Chou, "Binary Collision Monte Carlo Simulations of Cascades in Polyatomic Ceramics," in Fusion Reactor Materials Semiannual Progress Report, DOE/ER-0313/3, U.S. DOE, March 1988, pp. 143-148.

24. G. P. Pells and A. Y. Stathopoulos, Rad. Eff. 74 (1983) 181-191.

25. W. C. Mackrodt, "Calculated Point Defect Formation, Association and Migration Energies in MgO and α-Al_2O_3," in Structure and Properties of MgO and Al_2O_3 Ceramics, W. D. Kingery, Ed., American Ceramic Society, Columbus, 1984, pp. 62-78.

26. C. Kinoshita, K. Hayashi and T. E. Mitchell, "Migration Energies of Interstitials and Vacancies in MgO," in Structure and Properties of MgO and Al_2O_3 Ceramics, W. D. Kingery, Ed., American Ceramic Society, Columbus, 1984, pp. 490-505.

27. J. V. Sharp and D. Rumsby, Rad. Eff. 17 (1973) 65-68.

28. Y. Chen, D. L. Trueblood, O. E. Schow and H. T. Tohver, J. Phys. C: Solid State Phys. 3 (1970) 2501-2508.

29. R. E. Stoller and G. R. Odette, J. Nucl. Mater. 131 (1985) 118-125.

MICROSTRUCTURAL EVOLUTION OF NEUTRON IRRADIATED Fe-Cr-Ni ALLOYS AT 495°C IN RESPONSE TO CHANGES IN He/dpa RATIO, J. F. Stubbins and J. E. Nevling (University of Illinois), F. A. Garner (Pacific Northwest Laboratory) and R. L. Simons (Westinghouse Hanford Company)

OBJECTIVE

The objective of this study is to provide microstructural data that will provide information on the separate and synergistic roles of helium, composition, thermal-mechanical treatment and irradiation variables on the evolution of radiation-induced microstructure.

SUMMARY

A series of three Fe-15Cr-XNi alloys in both annealed and cold-worked conditions was irradiated in the Fast Flux Test Facility at 495°C to 14 dpa. The experiment was developed to determine the separate and synergistic effects of nickel and phosphorus content, cold-work, and helium/dpa ratio. This experiment was conducted without introducing variations in displacement rate, a variable known to strongly influence microstructural evolution. Each alloy condition was irradiated in two variants, one with natural nickel and one enhanced with the ^{59}Ni isotope. The latter variant produces helium/dpa ratios typical of fusion reactor spectra while the former yields a much lower level of helium. The results show that helium alters the microstructural evolution somewhat at 495°C but its effect is relatively small compared to the influences of the other variables studied. Increases in starting dislocation density, nickel content, or phosphorus level all retard swelling temporarily while higher rates of helium generation, usually, but not always, accelerate swelling. Phosphorus addition of 0.04 wt% not only decreased swelling but lead to refinement of dislocation loop microstructure and stabilization of dislocation networks created by cold working. Phosphide precipitates did not form at this temperature and dose level.

PROGRESS AND STATUS

Introduction

There has been continuing concern about the effects of helium production in neutron environments during elevated temperature irradiation. This interest stems from the fact that helium can help initiate and grow voids formed during irradiation. It also has the potential for causing embrittlement of alloys at elevated temperatures where it is mobile enough to segregate to grain boundaries. The extent of the effect is dependent not only on the levels of helium but also on the rate at which it is produced and the time during the irradiation history at which it is produced. This concern is particularly acute for materials for potential fusion applications since the amounts of helium generated in most materials through transmutation reactions are significantly higher than those generated in thermal and fast reactors. This is due to the fact that the transmutation cross-section for producing helium normallv exhibits an energy threshold which is above the average neutron energy found in fission spectra, but well within the range of neutron energies expected in fusion environments.

The significance of this problem was recognized many years ago, but the study of the effect has been limited due to the lack of a high flux source of high energy neutrons. While surrogate spectra are available for purposes of simulation, it is not always possible to simultaneously achieve high irradiation doses and concomitant high helium levels expected for technological applications. Other experimental approaches have been pursued to gain some insight into this potential problem. These approaches include the use of materials with pre-implanted helium, material infused with tritium which decays to helium, material alloyed with boron or nickel which have larger (n,α) cross-sections at low neutron energies, or materials with helium injected simultaneously during ion or electron irradiation. These approaches, while useful, all have drawbacks which limit their effectiveness for characterizing helium effects in anticipated fusion environments. These experimental techniques, along with several other aspects of the effects of helium on fusion reactor structural materials have been reviewed recently'.

One measure of the relevant helium production rate is the ratio of the rate of helium production to the atomic displacement rate. Since this is a ratio of rates, it is expressed as the helium to dpa ratio, normally atomic parts per million (appm) He/dpa. This ratio is expected to remain relatively constant during irradiation in fusion environments but can vary strongly in materials irradiated in fission neutron spectra. In some cases, where little or no transmutation occurs, the ratio will approach zero. But, in others, especially those where nickel is present in materials irradiated in mixed spectra reactors, the ratio is initially low, then builds up to a significant level. This is due to the fact that the isotope of nickel which has a significant (n,α) cross-section for thermal neutrons is not found in naturally occurring nickel. Instead, this isotope, ^{59}Ni, is formed by the capture of a neutron by ^{58}Ni. The ^{59}Ni, once formed, can capture a further neutron, to briefly form ^{60}Ni. This isotope decays by the emission of an alpha particle to ^{56}Fe. The alpha particle acquires the two electrons necessary to neutralize it during the slowing down process and becomes a stable helium atom. Since this is a two-step process, the amounts of helium produced

become significant only after a protracted irradiation period and then build to a nearly steady source for relevant displacement levels.

While this transmutation reaction is a means of producing high levels of helium in fission reactor spectra, it normally has the drawback that small amounts of helium are generated during the early stages of irradiation, the time during which the initial irradiation-induced microstructure is evolving. This is contrary to the case of anticipated fusion neutron environments where helium is produced during the very early stages of irradiation, and could strongly affect void nucleation and other features of microstructural development.

As a means of circumventing the drawback associated with the use of natural nickel in fission reactor, Simons et al.[2] initiated a program to fabricate nickel-bearing alloys enriched in the ^{59}Ni isotope. This was possible since a relatively large amount of that isotope was contained in an Inconel 600 compact tension specimen which had been irradiated in a thermal reactor for nearly six years. The first results of the examination effort on materials doped with ^{59}Ni are reported here. The subset of materials examined in the current study are those irradiated at 495°C with helium/dpa ratios of 0.35 and 4.7, or 0.57 and 4.9 appm/dpa, depending on the composition of the alloy. The experiment explored the separate and synergistic effects of helium, nickel, phosphorus and cold-work on swelling and microstructural development. Phosphorus, higher levels of nickel, and cold-work are all known to suppress void swelling and exert other strong effects on the development of microstructure.

The most important feature of this experiment is that the influence of helium is examined without introducing a variation in another important variable, namely the displacement rate. Swelling and microstructural evolution are very sensitive to both temperature and displacement rate and meaningful experiments on the influence of helium cannot be conducted if these are simultaneous variations in either of these variables.

EXPERIMENTAL PROCEDURE

Specimens suitable for transmission electron microscopy were prepared in the form of 3-mm discs from Fe-15Cr-XNi alloys having the compositions shown in Table 1. Half of the specimens were fabricated using nickel enriched in the ^{59}Ni isotope and the balance with natural nickel. In addition to the differences in the isotopic composition of nickel, two levels of nickel were used (25 and 45%), and 0.04% phosphorus was added to a variant of the lower nickel alloy.

Specimens were also prepared in both the solution annealed and the cold-worked state for all compositions. After a series of cold reductions and anneals in argon at 1030°C, the alloys were cold-reduced to 0.25 mm (10 mils) resulting in a 20% reduction in thickness. Microscopy specimens for irradiation were punched from these sheets. Half remained in the 20% cold-worked state, while the other half received a final solution treatment of 1030°C for 30 minutes.

A detailed description of the irradiation conditions for these alloys is given elsewhere[2]. The alloys in the present program were irradiated at ~3 x 10^{-7} dpa/s (~7.2 x 10^{19} n.m^2/s; E > 0.1 MeV) in the Fast Flux Test Facility (FFTF) at a temperature of 495°C which was actively controlled to ±5°C. One temperature excursion to 600°C for 10 minutes was experienced after approximately 2 dpa had been accrued. The irradiations were carried out in the Materials Open Test Assembly (MOTA) and the specimens were irradiated to a total of 14 dpa (3.35 x 10^{26} n/m^2; E > 0.1 MeV).

Table 1

Composition of Alloys (weight percent)

Condition	Alloy Oesisnation					
Soln. Anneal:	MB1A	MBZ6	MB1B	MBZ7	MB1E	MBZ9
Cold-Worked:	MBZ3	MBZX	MBZ4	MBZZ	MBZ5	MBZ1
Element						
Fe	60.0	60.00	60.0	60.0	40.0	40.0
Ni, total	25.0	25.00	25.0	25.0	45.0	45.0
Cr	15.0	15.0	15.0	15.0	15.0	15.0
P	0.0	0.0	0.04	0.04	0.0	0.0
^{59}Ni	0.434	0.0	0.412	0.0	0.420	0.0

Specimens were analyzed for macroscopic volume changes as well as microstructural parameters. Immersion density measurements accurate to ±0.16% change in volume were carried out on all specimens to determine the bulk density change. Each reported density is the average of three separate measurements on nominally identical specimens. The microstructural information was obtained using a JEM **JEOL** 100CX scanning transmission electron microscope (STEM) operated at 100 kV. This microscope was equipped with a double tilt stage for large angle tilting.

The helium levels of the various alloys were determined within 1% uncertainty by Brian Oliver of Rockwell International, yielding He/dpa ratios of 0.35 and **4.7** for the low and high helium cases of Fe-25Ni-15Cr. For **Fe-45-Ni-15Cr,** the He/dpa ratios were 0.57 and **4.9;** the increase is due to the (n,α) contribution of the natural nickel.

.RESULTS

The results of the immersion density measurements are shown in Figure 1. Several trends are clear from the data. The cold-worked material always shows lower bulk swelling than does the corresponding solution annealed material ; the phosphorus-doped low nickel compositions show lower swelling than do their undoped counterparts; and the higher nickel alloys show lower swelling than do their lower nickel counterparts. Another trend is also found with **one** exception. The bulk swelling increases a small to moderate amount from low to high helium content except for the solution annealed, low nickel alloy with no phosphorus. In all cases, however, the change due to increased helium is less than 0.8% swelling.

The immersion density measurements indicate in two cases that densification took place during irradiation. In the high nickel case, the apparent densification is within the range of uncertainty of the density measurement technique. (Densification is commonly observed in solute-free Fe-Cr-Ni alloys at such nickel levels). In the case of the phosphorus-doped, cold-worked, low helium, low nickel alloy, a substantial net densification is quite clearly indicated, however.

Microstructural analysis was carried out on all specimens, but it was possible to obtain only **a** limited amount of information on the high helium, cold-worked, low nickel alloy without phosphorus. In all cases, voids were found after irradiation, even in specimens which exhibited a net densification in the immersion density measurements. The results of void and dislocation measurements are reported in Table **2.** The loops frequently exhibited a bimodal distribution. Loops with diameters small than 6 nm are described as "small" in Table **2.**

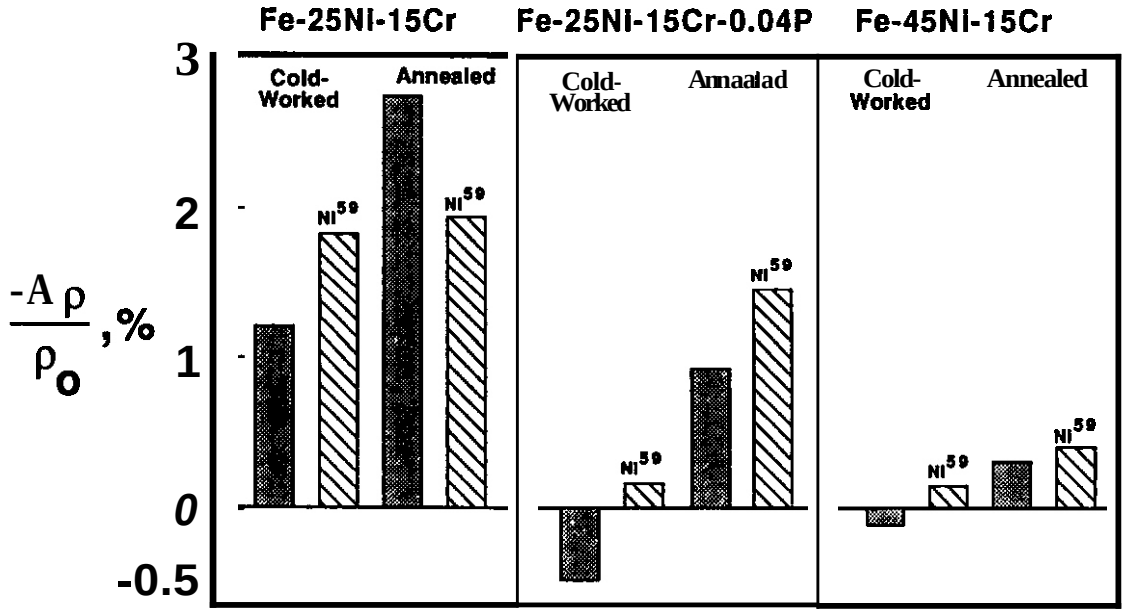

Figure 1. Density Changes Observed in the Twelve Alloy Conditions Irradiated in this Experiment.

Table 2

Microstructural Parameters for Irradiated Alloys

Specimen Number	Voids				Dislocations						Network Dislocations
					Total		Large		Small		
	$-\Delta\rho/\rho_o$ (%)	$\Delta V/V_o$ (%)	N_v ($\times 10^{21} m^{-3}$)	d_v (nm)	d_ℓ (nm)	N_ℓ ($\times 10^{21} m^{-3}$)	d_ℓ (nm)	N_ℓ ($10^{21} m^{-3}$)	d_ℓ (nm)	N_ℓ ($\times 10^{21} m^{-3}$)	($\times 10^{14} m^{-2}$)
FE-25Ni-15Cr											
MBZX (CW)[c]	1.2	0.4Z	1.21	22.2	19.4	4.0	21.3	1.3	<6	2.6	1.4
MBZ3 (CW,He)	1.8	0.2	1.82	26.8	(a)						
MBZ6 (SA)	2.7	1.1	3.70	20.9	9.1	4.0	24.4	0.7	< *	*9	2.0
MB1A (SA, He)	1.9	0.6	1.05	26.4	10.5	2.3	21.0	0.7	<6	1.8	2.3
Fe-25Ni-15C4-0.04P											
MBZZ (CW)	-0.5	0.08	0.74	13.4	(b)						
MBZ4 (CW, He)	0.1	0.25	1.37	15.2	(b)						
MBZ7 (SA)	0.9	0.41	1.67	19.3	11.8	2.4	22.0	0.8	<6	1.5	1.3
MB1B (SA, He)	1.4	0.51	2.13	18.8	9.1	6.2	16.9	1.7	<6	4.6	1.7
Fe-45Ni-15Cr											
MBZ1 (CW)	-0.16	0.04	0.12	18.6	19.8	3.1	27.8	2.0	<6	1.2	2.2
MBZ5 (CW,He)	0.08	0.09	0.11	28.6	12.5	3.3	20.1	1.7	<6	1.65	2.2
MBZ9 (SA)	0.2	0.09	0.39	18.2	16.9	0.7	33.7	0.3	<6	0.4	1.7
MB1E (SA,He)	0.3	0.11	0.51	17.8	14.1	3.1	31.0	1.0	<6	2.1	1.5

(a) Insufficient thin area to determine these parameters.
(b) Dislocation and loop density were too high to separate individual images for counting.
(c) CW = cold worked; SA = solution annealed, He = doped with ^{59}Ni.

In every solution annealed specimen, the measured void swelling underpredicts the bulk swelling measured by immersion density. For the high nickel alloys, this underprediction is within the range of uncertainty for both measurements. In the other cases, there is a clear difference between the swelling measured from the microstructure and that measured by immersion. However, the trends observed for void swelling determined by microscopy are the same as those observed in the density measurements. It was found by repeated measurements that neither the microscopy nor immersion measurements are in error. The reason for the difference in the absolute values produced by the two measurement techniques will be addressed in the Discussion section.

Figures 2, 3, and 4 show a comparison of the void size versus number density distribution for each set of samples. Figure 2 shows that the higher level of helium accelerates void nucleation in Fe-25Ni-15Cr as evidenced by the extension of the distribution to higher void sizes. In the cold-work case, however, this leads to more swelling, while in the annealed case, it leads to less swelling. These distributions indicate that the critical radius for bias-driven void growth at 495°C in Fe-25N-15Cr is rather small since no bimodal size population was observed in either the low helium or high helium condition.

The effect of phosphorus addition to Fe-25Ni-15Cr is to retard temporarily the swelling in the solution annealed alloys. Figure 3 shows that, for the phosphorus-bearing alloys, the average void sizes are somewhat smaller as are the void number densities. The retardation of swelling is counterbalanced somewhat by higher levels of helium. The shift to smaller void sizes with high helium levels is pdrticularly pronounced for the cold-worked irradiation however. In addition, TEM analysis indicates that the loop and dislocation structure are more refined in the case of alloys containing phosphorus. No precipitation of phosphides or other phases was observed.

The 45% nickel, solution annealed alloys exhibit very similar swelling behavior. Figure 4 indicates that the effect of helium on the size distribution of voids found in these alloy conditions is rather slight. The cold-worked condition at 45% nickel presents a quite different picture however. Note in Figure 4 that the combined influence of cold-work and high nickel content has made it sufficiently difficult at 495°C to nucleate voids that, for the first time in this experiment, the operation of a critical radius can be easily observed, as evidenced by the presence of a bimodal cavity population. When imaged at high magnification, there is a second population of cavities with smaller sizes ranging from 1 to 4 nm at a total density of ~3 x 10^{21} m^{-3}.

Cold working was shown in the immersion density results to have a distinct retarding effect on swelling in all of the alloy groups, especially for the low nickel alloy groups. The swelling values determined by microscopy for the high nickel alloys are all similar regardless of prior condition or nickel isotopic make-up. The dislocation and loop structures are similar in all cases. The void size distributions are peaked toward larger diameters, but smaller number densities, for the cold-worked specimens in this group (see Figure 4). However, the numbers of voids were small, resulting in less than normal accuracy in the counting statistics.

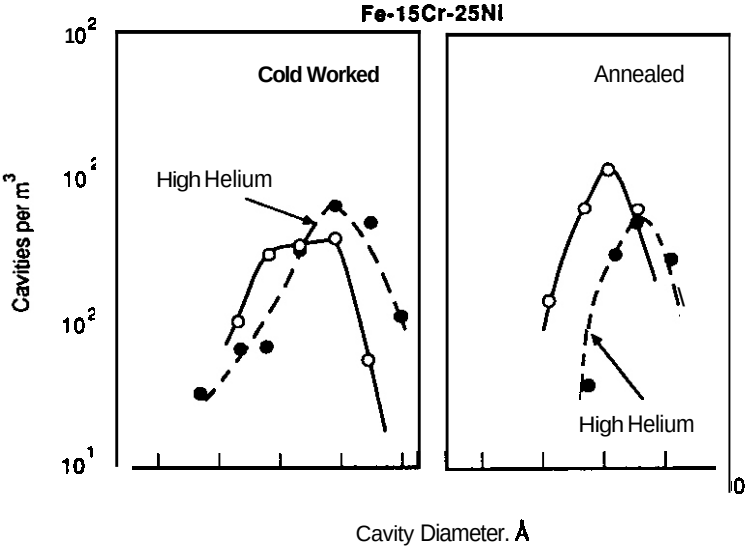

Figure 2. Void Size Distribution in Four Variants of Fe-15Cr-25Ni. Theswelling values calculated from void measurements are 0.42% for the cold-worked, low He case; 1.2% for the cold-worked, high He case; 1.1% for the annealed, low He case; and 0.65% for the annealed, high He case.

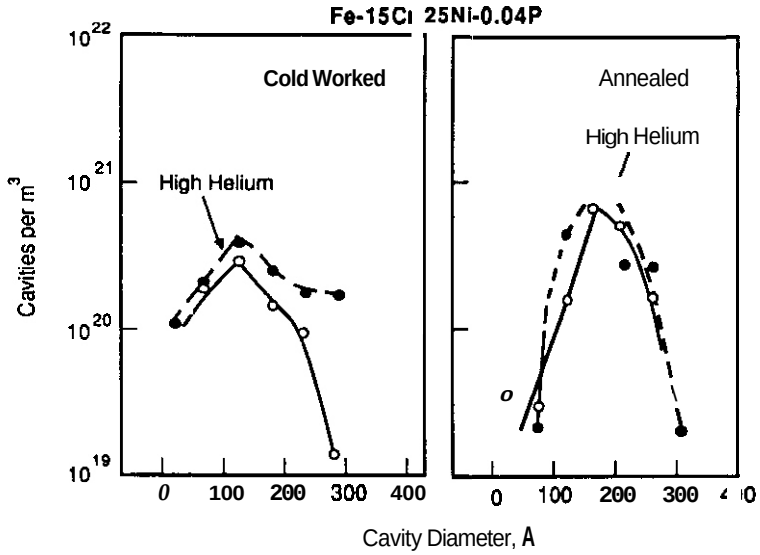

Figure 3. Void Size Distribution in Four Variants of Fe-15Cr-25Ni-0.04P. The swelling values calculated from void measurements are 0.08% for the cold-worked, low He case; 0.25% for the cold-worked, high He case; 0.41% for the annealed, low He case; and 0.51% for the annealed, high He case.

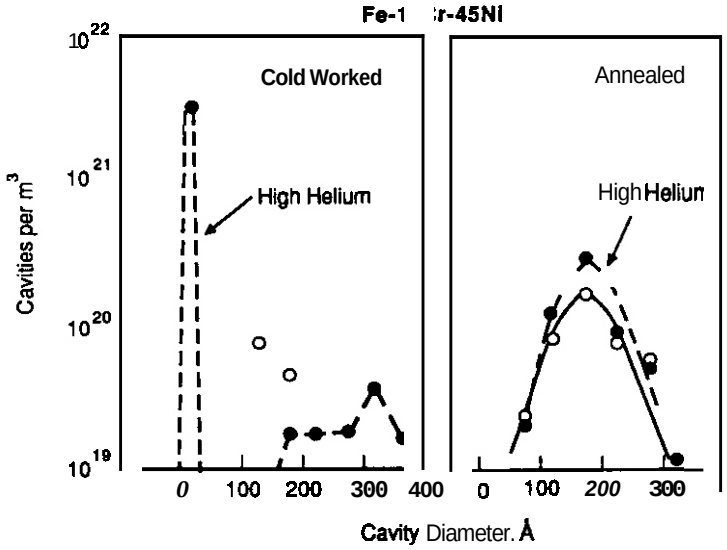

Figure 4. Void Size Distributions in Four Variants of Fe-15Cr-45Ni. No cavities were found in the cold-worked high helium case in the 50-150Å range. The swelling values calculated from void measurements are 0.04% for the cold-worked, low He case; 0.09% for the cold-worked, high He case; 0.09% for the annealed, low He case; and 0.11% for the annealed, high He case.

In the case of the phosphorus-doped alloys, cold working has the effect of suppressing swelling. Voids are unevenly distributed, often grouped in patches exhibiting larger sizes and number densities, surrounded by volumes of lower number densities and smaller void sizes. The swelling values were taken from an average over a wide range of volumes and should be representative of the volume average. Figure 3 indicates that the void number densities are higher in the specimen with the ^{59}Ni addition but that the size distribution follows the same trend, again with very similar average void sizes in the two cases.

The behavior is less clear for the low nickel, cold-worked specimens without phosphorus doping due to the difficulty in examining one of the two conditions. (Insufficient thin area was produced in those specimens.) It is clear, however, that the void sizes are larger on average as are the void number densities in the cold-worked specimens without phosphorus additions. In addition, the dislocation structures are much coarser than in the case of the phosphorus-containing alloys. In the cold-worked specimens, the initially high density of dislocations is maintained with phosphorus; but, in the absence of phosphorus, the network relaxes to the significantly lower levels typical of that developed in annealed specimens.

DISCUSSION

Helium Effects

With one exception, cavity size distributions in Fe-15Cr-25Ni and Fe-15Cr-45Ni at 495°C do not appear to be strongly affected by the simultaneous generation of significant levels of helium. (The exception is the bimodal population observed in the cold-worked 45% nickel specimens at high helium levels.) The immersion density data indicate, in all cases but one, that the higher helium content results in larger values of bulk swelling but in no cases are the absolute differences in swelling very large, being always less than 1%. These steels are known to swell at ~1%/dpa after a transient period on the order of 10 dpa or greater, the duration of the transient depending on the nickel content, displacement rate and temperature. Therefore, all helium-induced swelling differences observed in this study could be explained by a shift in incubation period of only 1 dpa or less.

On the other hand, the microstructural data regarding numbers and sizes of voids show that the visible void population is often very similar between the low and high helium conditions. Exceptional care was taken in looking for small voids or bubbles, but only in the cold-worked, 45% nickel, high helium case was it possible to identify a large population of small cavities. Nor was there a significant population of cavities found at grain boundaries, which might also have explained the differences in swelling measurements between the microscopy and immersion techniques.

The role of helium in cavity formation has been modelled by several investigators and reviewed in reference 1. Recent calculations[3,4] made with material parameters representative of the present Fe-Ni-Cr alloys indicate that helium in sufficient quantities can reduce the critical diameter for void formation by more than 10% or, alternately, reduce the dose required to attain significant void formation by a factor of more than ten. Nevertheless, at irradiation temperatures of 500°C (very similar to the 495°C in this study), much larger quantities of helium were required than at a temperature only 50°C lower. Thus the present experimental results, where only marginally larger swelling was found in the high helium specimens, are not surprising. In addition, the very similar void size distributions found for several of the pairs of alloy conditions with high/low helium indicate that, while the helium may facilitate the nucleation of voids initially, this head-start does not have significant long-term consequences. The presence of a few larger diameter voids in the high helium specimens would also indicate that nucleation occurs slightly more rapidly in those alloy conditions but in no way prohibits the growth of the early void/embryo population beyond the critical size.

The bimodal population found in the cold-worked, 45% nickel, high helium alloy shows clearly that helium was accumulating in small subcritical bubbles but conditions were not favorable for easy promotion to voids. The combined suppressing effect of cold-work and high nickel level must have significantly increased the size of the critical radius. At 25% nickel, the conditions were sufficiently favorable (even in the cold-worked condition) throughout the irradiation that bubbles were quickly promoted to voids.

This behavior is very similar to the observation of Lee and Mansur on ion-irradiated Fe-15Cr-15Ni and Fe-15Cr-35Ni[5]. These authors noted that one could use bimodal distributions to define the critical size for cavity promotion. Based on the largest size cavity in the smaller size population, it would appear in this study that the critical radius for cold-worked 45% nickel alloy at 495°C is ~4 nm.

Effects of Cold Working

The cold-worked specimens showed lower swelling in general than the solution annealed material. This suppression is usually attributed to the higher initial sink density for point defects, reducing the supersaturations driving cluster nucleation. In the two alloy conditions (25 and 45% Ni) without phosphorus, the cold-work dislocation structure had largely disappeared during irradiation, and a dislocation and loop structure similar to the solution annealed material was present. This phenomenon has been reported and modelled previously in alloys irradiated at similar temperatures[6]. It is also in line with predictions in more recent modelling work[4] that a saturation loop and dislocation structure is reached prior to 10 dpa for both solution annealed and 20% cold-worked material irradiated at 500°C. In addition, the saturation loop and dislocation densities are auantitatively identical reaardless of startina dislocation values[4,6]. The lower swelling in the cold-worked condition probably stem; from the temporary suppression of void formation during the initial period of dislocation restructuring under irradiation.

It was also noted that two of the cold-worked conditions showed densification upon irradiation when measured using an immersion technique while voids were clearly found in both cases. Very slight increases in volume due to cold working of stainless steel have been reported[9], but a recovery in the dislocation structure such as found here could not fully account for even the slight densification found in the higher nickel cold-worked alloy. This suggests that the lattice parameter of the alloy is being reduced. Since no precipitation was observed, some kind of segregation or short range ordering must be occurring on a very fine scale.

The cold-worked dislocation density in the phosphorus-containing alloy did not substantially recover during irradiation. Phosphorus additions have been shown in other studies to lead to retention of cold-worked dislocation microstructures[8] and to a refinement of loop microstructures in annealed specimens[9,10].

Phosphorus Effects

The effect of phosphorus additions was to retard swelling somewhat, with the maximum change being about 1.7% swelling. In every case studied, a phosphorus addition of 0.04% resulted in lower swelling than the same alloy condition without phosphorus. In earlier work to similar doses but at lower temperatures, 399 to 427°C, phosphorus was observed to first increase swelling in Fe-25Ni-15Cr at low phosphrous levels, then to decrease it strongly at higher levels[11]. In fact, no pronounced effect of phosphorus was found for irradiation temperatures slightly above and below the irradiation temperature of the present study.

Radiation-induced phosphide precipitation has also been proposed to influence swelling in both simple and moderately complex alloys, primarily by providing sites for helium precipitation at subcritical cavity sizes[5,9,12]. Previous irradiation studies[9] on more complex steels have also found voids associated with phosphides at temperatures of 525°C but only for doses in excess of 30 dpa. (Phosphides were also identified at lower doses but at much higher irradiation temperatures.) However, the microstructures found in this study show no trace of the development of phosphides, either through an identifiable precipitate morphology or as extra spots (reflections) in selected area diffraction patterns. While there is obvious merit to the phosphide-helium interaction model, it cannot explain the results of this study.

Phosphorus has also been proposed to retard void nucleation by strongly binding with vacancies, thereby raising their equilibrium concentration and strongly decreasing the supersaturation of vacancies[11,14,15]. This mechanism operates most strongly at higher irradiation temperatures with a relatively moderate influence predicted at 495°C. This model is, therefore, consistent with the results of the present study.

It does seem clear from the dislocation and loop morphologies that phosphorus acts to stabilize the dislocation structure. This is especially clear in the cold-worked material where the dislocation densities were still quite high after irradiation. The relative stability of this high sink density should also contribute to the reduction in swelling relative to that of the phosphorus-free alloys. In the solution annealed material, the dislocation loop structures are much finer than in the comparable conditions without phosphorus. Once again, this is in agreement with the results of other studies[8-10]. Watanabe and coworkers attribute the refinement to arise from a strong binding of phosphorus with interstitial atoms[10]. This mechanism would exert its strongest influence at relatively low irradiation temperatures.

Nickel Concentration Effects

As expected, the 45% nickel alloys all exhibited low swelling relative to that at 25% nickel. The increased swelling resistance at larger nickel levels is well established and has been related to the increased level of vacancy diffusivity at higher nickel content[11,16-19]. This results in an increase in the critical radius for void formation and a delay in the onset of steady-state swelling[19].

In the compositional regime of 25 to 45% nickel, there has also been observed a radiation-induced hardening component that increased with nickel content[20]. This hardening is thought to be associated with spinodal decomposition[21] accelerated by radiation[22-24]. At this irradiation temperature, however, the wavelength of the spinodal decomposition is expected to be below the limit of resolution associated with the EDX technique employed. Indeed, in the present case, the existence of spinodal-like microsegregation could not be established using an EDX technique whose resolution limit is on the order of 30 nm.

We are presented in this study with several indications of positive or negative lattice parameter changes resulting from irradiation that cannot be attributed to observable precipitation. The first of these was found in several cold-worked alloys and was discussed earlier. It is also proposed that the mismatch between the swelling determined by microscopy and immersion density, particularly at 25% nickel, arises due to some microsegregation process. This proposal is supported by some soon-to-be published work on two related experiments involving the same alloys. In each experiment, with microscopy conducted by different individuals, the 25% nickel alloy exhibits more density change than can be explained in terms of measured voidage. It should be noted that the spinodal-like decomposition mentioned earlier was discovered because a measured change of 1% in density occurred in a Fe-7.5Cr-35Ni solute-free alloy prior to the onset of swelling!'. The possibility of segregation-induced lattice parameter changes in irradiated Fe-25Ni-15Cr will be explored using x-ray diffraction and anomalous x-ray absorption.

Once again, we consider it important to note that this study was conducted under conditions which involve no influence of displacement rate. This variable has been shown to have a very large influence in determining the duration of the transient regime that precedes the onset of steady-state swelling.

CONCLUSIONS

A series of three Fe-Ni-Cr alloy compositions in both the annealed and cold-worked conditions, and each with two variants in helium generation rate, have been examined after irradiation in FFTF to approximately 14 dpa at 495°C. Other important variables in this experiment were the nickel and phosphorus contents and the initial dislocation densities. The major conclusions of this study are as follows:

1. Under the conditions examined, the generation of helium has only a minor, but nevertheless observable, effect on void induced swelling. This effect, in all cases but one, was to moderately increase swelling.

2. In most cases, the distribution in void sizes and void number densities was affected only to a minor degree by the presence of high helium generation rates. The single exception was when high nickel levels and cold-work acted together to strongly suppress swelling. In this situation, a high rate of helium generation resulted in a bimodal void size distribution and allowed a determination of the minimum critical radius.

3. Phosphorus additions of 0.04% decrease swelling in all cases when compared to the same compositional and microstructural alloy condition without phosphorus. This effect may be linked to the stabilizing influence phosphorus has on the dislocation population and to the strong binding of phosphorus atoms with vacancies. It was not related to precipitate formation in this study.

4. An increase in nickel concentration from 25 to 45% caused a notable decrease in void swelling, consistent with the results of earlier studies. Higher levels of helium do not greatly alter the impact of nickel on void nucleation at 495°C.

5. In all cases, prior cold working to levels of 20% caused lower swelling than was observed in the same alloy in the solution annealed state.

6. In general, the effect of helium is small at 495°C compared to the influence of the other variables studied in this experiment.

FUTURE WORK

Analysis of the ^{59}Ni experiment will continue, focusing on specimens irradiated to higher displacement levels.

REFERENCES

1. Ullmaier, H., Nuclear Fusion, Vol. 24, 1984, pp. 1039-1083

2. Simons, R. L., H. R. Brager, and W. Y. Matsumoto, Journal of Nuclear Materials, Vols. 141-143, 1986, pp. 1057-1060.

3. Stoller, R. E., and G. R. Odette, in Radiation-Induced Changes in Microstructure: 13th International Symposium (Part 1), ASTM STP 955, F. A. Garner, N. H. Packan and A. S. Kumar, Eds., Philadelphia, PA, 1987, pp. 358-370.

4. Stoller, R. E., and G. R. Odette, in Reference 3, pp. 371-392.

5. Lee, E. H. and L. K. Mansur, Philosophical Magazine A, Vol. 52, 1985, pp. 493-508.

6. Garner, F. A. and W. G. Wolfer, in Effects of Radiation on Materials: 11th Conference, ASTM STP 782, H. R. Brager and J. S. Perrin, Eds., Philadelphia, PA, 1982, pp. 1073-1087.

7. Garafalo, F. and H. A. Wriedt, Acta Metallurgica, Vol. 10, 1962, p. 1007.

8. Itoh, M., S. Onose, and S. Yuhara, in Reference 3, pp. 114-126.

9. Lee, E. H. and N. H. Packan, "Swelling Suppresion in Phosphorus-Modified Fe-Cr-Ni Alloys During Neutron Irradiation," accepted for publication in ASTM-STP.

10. Watanabe, H., A. Aoki, H. Murakami, T. Muroga and N. Yoshida, Journal of Nuclear Materials, Vols. 155 157, 815-822.

11. Garner, F. A., and A. S. Kumar, in Reference 3, pp. 289-314.

12. Lee, E. H. and L. K. Mansur, Journal of Nuclear Materials, Vols. 141-143, 1986, pp. 695-702.

13. Pedraza, D. F., and P. J. Maziasz, in Reference 3, pp. 161-194.

14. Garner, F. A., and H. R. Brager, Journal of Nuclear Materials, Vols. 133 and 134, 1985, pp. 511-514.

15. Garner, F. A. and H. R. Brager, Journal of Nuclear Materials, Vols. 155-157, 1988, pp. 833-837.

16. Esmailzadeh, B. and A. S. Kumar, in Effects of Radiation on Materials: 12th International Symposium, ASTM STP 870, F. A. Garner and J. S. Perrin, Eds., Philadephia, PA, 1985, pp. 468-480.

17. Garner, F. A., and W. G. Wolfer, Journal of Nuclear Materials, Vols. 122 and 123 (1984) pp. 201-206.

18. Garner, F. A., Journal of Nuclear Materials, Vols. 122 and 123 (1984) pp. 459-471

19. Coghlan, W. A. and F. A. Garner, in Reference 3, pp. 315-329.

20. Brager, H. R., F. A. Garner, and M. L. Hamilton, Journal of Nuclear Materials, Vols. 133 and 134, 1985, pp. 594-598.

21. Russell, K. C. and F. A. Garner, "High Temperature Phase Separation in Fe-Ni and Fe-Ni-Cr Invar Alloys," submitted to Acta Metallurgica.

22. Garner, F. A., H. R. Brager, and J. M. McCarthy, in Reference 3, pp. 775-787.

23. Garner, F. A., H. R. Brager, R. A. Dodd and T. Lauritzen, Nuclear Instruments and Methods in Physics Research, Vol. 168, 1986, pp. 244-250.

24. Dodd, R. A., F. A. Garner, J. J. Kai, T. Lauritzen and W. G. Johnston, in Reference 3, pp. 788-804.

PRECIPITATION AT GRAIN BOUNDARIES IN IRRADIATED AUSTENITIC Fe-Cr-Mn ALLOYS

3. M. McCarthy (Pacific Northwest Laboratory)[a]

OBJECTIVE

The objective of this work is to assess the suitability of Fe-Cr-Mn alloys for fusion reactor service.

SUMMARY

In previous work. the phase stability of Fe-Cr-Mn alloys during irradiation was investigated in a study that included simple binaries. simple ternaries and commercially produced alloys. These low activation alloys are being considered for fusion reactor service in the first wall and in other structural applications subject to high neutron doses. In addition to phase instabilities observed within the grains, grain boundaries were susceptible to varying levels of precipitation dependent upon alloy canposition. displacement dose and irradiation temperature. This report describes the grain boundary microstructures that developed in these Fe-Cr-Mn alloys during irradiation.

PROGRESS AND STATUS

Introduction

The Fe-Cr-Mn system has been proposed to replace the Fe-Cr-Ni system in the construction of components for fusion energy devices.[1-5] This change is directed tcuard the attainment of greatly reduced levels of long term radioactivity. Manganese is a much more reactive element than nickel, however. and there is concern that reduced activation will be achieved at the expense of phase stability. corrosion resistance, and other properties.

Stainless Fe-Cr-Mn austenitic steels have been found to be subject to more phase instability than austenitic Fe-Cr-Ni stainless steels.[6] At low Mn and Cr contents. these alloys are subject to martensitic transformations to epsilon and alpha martensite.[7,8] At high Cr contents. the simple ternary alloys are subject to phase transformations to body-centered cubic (bcc) chi. h solute modified commercial alloys. to tetragonal sigma and to face-centered cubic (fcc) $M_{23}C_6$ carbide.'" The latter three phases are the most important at grain boundaries although the martensitic transformations do create more grain boundary surface area for precipitation.

EXPERIMENTAL DETAILS

Simple binary, ternary and commercial Fe-Cr-Mn alloys in the form of disks 3000 μm in diameter and 250 μm thick were irradiated in the Materials Open Test Assembly of the Fast Flux Test Facility (MOTA/FFTF) to doses as high as 75 displacements per atom (dpa) at 420, 520, and 600 ± 5°C. The simple ternaries had chranium contents of 5, 10 and 15 wt% and Mn contents of 15, 20, 25. 30 and 35 wt%.[7] The commercial alloys that were examined had chranium contents of 4, 10, and 18 wt% and Mn contents of 12, 18 and 19 wt% with minor additions of Mo, Ni. Si, Cu. C and P. See tables 1 and 2. The disks were electrc-polished to transmission thickness and then examined in a JEOL 1200ex analytical transmission/scanning transmission electron microscope (TEM/STEM) equipped with a beryllium window energy dispersive X-ray detector and a TN-5500 multi-channel analyzer. Phases were identified by measuring d-spacings fran several low index zone axis electron diffraction patterns and by using a canputer program to generate the same zone axis pattern for the suspected phase using the camera constant of the microscope. Canpositions were determined using a semi-quantitative computer program for X-ray spectra analyses.

TABLE 1. Canposition of Commercial Fe-Cr-Mn Austenitic Alloys

Designation	Vendor	Composition wt%
Nitronic Alloy 32	ARMCO	18Cr-12Mn-1.5Ni-0.6Si-0.2Cu-0.2Mo-0.4N-0.1C-0.02P
18/18 Plus	CARTECH	18Cr-18Mn-0.5Ni-0.6Si-1.0Cu-1.1Mo-0.4N-0.1C-0.02P
AMCR 0033	CREUSOT-MARREL	10Cr-18Mn-0.7Ni-0.6Si-0.06N-0.2C
NMF3	CREUSOT-MARREL	4Cr-19Mn-0.2Ni-0.7Si-0.09N-0.02P-0.6C

(a) Operated for the U.S. Department of Energy by Battelle Memorial Institute under Contract DE-AC06-76RLO 1830.

TABLE 2. Thermal-Mechanical Starting Conditions

Description	Conditions
Nitronic Alloy 32	CW
18/18 Plus	CW, CWA
AMCR	CW, CWA, SAA
NMF3	CW

RESULTS

The alloys with chranium contents at and above 10 wt% were most susceptible to intergranular precipitation of chranium-rich bcc chi, fcc $M_{23}C_6$ carbide. and tetragonal sigma. See Table 3 and Figures 1, 2 and 3. A Simple ternary alloy. Fe-15Cr-20Mn, precipitated chi at grain boundaries. Alloys with greater than 10 wt% chranium and sane carbon. two of the commercial alloys, 18/18 Plus and Nitronic Alloy 32 precipitated chromium-rich $M_{23}C_6$ carbide at grain boundaries and at 600°C, chranium-rich sigma. AMCR with less chromium, but more carbon and with molybdenum and copper missing when canpared to 18/18 Plus and Nitronic Alloy 32, precipitated $M_{23}C_6$ instead of sigma when irradiated at 600°C. See Tables 1 and 2.

Decomposition to bcc alpha-ferrite, $M_{23}C_6$ carbide and retained austenite at the grain boundaries occurred in a 4 wt% chranium alloy. NMF3, irradiated at 520°C to 75 dpa (see Figure 4 and Tables 1 and 2), in a 10 wt% chranium alloy, AMCR, irradiated at 420°C to 75 dpa, and in an 18 wt% chranium alloy. 18/18 Plus, irradiated at 420 C to 75 dpa (see Figure 5). NMF3 was irradiated in the 20% cold-worked condition. AMCR and 18/18 Plus were irradiated in the 20% cold-worked and aged condition. In the canmercial alloy 18/18 Plus small rectangular prisms of sigma precipitated on an advancing recrystallization front as it passed, leaving a distribution of sigma within the recrystallized grain. precipitation ceasing or slowing once the grain boundary moved on. See Figure 6.

In several of the Irradiated alloys, the electropolishing preferentially attacked regions near grain boundaries indicating possible chranium depletion there. Energy dispersive X-ray microanalysis shared bulk chranium content in a region to be 8.1 wt% and the chranium content at the center of an austenite grain in that region to be 5.1 wt%.

TABLE 3. Identified Phases

Phase	Structure	Lattice Constants nm	Composition
austenite, γ	face-centered cubic	a = 0.358	bulk alloy canposition dependent on segregation
alpha martensite a'	body centered cubic	a = 0.287	canposition same as the parent austenite
epsilon martensite, ε	hexagonal close packed	a = 0.2532 c/a = 1.625	composition same as parent austenite
alpha ferrite, a	body-centered cubic	a = 0.287	95-100 wt% Fe
sigma, σ	tetragonal	a = 0.880 c = 0.454	58.5 Cr - 40 Fe - 1.5 Mo
chi, χ	body-centered cubic	a = 0.889	chranium-rich canpared to maxtrix
$M_{23}C_6$ carbide	face-centered cubic	a = 1.06 nm,	composed of Cr, Mn, Fe and C. chranium-rich canpared to the matrix

Note: CW = 1030°C/0.5 h/air cool t 20% cold-work. CWA = cold-worked condition t 650°C/h/air cool. SAA = 1030°C/1 h/air cool t 760°C/2 h/air cool.

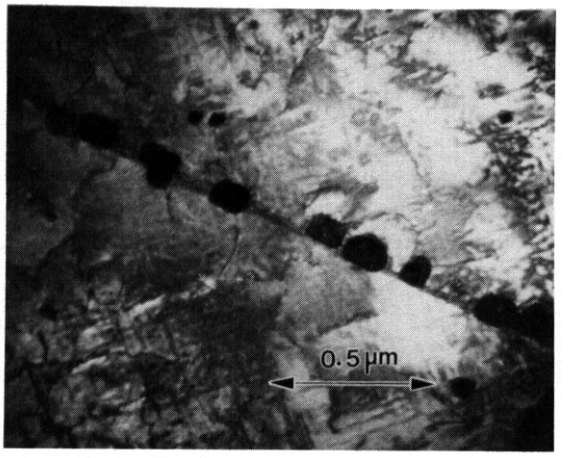

FIGURE 1. Bright field transmission electron microscopy (TEM) image of chromium-rich bcc chi at a grain boundary in Fe-15Cr-20Mn irradiated at 420°C to a dose of 9 dpa (420°C, 9 dpa).

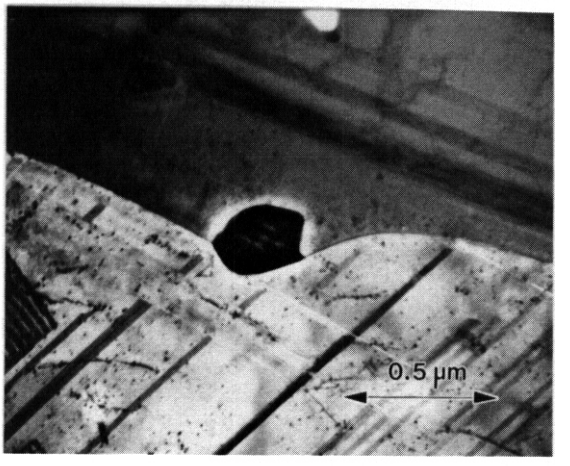

FIGURE 2. Bright field TEM image of fcc $M_{23}C_6$ carbide at a grain boundary in NMF3 (600°C, 60 dpa).

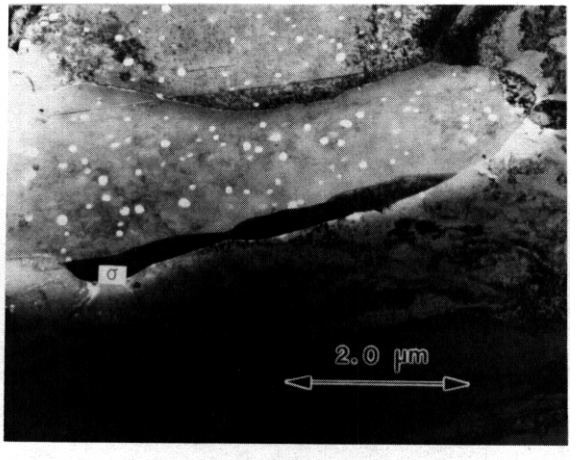

FIGURE 3. Bright field TEM image of tetragonal sigma coating a grain boundary in Nitronic Alloy 32 (600°C, 60 dpa).

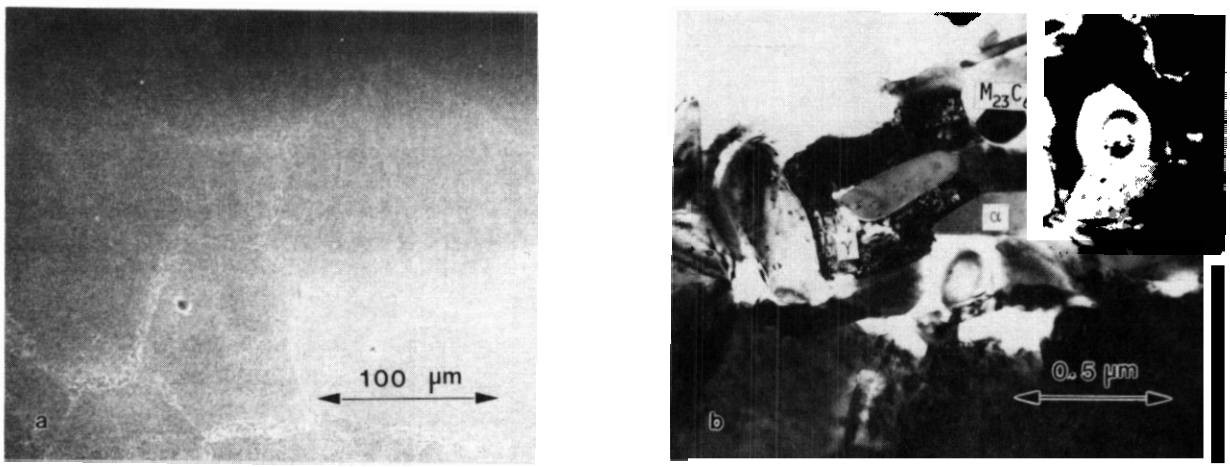

FIGURE 4. a. Low magnification SEM image of decomposed grain boundaries in NMF3 (520°C, 75 dpa).
b. High magnification TEM image of one of these grain boundaries.

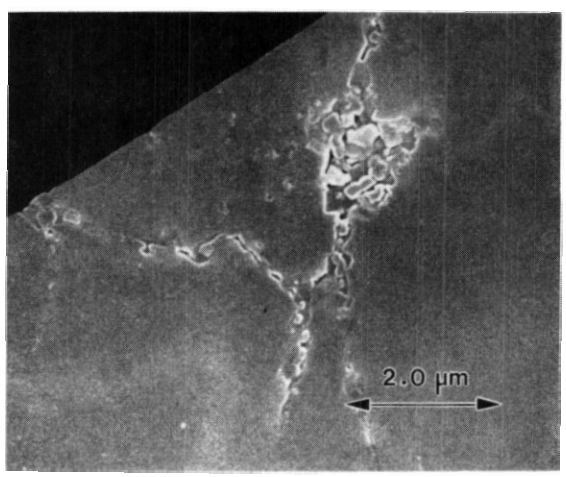

FIGURE 5. Scanning electron image of decomposed grain boundaries in 20% cold worked and aged AMCR (420°C, 75 dpa).

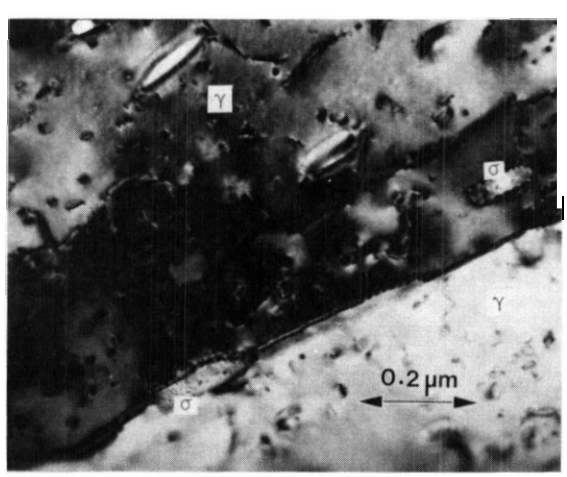

FIGURE 6 Bright field TEM image of small sigma precipitates within a recrystallized grain and at its grain boundaries in cold-worked 18/18 Plus (600°C, 60 dpa).

DISCUSSION

During irradiation a large supersaturation of vacancies is created and these vacancies move to sinks such as grain boundaries causing an equal and opposite movement of atoms away fran the sinks. This movement in turn leads to segregation of the slowest diffusing elements at these sinks. Mn is a fast diffuser and. therefore. concentrates Fe and Cr at the grain boundaries.[9,10] This mechanism is referred to as the Inverse Kirkendall Effect. This effect creates small regions which have canpositions that are very different fran the bulk canposition of the alloy. compositions at which multiple phases are likely to exist.

In addition to diffusion through the lattice. there is another major route by whlch atans are transported to precipitates at graln boundaries and that is along the grain boundaries. The diffusion coefficient here is orders of magnitude greater than that in the matrix.[11] This eventually leads to the coarsening of the grain boundary precipitates and finally to a coated grain boundary in sane regions. If the grain boundary is movlng as a result of a recrystallization process, its diffusion coefficient is Increased even more.[12,13] Sigma was observed to precipitate by this mechanism in cold worked 18/18 Plus irradiated at 600°C to 60 dpa in thls study and in thermally aged Fe-10.09 Cr-28.4Mn-0.46Si-0.01S-0.002P-0.006O-0.005N in a study by Garner. Abe and Noda.[14]

Chranium-rich phases such as bcc chi, fcc $M_{23}C_6$, and tetragonal sigma embrittle alloys by acting as nucleation sites for cracks whlch can initiate intergranular failure when these precipitates are located at grain boundaries. Therefore, it is desired that the grain boundaries in these austenitic Fe-Cr-Mn alloys remain relatively free of these brittle phases to preserve acceptable mechanlcal properties. The precipitation of chromium-rich phases also depletes the matrix of chranlum. This reduces the corrosion resistance of the alloy as a whole and. coupled with the depletion of manganese at the grain boundaries due to the Inverse Kirkendall Effect, increases the matrix iron content at the graln boundaries and subsequently can cause phase transformations to bcc alpha-ferrite.

In addition to the instabilities caused by segregation, cold work increases the dislocation density in the lattice adding to the free energy of these alloys, making them less stable and phase changes more likely. The initial dislocation density due to cold work is increased by the lattice misfit of the $M_{23}C_6$ carbides as grath proceeds. Therefore. regions near the grain boundaries in the cold-worked commercial alloys are likely sites for the nucleation of a recrystallization process driven by segregation and high free energy.

In this study regions near grain boundaries in austenitic Fe-Cr-Mn alloys decompose by a low temperature mechanism and a high temperature mechanism. Both mechanisms Involve the precipitation of a chromium-rich phase depleting the austenite matrix of chranium. At low temperatures (420°C and 520°C) grain boundaries were observed to decompose to alpha-ferrite. $M_{23}C_6$ carbide. and retained austenite as a result of thermal aging and irradiation. At high temperature. 600°C, sigma or $M_{23}C_6$ forms and coarsens to approach coating grain boundaries. The chranium and carbon contents of the canmercial alloys appears to determine whether sigma or $M_{23}C_6$ precipitates at 600°C. Alloys with 18 wt% chranium and lower carbon precipitated sigma and alloys with 10 wt% chranium and higher carbon precipitated $M_{23}C_6$.

CONCLUSIONS

Austenitic Fe-Cr-Mn alloys are susceptible to graln boundary decomposition during irradiation. Grain boundaries were observed to decompose by a la and high temperature mechanism to brittle phases such as chi. sigma and $M_{23}C_6$ carbide that can adversely change the mechanical properties of the bulk alloy. This decomposition leads to a chranium depleted austenite matrix and at la temperatures the formation of alpha iron ferrite, both having poor corrosion resistance.

FUTURE WORK

Detailed X-ray microanalysis needs to be done on various grain boundaries: γ/γ, $\gamma/M_{23}C_6$, γ/α and γ/σ in both low and high temperature specimens. this will provide detailed characterization of segregation and alla better understanding of the driving mechanisms.

TO attain more detailed characterization. a STEM microscope that can produce an intense 2 nm spot will be used. The small intense spot will give compositions fran smaller volumes than conventional STEMs. Corrosion and mechanical property tests on these Fe-Cr-Mn alloys need to be performed and the results related to microstructure.

REFERENCES

1. H. R. Brager, F. A. Garner, D. S. Gelles and M. L. Hamilton, J. Nuc. Mat. 133-134, 907 (1985).

2. F. A. Garner and H. R. Brager, Radiation Induced Changes in Microstructure. ASTM STP 955, Eds. F. A. Garner. N. H. Packan and A. S. Kumar (ASTM, Phlladelphia, 1987), p.195.

3. R. L. Klueh and E. E. Bloom in Optimizing Materials for Nuclear Applications, Eds. F. A. Garner, D. S. Gelles and F. W. Wlffen (The Metallurgical Society, AIME. Warrendale, PA. 1985), p.73.

4. A. H. Bott, F. B. Pickering and G. J. Butterworth, J. Nuc. Mat. 141-143, 294 (1986).

5. M. Snykers and E. Ruedl. J. Nucl. Mat. 103-104, 1075 (1981).

6. F. A. Garner, H. R. Brager, D. S. Gelles and J. M McCarthy. J. Nuc. Mat. 148, 294 (1987).

7. J. M. McCarthy and F. A. Garner, J. Nuc. Mat. 155-157, 877 (1988); Fusion Reactor Materials DOE/ER-0313/4, 146 March (1988).

8. J. M McCarthy. Fusion Reactor Materials DOE/ER-0313/5, in press (1988).

9. H. Oikawa, Tech. Reports, Tohoku Universlty 47, 251 (1982); 48, 7 (1983).

10. H. Takahashi, F. A. Garner, H. Itoh, B. Hu and S. Ohnuki Radiation Induced Changes in Microstructure. ASTM STP 955. Eds. F. A. Garner, N. H. Packan and A. S. Kumar (ASTM. Philadelphia. 1987). p.268.

11. D. Lazarus, Solld State Physics 10, 71 (1960).

12. M. Hillert and G. R. Purdy, Acta. Met. 26, 333, (1978).

13. K. Smidoda, C. Gottschalk and H. Gliefer, Met. Sci., 13 (1979) p.146.

14. F. A. Garner. F. Abe and T. Noda. J. Nuc. Mat. 155-157, 870, (1988).

THE EFFECT OF PHOSPHORUS ON MICROSTRUCTURES OF Fe-15Cr-25Ni ALLOYS IRRADIATED WITH FAST NEUTRONS, T. Muroga (Kyushu University), F. A. Garner and J. M. McCarthy (Pacific Northwest Laboratory)

OBJECTIVE

The objective of this study is to provide microstructural data to demonstrate the operation of the various roles proposed for phosphorus and assess the relative contribution of some of these roles in model austenitic Fe-Cr-Ni alloys.

SUMMARY

Fe-15Cr-25Ni austenitic alloys with various phosphorus contents were irradiated with fast neutrons in the EBR-II reactor at temperatures ranging from 399 to 649°C and doses between 8.2 and 14.3 dpa. Observations of microstructure and microchemical analyses were carried out to determine the various roles of phosphorus. At lower irradiation temperatures and lower phosphorus contents, where no precipitate formation was observed, the phosphorus remained in solution and had a strong but variable influence on swelling and void density. However, the results suggest that more than one mechanism involving phosphorus-point defect interaction were operating and that the net effect was a result of the competition of several mechanisms. Phosphide precipitates were observed to form at higher irradiation temperatures and phosphorus levels. The formation of these precipitates then exerted a further influence on the void density and distribution.

PROGRESS AND STATUS

Introduction

Recently, phosphorus addition to austenitic steels has been examined for the purpose of reducing void swelling and irradiation creep during displacive irradiation[1-17]. Under most conditions, phosphorus has been observed to delay the onset of swelling, but in some experiments it was shown that under certain conditions the addition of phosphorus can actually increase swelling[1,4,6,14]. In other cases, the effect of phosphorus in reducing swelling ranged from very small to very large, strongly dependent on variables such as temperature and the composition of the steel[2-4]. Such variability in response to phosphorus suggests that this element plays more than one role and that the specific results depend on a competition of each of these roles in response to the environmental and compositional variables operating in each experiment.

With the exception of the work of Watanabe et al.[14,18], no studies to date have advanced mechanisms which might account for an increase in swelling. Phosphorus is known to be a subsize and very chemically active element when in solution and, in certain conditions, can produce phosphide precipitates at very high densities and very small sizes. Phosphorus has been shown to interact very strongly with interstitial atoms[14,21], resulting in radiation-induced segregation of phosphorus and a strong increase in the rate of formation of interstitial loops[14,19,20]. Watanabe and coworkers[14,18] also demonstrated a strong interaction between vacancies and phosphorus. A similar conclusion was reached by Azarian and Kheloufi[22] using positron annihilation. The same conclusion is also supported by the observation of void formation during quenching and aging experiments conducted on phosphorus-containing steels[23-26]. Phosphorus has also been shown to increase the interdiffusion coefficient of Fe-Ni alloys[27,28], which implies some interaction with vacancies.

There are a number of consequences of these various interactions of phosphorus with point defects, and different researchers tend to focus on different aspects of these consequences when attempting to model the microstructural response of phosphorus-containing alloys. Garner and coworkers[2-4] focus primarily on the competitive roles of phosphorus while in solution as well as the consequence on the matrix chemistry when phosphorus is removed by segregation or precipitation. This approach considers not only the interaction of point defects with phosphorus but also the modification of the matrix composition that occurs when phosphides are formed. Phosphides are known to delay the formation of radiation-induced phases rich in silicon and nickel, both of which are also known to strongly retard void nucleation when in solution[4,29-32]. Itoh and coworkers also emphasized the retardation by phosphide formation of these phases, and they further noted that phosphorus additions tend to retard the recovery of dislocation networks induced by cold working. High initial dislocation densities are also known to retard the onset of void formation.

The studies and theories of Lee and Mansur and their coworkers[7-9,17,33,34] are more directed toward the role of phosphorus in forming precipitates. Precipitates are seen in their approach to act in a physical rather than chemical sense. The surfaces of these precipitates serve in several models as recombination centers for point defects and collectors for impurity atoms. The latter model in particular was developed to account for the influence of phosphorus in the presence of helium atoms[7-9,17]. In this model, the precipitates serve as collection surfaces for helium atoms, producing a profusion of small subcritical bubbles which cannot be easily promoted into bias-driven void growth.

It is quite probable, however, that all of these models, both chemical and physical, are operating to one extent or another at different stages in the microstructural evolution. The net outcome of the many roles of

phosphorus is determined by the environmental and compositional variables dominating the particular experiment being analyzed. It has been previously difficult to discriminate between the strength of the various potential roles of phosphorus since most earlier studies concentrated on a limited set of experimental conditions, allowing only one and sometimes two of the potential outcomes to develop from the competition.

In the study chosen for this paper, a set of neutron-irradiated specimens was selected for microstructural observation because their density changes indicated a wide range of behavior in response to irradiation temperature, displacement level and phosphorus content. The level of other solutes in these alloys was also low, allowing phosphorus to exhibit its influence without synergistic interactions that might obscure its influence. The objective of this study was to provide microstructural data to demonstrate the operation of the various roles proposed for phosphorus and hopefully assess the relative strength of some of these roles.

Experimental Details

The materials used in this study were nominally Fe-15Cr-25Ni austenitic alloys with various phosphorus levels. The compositions of these alloys are shown in Table 1. The specimens were in the form of rods (3-mm diameter by 12.7-mm long) and were irradiated in the AAIX experiment in the EBR-II reactor[4]. The eight irradiation temperatures varied from 399 (±5°C) to 650 (±15°C). The irradiation dose for each temperature was different (ranging from 8.2 to 14.3 dpa), reflecting axial differences in the displacement rate, which varied from 0.6 to 1.1 x 10^{-6} dpa/s.

The density of each specimen was determined using an immersion density technique demonstrated to be accurate to ±0.16%. The results were reported by Garner and Kumar[4] and are reproduced in Figure 1. In the present study, five of the eight irradiation temperatures were chosen for further study utilizing electron microscopy and microchemical analysis as indicated by asterisks in Figure 1 and listed in Table 2. The rod specimens were sectioned to produce microscopy disks and electropolished to perforation. In most cases, microstructural analyses were performed on a JEM-100CX electron microscope. In some cases, microchemical analyses were performed using a JEM-1200EX electron microscope equipped with a TN-5500 energy dispersive X-ray spectrometer (EDS) with an effective probe diameter of about 20 nm.

RESULTS

399°C and 8.2 dpa

No precipitation was observed at any phosphorus level at 399°C. Voids as well as tangled dislocation networks at relatively constant density were observed. The latter are shown in Figure 2 imaged in the off-Bragg condition. The voids were distributed relatively homogeneously at all phosphorus levels but decreased in density gradually with increasing phosphorus. The swelling increased initially, however, and declined thereafter with increasing phosphorus, mirroring the trend observed in the radiation-induced change in bulk density shown in Figure 1. The network dislocations were found to be tangled with very few loops remaining. The various microstructural parameters as influenced by phosphorus level are shown in Figure 3.

427°C and 11.2 dpa

In this irradiation condition, the measured void volume at 0% phosphorus was 1.06% with a void density of 5.9 x 10^{21}/m3 and at 0.1% phosphorus was 1.10% with a density of 1.75 x 10^{21}/m3. Relative to the (399°C, 8.2 dpa) case, the void density was lower at both phosphorus levels even though the displacement level at 427°C was higher.

At 0.1% phosphorus, a low density of the needle-like precipitates was observed. These precipitates were 2.9 x 10^{20}/m3 in density and 45 nm in average length. These were oriented along <100> directions, typical of those observed also at 510°C and above. Compared to the absence of precipitates at 399°C, it cannot be deduced from the limited observations whether the precipitation at 427°C arises simply as a result of the increase in temperature or whether the increase in dose is partially or totally responsible.

510°C and 13.2 dpa

The microstructures developed at this temperature are illustrated in Figures 4 and 5, and the microstructural parameters are shown in Figure 6. At the lower phosphorus level, the void density strongly decreased with phosphorus addition, once again indicating an effect of phosphorus unrelated to precipitation. Needle-like precipitates were observed only at the two highest phosphorus levels. The density and size of the precipitates at 0.1% phosphorus were larger than that observed in this alloy at 427°C and 11.2 dpa. The precipitate density was 3.3 x 10^{20}/m3 with an average size of 105 nm at the 0.055% phosphorus level and a density of 7.4 x 10^{20}/m3 with an average length of 185 nm at the 0.1% phosphorus level. As precipitation develops

TABLE 1

Chemical Compositions (wt%) of Alloys Examined in This Study

Designation	Fe	Cr	Ni	C	O	N	P
E33	Bal	14.8	25.8	0.005	0.023	0.0028	t0.005
E103	Bal	14.7	24.1	0.004	0.013	0.0019	0.013
E104	Bal	15.2	25.0	0.001	0.014	0.0018	0.055
E105	Bal	15.3	24.7	0.002	0.016	0.0019	0.10

TABLE 2

Specimens and Irradiation Conditions

		E33	E103	E104	E105
399°C	8.2 dpa	X	X	X	X
427°C	11.2 dpa	X	NA	NA	X*
510°C	13.2 dpa	X	X	X*	X*
593°C	14.3 dpa	NA	X*	X*	X*
649°C	14.3 dpa	X	X*	X*	X*

NA = not analyzed.
* = phosphide precipitates observed.

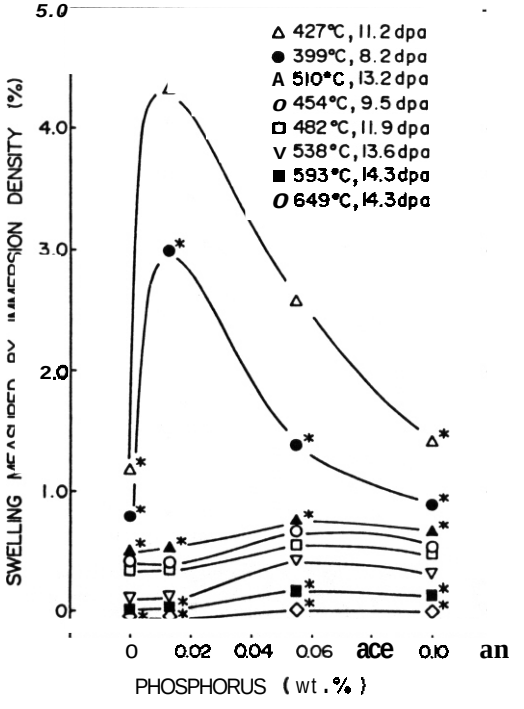

Figure 1. Swelling of Neutron Irradiated Fe-15Cr-25Ni-XP Alloys Measured by an Immersion Density Technique by Garner and Kumar[4]. The specimens marked with asterisks were chosen for the present experiment.

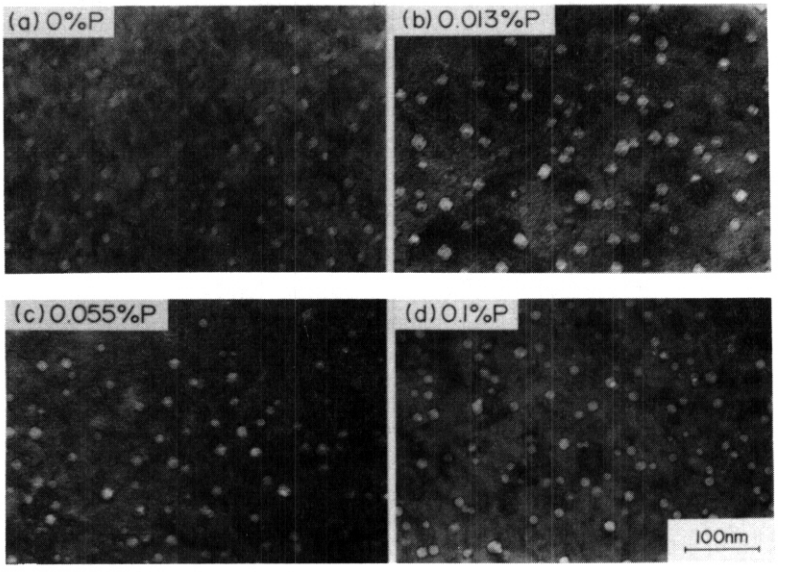

Figure 2. Voids Observed in Fe-15Cr-25Ni-XP Alloys at 399°C and 8.2 dpa.

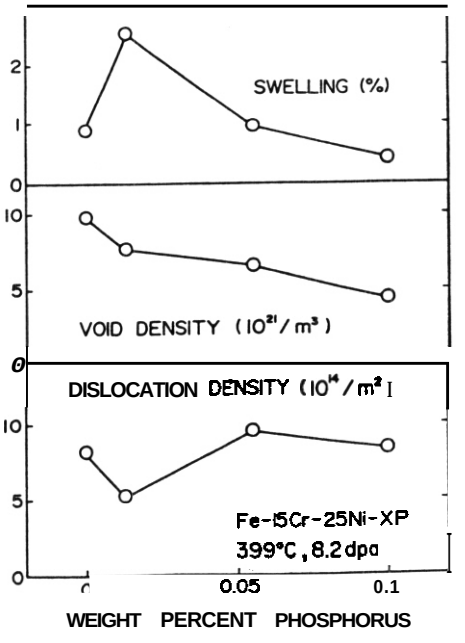

Figure 3. Swelling, Void Density and Dislocation Density as a Function of Phosphorus Content at 399°C and 8.2 dpa.

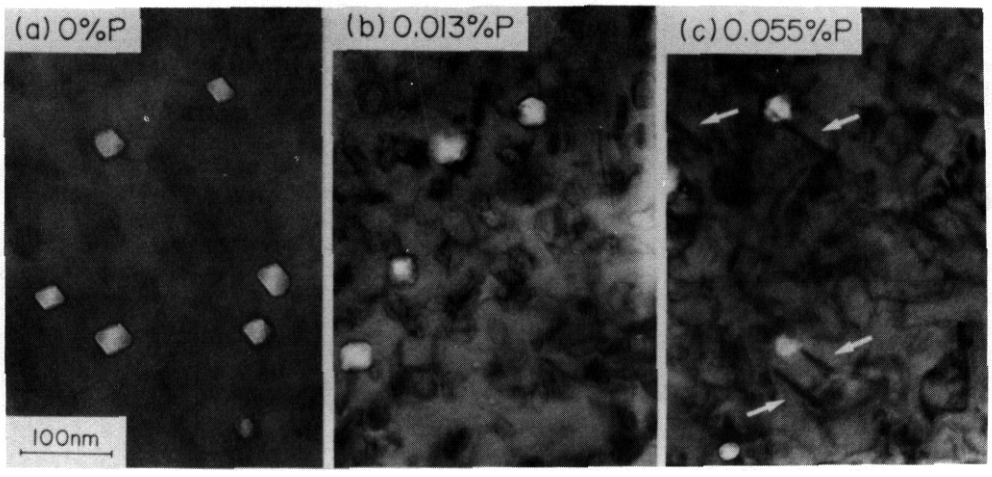

Figure 4. Voids and Precipitates Observed in Fe-15Cr-25Ni-XP Alloys at 510°C and 13.2 dpa. Precipitates are observed only at 0.055 and 0.1 wt% phosphorus levels.

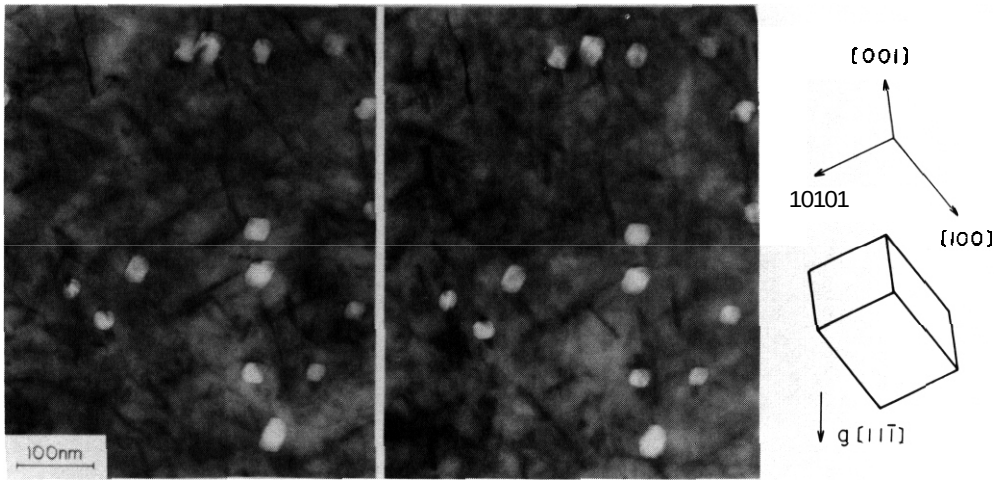

Figure 5. Stereomicrographs of Voids and Precipitates for 0.1 wt% P, 510°C, 13.2 dpa. They are observed from near the [101] direction with a a vector of [11$\bar{1}$]. The precipitates are oriented along <100> directions; some of the voids formed very close to precipitates.

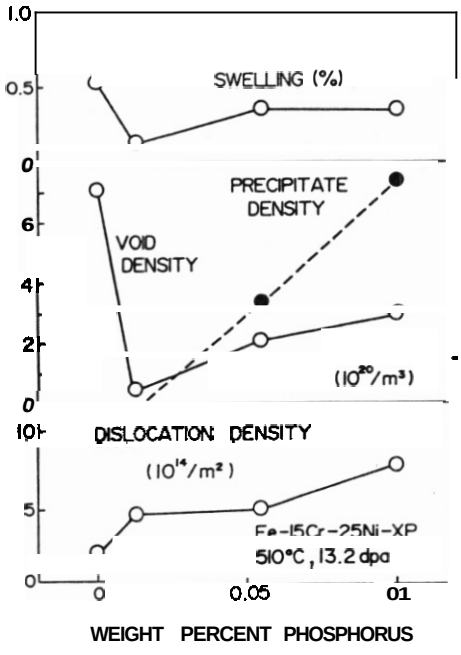

Figure 6. Swelling, Void Density, Phosphide Precipitate Density and Dislocation Density as a Function of Phosphorus Content at 510°C. Note that the precipitates are observed only at the two higher phosphorus levels.

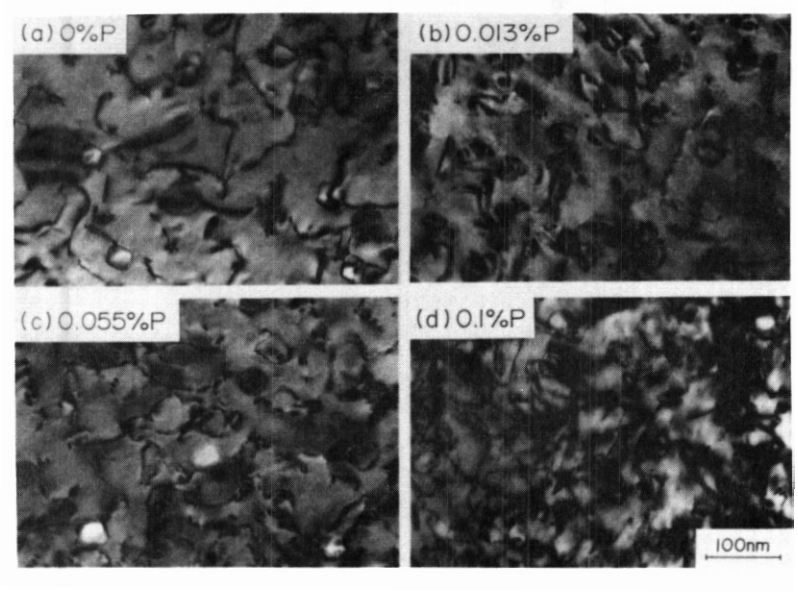

Figure 7. Dislocations and Dislocation Loops Observed in Fe-15Cr-25Ni-XP Alloys at 510°C and 13.2 dpa.

the void density increases relatively slowly, indicating some tendency toward enhancement with phosphide formation. The swelling vs. phosphorus behavior mirrors that of the void density.

Figure 5 is a stereo pair that illustrates the spatial relationship between voids and precipitates, indicating that some of the voids may have nucleated on or very near to the precipitates.

As shown in Figure 7, there was some dependente of the dislocation structure on phosphorus level. In a phosphorus-free specimen a low density of large faulted dislocation loops were observed among the perfect loops and the tangled dislocations. At 0.013% phosphorus level, some smaller loops, both faulted and perfect loops, remained within the tangled dislocations. At the two highest phosphorus levels, higher densities of tangled dislocations remained but with a lower density of visible loops. The total dislocation density gradually increased with phosphorus addition as shown in Figure 6.

593°C and 649°C at 14.3 dpa

Very few voids and a relatively low density of dislocations were observed at all phosphorus levels. Phosphide precipitates were observed in all three phosphorus-bearing alloys at both temperatures. The precipitate size in each case increased with irradiation temperature and phosphorus level.

Figure 8 shows a stereo pair of the precipitates observed at 0.1% phosphorus and 593°C. The precipitates tend to resist electropolishing and thus protrude through the foil surface. Stereoscopic observation shows that the curved precipitate images seen in Figure 8 are formed by bending of precipitates lying outside the foil volume. Portions of precipitates remaining within the foil are oriented along <100> directions as observed at lower temperatures. Figure 9 shows precipitate images at 649°C. On the other hand, the dislocation density was very small in a zero-phosphorus specimen at 649°C and in all alloys observed at 593°C. Thus it is inferred that these dislocations were produced via a punching process caused by the strain around precipitates.

At 593°C, the precipitates developed at 0.1% phosphorus were analyzed by EDS to ascertain their composition. This type of analysis inevitably includes some contribution from the matrix and some perturbation by the high radioactivity of the specimen. These effects were minimized by examining a precipitate protruding far from the edge of the foil and by subtracting the radiation background measured during a comparable period of time. Figure 10 shows the X-ray spectrum extracted from the precipitates and the spectrum of the radiation background. As seen in Figure 10, the precipitates are very rich in phosphorus and enhanced in chromium and nickel relative to that of the matrix.

Figure 11 shows a compositional profile of the matrix taken along a traverse that includes a void. The void surface is substantially enriched in both nickel and phosphorus, although no precipitation of phosphides or other phases was found at the void surface.

Figure 12 shows that blocky precipitates form along the grain boundary at 593°C in the 0.1% phosphorus alloy. An example of the composition of these precipitates is shown in Figure 13 [note that this spectrum includes the same radiation background as shown in Figure 10(b)]. These precipitates are also rich in phosphorus. Moreover, the chromium content is considerably higher compared with that of the needle-like precipitates shown in Figure 10(a). Since the electron diffraction pattern could not be used to clearly identify the crystal structure, it is not certain if these precipitates have the same phosphide structure as that of the needle-like precipitates or whether they possess a different structure. Figure 12 also suggests the movement of the grain boundary during the irradiation. A compositional trace conducted across the boundary in an area without large precipitates is shown in Figure 14, indicating that nickel segregates at the boundary largely at the expense of chromium. Note that phosphorus was not found to segregate in precipitate-free regions along this boundary. From this behavior it is inferred that phosphorus diffuses rapidly along the boundary, as pointed out by Ohnuki and coworkers for a Fe-0.5P alloy[35], and thus forms the blocky precipitates.

Figure 15 demonstrates that although the void density is decreased strongly at higher temperature, a large fraction of the cavities are directly associated with phosphorus precipitates.

DISCUSSION

From the above results we can draw some conclusions about the role of phosphorus in microstructural evolution during irradiation. Phosphorus obviously plays one or more roles associated with point defects that is not related to precipitation. We cannot from these data alone ascertain the relative importance of those roles associated with interstitials and those associated with vacancies. Phosphorus in the absence of precipitation was observed to influence void formation both at 399°C and 510°C. While the void density decreased monotonically with phosphorus in the absence of precipitation, swelling could either increase or decrease, suggesting a competition between one or more point defect related mechanisms. Other indications of

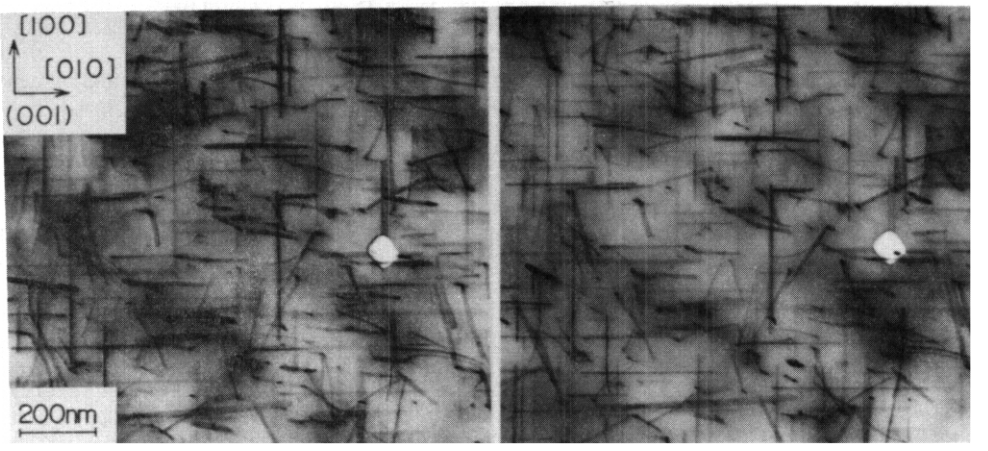

Figure 8. Stereomicrographs of the Precipitates Formed in Fe-15Cr-25Ni-0.1P Irradiated at 593°C and 14.3 dpa. The micrographs are taken from <100> directions. The curved precipitate images are formed by distorted precipitates protruding outside the foil volume.

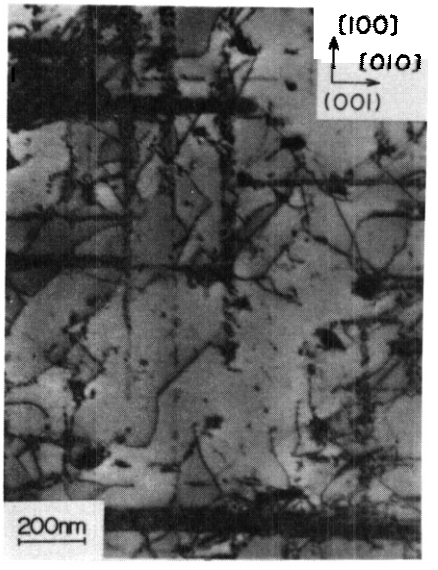

Figure 9. Precipitates and Tangled Dislocations Formed in the Fe-15Cr-25Ni-0.1P Alloy Irradiated at 649°C and 14.3 dpa.

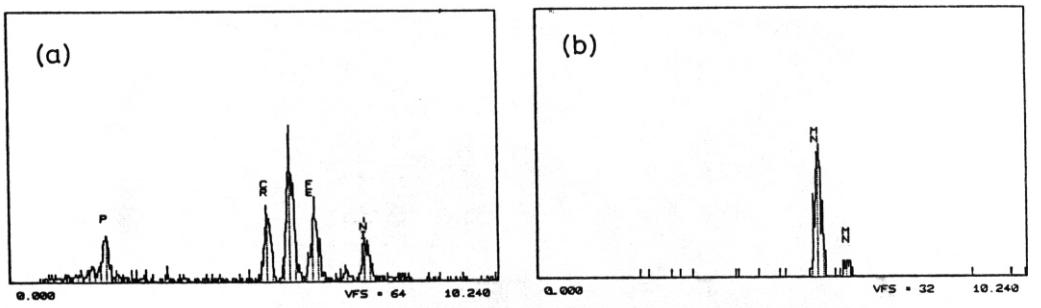

Figure 10. (a) X-ray Spectrum Excited from one of the Needle-Shaped Phosphide Precipitates; (b) The Radiation Background Spectrum Extracted from the Same Specimen (0.1 wt% P, 593°C, 14.3 dpa). This background arises from a K-capture event transforming ^{55}Fe to an excited state of ^{55}Mn, the latter emitting an x-ray as it returns to the ground state.

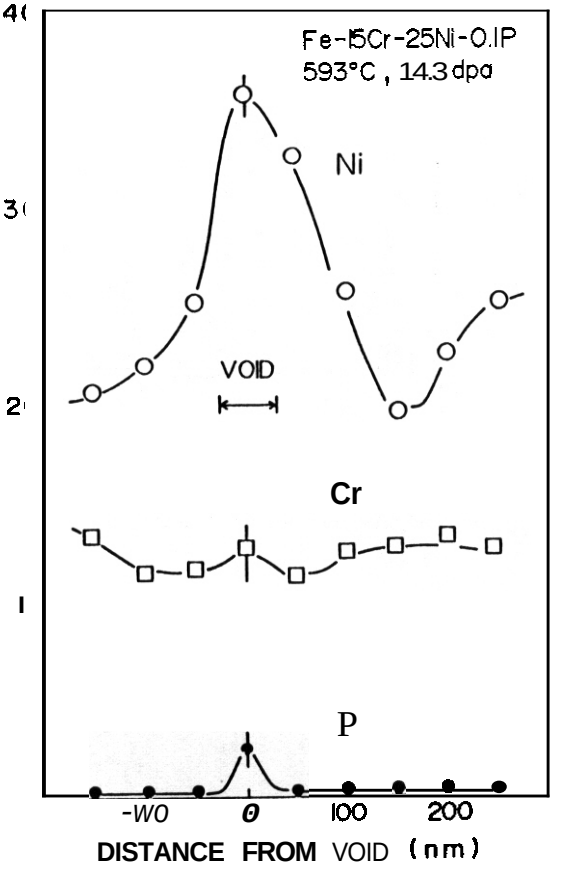

Figure 11. A Compositional Traverse of the Matrix Including a Void. The specimen thickness is about 70 nm. The diameter of the probe beam is about 20 nm (0.1 wt% P, 593°C, 14.3 dpa).

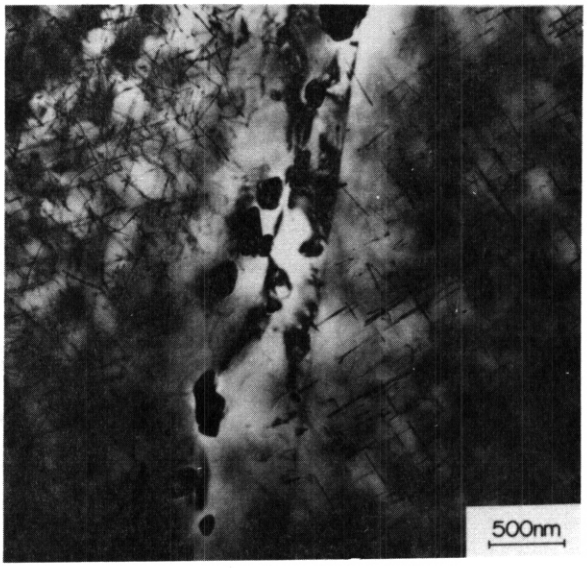

Figure 12. Grain Boundary Microstructure (0.1 wt% P, 593°C, 14.3 dpa).

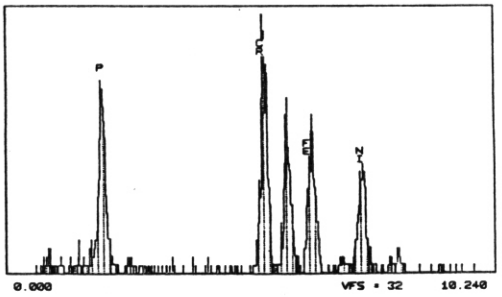

Figure 13. X-Ray Spectrum Excited from a Blocky Precipitate Formed at the Grain Boundary Shown in Figure 12. The unlabeled peak corresponds to ^{55}Mn x-ray emission following k-capture of ^{55}Fe. See figure 10(b) for the radiation background spectrum.

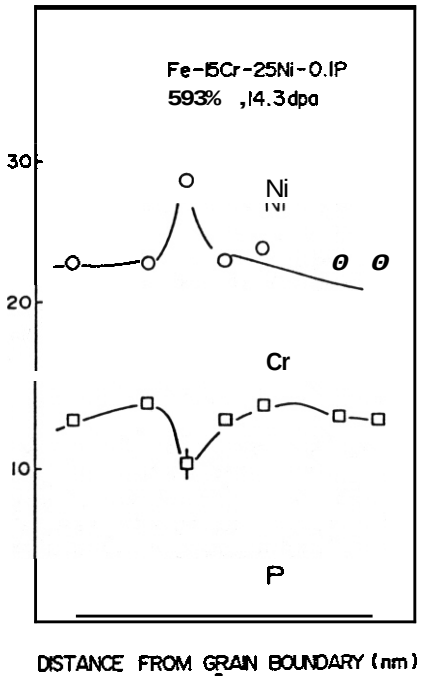

Figure 14. Compositional Traverse Across a Grain Boundary. An area without any visible precipitation nor any evidence of the-grain boundary migration was chosen (0.1 wt% P, 593°C, 14.3 dpa).

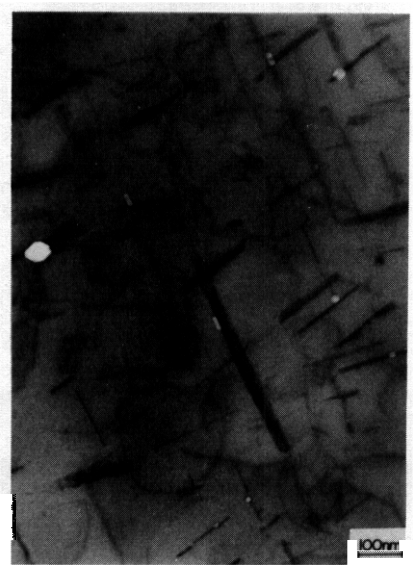

Figure 15. Relationship of Precipitates and Cavities at High Temperature (0.055 wt% P, 593°C, 14.3 dpa).

phosphorus interaction with point defects are its strong segregation at void surfaces and in the formation of needle-like precipitates. Watanabe et al.[36] have shown that phosphide precipitates do not form during thermal aging in austenitic alloys containing only phosphorus. They showed that other elements such as Ti or Si are required to form phosphides during thermal aging. Lee and Packan also demonstrated that phosphide precipitation during neutron irradiation was enhanced by the addition of silicon and titanium[17]. Garner and Kumar also noted that in the absence of these elements precipitation of phosphorus is inconsistent with the Fe-Ni-P equilibrium phase diagram[4]. Therefore, we must assume that the radiation induced formation of phosphides in these alloys is due to phosphorus-point defect associations of some type.

The segregation of nickel at void surfaces and grain boundaries during irradiation has been observed many times and is consistent with the operation of both the Inverse Kirkendall effect and interstitial binding[37]. While phosphorus was described in the Introduction section as having variety of interactions with both vacancies and interstitials, its segregation at void surfaces cannot be explained solely on the basis of the Inverse Kirkendall effect since as a fast diffusing solute it would be expected to flow away from sinks. Phosphorus binding with either (or both) vacancies or interstitials could lead to this type of segregation, however.

Since we assume that phosphide precipitation does not occur in the absence of irradiation in our alloy but requires radiation-induced segregation, one would expect that such precipitation depends on the total displacement level, displacement rate, temperature and phosphorus level. While we cannot unambiguously separate the influence of the first three of these variables using this data set, it does appear that the density and size of the precipitates increases with irradiation temperature and phosphorus level as expected. At lower temperatures, phosphide formation requires either higher phosphorus levels or higher dose levels than acquired in this experiment. Other neutron irradiation experiments on Fe-15Cr-25Ni phosphorus-bearing alloys also indicate that there exists for each phosphorus level some threshold temperature for phosphide formation[16,38]. At higher temperatures, phosphides form at all non-zero levels of phosphorus within the dose levels acquired in this experiment. This in turn implies that some substantial portion of the irradiation proceeded before phosphides formed and that any reduction observed in swelling cannot be attributed solely to the mere presence of the precipitates. Therefore, prior to the removal of phosphorus into the precipitate, there must have been interactions with point defects that contributed to the reduction of swelling. Moreover, even after precipitate formation, some fraction of phosphorus remains in the matrix, though not estimated in the present study, and will continue to affect defect behavior. The phosphorus segregation observed at a void at 510°C (Figure 11) implies a phosphorus-defect interaction even in the presence of the high density of precipitates.

We did observe in this study some indication that loop evolution was influenced by phosphorus level. These specimens were irradiated to doses and temperatures that carried the microstructure beyond the early stage dominated by interstitial loops. Therefore, we cannot address the observations by Watanabe et al.[14] and Fukuya et al.[19,20] that phosphorus additions enhance the formation of interstitial loops, possibly via phosphorus-interstitial binding. Such a mechanism would hasten the onset of dislocation evolution and could account for the relative increase of swelling at relatively lower irradiation temperatures and low phosphorus levels.

It is clear from this and many other studies that void nucleation becomes more difficult as either the temperature or phosphorus level is increased. Thus the relatively high density and homogeneous void distributions observed at low temperatures and low phosphorus levels are replaced with much lower density and more heterogeneous distributions at high temperature and high phosphorus levels. In this sense, phosphorus both inhibits void nucleation prior to precipitation and induces a shift toward more heterogeneous distribution by providing nucleation sites for voids after precipitation.

It is, therefore, difficult to determine whether phosphides per se increase or decrease swelling. Is the net influence an increase in swelling via enhancement of nucleation or a decrease via collection of gaseous impurities in such a way as to inhibit the attainment of critical cavity radii in the matrix? The data from this experiment cannot adequately address this question. Perhaps the phosphide effect depends on the densities of the phosphides themselves and the concentration of effective impurities as well as the temperature, dose and dose rate. The enhancement of void nucleation by phosphides may be a possible mechanism whereby swelling can eventually increase under certain conditions.

There is some indication that phosphorus has an effect on dislocation density, but it was not very large in these alloys which were irradiated only in the annealed condition. The studies of Itoh et al. showing a significant retardation of dislocation recovery of cold-worked solute-modified steels is not thought to be relevant to this experiment. However, there was a remarkable effect of phosphorus on dislocation structure observed at 510°C, namely, the large faulted loops remaining in the zero phosphorus alloy that were not seen in the phosphorus bearing alloys. A similar observation of dislocation loops including large faulted loops remaining to high doses in high nickel austenitic ternary alloys irradiated with heavy ions[39] and fast neutrons[40] can be compared with their disappearance at lower nickel levels. The present results suggest that the loop microstructure and swelling suppression effects of nickel might be related to the effects of phosphorus.

There is one aspect of these studies that still remains to be addressed. There is a persistent discrepancy between the values of swelling measured by microscopy and immersion density. In every case where both density and microscopy measurements were made, one would anticipate more voids than were actually found, although in every case the void swelling measurement mirrored that of the density change except for a persistent offset. This discrepancy was observed in alloys both without and with phosphorus. It was also observed in several other studies on similar alloys[16,38]. The origin of this apparent change in lattice parameter of the matrix is presently under study. The relative contributions of matrix and phosphide to this discrepancy are also being sought.

CONCLUSIONS

In simple Fe-Cr-Ni-P alloys it has been shown that phosphorus when in solution has a strong impact on void nucleation during neutron irradiation. The dependence of void behavior on matrix phosphorus level and irradiation temperature suggest that more than one mechanism involving point defect interaction is operating and that the net effect is determined by the competition of these mechanisms in response to the irradiation variables. It is not possible with these data alone to discriminate between interactions associated with vacancies and those associated with interstitials.

Other studies have shown that phosphorus addition in these simple alloys does not lead to phosphide formation in the absence of radiation. Segregation of phosphorus into phosphides does occur during irradiation, however, increasing strongly with irradiation temperature and phosphorus level. Upon the formation of these precipitates, there are further interactions that affect the void density and distribution and also dislocation evolution. This precipitate-related effect increases with irradiation temperature.

FUTURE WORK

The effect of further additions of titanium and/or silicon to Fe-Cr-Ni-P austenitic alloys on defect and precipitate structures will be examined. The effects of ^{10}B addition will also be investigated to determine the effect of helium on the evolution of defects and precipitates. The alloys designed for these purposes are scheduled to be irradiated in FFTF cycle 11 and beyond.

REFERENCES

1. J. F. Bates, R. W. Powell and E. R. Gilbert, ASTM-STP 625, eds. D. Kramer, H. R. Brager and J. S. Perrin (ASTM 1981) 713.

2. F. A. Garner and H. R. Brager, J. Nucl. Mater., 133 & 134 (1985) 511.

3. F. A. Garner and H. R. Brager, J. Nucl. Mater., 155-157 (1988) 833.

4. F. A. Garner and A. S. Kumar, ASTM-STP 955, eds. F. A. Garner, N. H. Packan and A. S. Kumar (ASTM 1987) 289.

5. M. Itoh, S. Onose and S. Yuhara, ASTM-STP 955, eds. F. A. Garner, N. H. Packan and A. S. Kumar (ASTM 1987) 114.

6. J. F. Bates and W. G. Johnston, Proc. AIME Int. Conf. on Radiation Effects in Breeder Reactor Structural Materials (TMS-AIME 1977) 625.

7. E. H. Lee and L. K. Mansur, J. Nucl. Mater., 141-143 (1986) 695.

8. E. H. Lee, P. J. Maziasz and A. F. Rowcliffe, in Phase Stability During Irradiation, eds. J. R. Holland, L. K. Mansur and D. I. Potter (TMS-AIME 1981) 219.

9. E. H. Lee, L. K. Mansur and A. F. Rowcliffe, J. Nucl. Mater., 122 & 123 (1984) 299.

10. M. Terasawa, M. Shimada, T. Kakuma, T. Yukitoshi, K. Shiraishi and K. Uematsu, Proc. AIME Int. Conf. on Radiation Effects in Breeder Reactor Structural Materials (TMS-AIME 1977) 687.

11. M. L. Hamilton, G. D. Johnson, R. J. Puigh, F. A. Garner, P. J. Maziasz, W. J. S. Yang, and N. Abraham, The effects of Phosphorus and Boron on the Behavior of a Titanium-Stabilized Austenitic Stainless Steel Developed for Fast Reactor Service, PNL-SA-15303, Battelle, Pacific Northwest Laboratory, 1988.

12. W. J. S. Yang, ASTM-STP 955, eds. F. A. Garner, N. H. Packan and A. S. Kumar (ASTM 1987) 888.

13. M. Fujiwara, H. Uchida, S. Ohta, S. Yuhara, S. Tani, and Y. Sato, ASTM-STP 955, eds. F. A. Garner, N. H. Packan and A. S. Kumar (ASTM 1987) 127.

14. H. Watanabe, A. Aoki, H. Murakami, T. Muroga and N. Yoshida, J. Nucl. Mater., 155-157 (1988) 815.

15. E. H. Lee and L. K. Mansur, Phil. Mag., accepted for publication.

16. J. F. Stubbins, J. E. Nevling, F. A. Garner and R. L. Simons, Microstructural Evolution of Neutron Irradiated Fe-Cr-Ni Alloys at 495°C in Response to Changes in He/dpa Ratio, accepted for publication in ASTM-STP; also in this report.

17. E. H. Lee and N. H. Packan, Swelling Suppression in Phosphorus-Modified Fe-Cr-Ni Alloys During Neutron Irradiation, accepted for publication in ASTM-STP.

18. H. Watanabe, E. Kuramoto and N. Yoshida, Trans. Japan Inst. Metals, 29 (1988) 769.

19. K. Fukuya, S. Nakahigashi, S. Ozaki, M. Terasawa and S. Shima, Proc. Third Int. Symp. on Environmental Degradation of Materials in Nuclear Power Systems--Water Reactors (Traverse City 1987).

20. K. Fukuya, S. Nakahigashi and M. Terasawa, Scripta Met., 19 (1985) 959.

21. J. M. Perks, C. A. English, and M. L. Jenkins, Radiation-Induced Segregation of Phosphorus in Nickel and Fe-Cr-Ni Alloys, accepted for publication in ASTM-STP.

22. A. Azarian and K. Kheloufi, J. Nucl. Mater. 97 (1981) 25.

23. A. F. Rowcliffe and A. B. Nicholson, Acta Met., 20 (1972) 143.

24. A. F. Rowcliffe and B. L. Eyre, J. Phys. F,1 (1971) 771.

25. L. Boulanger, Scripta Met., 14 (1980) 67.

26. A. Azarian, M. DaCunha Belo, and J. Leteutre, Scripta Met., 9 (1975) 185.

27. D. C. Dean and J. I. Goldstein, Met. Trans., 17A (1986) 1131.

28. T. R. Heyward and J. I. Goldstein, Met. Trans., 4 (1973) 2335.

29. H. R. Brager and F. A. Garner, J. Nucl. Mater., 73 (1978) 9.

30. F. A. Garner and W. G. Wolfer, J. Nucl. Mater., 102 (1981) 143.

31. F. A. Garner and W. G. Wolfer, J. Nucl. Mater., 122 & 123 (1984) 201.

32. B. N. Singh, T. Leffers, M. J. Makin, G. P. Walters, and A. J. E. Foreman, J. Nucl. Mater., 103 & 104 (1981) 1041.

33. A. D. Brailsford, and L. K. Mansur, J. Nucl. Mater., 103 & 104 (1981) 1403.

34. L. K. Mansur, M. H. Hayns, and E. H. Lee, in Phase Stability During Irradiation, eds. J. R. Holland, L. K. Mansur, and D. 1. Potter (TMS-AIME 1981) 359.

35. S. Ohnuki, H. Takahashi, and T. Takeyama, Proc. Int. Symp. on Behavior of Lattice Imperfections in Materials, (1985) 261.

36. H. Watanabe, Doctoral Thesis, Mar. 1989, Kyushu Univ.; H. Watanabe, A. Aoki, T. Muroga, N. Yoshida, Engineering Sciences Reports, Kyushu Univ., Vol. 10 (1988) 193 (in Japanese).

37. A. D. Marwick, R. C. Pillar, and M. E. Horton, in Dimensional Stability and Mechanical Behavior of Irradiated Metals and Alloys, BNES (London 1984) 11.

38. H. Kawanishi and F. A. Garner, Fusion Structural Materials Semiannual Progress Report, this report.

39. E. H. Lee and L. K. Mansur, Phil. Mag., A52 (1985) 493.

40. T. Muroga, F. A. Garner, and S. Ohnuki, Annual Progress Report for MONBUSHO-DOE Collaboration in Fundamental Studies of Irradiation Effects in Fusion Materials Utilizing Fission Reactors, Fusion Year 1988, also in this report.

6. DEVELOPMENT OF STRUCTURAL ALLOYS

6.1 Ferritic Stainless Steels

VOID FORMATION AND HELIUM EFFECTS IN 9Cr-1MoVNb AND 12Cr-1MoVW STEELS IRRADIATED IN HFIR AND FFTF AT 400°C — P. J. Maziasz and R. L. Klueh (Oak Ridge National Laboratory)

OBJECTIVE

The objective of this experiment is to evaluate the effects of increased He:dpa ratio on the microstructural evolution and void swelling behavior of 9 Cr and 12 Cr comnercial martensiticlferritic steels. Steels doped with up to 2 wt % Ni were irradiated in both FFTF and HFIR. The He:dpa for all the steels irradiated in FFTF is ~0.1 appm/dpa, whereas that ratio in the nickel-doped steels is 10 to 12 appm/dpa in HFIR, about the same as expected for fusion.

SUMMARY

Martensiticlferritic 9Cr-1MoVNb and 12Cr-1MoVW steels doped with up to 2 wt % Ni have up to 450 appm He after HFIR irradiation to ~38 dpa, but only 5 appm He after 47 dpa in FFTF. No fine helium bubbles and few or no larger voids were observable in any of these steels after FFTF irradiation at 407°C. By contrast, many voids were found in the undoped steels (30-90 appm He) irradiated in HFIR at 400°C, while voids plus many more fine helium bubbles were found in the nickel-doped steels (400-450 appm He). Irradiation in both reactors at ~400°C produced significant changes in the as-tempered lath/subgrain boundary, dislocation, and precipitation structures that were sensitive to alloy composition, including doping with nickel. However, for each specific alloy the irradiation-produced changes were exactly the same comparing samples irradiated in FFTF and HFIR, particularly the nickel-doped steels. Therefore, the increased void formation appears solely due to the increased helium generation found in HFIR. While the levels of void swelling are relatively low after 37 to 39 dpa in HFIR (0.1-0.4%), details of the microstructural evolution suggest that void nucleation is still progressing, and swelling could increase with dose. The effect of helium on void swelling remains a valid concern for fusion application that requires higher dose experiments.

PROGRESS AND STATUS

Introduction

Martensiticlferritic steels are attractive candidate structural first wall materials for magnetic fusion reactor (MFR) applications. They offer good thermal conductivity and lower thermal expansion together with excellent radiation resistance. Figure 1(a) shows the very low swelling observed in this type of steel relative to either type 316 or advanced Ti-modified austenitic stainless steels after fast breeder reactor (FBR) irradiation to 100 dpa or more.[1-5] However, helium generation during FBR irradiation is very low in martensitic/ferritic steels, as shown in Fig. 1(b), but will be much higher during MFR irradiation to similar displacement-damage doses. Helium is known to affect void swelling in austenitic stainless steels,[5,6] and it has been shown to increase void formation in martensiticlferritic steels as well.[7-10] Helium generation in nickel bearing steels is increased when they are irradiated in the High Flux Isotope Reactor (HFIR), with a mixed fast and thermal neutron spectrum, relative to an FBR like the Fast Flux Test Facility (FFTF), with only fast neutrons. The thermal neutrons produce helium from transmutation reactions with nickel atoms. Martensitic/ferritic steels often contain minor amounts (0.1-0.5 wt %) of nickel to stabilize them against 6-ferrite formation during normalizing treatments. This increases the He:dpa ratio slightly when a steel like 9Cr-1MoVNb (mod. 9Cr-1Mo or T-91) is irradiated in HFIR, as shown in Fig. 1(b). If, however, a martensiticlferritic steel is deliberately alloyed with about 2 wt % Ni, then the ratio of He:dpa generation during irradiation in HFIR increases into the same range expected during irradiation in an MFR first wall, as also shown in Fig. 1(b).

For several years, a portion of the MFR materials program at the Oak Ridge National Laboratory (ORNL) has been devoted to studying the sensitivity of properties and microstructure during irradiation to helium.[10-13] Initial studies have mainly compared the 9Cr-1MoVNb and 12Cr-1MoVW steels irradiated in HFIR with and without nickel-doping, to discern the effects of increased He:dpa ratios. While nickel-doping introduces no obvious microstructural effect on either 9Cr-1MoVNb or 12Cr-1MoVW (HT-9) steels prior to irradiation, other than the need to temper at lower temperatures for longer times (nickel lowers the A_{c_1} temperature), it does affect precipitation somewhat during irradiation at 400 to 500°C, particularly in 9Cr-1MoVNb-2Ni.[10,14] A better comparison would be obtained by irradiating the same material in HFIR and FFTF to obtain different He:dpa ratios at similar temperatures and fluxes. Therefore, the subject of this paper is a comparison of swelling and microstructure of 9 Cr and 12 Cr steels with and without nickel-doping irradiated in HFIR and FFTF at about 400°C, the temperature of maximum void formation.

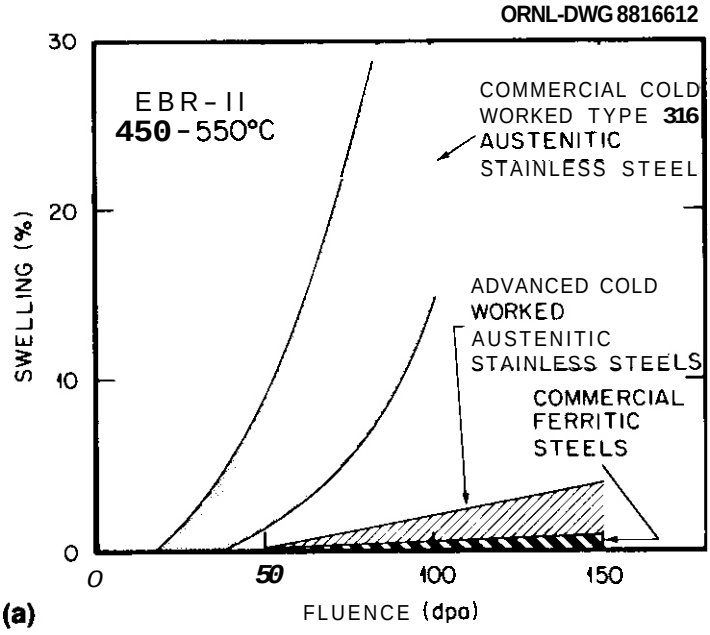

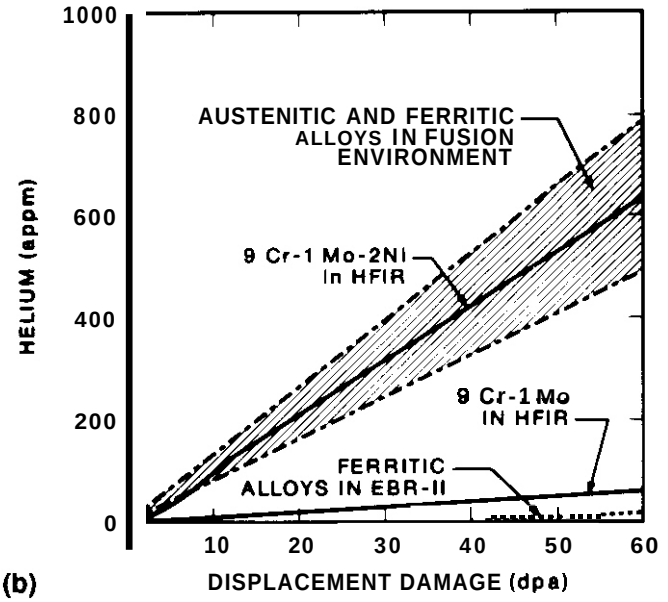

Fig. 1(a) Swelling behavior versus fluence for *20%* cold worked (CW) type 316, 20-25% CW advanced Ti-modified austenitic stainless steels and various 9-12 Cr martensitic/ferritic steels irradiated in EBR-II at 450-550°C.[1-6] The trend band for the ferritic steels includes data up to about 100 dpa and is linearly extrapolated to about 150 dpa. (b) Helium generation versus dose for various ferritic steels irradiated in EBR-II or a fusion reactor first wall, and for 9Cr-1MoVNb with and without *2* wt % Ni doping irradiated in HFIR.

EXPERIMENTAL

The compositions of the nickel-doped and undoped heats of 9Cr-1MoVNb and 12Cr-1MoVW are given in Table 1. Standard 3-mm-diam transmission electron microscopy (TEM) disks were punched from 0.25-mm-thick sheet stock, and then these disks were normalized and tempered as indicated in Table *2.*

Disks were irradiated in experiment CTR-30 in HFIR at 400°C to neutron fluences producing 36 to 37 displacements per atom (dpa) and 30 to 430 appm He, depending on the nickel content of the alloy. Irradiation conditions and damage parameters for various steels are found in Table 3. Disks were also irradiated in basket 1E2 for cycles 4-6 in the Materials Open Test Assembly (MOTA) of FFTF at 407°C to neutron fluences producing 47 dpa and about 5 appm He in all the alloys. Temperatures in FFTF are recorded during irradiation whereas temperatures in HFIR are determined by heat transfer calculations that have been verified by post-irradiation examination of monitors that measure temperature during irradiation.[15] Temperature uncertainties for experiments in both reactors appear to be t15 to 25°C or less. Displacement damage is calculated in both reactors from dosimetry measurements. For the HFIR experiment, both dpa and helium levels were calculated by L. R. Greenwood,[16] and dpa values include the extra contribution of nickel recoils when helium atoms are generated.

TEM specimens were thinned using an automatic TENUPOL electropolishing unit (with cooling) located in a hot cell. TEM disks were examined using a JEM 100C electron microscope equipped with a special objective lens pole-piece that lowers the magnetic field at the ferro-magnetic specimen. Quantitative cavity statistics and swelling values were obtained using a ZEISS particle analyzer; foil thicknesses were measured via stereomicroscopy. Some selected area electron diffraction (SAD) was performed in-foil to obtain crystallographic data for phase identification but good, low-order zone axis patterns (ZAPs) were difficult to obtain because tilting more than 5 to 10° is difficult with magnetic specimens.

Precipitates were also extracted onto carbon replica films from as-tempered and from irradiated samples for phase identification and compositional evaluation using X-ray energy dispersive spectroscopy (XEDS) and convergent beam electron diffraction (CBED). Replicas from the irradiated specimens were prepared in a special shielded hands-on facility because the HFIR specimens in particular were highly radioactive. XEDS was performed on either a Philips EM400T/FEG or a JEM 2000FX (LaB_6) analytical electron microscope (AEM). The EM400T/FEG has a field emission gun (FEG) that produces a very high electron intensity at probe sizes as small as 3 nm in diameter, so that the compositions of very small precipitate particles could be measured easily. XEDS spectra were quantified after measuring integral peak intensities using well-established standardless analysis techniques.[17,18] Individual elemental XEDS peaks contained 100 to 100,000 counts, giving a statistical significance of ±10 to 0.3% of the reported composition in atomic percent. Multiple particle measurements were made for each phase identified on the replica.

Table 1. Compositions of 9Cr-1MoVNb and 12Cr-1MoVW heats of steel with and without nickel doping

Alloy Designation	Heat No.	Concentration,[a] wt %										
		Cr	Mo	Ni	Mn	C	Si	V	Nb	Ti	W	N
9Cr-1MoVNb	(XA 3590)	8.6	1.0	0.1	0.36	0.09	0.08	0.21	0.063	*0.002*	0.01	0.05
9Cr-1MoVNb-2Ni	(XA 3591)	8.6	1.0	*2.2*	0.36	0.064	0.08	0.22	0.066	*0.002*	0.01	0.05
12Cr-1MoVW	(XAA 3587)	12	0.9	0.4	0.5	*0.2*	0.18	0.27	0.018	0.003	0.54	*0.02*
12Cr-1MoVW-2Ni	(XAA 3589)	11.7	1.0	2.3	0.5	*0.2*	0.14	0.31	0.015	0.003	0.54	*0.02*

[a]Balance iron.

Table 2. Normalizing and tempering conditions for various steels

Alloy	Normalization	Tempering
9Cr-1MoVNb	0.5 h at 1040°C	1 h at 760°C
9Cr-1MoVNb-2Ni	0.5 h at 1040°C	5 h at 700°C
12Cr-1MoVW	0.5 h at 1050°C	*2.5* h at 780°C
12Cr-1MoVW-2Ni	0.5 h at 1050°C	5 h at 700°C

Table 3. Damage parameters and helium levels for nickel-doped and undoped 9Cr-1MoVNb and 12Cr-1MoVW steels irradiated in FFTF and HFIR

Alloy	Reactor	Irradiation Temp. (°C)	Damage (dpa)[a]	Helium Content (appm)
9Cr-1MoVNb	FFTF	407	47	~5
	HFIR	400	36.5	30.5
9Cr-1MoVNb-2Ni	FFTF	407	47	~5
	HFIR	400	37.2	402.5
12Cr-1MoVW	FFTF	407	47	~5
	HFIR	400	36.4	85.3
12Cr-1MoVW-2Ni	FFTF	407	47	~5
	HFIR	400	37.1	429.0

[a]Displacement — dpa calculation includes the effect of nickel recoils.

RESULTS

Cavity Evolution and Swelling — FFTF Irradiation

There were very few voids (large cavities, bias-driven growth), no detectable bubbles (very small cavities, gas-driven growth) and, therefore, negligible cavity swelling in any of the 9 Cr and 12 Cr steels irradiated in FFTF to 47 dpa at 407°C. Cavity behavior and statistics are described in Table 4, and TEM microstructures of 9 Cr and 12 Cr steels with and without nickel doping are shown in Fig. 2. Some large matrix voids (7–23 nm in diameter) can be seen in the 9Cr-1MoVNb steel [Fig. 2(a)], and some are occasionally observed within χ phase particles in the 9Cr-1MoVNb-2Ni steel. Large voids (15–23 nm in diameter) are found only occasionally in the 12Cr-1MoVW or 12Cr-1MoVW-2Ni steels.

Cavity Evolution and Swelling — HFIR Irradiation

Abundant void (7–30 nm in diameter) formation was found in both the 9Cr-1MoVNb and 12Cr-1MoVW steels and those doped with 2 wt % Ni after HFIR irradiation at 400°C to 36 to 37 dpa, as shown in Fig. 3. Previous work on HFIR irradiation of these steels at 300 to 600°C established that void formation was maximum[10] at about 400°C. Very few fine helium bubbles (2–5 nm in diameter) were detected in the undoped 9 Cr and 12 Cr steels despite increased void formation relative to FFTF, as shown for 9Cr-1MoVNb at higher magnification in Fig. 4. Since the TEM resolution limit for bubbles is about 1.5 nm, these steels could contain subcritical bubbles. By contrast, the nickel-doped steels with much more helium, also had much higher concentrations of fine bubbles than found than found in FFTF, as shown for 9Cr-1MoVNb-2Ni in Fig. 5. Cavity behavior is described and quantitative microstructural data are presented in Table 4.

Swelling due to cavities was 0.3 to 0.35% in the 9Cr-1MoVNb and 9Cr-1MoVNb-2Ni steels, and slightly less, 0.23 to 0.25%. in the 12Cr-1MoVW and 12Cr-1MoVW-2Ni steels. While these are not alarmingly high levels of swelling, closer inspection of microstructural details suggests additional insight into the actual stage of void evolution that each specimen is experiencing, which in turn is important to any projections of behavior at higher doses. The swelling in the 9Cr-1MoVNb and 12Cr-1MoVW steels is primarily

Table 4. Quantitative cavity statistics determined via TEM for 9Cr and 12Cr steels irradiated in HFIR and FFTF

Alloy	Cavity Statistics (Average) Diameter (nm)	Density (m^{-3})	Comnents	Total Cavity Volume Swelling (%)	Cavity Character Ratio
			FFTF Irradiation at 407°C to 47 dpa		
9Cr-1MoVNb			A few detectable voids (7–23 nm diam)		
9Cr-1MoVNb-2Ni			A few detectable voids (7–23 nm diam)		
12Cr-1MoVW			A few detectable voids (15–23 nm diam)		
12Cr-1MoVW-2Ni			A few detectable voids (15–23 nm diam)		
			HFIR Irradiation at 400°C to ~37 dpa		
9Cr-1MoVNb	9.2	2.71×10^{21}	Few fine cavities below ~3 nm diam, somewhat nonuniform spatial distribution. Many 10 to 20-nm-diam voids	~0.3	0.04
9Cr-1MoVNb-2Ni	3.8 12	1.6×10^{22} 2.5×10^{21}	Fine bubbles Larger voids	0.35	0.33
12Cr-1MoVW	12.5	2.2×10^{21}	Abundant fine cavities and a smaller population of larger voids. Critical size appears to be about ~5 nm (diam). Voids range up to 22 μm in diameter, but many are in the 10 to 15 μm range. Some fine cavities, but many 8 to 20 nm (diam) voids, with some in the 20 to 30 nm range in larger subgrains. Somewhat nonuniform distribution with most voids in largest subgrains, but all subgrains have some voids.	0.23	0.13
12Cr-1MoVW-2Ni	3.5 9	3.5×10^{22} 1.6×10^{21}	Fine bubbles Larger voids	0.25	0.45
			Abundant fine cavities and a sparse, nonuniform distribution of larger voids, many within larger subgrains.		

due to voids. Cavity size distributions plotted from the larger cavities observed in the microstructures show broad tails at larger sizes in these undoped steels (Fig. 6). Calculations accounting for the helium needed to fill these cavities (cavity character ratio - generated appm He/calculated appm He for equilibrium bubbles) indicate that these cavities are quite empty, suggesting that they are voids; any accommodation of helium in unresolved bubbles would further support this assessment. Swelling in the 9Cr-1MoVNb-2Ni and 12Cr-1MoVW-2Ni steels is due to the abundant populations of both fine helium bubbles and voids. Bubbles cause about 50 to 66% of the measured swelling in the nickel-doped steels. While the generated helium can be accommodated in the visible cavity microstructure, all the helium could easily fit into the smallest cavities as equilibrium helium bubbles, again suggesting that the larger cavities are probably voids.

The nickel-doped 9 Cr and 12 Cr steels with 400 to 430 appm He both have high concentrations of fine bubbles (2–5 nm diam, 1.6–3.5 $\times 10^{22}$ m^{-3}) with much lower concentrations (6 and 22 times less, respectively) of larger voids (see Table 4). Void formation in the presence of these dense populations of fine bubbles appears to be similar or somewhat retarded in the nickel-doped relative to the undoped steels. Cavity size distributions in both nickel-doped steels [Fig. 6(b) and 6(d)] show shifts in the size distributions toward smaller sizes. The 9Cr-1MoVNb-2Ni steel in particular has fewer voids in the 17-35-nm-diam size range than does the 9Cr-1MoVNb steel. The void densities (neglecting the patchy, spatial nonuniformity in the undoped steel) are similar in the 9 Cr steels with and without nickel, but there are noticeably fewer voids in the 12 Cr steel with nickel as compared to the one without. It would appear, therefore, that the increased density of bubble-sinks was affecting void formation and growth in the Ni-doped steels with the highest helium contents.

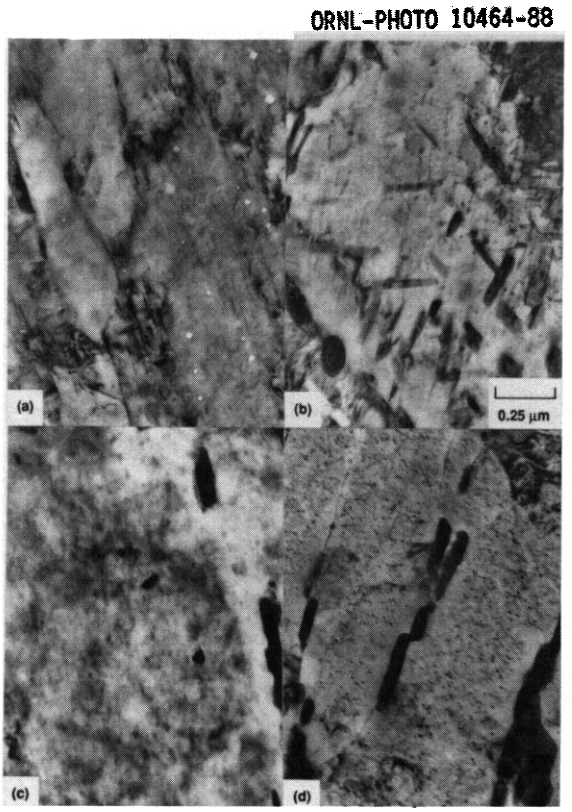

Fig. 2. Microstructure of various 9 Cr and 12 Cr martensitic/ferritic steels irradiated in FFTF at 407°C, to a dose of 47 dpa and helium level of ~5 appm. (a) 9Cr-1MoVNb (b) 9Cr-1MoVNb-2Ni, (c) 12Cr-1MoVW, and (d) 12Cr-1MoVW-2Ni.

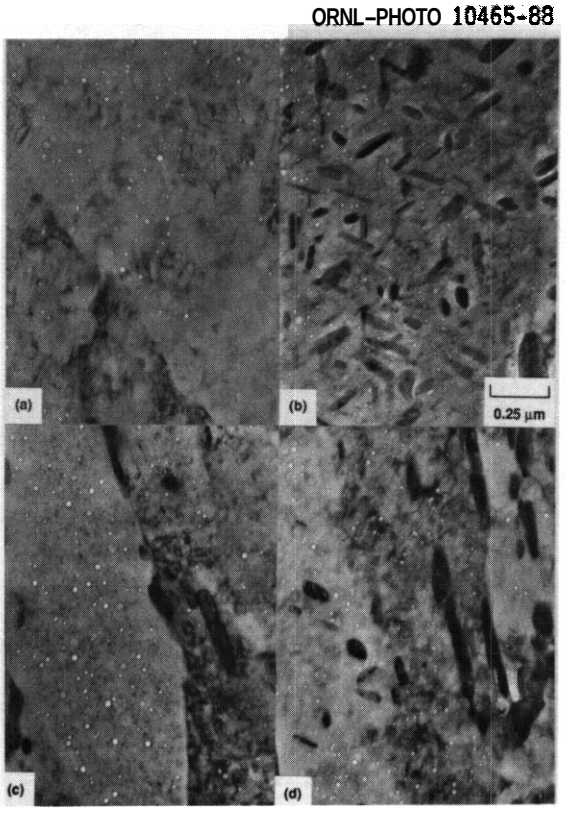

Fig. 3. Microstructure of various 9 Cr and 12 Cr martensiticlferritic steels irradiated in HFIR at 400°C to a dose of ~37 dpa and helium levels that depend on nickel content. (a) 9Cr-1MoVNb (30.5 appm), (b) 9Cr-1MoVNb-2Ni (402.5 appm), (c) 12Cr-1MoVW (85.3 appm), and (d) 12Cr-1MoVW-2Ni (429 appm)

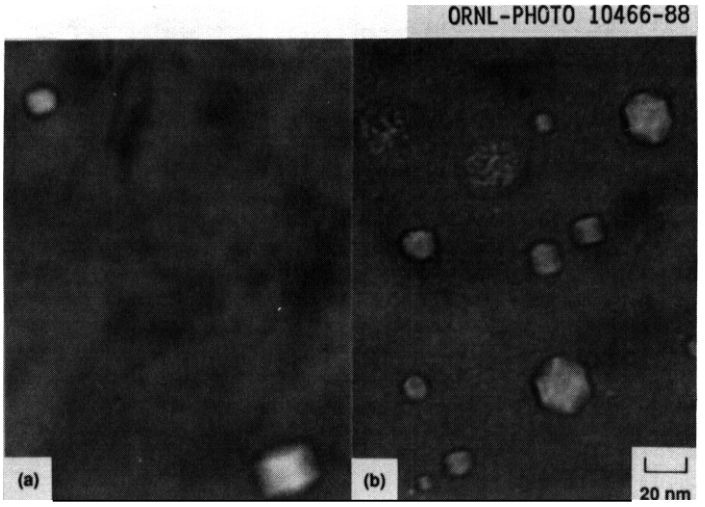

Fig. 4. Microstructure at higher magnification in kinematical contrast is used to show fine helium bubbles, when present, and larger voids in 9Cr-1MoVNb irradiated in (a) FFTF at 407°C to 47 dpa and 5 appm He and (b) HFIR at 400°C to 36.5 dpa and 30.5 appm He.

ORNL-PHOTO 10467-88

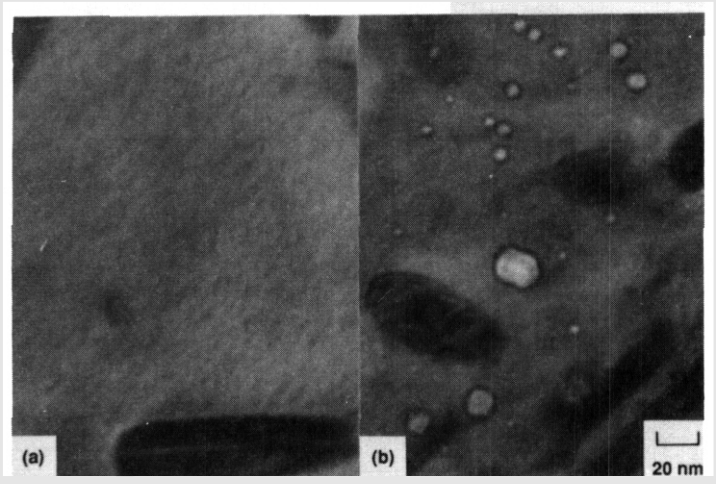

Fig. 5. Microstructures of 9Cr-1MoVNb-2Ni irradiated in (a) FFTF at 407°C to 47 dpa and 5 appm He and (b) HFIR at 400°C to 37.2 dpa and 402.5 appm He. Higher magnification in kinematical contrast shows fine helium bubbles and larger voids.

Cavity size distributions determined from higher magnification pictures that include both fine bubbles and large voids from the 9Cr-1MoVNb-2Ni and 12Cr-1MoVW-2Ni steels are shown in Fig. 7. These distributions with their large peaks at small sizes and broad tails to larger sizes empirically suggest that the critical cavity size is about 5 nm in diameter in the 9Cr-1MoVNb-2Ni steel, and is about 5 to 6 nm in diameter in the 12Cr-1MoVW-2Ni steel. Cavities below this size would be stable, subcritical bubbles, while the larger cavities would have converted from bubbles to unstable, rapidly-growing voids. By contrast to the steels with more helium, critical cavity sizes in the undoped steels irradiated in HFIR or any of the steels irradiated in FFTF appear to be below the TEM resolution limit, or less than 1.5 nm in diameter.

To summarize, the effects of increased helium generation on void and bubble formation can best be seen by comparing FFTF and HFIR irradiation for each heat of steel. In the 9 Cr and 12 Cr steels without nickel doping, a modest increase in helium generation causes a considerable increase in void formation. In

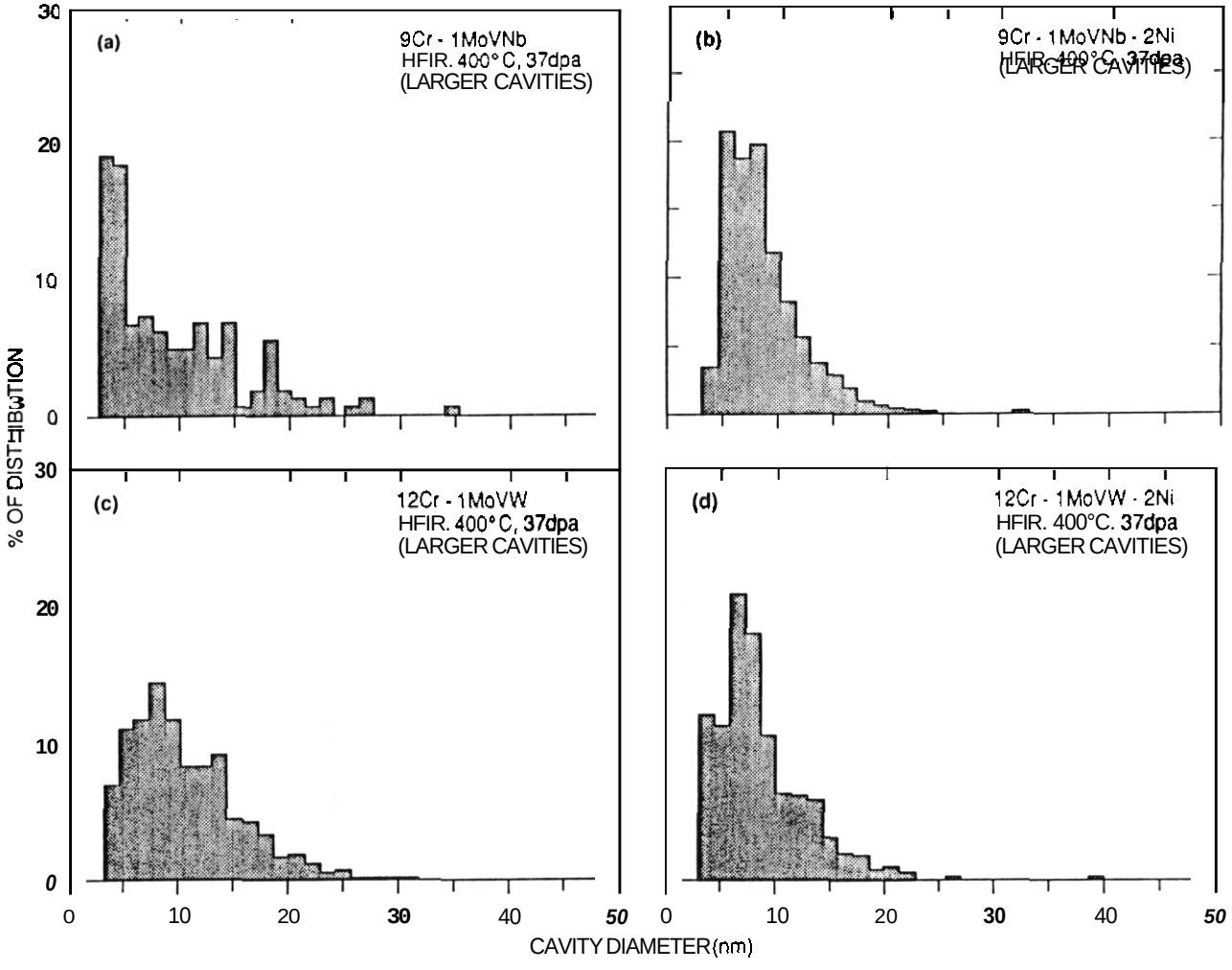

Fig. 6. Cavity size distribution histograms for various steels irradiated in HFIR, from quantitative analysis of low magnification photomicrographs which include the largest cavities (very fine bubbles would be obscure).

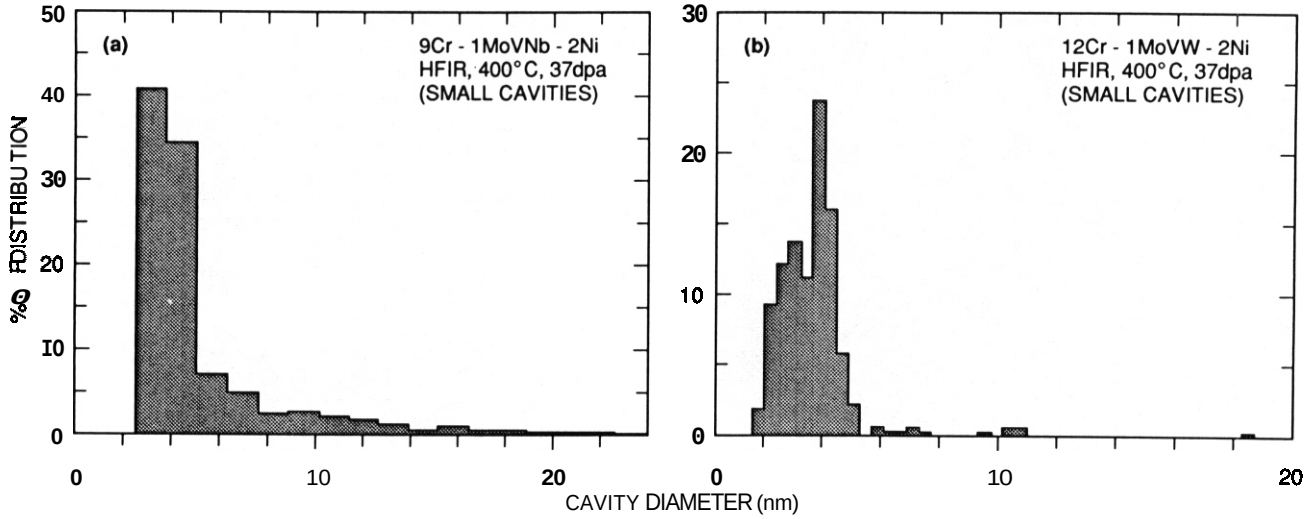

Fig. 7. Cavity size distribution histograms from quantitative analysis of higher magnification photomicrographs which include the smallest visible helium bubbles.

the 9 Cr and 12 Cr steels without nickel doping, a modest increase in helium generation causes a considerable increase in void formation. In the 9 Cr and 12 Cr steels with nickel doping, a large increase in helium generation not only increases void formation in HFIR relative to FFTF, but also greatly increases fine bubble nucleation. Both groups of samples appear to be still in the early stages of void formation. The critical cavity size appears to be below the resolution limit of the microscope in all of the FFTF-irradiated steels as well as in the HFIR-irradiated steels without nickel. If this critical size does not change. then it is easy for more voids to form as more helium is generated. In the nickel doped steels irradiated in HFIR, however, the critical cavity size becomes much larger while void formation becomes somewhat more difficult. These observations consistently suggest that the higher total densities of helium bubbles are becoming dominant sinks to hinder void formation.

Dislocation and Subgrain Boundary Structure Evolution — FFTF and HFIR Irradiation

By contrast to the large differences in cavity behavior between steels irradiated in FFTF and HFIR, there is little or no difference in the dislocation of subgrain structure evolution of a given steel irradiated in FFTF and HFIR. There are, however, differences in the evolution of this portion of the microstructure among the various heats of steel that depend on alloy composition and/or tempering conditions.

All of the irradiated steels had moderately to densely tangled dislocation networks that were spatially quite uniform, with a few larger loops visible. The 9Cr-1MoVNb steel irradiated in HFIR at 400°C had a total dislocation density (A) of 6×10^{13} m^{-2}, while the 9Cr-1MoVNb-2Ni had a higher A of 4×10^{14} m^{-2}. The dislocation structure in the as-tempered material was, by comparison, spatially quite non-uniform from grain to grain, with the degree of non-uniformity depending on the tempering conditions. The 9Cr-1MoVNb steel tempered for 1 h at 760°C was most non-uniform. This steel had a network dislocation density (A) that varied from 1 to 7×10^{13} m^{-2} within larger subgrains of the tempered martensite lath structure. The dislocation density was much less in many of the smaller subgrains, but A was quite high within the planar honeycomb arrays of dislocation network that defined most of the subgrain boundaries. Subgrains were somewhat smaller, but still had similar or higher dislocation concentrations in 9Cr-1MoVNb-2Ni tempered for 5 h at 700°C.[18] In both 9 Cr steels, irradiation obviously altered the dislocation structure, as can be seen in Fig. 8 for 9Cr-1MoVNb-2Ni irradiated in FFTF. This involves both some recovery of the as-tempered structure as well as the formation of new dislocations during irradiation. Although a detailed Burger's vector analysis was not done in this work, others have shown that unirradiated ferritic material has network segments of $a_0/2$ <111>, while such material irradiated at 400 to 500°C develops a structure with a mixture of $a_0/2$ <111> and a_0 <100> Burger's vectors.[3,19] Dislocation concentrations in the 9 Cr steels are either similar or slightly higher after irradiation at 400°C, but they are also spatially much more uniform compared to unirradiated material. This is most likely related to the significant coarsening of the as-tempered lath sub-grain boundary structure that also occurred in the 9 Cr steels irradiated at 400°C (Figs. 8 and 9).

The as-tempered grain and subgrain structure in various steels consists of large prior austenite grain boundaries and packet boundaries around groups of similarly aligned martensite laths, with both boundaries containing coarse $M_{23}C_6$ precipitates along them, and low-angle lath subgrain boundaries, which occasionally have coarse $M_{23}C_6$ or MC particles at junction points. The lath subgrain boundaries within the packet boundaries are almost completely removed during irradiation of the 9 Cr steels irradiated in

ORNL-PHOTO 10463-88

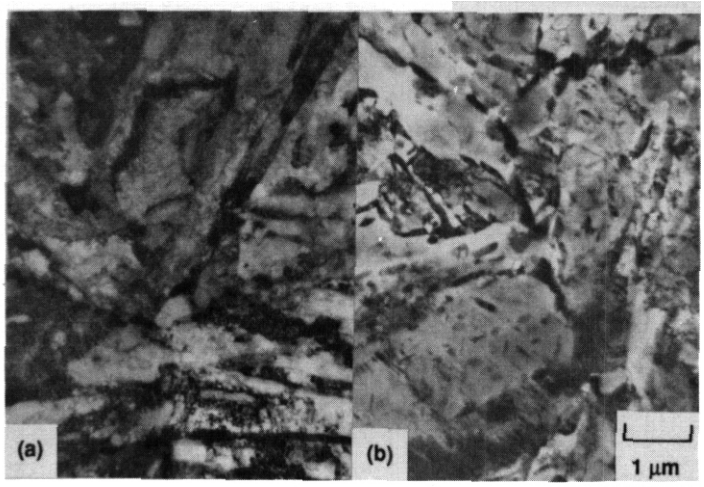

Fig. 8. Lower magnification TEM of 9Cr-1MoVNb-2Ni showing prior austenite grain size and lath packet and subgrain boundary structures in (a) as-tempered, and in (b) FFTF irradiated (407°C. 47 dpa, ~5 appm He material.

ORNL-PHOTO 10462-88

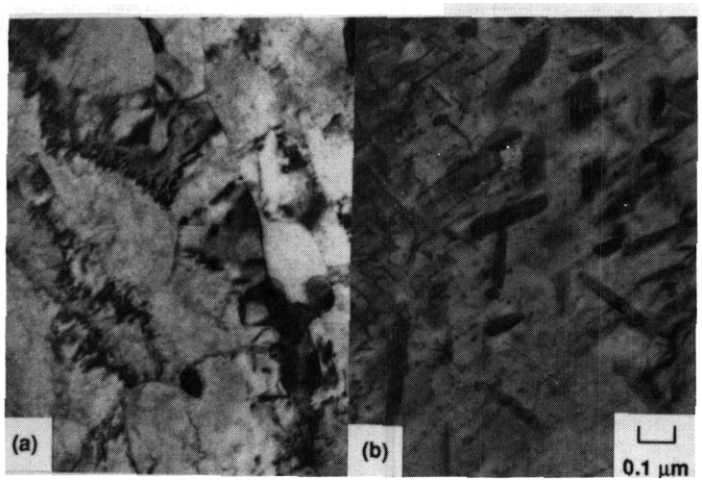

Fig. 9. Higher magnification TEM of 9Cr-1MoVNb-2Ni showing lath subgrain boundary and intra-lath dislocation structures in (a) as-tempered, and (b) FFTF irradiated (407°C, 47 dpa, ~5 appm He) material.

either HFIR or FFTF at about 400°C, as seen for 9Cr-1MoVNb-2Ni in Figs. 8 and 9. This can easily be seen in TEM because large regions of irradiated material have uniform contrast, whereas the as-tempered steel has a speckled appearance because contrast conditions change with the slight angular misorientations from lath to lath (Figs. 8 and 9).

In comparison to the behavior of the irradiated 9 Cr steels, the as-tempered lath subgrain boundary structure in both of the 12 Cr steels remains quite stable during irradiation in either FFTF or HFIR at 400°C. Within the larger subgrains of 12Cr-1MoVW tempered for 2.5 h at 780°C, Λ is very low, $<1 \times 10^{12}\ m^{-2}$. After irradiation in HFIR at 400°C, Λ is $3.5 \times 10^{14}\ m^{-2}$, so that the dislocation concentration in this steel has increased considerably during irradiation, as shown in Fig. 10. The 12Cr-1MoVW-2Ni steel tempered for 5 h at 700°C had a finer subgrain size and higher dislocation content within the subgrains prior to irradiation, so that irradiation produced only a modest increase, if any, in the dislocation content of this material.

In sumnary, irradiation at about 400°C clearly increases the dislocation concentration in the 12Cr-1MoVW steel that had a low dislocation content before-hand by virtue of its tempering conditions (higher temperature, longer time). Irradiation did not produce large increases in dislocation content of the other steels (12Cr-1MoVW-2Ni, 9Cr-1MoVNb, 9Cr-1MoVNb-2Ni), which had higher as-tempered dislocation contents to begin with. Irradiation did, however, evolve a more uniform dislocation network structure that includes some loops and probably a mixture of Burger's vectors. Irradiation appeared to cause almost complete recovery of the as-tempered lath subgrain boundary structure in both the 9 Cr steels, while such subgrain boundaries remained stable in the 12 Cr steels during irradiation. All aspects of dislocation/subgrain boundary evolution were identical when comparing the same steels irradiated in HFIR and FFTF.

Phase Formation and Stability - As-Tempered Precipitation

Tempering for the range of conditions shown in Table 2 produced carbide precipitation that differed between 9 Cr and 12 Cr steels, but was not affected by nickel doping. Table 5 lists phases and their relative abundances, while Tables 6 and 7 give the compositions of the $M_{23}C_6$ and MC phases, respectively, as determined by XEDS analysis on carbon film extraction replicas.

The 9Cr-1MoVNb and 9Cr-1MoVNb-2Ni steels have abundant coarse $M_{23}C_6$ and some finer MC distributed along the prior austenite grain boundaries, along some of the lath subgrain boundaries, and at junction points. The $M_{23}C_6$ phase contains primarily Cr with some Fe and lesser amounts of Mo and V (Table 6). Most of the finer MC phase particles are mainly rich in V (>60 wt %) with some Cr and Nb. A few MC particles have more Nb (>50%) than V (26-33%) with some Cr (Table 7). Bulk extraction techniques measured 1.4 wt % of total carbide precipitates in the 9Cr-1MoVNb (refs. 7,8) and broad-beam AEM analysis of relative phase fractions on extraction replicas indicates that 85% of the precipitate is $M_{23}C_6$ and 15% is MC. Precipitate phases, fractions, and compositions were about the same in 9Cr-1MoVNb and 9Cr-1MoVNb-2Ni steels.

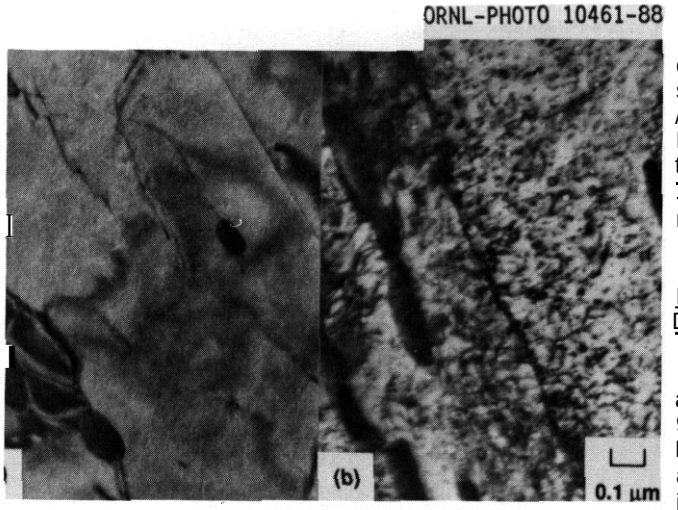

Fig. 10. Higher magnification TEM of 12Cr-1MoVW showing lath subgrain boundary and intra-lath dislocation structures in (a) as-tempered, and (b) HFIR irradiated (400°C, 36 dpa. 85 appm He) material.

The 12Cr-1MoVW steel contains more carbide precipitation (3.5 wt %) after tempering than the 9 Cr steels, with relative amounts of 99% $M_{23}C_6$ and 1% MC. All the MC is V-rich because these steels contain no Nb. Although a lower tempering temperature refines the $M_{23}C_6$ size distribution somewhat in the 12Cr-1MoVW-2Ni, there is otherwise no obvious effect of nickel doping on the precipitation.

Phase Formation and Stability — Evolution of $M_{23}C_6$ During FFTF and HFIR Irradiation

The as-tempered, coarse $M_{23}C_6$ precipitation appears to become unstable during irradiation of 9 Cr-1MoVNb and 9Cr-1MoVNb-2Ni at 400 to 410°C in FFTF and HFIR, dissolving at lath subgrain boundaries and somewhat along packet boundaries. This phase instability is coincident with the coarsening of the subgrain boundary structure noted above. While no additional precipitation occurs in the 9Cr-1MoVNb steel during irradiation [see Figs. 2(a), 3(a), and 41, abundant formation of new, coarse $M_{23}C_6$ particles occurs uniformly within the large matrix regions of the 9Cr-1MoVNb-2Ni steel that are free of prior

Table 5. Precipitate phase identification for 9Cr and 12Cr steels irradiated in HFIR and FFTF

Alloy	Phases after Tempering	Phases after Irradiation[a] HFIR (400°C, 37 dpa)	Phases after Irradiation[a] FFTF (407°C, 47 dpa)	Comments
9Cr-1MoVNb	$M_{23}C_6$ (85%)[b] MC (15%)	$M_{23}C_6$ MC	$M_{23}C_6$ MC M_2X	Partial dissolution of coarse $M_{23}C_6$ particles and coarsening of finer MC particles. Traces of very fine M_2X acicular needles are found only in FFTF-irradiated material. MC composition is modified — more Cr, less V.
9Cr-1MoVNb-2Ni	$M_{23}C_6$ (85%)[b] MC (15%)	$M_{23}C_6$ M_6C (η) MC	$M_{23}C_6$ M_6C (TI) MC M_2X	Some dissolution and coarsening of original as-tempered $M_{23}C_6$ particles and abundant precipitation of new $M_{23}C_6$ particles with slightly modified composition. MC evolution and modification are similar to that mentioned above. Many fine M_6C particles form in both reactors, but large M_6C particles are also found in FFTF-irradiated material. Some large M_2X particles are also found at boundaries in FFTF-irradiated material, but no fine needles.
12Cr-1MoVW	$M_{23}C_6$ (99%) MC (1%)	$M_{23}C_6$ M_6C (η)[c] MC	$M_{23}C_6$ M_6C (η)[c] MC	As-tempered $M_{23}C_6$ is stable while MC content increases during irradiation. MC composition is modified. Abundant, fine particles are found throughout the matrix, similar to M_6C mentioned above. In HFIR, these particles are very rich in Si and Cr, but in FFTF they have somewhat more Cr and less Si.
12Cr-1MoVW-2Ni	$M_{23}C_6$ (99%) M_6C (1%)	$M_{23}C_6$ M_6C (η) MC	$M_{23}C_6$ M_6C (TI) MC	Partial dissolution of as-tempered $M_{23}C_6$ occurs and some coarse M_6C forms to replace it, more so in HFIR than in FFTF. Abundant, fine M_6C forms in both reactors and more MC develops during irradiation with the same compositional modifications mentioned above.

[a] XEDS analysis on extraction replicas plus some SAD and CBED analysis.

[b] Relative phase fractions determined via broad-beam XEOS measurements.

[c] Mainly Cr- and Si-rich.

Table 6. Quantitative XEDS compositional analysis of $M_{23}C_6$ particles extracted from 9Cr-1MoVNb-2Ni steel specimens

Phase composition,[a] at. %									Number of Particles Analyzed	Comments
Si	Ti	V	Cr	Fe	Ni	W	Nb	Mo		
As-Tempered, 5 h at 700°C										
0.5	0.2	3.6	62	25.4	1.2	n.d.	0.8	6	6	Large, >350 nm diam
0.6	0.2	6.2	68	17.1	1.0	n.d.	0.4	6.2	3	Small, <150 nm diam
Irradiated in HFIR at 400°C to 37 dpa										
3.4	0.2	1.9	59	22.8	6.9	n.d.	0.2	5	2	Large, >350 nm diam. along boundaries
4.0	0.1	1.7	61	22.8	5.1	n.d.	0.2	4.4	2	Large, >200–500-nm long laths, in the matrix
Irradiated in FFTF at 407°C to 47 dpa										
3.4	0.2	1.5	60	20.9	6.8	n.d.	0.4	5.1	3	Large, >350 nm diam. along boundaries
2.0	0.2	0.8	63	24.9	2.9	n.d.	0.1	4.8	3	Large, >200–500-nm long laths, in the matrix

[a]Composition of metal atoms heavier than Al.

Table 7. Quantitative XEDS compositional analysis of MC particles extracted from 9 Cr steel specimens

Phase composition,[a] at. %									Number of Particles Analyzed	Comments[b]
Si	Ti	V	Cr	Fe	Ni	W	Nb	Mo		
9Cr-1MoVNb, As-Tempered. 1 h at 760°C										
1.6	0.6	62.6	16.6	1.6	n.d.	n.d.	14.2	1.1	6	V-rich, small, 17-60 nm
2.3	2.3	33	9.2	1.1	0.1	n.d.	49	1.3	2	Nb-rich, same
9Cr-1MoVNb-2Ni, As-Tempered, 5 h at 700°C										
0.3	0.6	69.2	14.0	0.8	n.d.	n.d.	14.0	0.8	7	V-rich, small, 17-60 nm
1.3	2.1	26.5	5.3	0.8	n.d.	n.d.	62.4	0.5	2	Nb-rich, same
9Cr-1MoVNb, FFTF, 407°C, 47 dpa										
2.3	n.d.	33.7	52.7	4.8	0.5	n.d.	2.9	1.2	4	V-rich, large, 70–160 nm
2.8	0.1	35.1	49.4	6.5	0.4	n.d.	3.0	1.0	3	V-rich. small, 17-50 nm
0.1	0.1	14.9	35.8	5.3	0.6	n.d.	40.3	1.1	4	Nb-rich, small
9Cr-1MoVNb-2Ni, FFTF, 407°C, 47 dpa										
4.4	0.2	37.5	35.0	8.7	3.6	n.d.	7.4	1.5	4	V-rich, large, >30 nm
3.7	0.4	38.5	31.1	6.3	3.0	n.d.	13.2	1.3	3	V-rich, small, 9-25 nm
3.2	1.1	9.8	21.6	5.0	6.2	n.d.	45.5	1.5	3	Nb-rich, large, >90 nm
9Cr-1MoVNb, HFIR, 400°C, 36.5 dpa										
3.2	0.5	34.9	46.5	5.5	0.4	n.d.	7.4	1.4	9	V-rich, 30–120 nm
0.4	1.2	8.8	34.2	4.5	0.8	n.d.	46.1	3.5	2	Nb-rich. same
9Cr-1MoVNb-2Ni, HFIR, 400°C, 37 dpa										
1.4	0.2	44.5	38.7	5.5	6.9	n.d.	5.6	1.4	4	V-rich, large, 40–80 nm
1.6	0.5	35.3	41.3	6.3	2.5	n.d.	9.6	1.6	4	V-rich, small, 8–25 nm

[a]Composition of metal atoms heavier than Al.
[b]Particle size, either diametre for equiaxed or larger dimension for other morphologies.

martensite lath subgrain boundaries [Figs. 2(b), 3(b), 5, 8, and 9]. Figure 9 of 9Cr-1MoVNb-2Ni irradiated in FFTF, shows coarse $M_{23}C_6$ particles at prior austenite grain boundaries and lath packet boundaries with odd, elongated shapes. These irregular shapes suggest that discrete smaller particles have grown together to form the larger ones. The composition of these irradiation-produced $M_{23}C_6$ particles is slightly different from the as-tempered phase (Table 6), with somewhat more Ni and Si, and slightly less Cr, Fe, and V, but still well within the characteristic compositional range for that phase.[6] While this abundant precipitation of $M_{23}C_6$ is a noticeable difference between the behavior of the Ni-doped and the undoped 9 Cr steels during irradiation [Figs. 2(a and b; 3(a and b)], it is important to note that the oroduction. distribution. and comoosition of these oarticles in the 9Cr-1MoVNb-2Ni steel is about the same in FFTF and HFIR [Figs. 2(b) and 3(b)]. There is some replacement of coarse $M_{23}C_6$ along boundaries by similarly coarse M_6C in the 9Cr-1MoVNb-2Ni irradiated to 47 dpa in FFTF (Table 5).

The as-tempered $M_{23}C_6$ is quite stable during irradiation of the 12Cr-1MoVW and 12Cr-1MoVW-2Ni steels in either FFTF or HFIR, in contrast to the instability found in the 9 Cr steels. Irradiation does not produce additional $M_{23}C_6$ nor does it alter its composition. The Ni-doped 12 Cr steel experiences some replacement of coarse $M_{23}C_6$ along boundaries by coarse M_6C during irradiation, similar to observations made in 9Cr-1MoVNb-2Ni, but this behavior is the same during both FFTF and HFIR irradiation (Table 5).

Phase Formation and Stability - Evolution of MC During FFTF and HFIR Irradiation

The as-tempered, finer MC precipitation also appeared to be unstable during irradiation in all the steels.. The MC coarsened and became more abundant, especially in the 9 Cr steels, as illustrated in Fig. 11 for 9Cr-1MoVNb irradiated in HFIR. Coincident with the microstructural coarsening, there was a considerable ch'ange in the composition of the MC phase during irradiation, as shown in Table 7 and in Fig. 12. The V-rich MC particles with low Nb contents were more abundant, and could be easily distinguished from the sparse Nb-rich MC particles in the irradiated 9 Cr steels. The two types of MC were similarly distinct in the as-tempered, unirradiated material. Both types of MC carbides became much richer in Cr at the expense of V (Fig. 12). Trace levels of Si, Ni, Fe and Mo were also detected in the irradiation-produced MC particles, but these were minor changes relative to the changes in Cr and V concentrations. There were some small differences in the effects of irradiation on the MC phase composition between the Ni-doped and undoped 9 Cr steels in HFIR, but almost no differences between these steels after FFTF irradiation (Table 7). Most importantly, there was little or no discernible difference in MC phase composition between either 9 Cr steel irradiated in HFIR and in FFTF. as emphasized by Fig. 13 for 9Cr-1MoVNb.

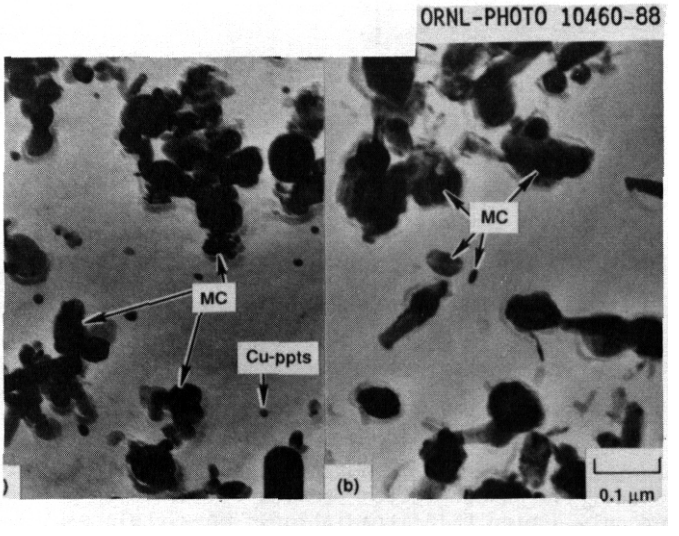

Fig. 11. Higher magnification TEM of carbon film extraction replicas from 9Cr-1MoVNb. (a) As-tempered and (b) after HFIR irradiation at 400°C to 36.5 dpa and 30.5 appm He. Changes (coarsening of the MC precipitate structure after irradiation can be seen.

The Cr enrichment and V depletion of MC during irradiation of the 12 Cr steels is very similar to that observed in the 9 Cr steels. Many MC particles show very high levels of Ti after irradiation in either reactor. The 12 Cr steels do not have Nb-rich MC particles before or after irradiation.

Phase Formation and Stability - Evolution of M_6C During FFTF and HFIR Irradiation

Abundant dispersions of fine M_6C (5-40 nm) were produced during irradiation in FFTF and HFIR at 400 to 410°C in all steels except the 9Cr-1MoVNb steel. These fine particles can be easily seen at higher magnification in Fig. 14. Diffraction information is consistent with the very similar crystal structures of either $M_{23}C_6$ (face-centered cubic) or M_6C (diamond cubic), but the Si, Cr and Ni-rich phase composition found clearly indicates that this phase is M_6C (η) (Table 8). The phase composition is about the same as the Si-Cr-Fe-Ni-Mo composition found for M_6C (η) in type 316 stainless steel irradiated in HFIR at 425 to 450°C, where the diamond cubic crystal structure has been positively identified by careful electron diffraction.[20]

Similarly, fine particles were found in the microstructure of the 12Cr-1MoVW steel after irradiation at about 400°C. These particles have an odd composition that are very rich in Si and Cr, has minor levels of Fe, Mo, and/or Nb, V, but has little or no Ni. The in-foil diffraction characteristics (where tilting is limited) are the same as found for the Ni-rich M_6C (η) in the other steels. Gelles and Thomas[3] have observed abundant, fine Cr-rich α' precipitation in similar steels, but our compositional

ORNL-DWG 88-11179

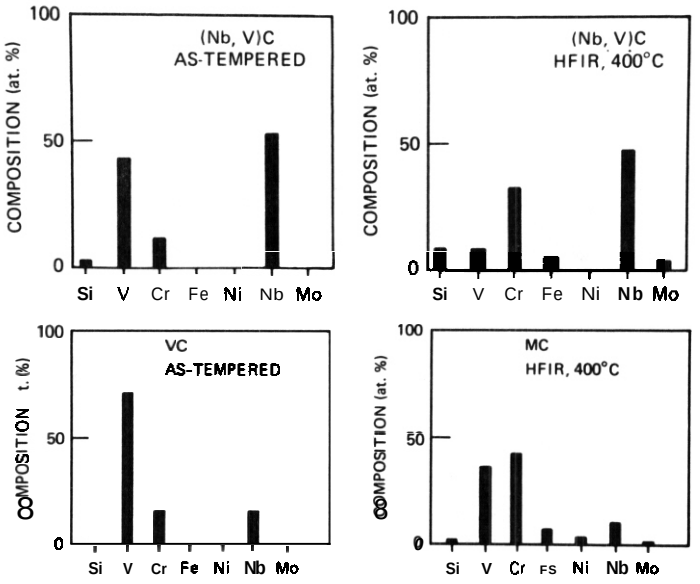

Fig. 12. Histograms of MC phase composition (metallic elements) for quantitative XEDS analysis of precipitate particles extracted on replicas from as-tempered and from irradiated 9Cr-1MoVNb.

ORNL-DWG 88-11180

9 Cr - 1 MoVNb

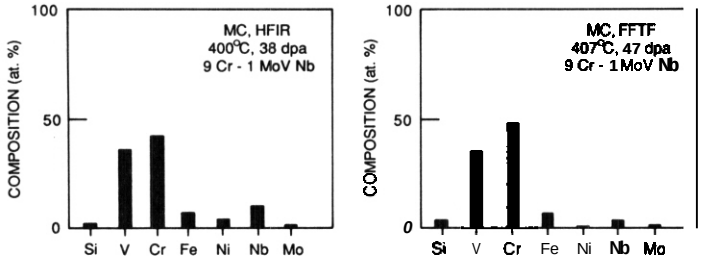

Fig. 13. Histograms of MC phase composition (metallic elements) from quantitative XEDS analysis of precipitate particles extracted on replicas from irradiated 9Cr-1MoVNb.

and diffraction results do not suggest α'. More work needs to be done to positively identify this phase; it is, however, consistently found in both HFIR- and FFTF-irradiated specimens.

As mentioned in the above section on the evolution of $M_{23}C_6$, irradiation at 400°C produces some coarse M_6C that replaces coarse, as-tempered $M_{23}C_6$ particles along prior austenite grain and lath-packet subgrain boundaries, but only in the Ni-doped steels (Table 5). Replacement is not noticeable in the in-foil microstructure, but becomes quite obvious during XEDS analysis on extraction replica films. Such coarse M_6C forms to a limited extent in 9Cr-1MoVNb-2Ni, but only during FFTF irradiation. More replacement M_6C particles form in 12Cr-1MoVW-2Ni in both reactors relative to 9Cr-1MoVNb-2Ni, but they occur more frequently during HFIR irradiation.

Despite some differences in formation characteristics and phase composition between finer and coarser M_6C particles in the various heats of steel, fine M_6C (η) precipitation is exactly the same in the various steels after FFTF and after HFIR irradiation. The fine M_6C phase composition is the same in both reactors, as emphasized in Fig. 15 for 9Cr-1MoVNb-2Ni. Even the composition of the fine, Ni-poor particles found in the 12Cr-1MoVW steel is fairly similar after HFIR and after FFTF irradiation (Table 8).

Table 8. Quantitative XEDS compositional analysis of fine M_6C (η) particles extracted from 9 Cr and 12 Cr steel specimens

Alloy	Number of Particles Analyzed	Composition, at. %[a]								
		Si	Ti	V	Cr	Fe	Ni	W	Nb	Mo
					FFTF, 407°C, 47 dpa					
9Cr-1MoVNb-2Ni	9	15	0.1	0.4	36	13	29.2	n.d.	0.4	3.6
12Cr-1MoVW	3	18.4	1.1	0.7	64.2	7.3	1.0	1.2	0.2	2.9
12Cr-1MoVW-2Ni	6	12	0.1	2.6	38.5	13.5	25.1	1.0	1.0	5.5
					HFIR, 400°C, 37 dpa					
9Cr-1MoVNb-2Ni	4	14.7	0.1	0.6	40.1	13.7	25.3	n.d.	0.4	3.9
12Cr-1MoVW	5	25	0.8	6.2	48	7.0	2.1	0.7	4.6	2.4
12Cr-1MoVW-2Ni	7	15	0.7	2.4	40.3	12.7	25.4	0.6	0.3	1.7

[a]Composition of metal atoms heavier than aluminum.

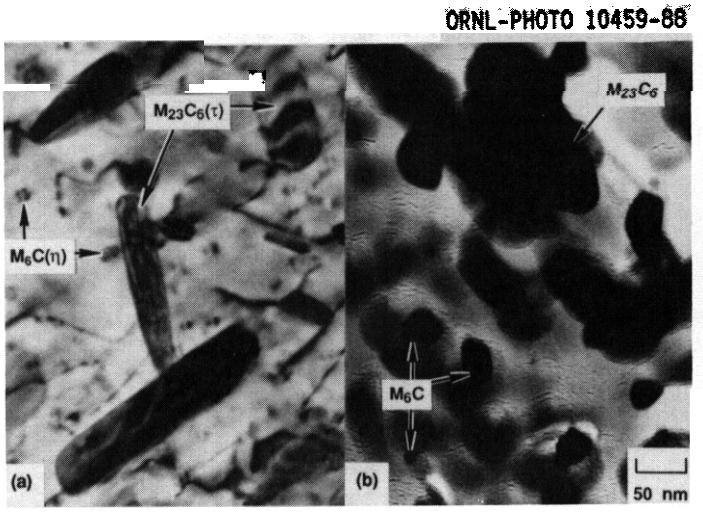

Fig. 14. Higher magnification TEM of fine M_6C (η) particles produced by irradiation of 9Cri-1MoVNb-2Ni irradiated in FFTF at 407°C to 47 dpa. (a) In-foil and (b) on a carbon film extraction replica.

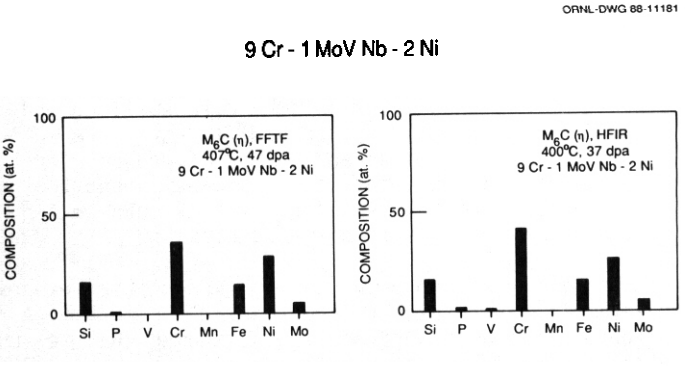

Fig. 15. Histograms of M_6C (η) phase composition (metallic elements) from quantitative XEDS analysis on precipitate particles extracted on replicas from irradiated 9Cr-1MoVNb-2Ni.

Phase Formation and Stability — Evolution of Other Phases

Traces of the fine, acicular M_2X needles, rich in Cr (75 at. %) and V (~20%) were found only in 9Cr-1MoVNb irradiated in FFTF. Some coarser particles with the same composition were found along boundaries in the 9Cr-1MoVNb-2Ni steel irradiated in FFTF. Although abundant formation of fine G phase ($Mn_6Ni_{16}Si_7$) particles has been observed by others in similarly irradiated steels,[3,4,21] we found no G phase in any of our steels irradiated in FFTF and HFIR at 400 to 410°C. We have, however, previously reported detecting trace levels of fine G phase precipitation in the 12Cr-1MoVW steel irradiated in HFIR at 500°C.[10]

DISCUSSION

The first portion of the discussion will compare the present swelling and microstructural data with data of others on similar steels, mainly from neutron experiments. The remainder will focus on the clear role that increased helium generation plays to enhance void formation in these martensitic/ferritic Steels, and the implications of such effects on the mechanism affecting or controlling void formation. Results on the evolution of other microstructural components will be discussed in the context of their relationship to the cavity microstructure. In general, except for cavities, microstructural evolution was similar for FFTF and HFIR irradiations of the same steel and, therefore, relatively unaffected by changes in helium level. Thus, these experiments can be interpreted as effectively straightforward, single-variable experiments of helium effects on cavity evolution, even in the steels doped with nickel.

The FFTF void-swelling behavior of the 9 Cr and 12 Cr steels (T91 and HT-9 base compositions, respectively) used in this work are generally consistent with the growing body of high-fluence FBR data on the martensitic class of ferritic steels.[22,25] This class includes such other steels as EM-12 (9Cr-2MoVNb, France), FV448 (12Cr-0.5MoVNb, United Kingdom), and DIN 1.4914 (12Cr-0.5MoVNb, West Germany). These steels have very good void-swelling resistance, with <0.6% swelling at doses of 100 to 125 dpa. Some coarse voids were seen in EM-12 at ~100 dpa by Gelles after EBR-II irradiation.[23] Our FFTF results, which show a few voids in the 9 Cr steel and almost none in the 12 Cr steel, are consistent with these observations.

There have been previous microstructural observations made on duplicate 9 Cr-1MoVNb and 12Cr-1MoVW specimens irradiated in HFIR at 400°C to ~37 dpa by Vitek and Klueh[7,8] and by Gelles and Thomas[3,14] on a similar heat of 12Cr-1MoVW (but with a different heat treatment) irradiated in HFIR at 400°C to 10 and 39 dpa. Gelles and Thomas also compared EBR-II irradiated HT-9 with their HFIR results to analyze for possible helium effects. For the 9Cr-1MoVNb steel, we found more of the smaller cavites and slightly more swelling than Vitek and Klueh,[8] but otherwise the cavity results are similar. For the 12Cr-1MoVW steels, we measured several times more swelling and almost 10 times more cavities (mainly smaller ones) than Vitek and Klueh,[9] but such differences are not unexpected, given the microstructural heterogeneity of these steels. Gelles and Thomas[3] found no effect of helium after 10 dpa in HFIR relative to EBR-II irradiation. On the other hand, Gelles[9] found that cavity formation is enhanced after 39 dpa in HFIR. but observed fewer and smaller cavities than we did, and about 4 times less swelling. Our reactor data on the nickel-doped steels are unique.

There have also been dual-ion irradiation experiments on these or similar steels to investigate helium effects on cavity formation.[26-29] Work by Ayrault,[26] using the dual-ion beam facility at the Argonne National Laboratory (ANL), showed that helium was essential to void formation at 410 to 470°C after 25 dpa in the same heats of 12Cr-1MoVW and 12Cr-1MoVW-2Ni used in the present work. The nickel-doping actually suppressed void swelling at 470°C. Farrell and Lee,[27,28] using the dual ion facility at ORNL, found that bias-driven voids could form at 450 to 550°C in 9Cr-1MoVNb (the same heat as used in this work) and 10Cr-6MoNb steels after 100 dpa. They found that helium enhanced void formation to produce maximum swellings of 0.4% and 0.75%, respectively, in the two steels. Horton and Bentley,[29] also using the ORNL facility, found that dual- and triple- (deuterium + tritium) ion beam irradiations of a binary Fe-10Cr alloy at 580°C produced a significant enhancement in void swelling after irradiation to 100 dpa (1.2 and 2.5% swelling, respectively).

There are few data available on the dislocation density in neutron-irradiated 9Cr-1MoVNb or 12Cr-1MoVW steels. Our 400°C values of Λ for 9Cr-1MoVNb are considerably less than the values measured after ion irradiation at 400 to 500°C by Farrell and Lee.[27] The range of Λ observed in our various steels irradiated in different reactors at 400 to 410°C (0.6 to 35 $\times 10^{14}$ m^{-2}) is also significantly less than the values observed by Gelles[30] for binary Fe-9Cr and -12Cr alloys irradiated in EBR-II at 400 to 450°C, or those observed by Horton and Bentley in ion-irradiated Fe-10Cr at ~580°C. Besides our data, there appear to be no other observations on subgrain structural instability during irradiation.[10]

Comparison of our precipitation results with the results of others and discussion about the role of radiation-induced solute segregation has been made elsewhere.[10,21] Our observations of fine M_6C (η) in irradiated HT-9 are consistent with findings by Little and Stoter[31] on FV 448. Our results differ considerably from those of Gelles and co-workers,[3,9] who report abundant precipitation of fine G and α' phases in 12Cr-1MoVW irradiated in EBR-II and HFIR at 400 to 500°C. Our observations of radiation-produced $M_{23}C_6$ in the nickel-doped 9 Cr steel and compositional modification of the MC phase in the various steels appear to be new findings.

There has been a considerable amount of theoretical work directed toward understanding the mechanisms that control void formation and swelling in ferritic steels, particularly during FER irradiation, where the resistance to void swelling is so obvious relative to austenitic stainless steels. Two recent reviews highlight the important mechanisms to consider:[25,32]

(a) Low intrinsic bias - This effect includes factors suggested to be inherent to the BCC crystal structure of the material. Sniegowski and Wolfer[33] proposed that the preferential attraction of dislocations for interstitials relative to vacancies (bias) is lower in ECC than in FCC materials because self-interstitials have smaller relaxation volumes in BCC material. Odette[32] also pointed out that

self-diffusion rates are considerably higher in BCC relative to FCC iron, which would enhance defect recombination.

(b) Low bias due to dislocation nature - Bullough and co-workers[34,35] proposed that a_0<100> loops with a strong interstitial bias cause the more neutral $a_0/2$<111> dislocation sinks to absorb vacancies, thus competing with cavities to reduce the net bias of the system.

(c) Solute effects - Little[36,37] and others[38] have suggested that there is substitutional trapping of point defects by solute atoms in BCC steels. Little[36] also suggested that substitutional solutes segregating to dislocations can reduce their bias for interstitials and inhibit climb. Both effects enhance point defect recombination. Gelles[39] has recently observed reduced swelling with oversize misfit solute atoms in dilute binary alloys and suggested radiation-induced segregation to dislocations and void surfaces was responsible.

(d) Microstructural sink balance effects - Horton and Mansur[40] in the context of a rate theory study of cavity growth rates and critical cavity size, indicated that domination of the microstructure by either dislocation or cavity sinks also contributes to the low swelling observed in BCC materials. Imbalanced partitioning leads to enhanced point defect recombination at the dominant sink. Their Fe-10Cr results suggest cavity-dominated microstructures, whereas similar interpretation of results on 9-10Cr steels indicated dislocation-dominated microstructures at low gas levels, and cavity dominated structures at high gas levels.

(e) Microstructural lath/subgrain boundary effects - Ayrault[26] and Maziasz et al.[10] have suggested that these boundaries are strong neutral sinks which enhance point defect recombination and lower the vacancy supersaturation in the as-tempered commercial steels.

(f) Microstructural precipitation effects - Gelles and Thomas[3] suggested that the fine G and α' precipitates that have been observed under irradiation contribute to void swelling resistance.

(g) Gas effects - Ferritic steels without nickel have lower helium generation rates during FBR irradiation than austenitic steels because nickel has a much higher (n,α) cross-section than Fe or Cr. All of the studies on the effect of helium[7-10,19,26-29] point to its stimulation of void nucleation. Triple-ion beam experiments also show an enhanced effect of helium and hydrogen together.[19,27-29]

Most of these mechanisms relate to the vacancy supersaturation available for void nucleation and growth. However, gas effects (g) and the critical size, r_c, for conversion of a stable gas bubble into a bias-driven void[32,40,41] are most relevant to void nucleation, which is the major issue addressed by our data. While most of the above-mentioned mechanisms probably contribute in concert to the void-swelling resistance observed in these steels during FBR irradiation, our data suggest that mechanisms (d) and (e) are most important to void growth during irradiation at higher helium generation levels.

Our data indicates that void nucleation is very difficult during FBR irradiation with little or no helium, and that increased helium generation greatly enhances void nucleation. Void nucleation can occur in austenitic stainless steels even without any helium present due to oxygen effects,[42,43] and elemental Ni used for alloying can have very high oxygen contents, usually higher than the Cr or Fe starting stock used to produce austenitic alloys and steels.[44] The martenistic/ferritic steels contain little Ni and much higher C contents (C is a very efficient deoxidizing element, as are Si and Ti) compared to austenitic steels and alloys, *so* that they mast likely have less oxygen available for void nucleation and are more dependent on helium generated during irradiation.

Macroscopic swelling with increasing fluence can be described in terms of a low-swelling transient regime or incubation period, followed by a steady-state regime of much more rapid swelling.[6,20] Voids nucleate and grow during the low-swelling transient regime, and usually rapid void growth and/or coalescence cause the onset of rapid swelling. Our data suggest that, while helium appears to have accelerated void nucleation to shorten the incubation period, perhaps by 75 to 100 dpa or more, none of our microstructures appear to be at the end of the transient regime and certainly not into the rapid-swelling regime.

Two closely related critical parameters from rate theory, the critical radius, r_c, and the critical number of gas atoms, n_g, whose mathematical equations are described by Odette[32] and Mansur and Coghlan,[41] help to interpret our microstructural data. Our data suggest empirical estimates for r_c; n_g^* is more difficult to estimate, but can be related to the duration of the incubation period. The r_c for the undoped 9 Cr and 12 Cr steels in this work appears to be t0.75 nm at 400 to 410°C in both FFTF and HFIR, whereas in the Ni-doped steels r_c increases from that value in FFTF to 2.5 to 3 nm in HFIR. The void formation in 9Cr-1MoVNb in FFTF may also indicate a very low value of n_g^* in that steel. At low values of both r_c and n_g^*, more helium would readily lead to more voids, as we observe for the undoped 9 Cr and 12 Cr steels irradiated in HFIR. Void formation appears more difficult in the nickel-doped steels in

HFIR because r_c and, presumably n_g^* increase. But void nucleation still increases. The value of r_c for the undoped steels appears to be consistent with that expected by others at about 400°C based on ion irradiation data,[27,28,40] but the value of 2.5 to 3 nm in the nickel-doped, HFIR irradiated steels seems large, as large as Horton and Mansur[40] find for Fe-10Cr ion irradiated at 580°C to 30 dpa. In SA 316 irradiated at 425 to 450°C, voids form easily and r_c appears to be ~1.5 nm, while in CW 316 or Ti-modified austenitic stainless steels that are resistant to void formation in HFIR at 400°C, r_c > 2.5 to 5 nm (refs. 20, 45).

Void formation and growth are also affected by the net bias or vacancy supersaturation and defect partitioning. The HFIR results on the nickel-doped steels with large r_c may suggest a larger vacancy supersaturation than might be anticipated and a more balanced partitioning of point defects among various sinks, despite the high density of bubbles. We can calculate a point defect partitioning factor Q for either vacancies or interstitials, defined for a two sink system as[41]

$$Q = Z^d \Lambda / 4\pi r N_c Z_c \quad , \tag{1}$$

where Z^d and Z^c are the capture efficiencies of dislocations and cavities, respectively, for that particular defect (usually ~1), Λ is the dislocation density, r is the average cavity radius, and N_c is the cavity concentration. Horton and Mansur[40] give an expression for the sink strength that includes a bimodal cavity distribution. The sink strength, S, for vacancies or interstitials can be expressed generally to include other sinks as follows,

$$S = 4 \Sigma_i r_i N_{c,i} Z^c(r_i) + \Lambda Z^d + r Z^b + 4 \Sigma_j r_{p,j} N_{p,j} Z_p(r_{p,j}) \quad , \tag{2}$$

where the first term sums over a cavity distribution with i size classes, r is the concentration of subgrain boundaries, j is the number of precipitate types with average size r_p and concentration N_p, and Z^b and Z^p are the capture efficiencies of subgrain boundaries and precipitates, respectively, for vacancies or interstitials. Using the simple form of Eq. (1), our steels irradiated in FFTF have Q > 40 so that they appear to be dislocation sink dominated. The values of Z^d and Z^c are assumed to be = 1 and values for the other parameters in Eq. (1) are obtained from the experimental data. The undoped steels irradiated in HFIR have Q ~ 0.2, while the Ni-doped steels have Q ~ 0.4, including the contribution of the bimodal cavity distribution. Clearly the HFIK irradiated specimens are closer to a balanced situation than the FFTF irradiated steels. and yet do not appear to have a sink structure totally dominated by cavities as do many cold-worked austenitic stainless steels irradiated in HFIR. The calculated Q values for the HFIR irradiated steels could be either closer or further from a balanced sink situation, depending on how the precipitates and subgrain boundaries compete with other sinks for point defects. The finer subgrain boundary structure may be a factor in reducing void formation and growth in the 12Cr-1MoVW-2Ni irradiated in HFIR.

Considering the bias, theoretical work suggests that the bias (B) in the ferritic steels can range from 0.05 to 0.4 (ref. 40). The normal B for austenitic steels is 0.15 to 0.2 (ref. 32). We cannot really estimate bias simply from void formation without knowing growth rates. However, it seems that enough bias exists for substantial void growth in these ferritic steels. From the various mechanisms that contribute to a low bias in ferritic steels, solute effects and dislocation nature effects appear constant in our comparison of FFTF and HFIR irradiation for each steel, and appear small among the various steels in either reactor. Helium generation itself could counter the low intrinsic bias suggested in mechanism (a) if helium trapped in vacancies hinders recombination with interstitials as suggested for austenitic steels.[6,20] Helium vacancy complexes may also be more mobile in the ferritc steels if the vacancy self-diffusion rate is higher. Increased helium accumulation at various sinks, governed by $D_v C_v$ (vacancy diffusivity times vacancy concentration) in the ferritic steels, could also alter defect capture efficiencies. Apart from defect-partitioning effects, subgrain boundaries and precipitates could also affect the bias as well. Fine precipitates could contribute to an increase in the bias if they preferentially attract interstitials on the basis of their volumetric misfit (undersized misfit would attract interstitials). Fine precipitates do not appear to contribute very much to void swelling resistance from this work, because void formation in HFIR often coincides with their formation. Previous data at 500°C actually show that fine M_6C develops cooperatively with voids in HFIR-irradiated 12Cr-1MoVW (ref. 10).

Finally, what do these results mean for the use of ferritic steels for fusion applications? While swelling in these 9 Cr and 12 Cr steels is not high and may not increase greatly at higher doses, several factors could still contribute to higher eventual void swelling rates during fusion irradiation than found during FBR irradiation. The voids in the steels with the fusion levels of helium could continue to grow, while new voids still form. These processes could then reduce the number of fine bubbles to lower r_c and achieve more balanced defect partitioning. which would further increase swelling. Odette[32] showed that an increase in bias and in the ultimate void density (a normal helium effect in austenitic stainless steels) could result in the ferritic steels swelling in a manner similar to 20% cold-worked type 316 stainless steel. If voids develop on coarse precipitates, swelling could be enhanced still further. Higher fluence experiments are necessary, but until then, the possibility of helium enhanced void swelling remains a legitimate concern for fusion.

CONCLUSIONS

1. By comparing nickel-doped and undoped 9Cr-1MoVNb and 12Cr-1MoVW steels irradiated in FFTF (47 dpa, ~5 appm He) and HFIR (~37 dpa, 400-430 appm He), it was found that increases in He:dpa ratio cause significant increases in the formation of large (7-30 nm diam), bias-driven voids at 400 to 410°C. Only the nickel-doped steels irradiated in HFIR with 400 appm He or more had visible helium bubbles, which were very fine (2-5 nm diam) and abundant (1 to 4 × 10^{22} m^{-3}).

2. Irradiation in both reactors produced a spatially uniform network of tangled dislocations and some larger loops, with A being 0.6 to 4 × 10^{14} m^{-2}. Irradiation produced a structure that was different than the initial as-tempered, spatially non-uniform structure in which A varied from <10^{11} to 7 × 10^{13} m^{-2}. Irradiation significantly increased A only in the 12Cr-1MoVW steel for which A was initially very low (<10^{11} m^{-2}). Irradiation at 400 to 410°C produced almost complete recovery of the as-tempered lath subgrain boundary structure in the 9Cr-1MoVNb and 9Cr-1MoVNb-2Ni steels. Such boundaries remained stable in similarly irradiated 12Cr-1MoVW and 12Cr-1MoVW-2Ni steels.

3. Irradiation produced some significant changes in the precipitate structure on all of the steels irradiated at 400 to 410°C in both reactors. There was dissolution of many of the coarse, as-tempered $M_{23}C_6$ particles during irradiation of both 9 Cr steels, whereas similar particles were relatively more stable in the 12 Cr steels. Irradiation produced an abundant dispersion of new coarse $M_{23}C_6$ particles only in the 9Cr-1MoVNb-2Ni steel. Finer MC precipitate particles, present in all the steels, experienced some coarsening and compositional changes (Cr enrichments and V depletions) during irradiation. Irradiation produced abundant dispersions of fine M_6C (TI) in all the steels except 9Cr-1MoVNb. These particles were Si, Cr and Ni rich in the nickel-doped steels, but had an odd composition with only Si and Cr in the 12Cr-1MoVW steel. Some coarse M_6C (TI) (Si, Cr and Ni rich) was found to replace coarse as-tempered $M_{23}C_6$ during irradiation in both nickel-doped 9 Cr and 12 Cr steels.

4. Although irradiation at 400 to 410°C had considerable effects on both the dislocation and subgrain boundary and the precipitate components of the microstructure in all the steels, these changes were nearly the same comparing irradiation in FFTF and HFIR for each heat of steel.

5. Interpretation of our data within the framework of existing rate theory and modeling indicates that there is a sufficient bias for void growth in ferritic/martensitic steels irradiated at about 400°C if there is enough helium for voids to nucleate. Our data indicates that the critical size and critical gas content for the conversion of stable gas clusters or bubbles (r_c and n_g^*, respectively) to voids are quite small (r_c 0.75 nm) in the 9Cr-1MoVNb and 12Cr-1MoVW steels irradiated in both reactors, because more helium causes more voids without producing resolvable bubbles. The higher helium content of the nickel-doped steels irradiated in HFIR produces many resolvable, but subcritical, helium bubbles, which increases r_c to 2.5 to 3 nm; however, voids still form and grow indicating the presence of some bias. All of the steels irradiated in FFTF appear to have point defect annihilation dominated by the sink strength of the dislocations. By contrast, the increased density of bubbles to act as sinks in the steels irradiated in HFIR appears to cause more balanced defect partitioning. Our data suggest that subgrain boundaries, and possibly precipitate particles, may also be important sinks in the system as well.

6. Our data clearly shows helium enhanced void formation where the low-swelling transient regime could be shortened by as much as 75 to 100 dpa. The levels of cavity swelling observed are small. less than 0.5%. However, microstructural details suggest that void formation is in the early stages of development, and that several mechanisms could easily lead to more void nucleation and growth as dose increases. The possibility of helium enhanced void swelling remains a legitimate concern for fusion that higher fluence experiments need to address.

REFERENCES

1. J. J. Huet et al., Proc. Irradiation Behavior of Metallic Materials for Fast Reactor Core Components, Ajaccio, France (CEA, 1979), p. 5.
2. J. Erler et al., Proc. Irradiation Behavior of Metallic Materials for Fast Reactor Core Components, Ajaccio, France (CEA, 1979), p. 11.
3. O. S. Gelles and L. E. Thomas, Proc. Topical Conference on Ferritic Alloys for Use in Nuclear Energy Technologies, eds. JW. Davis and D.J. Michel (The Metallurgical Society of AIME, 1984), p. 559.
4. D. S. Gelles, J. Nucl. Mater. 122-123 (1984) 207.
5. P. J. Maziasz, J. Nucl. Mater. 122-123 (1984) 472.
6. P. J. Maziasz and C. J. McHargue, International Materials Reviews 32 (1987) 190.
7. J. M. Vitek and R. L. Klueh, Proc. Topical Conference on Ferritic Alloys for Use in Nuclear Energy Technologies, eds. J. W. Davis and D. J. Michel (The Metallurgical Society of AIME, 1984) p. 551.
8. J. M. Vitek and R. L. Klueh, J. Nucl. Mater. 122-123 (1984) 254.
9. O. S. Gelles, ADIP Semiannual Progress Report, March 31, 1985, DOE/ER-0045/14, (Office of Fusion Energy, U.S. Oepartment of Energy, 1985) p. 129.

10. P. J. Maziasz, R. L. Klueh, and J. M. Vitek, J. Nucl. Mater. 141-143 (1986) 929.
11. R. L. Klueh, J. M. Vitek, and M. L. Grossbeck, J. Nucl. Mater. 1038104 (1981) 887.
12. R. L. Klueh, J. M. Vitek, and M. L. Grossbeck. Effects of Radiation on Materials: Eleventh Conference, ASTM STP-782, eds., H. R. Brager and J. S. Perrin, Am. Soc. for Testing and Matls., Philadelphia (1982), p. 648.
13. R. L. Klueh and J. M. Vitek. J. Nucl. Mater. 117 (1983) 295.
14. R. L. Klueh and P. J. Maziasz, "Helium Effects on Neutron-Irradiated Cr-Mo Ferritic Steels: A Review of Recent Results," elsewhere in this report.
15. M. L. Grossbeck, J. W. Woods, and G. A. Potter, ADIP Quarterly Progress Report, Sept. 30, 1980. DOE/ER-0045/4 (Office of Fusion Energy, U.S. Department of Energy, 1981) p. 36.
16. L. R. Greenwood, ADIP Semiannual Progress Report, March 31, 1985, DOE/ER-0045/14 (Office of Fusion Energy, U.S. Department of Energy, 1981), p. 22.
17. N. J. Zaluzec', Introduction to Analytical Electron Microscopy, eds. J. J. Hren, J. I. Goldstein, and D. C. Joy, Plenum Press, New York, NY, 1979, p. 121.
18. P. J. Maziasz and R. L. Klueh. ADIP Semiannual Progress Report, March 31. 1985. DOE/ER-0045/14 (Office of Fusion Energy, U.S. Department of Energy, 1981), p. 74.
19. L.L.S. Horton, A Transmission Electron Microscopy Study of Fusion Environment Radiation Damage in Iron and Iron-Chromium Alloys, Oak Ridge National Laboratory Report, ORNL/TM-8303 (July 1982).
20. P. J. Maziasz, Effects of Helium Content on Microstructural Development in Type 316 Stainless Steel During Neutron Irradiation, Oak Ridge National Laboratory Report, ORNL-6121 (November, 1985).
21. P. J. Maziasz, Materials for Nuclear Reactor Core Applications (Bristol Meeting, Oct. 27-29, 1987), vol. 2, British Nucl. Energy Soc., London (1988), p. 61.
22. D. R. Harries, Proc. Topcial Conference on Ferritic Alloys for Use in Nuclear Energy Technologies, eds. J. W. Davis and D. J. Michel (The Metallurgical Society of AIME, 1984), p. 141.
23. D. S. Gelles, J. Nucl. Mater. 148 (1987) 136.
24. K. Q. Bagley et al., Materials for Nuclear Reactor Core Applications (Bristol Meeting, Oct. 27-29, 1987), vol. 2, British Nucl. Energy Soc., London (1988), p. 37.
25. E. A. Little, Materials for Nuclear Reactor Core Applications (Bristol Meeting, Dct. 27-29, 1987), vol. 2, British Nucl. Energy Soc., London (1988), p. 47.
26. G. Ayrault, DAFS Quart. Progr. Rept., February, 1982, DOE/ER-0046/8, vol. 1 (Office of Fusion Energy, U.S. Department of Energy), p. 182.
27. K. Farrell and E. H. Lee, Effects of Irradiation on Materials: Twelfth International Symposium, ASTM STP-870, eds. F. A. Garner and J. S. Perrin. Am. Soc. for Testing and Matls., Philadelphia, PA (1985), p. 383.
28. K. Farrell and E. H. Lee, Radiation-Induced Changes in Microstructure: 13th Symposium (Part I), ASTM STP-955, eds. F. A. Garner, N. H. Packan, and A. S. Kumar, Am. Soc. for Testing and Matls., Philadelphia, PA (1987), p. 498.
29. L. L. Horton and J. Bentley, Proc. Topcial Conference on Ferritic Alloys for Use in Nuclear Energy Technologies, eds. J. W. Davis and D. J. Michel (The Metallurgical Society of AIME, 1984) p. 569.
30. D. S. Gelles, J. Nucl. Mater. 103&104 (1981) 975.
31. L. P. Stoter and E. A. Little, Advances in Physical Metallurgy and Applications of Steels, The Metals Society, London, U.K. (1981) p. 369.
32. G. R. Odette, J. Nucl. Mater. 155-157 (1988) 921.
33. J. J. Sniegowski and W. G. Wolfer, Proc. Topical Conference on Ferritic Alloys for Use in Nuclear Energy Technologies, eds. J. W. Davis and D. J. Michel (The Metallurgical Society of AIME, 1984), p. 579.
34. R. Bullough, H. M. Wood, and E. A. Little, Effects of Radiation on Materials: Tenth Conference, ASTM STP-725. eds. D. Kramer, H. R. Brager and J. S. Perrin. Am. Soc. for Testing and Matls., Philadelphia, PA (1981), p. 593.
35. E. A. Little, R. Rullough, and H. M. Wood, Proceedings of the Royal Society, A372 (1980) 565.
36. E. A. Little, J. Nucl. Mater. 87 (1979) 11.
37. E. A. Little and D. Stow, J. Nucl. Mater. 87 (1979) 25.
38. M. R. Hayns and T. M. Williams, J. Nucl. Mater. 74 (1978) 151.
39. D. S. Gelles, Fusion Reactor Materials Semiannual Progress Report, September 30, 1986, DOE/ER-0313/1, (Office of Fusion Energy, Department of Energy, 1987), p. 150.
40. L. L. Horton and L. K. Mansur, Effects of Irradiation on Materials: Twelfth International Symposium, ASTM STP-870, eds. F. A. Garner and J. S. Perrin, Am. Soc. for Testing and Matls., Philadelphia, PA (1985), p. 344.
41. L. K. Mansur and W. A. Coghlan, J. Nucl. Mater. 119 (1983) 1.
42. R. S. Nelson and D. J. Mazey, Radiation Damage in Reactor Materials, IAEA-SM-120, vol. 2, International Atomic Energy Agency, Vienna, Austria (1969), p. 157
43. E. H. Lee and L. K. Mansur, "Effect of Residual and Injected Oxygen on Swelling in Irradiated Fe-Ni-Cr Alloys - Part II," submitted to Philosophical Magazine, 1988.
44, Chemical analyses on steels melted at ORNL, 1986-1988.
45. P. J. Maziasz and D. N. Rraski, J. Nucl. Mater. 1228123 (1984) 311.

TENSILE PROPERTIES OF 9Cr-1MoVNb AND 12Cr-1MoVW STEELS IRRADIATED TO 23 dpa AT 390 TO 550°C — R. L. Klueh (Oak Ridge National Laboratory)

OBJECTIVE

The goal of this study is to evaluate the tensile properties of irradiated ferritic steels and relate the change in properties to the irradiation damage and precipitation processes that occur during irradiation.

SUMMARY

Normalized-and-tempered 9Cr-1MoVNb and 12Cr-1MoVW steels were irradiated in the Experimental Breeder Reactor II (EBR-II) at 390, 450, 500, and 550°C to displacement damage levels of up to 25 dpa. Tensile tests were made at the irradiation temperatures on three types of specimens: irradiated specimens, normalized-and-tempered specimens, and specimens thermally aged 10,000 h at the irradiation temperatures. Observations from these tests were compared with results on these same materials irradiated in EBR-II at the same temperatures up 13 dpa and thermally aged 5000 h. Results were interpreted in terms of the precipitate and dislocation microstructures developed during heat treatment, thermal aging, and irradiation.

PROGRESS AND STATUS

Introduction

Chromium-molybdenum steels are candidates for the structural components of fusion reactors operating at temperatures up to about 520°C. Steels of interest include 9Cr-1MoVNb, 12Cr-1MoVW, and 2¼Cr-1Mo steels. These ferritic steels are being irradiated in various fission reactors to determine the effect of irradiation on mechanical properties. Tensile specimens of all three of the steels were included in the large AD-2 irradiation experiment conducted by Hanford Engineering Development Laboratory (HEDL).[1] In the first phase of the experiment,[2,3] 9Cr-1MoVNb steel was irradiated to 10 to 12 dpa, and 12Cr-1MoVW steel was irradiated to 13 dpa. The second phase, to be presented in this paper, involved specimens of 9Cr-1MoVNb steel irradiated to ~23 dpa and 12Cr-1MoVW steel irradiated to ~25 dpa. For both phases, irradiation was at 390, 450, 500, and 550°C.

Experimental procedure

The processes used to melt and fabricate the materials and the chemical compositions of the materials have been published.[2,3] Prior to irradiation, the 9Cr-1MoVNb steel specimens were normalized and tempered as follows: 1 h at 1038°C, air cool; 1 h at 760°C, air cool.[2] Two different normalizing-and-tempering treatments were used for the 12Cr-1MoVW steel.[3] The first, referred to as HT1, was 0.08 h at 1038°C. air cool; 0.5 h at 760°C, air cool. The second, referred to as HT2, was 0.5 h at 1038°C, air cool; 2.5 h at 760°C, air cool.

Miniature sheet tensile specimens with a gauge section 20.3 mm long by 1.5 mm wide by 0.76 mm thick were irradiated and tested. The specimen design was in accordance with ASTM Specification E8. All specimens were machined with their gauge lengths perpendicular to the rolling direction of the sheet.'

Specimens were irradiated in capsules designed to maintain temperatures of 390, 450, 500, and 550°C.' Irradiation was in row 4 of EBR-II, and the fluence depended on the level of the specimens in the capsule relative to the reactor core center line. The 9Cr-1MoVNb steel specimens were irradiated at two levels: 4.6 and 5.0 × 10^{26} n/m^2, which produced *22* and 24 dpa, respectively. The HT1 12Cr-1MoVW steel specimens were irradiated at 5.1 and 5.4 × 10^{26} n/m^2, which produced 24.6 and *26* dpa, respectively. The HT2 specimens were all irradiated to 5.1 × 10^{26} n/m^2, approximately 24.4 dpa. For simplicity, the irradiation damage levels for the three materials will be referred to as 23, *25*, and 24 dpa for the 9Cr-1MoVNb, 12Cr-1MoVW HT1, and 12Cr-1MoVW HT2, respectively. The irradiations previously reported[2,3] will be referred to as damage levels of approximately 10, 13, and 9 dpa for the 9Cr-1MoVNb, HT1, and HT2, respectively. The uncertainty in fluence was estimated at ±10%, and the temperature uncertainties were 390 ± 10°C, 450 ± 15°C, 500 ± 20°C, and 550 ± 30°C.[2,3]

After irradiation, tensile tests were conducted at the irradiation temperature. Tests were made in a vacuum chamber on a 44-kN-capacity Instron universal testing machine at a crosshead speed of 8.5 μm/s, which results in a nominal strain rate of 4.2 × 10^{-4}/s. As-heat-treated (normalized-and-tempered) and thermally aged control samples were also tested to separate the effect of irradiation from thermal-aging effects. Thermal aging was conducted at the irradiation temperatures for 10,000 h, the approximate time of the irradiation. Unfortunately, there were only a limited number of specimens available, including

unirradiated control specimens for conducting the thermal aging treatments. As a result, only one test per condition was possible, and in some cases there were not sufficient specimens for each experimental condition.

Results

Microstructure and precipitate extraction — The microstructure of the normalized-and-tempered 9Cr-1MoVNb steel and 12Cr-1MoVW steel — in both heat-treated conditions — was tempered martensite, which consists of a ferrite matrix and carbide precipitates.[2,3] Thermal aging for up to 10,000 h over the range 400 to 550°C Droduced little noticeable change in the optical microstructure over that after 5000 h. The microhardness after 10,000 h at 550°C (the only temperature examined) was higher than after 5000 h at the same temperature.

The precipitates were electrolytically extracted from the normalized-and-tempered specimens and from those aged 5000 and 10000 h. The amount of precipitate extracted is plotted in Fig. 1 as a function of the aging temperature. There was little change in the amount of precipitate extracted from the 9Cr-1MoVNb steel as a result of the thermal aging. The 12Cr-1MoVW steels did show a change. In both heat-treated conditions, there was an increase in the amount of precipitate extracted at the highest aging temperatures. The HT1 steel showed an increase in amount of precipitate extracted at all temperatures after aging for 5000 h. After aging for 10,000 h, an increase was only observed for specimens aged at 500 and 550°C (no specimen was aged at 400°C). The HT2 steel showed increased amounts of precipitate only after aging at 550°C. No extractions were obtained from irradiated specimens.

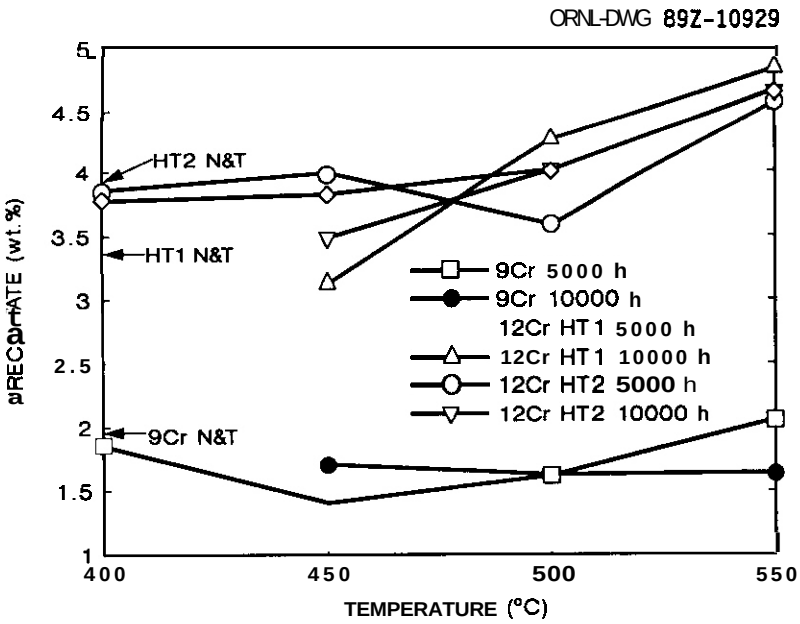

Fig. 1. Weight percent of precipitate extracted from the 9Cr-1MoVNb and 12Cr-1MoVW steels as a function of aging temperature for the normalized and tempered steels and the steels aged for 5,000 and 10,000 h.

An attempt was made to identify the extracted precipitates by x-ray diffraction. Only $M_{23}C_6$ and MC carbides were positively identified; these are the precipitates that are generally found in these steels in the normalized and-tempered condition.[4] Examination of extraction replicas by transmission electron microscopy (TEM) revealed that an additional precipitate was present in the specimen aged at 550°C. By the use of x-ray energy-dispersive spectroscopy, this precipitate was tentatively identified as Laves phase.

Tensile behavior of 9Cr-1MoVNb steel — Tensile data for the 9Cr-1MoVNb steel are presented in Figs. 2 and 3. In addition to the results obtained during the present study for the specimens irradiated to 23 dpa and those that were aged 10,000 h, the results from the previous tests on normalized-and-tempered specimens, specimens thermally aged for 5000 h, and specimens irradiated to 10 dpa are also shown.'

One noteworthy observation involves the specimens thermally aged for 10,000 h. Although specimens were aged for 10,000 h only at 450 and 550°C. both showed a substantial increase in yield stress (YS) and ultimate tensile strength (UTS) over those in the normalized-and-tempered condition and those aged 5000 h. After aging for 5000 h, there was little change in YS and UTS. The specimens aged 10,000 h were also stronger than specimens irradiated at 450 to 550°C. After irradiation to 23 dpa, there was a slight reduction in YS and UTS at all temperatures from the strength of the specimens irradiated to the lower fluence,[2] while those irradiated to 10 dpa had strengths similar to those of the normalized-and-tempered steel and the specimens aged 5000 h.

For the normalized-and-tempered and the thermally aged specimens, the total elongation (Fig. 3) reflected the strength behavior: an increase in strength due to aging was accompanied by a decrease in elongation. Specimens aged 10,000 h, which were the strongest at the temperatures where they were tested, also had a lower ductility (<3%); it was significantly lower at 550°C. Although the specimens irradiated to 23 dpa had a lower strength than those irradiated to 10 dpa, they had similar or slightly

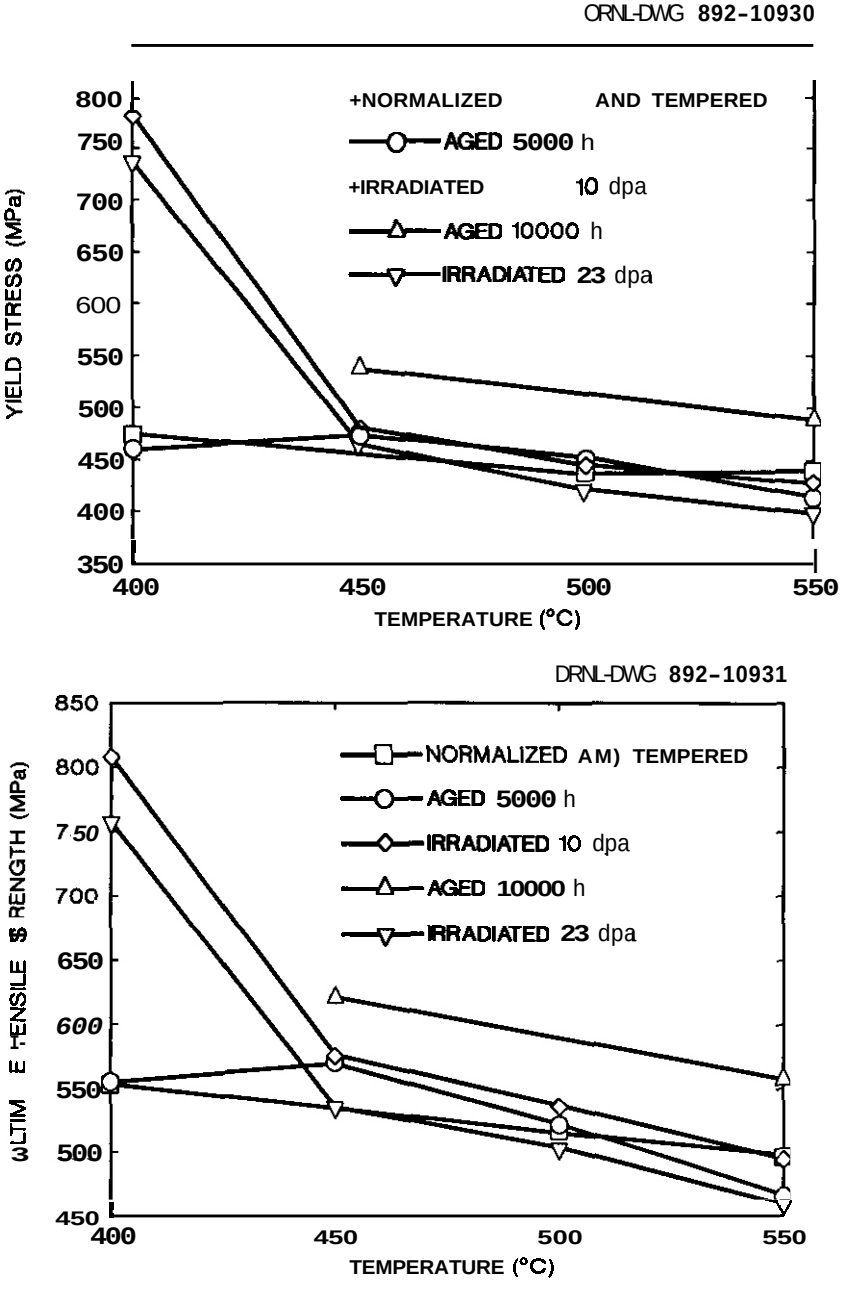

Fig. 2. (a) Yield stress and (b) ultimate tensile strength as a function of irradiation temperature for 9Cr-1MoVNb steel as normalized and tempered, as aged 5,000 and 10,000 h, and as irradiated to 10 and 23 dpa.

lower total elongations at 400, 450, and 500°C. However, at 550°C the total elongation of the specimen irradiated to 10 dpa was substantially greater than that for the specimen irradiated to 23 dpa, even though the latter specimen was weaker. At 400°C, where the irradiated steel hardened, the ductility of the irradiated specimens was less than that of the normalized-and-tempered steel. For irradiation at 500°C, there was little difference in the total elongation of the normalized-and-tempered and irradiated specimens. After irradiation at 550°C, there was also little difference between the total elongation of the normalized-and-tempered steel and the specimen irradiated to 10 dpa, but these two specimens were considerably more ductile than the specimen irradiated to 23 dpa (Fig. 3). Nevertheless, the specimen irradiated to 23 dpa was considerably more ductile than the specimen aged for 10,000 h. Further, the specimen irradiated to 23 dpa still had a total elongation of almost 7%.

Tensile behavior of 12Cr-1MoVW steel – The tensile behavior of the 12Cr-1MoVW steel in both heat-treated conditions was generally similar to the behavior of the 9Cr-1MoVNb steel (Figs. 4 to 7). Again, the specimens aged 10,000 h at 450 to 550°C had the highest YS and UTS at these test temperatures (Figs. 4 and 6). However, the ductility behavior (Figs. 5 and 7) appeared to have considerably more scatter than was the case for the 9Cr-1MoVNb steel.

For the HT1 heat treatment (a short austenitization and tempering treatment) where specimens were irradiated to approximately 25 dpa at all four temperatures, the strengths (Figs. 4) after 25 dpa were only slightly changed from the specimens irradiated to 13 dpa. At 400°C, there was no difference in the YS and the soecimen irradiated to 25 dpa was the weakest at 450, 500 and 550°C [Fig. 4(a)], similar to the observations on the 9Cr1MoVNb steel. The UTS [Fig.4(b)] after 25 dpa was the same as that after 13 dpa at 400°C, less than that after 13 dpa at 450 and 500°C. and slightly greater at 550°C. Note that the YS and UTS of the specimens aged 5000 h at 400 and 450°C were considerably weaker than the respective normalized-and-tempered specimens, but the two strengths were similar at 500 and 550°C.

The specimens irradiated at 390°C displayed the most hardening and also had the lowest ductility (Fig. 5). At the three highest temperatures, good total elongation was obtained for the irradiated specimens. The elongation of the specimens irradiated at 550°C did not show the decrease that was observed for the 9Cr-1MoVNb steel. In fact, at 550°C there was only a small difference between the total elongation of the two irradiated specimens and the normalized-and-tempered specimen. All three of these specimens had considerably more ductility than the aged specimens.

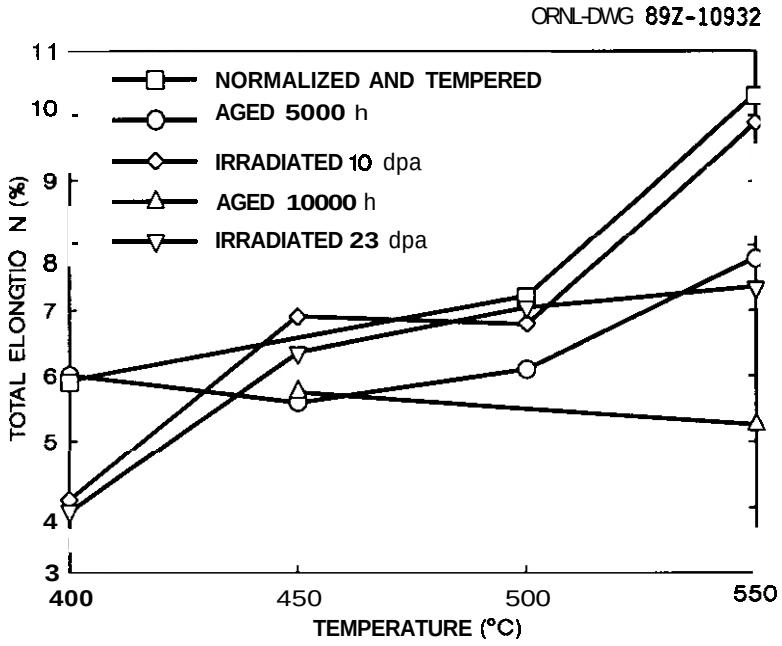

Fig. 3. Total elongation as a function of irradiation temperature for 9Cr-1MoVNb steel as normalized and tempered, as aged 5,000 and 10,000 h, and as irradiated to 10 and 23 dpa.

Fewer specimens with the HT2 heat treatment were available for testing than for HT1 (Figs. 6 and 7). However, the qualitative behavior was similar to that observed for the HT1 material. The only unusual behavior was that the specimen aged 5000 h had the highest total elongation at 550°C, and the total elongation of the two irradiated specimens exceeded that for the normalized-and-tempered steel.

To examine the relative effect of irradiation on the strength of the 12Cr-1MoVW steel with the different heat treatments, Fig. 8 compares the YS behavior of HT1 and HT2 in the normalized-and-tempered and irradiated conditions. Because HT1 was tempered only 20% as long at 760°C as HT2, it had a higher as-tempered strength. Thermal aging for 5000 h at 400°C continued the tempering process for both HT1 and HT2 and lowered the YS below that for the normalized-and-tempered steel (Figs. 4 and 6). After this aging treatment, similar amounts of precipitate were extracted from HT1 and HT2, and the amounts were similar to the amount obtained from HT2 after the 2.5 h tempering treatment at 760°C (Fig. 1).

As a result of these observations. it might be expected that irradiation at 390°C would also continue the tempering process, especially for HT1. Since this is the temperature at which irradiation hardening occurs, it might be expected that irradiation-aided tempering would offset some of the irradiation-induced hardening. This was not the case. Rather, irradiation at 390°C caused about twice as much hardening in HT1 as in HT2 (Fig. 8). The HT1 also remained harder than the HT2 at the higher temperatures, although the differences were smaller.

Discussion

Various studies indicate that precipitate reactions occur in these steels during tempering, aging, and irradiation,[4-11] and these reactions must be related to the observed changes in mechanical properties. A previous study showed that essentially all of the carbon precipitated from solution when the 9Cr-1MoVNb and 12Cr-1MoVW steels were tempered for 1 h or more at 700°C and higher (i.e., tempering for longer times did not cause further precipitation).[4] Precipitates that formed were mainly $M_{23}C_6$ with some MC. The 9Cr-1MoVNb and the HT2 of 12Cr-1MoVW steels were tempered under conditions where carbide precipitation should be complete, and after 5000 h at 400°C, there was little change in the amount of precipitate extracted.

For HT1, on the other hand, more (~15%) precipitate was extracted after 5000 h at 400°C than after the tempering treatment, indicating that the carbide precipitation was not quite complete after tempering for 0.5 h at 760°C. Furthermore, after 5000 h at 400°C, the amount of precipitate extracted from HT1 was similar to that extracted from HT2 after tempering 2.5 h at 760°C and after 5000 h at 400°C. Based on the results of the previous work,' it is concluded that the shorter austenitization time for HT1 (0.08 h at 1050°C) probably had only a minor effect on the amount of precipitate formed. The previous work showed that an 0.08-h austenitization period resulted in a small amount of carbide not dissolving (~0.1 wt %), which should not significantly affect the subsequent precipitation during tempering.'

Although essentially all of the carbon precipitated in the 9Cr-1MoVNb and the HT2 during tempering, further precipitation occurred during the aging, especially after 10,000 h and 550°C (Fig. 1). Most of that precipitate is probably Laves phase (Fe_2Mo).[5-7] Laves phase was identified in the aged steel in the present study and in previous studies on aged 9Cr-2MoVNb,[5] 9Cr-1MoVNb,[7] 12Cr-1MoV (CRM-12), and 12Cr-0.5MoVNb (FV 448).[6] All but the first of these steels are essentially 100% martensitic, as was the case for the 9Cr-1MoVNb and 12Cr-1MoVW steels used in the present work; 9Cr-2MoVNb is a duplex steel with 20 to 25% delta-ferrite and the balance martensite.

Hosoi et al. examined the effect of thermal aging at 500 and 600°C on the impact behavior of normalized-and-tempered 9Cr-2MoVNb steel. They found that the ductile-brittle transition temperature (DBTT) increased and the upper shelf energy decreased on aging at both temperatures, but the effect was greater for a high-silicon (0.67%) heat of the steel than for a low-silicon (< 0.001%) heat. Before

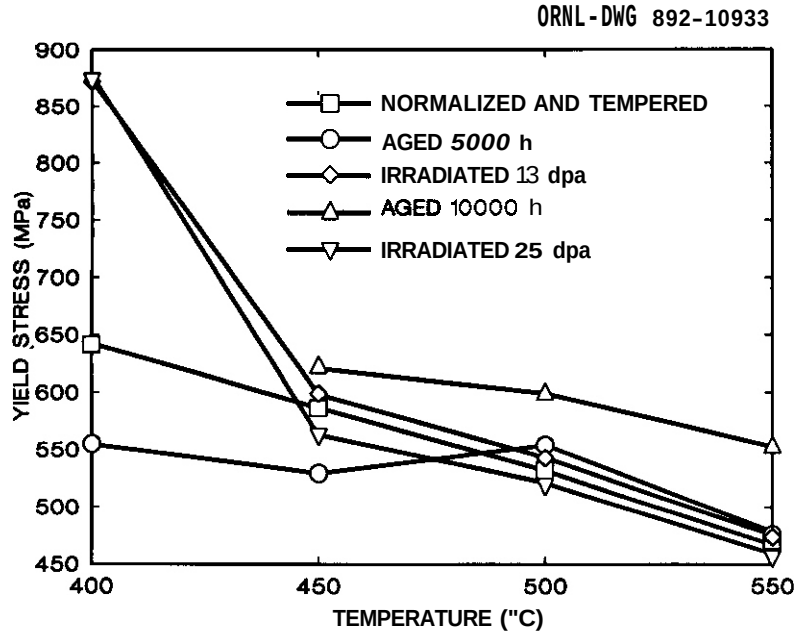

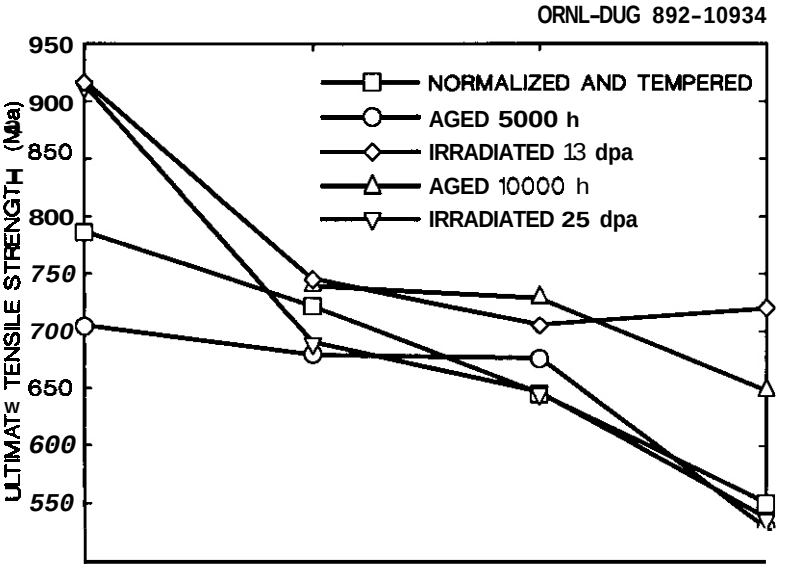

aging, the precipitates present were $M_{23}C_6$ and M_6C (the higher molybdenum content in the steel used by Hosoi et al. evidently leads to the M_6C). After aging for 1000 h, the changes in impact behavior were correlated with the appearance of Laves phase for the high-silicon heat at 500°C and by the total amount of precipitate (Laves + carbides) at 600°C.

Maziasz and Sikka' examined two heats of normalized-and-tempered 9Cr-1MoVNb steel after aging for 10,000 and 25,000 h at 482, 538, 593, 650, and 704°C. One heat of steel contained 0.11% Si and the second contained 0.4% Si. In the as-tempered condition, the steels contained $M_{23}C_6$ and MC. After aging at 482, 538, and 593°C, the amount of bulk precipitate extracted went through a maximum at 538°C. Considerably more precipitate formed in the high-silicon heat than in the low-silicon heat. At 650°C. there was little difference in the amount of precipitate before and after aging, and similar amounts of precipitate were extracted after aging for 10,000 and 25,000 h. However, at 538°C, more precipitate was extracted after 25,000 h, indicating that equilibrium had not been reached in 10,000 h.[7]

TEM examination indicated that the precipitate that formed during aging at temperatures below 650°C was Laves phase.[7] The Laves phase appeared to be superimposed on the $M_{23}C_6$ and MC in the as-tempered structure, which appeared to remain stable at 482, 538, and 593°C. The formation of the Laves phase at 538 and 593°C was accompanied by an increase in the dislocation density. At 650 and 704°C, the dislocation density decreased, and at 704°C. $M_{23}C_6$ and MC present in the tempered structure coarsened.[7]

In normalized-and-temoered 12Cr-1MoV and 12Cr-0.5MoVNb steels examined by Little

After irradiation to 30 dpa, Little and Stoter[6] found some Laves phase in the 12Cr-1MoV irradiated at 615°C, but not in the 12Cr-0.5MoVNb, even though it was found in both of these steels when aged at 600°C. The Laves formed after irradiation was chromium enriched and molybdenum depleted relative to that formed during aging.[6] No Laves phase was found after irradiation at 420 and 460°C.[6] New phases that were introduced in significant quantities by irradiation included M_6C, chi phase, and sigma phase. Considerable M_6C formed by irradiation at 420 and 460°C, but lesser amounts at 615°C. There were some minor variations in the distributions of phases that had been present in the as-tempered condition.

Microstructural studies of the TEM specimens of 9Cr-1MoVNb and 12Cr-1MoVW steels as normalized and tempered and after irradiation to ~11 dpa in the AD-2 experiment, from which the specimens of this study were obtained, were carried out by Peterson[8] and Gelles and Thomas[9] of HEDL. In the as-heat-treated condition, both HT1 and HT2 had similar carbide distributions:' "heavy $M_{23}C_6$ precipitation on prior-austenite grain boundaries and martensite lath boundaries." No difference in amounts could be detected. The substructure in the tempered martensite of HT2 appeared more refined than that in HT1 due to greater

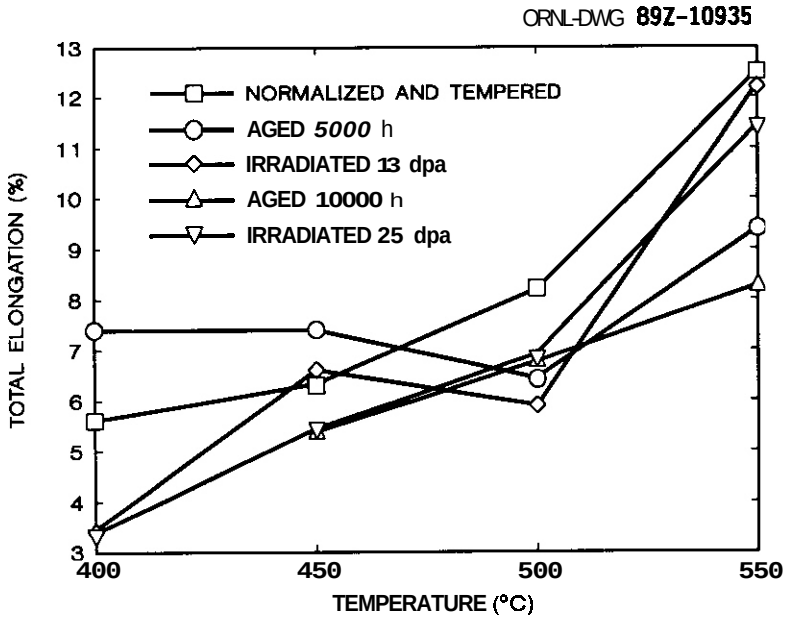

Fig. 5. Total elongation as a function of irradiation temperature for 12Cr-1MoVW steel as normalized and tempered, as aged 5,000 and 10,000 h, and as irradiated to 13 and 25 dpa.

recovery. Because of the shorter tempering time, the HT1 still contained a higher density of lattice dislocations that had formed during the martensite transformation.[8]

Only HT1 was examined by TEM after irradiation.[9] After irradiation at 390°C, the microstructure contained large amounts of irradiation-induced loops and tangles along with a high density of equiaxed matrix precipitates on the order of 8 nm in diameter, which were tentatively identified as G-phase.[9]

Irradiation at 450°C produced few irradiation-induced dislocations or extensive precipitation of the type developed at 390°C.[9] Microstructures of specimens irradiated at 500 and 550°C suggested that the $M_{23}C_6$ on prior-austenite grain boundaries had coarsened and that some additional $M_{23}C_6$ had formed within subgrains; the subgrain tilt boundaries at 550°C were extremely well developed due to recovery. It was concluded that the change in precipitate distribution would not be expected to significantly alter bulk properties.[9]

Gelles and Thomas[10] also investigated the microstructures of the steels used in this experiment after irradiation to 50 to 75 dpa and found similar precipitation effects to those described after 11 dpa. In 12Cr-1MoVW steel irradiated to ~15 dpa in EBR-II at 400 and 425°C, G-phase and a prime were identified. At 455, 480, and 540°C. chi phase was observed to have formed.[10] The as-tempered microstructure (lath subgrain boundaries and $M_{23}C_6$ precipitates) was found to be stable, with the additional phases being superimposed upon that structure.[10] They also examined several commercial Cr-Mo steels after irradiation to high doses. Some Laves phase was found in a 9Cr-2MoVNb steel (EM-12) irradiated at 650°C to ~25 dpa in the EBR-II reactor. However, none was found after irradiation at 425 and 510°C.

No Laves phase was found by Maziasz, Klueh, and Vitek,[11] who examined 9Cr-1MoVNb and 12Cr-1MoVW steels by TEM after irradiation in HFIR to 39 dpa at 300 to 600°C. For 9Cr-1MoVNb, no new phases, in addition to the $M_{23}C_6$ and MC present before irradiation, were identified. Some dissolution of the existing phases was observed, along with considerable coarsening of the subgrain structure.[9] The 12Cr-1MoVW steel appeared stable after irradiation at 300, 400, and 600°C. At 500°C, there was considerable coarsening of the subgrain and precipitate structure and the replacement of some of the $M_{23}C_6$ by irradiation-produced M_6C (ref. 9).

To summarize the TEM observations, Laves phase forms when these Cr-Mo steels are thermally aged at the upper end of the temperature range used in this study. However, when irradiated, microstructural changes occur and new precipitates form, but the involvement of Laves phase is not established below ~600°C.

The 9Cr-1MoVNb and HT1 and HT2 showed a definite strength increase when aged 10,000 h at 450 to 550°C. This strength increase was accompanied by a decrease in the total elongation, especially after aging at 550°C. After aging at the lower temperatures, there was much less difference in the elongation of the respective steels aged 10,000 h and the unaged steels and those aged 5000 h. Based on previous work[5-11] and the TEM observations of this study, the change in tensile properties after thermal aging for 10,000 h is attributed to Laves phase formation. Both steels contain a moderate amount of silicon (~0.2%)[2,3] which should enhance Laves-phase formation.[5-7]

In general, irradiation to 23 to 25 dpa produced only a small change in strength compared with that which occurred for 9 to 13 dpa (refs. 2,3). For most cases, the strength of the steels irradiated to 23 to 25 dpa was slightly less than that for the steel irradiated to 9 to 13 dpa. Irradiation at 400°C hardens the steels relative to the normalized-and-tempered and aged steels. In the previous work,[2,3] it was concluded that hardening is caused by the formation of irradiation-induced dislocation loops and precipitate~.~- "From the present work, where little change in hardening occurred between 9 and 23 dpa for 9Cr-1MoVNb and 13 and 25 dpa for HT1, it appears that hardening probably saturates by ~10 dpa.

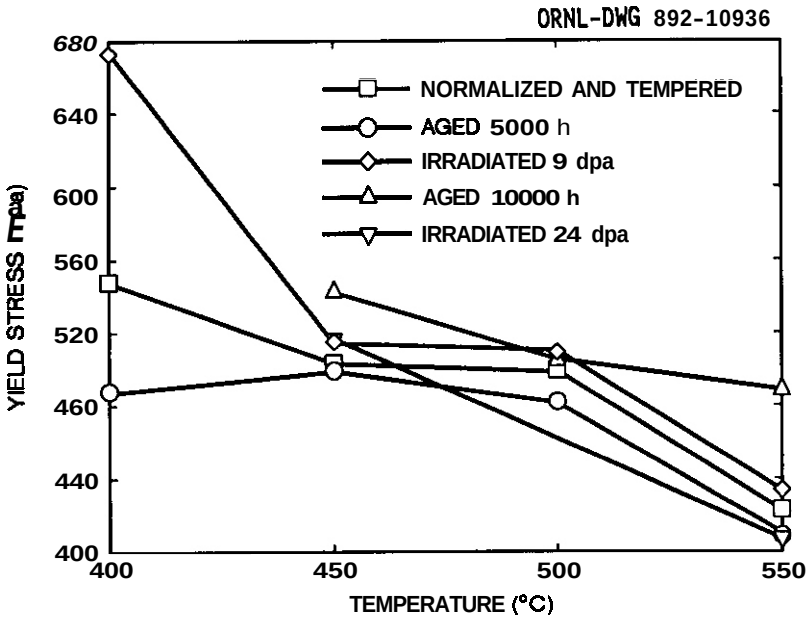

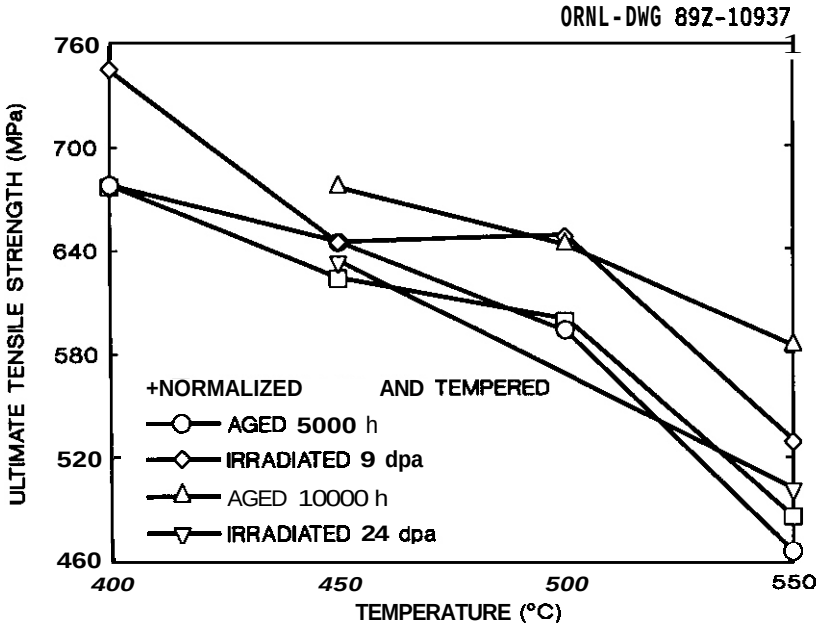

Fig. 6. (a) Yield stress and (b) ultimate tensile strength as a function of irradiation temperature for 12Cr-1MoVW steel HT2 as normalized and tempered, as aged 5,000 and 10,000 h, and as irradiated to 9 and 24 dpa.

Although there was considerable scatter for the respective steels between 450 and 550°C, there was no large difference between the irradiated steel, the normalized-and-tempered steel, and the steel aged for 5000 h (Figs. 2, 4, and 6). For this temperature range, there was a softening of the irradiated steels relative to the steel aged for 10,000 h. This observation of the difference in strength of irradiated steels and steels aged for 10,000 h agrees with the observation that much less Laves phase forms during irradiation[6,7,9-11] than during aging.[5-7] Note, however, that for all three steels at 550°C, the total elongation of the steel irradiated to the higher fluence is less than that irradiated to the lower fluence, despite the fact that the steel irradiated to the higher fluence was usually the weakest. Whether this means that an embrittling phase is beginning to form can only be determined by further experiments.

In the previous paper, we discussed the decrease in strength of the 12Cr-1MoVW steel aged at 400 and 450°C and attributed it to interaction solid-solution hardening.[3] We will not discuss it here.

The original objective for using two heat treatments was to determine the effect of prior-austenite grain size on the irradiated tensile properties.[3] A grain size difference was obtained (ASTM Nos. 7 and 5 for HT1 and HT2, respectively) with the two different austenitization times (0.08 and 0.5 h).[3] However, because different tempering times at 760°C were also used (0.5 and 2.5 h), somewhat different substructures and dislocation densities formed.[8] In addition, the HT1 and HT2 specimens were exposed to different irradiation fluxes. Thus. the strenath differences before and after irradiation cannot be attributed solely to grain size, although the grain size difference should contribute to the strength difference.

The differences in the effect of irradiation on the hardening of HT1 and HT2 at 390°C (Fig. 8) appear to be unusual (note that no HT2 specimen was irradiated to 24 dpa). Since HT1 was not tempered to the extent of HT2, irradiation-aided tempering was expected to offset some of the irradiation-induced hardening, and since more tempering was possible in the HT1, this steel might not be expected to harden as much as HT2. In the absence of tempering, the two steels might have been expected to harden by similar amounts. In fact, HT1 after 13 dpa hardened over 1.5 times the amount of change observed for HT2 in 9 dpa (in accordance with the discussion above, we assume hardening has saturated in both steels, and the different fluxes for the two steels does not matter).

A possible explanation for this observation is that since precipitation in HT1 occurs from a different starting point (the steel is under tempered), the hardening caused by the irradiation could be quite different. Irradiation embrittlement is of most concern for the impact properties of ferritic steels, because irradiation can lead to large increases in the ductile-brittle transition (OBTT) temperature and a decrease in the upper shelf energy. If the OBTT shift at 390°C is proportional to the amount of hardening, as is generally assumed, then the tempering of these steels prior to service in a fusion reactor could prove to be of considerable importance.

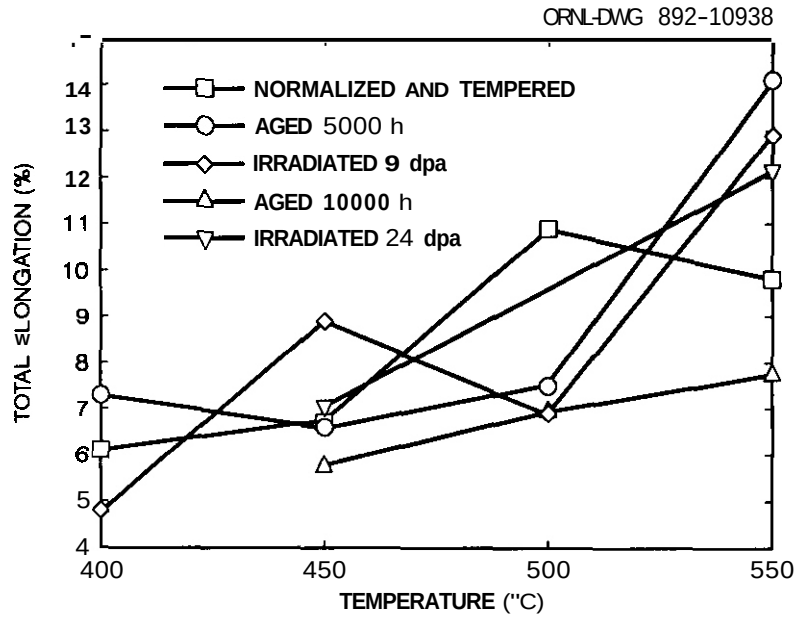

Fig. 7. Total elongation as a function of irradiation temperature for 12Cr-1MoVW steel, HT2, as normalized and tempered, as aged for 5,000 and 10,000 h, and as irradiated to 9 and 24 dpa.

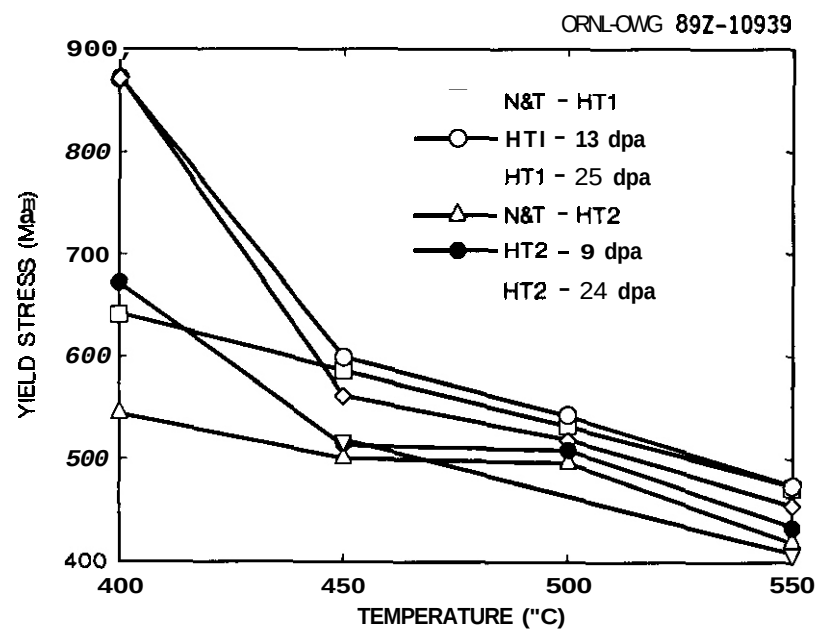

Fig. 8. A comparison of the yield stress behavior of the 12Cr-1MoVW steel given the two different heat treatments (HT1 and HT2) after irradiation and after normalizing and tempering.

SUMMARY AND CONCLUSIONS

Tensile specimens of normalized-and-tempered 9Cr-1MoVNb steel and normalized-and-tempered 12Cr-1MoVW steel with two different tempering treatments (HT1 and HT2) were irradiated in EBR-II to produce a displacement damage level of 23 to 25 dpa. Irradiation was at 390, 450, 500, and 550°C, and specimens were tested at the irradiation temperatures (the specimens irradiated at 390°C were tested at 400°C). Specimens aged to 10,000 h — the approximate time in the reactor — werealso tested. Results were compared with results previously obtained for the steels thermally aged to 5000 h and for 9Cr-1MoVNb irradiated to 10 dpa and the 12Cr-1MoVW irradiated to 13 (HT1) and 9 (HT2) dpa. Observations and conclusions can be summarized as follows:

1. Thermal aging for 10,000 h at 450 to 550°C caused an increase in strength and a decrease in total elongation relative to the normalized-and-tempered specimen. This change is probably related to the formation of Laves phase. Little change was observed after aging for 5000 h.

2. Irradiation to 23 to 25 dpa caused an increase in strength at 390°C relative to aged and unaged material; there was little change relative to the steels irradiated to 9 to 13 dpa. This hardening was accompanied by a loss in ductility. Hardening was attributed to radiation-induced damage structures and precipitation.

3. Irradiation caused a decrease in strength at 450, 500, and 550°C relative to thermally aged specimens. There was little difference between the two different irradiation levels. The greatest loss of ductility occurred for the specimens aged 10,000 h at 550°C. This embrittlement was attributed to Laves phase formation during aging. Indications are that Laves phase does not have the embrlttling role in tensile tests after irradiation that it does on specimens thermally aged at the same temperature.

REFERENCES

1. R. J. Puigh and N. F. Panayotou, US Oepartment of Energy Report DOE/ER-0045/3 (Office of Fusion Energy, Washington, DC, 1980), p. 260.

2. R. L. Klueh and J. M. Vitek, J. Nucl. Mater. 132 (1985) 27.

3. R. L. Klueh and J. M. Vitek, J. Nucl. Mater. 137 (1985) 44.

4. J. M. Vitek and R. L. Klueh, Met. Trans. A 14A (1983) 1047.

5. Y. Hosoi, N. Wade, S. Kunimitsu, and T. Urita, J. Nucl. Mater. 141-143 (1986) 461.

6. E. A. Little and L. P. Stoter, Effects of Radiation on Materials: Proceedings of Eleventh International Symposium, ASTM STP 782, Eds. H. R. Brager and J. S. Perrin (American Society for Testing and Materials, Philadelphia, 1982), pp. 207.

7. P. J. Maziasz and V. K. Sikka, US Oepartment of Energy Report DOE/ER-0045/15 (Office of Fusion Energy, Washington, DC, 1985), p. 102.

8. D. T. Petersen, US Department of Energy Report DOE/ER-0045/5 (Office of Fusion Energy, Washington, DC, 1980), p. 212.

9. D. S. Gelles and L. E. Thomas, US Department of Energy Report DOE/ER-0045/8 (Office of Fusion Energy, Washington, OC, 1982), p. 343.

10. 0. S. Gelles and L. E. Thomas, Ferritic Alloys for use in Nuclear Energy Technologies, Eds. J. W. Davis and 0. J. Michel (The Metallurgical Society of AIME, Warrendale, Pennsylvania, 1984), pp. 559.

11. P. J. Maziasz, R. L. Klueh, and J. M. Vitek, J. Nucl. Mater. 141-143 (1986) 929.

IMPACT BEHAVIOR OF 9Cr-1MoVNb AND 12Cr-1MoVW STEELS IRRADIATED IN HFIR — R. L. Klueh and O. J. Alexander (Oak Ridge National Laboratory)

OBJECTIVE

The goal of this study is to evaluate the impact behavior of irradiated ferritic steels and relate the change in properties to the irradiation damage.

SUMMARY

Impact specimens of 9Cr-1MoVNb and 12Cr-1MoVW steels were irradiated in the High Flux Isotope Reactor (HFIR) at 300 and 400°C to as high as 42 dpa. Irradiation caused large increases in the ductile-brittle transition temperature (DBTT) of both steels, with the increase being greater at 400°C than at 300°C. At 400°C, shifts in DBTT of 204 and 242°C were observed for the 9Cr-1MoVNb and 12Cr-1MoVW steels, respectively. These are the largest shifts ever observed for these steels and are attributed to the higher helium concentration generated during irradiation in HFIR.

PROGRESS AND STATUS

Introduction

A major concern with the ferritic steels for fusion reactor applications involves the effect of irradiation on the impact properties. Irradiation can cause large increases in the ductile-brittle transition temperature (DBTT) and decreases in the upper-shelf energy (USE). Even if the DBTT is below room temperature before irradiation, it can be well above room temperature after irradiation.[1-7]

Neutron irradiation of 12Cr-1MoVW steel in the Experimental Breeder Reactor II (EBR-II) and the High Flux Isotope Reactor (HFIR) up to 6×10^{26} n/m^2 at 50 to 550°C has indicated that the shift in DBTT (ADBTT), as measured by Charpy impact tests, can vary, depending on irradiation conditions. In many cases shifts of over 100°C have been observed,[1-8] and in some instances they approach 200°C.[5] There is some indication that the shift in DBTT saturates after irradiation to ~13 dpa in EBR-II.[3] A maximum in the ADBTT with irradiation temperature was found to occur for 12Cr-1MoVW steel at ~400°C.[5] Below the maximum, there was a fairly large shift, and above 400°C the magnitude of the shift decreased rapidly to quite low values.[4] No such maximum was observed for irradiated 9Cr-1MoVNb steel,[7] although less data were available for this steel. Instead, the limited data for the 9Cr-1MoVNb steel indicated that the ADBTT decreased slowly between 50 and 400°C, after which it decreased rapidly to a low value.[7]

A steel in a fusion reactor first wall will experience displacement damage from the high-energy neutrons from the fusion reaction. In addition, large amounts of transmutation helium will form in the material. To study the effect of simultaneously produced displacement damage and transmutation helium, nickel has been added to the 9Cr-1MoVNb and 12Cr-1MoVW steels.[9] When these nickel-doped steels are irradiated in a mixed-spectrum reactor, such as HFIR, displacement damage is produced by the fast neutrons in the spectrum, and helium is produced by a two-step transmutation reaction of ^{58}Ni with the thermal neutrons in the spectrum. This technique has been used to examine the effect of helium on the tensile properties,[9,10] and a previous paper considered the effect of helium on the impact properties after irradiation at ~50°C.[7] Although nickel-doped steels will not be discussed in this report, helium is also produced in the standard 9Cr-1MoVNb and 12Cr-1MoVW steels when irradiated in HFIR, because of the nickel present in the compositions of these steels.

In this report, impact properties of 9Cr-1MoVNb and 12Cr-1MoVW steels irradiated in HFIR at 300 and 400°C up to 42 dpa will be presented. Such high-fluence data in the vicinity of the observed peak for 12Cr-1MoVW steel should allow a better comparison of the effect of irradiation on the two steels.

Experimental Procedure

Charpy impact specimens were obtained from 25-kg electroslag-remelted heats of standard 9Cr-1MoVNb (heat XA 3590) and standard 12Cr-1MoVW (heat XAA 3587) steel prepared by Combustion Engineering, Inc., Chattanooga, Tennessee. The chemical composition of these steels is given in Table 1.

Specimens were obtained from hot-rolled plate in the normalized-and-tempered condition. The normalizing treatment for the 9Cr-1MoVNb steel was 0.5 h at 1040°C and for the 12Cr-1MoVW steel was 0.5 h

Element	9Cr-1MoVNb (Heat XAA 3590)			Element	12Cr-1MoVW (Heat XA 3587)		
C	0.09	Ti	0.002	C	0.21	Ti	0.003
Mn	0.36	Co	0.013	Mn	0.50	Mn	0.017
P	0.008	cu	0.03	P	0.011	Cu	0.05
S	0.004	Al	0.013	S	0.004	Al	0.030
Si	0.08	B	<0.001	Si	0.18	B	<0.001
Ni	0.11	W	0.01	Ni	0.43	W	0.54
Cr	8.62	As	<0.001	Cr	11.99	As	<0.001
Mo	0.98	Sn	0.003	Mo	0.93	Sn	0.002
V	0.209	Zr	<0.001	V	0.27	Zr	tO.001
Nb	0.063	N	0.050	Nb	0.018	N	0.020
		O	0.007			O	0.005

microstructures were obtained by such heat treatments. Details on heat treatment and microstructure have been published.[9]

Miniature Charpy V-notch (C_v) specimens were machined from the heat-treated plate in the longitudinal (LT) orientation. The subsize specimens were essentially one-half the standard size. They measured 5 by 5 by 25.4 mm and contained a 0.76-mm-deep 30° V-notch with a 0.05- to 0.08-mm-root radius. Such miniature specimens show impact behavior similar to that found in full-sized C_v specimens.[11,12]

upper-shelf energy (USE), impact energy-temperature curves were generated by fitting the data with a hyperbolic tangent function.

Because of space limitations in the HFIR irradiation capsules, only five specimens were available for each steel. The major objective of these studies was the determination of the shift in DBTT, and the USE often had to be determined based on a limited number of specimens. The DBTT was calculated for the energy corresponding to one-half of the USE and at fixed energy levels of 5.5 and 9.2 J (analogous to the 41 and 68 J often used for full-size Charpy specimens). For this report, the ½-USE value will be used.

Results and Discussion

Charpy impact results are given in Table 2. Also given are the displacement-damage levels and helium concentrations for each set of specimens. Specimens irradiated at 400°C had damage levels of 38 to 42 dpa, while those irradiated at 300°C had levels of 20 to 34 dpa. Helium concentrations were considerably different in the 9Cr-1MoVNb and 12Cr-1MoVW steels, because of the greater nickel content of the 12Cr-1MoVW (0.43% in the 12Cr-1MoVW compared to 0.11% Ni in 9Cr-1MoVNb).

Figures 1 and 2 show the Charpy curves for each steel in the irradiated and unirradiated condition. Values for ADBTT determined using the DBTT determined as ½ USE are shown in Table 2. For both steels, increases in DBTT of over 100°C occurred at 300°C and over 200°C at 400°C.

Corwin, Vitek, and Klueh[6] irradiated half-size specimens of the same heat of 12Cr-1MoVW steel used in this experiment to 12 dpa at 390°C in EBR-II and found a ADBTT of 122°C. Hu and Gelles[3] reported Charpy results for 12Cr-1MoVW steel irradiated at 390°C in EBR-II to 13 and 26 dpa and observed ADBTT changes of 124 and 144°C. respectively, which is similar in magnitude to the change observed by Corwin, Vitek, and Klueh.[6] Smidt et al.[1] irradiated 12Cr-1MoVW steel at a somewhat higher temperature (419°C) to about 6 dpa (ref. 1). They observed a DBTT of ~108°C. As discussed above, the DBTT decreases at irradiation temperatures above about 400°C,[4] so a lower ADBTT might be expected at the higher irradiation temperature.

Table 2. Impact properties of Cr-Mo steels irradiated in HFIR

Conditions			Transition Temperature, °C				
Temperature (°C)	Displacement (dpa)	Helium (appm)	1/2 USE	55 J	9.2 J	ΔDBTT[a] (°C)	USE (J)
			12Cr-1MoVW (Heat XAA 3587)				
Control	0	0	–18	–58	–35		26
300	20–34	51–90	87	86	87	105	15
400	38–42	99–111	224	226	--	242	8
			9Cr-1MoVNb (Heat XA 3590)				
Control	0	0	–29	-49	–37		25
300	20-34	16–27	138	136	138	167	20
400	37-42	30–34	175	114	182	204	12

[a]Calculated from 1/2 USE DBTT.

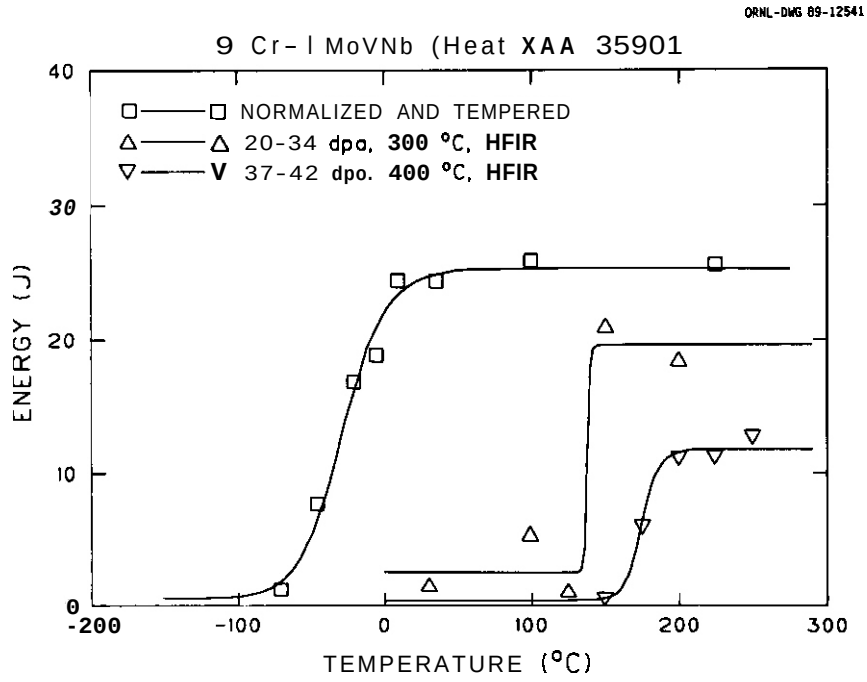

Fig. 1. Charpy impact properties of 9Cr-1MoVNb steel in the unirradiated condition and after irradiation to 20 to 34 dpa (16–27 appm He) at 300°C and to 37 to 42 dpa (30–34 appm He) at 400°C in HFIR.

Hu and Gelles[3] also irradiated 9Cr-1MoVNb to 13 and 26 dpa and found ΔDBTTs of 52 and 54°C, respectively. These results were taken to indicate that a saturation in ADBTT must occur after irradiation to ~13 dpa. Likewise, saturation apparently also occurred for the 12Cr-1MoVW steel, because the difference between 124 and 144°C for 13 and 26 dpa (ref. 3), respectively, is probably within experimental error.

Results from the present studies on the 9Cr-1MoVNb and 12Cr-1MoVW steels irradiated in HFIR at 400°C are significantly different from those obtained when these steels are irradiated at 390°C in EBR-II. The change observed for the 9Cr-1MoVNb after ~40 dpa in the present experiment was 204°C compared to 54°C in EBR-II after 26 dpa. For the 12Cr-1MoVW steel, a 242°C shift was found in HFIR, compared to only 144°C after 26 dpa in EBR-II. Thus, the saturation indicated after irradiation in EBR-II does not apply to specimens irradiated in HFIR. Furthermore, the shift in DBTT is considerably higher when irradiated in HFIR than the saturation values found in the steels irradiated in EBR-II.

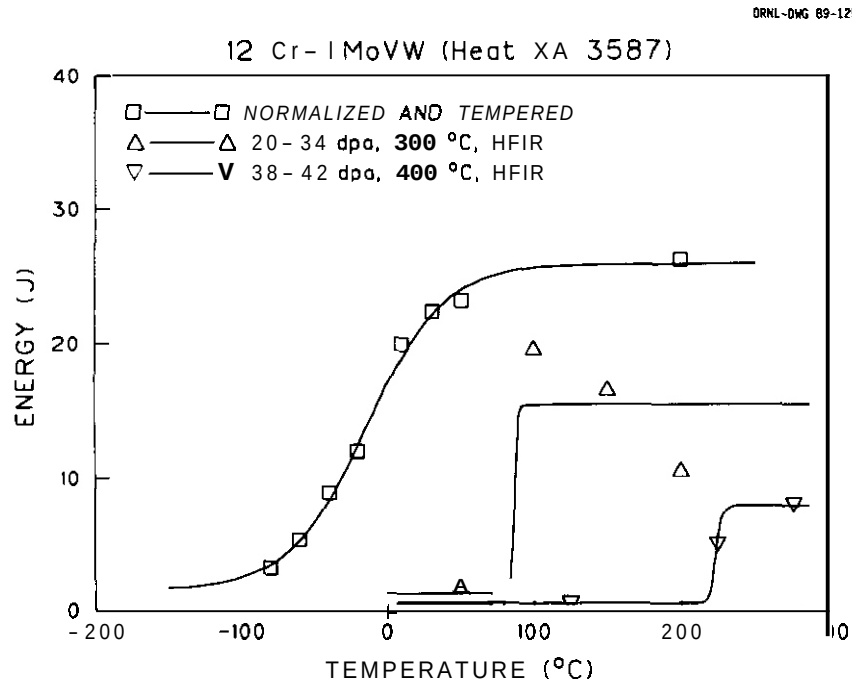

Fig. 2. Charpy impact properties of 12Cr-1MoVW steel in the unirradiated condition and after irradiation to 20 to 34 dpa (51–90 appm He) at 300°C and to 38 to 42 dpa (99–111 appm He) at 400°C in HFIR.

Similar differences were observed between HFIR and EBR-II in the only other Charpy specimens irradiated in HFIR.[5] In that experiment, capsules that contained half-size specimens of a different heat of 12Cr-1MoVW steel (heat 9607-R2) were irradiated to 4 to 9 dpa at 400°C. A ADBTT value of 195°C was obtained.[5] This value was also considerably larger than the 144°C observed in EBR-II. It is also quite a bit lower than the 242°C observed in the present experiment. Therefore, with respect to a saturation in ADBTT in HFIR, none has yet been observed, and irradiations to higher dpa levels are required. The results from the previous experiment led to the conclusion that the difference between HFIR and EBR-II irradiation was caused by the larger amounts of helium generated in HFIR, compared to the insignificant amounts formed in EBR-II.[5] Results from the present experiment give no reason to reject that hypothesis.

According to Table 2, ADBTT was always larger after irradiation at 400°C than at 300°C. This was true for both the 9Cr-1MoVNb and 12Cr-1MoVW steels. Previously, such results for 12Cr-1MoVW steel led to the conclusion that the ADBTT went through a maximum with irradiation temperature around 400°C.[5-7] The earlier work, which included a combination of results from EBR-II and HFIR, gave no indication of such a peak for 9Cr-1MoVNb steel. Prior to the present work, however, data were only available for 9Cr-1MoVNb steel irradiated in HFIR at 50°C and in EBR-II at 390, 450, 500, and 550°C.[9] Based on the present results, a maximum also occurs for 9Cr-1MoVNb steel. Furthermore, the ADBTT at 300°C for the 9Cr-1MoVNb steel is greater than that after irradiation at 50°C, which was also observed for the 12Cr-1MoVW steel.[5,7] It was previously suggested[7] that the subgrain coarsening observed at 400°C in 9Cr-1MoVNb and not in 12Cr-1MoVW[13] retarded a maximum in the 9Cr-1MoVNb steel. That suggestion was obviously incorrect.

One explanation of the maximum is that it is caused by the combination of helium and the irradiation-induced dislocation and precipitate structure that results when the steel is irradiated near 400°C.[13,14] This dislocation and precipitate structure could have a maximum effect near 400°C, because at lower temperatures precipitate reactions are inhibited by unfavorable kinetics and at higher temperatures softening occurs because of precipitate coarsening. Microstructures of both 9Cr-1MoVNb and 12Cr-1MoVW steels irradiated in HFIR to 37 to 39 dpa at 300 to 600°C have been examined.[13] These studies demonstrated the subgrain coarsening in the 9Cr-1MoVNb noted above, but also that irradiation at 300 to 500°C produced a dense dislocation structure. Such a dislocation structure was also noted for the 12Cr-1MoVW steel. Another possible explanation is that the helium Droduced in the HFIR-irradiated steels has an enhanced effect on the impact properties in this temperature range. Helium has been shown to affect tensile properties of 9Cr-1MoVNb and 12Cr-1MoVW steels at 300 and 400°C.

An inconsistency is observed when the data for 12Cr-1MoVW steel specimens previously irradiated in HFIR at 300°C to 4 to 9 dpa (11-25 appm He)[5] are compared to those irradiated in this experiment to 20 to 34 dpa (50-90 appm He). Although different heats of steel were involved, the ADBTT for the steel irradiated to the lower dpa had a higher ADBTT (166°C against 105°C). However, data for both heats displayed considerable scatter in the upper-shelf region. Perhaps this scatter made an accurate determination of the DBTT impossible. The 400°C data appear to be consistent, as discussed above.

If helium is the cause of the large AOBTT for the steel irradiated in HFIR, the shift for the 12Cr-1MoVW and 9Cr-1MoVNb steels would appear incongruous. Although the 9Cr-1MoVNb steel contained considerably less helium than the 12Cr-1MoVW steel, the ADBTT of the 9Cr-1MoVNb after irradiation at 300°C exceeded that for the 12Cr-1MoVW. The AOBTT for the 12Cr-1MoVW exceeded that for 9Cr-1MoVNb after irradiation at 400°C, but the difference (38°C) was quite small, considering that the 12Cr-1MoVW contained about three times as much helium after irradiation at this temperature. It should be noted, however, that this observation on the possible relative effect of helium in these two steels is in agreement with the observation that the amount of swelling was noticeably greater in 9Cr-1MoVNb than 12Cr-1MoVW when irradiated to ~39 dpa in HFIR (0.19% vs. 0.07%).[15,16] Helium was found to enhance swelling in these steels.[15,16] Further, the ADBTT for 9Cr-1MoVNb was also greater than that for 12Cr-1MoVW when the two steels were irradiated at 50°C.[7]

Regardless of whether the effect of helium is accepted to explain the enhanced embrittlement when these steels are irradiated in HFIR, the ADBTT of 204 and 242°C for the 9Cr-1MoVNb and 12Cr-1MoVW steels, respectively, are the largest shifts ever observed for these steels.

CONCLUSIONS

Charpy impact studies were conducted on specimens of 9Cr-1MoVNb and 12Cr-1MoVW steels irradiated at 300 and 400°C in HFIR to displacement-damage levels of up to 42 dpa. Because of the nickel present in the steels, irradiation in HFIR produced up to ~110 appm He in the 12Cr-1MoVW and ~35 appm He in the 9Cr-1MoVNb. For both steels, the AOBTT at 400°C was greater than at 300°C, resulting in a maximum in the ADBTT-temperature relationship at 400°C. The ADBTT observed for 9Cr-1MoVNb and 12Cr-1MoVW steels irradiated at 400°C in HFIR were the largest values ever observed. They were considerably larger than any shift observed after irradiation in a fast reactor, where a saturation of the shift in OBTT of 54°C was observed for 9Cr-1MoVNb and 144°C for 12Cr-1MoVW after 13 dpa. An effect of helium was proposed as a possible explanation for the difference between HFIR and EBR-II irradiation. A larger amount of helium is generated in these specimens when irradiated in HFIR. Irradiation in HFIR to a still-larger displacement-damage level is required to determine if a saturation of AOBTT occurs under test conditions present in HFIR.

REFERENCES

1. F. A. Smidt, Jr., J. R. Hawthorne, and V. Provenzano, in: Effects of Radiation on Materials, STP 725, Eds. D. Kramer, H. R. Braqer, and J. S. Perrin (American Society for Testing and Materials, Philadelphia, 1981), p. 269.
2. W. L. Hu and D. S. Gelles, in: Ferritic Alloys for Use in Nuclear Energy Technologies, J. W. Davis and D. J. Michel, Eds. (Metallurgical Society of AIME, Warrendale, PA, 1984), p. 631.
3. W. L. Hu and D. S. Gelles, in: Influence of Radiation on Material Properties: 13th International Symposium (Part 11), ASTM STP 956, F. A. Garner, C. H. Henager, Jr., and N. Igata, Eds. (American Society for Testing and Materials, Philadelphia, 1987), p. 83.
4. D. S. Gelles, J. Nucl. Mater. 149 (1987) 192.
5. J. M. Vitek, W. R. Corwin, R. L. Klueh, and J. R. Hawthorne, J. Nucl. Mater. 141-143 (1986) 948.
6. W. R. Corwin, J. M. Vitek, and R. L. Klueh, J. Nucl. Mater. 149 (1987) 312.
7. R. L. Klueh, J. M. Vitek, W. R. Corwin. and D. J. Alexander, J. Nucl. Mater. 155-157 (1988) 973.
8. J. R. Hawthorne, J. R. Reed, and J. A. Sprague, in: Effect of Radiation on Materials: Twelfth International Symposium, ASTM STP 870, F. A. Garner and J. S. Perrin, Eds. (American Society for Testing and Materials, Philadelphia, 1985), p. 580.
9. R. L. Klueh, J. M. Vitek, and M. L. Grossbeck, in: Effects of Irradiation on Materials: Eleventh Conference, ASTM STP 782, H. R. Brager and J. S. Perrin, Eds. (American Society for Testing and Materials, Philadelphia, 1982), p. 648.
10. R. L. Klueh and J. M. Vitek, J. Nucl. Mater. 150 (1987) 272.
11. W. R. Corwin, R. L. Klueh, and J. M. Vitek, J. Nucl. Mater. 122 & 123 (1984) 343.
12. W. R. Corwin and A. M. Hougland, in: The Use of Small-Scale Specimens for Testing Irradiated Material, ASTM STP 888, W. R. Corwin and G. E. Lucas, Eds., (American Society for Testing and Materials, Philadelphia, 1986), p. 325.
13. P. J. Maziasz, R. L. Klueh, and J. M. Vitek, J. Nucl. Mater. 141-143 (1986) 929.
14. 0. S. Gelles and L. K. Thomas, in: Ferritic Alloys for Use in Nuclear Energy Technologies, J. W. Oavis and 0. J. Michel, Eds. (Metallurgical Society of AIME, Warrendale, PA, 1984), p. 559.
15. J. M. Vitek and R. L. Klueh, in: Ferritic Alloys for Use in Nuclear Energy Technologies, J. W. Davis and D. J. Michel, Eds. (The Metallurgical Society of AIME, Warrendale, PA, 1984), p. 551.
16. J. M. Vitek and R. L. Klueh, J. Nucl. Mater. 122 & 123 (1987) 272.

THE FRACTURE TOUGHNESS DATA BASE FOR HT9 AND MODIFIED 9Cr-1Mo IRRADIATED IN SEVERAL REACTORS UP TO ~100 DPA

- F. H. Huang, Westinghouse Hanford Company and M. L. Hamilton, Pacific Northwest Laboratory

OBJECTIVE

The purpose of this work was to determine the fracture toughness behavior of HT9 and modified 9Cr-1Mo fer ritic steels after neutron exposure to high doses.

SUMMARY

A summary is presented of the entire fracture toughness database for HT9 and 9Cr-1Mo generated at Hanford. Fracture toughness tests were recently performed on miniature specimens of HT9 and modified 9Cr-1Mo irradiated in FFTF to exposures ranging from 35 to about 100 dpa. At test temperatures ranging from 20 to 430°C values of toughness and tearing modulus at 35 to 100 dpa were no lower than those obtained previously in tests conducted on specimens irradiated in EBR-II, despite differences in orientation between the EBR-II and FFTF specimens.

PROGRESS AND STATUS

Introduction

The ferritic alloys HT9 and modified 9Cr-1Mo are candidates for the fusion first wall and blanket due to their swelling resistance and low thermal expansion. Fracture behavior following irradiation, however, is of concern for these alloys since they are known to embrittle with neutron irradiation, particularly at low temperatures. Conventional compact tension specimens are not feasible for the determination of post-irradiation fracture behavior due to the large amount of irradiation space required and the large associated temperature and neutron gradients. A miniature compact tension specimen was therefore developed and the validity of the data obtained using this specimen was demonstrated.[1-4] A single specimen, electropotential technique was subsequently developed using the miniature specimens.[5-7] Tests have been conducted on several heats of both alloys irradiated in both fast and mixed spectrum reactors. Specimen descriptions are provided in Table 1 for HT9 and in Table 2 for modified 9Cr-1Mo. Each different type of specimen has a separate identification code. Figure 1 provides the geometry of the miniature specimens referred to in Tables 1 and 2. The database is summarized in Tables 3 and 4. The results of the most recent tests, on specimens irradiated in FFTF to between 35 and ~100 dpa, are presented here and compared to data obtained previously.

ExDerimental Procedure

Miniature compact tension specimens of HT9 and modified 9Cr-1Mo were irradiated in MOTA 1B, 1C, 1D and 1E in the FFTF. The specimen descriptions are given in Tables 1 and 2 under code 7 and code 11, respectively. Irradiation temperatures ranged from 411 to 600°C; neutron damage levels ranged from 35 to approximately 100 dpa. Fracture toughness tests were recently performed on these specimens at test temperatures ranging from 33 to 430°C using the single specimen, electropotential technique developed previously.[5-7]

Results

The fracture toughness data obtained recently for HT9 and modified 9Cr-1Mo are listed by specimen code in Tables 3 and 4, respectively. The entire database has been included to facilitate future considerations of the data. A brief discussion of the database followed by a discussion of the current results at 100 dpa is given in the next section.

Discussion

Inspection of Tables 1 and 2 show that data have been generated for a variety of specimen sizes, alloy heats, specimen orientations and heat treatments. The appropriate publication references for each data set are included in Tables 1 and 2. Several specimen sizes were used to validate the use of the miniature specimens and the electropotential technique. Three heats each of HT9 and modified 9Cr-1Mo have been investigated, with heat treatment variations designed to modify grain size or temper TIG welds. The compositions of the various heats are given in Table 5. Orientation differences were designed to force crack propagation either parallel or perpendicular to the rolling direction and delta ferrite stringers known to exist in the material, or to determine the effect of the fusion or heat affected zones (HAZ) on crack propagation. Strain rate variations have also been studied to evaluate the "transition temperature" phenomenon more typically examined using Charpy impact data.

Each parameter variation investigated will be discussed briefly below. Since the publication references for each data set are included in Tables 1 and 2, they are not repeated in the text. All data reported for miniature specimens satisfy the size criterion for the production of valid J_{1c} data.

TABLE 1

Codes Labeling Specimens Used for Fracture Toughness Tests on HT-9

Code	Ref	Heat	TMT[a]	Starting Stock	Orientation[b]	ID Code	B/W[c] (mm)	Use
1a	5,6	91354	A	Bar	C-R	HLxx	2.54/11.94	technique development
	9	91354	A	Bar	C-R	HRxx	2.54/11.94	Instron/MTS comparison
1b	7,8, 10,14, 15,16., 20,21	91354	A	Bar	C-R	T4xx	2.54/11.94	small grain size, size, low temperature, AD-2 irradiation
1c	4	91354	A	Bar	C-R	HDxx	2.54/11.94	size effects
1d	4	91354	A	Bar	C-R	HCxx	2.54/23.88	size effects
1e	4	91354	A	Bar	C-R	HBxx	7.62/23.88	size effects
1f	4	91354	A	Bar	C-R	HAxx	11.94/23.88	size effects
2	7,8, 10,15 16	91354	B	Bar	C-R	T5xx	2.54/11.94	large grain size, AD-2 irradiation
3	8,10, 11,12 15,17, 19	91353	E	Sheet	T-F	T7xx	2.54/11.94	welded unirradiated, AD-2 irradiation
4	8,10, 11,19	91353	E	Sheet	T-H	TAxx	2.54/11.94	weld/HAZ unirradiated, AD-2 irradiation
5	7,14, 20,21	84425	C	Sheet	T-L	Dx	2.54/11.94	low temperature and high/low strain rate, unirradiated
6	13	91353	F	Sheet	T-L	BAxx	2.54/11.94	HFIR irradiation
7	18, new data	9607R2	D	Sheet	T-L	KNxx	2.54/11.94	MOTA irradiation

(a) TMT codes:

A	(Mill annealed1	t	1149°C/1h	t	hot worked	t 740-760°C/1h/AC
B	TMT A	t	1050°C/30m/AC	t	780°C/2.5h/AC	
C	Cold worked	t	1038°C/5m/AC	t	760°C/0. 5h/AC	
D	Cold worked	t	1050°C/30m/AC	t	760°C/2.5h/AC	
E	TMT D	t	weld	+	780°C/1h/AC	
F	Cold worked	+	1038°C/10m/AC	t	760°C/0.5h/AC	

(b) Orientation of normal to crack plane - Orientation of crack propagation: standard terminology except
F = In weld, parallel to fusion line of weld
H = in HAZ, parallel to fusion line of weld.

(c) B/W = Thickness/Width.

TABLE 2

Codes Labeling Specimens Used for Fracture Toughness Tests on Modified 9Cr-1Mo

Code	Ref	Heat	TMT[a]	Starting Stock	Orientation[b]	ID Code	B/W[c] (mm)	Use
8	8	30182	G	Sheet	T-L	T6xx	2.54/11.94	AD-2 irradiation
9	8,11, 19	30182	I	Sheet	T-F	T3xx	2.54/11.94	welded unirradiated
10	13	30176	H	Sheet	T-L	HAxx	2.54/11.94	HFIR irradiation
11	18, new data	30176	H	Sheet	T-L	NPxx	2.54/11.94	MOTA irradiation
12	9,20	XA3364	J	Sheet	T-L	xxE	2.54/11.94	unirradiated

(a) TMT codes:
G Cold worked t 1038°C/60m/AC + 760°C/1h/AC
H Cold.worked + 1038°C/30m/AC + 760°C/0.5h/AC
I TMT G t weld + 780°C/1h/AC
J Cold worked t 1038°C/5m/AC + 760°C/1h/AC

(b) Orientation of normal to crack plane - Orientation of crack propagation: standard terminology except F = In weld, parallel to fusion line of weld

(c) B/W = Thickness/Width

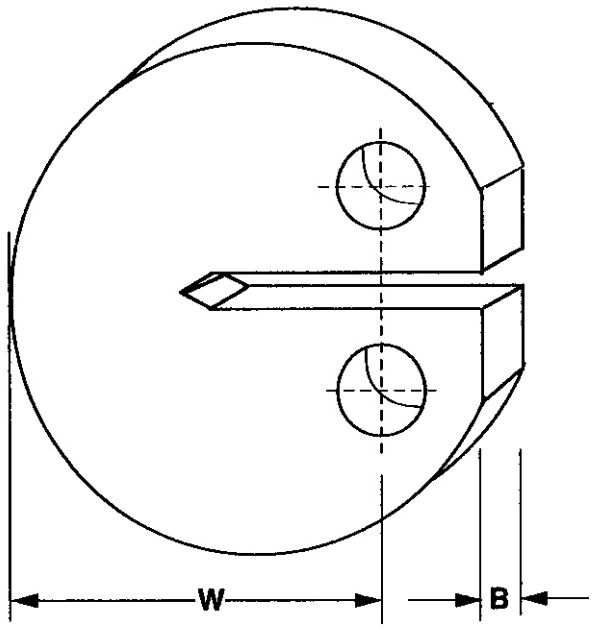

Figure 1. Miniature compact tension specimen geometry (8 and W are specimen thickness and width, respectively, as given in Tables 1 and 2)

TABLE 3

Fracture Toughness Data on HT-9

Code	Test Temp. (°C)	Irr. Temp. (°C)	Nominal Dose (dpa)	Nominal YS (MPa)	Nominal UTS (MPa)	J_{1c} (kJ/m^2)	T	Comments
1a	25	--	--	621	814	100	121	Miniature specimen
	149	--	--	600	766	67	131	test technique
	232	--	--	579	731	59	146	development
	316	--	--	552	690	53	118	
	427	--	--	503	614	72	147	
	539	--	--	407	483	112	130	
1b	-191	--	--	2520	--	2.5	--	High strain rate
	-74	--	--	1113	--	11	--	tests - 1.5E3
	-58	--	--	1064	--	17	--	greater than
	-36	--	--	1011	--	22	--	normal
	-6	--	--	937	--	57	--	
	25	--	--	621	814	97	166	High strain rate test - 1.0E3 greater than normal
	205	390	14	865	928	67	61	AD-2 2nd discharge,
	205	450	14	642	835	61	113	small grain size
	90	390	28	936	995	57	61	
	205	390	28	872	916	69	80	
	450	390	28	509	646	65	81	
	90	500	28	685	880	72	110	
	206	500	28	601	780	72	110	
1c	25	--	--	621	814	100	77	Smallest size - diameter
	232	--	--	579	731	50	103	and thickness
1d	25	--	--	621	814	96	63	Smallest diameter -
	232	--	--	579	731	52	103	thick specimens
1e	25	--	--	621	814	91	83	Medium diameter
	232	--	--	579	731	46	74	thick specimens
1f	25		--	621	814	91	0	Biggest size - diameter and thickness
2	205	390	26	872	916	53	109	AD-2 2nd discharge,
	205	500	26	630	818	64	214	large grain size
	205	500	12	627	813	55	142	
3	93	--	--	656	860	99	86	Unirradiated weld
	205	--	--	609	769	91	94	specimens
	427	--	--	552	674	66	92	
	538	--	--	447	531	62	193	
	93	390	12	962	1022	102	38	Weld specimens
	205	390	12	874	917	99	42	irradiated in AD-2
	316	390	12	820	862	96	45	
	427	390	12	698	887	76	48	
	205	450	14	720	755	80	35	
	205	500	14	673	706	82	32	
	205	550	14	639	671	87	65	
	205	390	26	872	916	58	44	AD-2 2nd discharge
4	93	--	--	656	860	89	105	Unirradiated weld/HAZ
	205	--	--	609	769	89	98	specimens
	427	--	--	552	674	65	106	
	538	--	--	447	531	58	202	

TABLE 3 (contd)

Code	Test Temp. (°C)	Irr. Temp. (°C)	Nominal Dose (dpa)	Nominal YS (MPa)	Nominal UTS (MPa)	J_{1c} (kJ/m²)	1	Comments
5	-192	--	--	1943	--	5	--	Low temperature tests
	-130	--	--	1154	--	15	--	at standard strain
	-74	--	--	962	--	32	--	rate
	-58	--	--	924	--	57	--	
	-42	--	--	894	--	77	--	
	25	--	--	620	814	100	120	
	-74	--	--	1072	--	27	--	Low temperature tests
	-42	--	--	995	--	75	--	at a strain rate 1.5E3 greater than normal
6	25	55	5	992	992	63	--	Specimens irradiated
	93	55	5	954	954	52	33	in HFIR
	205	55	5	898	898	57	28	
7	37	520	15	634	814	107	132	Specimens irradiated
	208	420	12	659	857	95	67	in MOTA 1B
	428	420	12	539	701	62	49	
	204	600	35	524	633	75	131	Specimens irradiated
	204	600	35	524	633	75	131	through MOTA 1C
	33	415	73	705	867	81	53	Specimens irradiated
	400	415	73	425	540	40	74	through MOTA 1D
	33	411	108	723	890	90	55	Specimens irradiated
	204	411	108	643	791	53	70	through MOTA 1E

TABLE 4

Fracture Toughness Data on Modified 9Cr-1Mo

Code	Test Temp. (°C)	Irr. Temp. (°C)	Nominal Dose (dpa)	Nominal YS (MPa)	Nominal UTS (MPa)	J_{1c} (kJ/m²)	T	Comments
12	25	--	--	572	689	87	161	Unirradiated base
	232	--	--	503	621	72	171	metal
	427	--	--	483	538	78	167	
9	93	--	--	594	715	87	133	Unirradiated weld
	205	--	--	543	670	78	107	specimens
	427	--	--	528	588	82	145	
	538	--	--	430	480	66	189	
10	93	55	5	847	847	33	23	Specimens irradiated
	205	55	5	792	792	35	16	in HFIR
	450	55	5	673	673	31	59	
11	41	420	11	700	816	57	66	Specimens irradiated
	427	420	11	473	552	43	83	in MOTA 1B
	202	520	15	531	631	77	81	
	316	520	15	500	594	49	86	
	33	415	70	712	777	52	109	Specimens irradiated
	400	415	70	527	575	47	79	through MOTA 1D
	33	411	105	732	798	56	122	Specimens irradiated
	204	411	105	646	705	71	86	through MOTA 1E

TABLE 5

Compositions of HT-9 and Modified 9Cr-1Mo Compact Tension Specimens

Element	HT-9 91353	HT-9 91354	HT-9 84425	9Cr-1Mo XA3364	9Cr-1Mo 30176	9Cr-1Mo 30182
C	0.21	0.21	0.20	0.10	0.092	0.088
Mn	0.49	0.50	0.58	0.39	0.48	0.31
P	0.008	0.008	0.003	0.008	0.012	0.011
S	0.003	0.003	0.004	0.009	0.004	0.004
Si	0.22	0.21	0.27	0.04	0.15	0.19
Ni	0.57	0.58	0.53	0.05	0.09	0.09
Cr	11.97	12.11	11.87	8.92	8.32	8.47
Mo	1.03	1.03	1.02	1.09	0.86	0.88
V	0.33	0.33	0.30	0.20	0.20	0.21
Nb		--	<0.010	0.07	0.06	0.07
Ti	0.002	0.002	<0.01	0.001	0.001	0.001
Co	0.01	0.01	0.011	0.018	0.017	0.017
Cu	0.074	0.04	0.013	0.03	0.03	0.03
Al	0.023	0.034	0.002	0.005	0.011	0.009
B	0.001	0.0007	0.0010	0.001	<0.001	t0.001
W	0.52	0.53	0.55	t0.01	<0.01	t0.01
As	t0.005	<0.005	t0.005	t0.001	t0.001	t0.001
Sn	--	--	--	t0.001	0.002	0.002
Zr	--	--	--	<0.001	t0.001	t0.001
N	0.004	0.004	0.0017	0.032	0.055	0.054
O	--	--	--	0.013	0.010	0.008
Pb	--	--	--	--	t0.001	<0.001
Sb	--	--	--	--	t0.001	t0.001
Fe	bal.	bal.	bal.	bal.	bal.	bal.

HT9: Size effects. Figure 2 shows the original HT9 data (codes 1a, 1c, 1d, 1e and 1f) used to demonstrate the validity of the single specimen, electropotential technique applied to miniature specimens. While J_{1c} (Figure 2a) appears to be reasonably reproducible and only slightly dependent on specimen size, the tearing modulus (Figure 2b) exhibits much more scatter and is generally higher with decreased specimen thickness. The toughness of HT9 decreases from room temperature up to roughly 300°C, increasing back to the room temperature level by approximately 500°C. This temperature dependence of J_{1c} is not uncommon in ferritic steels.[4]

HT9: Effect of increased strain rate and low temperature. Compact tension tests were performed at low temperatures and high strain rates to quantify the fracture toughness of HT9 in the temperature range where the alloy is known to exhibit a ductile-brittle transition temperature (DBTT) in Charpy impact tests. Two heats of HT9 were tested, one in a "mill annealed" (normalized, hot-worked and then tempered) condition and the C-R orientation (codes 1a, 1b and 1c), the other in a normalized and tempered condition and the T-L orientation (code 5). The data are shown in Figure 3. No tearing modulus data are provided as the specimens in the transition and lower shelf regions failed by fast fracture (i.e., tearing resistance was effectively zero).

It is evident in Figure 3 that the two heats of HT9 exhibited different transition behavior. The DBTT of the code 1 specimens was about -10°C, approximately 50°C above the DBTT of the code 5 specimens. Possible explanations for the difference include strain rate, orientation, composition and TMT. The data at various strain rates at 25, -42 and -74°C on both heats indicate that the fracture toughness of HT9 at low temperatures is relatively insensitive to strain rate. The difference in the behavior of the two heats therefore probably cannot be attributed to differences in strain rate. Likewise, the compositions of the two heats are very similar and this variable can also most likely be eliminated.

The difference in specimen orientation would be expected to cause the opposite of the observed behavior; i.e., the T-L orientation should lead to worse fracture behavior than the C-R orientation since crack propagation is parallel to the delta ferrite stringers in the T-L orientation and perpendicular in the C-R orientation. The only plausible explanation is the fact that the C-R oriented specimens were fabricated from bar stock in an as-forged condition, whereas the T-L oriented specimens were fabricated from cold worked and heat treated sheet stock in which the delta ferrite stringers were significantly broken up during processing. Thus TMT appears to be a more important variable in the fracture toughness of HT9 than strain rate, orientation or heat-to-heat variability in composition.

HT9: Effect of welding. Figure 4 shows the data obtained on unirradiated specimens fabricated from welded and tempered HT9 sheet stock. The toughness in both the fusion and heat affected zones (Figure 4a) appears

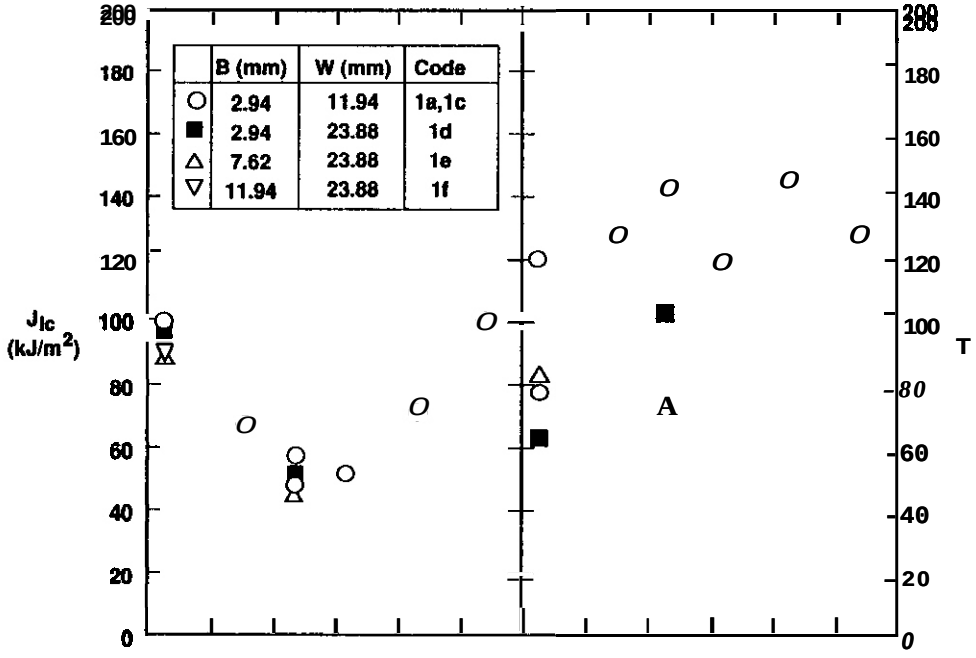

Figure 2. Effect of specimen size variations on a) fracture toughness and b) tearing modulus of unirradiated HT9 (B and W are specimen thickness and width, respectively)

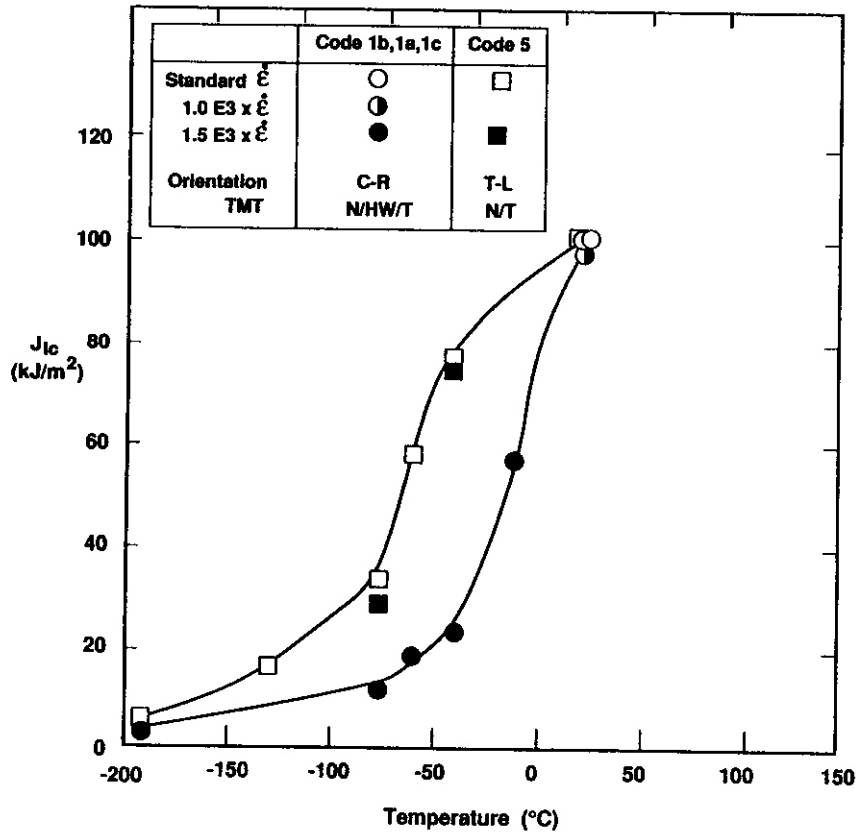

Figure 3. Fracture toughness of HT9 at high strain rates and low temperatures. Standard strain rate is 3×10^{-5} sec^{-1}.

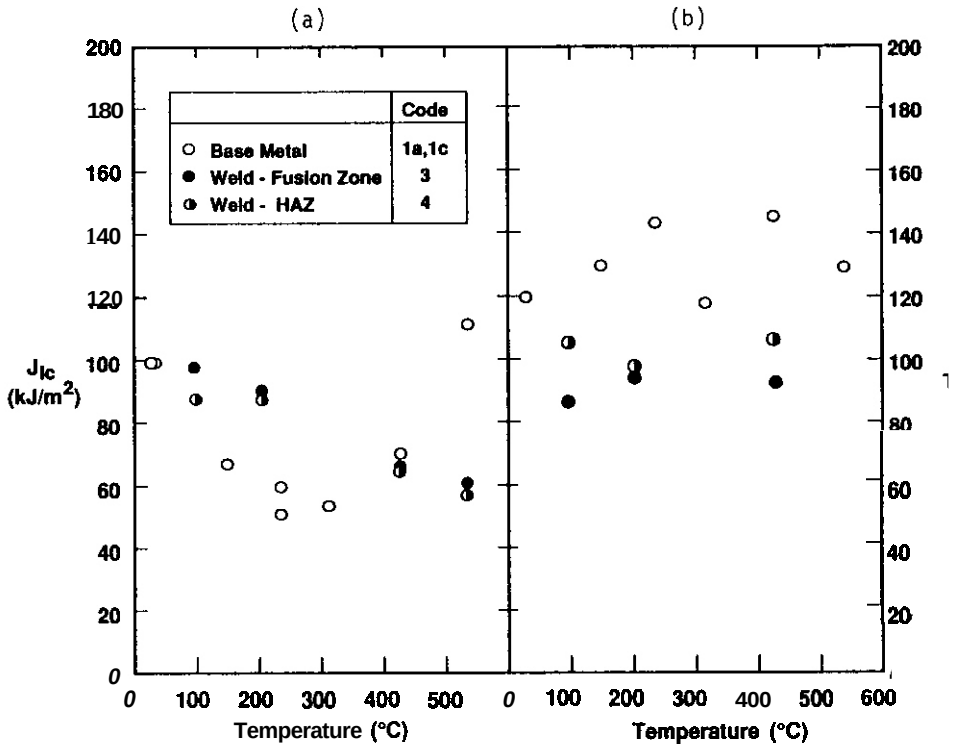

Figure 4. Effect of TIG welding on a) fracture toughness and b) tearing modulus in the fusion zone and heat affected zone of unirradiated HT9

to be somewhat higher at 205°C and somewhat decreased at 540°C relative to the base metal, although the tendency to decrease fracture toughness with increasing temperature is maintained. The tearing modulus (Figure 4b) in the welded regions was reduced approximately 25%. Overall, the crack initiation toughness of the unirradiated metal was not significantly affected by welding, although resistance to crack propagation was decreased in the temperature range of interest.

The data produced on irradiated specimens fabricated from the same welded sheet as the control specimens are shown in Figure 5. These specimens were irradiated in the AD-2 experiment in the EBR-II reactor. J_{Ic} exhibits very little effect of irradiation at 12-14 dpa (Figure 5a) while maintaining the dependence on test temperature seen in the unirradiated base and weld metal. Very little dependence is observed on irradiation temperature, although there is some indication (one data point) that continued irradiation of welded material at low temperatures to neutron exposures of about 26 dpa will cause a degradation in fracture toughness, albeit to a level no lower than observed in unirradiated material. While fracture toughness does not appear to be significantly affected by irradiation to 12-14 dpa, resistance to crack propagation (Figure 5b) is reduced approximately 50% compared to the unirradiated welded material, with no additional effect of irradiation to 26 dpa. Overall, in comparison to the base metal, a 60% loss in resistance to crack propagation is produced by the combination of welding and irradiation.

Modified 9Cr-1Mo: Effect of welding. Figure 6 shows a comparison between the fracture toughness data obtained on weld specimens (code 9) and control specimens (code 12). Note that the specimens were fabricated from two heats with very similar compositions. The effect of welding on the fracture behavior of modified 9Cr-1Mo is similar to its effect on HT9; viz., that J_{Ic} shows very little effect of welding over the temperature range of interest while T drops roughly 25%. No weld specimens were tested in an irradiated condition.

HT9: HFIR irradiation. The toughness of HT9 was evaluated after irradiation in HFIR at 55°C to a nominal dose of 10 dpa (actually determined to be 5 dpa).[21] The data are shown in Figure 7. No control data are available for the particular specimen fabrication process and orientation which were irradiated. The HFIR irradiation was applied to the code 6 specimens: cold worked, normalized and tempered heat 91354 in the T-L orientation. The only control data available for comparison are the data on code 1a specimens, fabricated from an essentially identical heat (91353) in the "mill annealed" condition and the C-R orientation.

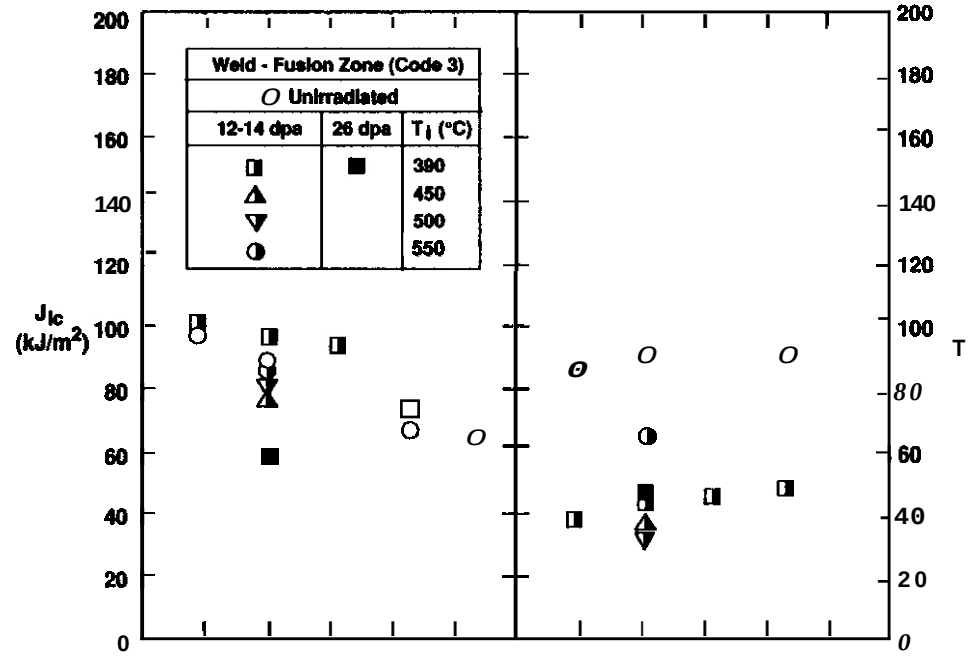
Weld - Fusion Zone (Code 3)
O Unirradiated
12-14 dpa
26 dpa
T_I (°C)
390
450
500
550
J_Ic (kJ/m²)
T
200
180
160
140
120
100
80
60
40
20
0

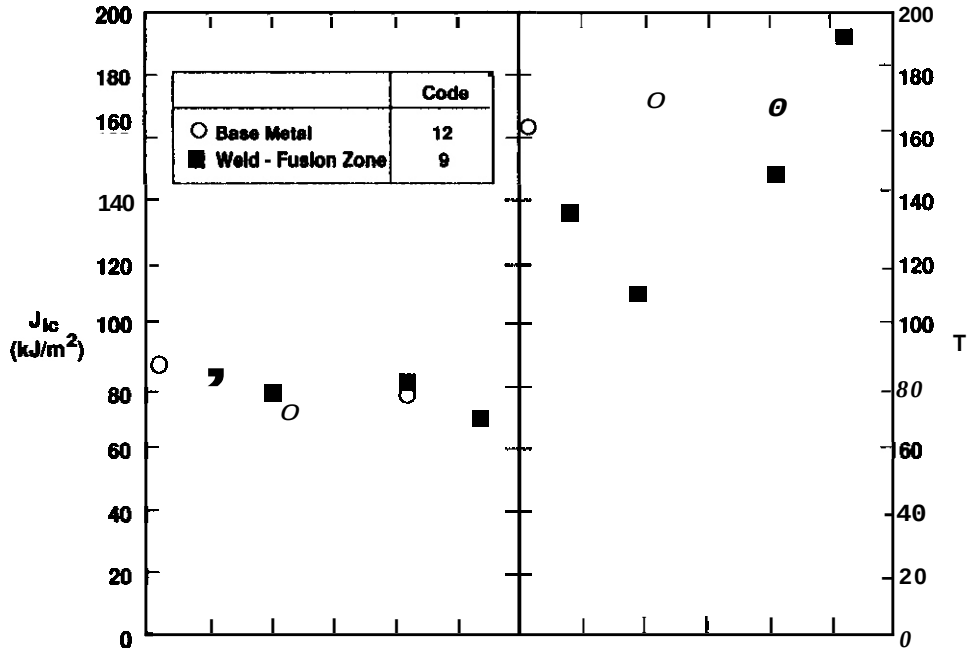
Code
Base Metal
12
Weld - Fusion Zone
9
J_Ic (kJ/m²)
T
200
180
160
140
120
100
80
60
40
20
0

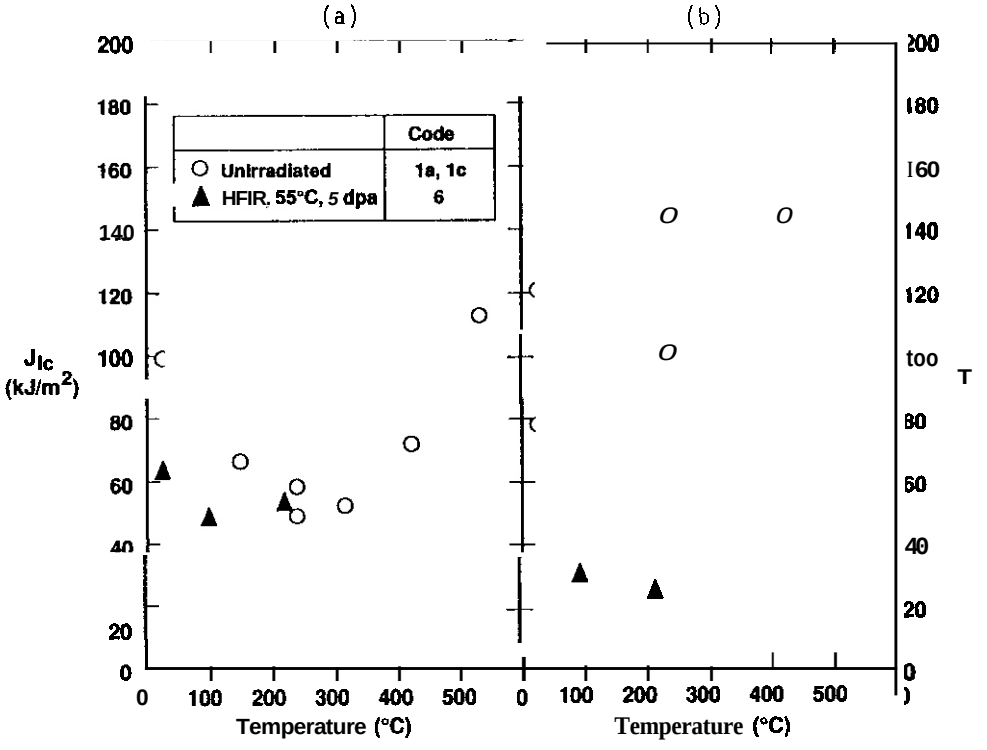

Figure 7. a) Fracture toughness and b) tearing modulus of HT9 after irradiation in HFIR at 55°C to 5 dpa

As is demonstrated in Figure la, fracture toughness decreased about 40% at room temperature following irradiation in HFIR, although it did not decrease below the level observed in unirradiated material at 205°C. Tearing resistance (Figure 7b) dropped about 15% to a very low value, on the order of 30. It is possible that the apparent embrittlement is due to some extent to the differences mentioned above between the control and the irradiated specimens. It is believed, however, that the embrittlement observed at low temperatures reflects the elevation of DBTT produced in ferritic steels by low temperature irradiation, particularly temperatures as low as in HFIR, where significant strengthening of the alloy is known to occur. It is also believed on the basis of impact data that additional degradation will occur with further low temperature irradiation. Impact data obtained on HFIR-irradiated HT9 showed additional elevation of the DBTT between 5 and 10 dpa.

9Cr-1Mo: HFIR irradiation. Irradiation in HFIR at 55°C to 5 dpa had a much stronger effect on modified 9Cr-1Mo than it did on HT9. While J_{Ic} for HT9 dropped only to the minimum value observed in the unirradiated condition, it dropped about 55% for 9Cr-1Mo over the entire range of temperatures considered (Figure 8a). Similarly, the tearing modulus of 9Cr-1Mo (Figure 8b) dropped approximately 90% to a value of about 20 following HFIR irradiation, whereas in HT9 it dropped 75% to a value of about 30 under the same irradiation conditions. It is also believed on the basis of impact data that additional degradation will occur with further low temperature irradiation. Impact data obtained on HFIR-irradiated 9Cr-1Mo showed additional elevation of the DBTT between 5 and 10 dpa.

HT9: Effect of grain size. The effect of grain size on the fracture toughness of irradiated HT9 was investigated using specimens fabricated from the same bar stock, in the same orientation (C-R), and given slightly different tempering treatments. TMT A, used for the code 1b specimens, produced a prior austenite grain size of ASTM 8-9, while TMT B, used for the code 2 specimens, yielded a prior austenite grain size of about ASTM 3-4 by means of a temper which was about 30°C higher for 2.5 times as long. No control data are available for the large grain size specimens. This section will discuss only the data comparison between the large and small grain sizes; the effect of continued irradiation on the small grain size material will be addressed in the next section, with data at a larger number of doses than are relevant to the larger grain size material.

The data are presented in Figure 9. Similar data are available at two exposure levels, about 13 and 27 dpa, and two irradiation temperatures, 390 and 500°C. The larger grain size material exhibits slightly less resistance to crack initiation (Figure 9a) and more resistance to crack propagation (Figure 9b), as might be expected since the smaller the grain size the more easily a fracture path can be established. J_{Ic} does not exhibit a strong dependence on either test or irradiation temperature, while T is consistently lower for

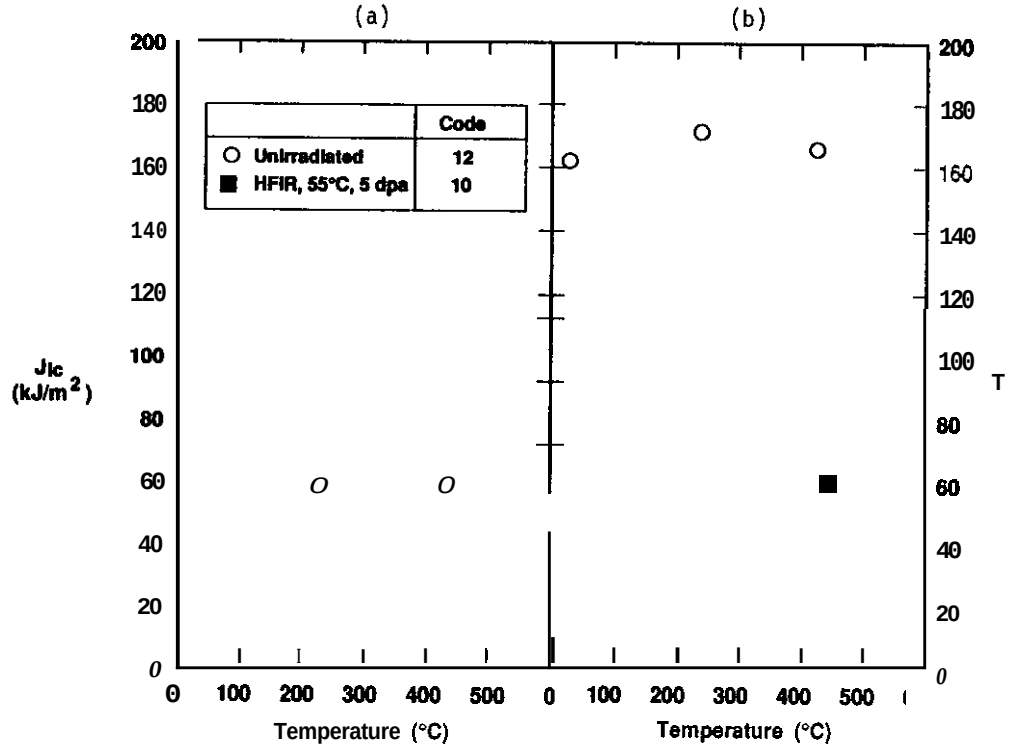

Figure 8. a) Fracture toughness and b) tearing modulus of 9Cr-1Mo after irradiation in HFIR at 55°C to 5 dpa

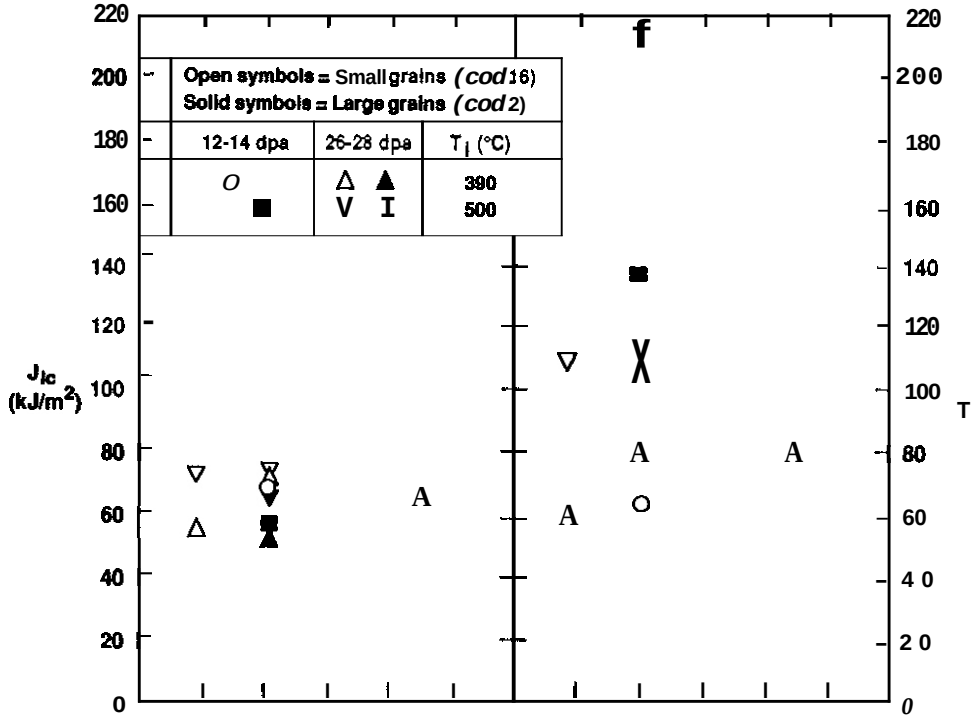

Figure 9. Effect of grain size on a) fracture toughness and b) tearing modulus of irradiated HT9

material strengthened by irradiation at the lower temperature. Neither parameter displays much sensitivity to increased neutron exposure.

HT9: Effect of EBR-II and FFTF irradiation. Figures 10 and 11 contain the data obtained in EBR-II and FFTF in the AD-2 and MOTA experiments. Neutron exposure levels range up to roughly 30 dpa in EBR-II at temperatures ranging from 390 to 500°C. FFTF irradiations have gone to exposures as high as about 100 dpa at temperatures ranging from 411 to 600°C. Note that the specimens irradiated in the two reactors are not identical: they were fabricated from different heats in different orientations and were given different tempering treatments. They will be referred to for simplicity by the reactor in which they were irradiated, although this is obviously not the most likely source of any differences observed in their mechanical properties.

Overall, the loss in toughness (J_{Ic}) induced by irradiation at any temperature is to a level no lower than the lowest observed in the unirradiated condition (Figures 10a and 11a). Resistance to crack propagation (T), however, is significantly decreased by irradiation, especially at low temperature, to a level about half that observed in the unirradiated condition (Figures 10b and 11b). The FFTF toughness values remain on the high side of the EBR-II toughness data up to doses of about 30 dpa; above this level the FFTF data begin to drop below the EBR-II data. The data suggest that a continued drop in toughness may be observed with increasing neutron exposures, while decreases in the tearing modulus appear to have saturated.

HFIR irradiation to 5 dpa at 55°C did not cause significantly more degradation in the toughness of HT9 than fast reactor irradiation to much higher doses at higher temperatures. While HFIR irradiation caused more of a decrease in low temperature (i.e., in the vicinity of room temperature) toughness, the actual values of toughness observed were at least as high as the lowest levels observed in unirradiated HT9. HFIR irradiation did cause, however, a much greater loss in tearing resistance than did fast reactor irradiation, dropping to about 30 after HFIR irradiation and only to about 50 following FFTF irradiation. Further degradation, anticipated on the basis of impact data, may very well be induced by additional low temperature irradiation.

9Cr-1Mo: Effect of FFTF irradiation. Irradiation generally causes a decrease in the toughness of 9Cr-1Mo of about 35%, regardless of the irradiation temperature or level of neutron exposure (Figure 12a). There is some inconsistency in the data, however, in that no degradation is observed at about 200°C while the 35% loss is observed at both lower and higher temperatures. Tearing modulus is reduced by approximately 50%. the reduction apparently saturating relatively quickly. Data obtained at room temperature suggest that the tearing modulus is actually increasing with continued neutron exposure at about 400°C, a phenomenon for which there is currently no microstructurally based explanation.

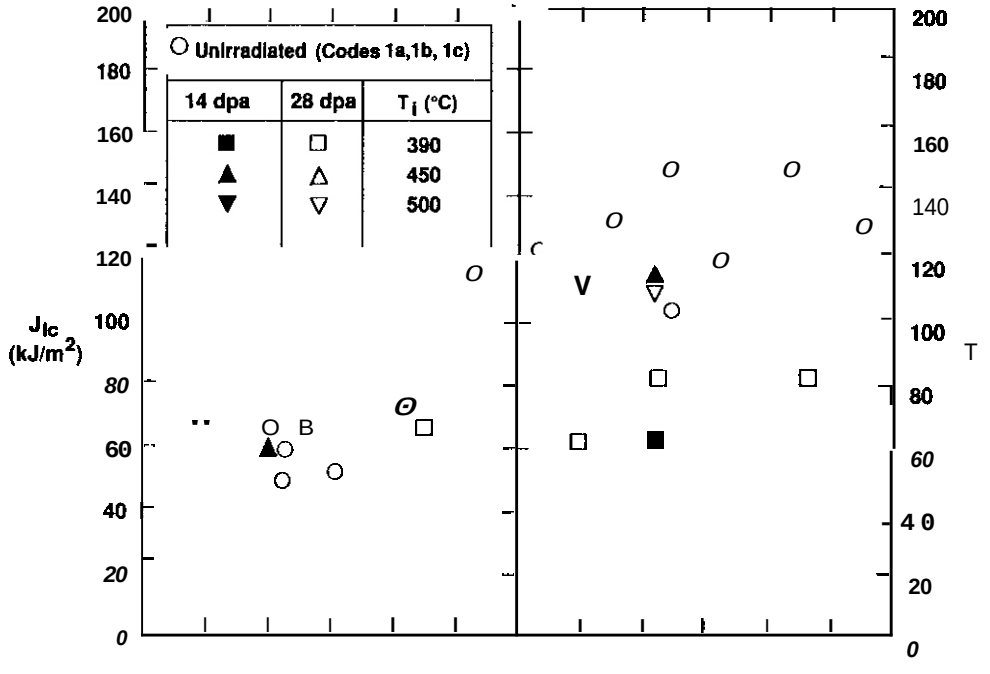

Figure 10. Effect of irradiation in EBR-II on a) fracture toughness and b) tearing modulus of HT9

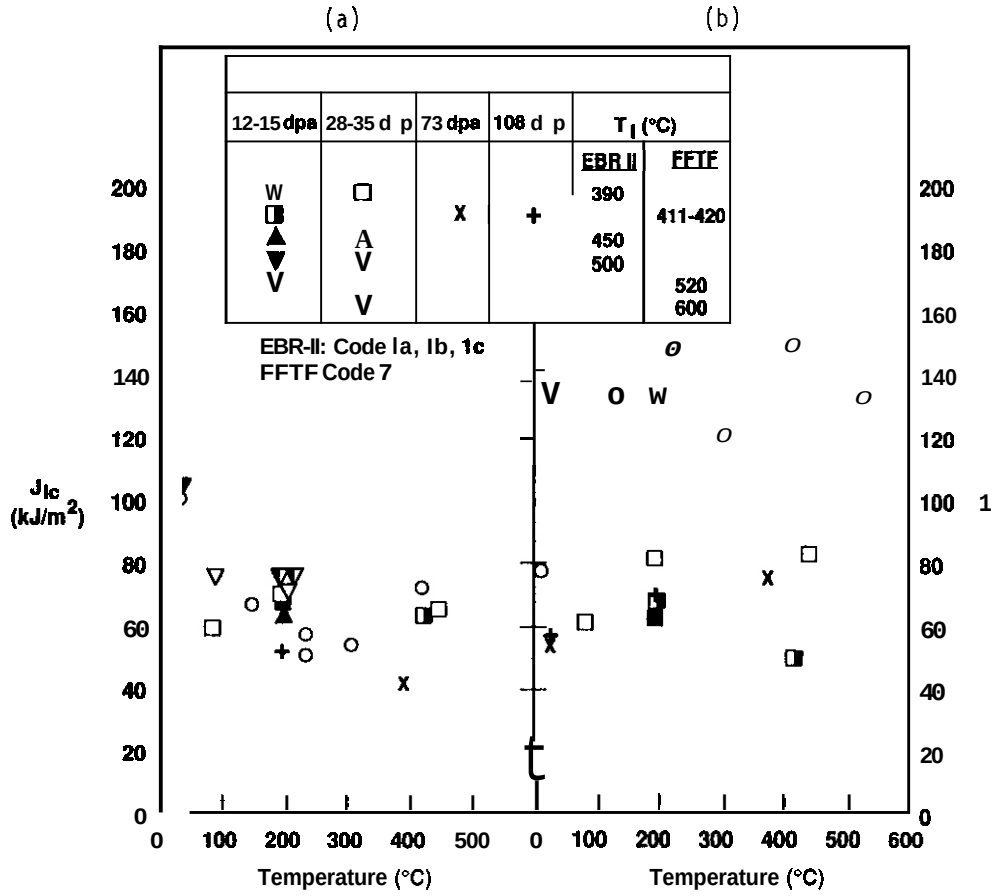

Figure 11. Effect of irradiation in FFTF on a) fracture toughness and b) tearing modulus of HT9

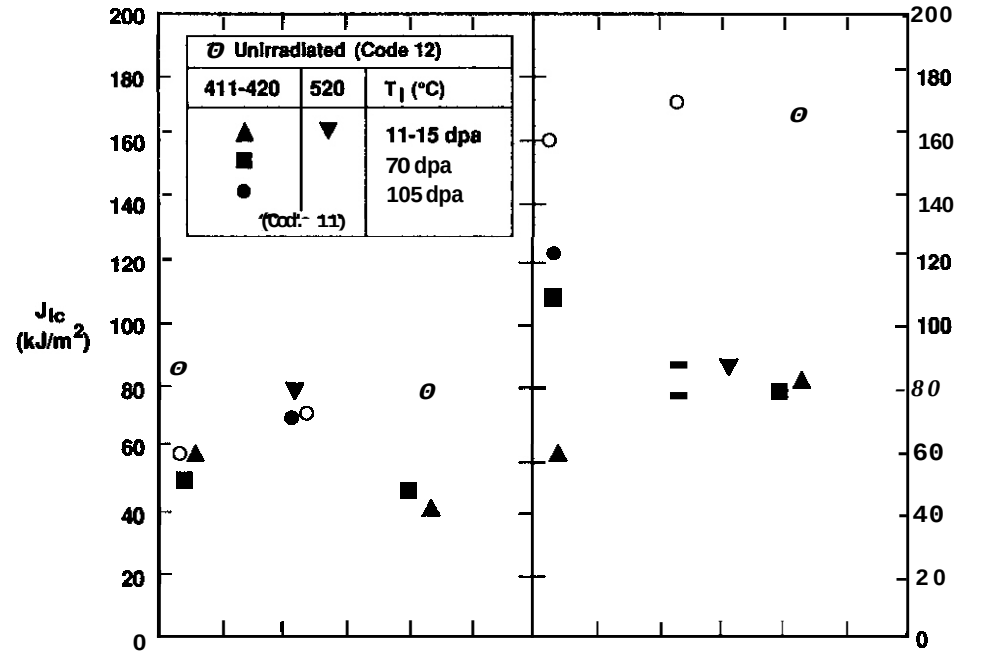

HFIR irradiation at 55°C was significantly more damaging to the fracture properties of 9Cr-1Mo than fast reactor irradiation at higher temperatures, even at the low neutron exposures for which there are HFIR data and the low helium levels produced in 9Cr-1Mo. While HFIR irradiation to 5 dpa at 55°C decreases the fracture toughness and tearing modulus to approximately 35 kJ/m2 and 20, respectively, the values of these parameters following FFTF irradiation to as much as 105 dpa did not drop below about 45 kJ/m^2 and 80, respectively. Presumably the effect is related primarily to the difference in irradiation temperature rather than differences in specimen preparation.

CONCLUSIONS

While the available data are sparse, no additional loss of fracture toughness appears to occur with fast reactor irradiation beyond about 30 dpa in HT9 and 9Cr-1Mo, up to doses as high as approximately 100 dpa. Tearing modulus values show more scatter, but within the limits of the data a similar conclusion can be drawn. After irradiation in HFIR at 55°C, HT9 exhibits slightly lower room temperature toughness than HT9 irradiated in fast reactors, while 9Cr-1Mo shows a large reduction in toughness at all temperatures of interest.

FUTURE WORK

Miniature compact tension specimens of both HT9 and 9Cr-1Mo (codes 7 and 11, respectively) continue to be irradiated in the FFTF. They will be discharged at much higher damage levels and tested under conditions similar to previous tests.

REFERENCES

1. F. H. Huang, B. A. Chin and G. L. Wire. "Application of the Electropotential Techniaue to J-Integral Measurements," Alloy Development for Irradiation Performance Quarterly Progress Repdrt for Period Ending September 30, 1979, DOE/ET-0058/7, pp. 16-28.

2. F. H. Huang and G. L. Wire, "Initial Test Results on Miniature Compact Tension Fracture Toughness Specimen," Alloy Development for Irradiation Performance Quarterly Progress Report for Period Ending December 31, 1979, DOE/ER-0045/1, pp. 18-25.

3. F. H. Huang and G. L. Wire, "Fracture Toughness Tests on HT-9 at Elevated Temperatures," Alloy Development for Irradiation Performance Quarterly Progress Report for Period Ending March 31, 1980, DOE/ER-0045/2, pp. 156-162.

4. F. H. Huang and D. S. Gelles, "Influence of Specimen Size and Microstructure on the Fracture Toughness of a Martensitic Stainless Steel," Engineering Fracture Mechanics 19 (1984) pp. 1-20.

5. F. H. Huang and G. L. Wire, "Analysis of Single Specimen Tests on HT-9 for J_{Ic} Determination," Alloy Development for Irradiation Performance Quarterly Progress Report for Period Ending June 30, 1980, DOE/ER-0045/3, pp. 236-254.

6. F. H. Huang and G. L. Wire, "Fracture Toughness Testing on Ferritic Alloys Using the Electropotential Technique," J. Nucl. Mat. 104 (1981) 1511-1516.

7. F. H. Huang, "Fracture Toughness of Irradiated HT-9 for Structural Applications," Nuclear Engineering and Design 90 (1985) pp. 13-23.

8. R. J. Puigh and N. F. Panayotou, "Specimen Preparation and Loading for the AD-2 Experiment," Alloy Development for Irradiation Performance Quarterly Progress Report for Period Ending June 30, 1980, DOE/ER-0045/3, pp. 260-293.

9. F. H. Huang and T. L. Wire, "Fracture Toughness Measurements for Unirradiated 9Cr-1Mo Using Electropotential Techniques," Alloy Development for Irradiation Performance quarterly Progress Report for Period Ending September 30, 1981, (DOE/ER-0045/7, pp. 220-229.

10. A. M. Ermi, "Reconstitution of the AD-2 Ferritics Experiment," Alloy Development for Irradiation Performance Quarterly Progress Report for Period Ending March 31, 1982, DOE/ER-0045/8, pp. 431-441.

11. F. H. Huang, "Fracture Toughness of Unirradiated HT-9 and Modified 9Cr-1Mo Welds," Alloy Development for Irradiation Performance Quarterly Progress Report for Period Ending September 30, 1982, DOE/ER-0045/9, pp. 221-229.

12. F. H. Huang and D. S. Gelles, "Fracture Toughness of Irradiated HT-9 Weld Metal," Alloy Development for Irradiation Performance Quarterly Progress Report for Period Ending March 31, 1983, DOE/ER-0045/10, pp. 125-130.

13. F. H. Huang, "The Fracture Toughness of Ferritic Alloys Irradiated in HFIR," Alloy Development for Irradiation Performance Quarterly Progress Report for Period Ending September 30, 1983, DOE/ER-0045/11, pp. 180-184.

14. F. H. Huang, "The J_c Fracture Toughness Transition Behavior of HT-9," Alloy Development for Irradiation Performance Quarterly Progress Report for Period Ending September 30, 1983, DOE/ER-0045/11, pp. 172-179.

15. F. H. Huang, "Fracture Toughness of Irradiated HT-9," Alloy Development for Irradiation Performance Quarterly Progress Report for Period Ending March 31, 1984, DOE/ER-0045/12, pp. 104-109.

16. F. H. Huang, "Effects of Irradiation on the Fracture Toughness of HT-9," Alloy Development for Irradiation Performance Quarterly Progress Report for Period Ending September 30, 1984, DOE/ER-0045/13, pp. 156-160.

17. F. H. Huang and D. S. Gelles, "Fracture Toughness of Irradiated HT-9 Weld Metal," J. Engineering Materials and Technology, 107 (1985) pp. 329-333.

18. F. H. Huang, "Fracture Toughness of Ferritic Alloys Irradiated in FFTF," Alloy Development for Irradiation Performance Quarterly Progress Report for Period Ending March 31, 1986, DOE/ER-0045/16, pp. 145-149.

19. F. H. Huang and D. S. Gelles, "Fracture Behavior of Unirradiated HT-9 and Modified 9Cr-1Mo Welds," Proceedings of Topical Conference on Ferritic Alloys for Use in Nuclear Energy Technologies, 1983, pp. 337-346.

20. F. H. Huang, "J_{1c} Measurements on Single Subsized Specimens of Ferritic Alloys," J. Test. Eval. 13 (1985) pp. 257-264.

21. D. S. Gelles and F. H. Huang, "Fractographic Examination of HT-9 Miniature Compact Tension Specimens Tested at Low Temperatures," Alloy Development for Irradiation Performance Quarterly Progress Report for Period Ending September 30, 1983, DOE/ER-0045/11, pp. 128-135.

EFFECT OF SPECIMEN SIZE ON THE UPPER SHELF ENERGY OF FERRITIC STEELS, A.S. Kumar (University of Missouri-Rolla) and F.A. Garner and M.L. Hamilton (Pacific Northwest Laboratory)[a]

OBJECTIVE

The object of this effort is to provide methods which use subsize specimens to determine the changes induced by radiation in metals employed for fusion service.

SUMMARY

A previous effort led to the development of size effect correlations for the ductile-brittle transition temperature (DBTT) and upper shelf energy (USE) of ferritic steels. An improved methodology is proposed that can be used to better predict the USE based on subsize specimen data. The proposed methodology utilizes the partitioning of the USE into energies required for crack initiation and crack propagation. Notched-only Charpy specimens are used in conjunction with precracked specimens to separate the two components. An unirradiated ferritic steel, HT-9, was used to demonstrate the validity of the methodology. Unlike previous correlations that were limited in their applicability to either highly ductile or brittle material, the proposed methodology is expected to be applicable over a wide range of ductility and to be particularly useful for materials which harden significantly during irradiation.

PROGRESS AND STATUS

Introduction

Ferritic steels are being considered as possible candidates for structural applications in fusion reactors. The steel designated HT-9 (12 Cr-1Mo-VW) has been found to be particularly promising[1,2]. In order to assess the effects of neutron exposure on the impact properties of this steel, studies are in progress using subsize specimens which are considerably smaller than the standard size specified in ASTM standard E23-86. While the use of subsize specimens allows a larger number of specimens to be irradiated in the limited reactor space available, there are size-related consequences that influence the usefulness of the data.

Full-size specimens are designed to ensure that a state of plane strain exists below the notch root, a condition that promotes brittle fracture. A reduction in size not only reduces the remaining load-bearing ligament but also alters the stress state under the notch.

Reduction of the specimen size eventually leads to a plane stress condition, which promotes a relatively ductile fracture compared to that of full-size specimens. This limits somewhat our ability to predict the upper shelf energy (USE) and ductile to brittle transition temperature (DBTT) of full-size specimens based on data derived from subsize specimens.

There have been a number of attempts to correlate the USE of full-size, half-size and third-size specimens[3-8]. In these studies, a normalized USE was defined as the ratio of the measured USE to a normalization factor. For the correlation to be valid, the normalized values of the USE for full- and subsize specimens should be equal.

Past attempts to correlate USE values can be divided into two main categories. The first category consists of correlations based on a normalization factor that is defined by the fracture volume below the notch root. In some investigations[3,4,8] the fracture volume is estimated as $(Bb)^{3/2}$ and in others[6,7] it is estimated as Bb^2, where B is the specimen thickness and b is the ligament size below the notch root. Correlations based on using the fracture volume as the normalization factor have been found to be satisfactory for relatively ductile steels having USE values larger than 200 J. It is important to note, however, that this type of normalization factor does not take into account either the length of the specimen or the geometry of the notch.

In the second category of correlations, the normalization factor includes all of the specimen dimensions as well as the stress concentration factor at the notch root, which incorporates the effect of notch geometry. Such a correlation was first proposed in an earlier stage of the present effort and has been found to work satisfactorily for steels in relatively brittle conditions (USE < 100 J) characteristic of irradiation to very high neutron fluences[4]. Similar success has also been obtained for DBTT correlations as a function of size.[9]

Neither of the above mentioned correlations would be suitable, however. when a normallv ductile material with USE > 200 J becomes embrittled by radiation such that its USE falls considerably below200 J. The purpose of

---

(a) Operated for the U.S. Department of Energy by Battelle Memorial Institute under Contract DE-AC-06-76RLO 1830.

the current study is to develop a methodology for the correlation of full-size and subsize USE values that is applicable to a wide variety of steels irrespective of their USE value in either the irradiated or unirradiated state. To demonstrate the improved methodology, HT-9 steel was selected in the T-L orientation, having a full-size USE of 129 J.

The methodology is based on the partitioning of the USE into two contributions, i.e., that required for crack initiation and that for crack propagation. To accomplish this partition both precracked and notched-only specimens were used. Whereas the USE of notched-only specimens is the sum of both crack initiation and propagation energies, the use of precracked specimens reflects only crack propagation. The difference in USE values for the two types of specimens is thus a measure of the crack initiation energy. We will expand on the utility of this partition in later sections of the paper.

Exoerimental Procedure

All specimens used in this study were machined from HT-9 plate material of heat 9607R2, which was manufactured by Electralloy Corporation for the U.S. DOE fusion materials program. The chemical composition and tensile properties of this heat are given elsewhere[10]. A series of heat treatments was performed on the plate stock to produce a tempered martensitic structure with a hardness of 255 DPH and a prior austenite grain size of ASTM 5 to 6. All specimens were taken from the base material in the transverse (T-L) orientation, in which the long axis of the specimen lies perpendicular to the rolling direction and the direction of elongation of the grains is the same as the direction in which the crack propagates. Specimens in this orientation will have the least resistance to fracture and will therefore provide a minimum estimate of fracture energy.

Dimensions for both full-size and subsize specimens are given in Figure 1. The full-size specimen dimensions are in accordance with ASTM standard E23-86. While there are no standards available for subsize specimens, the dimensions used in this study for half-size and third-size specimens are similar to those used in other investigations.[4,5]

Precracked specimens were prepared by loading the notched specimen in a three-point-bend arrangement and subjecting it to an oscillating load in a closed-loop hydraulic system. The minimum and maximum loads for the oscillations were determined in advance according to ASTM standard E399 modified for miniature specimens.

Adjustable anvils and interchangeable crossheads made possible the testing of different size specimens on the same instrumented drop tower. Data from each test were recorded on a digital oscilloscope and transferred to a desktop computer for storage and analysis.

Calibration of the instrumented hammer was performed by adjusting the load signal gain so that the maximum load obtained during dynamic testing was the same as the maximum load determined during the slow bend testing of a strain-rate insensitive alloy (6061 aluminum in the T651 heat-treatment). In addition, a static calibration of the load cell was performed to insure that its response was linear over the desired range.

The impact velocity of the crosshead was calibrated by attaching a 1-cm-long flag to the crosshead, positioned so that the flag passed an infrared sensor just prior to impact, causing a change in voltage during interruption by the flag. The duration of this change was measured on the oscilloscope and the velocity calculated. Velocity was calculated as the average of at least ten calibration runs.

Temperature control for full-size specimens was accomplished in a conditioning chamber where high temperatures were attained with a heated stream of air and low temperatures were reached by using cold nitrogen gas. Temperature control was achieved by adjusting the rate of gas flow into the conditioning chamber. Each specimen was kept at the test temperature for five to ten minutes prior to testing to ensure temperature stabilization to within 2°C. Temperature control for the subsize specimens used the same sources of heated or cooled gas, but because the conditioning chamber was designed specifically for full-size Charpy specimens, the miniature specimens were manually placed and aligned in the testing position and the gas was directed across the specimen surface. A thermocouple spot-welded across from the notch (opposite the surface being impacted) was used to monitor the temperature for each test.

Specimen placement for full-size specimens was achieved by air-driven pistons that moved the specimen from its initial position, into and out of the conditioning chamber, and finally into the testing position using a rotary positioning arm. ASTM standard E23-86 provides for a maximum 5-second delay between obtaining the desired temperature and impacting the specimen. For full-size specimens, the elapsed time between the exit of the sample from the conditioning chamber and the impact was approximately 0.2 seconds. For subsize specimens, no specimen transfer was involved.

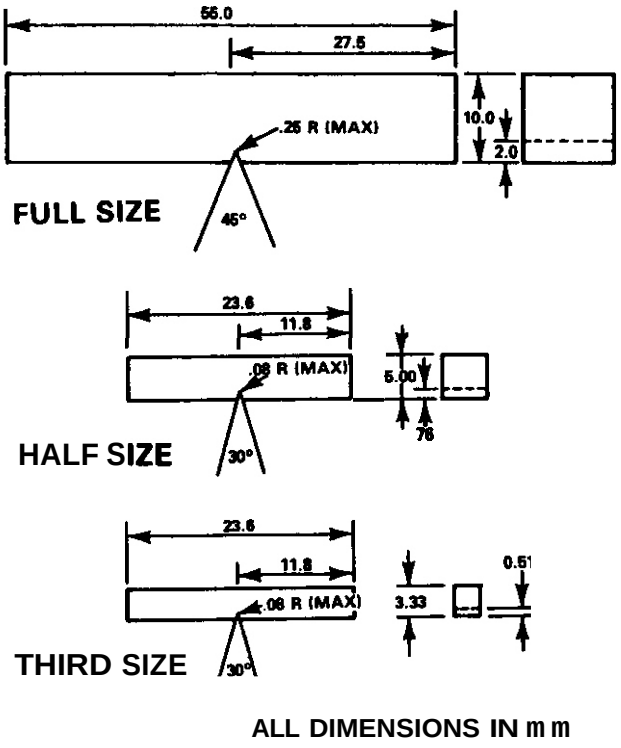

Figure 1. Dimensions of Full- and Subsize Charpy Specimens.

RESULTS AND DISCUSSION

A comparison of typical load traces for a precracked Charpy specimen and a notched specimen tested in the neighborhood of the transition temperature is shown in Figure 2. The precracked specimen generally shows a sharp, well-defined peak load. The crack starts to propagate either at the maximum load or just prior to maximum load. As the crack propagates through the specimen, the load subsides. The energy absorbed by the specimen up to the point of crack initiation could be used to evaluate the dynamic fracture toughness of the material. On the other hand, a notch is not as sharp as the fatigue precrack and hence is a less efficient stress raiser. Consequently, much more energy is required to deform the material at the notch root. The volume of material deformed in this case is an order of magnitude more than the volume of material deformed at the crack tip in a precracked specimen. Therefore, a plateau of high load is observed. Since the energy stored in the specimen prior to failure initiation could be very large, the velocity of failure propagation through a notched specimen is much higher than the propagation velocity in a precracked specimen. A rather sharp load drop illustrates this point.

In a notched-only specimen, plastic deformation occurs below the notch root prior to crack initiation. At high temperatures when deformation proceeds on the upper shelf, work hardening precedes fracture and crack initiation occurs in a microscopic manner. During this stage microcracks may initiate at different times at different locations across the specimen width before linking up to generate a macrocrack across the entire width[11]. The crack then propagates across the ligament in a relatively uniform manner. At this point, called the macroinitiation point, the slope of the curve of absorbed energy versus crack depth falls abruptly to a lower value. Before the macroinitiation point the absorbed energy is related only to the dimensions of the specimen, primarily the width and ligament size. After macroinitiation, crack propagation becomes strongly dependent on the stress concentration factor as well.

The work of Louden et al.[9] shown in Figure 3 provides support for this view of how the fracture energy is partitioned. The upper portion of Figure 4 shows Louden's normalized values of USE for full-size and subsize specimens. This correlation, based on a normalization factor which is equal to the product of the stress concentration factor, the specimen length and the inverse of the fracture volume, works very well for materials having a full-size USE less than 100 J. Examples are precracked HT-9 in the T-L orientation, quenched

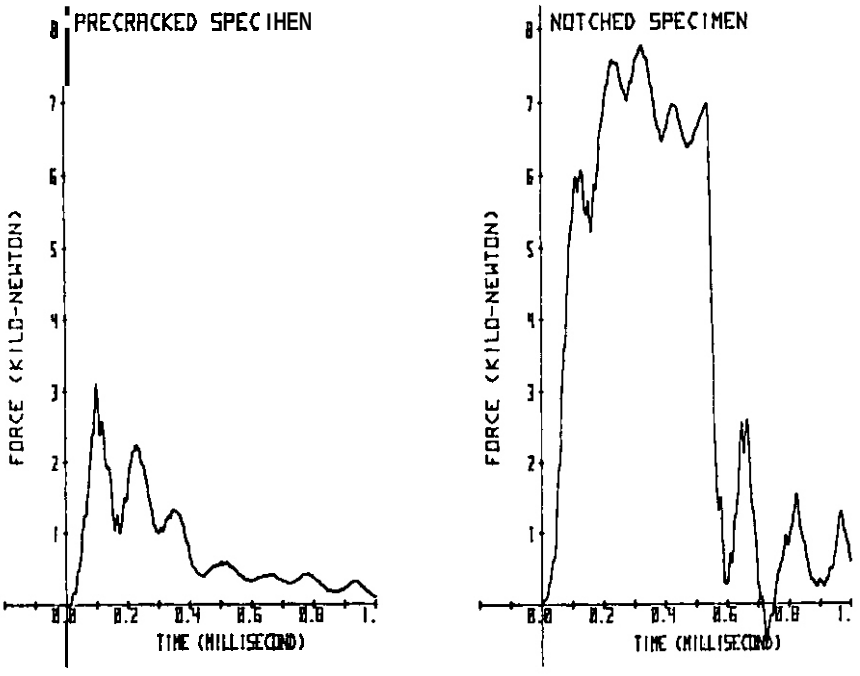

Figure 2. Typical Load Traces for Specimens Tested Near the Transition Temperature.

9Cr-1Mo-VNb in the T-L orientation and 12Cr-1Mo-VW steel in both the L-T and T-L orientations. All of these have a normalized **USE** that is approximately equal for full-size, half-size and third-size specimens as shown in Figure 4, suggesting an excellent correlation for materials with low levels of ductility (**USE** <100J). "Average" in the ordinate of Figure 4 represents the average of the normalized **USE** of full- and subsize specimens.

In contrast, as shown by the work of Corwin et al.[3] (see lower portion of Figure 4) correlations for highly ductile materials can be obtained with consideration of the fracture volume only. Sufficient blunting of the crack tip occurs in such cases to significantly reduce the stress concentration.

Even highly ductile materials will become embrittled, however, after exposure to high fluences of fast neutrons. Neither Louden's nor Corwin's correlation will therefore be valid in both the preirradiation and postirradiation conditions. The methodology presented here will permit determination of the crack initiation energy, which scales well with the fracture volume. Testing of precracked specimens yields that portion of the **USE** that is absorbed after the macroinitiation of crack. The **USE** of precracked specimens therefore approximates the crack propagation energy. The difference between the USE of notched-only and precracked specimens, ΔUSE, is therefore a measure of the crack initiation energy and should scale with fracture volume. The **USE** of Charpy specimens can thus be written as the sum of two terms as follows:

$$\text{USE (notched)} \approx F_1 \left[\frac{1}{B(W-A)^2}\right] + F_2 \left[\frac{L\,K_T}{B(W-A)^2}\right]$$

where F_1 is the crack initiation energy and F_2 is the crack propagation energy. L,B,W, (W-A), K_T are the length, thickness, width, ligament size and stress concentration factor, respectively. Since

$$\text{USE (precracked)} = F_2 \left[\frac{L\,K_T}{B(W-A)^2}\right], \quad \text{then}$$

$$\Delta\text{USE} = F_1 \left[\frac{1}{B(W-A)^2}\right]$$

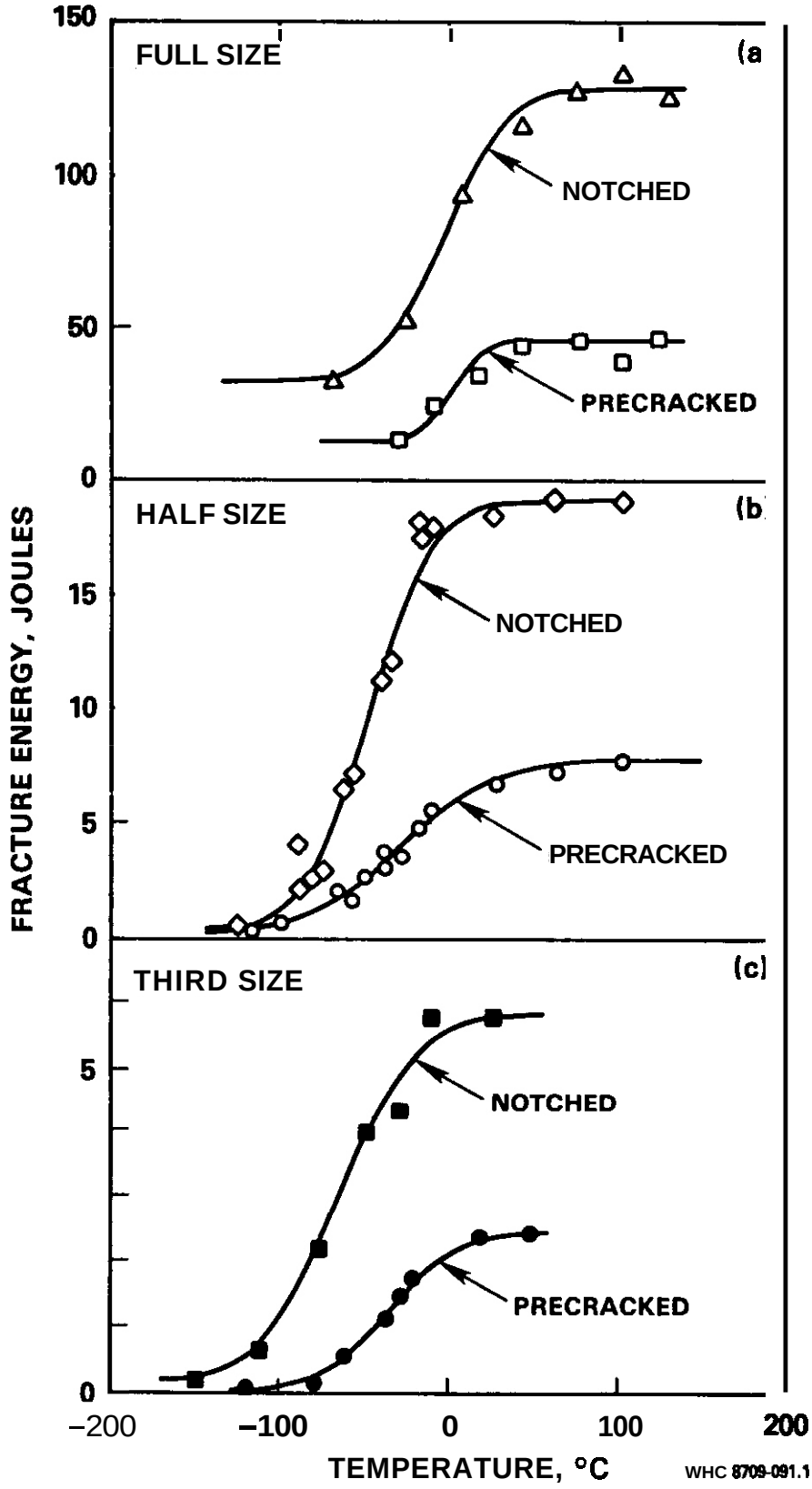

Figure 3. Dependence of fracture energy on temperature for both notched-only and precracked specimens for (a) full size, (b) half size, (c) third size.

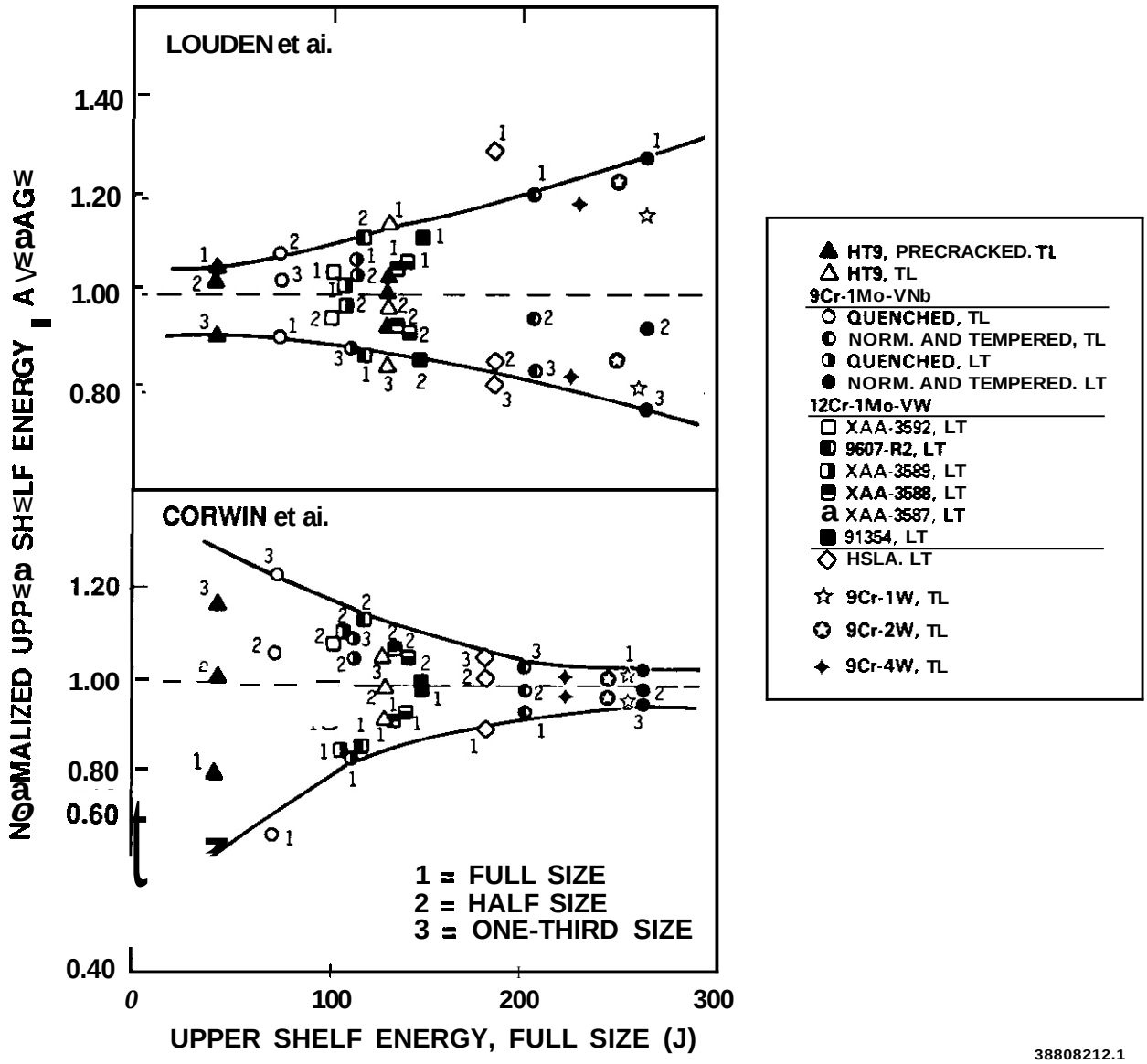

FIGURE 4. Comparison of normalized USE's of various materials. Superscripts 1, 2, and 3 on data points refer to full-, half- and third-size specimens. All specimens are notched-only, except those labeled precracked. TL means that the specimen axis is perpendicular to the rolling direction. LT means that the axis of the specimen is parallel to the rolling direction. The specimen geometries for all specimens are shown in Figure 1.

(a) Normalization of Louden et al.[9]
(b) Normalization of Corwin et al.[3,4]

Figure 3 shows Charpy data on the USE of HT-9 tested in both notched-only and precracked conditions. The USE values for notched-only specimens were 129 J, 19.1 J and 5.84 J for full-, half- and third-size specimens. The USE of precracked specimens, as shown in Table 1, drops off sharply compared to the notched-only specimens. The ligament sizes of the precracked specimens were 62.5%, 68.3%, and 63.1% of the respective ligament sizes of notched-only specimens. If the ligament sizes of the precracked subsize specimens were smaller such that they were each 62.5% of the respective notched-only specimens, the resulting precracked subsize USE would also be smaller. The "adjusted" value of the USE (for a 62.5% ligament) of half-size and third-size precracked specimens would then be 7.32 J and 2.28 J. The adjusted value is based on the premise that if the full-size and subsize specimens were precracked to the same fraction of the ligament size of the notched-only specimens, the USE would drop from the notched-only value to the precracked value by the same factor for full-, half- and third-size specimens. The assumption appears to be reasonable since, as shown in Table 2, the ratios of the notched-only and precracked USE values are roughly equal. Table 3 shows the normalized values of AUSE, where the normalization factor is the fracture volume and AUSE is the difference between the USE of notched-only specimens and the adjusted USE value of the precracked specimens. The normalized values of AUSE are within ±3% of the average value, signaling an excellent correlation.

Knowledge of the ΔUSE and the ratio of the USE and USE_p provides the following three equations with three unknowns to determine the USE of full-size specimens based on subsize data. Superscripts f and s represent full- and subsize specimens, respectively, and subscript p means crack propagation.

$$(\Delta USE/F.V.)^f = (\Delta USE/F.V.)^s \quad (1)$$

$$(USE/USE_p)^f = (USE/USE_p)^s \quad (2)$$

$$USE^f = \Delta USE^f \; t \; USE_p{}^f \quad (3)$$

where F.V. is the fracture volume. F.V. equals $B(W-A)^2$, B being the thickness and (W-A), the ligament size.

CONCLUSION

The upper shelf energy (USE) of full-size Charpy specimens can be predicted based on subsize specimen data. USE is a sum of the crack initiation energy (ΔUSE) and the crack propagation energy (USE_p). USE_p equals the upper shelf energy of precracked specimens. The ratios of USE and USE_p for full-size and subsize specimens were found to be equal. A normalized value of ΔUSE is defined as the product of the actual value and the reciprocal of the fracture volume. Normalized values of ΔUSE for full-size specimens were found to be equal to the subsize normalized values. ΔUSE represents the difference between USE and USE_p. Knowing both the difference and the ratio of USE and USE_p for full-size specimens based on subsize data, USE for full-size specimens can be calculated.

FUTURE WORK

No further work is planned until additional data become available.

TABLE 1

Measured Upper Shelf Energy of HT-9

	Notched-Only (J)	Pre-Cracked (J)
Full Size	129	44.0
Half Size	19.1	8.0
Third Size	5.84	2.30

TABLE 2

Adjusted Values of Upper Shelf Energy. The adjustment is made only for half-size and third-size precracked specimens. It is assumed that the ligament size in these specimens is the same fraction of respective notched-only specimens as in the case of full-size specimens.

	Notched-Only (J)	Pre-Cracked (J)	Ratio
Full Size	129	44.0	2.93
Half Size	19.1	7.32	2.61
Third Size	5.84	2.28	2.56

TABLE 3

Normalized ΔUSE for Full-, Half- and Third-Size Specimens. "AVG" (ΔUSE) is the average of the three normalized ΔUSE values.

	Notched-Only (J)	Pre-Cracked (J-adjusted)	ΔUSE Fract. Vol. (J/cm^3)	ΔUSE Avg.
Full Size	129	44.0	133	0.99
Half Size	19.1	7.32	131	0.98
Third Size	5.84	2.28	138	1.03

REFERENCES

1. W. L. Hu and D. S. Gelles, Proc. Conf. on Ferritic Alloys for Use in Nuclear Energy Technologies, Snowbird, UT, (June 1983) p. 631.

2. R. W. Powell, G. D. Johnson, M. L. Hamilton and F. A. Garner, in the Proc. of the ANS International Conf. on Reliable Fuels for Liquid Metal Reactors, Tucson, AZ, (September 1986) pp. 4-17.

3. W. R. Corwin, R. L. Klueh, and J. M. Vitek, J. Nucl. Mater. 122-123, (1984) p. 343.

4. W. R. Corwin and A. M. Hougland, ASTM STP 888, Eds., W. R. Corwin and G. E. Lucas, American Society for Testing and Materials (1986) p.325.

5. G. E. Lucas, G. R. Odette, J. W. Sheckherd, P. McConnell, and J. Perrin, ASTM STP 888, eds., W. R. Corwin and G. E. Lucas, American Society for Testing and Materials (1986) p. 305.

6. G. E. Lucas, G. R. Odette, J. W. Sheckherd, and M. R. Krishnadev, Fusion Tech., 10 (1986) p. 728.

7. B. L. Ferguson, ASM Proc. of AIME Annual Meeting on "What Does the Charpy Test Really Tell Us?", Denver, CO, Feb. 1978, Eds. A. R. Rosenfield, et al., pp. 90-107.

8. F. Abe, T. Noda, H. Araki, M. Okada, M. Naraui and H. Kayano, Journal of Nuclear Materials, 150 (1987) 292-301.

9. B. S. Louden, A. S. Kumar, F. A. Garner, M. L. Hamilton and W. L. Hu, Journal of Nuclear Materials, 155-157 (1988) 662-667.

10. T. A. Lechtenberg, ADIP Semiannual Progress Report, DOE/ER-0045/8, p. 363

11. W. Server, D. Norris, Jr. and M. Prado, ASM Proc. of AIME Annual Meeting on "What Does the Charpy Test Really Tell Us?", Denver, CO, Feb 27-28, 1978, Eds. A. R. Rosenfield et al., pp. 187-200.

PROCESSING OF TWO IRON-CHROMIUM OXIDE DISPERSION STRENGTHENED STEELS BY MECHANICAL ALLOYING - A. N. Niemi, M. G. McKimpson (Michigan Technology Institute), and D. S. Gelles (Pacific Northwest Laboratory)[a]

OBJECTIVE

The objective of this effort is to detennine if oxide dispersion strengthened (ODS) alloys produced by mechanical alloying are suitable for first wall applications.

SUMMARY

Two low activation ferritic OOS alloys have been manufactured. using mechanical alloying procedures. into extruded bar. The alloy canpositions in weight percent are: Fe-14Cr-1.0Ti-0.5W-0.25Y_2O_3 and Fe-9Cr-2.0W-0.3V-0.08C-0.25Y_2O_3. Dispersoid phase instability is indicated in the Fe-9Cr carbon-containing alloy, but the 14Cr alloy appears to offer a novel material which may be suitable for first wall applications and warrants further study.

PROGRESS AND STATUS

Introduction

An OOS alloy made by mechanical alloying methods is receiving continued international consideration for liquid metal', fast breeder reactor fuel cladding applications.[1] The alloy shows excellent long term microstructural stability in irradiation environments and is expected to retain superb high temperature strength. The alloy. called MA957, has the canposition Fe-14Cr-1Ti-0.25Mo-0.25Y_2O_3 and is made by a powder metallurgy process involving high energy ball milling. The resultant microstructure consists of a metal matrix with a uniformly distributed yttria dispersoid on the order of 5 nm in diameter. It also contains a highly elongated subgrain structure which is introduced by thermo-mechanical processing. Based on performance demonstrated to date. this technology should be considered for fusion first wall applications.

Therefore. an effort has been initiated to consider the use of mechanically alloyed OOS alloys for fusion by altering the alloy canposition to be in line with low activation criteria. However. the manufacturer of MA957, the INCOMAP division of the International Nickel Canpany. Huntington. W. Va., was unwilling to manufacture a low activation variant. and therefore. a request was made and a responding proposal was submitted by The Institute of Materials Processing (IMP). Michigan Technology University to produce two extrusions from mechanically alloyed powder. As accepted. the agreement called for the production of extrusions fran mechanically alloyed powder of the following compositions (in weight percent): Fe-14Cr-1.0Ti-0.5W-0.25Y_2O_3 and Fe-9Cr-2.0W-0.3V-0.08C-0.25Y_2O_3. The alloy compositions and method of processing were defined by Pacific Northwest Laboratory (PNL) so that the 14Cr alloy was a low activation variant of MA957 and the 9Cr alloy was a mechanically alloyed version of GA3X, with the development of appropriate process parameters by IMP on a best effort basis. The extrusions were to be supplied to PNL with a 19 mm (3/4 in.) diameter and a minimum 410 mm (16 in.) length. This report describes the manufacturing process used to produce the requested materials based on the IMP Project No. R-419 report. and provides sane preliminary measurements on the products.

Experimental Procedure

The starting powder compositions and the maximum mesh sizes are shown in Table 1. Master alloy powders were used, where possible, in an attempt to minimize inhomogeneity in the final product. A 1S Szegvari attritor with a tank capacity of 9.5 L (2.5 gal.) was used for the mechanical alloying. The tank was charged with 27.3 kg (60 lb) of 9.53 mm (3/8 in.) 440C stainless steel balls and 1.82 kg (4 lb) of powder. Two batches of each composition were required. The attritor was operated at 350 rpm with a positive pressure, high purity argon purge rate of 5 L/min. Each batch was attrited for 12 h, held overnight under A, and attrited for 8 h the next day. During attrition. the drive torque and tank lid temperature were monitored. The torque ran between 556 and 570 N-m (410 and 420 in.-lb) and the lid temperature ran between 363 and 380K. The tank and discharge valve were wiped clean after each batch and the powder was screened to -100 mesh to remove any large chunks (there were roughly 16 g of +100 mesh per batch). A sample of powder fran each alloy canposition was mounted, polished. and examined metallographically to establish that sufficient alloying had been achieved. As shown in the photanicrographs in Figure 1, the powder particles appear to be quite hanogeneous. Although not shown in Figure 1, a fer powder particles were observed which had not been completely alloyed. Nevertheless. the attrition time was limited to 20 h in order to prevent caking of powder on the walls and bottom of the attritor. Once this problem develops. the pader continues to accumulate until it causes a motor stall or a fracture of sane of the stirring components.

(a) Operated for the U.S. Department of Energy by Battelle Memorial Institute under Contract DE-AC06-76RLO 1830.

Table 1. Compositions and maximum mesh sizes of starting powders

Powder	Composition	Mesh Size
Fe	99.5%	-100
Fe-Cr	74%Fe,26%Cr	-200
Fe-Ti	60%Fe,40%Ti	-100
W	99.9%	6 μm
V-Cr	75%V,25%Cr	-100
Y_2O_3	99.9%	40 nm

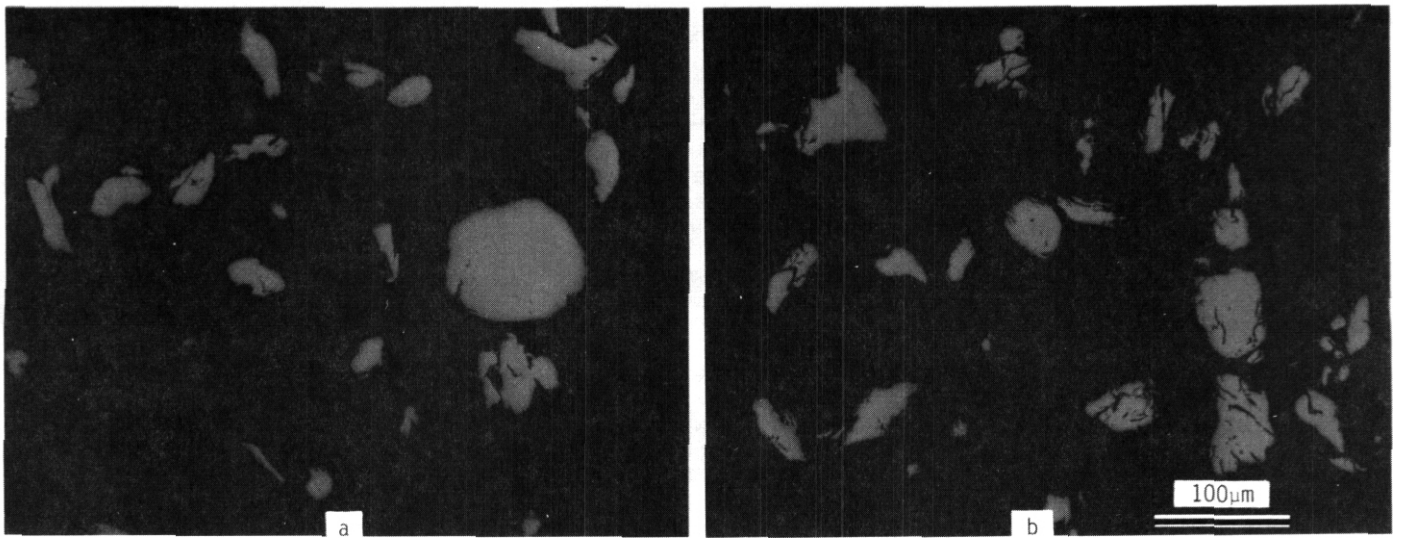

Figure 1. The 14Cr and 9Cr mechanically alloyed powder samples were mounted in molding compound, polished and etched (Vilella's reagent) to reveal a cross section of the particles. The 14Cr alloy is shown in (a) and the 9Cr alloy in (b).

After screening. the two batches of each canposition were combined in a v-cone blender for 15 min before consolidation. An attempt was made to cold isostatically press the pader at 400 MPa but did not result in sufficient green strength for handling. Hence. the hot isostatic press (HIP) consolidation was carried Out on loose powder. The HIP parameters and can material were determined fran trial runs using mild Steel or copper tubing for HIP cans. It was found that densities greater than 98% of theoretical could be achieved using the copper tubing at 1223K for 30 min at 200 MPa. Copper was also chosen for the extrusion billet HIP cans because the steel cans were too rigid to obtain full densification during trial runs using iron powder. The extrusion billets were given a second. higher temperature HIP treatment after removal of the copper can to help ensure full densification. This was done because of a concern about scaling the HIP parameters fran copper tubing to the larger size of the extrusion billets. Powder for the extrusion billets was poured through the evacuation stem of a 80-mm diameter x 100-mm length copper can with intermittent vibration to ensure a maximum packing density. After filling, the cans were evacuated and heated under vacuum to 673K where they were maintained for 16 h before sealing the evacuation tubes. Following evacuation and canning. the billets were HIPed at 1223K for 2 h at 200 MPa. After removal of the copper can. the billets were HIPed again at 1373K for 1 h at 200 MPa. They were then machined to dimension (63.5-mn diameter x 66 mm long) for extrusion. A calculation of the bulk density from the machined dimensions showed the billets to be 98% dense. assuming theoretical densities of 1.73 g/cc and 7.90 g/cc for the Fe-14Cr and Fe-9Cr alloys, respectively.

After soaking at 1422K for 2.25 h the billets were extruded at RMI Canpany of Ashtabula, Ohio. They were given a glass coating as a die lubricant and extruded to 19 mm in diameter with a ram speed of -1.27 m/min. The maximum ram pressure was 20.7 MPa for both alloys. After extrusion. the Fe-14Cr alloy had severe surface cracks over one-third of its length and the Fe-9Cr alloy had cracks over one-half its length. Figure 2 shows examples of each side of each of these bars. The alloys were shipped to PNL in the as-extruded condition wtth a recommendation that they be hanogenized for 20 h at 1273K. Table 2 shows the results of chemical analyses on samples of the extruded bars.

Discussion

The density. hardness. and microstructure of the alloys were monitored during the consolidation. extrusion. and hanogenization processes. Initial characterizations were done on test coupons HIPed separately from the extrusion billets. The reason for this was simply that there was not enough room in the HIP chamber for both an extrusion billet and a coupon. Figure 3 compares the microstructure of the two alloy coupons after the first and second HIP treatments. The most notable features are sane second phase particles that have been identified by energy dispersive x-ray analysis as Fe-. Cr-. Ti-. V-, and W- rich regions. They are most likely remnant precursor powder particles which escaped the mechanical alloying process. The distribution of these particles is better shown at lower magnification in Figures 4a and 4b. The Fe-. Cr-, Ti-. V-. and W- rich particles (identified in Figure 4a by chemical symbols) seem to appear in relative numbers proportional to the amount of master alloy added to the powder blend. Figure 4b shows the coupon microstructure after hanogenization. Note that the particles have almost entirely disappeared. Figure 5 is a ccmparison of the extrusions before and after homogenizing 20 h at 1273K. Before hanogenization. a few precursor particles remain with a fine dispersion of porosity. After hanogenization, the porosity becomes very prcminent. Table 3 summarizes the hardness and density data for the various stages of consolidation. extrusion. and hanogenlzation. Note that the density of the 14Cr coupon remains nearly constant fran the first HIP treatment through the hcmogenization. The density of the billet increases slightly after extrusion. The density of the 9Cr coupon, however. decreases with each successive high temperature exposure. Although the 9Cr density increases on extrusion, it drops to its original value after hanogenization. Also. the hardness of both alloys decreases after each high temperature excursion with the most dramatic drop occurring in the 9Cr extrusion after hanogenization. This sudden drop might be at least partly due to the changes in pore size and content. as discussed.

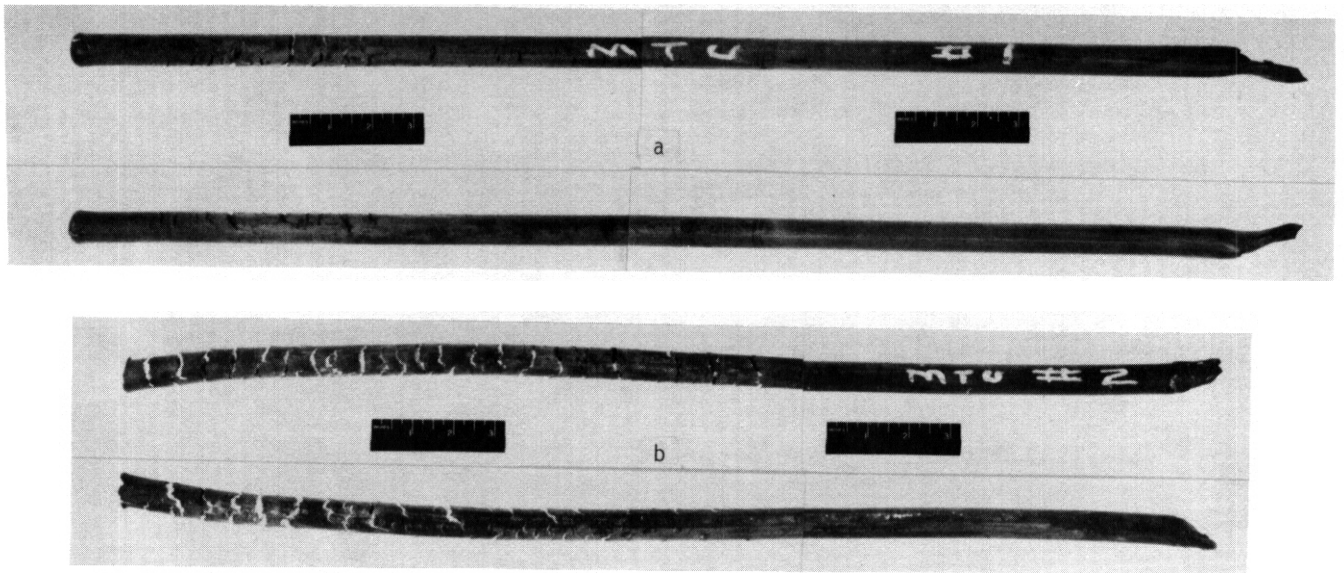

Figure 2. As-extruded bars Fe-14Cr (a) and Fe-9Cr (b) showing both sides of each bar at low magnification. Sufficient uncracked material is available for tube fabrication studies.

Table 2. Results of chemical analyses on as-extruded bar

Element	Fe-14Cr		Fe-9Cr	
	Measured	Stated	Measured	Stated
Cr	13.8	14.0	9.10	9.0
W	0.73	0.5	2.01	2.0
V	----	0	0.30	0.3
Ti	0.62	1.0	0.0	---
C	0.051	0	0.096	0.08
Y	0.23	0.20	0.23	0.20

In order to better understand the reason for the degradation in hardness in the 9Cr alloy with further hanogenization. a cooling rate experiment was performed on the 9Cr extruded bar to determine if a martensite transformation was operating and had any effect on properties. Three specimens were aged at 1100 C for 5 min and then cooled either by quenching in water. cooling in air or cooling in the furnace to 700 C (cooling took 1.7 h) and holding for two hours. Resulting hardness measurments are given in Table 4. Fran caparison of Tables 3 and 4, it can be shown that the hardness of the 9Cr alloy can be raised by suitable heat treatment procedures, but the hardness can also be reduced to values on the order of 20 R_C by furnace cooling. This suggests that the yttria is reacting with the carbon and being redistributed so that hardness is controlled by the martensite structure. Therefore, mechanical alloying benefits are probably not retained.

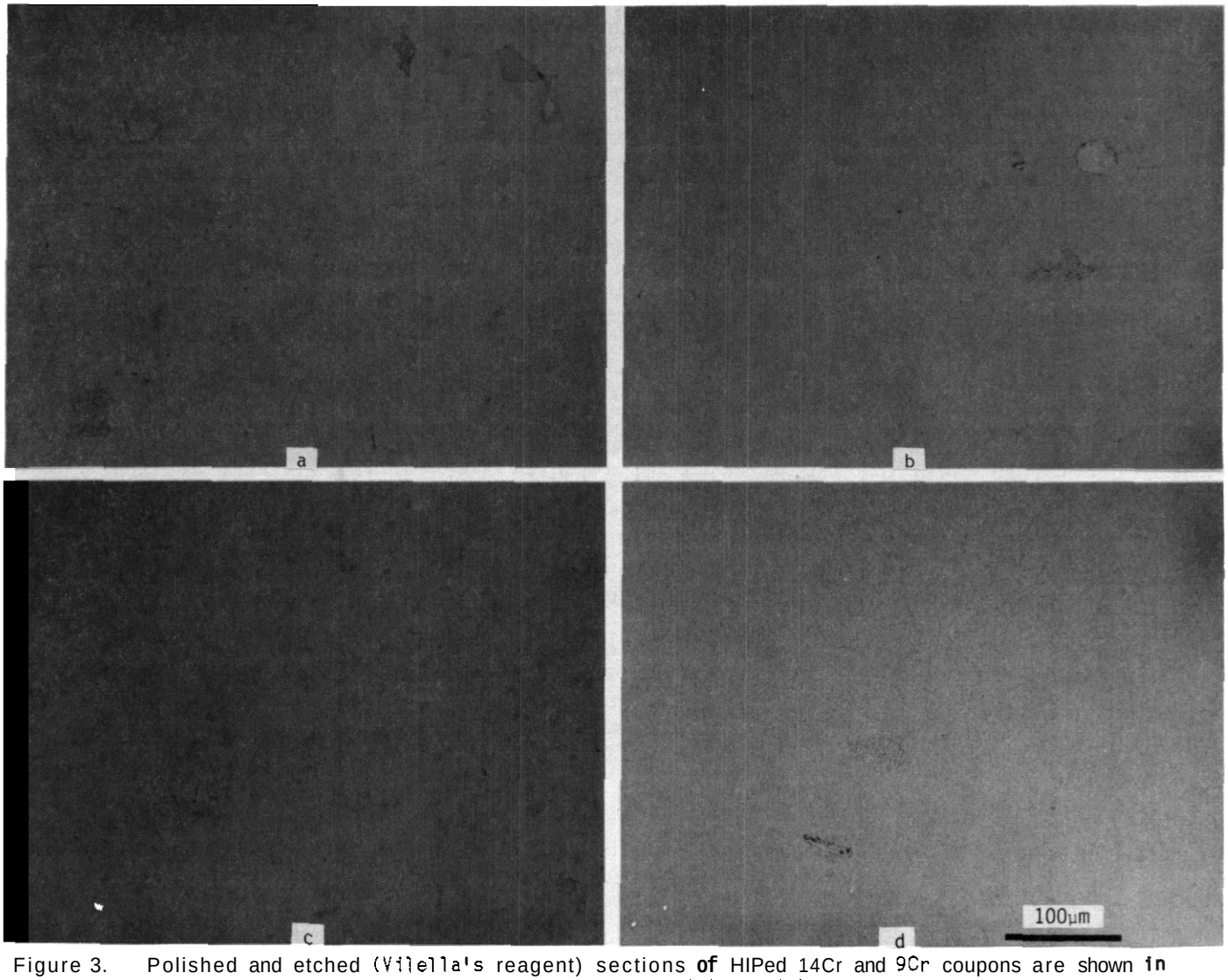

Figure 3. Polished and etched (Vilella's reagent) sections of HIPed 14Cr and 9Cr coupons are shown in (a) and (b). ReHIPed 14Cr and 9Cr are shown in (c) and (d). The most notable features are apparent remnant precursor particles.

Although the fabrication of extrusions fran the experimental mechanical alloys turned out quite well, there are several areas which could benefit fran some additional work. One area is the effect of a smaller batch size and extended milling times on the degree of mechanical alloying and the need for homogenization. The batch size used in this program corresponded to a 15:1 ball-to-charge ratio. The INCO patents on commercial alloys MA956 and MA957[2] refer to a 20:1 ball-to-charge ratio. The higher ratio would unfortunately mean that more batches would be required to process the same amount of powder. Another area in need of further study is the outgassing procedure used to evacuate the powder cans before HIPing. There is no reliable way of predicting, from theory. the temperatures at which various gas species will evolve during outgassing. We have found that residual gas analysis (RGA) is an effective technique for detecting small amounts of gas evolved during a vacuum heat treatment. This information can be used to establish an effective outgassing schedule ultimately leading to reduced porosity in the consolidated product. The additional work described should result in a major improvement in the homogeneity and quality of mechanically alloyed Fe-Cr extrusions.

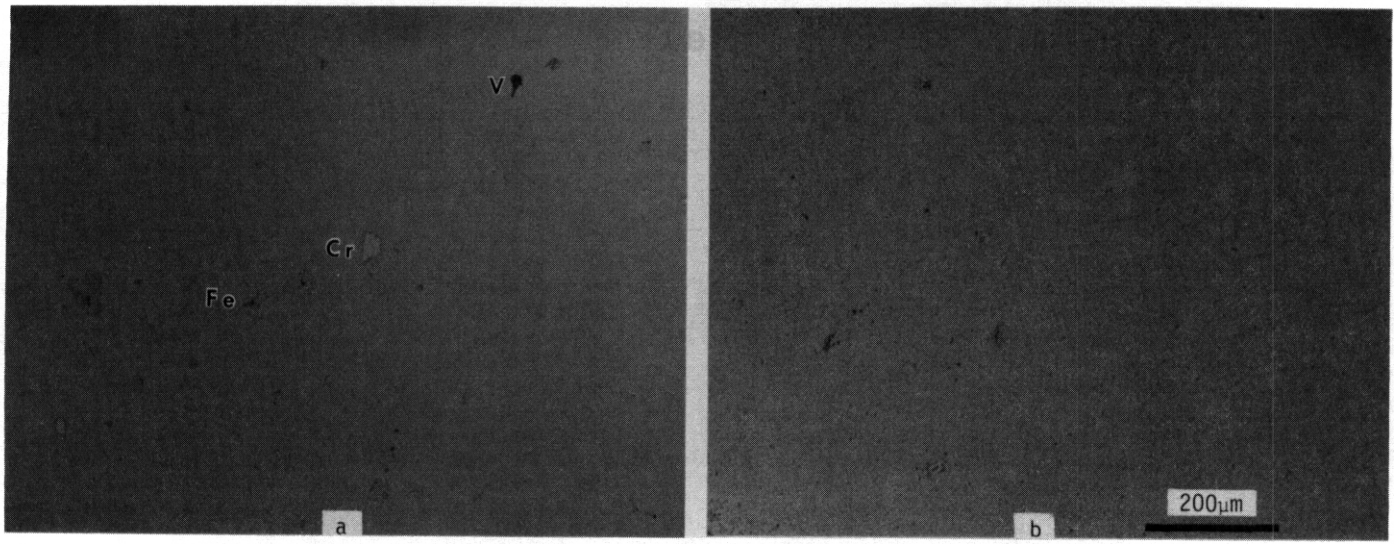

Figure 4. Lower magnification photomicrographs of 9Cr HIPed coupon In (a) and reHIPed and homogenized 9Cr In (b) show typical distribution of remant precursor pader particles.

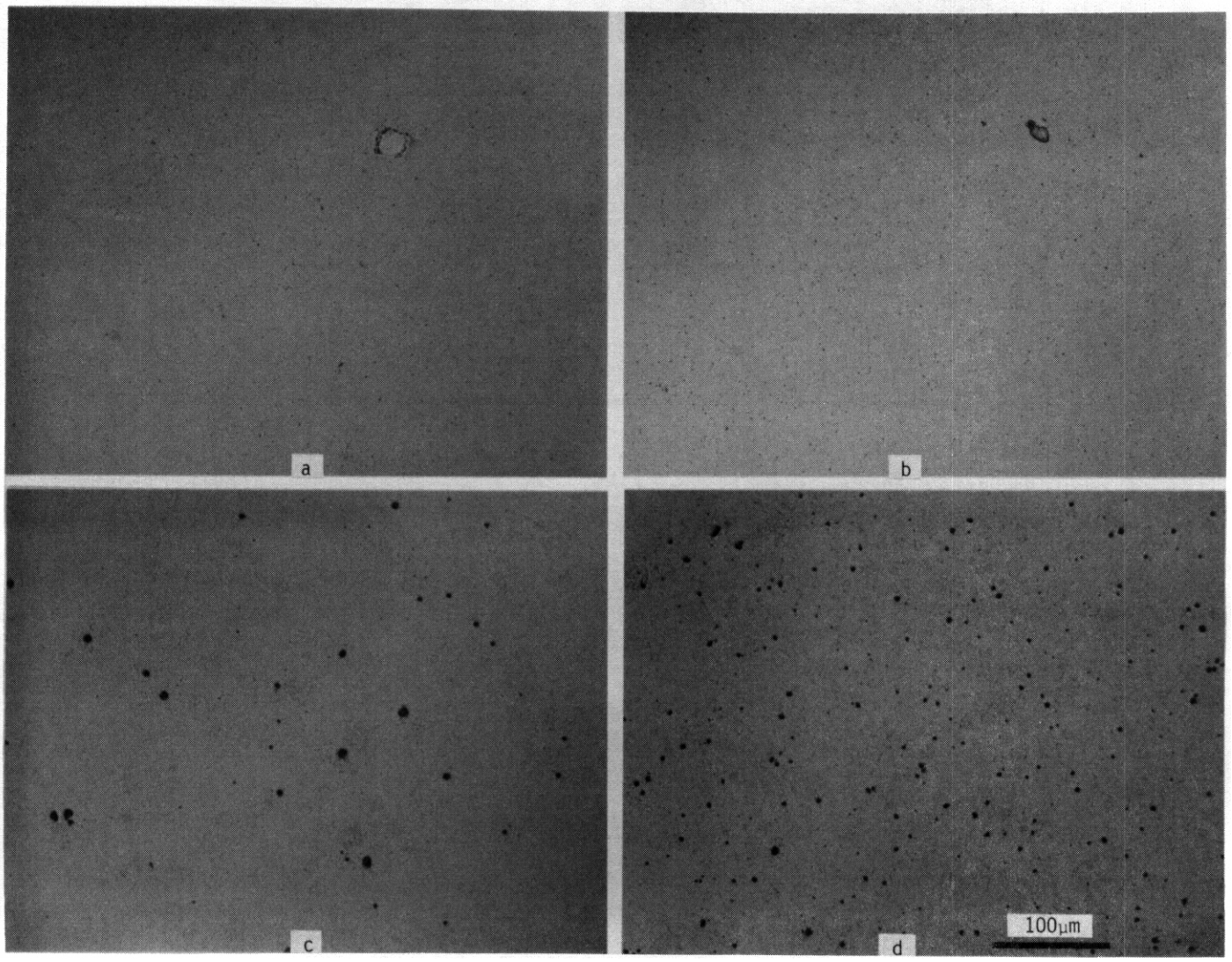

Figure 5. Microstructure of extrusions before hanogenization (a) and (b) and after hanogenization (c) and (d). The most obvious change after homogenization is the Increase in pore size.

Table 3. Summary of hardness and density data for the various stages of consolidation. extrusion, and homogenization

Condition	Alloy	Density (g/cc)	Hardness (R_C)
HIPed Coupon	14Cr	7.65	48.5
ReHIPed Coupon	14Cr	7.64	39.5
Homogenized Coupon	14Cr	7.64	37.9
HIPed Coupon	9Cr	7.80	49.4
ReHIPed Coupon	9Cr	7.76	42.2
Homogenized Coupon	9Cr	7.74	30.3
ReHIPed Billet	14Cr	7.61	----
Extrusion	14Cr	7.67	37.5
Homogenized Ext.	14Cr	7.66	36.3
ReHIPed Billet	9Cr	7.71	----
Extrusion	9Cr	7.79	32.9
Homogenized Ext.	9Cr	7.71	20.3

Table 4. Hardness as a function of cooling rate for the 9Cr alloy

Condition	Hardness (R_C)
Water quenched	44.5
Air cooled	42.2
Furnace cooled to 700/2h	19.2

CONCLUSIONS

Two low activation ferritic ODS alloys have been successfully manufactured using mechanical alloying processes and extruded into bar. One of the alloys, Fe-14Cr-1.0Ti-0.5W-0.25Y_2O_3, is considered worthy of further study as a candidate first wall material.

FUTURE WORK

Fabrication of two more. ODS alloys is planned for the next reporting period.

REFERENCES

1. D. J. Sherwood, A L. Ward, and G. D. Johnson. Nuc. Tech. 78, 83 (1987).

2. Cairns et al., U.S. Patents 3,837,930 (September 24, 1974) and 3,992,161 (November 16, 1976).

MICROSTRUCTURAL EXAMINATION OF HT-9 IRRADIATED IN THE FFTF/MOTA TO 110 OPA - D. S. Gelles (Pacific Northwest Laboratory)[a] and Akira Kohyama (University of Tokyo)

OBJECTIVE

The objective of this effort is to determine the applicability of martensitic stainless steels for first wall applications.

SUMMARY

HT-9 in two heat treatment conditions has been examined following irradiation at 420°C to 114 dpa. The irradiations were performed in the Fast Flux Test Facility Materials Open Test Assembly (FFTF/MOTA). Void swelling is found in both conditions, with swelling values as high as 0.9% in isolated regions. Voids show a wide range of truncation, between cubic and octahedral shapes. Void swelling appears to vary as a function of preirradiation heat treatment, whereas the dislocation structure and precipitation that developed during irradiation is unaffected. Quantitative microstructural measurments are in good agrement with results on similar simple alloys.

PROGRESS AND STATUS

Introduction

Martensitic stainless steels are receiving increased consideration as structural materials for fusion first wall applications. based in large part on good irradiation creep and swelling resistance properties In the temperature range 400 to 600°C.[1] The martensitic stainless steel for which the greatest irradiation effects data base exists is HT-9, of canposition 12Cr-1Mo-0.2C-WV. The present effort is intended to increase the data base by reporting on microstructural development for two heat treatment conditions of HT-9 following irradiation to 110 dpa at 420°C, the peak swelling tmperature for ferritic alloys.

On several occasions. HT-9 was previously examined for microstructural evolution following fast neutron irradiation. Gelles and Thomas[2] reported behavior following irradiation in the Experimental Breeder Reactor II (EBR-II) to 1.4 x 10^{22} n/cm^2 or 70 dpa. They noted that dislocation loops and tangles formed in the tmperature range 400 to 450°C, but no voids formed. However. helium bubbles were found at temperatures as low as 400°C, and precipitation in the form of a high density of equiaxed particles. identified as chromium-rich α' and nickel silicide Gphase. was recognized as the cause of irradiation hardening. Also of note was the observation of molybdenum- containing intermetallic chi phase at grain boundaries.

Void swelling was identified in HT-9 specimens irradiated In the High Flux Isotope Reactor (HFIR)[3,4] at 400°C to damage levels of 36 or 39 dpa. The swelling was low, less than 0.1%, whereas canpanion specimens irradiated in EBR-II were found to contain no void swelling. The results were sufficiently comprehensive to rule out the possibility of heat-to-heat variations. and the effect was tentatively ascribed to a helium effect on void nucleation. based on differences in helium production in EBR-II and HFIR.

More recently. however. it has been shown that void swelling occurs in HT-9 following irradiation in FFTF at 420°C to 34 dpa.[5] Microstructural examination reveal'ed several small. facetted cavities typical of irradiation-induced voids in ferritic alloys. and equiaxed precipitates of both α' and Gphase type. Since helium generation is low in FFTF. it is apparently not necessary to have significant amounts of helium present for void swelling to occur in HT-9. Instead. it could be argued that the behavior appeared to be different in different reactors.

Most recently, Maziasz and Klueh[6] have summarized comparisons of results of microstructural examinations in HT-9 following irradiation in HFIR and FFTF. Their experiment included variation in the nickel content in order to provide a larger variation in helium production. Very few voids were found following irradiation in FFTF to 47 dpa at 407°C, whereas abundant void formation was found in the same steels following irradiation in HFIR at 400°C to 37 dpa. It was concluded that increases in He/dpa ratio cause abundant increases in the formation of large bias-driven voids. The microstructures were otherwise similar. with little difference observed in dislocation structure or precipitate formation. An alternate interpretation of precipitate development during neutron irradiation was proposed. me abundant dispersions of fine precipitate particles that formed both in HFIR and FFTF at 400°C were identified as M_6C (n), but with an unusual canposition that is rich in silicon, rich in chromium. has minor levels of iron. molybdenum and/or niobium and vanadium. but little or no nickel. The possibility of the presence

(a) Operated for the U.S. Department of Energy by Battelle Memorial Institute under Contract DE-AC06-76RLO 1830.

of G phase was ruled out. However, it was noted that more work was needed to positively identify the phase.

Therefore. HT-9 irradiated in FFTF can be expected to show sane void swelling. but it is of considerable interest to determine the degree of swelling at doses in excess of 100 dpa. Questions remain concerning precipitate development. Also, it is of interest to compare the microstructures with those produced under dual-beam charged particle irradiation to high dose. 7

Experimental procedures

Specimens of the fusion heat of HT-9 (heat 9607R2)[8] were included in the MOTA 1B irradiation test matrix in two heat treatment conditions, condition RF: 1000°C/20h/AC to RT + 1100°C/5m/AC + 700°C/2h/AC; and condition RH: 1050°C/5m/AC + 760°C/30m/AC. The purpose of the heat treatment variation was to consider consequences of improved hanogenization (1000°C/20h), WC dissolution (1100°C/5m) and a high strength tempering condition (700°C/2h) on microstructural evolution in canparison to a more standard condition.

Duplicate specimens of each of the two conditions in multiples of five were irradiated as 0.008 in. thick Transmission Electron Microscopy (TEM) disks side by side in TEM packet FL. The packet was of weeper design in a weeper canister so that specimens were in contact with reactor sodium. Canpanion specimens in the packet were low activation ferritic alloys. E M packet FL began irradiation in MOTA 1B (FFTF cycle 4) in early 1984 in position 1E4 at an average temperature of 407°C to 9.8 dpa. In MOTA 1C (FFTF cycles 5 and 6), it was transferred to position 2C4 at an average temperature of 426°C to a total dose of 43 dpa. For MOTA 1D (cycles 7 and 8), packet FL was located in position 2C2 at an average temperature of 420°C and accumulated a total dose of 73 dpa. Finally. in MOTA 1E (FFTF cycle 9) it remained in position 2C2 at an average temperature of 420°C and accumulated a total dose of 114 dpa. Therefore. the specimen tmperature varied between about 407 and 426°C. but will be reported as the average. 420°C.

Following irradiation, the TEM packet was opened and specimens were removed and sorted to provide specimens both for microstructural examination and density measurement. Reported here are results of microstructural examination by TEM and results on precipitate canposition analysis using analytical electron microscopy of precipitate extraction replicas. Procedures for preparation of specimens for electron microscopy have been previously described.[9] Microscopy was performed on a 120keV scanning transmission electron microscope. and canpositional analysis used a standard x-ray detector coupled to a canputer analyzer.

Results

The microstructures of conditions RF and RH were found to be similar. indicating that heat treatment variations did not have a major effect on a microstructural scale. Figure 1 provides canparison of specimen conditions RF and RH at low magnification. Both conditions have well developed martensite lath structures decorated with carbide precipitate of similar size. The dislocation structure has relaxed into better defined subgrain boundaries in the RH case, but other differences are difficult to demonstrate due to area to area variability in a given sample.

The microstructures of specimens RFFL and RHFL irradiated at 420°C to 114 dpa were typical of irradiated HT-9 that had begun to swell due to void growth. The martensite lath structures were retained. but irradiation had resulted in a rearrangement of the dislocation structure. precipitation of a high density of small equiaxed particles, and formation of a non-uniform distribution of facetted cavities within martensite laths.

An example of the structure of specimen RFFL at low magnification is shown in Figure 2. The martensite laths are clearly defined. many decorated with blocky precipitate. Several regions appear in void contrast so that voids appear as white features with well defined facetted surfaces. These regions also show darker equiaxed features typical of precipitates that form in irradiated HT-9 at this temperature. It is possible to convince oneself that two types of equiaxed precipitates are present. one sanewhat larger and darker than the other. Other regions appear darker in contrast and do not reveal the presence of voids. These regions are in strain contrast and show linear features due to dislocation development.

The microstructure developed in specimen RFFL is shown at higher magnification in Figure 3. Figure 3 provides canparison of the same region of the specimen in a) void contrast. b) and c) dislocation contrast near a (001) orientation using bright field $\bar{g}$=110 and dark field $\bar{g}$=200 respectively, and d) precipitate dark field contrast using $\bar{g}$=1/3 <222>. The thickness of the foil in this region is approximately 220nm. In Figure 3a, several void shapes can be identified. Voids with haloes are voids that intersect the foil surface (easily demonstrated by stereo examinations), the haloes forming as a result of electrochemical attack. These voids have had their shapes altered during specimen preparation. The remaining voids have several projected shapes ranging fran squares in two orientations. to truncated shapes approaching octagons. to circular projections. Therefore. void shape varies in this condition. the shapes corresponding to truncated cubes and octahedra.

In Figures 3b and c, many examples of dislocation loops and line segments can be identified. Canparison of these two micrographs provides sufficient information to evaluate Burgers vector distributions. Figure 3b in 110 dislocation contrast reveals 2/3 of the dislocations with a<100> Burgers vectors and half the

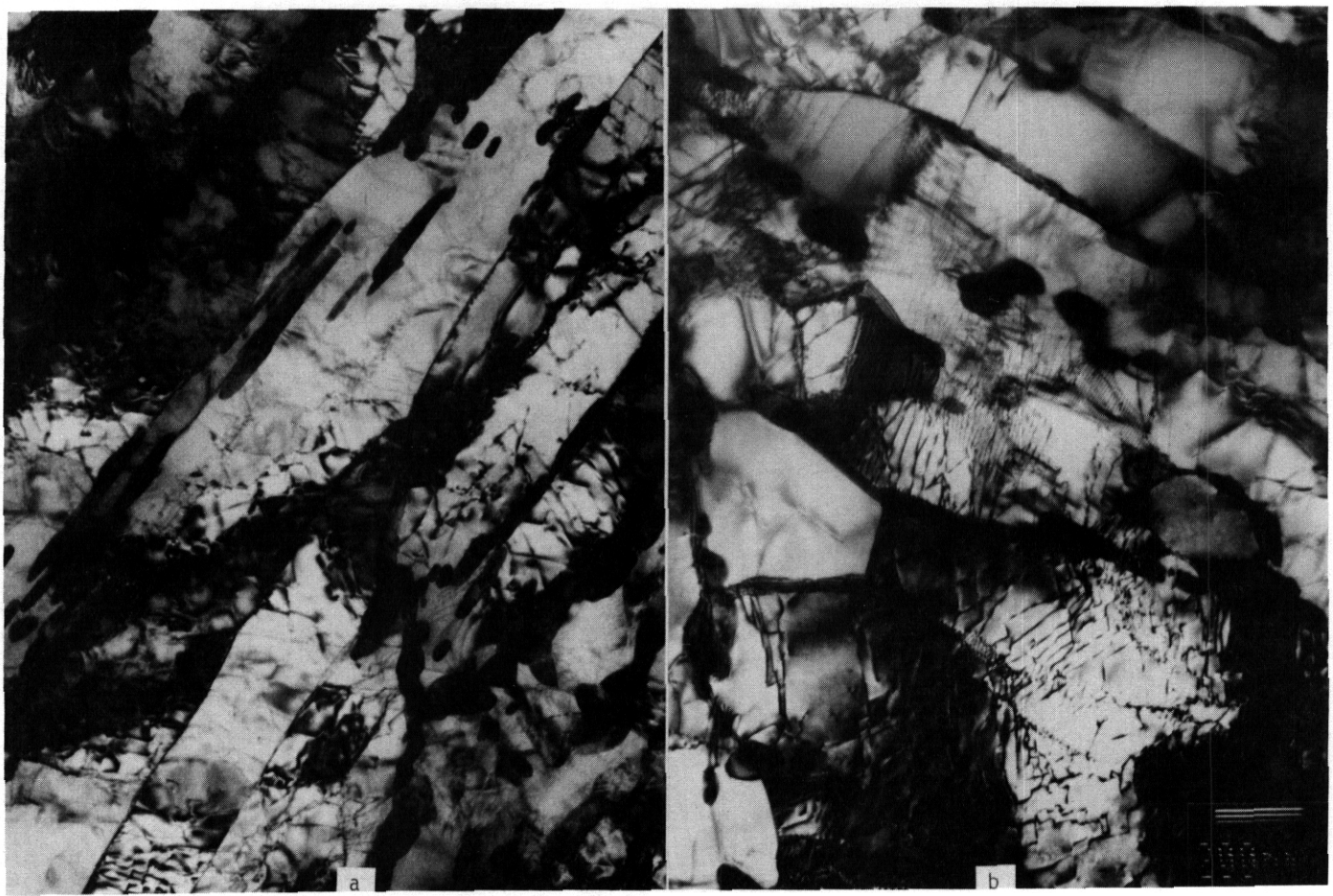

Figure 1. Comparison of the microstructure of a) heat treatment condition RF and b) heat treatment condition RH prior to irradiation at low magnification.

dislocations with a/2 <111> Burgers vectors. whereas Figure 3c shows all a/2 <111> Burgers vectors but only a third of the a<100> Burgers vector possibilities. From this comparison, it can be shown that only a few a/2 <111> dislocation line segments are present. The loops in Figure 3b elongated in the horizontal direction are of type a[010]. Therefore. most of the dislocations present are of a<100> type. As a consequence, void development probably is due to growth of a<100> loops.

The precipitate dark field image shown in Figure 3d reveals two size distributions of precipitates. These are the precipitates that have been identified as G-phase by Gelles and Thomas[2] and as η by Mazlasz and Klueh.[6] Insufficient information was obtained in the present work to differentiate between these possibilities. However. comparison with the precipitate images of Figure 3a demonstrates that an intermediate size predominates In void contrast imaging conditions. The particles of Intermediate size probably correspond to α', the chranium-rich, body-centered cubic phase. The α' phase is difficult to image in steels due to its cube-on-cube orientation relationship. and generally appears only as a surface feature in void contrast imaging conditions. Therefore. α' is probably present at a higher number density than the phase imaged in Figure 3d.

Specimen RHFL appeared similar to specimen RFFL. Figure 4 shows a region near a $(\bar{1}10)$ foil orientation in a) void contrast. b) dark field $\bar{g}$=110 dislocation contrast and c) precipitate dark field contrast. Several void shapes are present. the precipitates imaged in dark field are similar in size to those in specimen RFFL, and the dislocation structure includes dislocation line segments and loops. Because the foil is in a different orientation. the a<100> loops are less steeply inclined. making them appear more circular. The Burgers vector distribution was not determined for this condition.

Quantitative measurements based on stereographic thickness measurenents were made for void swelling. dislocation density. and precipitate volume fraction as indicated by dark field imaging. Because of the nonuniform distribution of void swelling, several areas were analyzed. The results. given in Table 1, include void volume, void mean diameter. void number density. dislocation loop number density, loop line length per unit volume, total dislocation line length per unit volume based on $\bar{g}$=110 images. precipitate volume fraction, number density and mean particle sire based on precipitate dark field images in Figures 3d and 4c. The results indicate that void swelling is higher in the RHFL condition than the RFFL condition as a result of higher void densities. but that most other microstructural details are very similar. The values of welling measured in specimen RFFL varied from 0.24 to 0.701, whereas the values for RHFL were



Figure 2. Low magnification example of microstructure in specimen RFFL Irradiated at 420 C to 114 dpa.

Table 1. Summary of void. dislocation. and precipitate quantitative microstructural measurements

Spec. I.D.	Voids			Dislocations			Precipitates		
				LOOPS		line			
	ΔV/V	d	# density	# density	disl. dens.	length	fraction	density	d
	(%)	(nm)	(/cm^3)	(/cm^3)	(cm/cm^3)	(/cm^2)	(%)	(/cm^3)	(nm)
RFFL	0.24	20.2	5.9×10^{14}						
	0.45	18.1	1.30×10^{15}						
	0.41	18.1	1.29×10^{15}	5.1×10^{14}	4.3×10^{9}	9.8×10^{9}			
	0.70	20.8	1.44×10^{15}						
							0.32	8.7×10^{15}	6.9
RHFL	0.78	20.4	1.82×10^{15}						
	0.91	20.7	2.09×10^{15}			1.5×10^{10}	0.32	9.2×10^{15}	7.0

0.78 and 0.91%. Although it is possible that this difference may not be statistically meaningful. It suggests that variations in heat treatment may result in swelling differences. Density measurements are expected to validate this point. Of particular note is the fact that heat treatment does not appear to alter precipitation behavior (be It Gphase or n); volume fraction, number density. and mean diameter are unchanged.

Results of compositional analysis of particles on extraction replicas are provided in Table 2. The results indicate that $M_{23}C_6$ compositions are changed little as a result of irradiation to 110 dpa at 420°C. Indications of Mo rich Chi phase are indicated and a high Cr phase. containing Mn and not yet clearly identified. was found in RFFL.

Discussion

This work has shan that HT-9 can develop void swelling that approaches one percent in isolated regions at fast neutron irradfatfon doses of 110 dpa. It has previously been shan that swelling rates can be as hlgh as 0.06%/dpa in simple ferritic alloys,[10] and the levels found in the present work can be shan

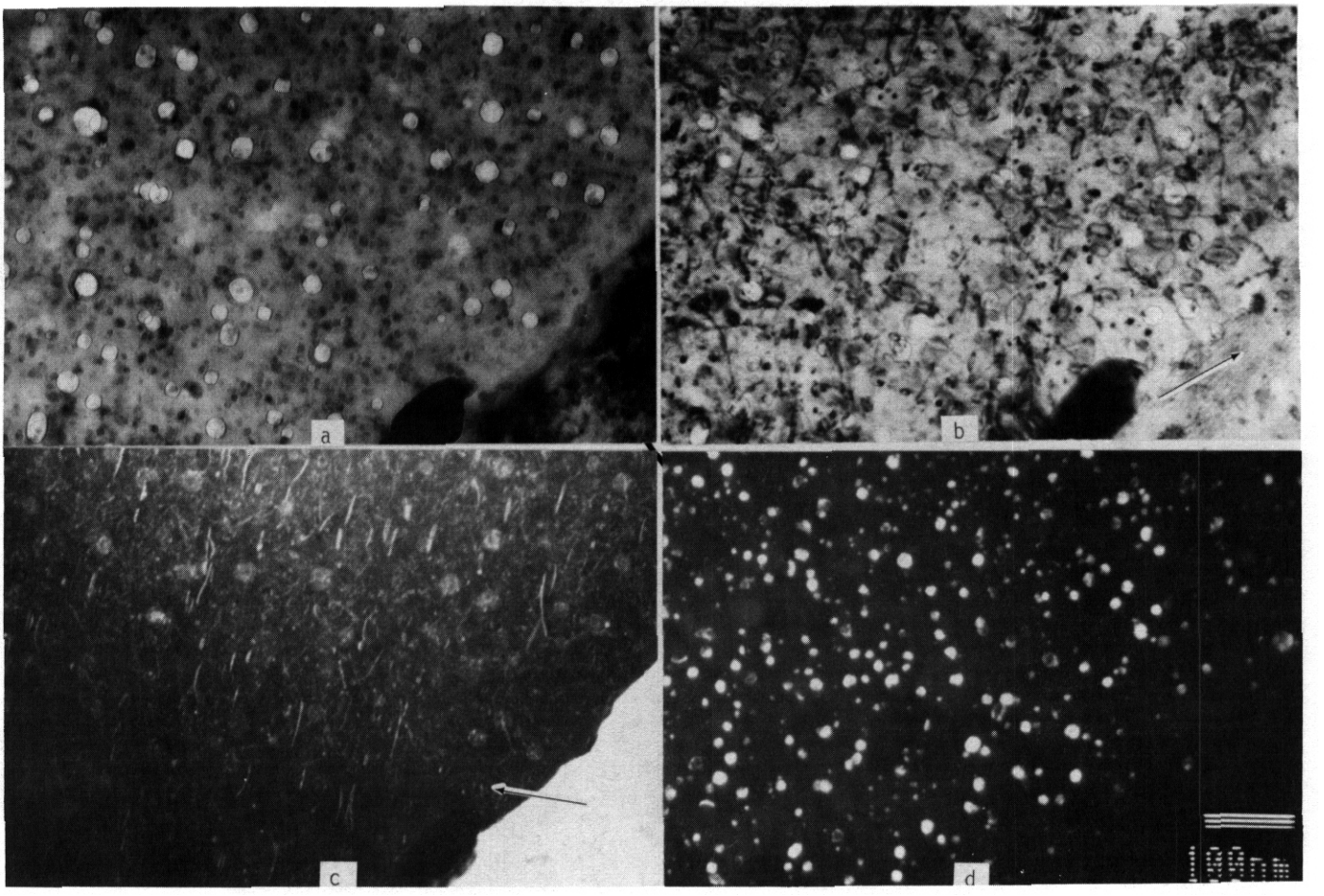

Figure 3. Comparison of the same area of specimen WFL in a) void contrast. b) bright field g=110 dislocation contrast. c) dark field $\bar{g}$=200 dislocation contrast and d) dark field $\bar{g}$=1/3 <222> precipitate contrast.

Table 2. Canpositions of precipitate particles extracted fran HT-9 specimens

Sample Identity	Composition (wt%) Fe	Cr	Mo	V	Si	Mn	Ni	W	No. Measured	Identification
RF	27-31	56-62	7-8	2-4	1-3	0-1	0-2		6	$M_{23}C_6$
RFFL	25-31	59-68	5-7	0-1	0-2	0-5	--	0-6	13	$M_{23}C_6$
	23-26	62-70	--	--	--	7-12	--		2	η or a' ?
	24	58	lo	--	--	8	--		1	Chi ?
RHFL	25-31	54-64	4-7	0-4	1-4			0-3	4	$M_{23}C_6$

to be in accord with simple ferritic alloy behavior. A swelling rate of 0.015%/dpa can be estimated for 0.9% swelling between 50 and 114 dpa. The void densities found in HT-9 are in good agrement with observations in Fe-12Cr binary alloys,[11] but the dislocation densities observed appear to be somewhat lower. In the binary alloys. a<100> dislocation line length was found to be as high as 4×10^{10} cm/cm^3 following irradiation in FFTF at 431°C to 15 dpa and swelling levels 0.1 to 0.3%.[11] This observation suggests that the presence of nearby lath boundaries may be suppressing the dislocation density. Nonetheless. the present microstructural observations indicate that swelling rates in HT-9 may approach those in simpler alloys. Higher dose experiments are needed to determine the actual steady state swelling rate.

The present results also indicate that variations in heat treatment procedures can alter void swelling response. but. surprisingly. precipitation that develops during irradiation is unaffected. Swelling is found to be sanewhat greater in the heat treatment condition that promotes greater toughness but lower strength. This is due to higher void densities: dislocation densities are slightly higher also. Explanations for why void and dislocation densities would be Increased under these conditions are not

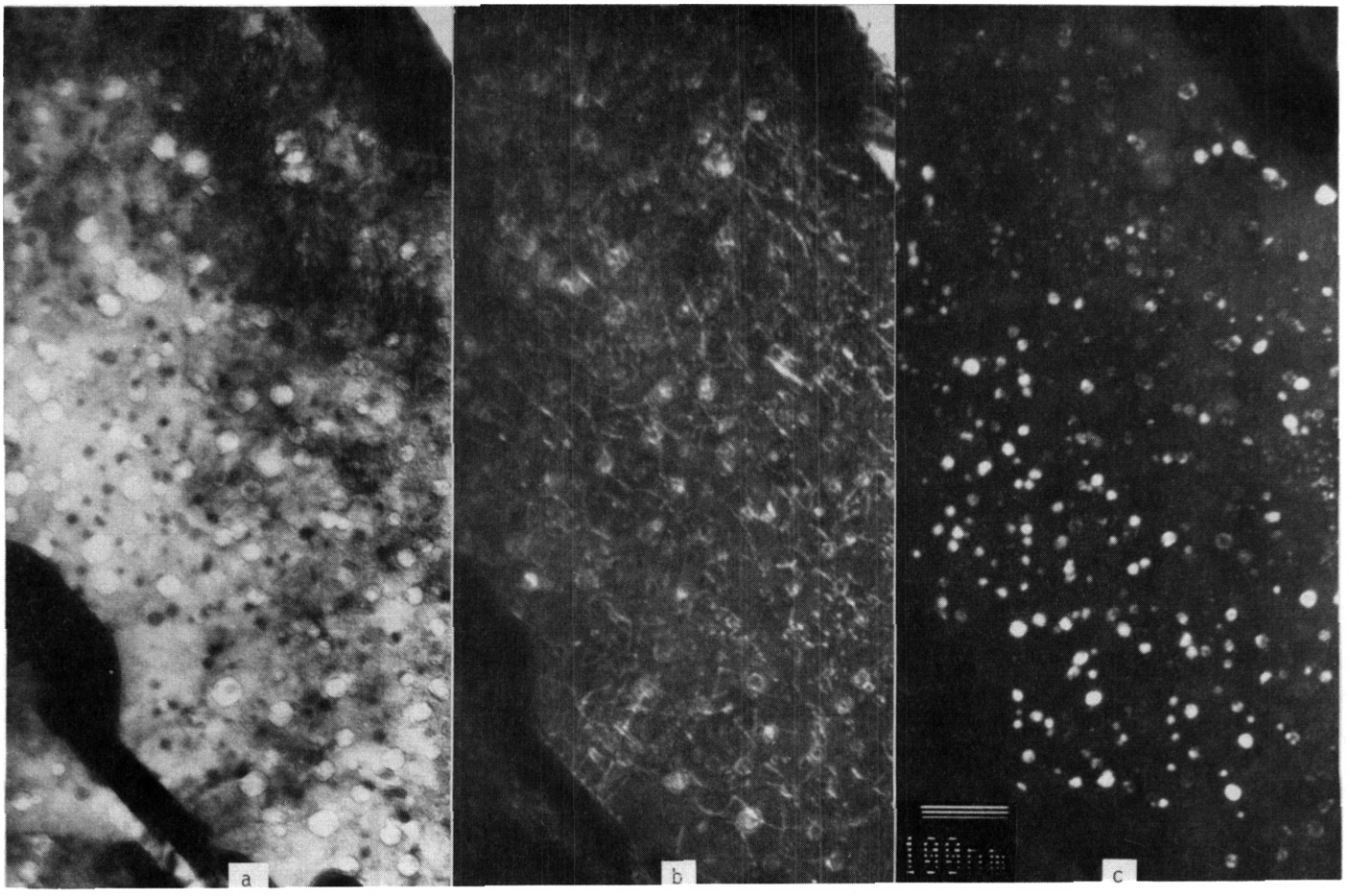

Figure 4. Comparison of the same area ot specimen HHFL Irradiated at 420 C to 144 dpa in a) void contrast, b) dark field $\bar{g}$=110 dislocation contrast and c) dark field $\bar{g}$=1/3 <222> precipitate contrast.

apparent. If precipitation that forms during irradiation is unaffected by variations in heat treatment. then improvements to fracture toughness in irradiated steels may not be possible by variations in preirradiation heat treatment.[12] Efforts to improve postirradiation fracture toughness should instead be directed toward composition control.

Canparison of the present results with those obtained during dual-beam charged particle irradiation[7] provides the following observations. Irradiation in FFTF produced significantly higher levels of swelling than did dual-beam irradiation. 0.14% at 100 dpa for the former versus as high as 0.9% in the FFTF irradiation. Void shape is found to vary in both cases. (See figure 3 of reference 7.) Therefore. it can be assumed that solute segregation to void surfaces occurs In both irradiation environments. However. no evidence was found for formation of precipitate particles during dual-beam irradiation. It is often found that higher damage rates do not promote precipitation and swelling to the same extent as in low damage rate irradiations. Therefore. in those materials where precipitation that formed during irradiation plays a role in microstructural development, care must be taken in interpreting the results of high damage rate irradiation.

CONCLUSIONS

Specimens of HT-9 in two heat treatment conditions have been examined by TEM following irradiation in the FFTF/MOTA at 420°C to 114 dpa. The results show that swelling in HT-9 can be as high as 0.9% in localized regions. and that the level of swelling observed can be affected by preirradiation heat treatment. However. the precipitates formed during irradiation were found to be unaffected by heat treatment and therefore efforts to control postirradiation mechanical properties by suitable heat treatment may not work.

FUTURE WORK

This work will be continued when specimens irradiated to a higher dose become available.

REFERENCES

1. D. S. Gelles, "Effects of Irradiation on Ferritic Alloys and Implications for Fusion Reactor Applications," J. Nucl. Mater., 149, 192-199 (1987).

2. D. S. Gelles and L. E. Thanas. "Effects of Neutron Irradiation on Microstructure in Experimental and Commercial Ferritic Alloys." Proceedings of: Topical Conference on Ferritic Alloys for Use in Nuclear Energy Technologies, J. W. David and 0. J. Michel. Eds., AIME. Warrendale, PA. 1984, 559-568.

3. J. M. Vitek and R. L. Klueh, "Microstructure of HFIR-Irradiated 12Cr-1MoVW Ferritic Steel." Ibid. 551-558.

4. D. S. Gelles. "Microstructural Comparison of HT-9 Irradiated in HFIR and EBR-II." Alloy Development for Irradiation Performance Semiannual Progress Report for the Period Ending March 1985, DOE/ER-0045/14, 129-136.

5. C. Y. Hsu, D. S. Gelles. and T. A. Lechtenberg. "Microstructural Examination of 12% Cr Martensitic Stainless Steel After Irradlation at Elevated Temperatures." Radiation-Induced Changes in Microstructure: 13th International Symposium (Part 1), ASTM STP 955. F. A. Garner, N. H. Packan. and A. S. Kumar. Eds., ASTM. Philadelphia. 1987. 545-559.

6. P. J. Maziasz and R. L. Klueh. "Void Formation and Helium Effects in 9Cr-1MoVNb and 12Cr-1MoVW Steels Irradiated in HFIR and FFTF at 400°C," to be published in the proceedings of the 14th International Symposium on the Effects of Radiation on Materials. held June 27-29. 1988 in Andover. MA.

7. K. Asano. Y. Kohno. A. Kohyama, and G. Ayrault, "Microstructural Evolution of HT9 Under Dual-Beam Charged Particle Irradiation." J. Nucl. Mater. 155-157, 912-915 (1988).

8. T. A. Lechtenberg. "The Procurement and Characterization of the Electroslag Remelted Fusion Program Heat of 12Cr-1Mo Steel," Ibid reference 4, DOE/ER-0045/8, 3/1982, 363-369.

9. D. S. Gelles and L. E. Thanas. "Microstructural Examination of HT-9 and 9Cr-1Mo Contained in the AD-2 Experiment." Ibid reference 4, DOE/ER-0045/8, 12/1982, 343-361.

10. D. S. Gelles and R. L. Meinecke Ermi, "Swelling in Simple Ferritic Alloys Irradiated to High Fluence." Ibid reference 4, DOE/ER-0045/11, 7-9/1983, 103-107.

11. D. S. Gelles. "Microstructural Examination of Fe-Cr Binary Ferritic Alloys Following Irradiation to 15 dpa in FFTF," Damage Analysis and Fundamental Studies Quarterly Progress Report for the period 10-12/1985, DOE/ER-0046/24, 10-12/1986, 43-56, to be published in the ASTM 14th Symposium on the Effects of Radiation on Materials.

12. E. A. Little. O. R. Harries and F. B. Pickering. "Sane Aspects of the Structure-Property Relationships in 12%Cr Steels," Ferritic Steels for Fast Reactor Steam Generators, S. F. Pugh and E. A. Little, Eds., (BNES, London, 1978) 136-144.

IRRADIATION CREEP OF FERRITIC (AND OTHER BCC) ALLOYS

R. J. Puigh (Westinghouse Hanford Company) and D. S. Gelles (Pacific Northwest Laboratory)(a)

OBJECTIVE

The objective of this work is to determine the effect of irradiation on creep deformation behavior of ferritic alloys. based in part on a review of the literature. to aid in determining of the applicability of martensitic stainless steels for first-wall applications. It is intended for publicatton as part of a special volume on "Irradiation Creep" in Diffusion and Defect Data. Solid State Data.

SUMMARY

Ferritic/martensitic alloys are now being used as structural materials in several reactor systems and are being considered as structural materials for future fusion reactors. The irradiation creep response of body centered cubic (BCC) alloys has been studied for over 20 years; however, only in the last 10 years has the effort narrowed to concentrate on the irradiation creep behavior of ferritic/martensitic alloys. This paper reviews our current understanding of irradiation creep behavior in ferritic alloys by reviewing the literature and reporting new data on the topic.

INTRODUCTION

The current high interest in the irradiation creep behavior of ferritic/martensitic alloys is demonstrated by the large number of recent review papers which have included a discussion of the subject.[1-7] These publications have been stimulated by the increasing use of ferritic and martensitic steels as structural materials in liquid metal fast breeder reactors and by the consideration of these alloys for fusion reactor first walls. Much of the attraction of these steels lies in their good irradiation creep and swelling resistance properties in the temperature range 400 to 600 C. In concert with this increased interest, the number of papers that provides irradiation creep results for ferritic alloys is also increasing.[8-28] Therefore, it is appropriate to review this body of knovledge in order to better understand the underlying behavior.

Although irradiation creep data on ferritic alloys have been collected and studied for over 10 years, the metallurgical processes involved are not nearly as well understood as in the austenitic class of alloys. Most of the discussion of irradiation creep in ferritic alloys has been phenomenological; little attention has been given to the associated microstructural evolution. The present review will therefore be primarily a phenanenological treatise.

Irradiation creep measurements have been performed on many ferrous metals including pure iron. martensitic steels, and a precipitation-strengthened ferritic steel.[8-28] A listing of the ferrous alloys for which irradiation creep data exist is provided in Table 1, giving composition and pre-irradiation heat treatment information. From Table 1, it can be seen that several experiments have been performed on the same material with different heat treatment, or on similar compositions, providing the possibility of comparison to determine the effect of varying heat treatment and/or composition. Some effort has been made to develop oxide dispersion strengthened (ODS) ferritic alloys,[8, 14, 20] predominantly in support of the Liquid Metal Reactor programs in several countries. However, this class of alloys will be covered briefly in this review.

SUMMARY OF THE LITERATURE ON CREEP FOR NEUTRON IRRADIATION

Publication of irradiation creep data for ferritic alloys began in 1979, with data reported fran researchers at three laboratories during the Conference on Irradiation Behavior of Metallic Materials for Fast Reactor Core Components in Ajaccio Corsica: Vandermeulen et al. from Centre d'Etude de l'Energie Nucleaire (S.C.K./C.E.N.), Belgium,[8] Herschbach et al. fran Karlsruhe, West Germany,[9] and Little et al. from Harwell. England.[1] The Belgian effort compared ODS ferritic alloys with a ferritic alloy of similar composition, a martensitic alloy. and a duplex (martensite/ferrite) alloy. Specimens were long pressurized tubes. 5.75 mm in diameter with 0.37 mm wall thickness, Irradiated in Rapsodie. a fast reactor. in contact with slowly flowing reactor sodium. Maximum dose was 3.7 x 10^{22} n/cm^2 (E > 0.1 MeV). or about 18 dpa, and temperatures were in the range from 405 to 502°C. The results shoved deflections due to irradiation creep of 11 μm or less for stress levels of 150 MPa and 29 μm or less at 200 MPa. Because the irradiation creep was so small. it was difficult to interpret the results definitively. However, it could be shown that the results were reproducible and that ODS alloys were significantly more resistant irradiation creep than martensitic or duplex alloys.

(a) Operated for the U.S. Department of Energy by Battelle Memorial Institute under Contract DE-AC06-76RLO 1830.

Table 1. Irradiation creep data base on ferritic/martensitic alloys. with compositions and heat treatments of the alloys studied.

	Composition, wt%									
Alloy	Fe	Cr	Mo	W	V	Nb	C	Test Temp., (°C)	Heat treatment*	Ref.
EM12	87.3	9.5	2.0	--	--	--	0.1	414-489	not given	8,14
1.4914	84.8	11.5	0.7	--	0.2	0.1	<0.2	405-502	not given	8,14
OT02	79.9	13	1.5	--	--	--	<0.1	428-481	not given	8,14
DY005	81.4	13	1.5	--	--	--	<0.1	436-496	not given	8,14
HT-9	84.4	12.0	0.99	0.52	0.30	--	0.20	540, 595	1052/30m/AC+780/2.5h/AC	10,12
403	86.6	12.5	--	--	--	--	0.1	67, 300	solution treated	11
410	86.0	13	--	--	--	--	0.1	67, 300	solution treated	11
AIS14140	97.2	1.0	--	--	--	--	0.4	67, 300	solution treated	11
1.4914	85.7	11.1	0.66	--	0.33	0.28	0.17	400-600	1075/30m/OQ+675/2h/AC	15,18,21
HT-9	84.8	11.8	0.94	0.52	0.24	--	0.17	443-572	1038/5m/AC+760/30m/AC	16
9Cr-2Mo	87.9	9.0	1.99	--	--	--	0.06	443-572	1050/30m/AC+760/1h/AC	16
2¼Cr-1Mo	95.7	2.2	0.95	--	--	--	0.09	443-572	900/30m/AC+700/1h/AC	16,22,23
HT-9	84.4	12.1	1.03	0.52	0.33	--	0.21	432, 540	1052/30m/AC+780/2.5h/AC	17
EM12	88.2	10.5	2.3	--	0.4	0.55	0.1	400-440	1050-1125/AC+750	19
HT-9	85.1	11.8	0.94	0.52	0.24	--	0.17	380-570	1038/5m/AC+760/30m/AC	22
9Cr-1Mo	89.0	9.0	0.94	--	0.19	0.17	0.10	380-570	1038/5m/AC+760/1h IAC	22
HT-9	84.5	12.1	1.04	0.45	0.28	--	0.20	400-540	1038/5m/AC+760/2.5h/AC	25
9Cr-1Mo	89.4	8.6	0.89	<.01	0.21	0.07	0.08	400-540	1038/5m/AC+760/1h/AC	25
D57	82.2	11.1	5.14	--	0.40	--	0.06	425	1025/5m/AC+25%CW	unpublished
F5	98.5	<.01	--	--	--	--	0.032	400	700/2h/FC	27
F7	98.8	<.01	--	--	--	--	0.054	400	700/2h/FC	27
1.491411		10.6	0.52	--	0.26	0.012	0.16	400-500	1075/30m/Q+700/2h/SC	28
1.4914/2		10.7	0.75	--	0.22	0.015	0.13	400-500	1075/30m/Q+700/2h/SC	28

* Temperature (°C)/Time (minutes or hours)/Quench (AC = air-cooled, OQ = oil quenched, CW = cold-worked, FC = furnace-cooled, Q = quenched, SC = slow-cooled)

The Karlsruhe paper[9] reported on irradiation creep of 1.6770 steel (2.25Cr-1Mo type) at 400 and 500°C. Specimens were tested in the BR2 reactor in Mol. Belgium using cylindrical geanetry in uniaxial tension with hydraulic loading. Stress covered the range 100 to 200 MPa, and doses were limited to 0.8 x 10^{22} n/cm^2 or 4 dpa. Testing at 400°C produced no detectable creep rate (strain rate < 8 x 10^{-8} h^{-1}), but a permanent transient deflection was measured. At 500°C, creep behavior shared typical transient behavior. but it was follared by accelerated rather than steady-state creep. An example is given in Figure 1, showing response at 100 MPa to 2600 h, followed by continued creep at 80 MPa. A stress exponent value of n = 3.3 was found to fit the experimental data. No changes in microstructure were detected. The conclusions drawn were as follows: irradiation creep in 1.6770 is fundamentally different fran the phenanenon found in face-centered cubic (FCC) metals; there is no measurable effect at 400°C; nonlinear stress dependence behavior is exhibited at 500°C. In canparlson with thermal creep at 500°C, in-reactor creep was more rapid but apparently was based on the same creep mechanism.

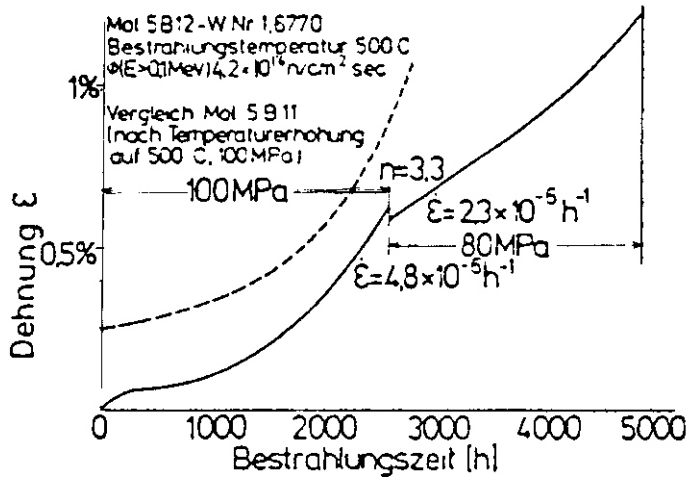

Figure 1. In-pile creep of bainitic steel 1.6770 at 500°C showing the effect of a load decrease fran 100 to 80 MPa at 2600 h. The dashed curve defines power law behavior with n = 3.3.[9]

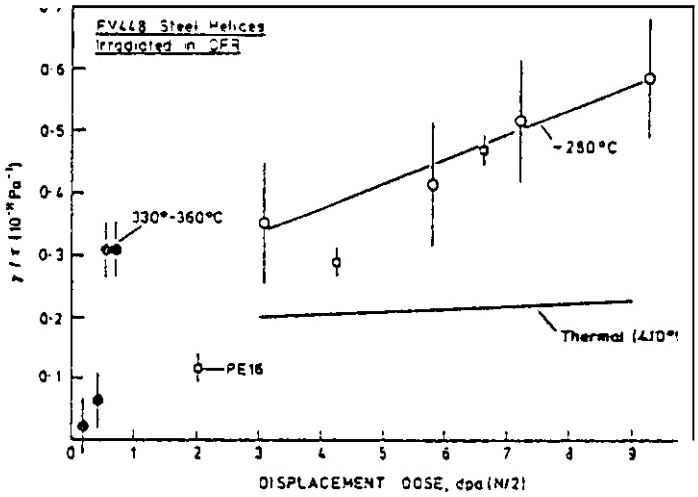

Figure 2. In-reactor creep of FV448 using helical springs in DFR.

The Harwell work[1] focused on development of a 12%Cr ferritic/martensitic steel for fast reactor applications and included irradiation creep results for FV448, a niobium-stabilized martensitic steel. Specimens were helical springs In tension exposed In sodium at temperatures of 280 to 380°C to doses of up to 9 dpa (N/2). The results. reproduced in Figure 2, showed that at 280°C the irradiation creep rate was significantly higher than the thermal creep rate. Creep strain rate reached a steady-state value that was a linear function of displacement dose, similar to. but one order of magnitude less than that found in austenitic alloys and even below that found for the nickel-base alloy, PE16. This alloy had Previously been considered the most resistant to irradiation creep. It was also tentatively concluded that based on comparison with results at a lower displacement rate but with higher operating temperatures of 330 to 360°C. the creep rate per unit displacement dose is higher the lower the displacement rate. in agreement with data for sane austenitic steels and nickel-base alloys.

At the same time, Paxton et al.[10] at Hanford reported results on short pressurized tubes irradiated in the Experimental Breeder Reactor II (EBR-II) at 540°C to 2 and 4 x 10^{22} n/cm^2 (E > 0.1 MeV) or 10 and 19 dpa. The specimen matrix included HT-9, a 12%Cr martensitic steel. It was found that following irradiation to 2 x 10^{22} n/cm^2, HT-9 was one of the least irradiation creep resistant materials tested; after 4 x 10^{22} n/cm^2, its ranking had improved so that it was better than 20% CW AISI 316 and canparable to most of the other alloys in the experiment. These results suggest a higher transient creep response but a lower steady-state creep rate. However, in both cases a plot of the creep strains as a function of applied stress gave nonlinear behavior; the stress exponent was between 1 and 2, which is uncharacteristic of thermal creep. These results for HT-9 are compared with several austenitic steels in Figures 3a and 3b.

Causey et al.[11] later reported in-reactor stress relaxation measurements on selected metals and alloys, including two martensitic stainless steels (403 and 410) and a bainitic steel (AISI 4140) in solution-treated (sic) conditions. Bent beams were allowed to relax while immersed in flaring water in fast-neutron fluxes of 1.5 x 10^{13} n/cm^{2}s at 340K and/or 2.1 x 10^{13} n/cm^{2}s at 570K. Analysis of the data provided irradiation creep coefficients that showed the martensitic and bainitic steels to have sane of the lowest creep coefficients in the test matrix: between 0.2 and 0.6 x 10^{-30} $(n/m^2)^{-1}$ MPa^{-1}. It was also found that for both the ferritic alloys as well as the other alloys in the matrix, the creep coefficient at 340K was higher than the creep coefficient at 570K. For the ferritic alloys, the ratios of creep Coefficients C_{340}/C_{570} were 1.4, 2.0. and 3.0 for the 403. 410, and AISI 4140 steels. respectively. Therefore, irradiation creep in ferritic alloys appears to be more rapid at very low temperatures than at sanewhat higher temperatures however. the authors were unable to provide a theoretical explanation for this weak temperature dependence.

Paxton et al.[12] followed with results on pressurized tubes irradiated in EBR-II under conditions similar to those used for their previous experiment[10] but at higher irradiation temperatures, 605 and 630°C. Their results. shown in Figure 4, demonstrate that at higher temperatures the martensitic alloy HT-9 creeps more rapidly than austenitic alloys such as AISI 310 or 330, both at 2 and 4 x 10^{22} n/cm^2. The creep behavior is nonlinear as a function of stress; this observation was attributed to a large thermal creep component. If thermal creep is the controlling behavior. as is likely. then this data base is not representative of irradiation creep, and indicates that for fluxes similar to those in EBR-II, thermal creep is the dominant deformation mechanism for ferritic steels at temperatures of 600°C and above.

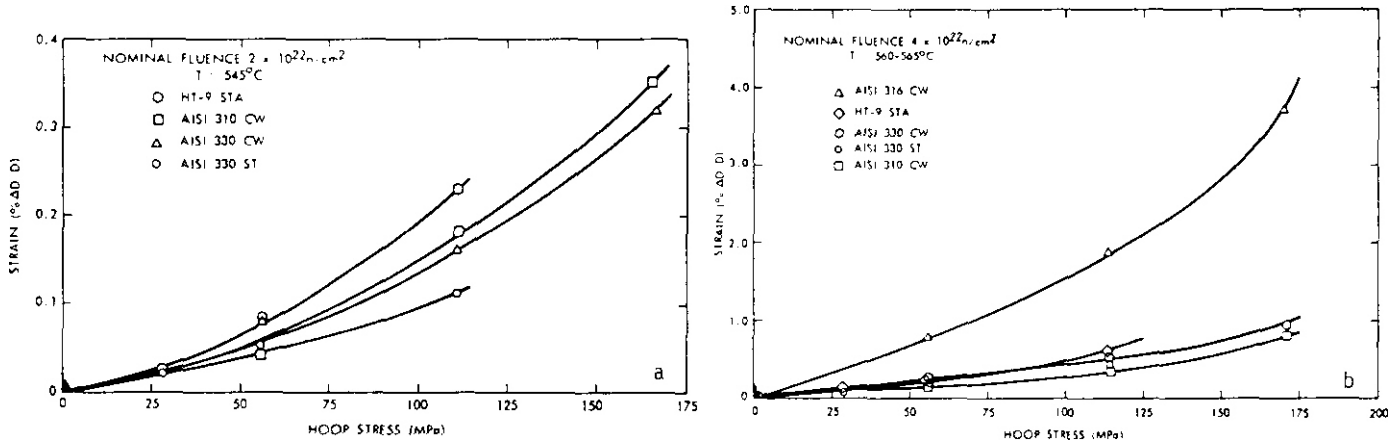

Figure 3. Diameter change as a function of stress for pressurized tubes in EBR-II at a) 545 C to 2 x 10^{22} n/cm^2 and b) 560 C to 4 x 10^{22} n/cm^2.[10]

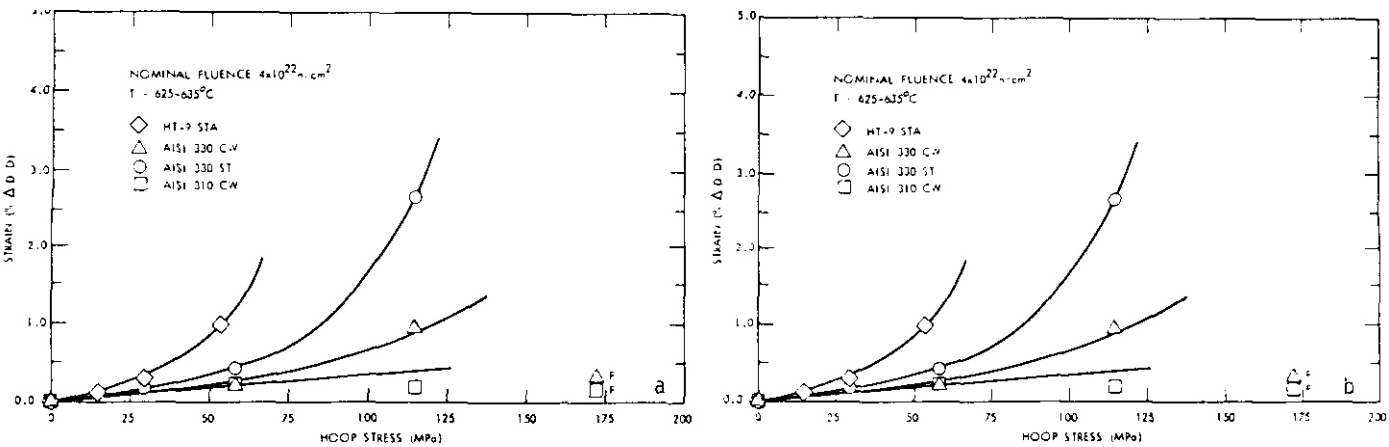

Figure 4. Diameter change as a function of stress for pressurized tubes in EBR-II at a) 605 C to 2 x 10^{22} n/cm^2 and b) 625 C to 4 x 10^{22} n/cm^2.[12]

The Paxton et al. results[12] for Irradiation at 630°C to 4 x 10^{22} n/cm^2 were replotted by Gilbert and Chin,[13] as shown in Figure 5, to demonstrate that even at 630°C HT-9 was more resistant to irradiation creep than was AISI 316. Also, Straalsund et al.[2] reported an extension of the results of Paxton et al. at 540°C to 10^{23} n/cm^2 (50 dpa) and showed that with increasing dose, HT-9 demonstrated significantly better irradiation creep resistance than developmental austenitic alloys. as shown in Figure 6. Comparisons between Figures 3a. 3b, and 6 further support the observation that HT-9 has a lower steady-state creep rate.

An update by De Bremaecker and Huet[14] of the Belgian work on ODS ferritic alloys and German studies by Herschbach and Doser[15] on 1.4914. a martensitic steel, were reported at the BNES conference on Dimensional Stability and Mechanical Behavior of Irradiated Metals and Al'loys held at Brighton, England, in 1983. The Belgian irradiation creep experiment was extended to a peak dose of 56 dpaF [dpaF corresponds to dpa as defined in the French Atomic Energy Program, where 1 dpa (NRT) = 0.87 dpa (N/2) = 0.17 dpaF[4]; their data are reproduced in Figure 7. Figure 7a plots deflection of internally pressurized tubes as a function of temperature (and corresponding position so that dose also varies, as indicated by the curve labeled ϕt). Deflections remain small, less than 0.5%. Figure 7b shows these results replotted. giving in-reactor creep strain as a function of applied stress for dose levels of 10 and 50 dpaF. ODS alloys remain most irradiation-creep resistant, the martensitic steel 1.4914 is least resistant, and the duplex alloy EM12 is intermediate. All results were plotted showing a linear dependence of creep with stress. A replot of the data. Figure 7c, to show the in-pile creep modules [$K = (\epsilon/\sigma) \cdot \phi t^{-1}$ where ϵ is the creep strain, σ is the applied stress. and t is the irradiation dose] as a function of temperature indicates increasing creep rates with decreasing temperature for 1.4914 and EM12, but not for ODS alloys. After subtracting thermal creep behavior to obtain the irradiation creep modules. one-third of the values obtained were found to be negative, Indicating. as noted by the authors. that thermal creep must be considered in analyzing such data. or, as will later be shown. that some other irradiation-controlled mechanism such as precipitation is important. The irradiation creep modules plotted as a function of inverse temperature are shown in Figure 7d, which indicates that negative behavior is most prevalent at the highest temperature of 500°C. These results further demonstrate the excellent irradiation creep resistance of ferritic steels,

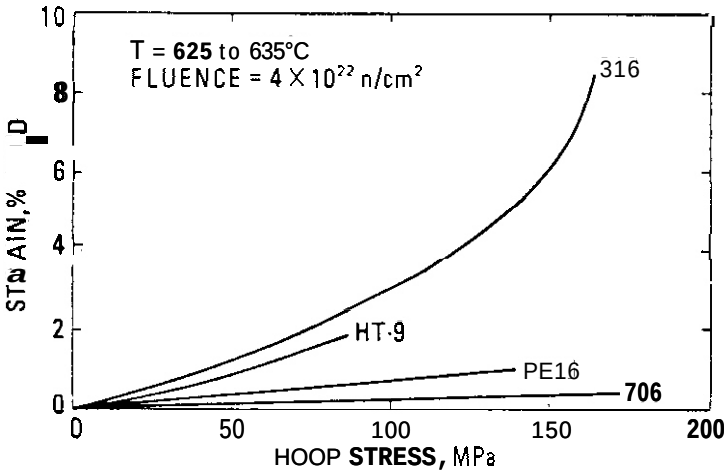

Figure 5. Data of Figure 4b replotted in comparison to AISI 316, PE16 and Inconel 701.[13]

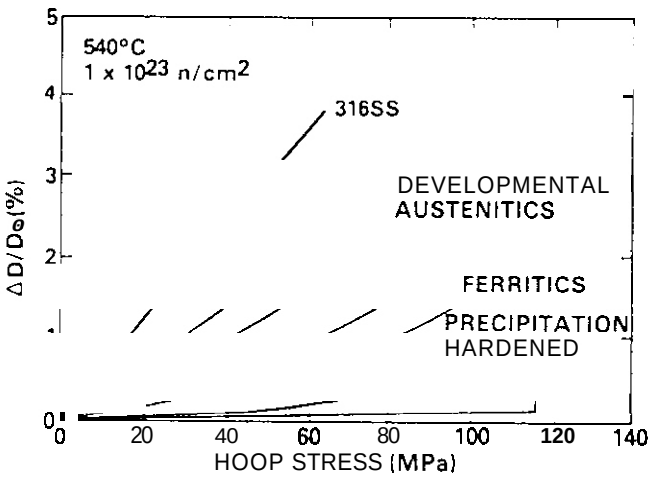

Figure 6. Diameter change as a function of stress for pressurized tubes in EBR-II at 540°C to 10^{23} n/cm^2.[2]

support the concept of increasing irradiation creep rates with decreasing temperature. and indicate that the phenanenon is probably quite complex in complex materials.

Herschbach and Doser[15] reported behavior of the martensitic steel 1.4914 between 400 and 600°C in the Mol BR2 reactor to doses of 5 dpa (NRT) or less. It was found that experiments using stresses of 100 MPa at 400 and 450°C gave very small creep coefficients (<< 1 x 10^{-6} MPa^{-1} dpa^{-1}), whereas at 450°C. 150 MPa gave 2 x 10^{-6} MPa^{-1} dpa^{-1} and 200 MPa gave 7 x 10^{-6} MPa^{-1} dpa^{-1} At 500°C. 100 MPa gave 6.0 x 10^{-6} MPa^{-1} dpa^{-1} and 200 MPa gave 5.1 x 10^{-5} MPa^{-1} dpa^{-1}; at 600°C, 50 Mia gave 2.7 x 10^{-5} MPa^{-1} dpa^{-1}. The stress dependence at 500°C was nonlinear, yielding a stress exponent on the order of 3.1. Also, temperature change experlments indicated an apparent activation energy of 1.9 eV. Finally, recovery was observed during reactor shutdowns and a "primary" creep period followed on subsequent restarts. Unfortunately, thermal control results were not then available for comparison.

Also in 1983, the AIME Topical Conference on Ferritic Alloys for Use in Nuclear Energy Technologies attracted six papers concerned with the topic of irradiation creep in ferritic alloys. Straalsund and Gelles[3] reported further results on pressurized tube tests begun by Paxton et al.[10] Results included behavior at 430, 550, and 620°C to 1.6 x 10^{22} n/cm^2 and comparison of behavior with other alloys at 425, 540, and 590°C to 1.0 x 10^{22} n/cm^2. The results are shown in Figures 8a through 8f. Figures 8a, 8b, and 8c provide Comparison of change in diameter as a function of either fluence or stress in specimens of HT-9 and D57 (a Laves phase precipitation-strengthened ferritic alloy) with those of two austenitic stainless steels, 316SS and D9, and two experimental, austenitic. precipitation-strengthened steels, 021 and D68. Figures 8a and 8c demonstrate linear behavior as a function of dose at 425 and 590°C. respectively, with strains comparable to all the austenitic alloys except 068. Figure 8b provides a similar comparison at 540°C, showing nonlinear response as a function of stress. Figures 8d through 8f show creep in HT-9 as a function of stress at 430, 550, and 620°C following irradiation to 1.6 x 10^{22} n/cm^2, with predictions for the behavior of 316SS shown for Comparison. The HT-9 is more irradiation creep resistant in all three cases. Irradiation creep as a function of stress is again demonstrated to be nonlinear. Therefore. as a general rule, irradiation creep in ferritic alloys is linear with dose but nonlinear with stress.

A paper by Harries[4] considers the use of ferritic/martensitic steels for fusion reactors and provides a good review of the irradiation creep data base. The results of that review were sumnarized in a plot of irradiation creep modules as a function of temperature, reproduced in Figure 9. This figure indicates that above 500°C. creep increases rapidly with increasing temperature. Below 500°C. creep appears to be a function of alloy tested.

Dupouy et al.[19] reported on possible use of EM12, a 9%Cr duplex martensiticlferritic steel. in fast reactor core applications. They discussed results for pressurized tubes at a hoop stress of 70 MPa and 430°C, and concluded that an irradiation creep coefficient of 6.1 x 10^{-7} $dpaF^{-1}$ MPa^{-1} [4.7 x 10^{-7} $dpa(NRT)^{-1}$ MPa^{-1}] applies. Therefore, the results on EM12 agree closely with those given by Harries,[4] lying between values for 1.4914 and EM12 in Rapsodie, as shown in Figure 9.

Huet et al.[20] submitted a paper on ODS ferritic alloy development that included irradiation creep data. The irradiation creep results duplicated those reported at the ENES conference held earlier in the year.

Puigh and Wire[16] reported irradiation creep results for two martensitic alloys (HT-9 and 9Cr-2Mo) and one bainitic alloy (2 Cr-1Mo). Specimens were short pressurized tubes (similar to those reported by Paxton et al.[10]) irradiated in EBR-II at 443, 505; and 572°C to a peak dose of 2.8 x 10^{22} n/cm^2 or 14

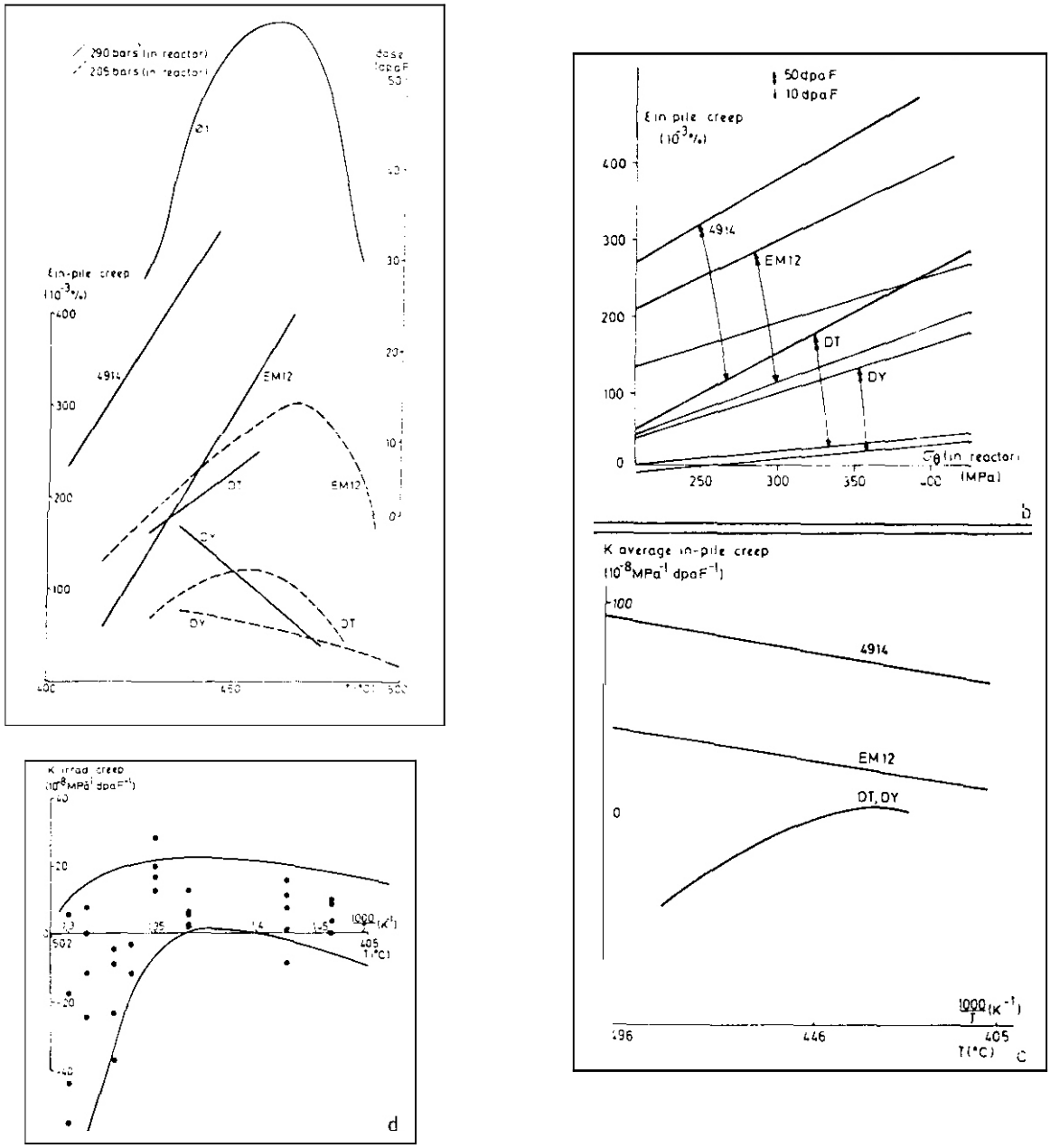

Figure 7. In-pile creep of martensitic and ODS ferritic alloy tubes in Rapsodie. a) showing behavior as a complex function of location in reactor, b) showing creep strain as a function of stress at dose levels of 10 and 50 dpaF, c) showing average in-pile creep Coefficient as a function of temperature, and d) sharing results for irradiation creep as a function of temperature after correcting for thermal creep.[14]

dpa. The results showed that all three alloys gave deformations well belar those expected for 316SS at 443 and 505°C, but at 572°C. the deformation found for 2 Cr-1Mo was similar to that expected for 316SS. Their results are shown in Figure 10, plotted as a function of hoop stress. There is sufficient scatter in the data to obscure the stress dependence of creep in the data base, but it was noted that these results and the earlier work of Paxton et al[10,12] on a different heat of material are in good agreement. Also, Puigh and Wire noted that the data were consistent with a long transient-for primary creep. Modeling, the in-reactor creep behavior by using the equation $\bar{\epsilon} = \bar{B}\, Qt\, \sigma^n$ [where ϵ is the effective creep strain, ϕt is the fast fluence, σ is the effective stress. and $\bar{B}$ is the average creep coefficient (which is a function of temperature)], gave a best value for the stress exponent of $1 \leq n < 2$ and gave a plot of $\bar{B}$ as a function of temperature as shown in Figure 11. Therefore, for temperatures below 540°C, the average creep coefficient is insensitive to temperature. and thermal creep becomes important only above 570°C. Also, the scatter in the values at largest $\bar{B}$ is only for the specimens with the highest stress, indicating that the stress exponent is larger than 1. (Even at 570°C, use of a stress exponent of 1 still coalesced

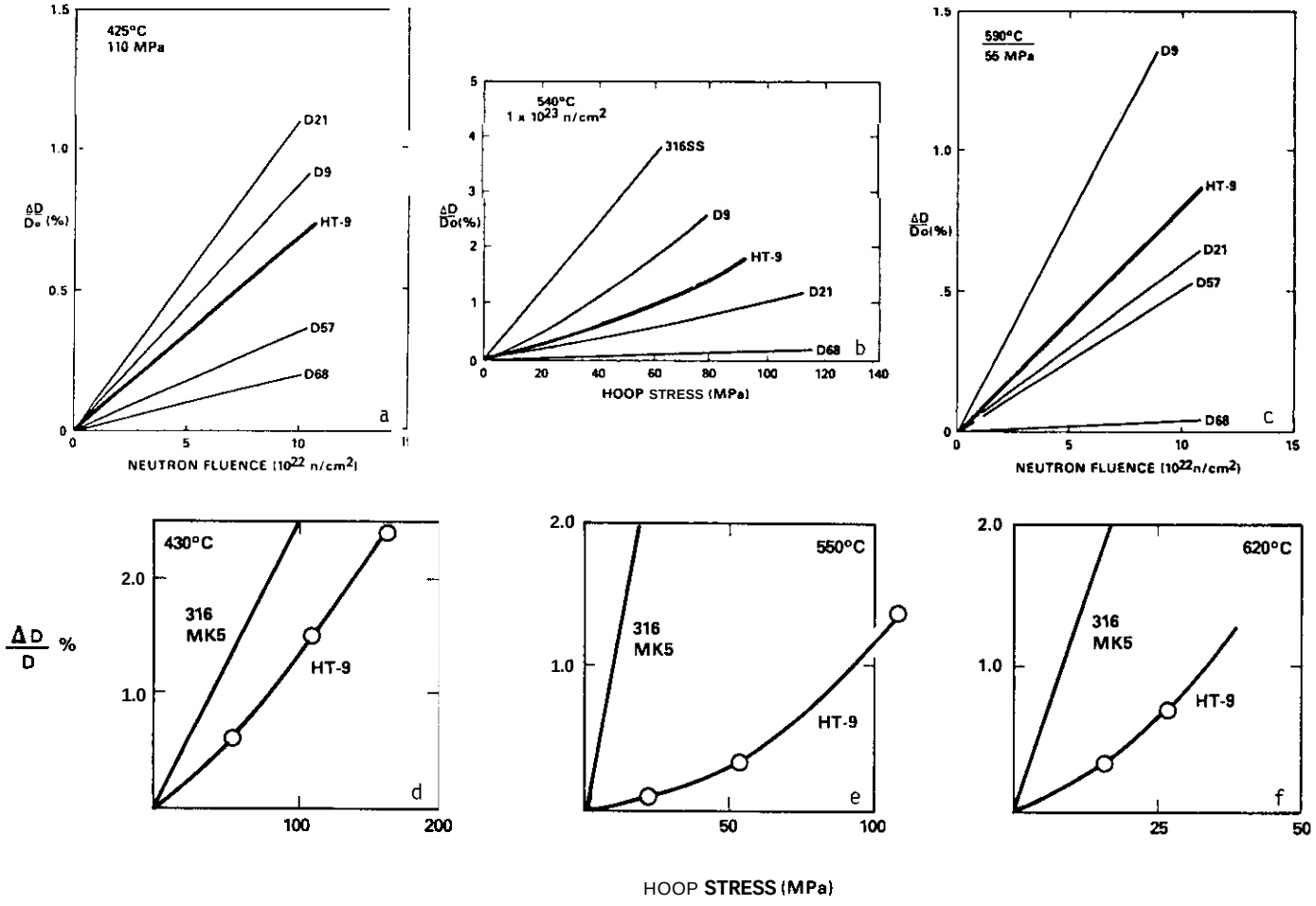

Figure 8. Diameter change for pressurized tubes in EBR-II to 10^{23} n/cm^2 at a) 425°C and 110 MPa, b) 540°C as a function of hoop stress, and c) 590°C and 55 MPa; and to 1.6 x 10^{23} n/cm^2 as a function of hoop stress at d) 430°C, e) 550°C, and f) 620°C.[3]

the data for HT-9 and 9Cr-2Mo.) Therefore, these results confirm the insensitivity of irradiation creep to temperature and composition. but indicate that the temperature above which thermal creep is controlling is a function of alloy cmposition.

Chin submitted an analysis and comparison of the in-reactor and thermal creep behavior of HT-9 pressurized tubes for the AIME proceedings.[17] The irradiation creep data were taken frm the experiments started by Paxton et al.[10] and included data for 425, 485, 540, and 600°C at doses of 2, 5, 7, and 10 x 10^{22} n/cm^2. Little difference was found between thermal and in-reactor behavior. An example providing comparison between thermal and in-reactor response at 540°C and 50 MPa is shown in Figure 12. From this figure. it is apparent that the steady-state creep rates are identical, but primary creep has been eliminated in-reactor. The elimination of primary creep in-reactor was consistently observed. resulting in better reproducibility than found in thermal control data. The temperature dependence of in-reactor creep was demonstrated using the same approach as that used by Puigh and Wire,[16] with results reproduced in Figure 13. Behavior is very insensitive to temperature changes below 600°C. Above 600°C, Chin noted that the creep strengthening mechanisms rapidly deteriorate. resulting in large creep rates and creep strains. However. the in-reactor creep rates below 600°C are very similar to thermal behavior. For example, when the in-reactor steady-state creep rates were compared with thermal steady-state creep rates for log σ/E values less than -3.0. very little difference was found: as shown in Figure 14. Only for the lowest temperature. 416°C, was there a difference between the steady-state in-reactor and thermal creep specimens. For this low temperature. the specimens tested in-reactor displayed an irradiation-enhanced creep rate. However, this work confirms the conclusion of De Bremaecker and Huet[14] that thermal and irradiation creep are similar. even in the irradiation creep regime.[14]

Finally, Wassilew et al.[18] reported on the continuation of their work on 12%Cr steels.[15] They described experiments on two 12%Cr steels. 1.4914 and 1.4923, including heat-to-heat and heat treatment variation behavior for 1.4914. The major differences between these steels are that 1.4914 has a lower carbon level and contains intentional additions of niobium, nitrogen, and boron. Cylindrical uniaxial tension specimens

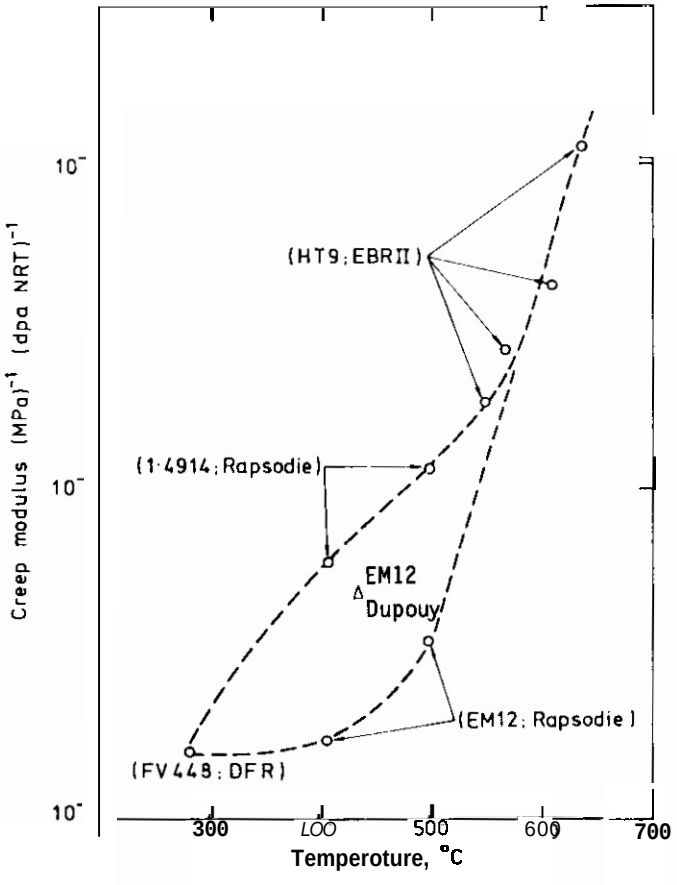

Figure 9. Compilation of results for in-reactor creep modules of 10 to 12%Cr martensitic steels as a function of temperature.[4] with additional data.[19]

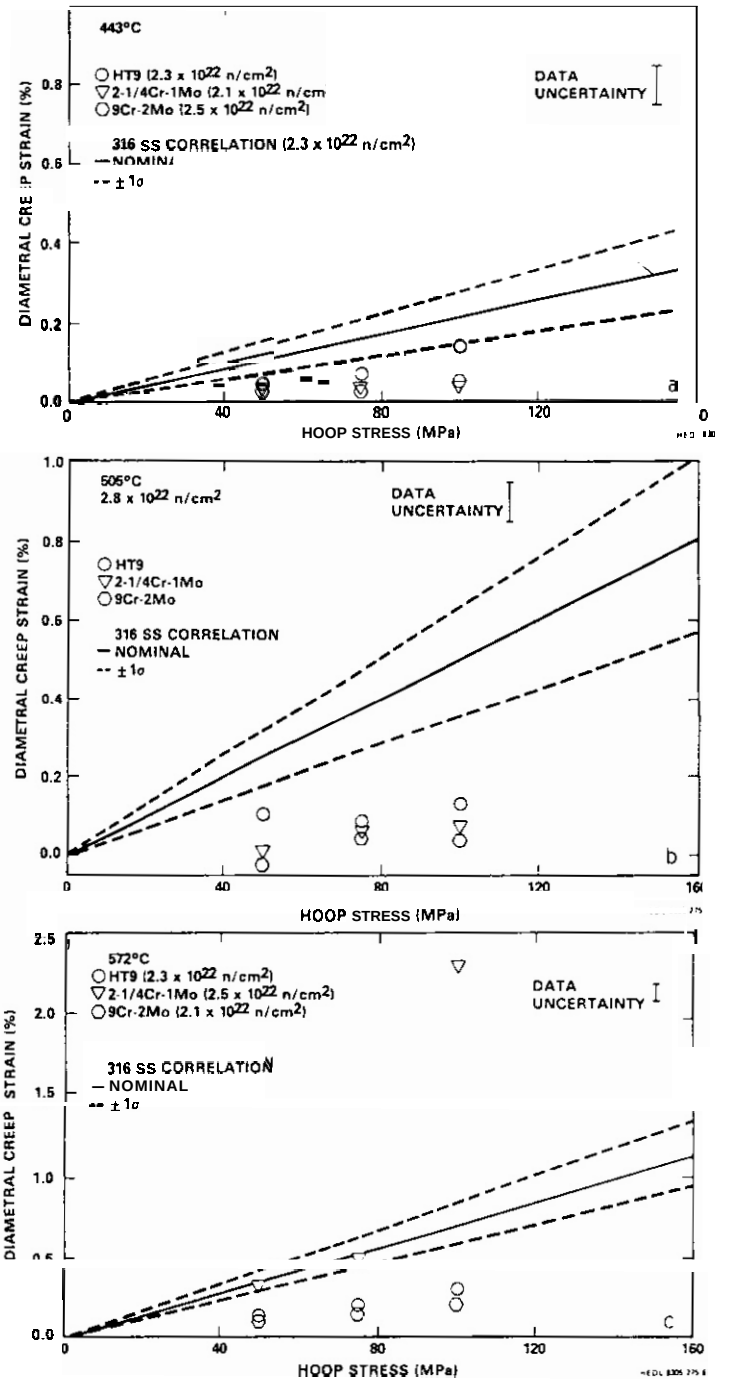

Figure 10. Diameter change as a function of stress for balnitic and martensitic steel pressurized tubes to about 2 x 10^{22} n/cm^2 in EBR-II at a) 443°C. b) 505°C, and c) 572°C.[16]

were tested in the Mol BR2 reactor to doses as high as 5.7 dpa at a flux corresponding to 1.2 dpa_{NRT}/1000 h, temperatures in the range 400 to 600°C, and stresses between 50 and 200 MPa. The results are in close (but not exact) agreement with previous results[15] and published creep curves appear to exactly match those published previously. The authors do not discuss the effect of heat-to-heat variations or heat treatment on irradiation creep; nor are irradiation creep results given for 1.4923. Therefore, it is likely that the only new results were at 600°C and 100 MPa, where a creep coefficient of 2.3 x 10^{-3}

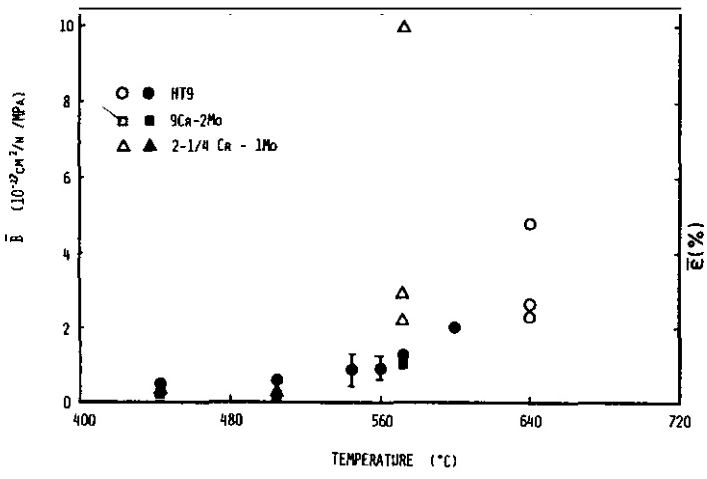

Figure 11. Temperature dependence of the average creep Coefficient for bainitlc and martensitic steels. (Open symbol calculated for a given specimen, closed symbols are average values for a set of specimens at a given temperature and fluence.)[16]

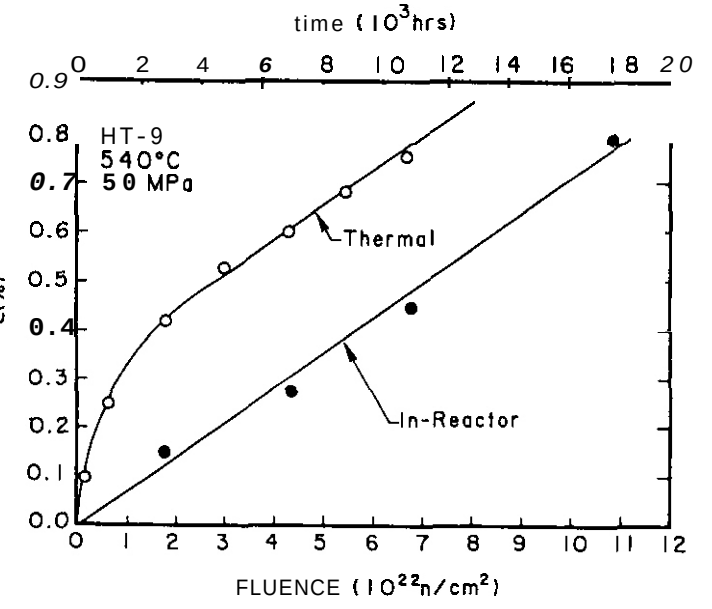

Figure 12. Comparison of HT-9 thermal and in-reactor pressurized tube data for tests in EBR-II at 540°C and 50 MPa. The same steady-state creep rate controls.[17]

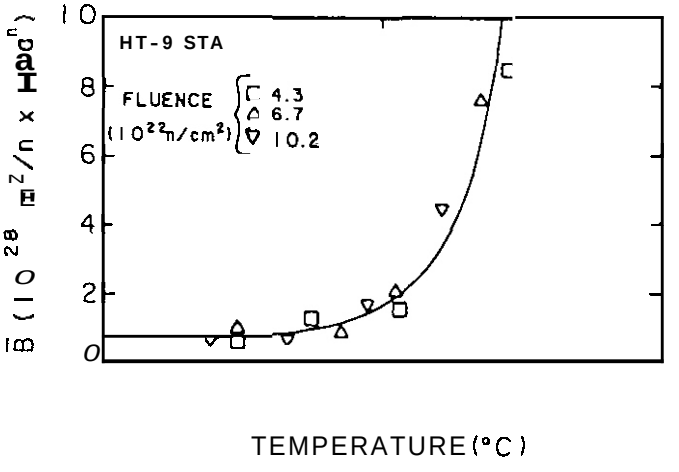

Figure 13. Temperature dependence of the in-reactor creep coefficient for HT-9 pressurized tubes.[17]

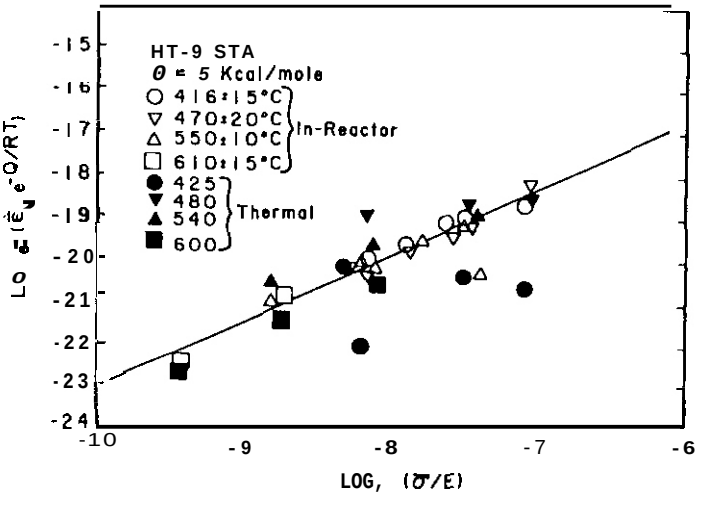

Figure 14. Comparison of in-reactor and thermal creep rates (for log /E values less than -3.1) obtained fra HT-9 pressurized tube specimens. Only thermal tests at 425°C give results significantly below the in-reactor response.[17]

MPa^{-1} dpa^{-1} was measured. Two polnts made in discussion are noteworthy, however. It is concluded that creep is nonlinear with stress, and that the value of the stress exponent is on the order of 5, with a strong temperature dependence. Also. thermal creep tests were done in parallel for the 500°C tests, and the thermal tests did not show noticeable creep strain for caparable time periods. The authors conclude that these results are inconsistent with a stress induced preferrentlal absorption mechanism for irradiation creep.

The ASTM Effects of Radiation Conference held in 1984 included two papers on irradiation creep. Puigh[22] reported results on pressurized tubes of HT-9, 9Cr-1Mo, and 2 Cr-1Mo irradiated at 380 to 570 C in EBR-II to a higher dose than was previously reported.[16] Peak dose in this case was 5.7 x 10^{22} n/cm^2 or 29 dpa. Results for irradiation at 650°C to 2.9 x 10^{22} n/cm^2 or 14 dpa were also reported. The response at higher dose was similar to that found at lower dose.[16] As shown by comparison of the results reproduced in Figures 15a and 15b and those given in Figure 10 for the earlier discharge, all three alloys continue to perform better than 316SS at 419 and 490°C (in fact getting relatively more creep resistant with higher dose). At 570°C, as shown in Figure 15c, performance is almost identical to that found at lower dose. with 2 Cr-1Mo at creep strains identical to those predicted for 316SS. However. the results for behavior to lower dose at 653°C in Figure 15d show that at sufficfently high temperatures. 316SS has properties superior to those of HT-9. As a function of temperature, behavior remained unchanged with increasing dose, with temperatureindependent behavior found for temperatures of 510°C and below. Several other observations are worthy of note. The Hi-9 exhibited an average creep coefficient approximately a factor of 2 larger than the other ferritic alloys for irradiation temperatures below 505°C. At 570°C. the values for the average creep coefficient appeared larger at the lower dose than at the higher dose, but if the creep coefficients were normalized to time at temperature, then they appeared to be the same. consistent with a thermal creep mechanism controlling behavior. The average creep coefficient for 2 Cr-1Mo at 419°C was qualitatively higher at the higher fluence and lower temperature. and the volume change for the zero stress specimen was 0.3% (assuming isotropic volume change). Therefore, an effect due to swelling enhanced creep was indicated. Finally, at 653°C, ductilities for HT-9 were large. indicating that strains in excess of 24% were possible.

The second paper at the ASTM conference. by Gelles and Puigh,[23] was concerned only with 2 Cr-1Mo and. in fact, reported the same pressurized tube measurements as those previously given.[12, 18] However, the lowest irradiation temperatures were reported as 392 and 383°C for the two dose levels, and the doses were reported at 10 and 25 dpa. The major contribution of the paper was an analysis that included correction for Swelling assisted creep and provided equations for in-reactor creep and sdelling. The magnitude of the swelling assisted irradiation creep contribution is indicated in Figure 16, which shows the results of the 390°C tests plotted as a function of dose with the in-reactor creep correlation prediction shown by the curves. The dashed curves define the irradiation creep contributions without swelling enhanced creep. The in-reactor creep equation used was of the form in-reactor creep strain (E):

$$\varepsilon = \varepsilon_I + \varepsilon_T$$

where subscripts I and T refer to irradiation and thermal components, respectively. and

$$\varepsilon_I = B\,\sigma^n\,\phi t + DS_o$$

where D is the swelling enhanced creep coefficfent and S_o the fractional swelling. Design correlation parameters were provided to allow estimation of swelling and irradiation creep, but evaluating the thermal creep contribution proved to be too unwieldly for the scope of the work. Following work by Gelles.[24] presented at the next ASTM Irradiation Effects Conference, used transmission electron microscopy to confirm that void swelling occurs in 2 Cr-1Mo over the temperature range 400 to 480°C, and that interpretation of diameter change in unstressed tubes as void swelling was therefore valid.

The next year, Herschbach[21] updated and analyzed the previous results on irradiation creep of 1.4914 12%/Cr martensitic steel.[15,18] He found that if he assumed linear creep response with dose, he could normalize the data to dose and show creep rate as a function of stress as reproduced in Figure 17. This analysis fitted the phenomenological expression:

$$\varepsilon = 2.0 \times 10^{-6}\,\sigma^{5.0}\,\exp(-3.0/kT) \quad [1/\text{dpa}]$$

The high stress exponent confirmed the previous statement that no SIPA-type in-pile creep was operating. However, the creep strains were one to two orders of magnitude larger than for thermal creep: a stress exponent of 6 determined for thermal creep.

More recently, Puigh and Garner[25] reported results of pressurized tube specimens irradiated in the Fast Flux Test Facility (FFTF) at Hanford. They compared two martensitic alloys, HT-9 and 9Cr-1Mo, following irradiation to doses as high as 50 dpa over the temperature range 400 to 540°C, with hoop stresses fran 0 to 200 MPa. The HT-9 specimens were machined fran plate stock. the 9Cr-1Mo was fabricated into tubing by standard drawing procedures. The creep behavior of the two alloys was found to be similar and to be consistent with creep data on related alloys irradiated in either EBR-II or FFTF. The zero- stress specimens had negligible diametral strain and showed no evidence of irradiation-induced dimensional change. The data suggested a nonlinear dependence on stress similar to that observed in other ferritic alloys. The model used to investigate the temperature dependence of creep was described previously by Puigh and Wire[16] and Chin,[17] consistent with a stress exponent of $1 \le n \le 2$ with best fit for n = 1.3. A plot of the value B for the data base, examined as a function of temperature, is shown in Figure 18. For irradiation temperatures lower, than 520°C. the values *for* B for each of the ferritic alloys increase Only slightly, indicating that the average in-reactor creep coefficient for ferritic alloys is relatively insensitive to temperature. However, with decreasing temperature, the creep rate does decrease. Minor

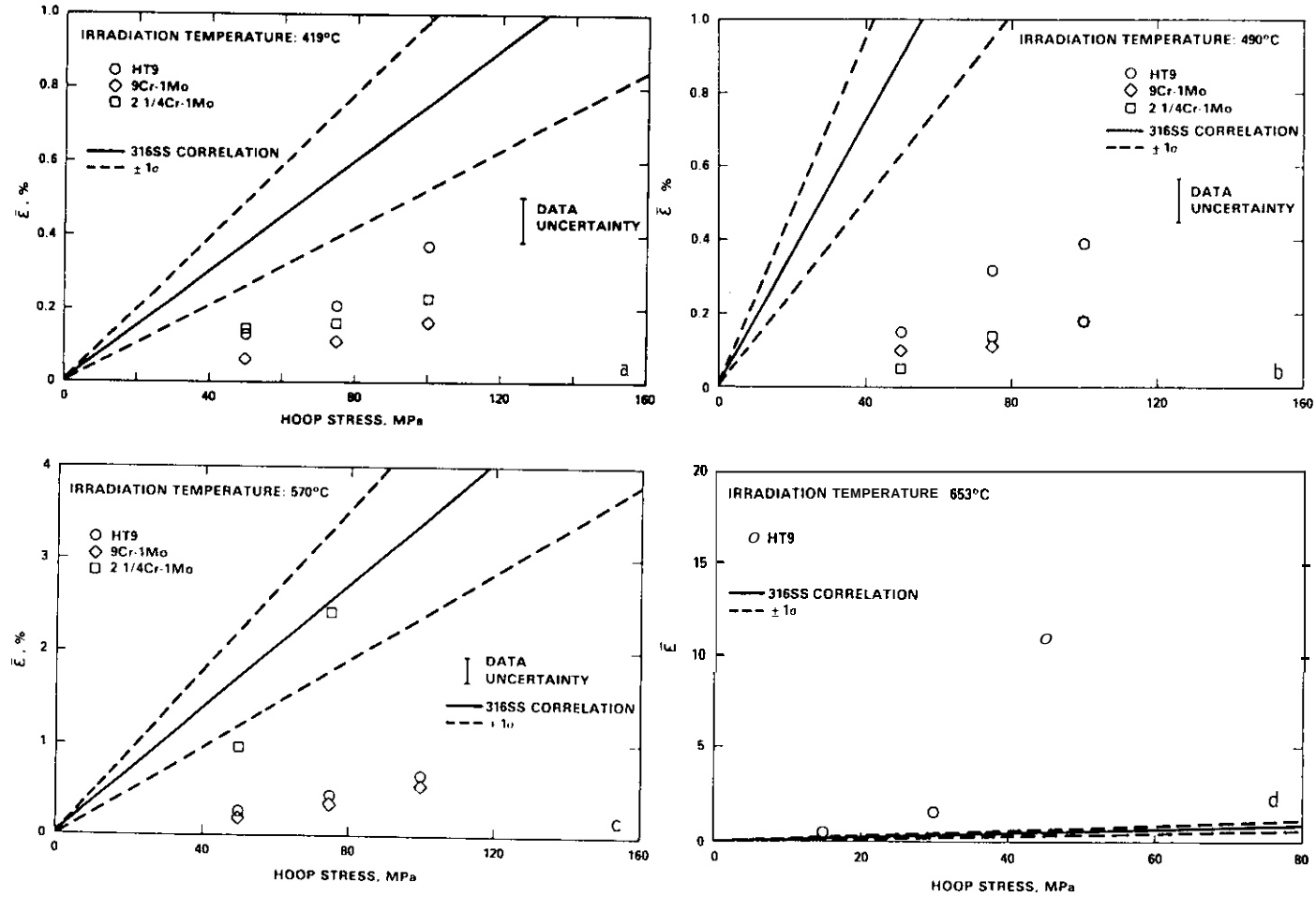

Figure 15. Canparison of diameter change in pressurized tubes as a function of stress between 316 SS and bainitic and martensitic steel to about 6 x 10^{22} n/cm^2 in EBR-II at a) 420°C, b) 490°C, c) 570°C, and to 2 x 10^{22} n/cm^2 at d) 650°C.[22]

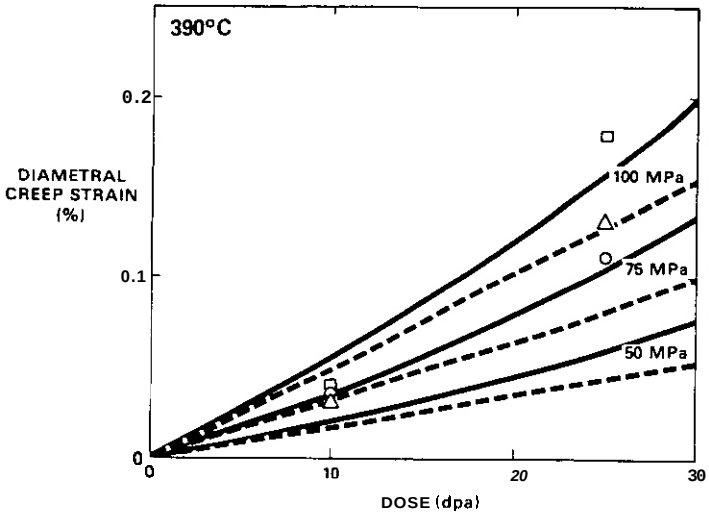

Figure 16. Diameter change corrected for swelling as a function of dose at 390°C for midwall hoop stress levels as high as 100 MPa. The solid curves define in-reactor creep predictions for the stress indicated. Dashed curves show the irradiation creep contribution without swelling-enhanced creep.[23]

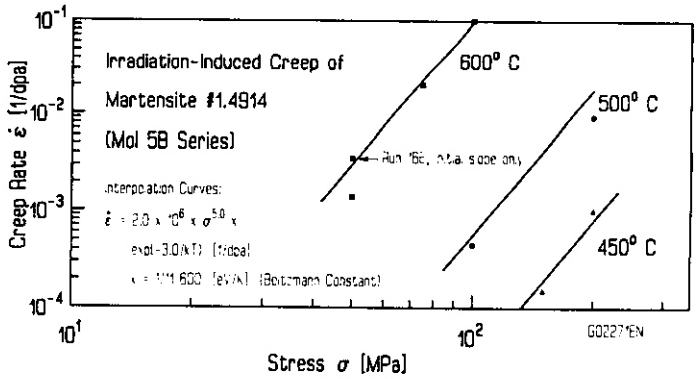

Figure 17. Stress dependence of creep rate for martensitic steel 1.4914 uniaxial tensile specimens irradiated in BR-2.[21]

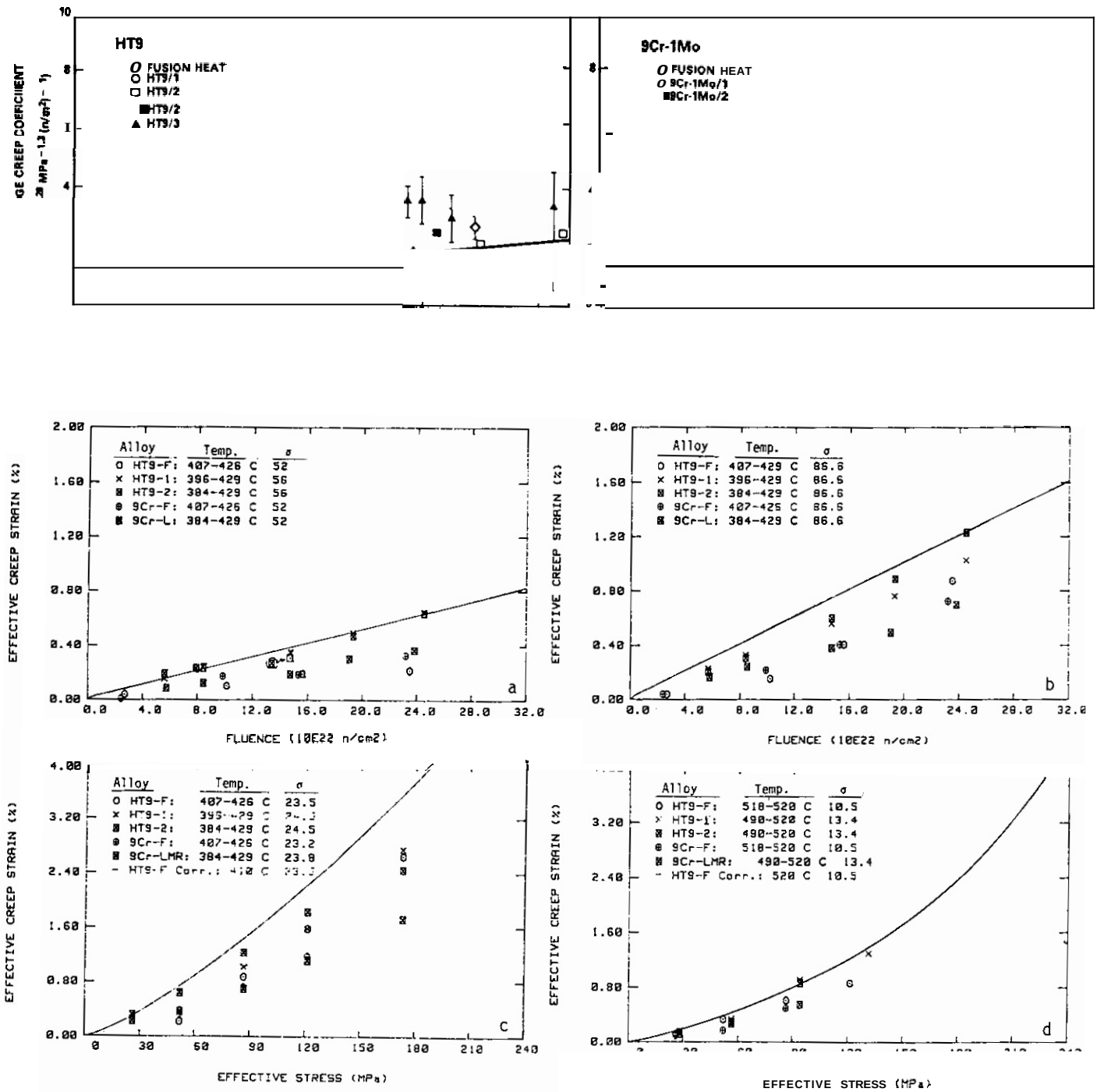

Figure 19. Canparison of effective creep strain for several conditions of HT-9 and 9Cr-1Mo in FFTF at ~400°C as a function of fluence a) ~55 MPa, b) 87 MPa, and as a function of stress c) at ~400°C, and d) at ~500°C.

PHENOMENOLOGICAL REVIEW OF BEHAVIOR IN FERRITIC ALLOYS

The major environmental parameters affecting the creep behavior of all steels are stress, accumulated Irradiation damage, and temperature. Secondary environmental effects include irradiation damage rates. temperature history. and stress state. In most instances, it is difficult to separate thermal versus Irradiation induced creep without having a complete data set that includes thermal control creep data and sufficient microstructural examinations. Within this review. an attempt will be made to segregate the secondary effects from the three major environmental parameters; however. it will become apparent that the irradiation temperature has a significant impact on the in-reactor ferritic creep behavior.

The stress dependence of irradiation induced creep in ferritic alloys is dependent on irradiation dose (exposure time), temperature. and stress range under consideration. For all ferritic alloys, this stress dependence is nonlinear. For example. the stress dependence of several ferritic alloys irradiated in the form of pressurized tube creep specimens to a nominal damage accumulation of 80 dpa at irradiation temperatures of ~400, 500, and 600°C is shown in Figure 20. At 400 and 500°C, the stress exponent derived fra the data is between 1 and *2;* at 600°C. it is greater than 3. Similar behavior has been observed in earlier studies of in-reactor ferritic creep behavior.[8,12] In-reactor ferritic creep studies on the alloys 1.6770[9] and 1.4914[15] and 1.4923[18] have led to stress exponents of 3 to 5 at irradiation temperatures of 500°C and above.

The irradiation dose dependence for ferritic creep behavior is qualitatively similar for all alloys that have been investigated to date. Primary creep is typically small. if observed at all. in the irradiation induced creep behavior of ferritic steels. For example, the thermal and irradiation induced creep behavior of HT-9 is shown at 540°C as a function of neutron fluence in Figure 12. While primary creep behavior is observed in the thermal creep response, the in-reactor creep behavior provides no evidence for a primary creep response.[17] Evidence for primary creep behavior has been observed in the ferritic steel 1.4914.[15] At intermediate to high doses. the ferritic creep rate is relatively constant.[1,26] For example. the fluence dependence for HT-9 and 9Cr-1Mo is shorn in FIgure 21 for nominal hoop stresses of 60 and 100 MPa for an irradiation temperature of 500°C. A linear fluence dependence is observed to the maximum measured fast fluence of 13 x 10^{22} n/cm^2 (E > 0.1 MeV). Irradiation temperature influences the creep rates at intermediate to high fluences in two ways. At temperatures of ~400°C, the creep rate begins to increase slightly at intermediate to high dose for sane alloys and heat treatments. This can be seen in Figure 22 in the fluence dependence of one heat of HT-9 that has been irradiated in the Materials Open Test Assembly (MOTA) to a peak fast neutron fluence of 23 x 10^{22} n/cm2 (E > 0.1 MeV). Also. for temperatures above 500°C. the creep rate increases rapidly with fluence, depending on alloy and stress. For example, the creep dependence of HT-9 shows a nonlinear fluence dependence at ~600°C (see Figure 23). The creep dependence of the ferritic alloy 1.6670 also shows a nonlinear fluence dependence at 500°C.[9]

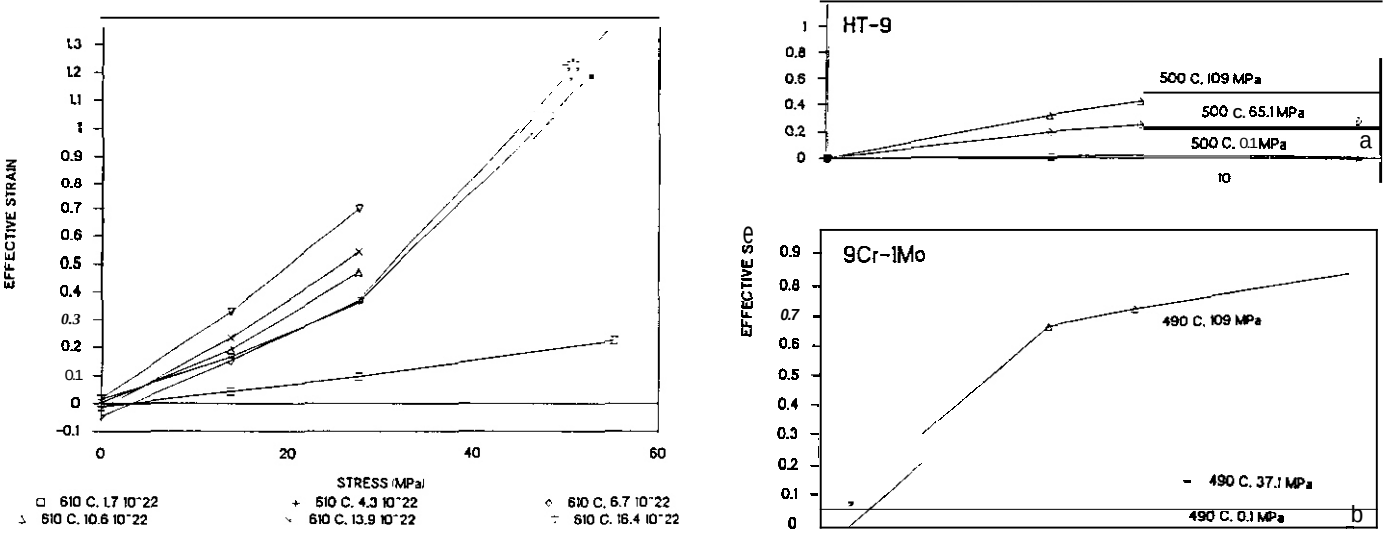

Figure 20. Stress dependence for in-reactor creep of HT-9 at ~400, 500, and 600°C. The nominal damage accumulation is 16 x 10^{22} n/cm^2 (E > 0.1 MeV).

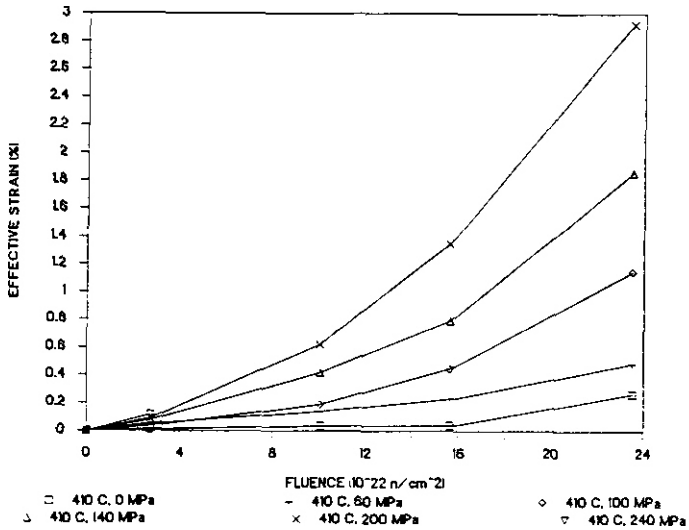

Figure 22. Fluence dependence of HT-9 heat 9607R2 at an irradiatlon temperature of ~410°C.

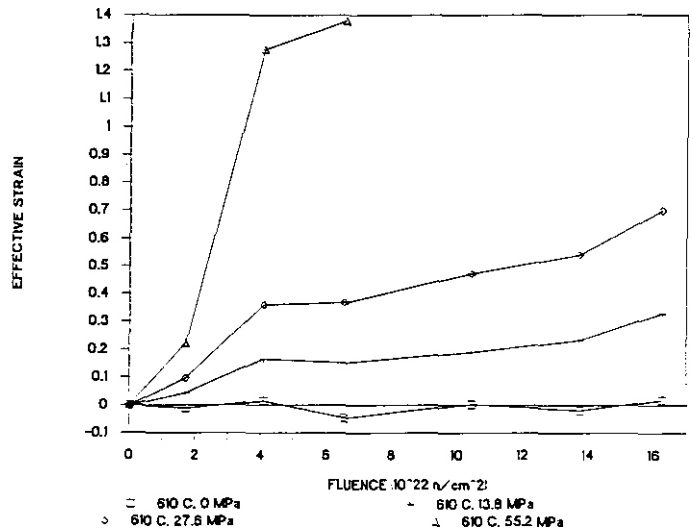

Figure 23. Fluence dependence of HT-9 at an irradiation temperature of -600°C.

The temperature dependence of the irradiation induced creep of ferritic alloys has the most profound effect on the creep behavlor. The evidence to date suggests that irradiation creep in ferrltic steels Is relatlvely insensitive to temperature for exposure temperatures below 500°C. In sane alloys the creep strains are slightly higher at 400°C than at 500°C. For example. certain heats of HT-9 and 2 Cr-1Mo show such a behavior. The ferritic alloys HT-9 and 9Cr-1Mo exhibit a slight increase in creep strains with increasing Irradiation temperatures between 400 and 550°C.[26] The ferritic alloys EM12 and 1.4914 also show an increase in their creep rates wlth Increasing Irradiation temperature over thls temperature range.[14] Sane evidence exfsts *for* the *irradiation* creep modules increasing slightly as the temperature is reduced from 300 to 70°C.[11] Dependlng on the alloy considered, the creep strains can increase rapidly for irradlation temperatures greater than 500°C. For example, the stress dependence for the creep modules for HT-9[17] is shown for several temperatures In Flgure 24. (Similar behavior for ferritic steels was shown.[4]) Also. the temperature can influence the stress dependence for irradiatlon creep in the temperature range of 400 to 600°C. For example, the HT-9 steady-state thermal creep dependence on temperature and stress exhibits a bilinear stress dependence (Figure 24). At low stresses, the stress exponent is between 1 and 2. At high stresses. the stress exponent can be as high as ~20. At la stresses, the in-reactor creep of HT-9 shows a similar behavior, with stress exponents between 1 and 2 (Figure 14).

The impact of secondary environmental effects on the irradiation creep of ferritic alloys has not been systematically explored. Limited data fran Harwell[1] suggest that a flux effect exists for the ferritic steel FV448, which was irradiated at ~330 to 360°C. Specifically, the data suggest that an increase in the neutron flux by a factor of 5 leads to a decrease in the observed in-reactor creep strains at a given fluence by approxlmately a factor of 2. A slmilar flux effect has been observed In several austenitic stainless steels.

A comparison between the in-reactor and thermal creep behaviors of selected ferrltic alloys has produced sanewhat confusing and contradictory observations. For HT-9. the thermal and in-reactor steady-state creep rates have been found to be similar over the temperature range of 440 to 600°C.[13] The data on the ferritic steels 1.667. 1.4914, and 1.4923 in the temperature range of 400 to 600°C show that the in-reactor creep strains are significantly larger than the measured thermal strains. Nevertheless. the authors indlcated that the In-reactor behavior of these ferritic steels exhibits thermal-like creep processes at 500°C and higher. Comparisons between thermal and in-reactor creep strains at lower temperatures (<400°C) also demonstrate that the thermal strains are significantly lower.[1]

Canparisons of the in-reactor creep behavtor of ferritlc steels with the austenitlc steels have been made by several authors.[3,10,12,16,22,26] Typically, it has been found that the ferritic steels creep less than the austenitlc alloys if canpared at high dose and Intermediate irradiatlon temperatures (i.e., temperatures below which thermal creep mechanisms manifest themselves). For example. the in-reactor creep behavior of HT-9 is compared to several austenitic alloys.[3] As seen in Figure 8, HT-9 exhibits less creep strain than 316SS and the developmental austenitic alloy D9 for frradlation temperatures between 425 and 590°C. The alloy D57 is a preclpltation-strengthened ferritlc alloy that shas superior creep resistance. Finally, the alloys D21 and 068 are precipitation-strengthened austenitic alloys that exhibit the best resistance for austenitic alloys to In-reactor creep over this temperature range. While the

ferritic alloys show comparable to better creep resistance in the temperature range of 400 to ~550°C, the ferritic steels rapidly lose their creep strength as thermal-like mechanisms begin to dominate. Limited data at 280 to 350°C have shown that the creep strength of FV544 is superior to PE-16 (a solution-strengthened austenitic alloy).[1]

LITERATURE ON CREEP FOR LIGHT ION IRRAOIATION

Two recent papers have described irradiation creep experiments on ferrous alloys using other than neutron damage. Henager and Simonen[27] examined the effect of 14-MeV deuteron irradiation on two pressure vessel

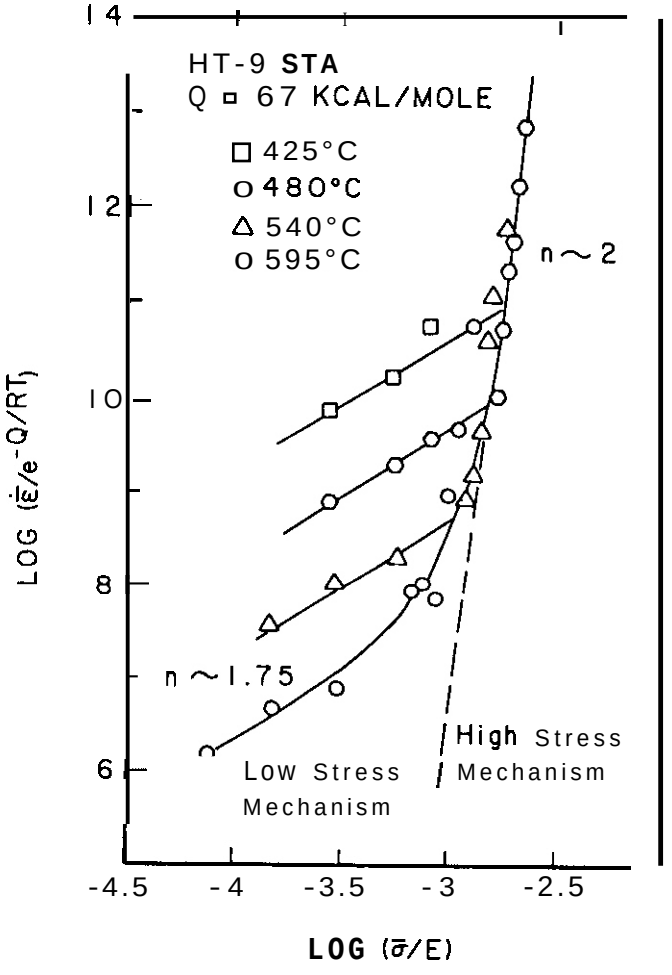

Figure 24. HT-9 thermal creep dependence is shown to exhibit a transition in the controlling creep behavior, which is indicated by a change in the activation energy and stress dependence.[17]

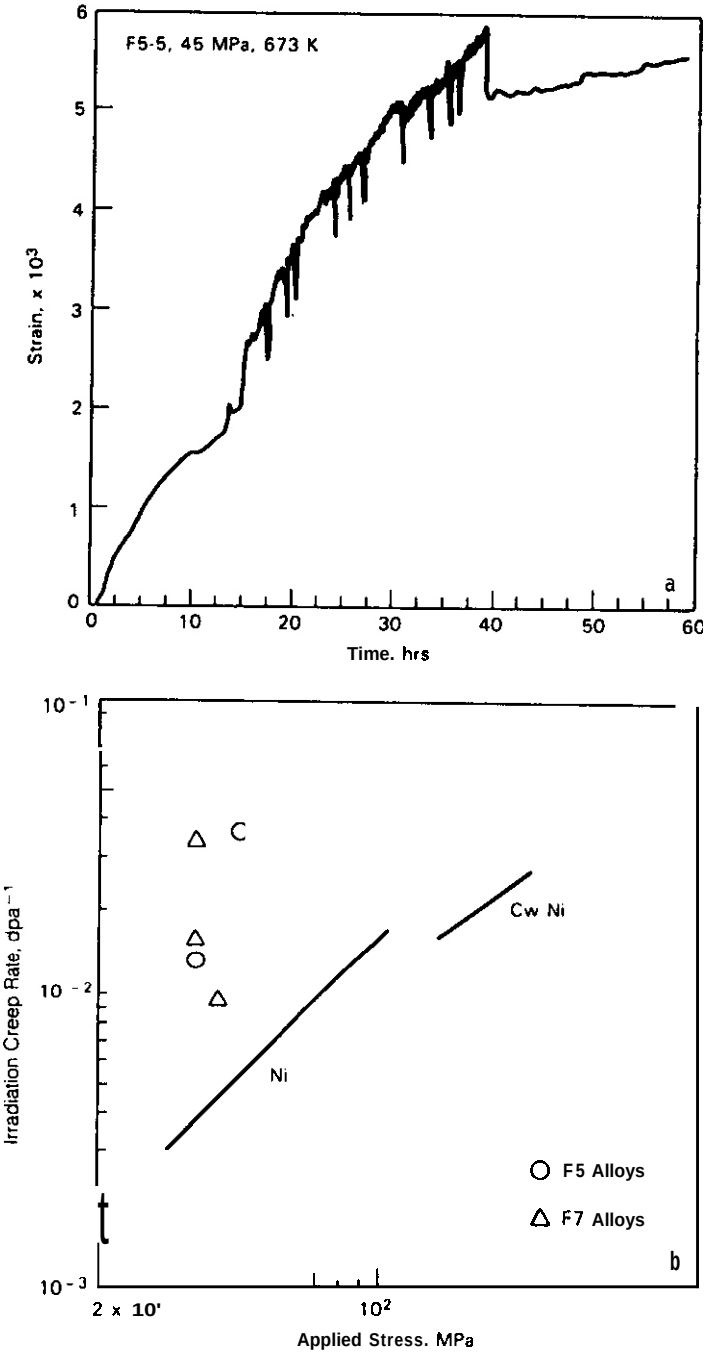

Figure 25. Deuteron irradiation creep results for pressure vessel steels showing a) a typical example of behavior for an applied stress of 45 MPa at 200°C, and b) a comparison of creep rates with those of annealed and cold-worked nickel.[27]

steels. one with a copper level of 0.29%. Irradiation tests were conducted for 24 h at a displacement rate of 6 x 10^{-7} dpa/s, followed by 12 h of post irradiation thermal creep. Peak dose was on the order of 0.05 dpa. Creep enhancement and radiation hardening were observed in each of the irradiated alloys. A typical test, shown in Figure 25a, displays primary behavior followed by the onset of steady-state irradiation creep. Post irradiation thermal creep, starting after 39 h, is slower. Figure 25b summarizes the results of irradiation creep rate as a function of applied stress. The creep rates observed were higher than those for annealed pure nickel, but no effect of copper content was apparent. (Alloy F5 contained the higher copper content.) Microstructural examinations of a postirradiation thermal creep specimen revealed small irradiation induced dislocation loops, with carbide decorated network dislocations bowing around the loops. The paper included models of creep and irradiation hardening. The creep model used calculated loop growth rates and dislocation climb velocities in the context of a climb-glide model. Loop growth predictions were found to underpredict the creep strain by a factor of 10, but loop size predictions agreed well with experiment. An explanation for the discrepancy was not apparent. An increase in glide distance by a factor of 10 was not plausible, and reasonable increases in bias for self-interstitial atoms did not provide the necessary increase in creep strain.

A second paper by Jung and Afify[28] examined the creep response of two heats of DIN 1.4914 martensitic steel in an annealed condition. Specimens were in the form of foils and irradiation was by 6.2-MeV protons with doses limited to a maximum of 0.76 dpa at temperatures of 400 to 500°C and stress ranging from 150 to 480 MPa. It was concluded that all behavior observed was of primary creep type. with no significant difference between creep rates with and wlthout irradiatlon. Composition was found to affect creep and the temperature dependence could be described by an activation energy of about 3.0 eV.

REVIEW OF THE CREEP LITERATURE ON REFRACTORY ALLOYS

The early work on the effect of radiation damage on BCC alloys was primarily concerned with BCC refractory alloys. Hesketh[29] reported helical spring results for a number of materials irradiated with neutrons, including tungsten and niobium at roan temperature. The deformation rates reported for tungsten and niobium were similar to rates reported for FCC and hexagonal close-packed (HCP) materials. A published extension curve for tungsten. reproduced in Figure 26, shows a primary creep transient that is exponential in neutron dose; followed by steady-state creep. Hesketh identified the steady-state response with the collapse of dislocation loops. It was noted that a higher atanic weight corresponded to a more rapid creep rate. and was explained by the larger cascade sizes associated with heavier atans. Hesketh concluded that the small variation in the comparative creep rates over the range of atanic weights he investigated indicated that normal metallurgical processes involving the thermal creep process of dislocation glide could be ruled out canpletely.

However, Buckley[30] arrived at a different conclusion based on foil flexure irradiation creep studies using various materials. including Armco iron and BCC gama uranium, in a recoil fission fragment spectrum. Doses were 1imited to 10^{17} fissions/cm^3. Examples of response in cold-worked material. reproduced in Figure 27. showed nonlinear behavior with dose, typical of primary creep response but. as noted by Buckley, not of dislocation-glide-controlled behavior. Deformation rates were found to be dependent on thermomechanical treatment: annealed material crept more slowly than 15% cold-rolled material. Deformation was anisotropic with respect to the cold-working direction. producing greater strain rates in the direction parallel to the rolling direction. Like Hesketh, Buckley noted that heavy elements tended to be more susceptible than light elements, and that there was no obvious correlation with crystal structure. Buckley concluded that dislocation glide, in addition to dislocation climb, had to be invoked to explain the results. Subsequent discussion by Hesketh suggested that transient response was responsible for the higher creep rates in cold-worked material, and that steady-state creep response would be independent of thermomechanical treatment history.

Ponsoye[31] reported uniaxial creep measurments on tungsten irradiated with fission fragments at low temperature (20K). To monitor resistance and length change, strip specimens were coated with uranium, loaded into a straining stage, and tested in tension at 6 (approximately zero). 60, 72, and 87 kg/mm^2 (and at 120 kg/mm^2 for an uncoated wire specimen) in the TRITON test reactor. Results showed that resistivity changes were insensitive to applied stress during irradiation. whereas length changes were increased significantly with increased stress. For example, at a dose of 5 x 10^{17} FF/cm^3, the elongation is 2.6 times greater at 72 kg/mm^2 than at 6 kg/mm^2. As with Hesketh's results. deformation response under applied stress showed initial transient behavior followed by an approach to steady state, as shown reproduced in Figure 28. The behavior was interpreted as a result of anisotropic dislocation loop formation and growth as a result of applied stress during irradiation.

Hesketh[32] compared his earlier results[30] with those of Ponsoye[29] and noted that the strain rate sensitivity was larger at 253°C (14^a) than at 43°C (8^a) for tungsten. but that. in agrement with results on nickel, uranium dioxide, and Zircaloy, irradiation creep was insensitive to temperature over a broad range of low temperatures. or even rose at low temperature.

(a) Natural strain rate sensitivity units, "per unit elastic strain, per atomic displacement"[31]

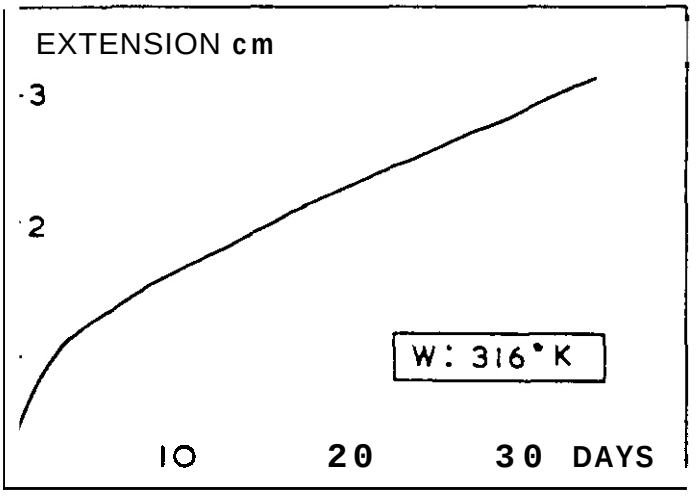

Figure 26. Extension of a helical spring of tungsten in a fission flux of 1.4 x 10^{17} fission fragments per m^2 s at 43'C. The strain is 10^{-4} per cm extension.[30]

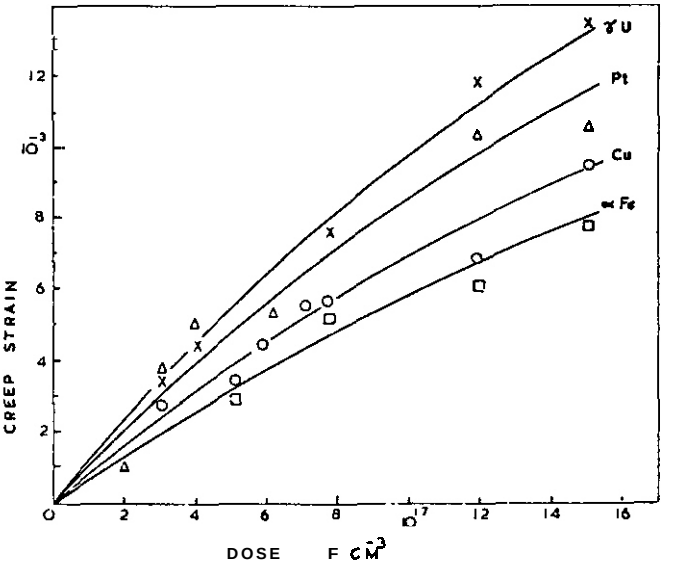

Figure 21. Dose dependence of fission-fragment-induced irradiation creep in various cold-worked metals. Prestrain = 11%, irradiation temperature = 90°C, and peak stress = 9.3 x 10^3 g/mm^2.[33]

Mosedale et al.[33] reported results on loaded helical spring specimens irradiated at about 280°C in the Dounreay Fast Reactor. and including results for molybdenum and its alloy RM. Molybdenum and TZM were found to behave similarly, as shown in Figure 29; the response was like that found by Hesketh[30] and Ponsoye[29] as a function of dose. showing an initial transient followed by behavior approaching steady state. Reduced strain (strain per unit stress) for molybdenum was above that for stainless steels but belcw that for nickel and En 58B, an austenitic steel in a cold-worked condition.

Early results on refractory BCC alloys therefore suggest that irradiation creep rates in BCC alloys are canparable to other cubic metals but are higher for heavier atoms. Irradiation creep is insensitive to temperature. Surprisingly. irradiation creep at very low temperature is greater than at somewhat higher temperature. As a function of dose. creep is first found to be transient and then to approach steady state. similar to primary and secondary creep, but with a lower transient decay rate. All experiments were to low dose, the highest being for molybdenum to 8 dpa.[32]

UNPUBLISHED RESULTS ON CREEP FROM HANFORD STUDIES

In order to better understand irradiation creep in ferritic alloys, the pressurized tube irradiation creep data base for ferritic alloy specimens in EBR-II and FFTF has been compiled and re-examined. The trends that can be identified in that data base confirm the behavior described in the literature. but further insights can be obtained. For example, the pressurized tube measurements on the original HT-9 tested in EBR-II have been taken to almost 20 x 10^{22} n/cm^2 (E > 0.1 MeV; all subsequent fluences for EBR-II and FFTF will be so expressed) or 100 dpa. The results are shown as a function of fluence in Figure 30 and as a function of hoop stress in Figure 31. Due to changes in reactor operating conditions. temperature fluctuations as large as 40°C occurred from one irradiation discharge to the next. but standard deviations from the average temperatures that are given were generally between 15 and 20 C. These temperature fluctuations can account for the minor changes in slope, for example, in the higher stress level conditions in Figure 30a. At 435°C, as shown in Figure 30a primary creep is negligible, creep is linear with increasing fluence, and densification occurs in the zero stress Specimen to strain levels of 0.05% or about 0.15% densification by volume; the process saturates after about 4 x 10^{22} n/cm^2 or 20 dpa. The measurements at 490°C are shown in Figure 30b, In this case. irradiation on the two higher stress conditions was discontinued after 6 x 10^{22} n/cm^2. The reduction in creep rates observed in specimens just prior to removal is probably a result of densification, shown clearly in the zero stress specimen to occur after 4 x 10^{22} n/cm^2 and to produce negative strains as large as 0.2%, indicating volumetric densification as large as 0.6%. Similar behavior was observed at 550°C as shown in Figure 30c, but at 610°C. the densification was significantly reduced. The most likely explanation for the densification response is formation of FeCrMo chi phase. which occurs in the 400 to 550°C temperature range.[34]

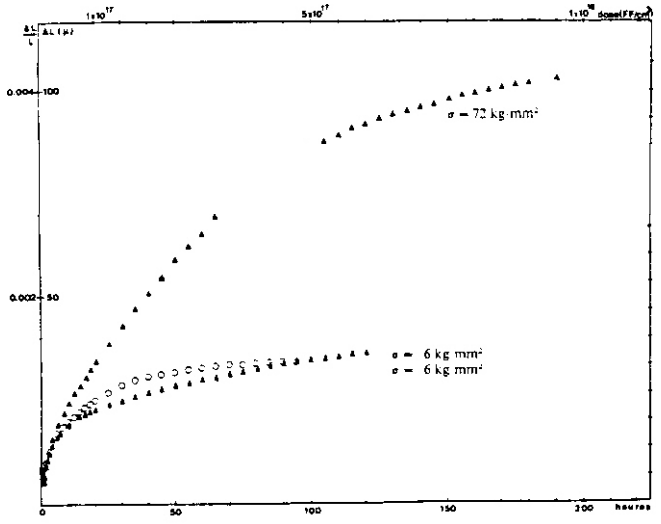

Figure 28. Change in length as a function of fission-fragment irradiation time for tungsten specimens tested at 20K for low and high applied stress states. Triangles denote preirradiation strain hardening treatments.[29]

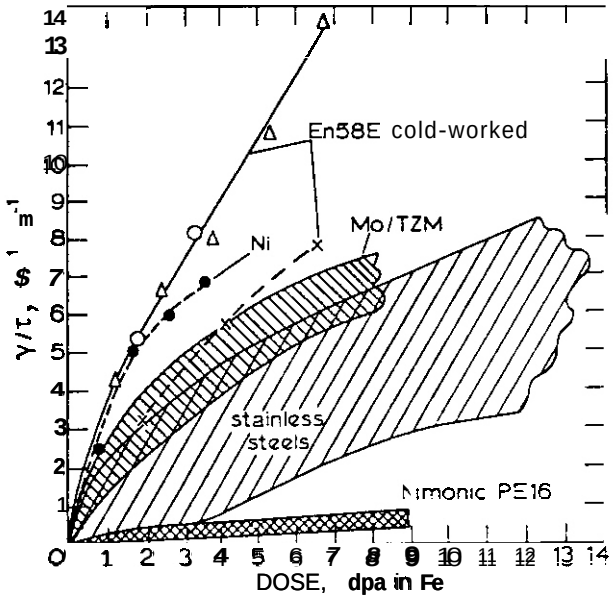

Figure 29. Creep of helices of various materials at ~280°C in DFR.[32]

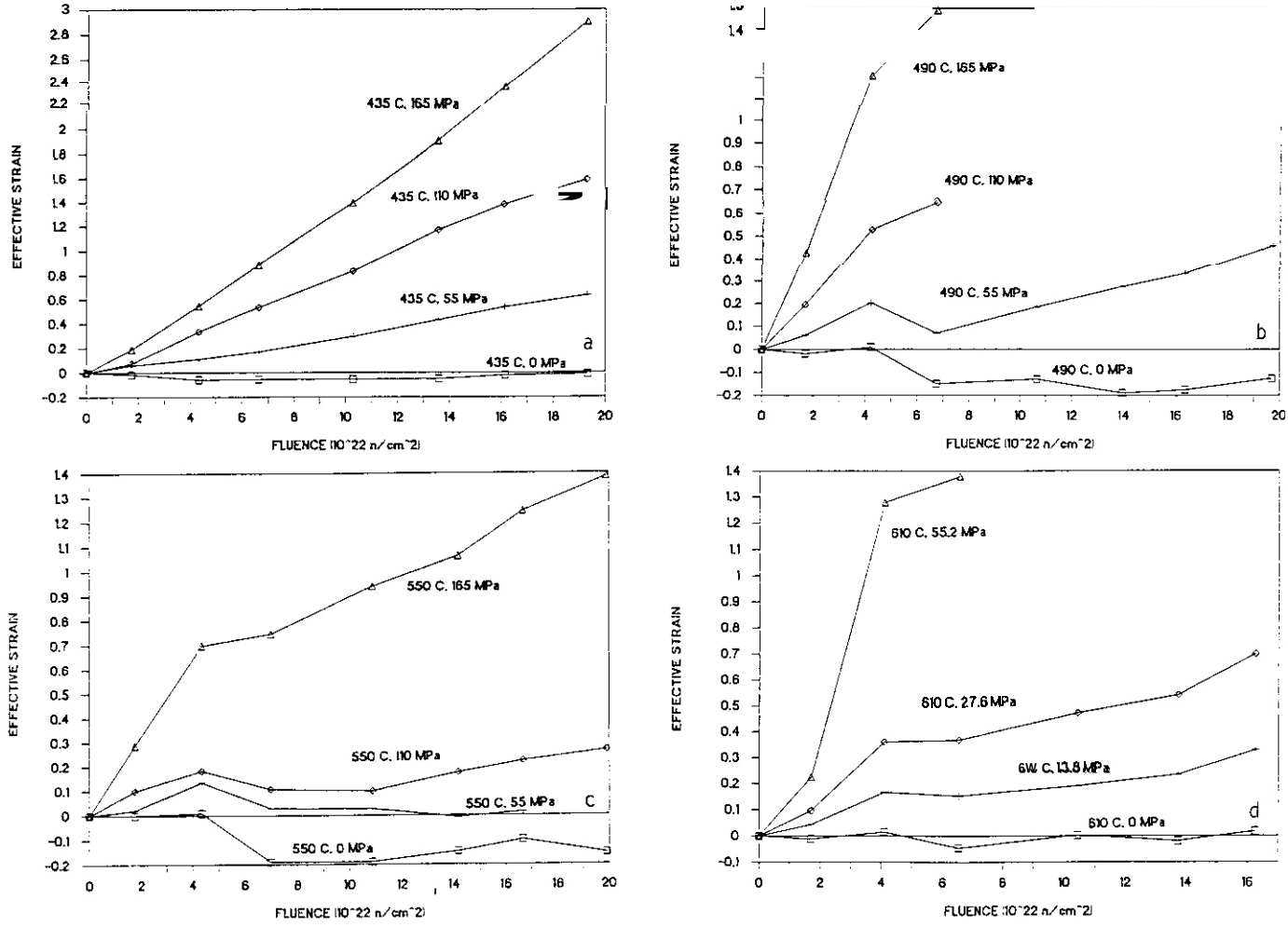

Figure 30. Compilation of creep strain results for pressurized tube specimens of HT-9 in EBR-II as a function of fluence at a) 435°C, b) 490°C. c) 550°C. and d) 610°C. Note that in all cases densification is indicated in the zero-stress condition.

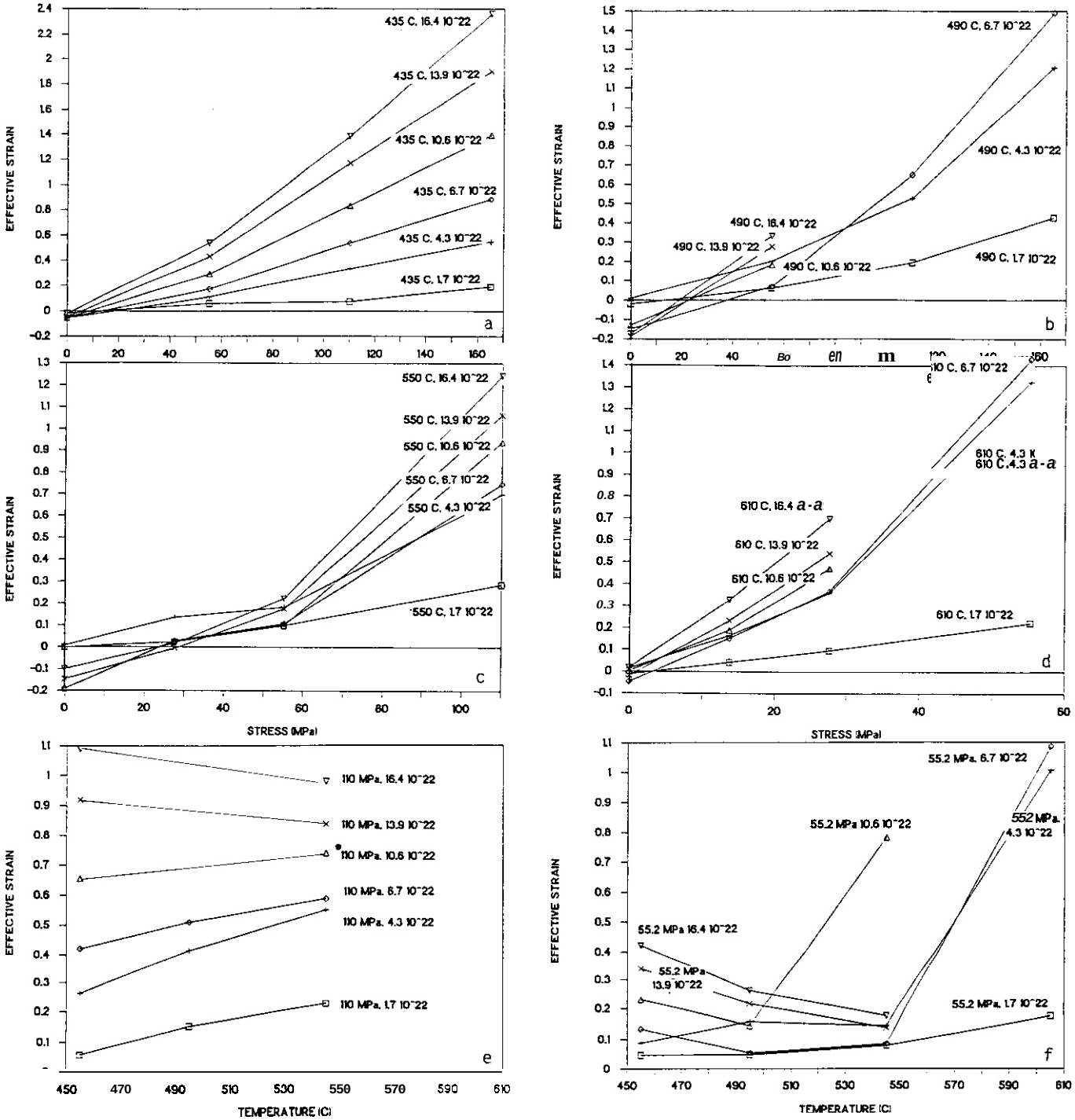

Figure 31. Compilation of creep strain results for pressurized tube specimens of HT-9 in EBR-II as a function of hoop stress at a) 435°C, b) 490°C, c) 550°C. and d) 610°C and as a function of temperature e) at 110 MPa and f) at 55 MPa.

In-reactor creep response in HT-9 pressurized tubes as a function of stress is nonlinear, as shown in Figures 31a through 31d. Densification canplicates the interpretation. but in all cases. nonlinear behavior is clearly seen. Plots of creep strain as a function of temperature for this data base were weakly a function of temperature. except in cases where a change in creep mechanism was indicated. However, the dependence changed from negative to positive slope when the stress changed from 55 to 110 MPa. The behavior can be seen in Figures 31e and 31f.

Similar response was observed in pressurized tube specimens irradiated at FFTF. Figure 32 allows comparison of six similar martensitic steel conditions. five compositional/heat-treatment variations of HT-9, and one condition for 9Cr-1Mo; many of these test results are reported to fluences of 2 x 10^{23} n/cm^2 or 100 dpa. Figure 32a shows results for the fusion heat of HT-9, which are notable for several

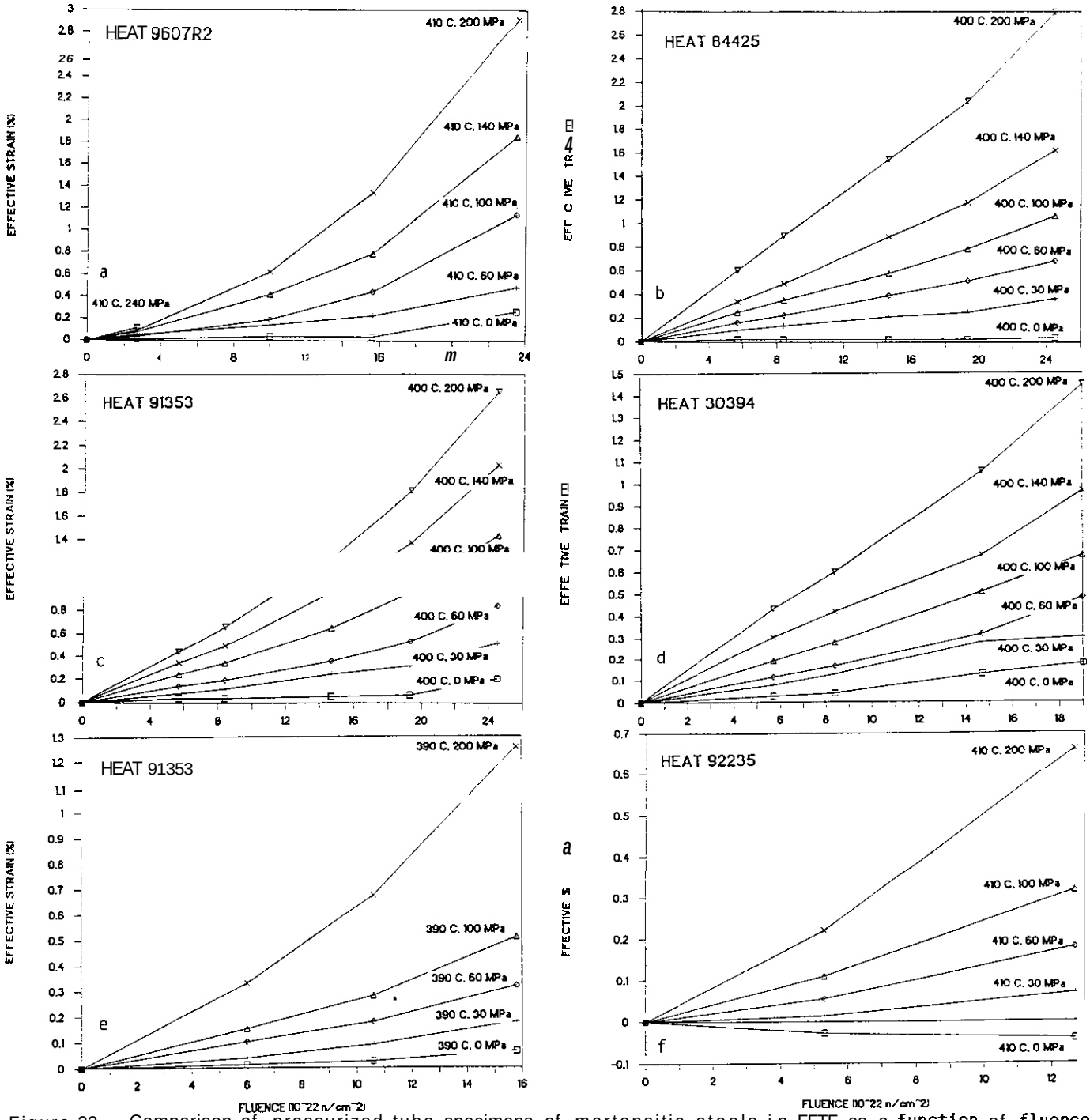

Figure 32. Comparison of pressurized tube specimens of martensitic steels in FFTF as a function of fluence at 400°C: a) HT-9 fusion heat 9607R2, b) HT-9 heat 84425, c) HT-9 heat 91353, d) 9Cr-1Mo heat 30394. e) HT-9 heat 91353 in a stronger heat-treatment condition. and f) HT-9 heat 92235 in the stronger heat-treatment condition.

reasons. Strain is nonlinear with fluence. but canparison of strains with those for heat R74075 in EBR-II shows that the fusion heat is stronger. No evidence of densification is apparent. suggesting heat-to-heat variations on precipitation response. Also, diameter increase occurs in the zero stress condition at fluences above 1.6 x 10^{23} n/cm^2, an indication of the onset of void swelling, with levels of 1% volumetric swelling indicated at 2.4 x 10^{23} n/cm^2. At least a part of the nonlinearity can therefore be attributed to swelling enhanced creep.

The effect of heat-to-heat variations on creep can best be demonstrated by canparison of Figures 32a, 32b and 32c. For example. all three figures demonstrate strains of just under 3% at 200 MPa and 2.4 x 10^{23} n/cm^2, but the stress dependencies differ and creep strains therefore appear to be fairly insensitive to canposition variations. Much of the difference between these curves can be ascribed to variations in

the fluence required for the onset of swelling. Also of note in Figure 32b is the linear response found for heat 84425 to 2.0 x 10^{23} n/cm^2, followed by deviation from linearity above 2.0 x 10^{23} n/cm^2. This deviation from linearity can be seen in the other two curves at the fluence level just before the onset of swelling. As a consequence, volumetric swelling can be expected in specimens shown in Figure 32b on the next discharge from reactor. Therefore. as had been shown with 2 Cr-1Mo, the effect of swelling-enhanced creep must be taken into account, and the onset of the effect can be identified prior to measurement of the actual swelling.

Canparison of the creep response in 9Cr-1Mo (Figure 32d) with those for HT-9 further shows heat-to-heat differences. The 9Cr-1Mo and HT-9 specimens have similar microstructures but quite different compositions. As demonstrated previously,[22] 9Cr-1Mo is more creep resistant than HT-9. Also, the onset of swelling occurs at a lower fluence, about 8 x 10^{22} n/cm^2. Therefore, canpositional variations can result in differences in irradiation creep response, but the differences appear to result in no more than a factor of 2 variation in creep strain.

Finally, Figure 32 allows comparison of the effect of heat treatment on creep resistance. Two sets of specimens were given heat treatments to promote higher tensile strength. primarily by lowering the tempering temperature. Comparison of Figures 32c and 32e shows a negligible effect of creep strength due to heat treatment: some differences may be identified. however. The high-strength condition indicates volumetric swelling in the zero stress condition starting at about 10 x 10^{22} n/cm^2, with a corresponding nonlinear effect of fluence at higher stress levels: the lower strength condition shows the start of swelling response at about 18 x 10^{22} n/cm^2. Heat 92235, shown in Figure 32f, gives similar creep strains at comparable stress and fluence. but shows densification in the zero stress condition. similar to that observed in heat R74075 tested in EBR-II (Figure 30a). It is concluded that changes in heat treatment. and therefore differences in microstructure. do not significantly change creep resistance. but they can alter the onset of volumetric swelling.

A further example is also instructive. A Laves precipitation strengthened alloy. known as D57, was tested in the solution-treated and cold-worked condition in FFTF (see Figure 33). This experiment provides an excellent example of the consequences of densification due to phase instability on irradiation creep.

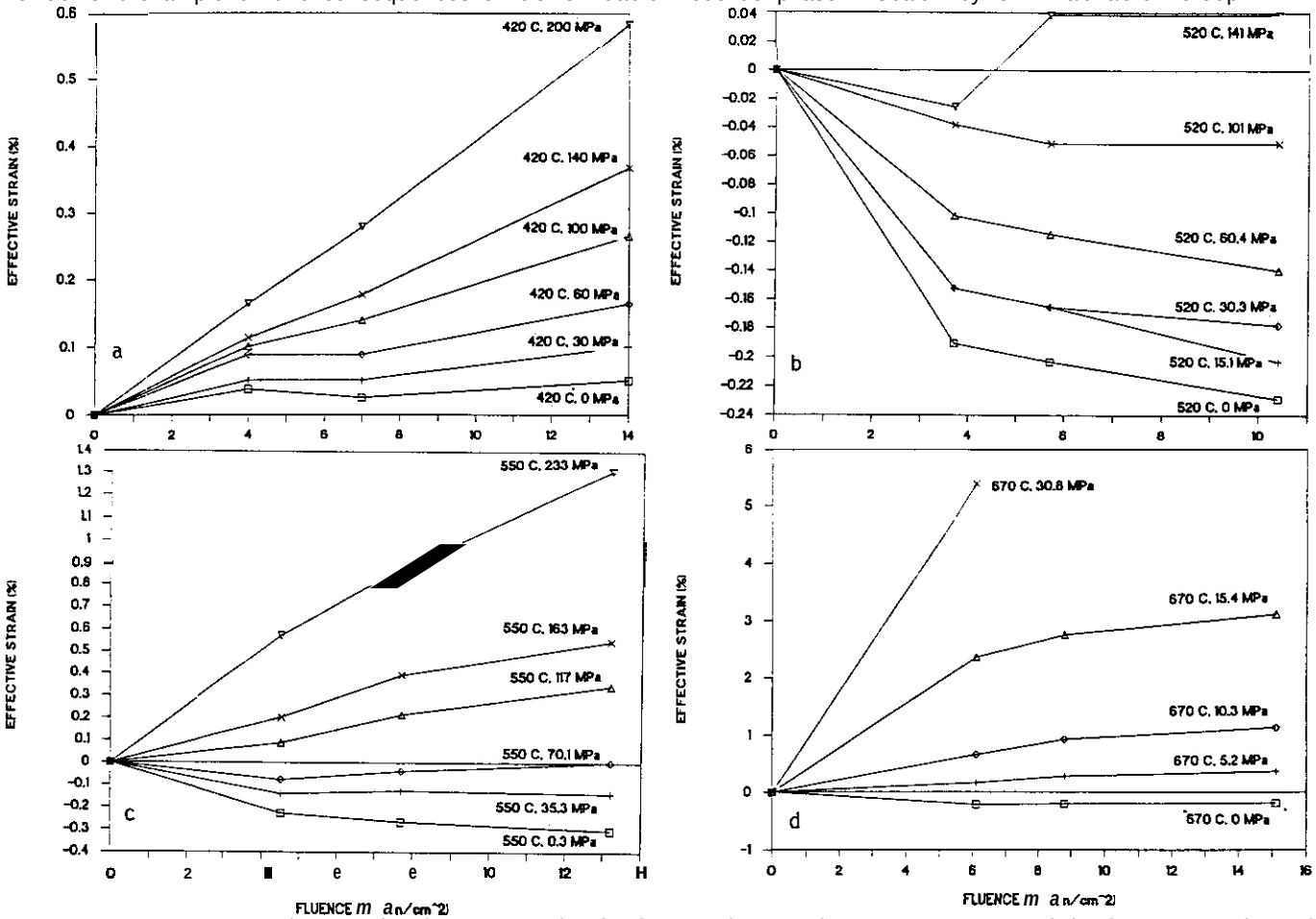

Figure 33. Creep strain results for pressurized tube specimens of D57, a Laves precipitation-strengthened delta ferritic alloy, tested in the solution-treated and cold-worked condition at a) 420°C. b) 520°C, c) 550°C, and d) 670°C.

The instability is again due to FeCrMo chi phase formation, and the densification is as large as 0.3% strain corresponding to a volumetric densification of 1%. At each irradiation temperature, the creep response is affected by densification, but the greatest effect is at 520°C (Figure 33b), where all but one of the pressurized tubes shrank even up to fluences as high as 10 x 10^{22} n/cm^2. Also of note is the observation that creep rates decrease with increasing fluence, possibly due to hardening fran precipitation.

CONCLUSIONS

As has been shown, there is now a large body of data describing irradiation creep in ferritic/martensitic steels and a much less canplete data base for other refractory alloys. The behavior can be sumnarized as follows: primary creep is often absent, behavior is often linear with dose but rarely linear with stress, and strains to failure can be as large as 25%. Some researchers report stress exponents between 1 and 2, but others report values near 6. (Values near 6 are expected to correspond to a thermal creep mechanism.)

It has been shown that composition variation can alter creep response, but variations in heat treatment that lead to significant changes in yield strength appear to be of little consequence to irradiation creep rates. The major impact of composition is on the onset of thermal-like creep mechanisms in the in-reactor creep behavior of different ferritic alloys. Canpositional modifications can extend the useful tmperature range for ferritic alloys. Composition variation not only changes the effective creep coefficient, but can also result in the enhancement or delay of other deformation mechanisms, such as swelling. As a result. if prediction of performance is critical. experiments must employ the proper canposition and the proper irradiation environment.

The data base suggests the unexpected and unexplained result that irradiation creep rates can be higher at very low temperatures than at intermediate temperatures. The relevant data tend to be only to low doses. and therefore this response may turn out to be transient. However, the consequences of this result to real machines operating at low temperatures necessitate the performance of further low temperature tests.

ACKNOWLEDGMENTS

The authors wish to thank F. A. Garner for providing a copy of his manuscript prior to publication.

REFERENCES

1. E. A. Little, D. R. Arkell, D. R. Harries, G. R. Lewthwaite. and T. M Williams, "Development of Ferritic-Martensitic Steels for Fast Reactor Applications." pp. 31-37 in the proceedings of the international conference Irradiation Behavior of Metallic Materials for Fast Reactor Core Components, Ajaccio, Corsica. France, June 4-8, 1979.

2. J. L. Straalsund. R. W. Powell, and B. A Chin. "An Overview of Neutron Irradiation Effects in LMFBR Materials," J. Nucl. Mater. 108-109 (1982) 299-305.

3. J. L. Straalsund and D. S. Gelles. "Assessment of the Performance of the Martensitic alloy HT-9 for Fast Breeder Reactor Applications," presented at the Topical Conference on F———— for Use in Nuclear Energy Technologies, HEOL-SA-2771 FP, Snowbird, UT. June 19-23, 1983.

4. D. R. Harries. "Ferritic/Martensitic Steels for Use in Near-Term and Commercial Fusion Reactors," pp. 141-155 in Proceedings of Topical Conference on Ferritic Alloys for Use in Nuclear Energy Technologies, J. W. Davis and D. J. Michel. Eds., AIME, Warrendale, Penn. (1984).

5. T. Lechtenberg. "Irradiation Effects in Ferritic Steels." J. Nucl. Mater. 133-134, 149-155 (1985).

6. D. S. Gelles. "Effects of Irradiation on Ferritic Alloys and Implications for Fusion Reactor Applications." J. Nucl. Mater. 149, 192-199 (1987).

7. K. Q. Bagley, L. E. Little. V. Levy, A Alamo, K. Ehrlich. K. Anderko. and A. Calza Bini, "European Development-of Ferritic-Martensitic Steels for Fast Reactor Wrapper Applications." Nucl. Energy, 27, 295-303 (1988).

8. W. Vandermeulen, A. De Bremaecker, S. de Burbure. J.-J. Huet. and P. Van Asbroeck. "Irradiation Creep in Ferritic Steels," pp. 1-4 in the proceedings of the international conference Irradiation Behavior of Metallic Materials for Fast Reactor Core Components, Ajaccio, Corsica. France, June 4-8, 1979.

9. K. Herschbach, K. Ehrlich, and E. Materna, "Uber Das Kriechverhalten und Mikrostructur de Ferritischen Werkstoffes Nr. 1.6770 unter Bestrahlung," pp. 25-29 in the proceedings of the international conference Irradiation Behavior of Metallic Materials for Fast Reactor Core Components, Ajaccio, Corsica, France. June 4-8, 1979.

10. M. M Paxton. E. A Chin, E. R. Gilbert. and R. E. Nygren, "Comparison of the In-reactor Creep of Selected Ferritic. Solid Solution Strengthened. and Precipitation Hardened Commercial Alloys." J. Nucl. Mater. 80, 144-151 (1979).

11. A. R. Causey, G. J. C. Carpenter, and S. R. MacEwem, "In-Reactor Stress Relaxation of Selected Metals and Alloys at Low Temperatures," J. Nucl. Mater. 90, 216-223 (1980).

12. M. M Paxton. E. A. Chin. and E. R. Gilbert, "The In-Reactor Creep of Selected Ferritic, Solid Solution Strengthened and Precipitation Hardened Alloys." J. Nucl. Mater. 95, 185-192 (1980).

13. E. R. Gilbert and B. A. Chin. "In-Reactor Creep Measurements," Nuc. Tech. 52, 273-283 (1981).

14. A. De Erenaecker and J.-J. Huet. "Irradiation Creep and Swelling of Ferritic Steels Irradiated in Fast Reactors: New Results," pp. 117-120 in Dimensional Stability and Mechanical Behavior of Irradiated Metals and Alloys, BNES. London (1983).

15. K. Herschbach. D. P. Ooser. and W. Doser, "Irradiation Creep of the Martensitic Steel No. 1.4914 Between 400°C and 600°C (Mol 5B)," pp. 121-124 in Dimensional Stability and Mechanical Behavior of Irradiated Metals and Alloys, ENES, London (1983).

16. R. J. Puigh and G. L. Wire, "In-reactor Creep Behavior of Selected Ferritic Alloys," pp. 601-606 in Proceedings of Topical Conference on Ferritic Alloys for Use in Nuclear Energy Technologies, J. W. Davis and D. J. Michel. Eds., AIME, Warrendale, Penn. (1984).

17. E. A. Chin. "An Analysis of the Creep Properties of a 12Cr-1Mo-WV Steel." pp. 593-599 in Proceedings of Topical Conference on Ferritic Alloys for Use in Nuclear Energy Technologies, J. W. Davis and D. J. Michel, Eds., AIME, Warrendale. Penn. (1984).

18. C. Wassilew. K. Herschbach, E. Materna-Morris. and K. Ehrlich. "Irradiation Behavior of 12%Cr Martensitic Steels," pp. 607-614 in Proceedings of Topical Conference on Ferritic Alloys for Use in Nuclear Energy Technologies, J. W. Davis and D. J. Michel. Eds., AIME, Warrendale. Penn. (1984).

19. J. M. Dupouy, Y. Carteret, H. Aubert and J. L. Eoutard. "EM 12, A Possible Fast Reactor Core Material." pp 125-128 in Proceedings of Topical Conference on Ferritic Alloys for Use in Nuclear Energy Technologies, J. W. Davis and D. J. Michel. Eds., AIME, Warrendale, Penn. (1984).

20. J.-J. Huet. L. Coheur, L. De Wilde, J. Gedopt. W. Hendrix. and W. Vandermeulen. "Fabrication and Mechanical Properties of ODS Ferritic Alloys Canning Tubes for Fast Reactor Fuel Pins." pp. 329-334 in Proceedinas of Topical Conference on Ferritic Alloys for Use in Nuclear Energy Technologies, J. W. Davis and O. J. Michel. Eds., AIME, Warrendale. Penn. (1984).

21. K. Herschbach. "In-Pile Creep of the Martensitic 1.4914: Some Fundamental Observations." J. Nucl. Mater. 127, 239-241 (1985).

22. R. J. Puigh. "In-Reartor Creep of Selected Ferritic Alloys," pp. 7-18 in Effects of R[illegible] Materials: Twelfth International Symposium, ASTM STP 870, F. A. Garner and J. S. Perrin. Eds., ASTM. Philadelphia, Penn. (1985).

23. O. S. Gelles and R. J. Puigh, "Evaluation of Ferritic Alloy Fe-2 Cr-1Mo After Neutron Irradiation: Irradiation Creep and Swelling." pp. 19-37 in Effects of Radiation on Materials: Twelfth International Symposium, ASTM STP 870, F. A Garner and J. S. Perrin, Eds., ASTM. Philadelphia, Penn. (1985).

24. O. S. Gelles, "Evaluation of Ferritic Alloy Fe-2 Cr-1Mo After Neutron Irradiation: Microstructural Development." pp 560-587 in Radiation-Induced Changes in Microstructure: Thirteenth International Symposium (Part I), ASTM STP 955, F. A. Garner, N. H Packan, and A. S. Kumar, Eds., ASTM. Philadelphia, Penn. (1987).

25. R. J. Puigh and F. A. Garner. "Irradiation Creep Behavior of the Fusion Heats of HT-9 and Modified 9Cr-1Mo," submitted for publication in the proceedings of Effects of Radiation on Materials: Fourteenth International Symposium, PNL-SA-15472. Pacific Northwest Laboratory, Ricnalana. Washington.

26. F. A Garner and R. J. Puigh, "Irradiation Creep Observed in FFTF-MOTA for HT-9, 9Cr-1Mo, AISI 316 and PCA" to be submitted for publication in Fusion Reactor Materials, DOE/ER-0313/6.

27. C. H. Henager and E. P. Simonen. "Light-Ion Irradiation Creep and Hardening of Model Ferritic Alloys." pp. 69-80 in Influence of Radiation on Materials Prooerties: Thirteenth International Symposium (Part II), ASTM STP 956, F. A Garner, C. H. Henager, Jr. and N. Igata, Eds., ASTM, Philadelphia, Penn. (1987).

28. P. Jung and N. M. Afify. "Creep of DIN 1.4914 Martensitic Stainless Steel Under Proton Irradlation," J. Nucl. Mater. 155-157, 1019-1024 (1988).

29. R. V. Hesketh, "Collapse of Vacancy Cascades to Dislocation Loops," pp. 389-401 in Proceedings of the International Conference on Solid State Physics Research with Accelerators, A. N. Goland. Ed.. BNL-50083 (C-52) September 25-28. 1967.

30. S. N. Buckley. "Irradiation Growth and Irradiation Enhanced Creep in F.C.C and B.C.C. Metals," pp. 547-565 in The Interactions Between Dislocations and Point Defects, AERE-R 5944 Vol 2, Harwell, England. July 4-12. 1968.

31. J. Ponsoye. "Irradiation de Tungstene sous Contrainte Uniaxiale a Basse Temperature." Rad. Effects. translation AEC-tr-7451 8, 13-26, (1971).

32. R. V. Hesketh, "Irradiation Creep," pp. 221-231 in Irradiation Embrittlement and Creeo of Fuel Cladding and Core Components, London. BNES November 9-10, 1972

33. D. Mosedale, G. W. Lewthwaite. and I. Ramsay, "Irradiation Creep of Fast Reactor Materials," pp. 132-135 In Physical Metallurgy of Reactor Fuel Elements, J. E. Harris and E. C. Sykes, Eds., Berkeley. UK., September 2-7, 1973.

34. D. S. Gelles and L. E. Thomas, "Effects of Neutron Irradiation on Microstructure in Experimental and Commercial Ferritic Alloys." pp. 329-334 in Proceedings of Topical Conference on Ferritic Alloys for Use In Nuclear Energy Technologies, J. W. Davis and D. J. Michel, Eds., AIME, Warrendale. Penn. (1984).

6.2 Austenitic Stainless Steels

THE DEVELOPMENT OF AUSTENITIC STAINLESS STEELS FOR FAST INDUCED-RADIOACTIVITY DECAY -- R. L. Klueh and P. J. Maziasz (Oak Ridge National Laboratory)

OBJECTIVE

Induced radioactivity in the first-wall and blanket-structure materials will make these components highly radioactive after their service lifetime, leading to difficult radioactive waste-management problems. One way to minimize the disposal problem is to use structural materials in which radioactive isotopes induced by irradiation decay quickly to levels that allow simplified disposal techniques. We are assessing the feasibility of developing such austenitic stainless steels.

SUMMARY

A program is under way to develop a nickel-free austenitic stainless steel for fusion-reactor applications. Previous work has shown that an austenite-stable alloy should be possible with a base composition of Fe-20Mn-12Cr-0.25C. Tensile properties for this base composition were comparable to those of type 316 stainless steel. To improve strength and irradiation resistance, closely controlled quantities of W, Ti, V, C, B, and P were added to this base. Such additions resulted in improved tensile properties over those for type 316 stainless steel in both the solution-annealed and 20% cold-worked conditions.

PROGRESS AND STATUS

Introduction

An alloy-development program is in progress[1] to develop fast induced-radioactivity decay (FIRD) austenitic stainless steels to replace the high-nickel stainless steels that are among the present candidate alloys for fusion applications. These steels are designed to meet the criteria for shallow land burial of radioactive isotopes, as decribed in the Nuclear Regulatory Comnission Guidelines 10CFR61. According to 10CFR61, Ni, N, Nb, Mo and Cu must be minimized. For a FIRD stainless steel, manganese is to be used as a replacement for nickel.

Work to develop high-manganese reduced-activation austenitic steels is also in progress elsewhere.[2-6] However, nitrogen is often used for austenite stabilization,[2,3,5] and in other instances, some nickel was allowed.[2,3] In keeping with 10CFR61, neither nitrogen nor nickel were used for austenite stabilization in the present work.

It was proposed that an effort be made to first determine Fe-Mn-Cr-C compositions that produce a fully austenitic microstructure.[7] This base composition could then be modified to obtain strength and irradiation resistance at least equal to that of current candidate fusion-reactor structural materials. By investigating a series of Fe-Mn, Fe-Mn-Cr, and Fe-Mn-Cr-C alloys, the austenite-stable region for the Fe-Mn-Cr-C system was determined.[7] The result was a "modified Schaeffler diagram" for high-manganese alloys, which differed from the standard diagram for high-nickel steels containing only small amounts of manganese.[7] With the nmdified diagram it was possible to pick a stable austenite composition for a high-manganese Fe-Mn-Cr-C alloy. A composition range of Fe-12/14%Cr-20/25%Mn0.1/0.25%C was suggested.[7]

In the present report a base composition was chosen and the tensile properties were determined. That base was then alloyed for strength and irradiation resistance. The objective was an alloy with strength and irradiation resistance equivalent to or better than that of type 316 stainless steel, which is considered a possible fusion-reactor structural material.

Experimental Procedure

Based on the results of the previous work,[7] a nominally Fe-20 Mn-12Cr-0.25C steel was chosen as a base composition. This composition was alloyed for strength and irradiation resistance by adding Ti, W, V, P, and B. All but tungsten have been successfully used to improve the properties of nickel-stabilized stainless steels.[8,9] Tungsten was substituted for rmlybdenum, which cannot be used in a FIRD steel.

Seven experimental alloys, including the base composition, were obtained in the form of 600-g button heats. Table 1 lists the alloys and their designations. By making elemental additions to the base composition (designated MnCrC), alloys were obtained with titanium (MnCrCTi), tungsten (MnCrCW), a combination of titanium and tungsten (MnCrCWTi), and combinations of these elements with V, B, and P (MnCrCTiBP. MnCrCTiVBP, and MnCrCWTiVBP). When additions of the various elements were made. nominal levels of Ti, W, V, B. and P of 0.1, 1, 0.1, 0.005, and 0.03, respectively, were sought. Actual compositions are shown in Table 1.

Table 1. Fe-Cr-Mn Alloys Tested

Alloy Designation	Composition,[a] wt %							
	Cr	Mn	C	Ti	W	V	P	B
MnCrC	11.83	20.51	0.24			0.01	0.003	
MnCrCTi	11.73	20.50	0.25	0.11	0.09	0.01	0.003	
MnCrCW	11.80	20.46	0.23		0.83	0.01	0.004	
MnCrCTiW	11.71	21.13	0.25	0.12	0.77	0.01	0.003	
MnCrCTiPB	11.85	20.50	0.24	0.10		0.01	0.034	0.005
MnCrCTiVPB	11.84	20.82	0.22	0.10		0.10	0.033	0.005
MnCrCTiWVPB	11.70	20.39	0.25	0.10	1.08	0.10	0.027	0.005

[a]Balance iron.

Alloys were cast into a rectangular cross section of 12.7 mm by 25.4 mm by 152 mm. They were hot rolled at 1050°C to a thickness of approximately 6.4 mm. After homogenizing for 5 h at 1200°C, the steel was cold rolled to a thickness of 0.76-mm in five stages. Between each stage, the steel was annealed 1 h at 1150°C. The final sheet was in a 20% cold-worked condition.

Tensile tests were made at room temperature, 200, 300, 400, 500, and 600°C on specimens in the cold-worked condition and after two annealing treatments: 1 h at 1050°C and 2 h at 1150°C. Specimens had a reduced gage section 20.3-mm long by 1.52-mm wide by 0.76-mm thick. All specimens were machined with gage lengths parallel to the rolling direction. Tests were made in vacuum on a 120-kN-capacity Instron universal testing machine at a crosshead speed of 8.5 μm/s, which resulted in a nominal strain rate of ~4.2 × 10^{-4}/s.

Results and Discussion

Optical Microscopy – Microstructures for the Fe-20Mn-12Cr-0.25C base alloy (the MnCrC) and type 316 stainless steel are shown in Fig. 1 after both were solution annealed 1 h at 1050°C. Overall microstructures were quite similar: both appeared to contain scattered precipitates in the cross section. Grain size for both steels was estimated as ASTM number 4.

ORNL-PHOTO 4967-89

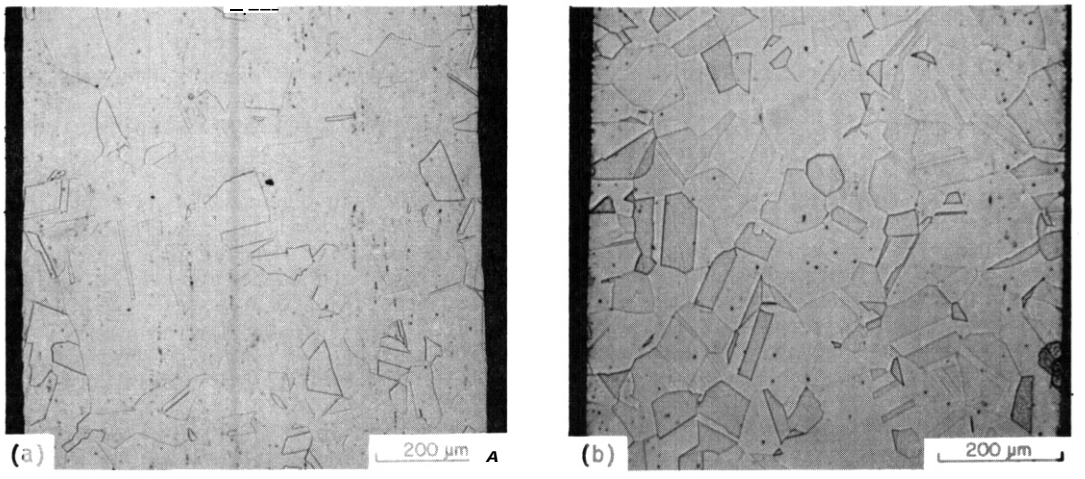

Fig. 1. Microstructures of (a) type 316 stainless steel and (b) Fe-20%Mn-12%Cr-0.25%C alloy annealed 1 h at 1050°C.

When alloying elements were added to the base composition [Fig. 2(a)], the primary change appeared in the amounts of precipitate present and the grain size (Fig. 2 and Table 2). Figure 2 shows the microstructures for the steels after annealing at 1050°C. A tungsten addition (MnCrCW) [Fig 2(b)] had only a small effect on the grain size and precipitation relative to MnCrC, but the addition of titanium (MnCrCTi) [Fig. 2(c)] led to a smaller grain size and an increase in the amount of precipitate. There was somewhat more precipitate present when tungsten and titanium were present in the same alloy (MnCrCWTi) [Fig. 2(d)]. Still more precipitate formed on the alloy with Ti, B, and P (MnCrCTiBP) [Fig. 2(e)] and then still more formed in the steel to which Ti, V, B, and P were added (MnCrCTiVBP) [Fig. 2(f)]. The steel with all the elements added (MnCrCWTiVBP) [Fig. 2(g)] contained the most precipitate. The primary difference between microstructures of steels annealed at 1050°C (Fig. 2) and those produced by annealing at 1150°C was that after the 1150°C anneal, a smaller portion of the precipitate appeared in the matrix and more at grain boundaries. As shown in Table 2, grain size was considerably larger after the 1150°C anneal. This is demonstrated in Fig. 3, where the microstructures of the MnCrCTiBP and MnCrCWTiVBP annealed at 1050 and 1150°C are compared.

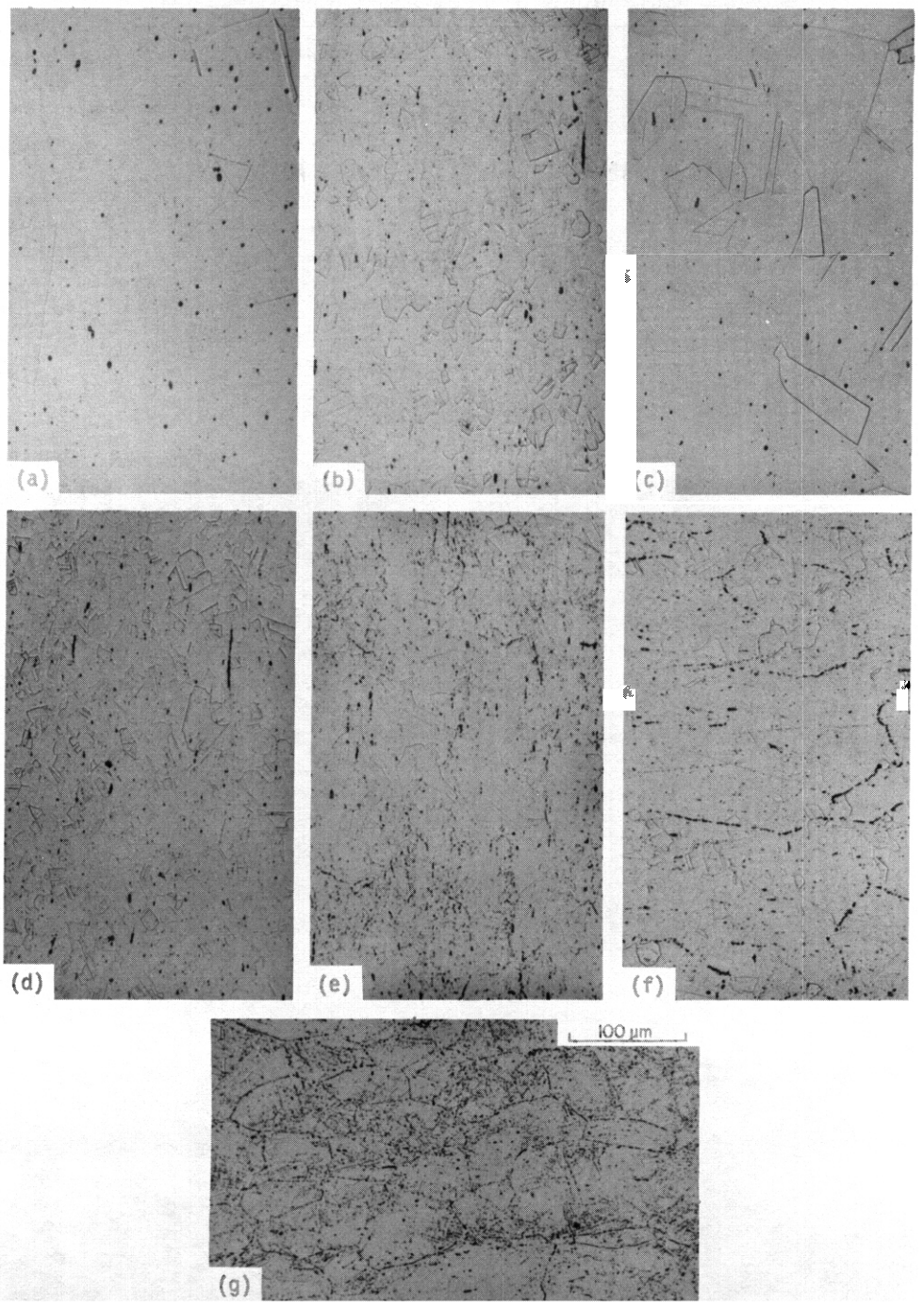

Fig. 2. Optical microstructures of seven experimental heats of high-manganese steels annealed 1 h at 1050°C. (a) MnCrC, (b) MnCrCTi, (c) MnCrCW, (d) MnCrCTiW, (e) MnCrCTiBP. (f) MnCrCTiVBP, and (g) MnCrCTiWVBP.

Electron Microscopy — For the MnCrC, neither the specimen annealed 1 h at 1050°C nor the one annealed 2 h at 1150°C contained any matrix precipitate, although the specimen annealed at 1150°C contained a few precipitates along grain boundaries (Fig. 4).

When titanium was added (MnCrCTi), a relatively high density of precipitates formed within the grains of the steel annealed at 1050°C (Fig. 5); these precipitates often appeared to have formed in rows or bands, as shown in Fig 5. After annealing at 1150°C, most of the precipitation occurred on grain boundaries [Fig. 6(a)]. Matrix precipitates were coarser than those for the steel annealed at 1050°C, and they were generally surrounded by tangled dislocations [Fig. 6(b)].

Table 2. ASTM Grain Size of Manganese-Stabilized Steels

Alloy Designation	Heat Treatment	
	1 h at 1050°C	2 h at 1150°C
MnCrC	3	1
MnCrCTi	8	6
MnCrCW	4	3
MnCrCTiW	8	6
MnCrCTiPB	8	6
MnCrCTiVPB	8	4
MnCrCTiWVPB	8	5
316 SS	4	5

ORNL-PHOTO 4969-89

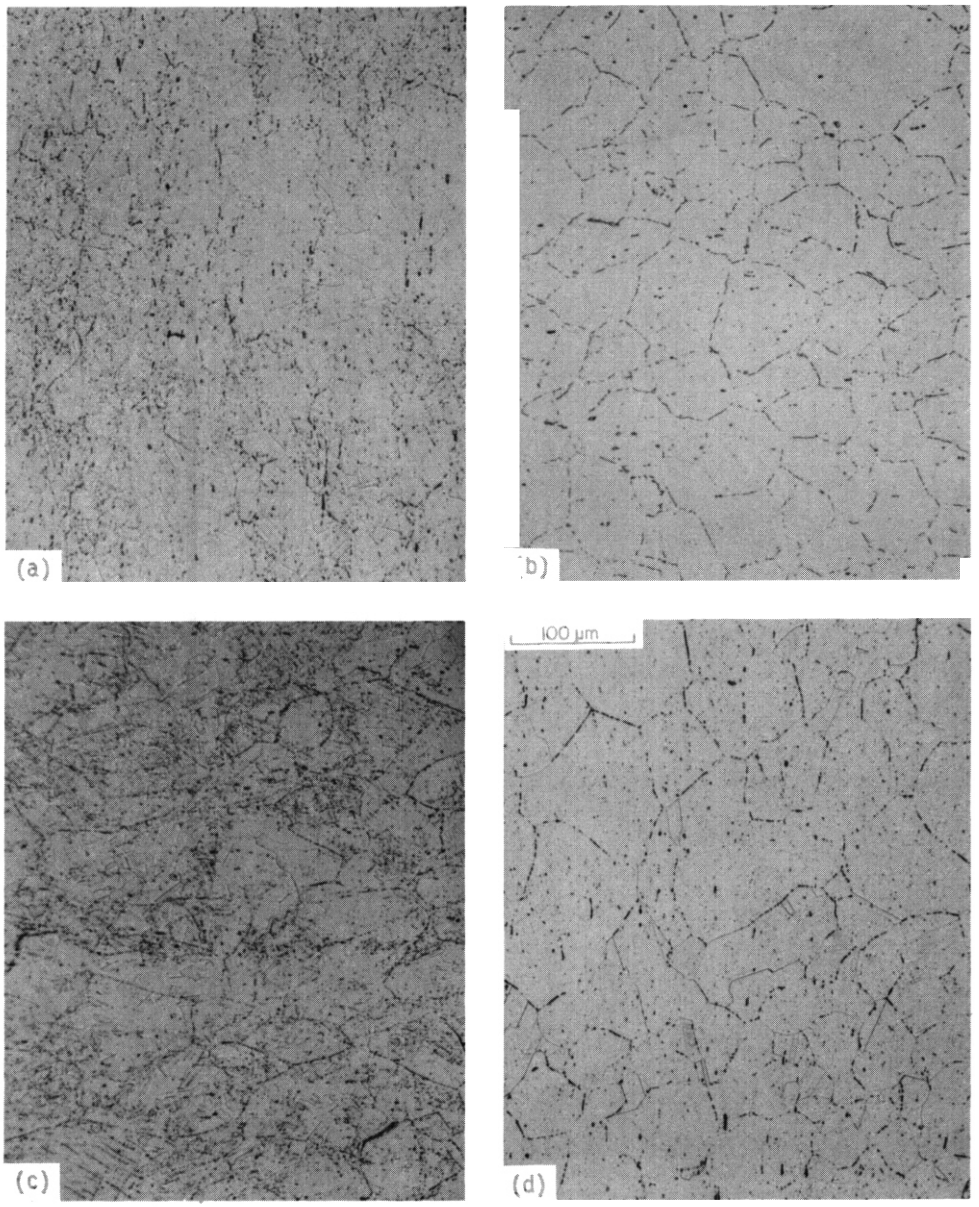

Fig. 3. A comparison of the microstructures of (a) and (b) MnCrCTiBP and (c) and (d) MnCrCTiWVBP after annealing 1 h at 1050°C [(a) and (c)] and 2 h at 1150°C [(b) and (d)].

YE-13826

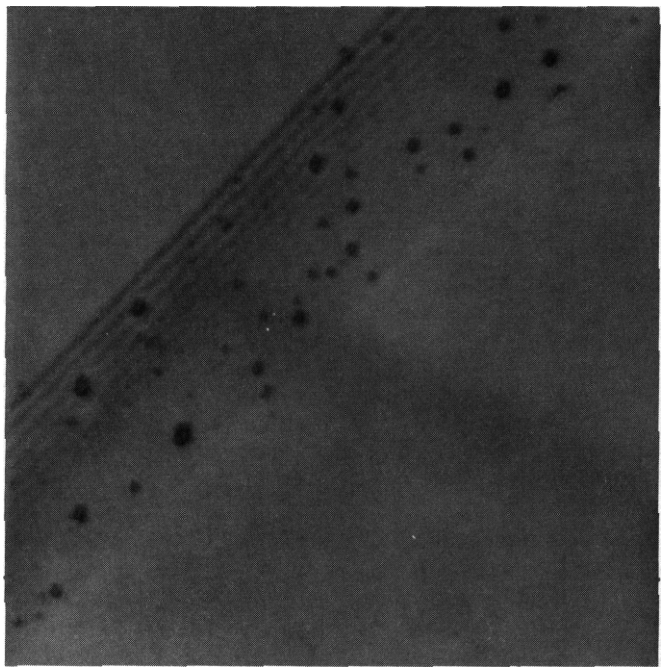

Fig. 4. Precipitates in grain boundary of the Fe-Mn-Cr-C (MnCrC) base alloy after annealing 2 h at 1150°C.

YE-13932

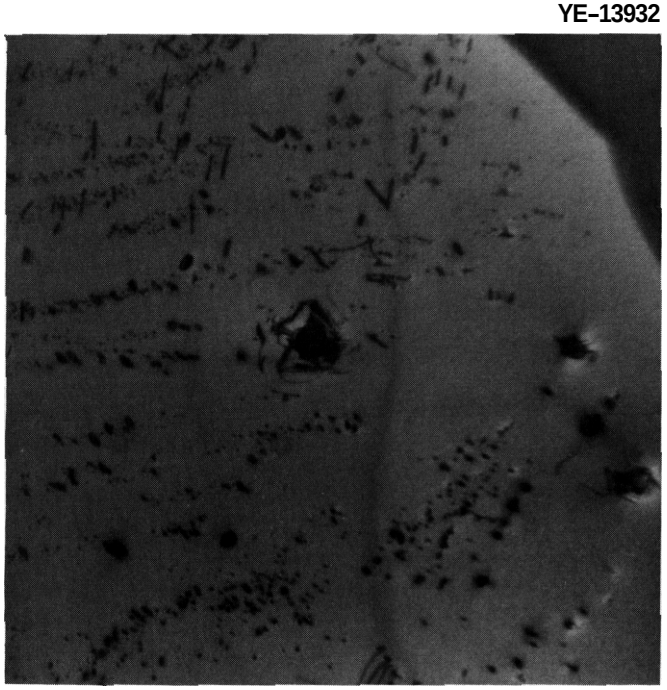

Fig. 5. Matrix precipitates in MnCrCTi annealed 1 h at 1050°C.

The base composition with tungsten added (MnCrCW) contained a few fine precipitates scattered through the matrix after annealing at 1050°C. Annealing at 1150°C resulted in a few large precipitates in the matrix. These precipitates were generally not surrounded by dislocations, as were precipitates formed in the MnCrCTi. Precipitates were also present on grain boundaries after annealing at 1150°C; these were larger and of lower density than for those in MnCrCTi (Fig. 7).

For the base steel with additions of both titanium and tungsten (MnCrCTiW), a relatively fine precipitate formed in the matrix when annealed at 1050°C [Fig. 8(a)]. In the specimen annealed at 1150°C, a much coarser distribution of precipitates formed, and these were surrounded by dislocations [Fig. 8(b)]. Neither of the specimens gave much indication of precipitation on grain boundaries.

Additions of phosphorus and boron in combination with titanium (MnCrCTiPB) seemed to lead to a non-uniform distribution of fine precipitates in both the matrix and grain boundaries of the specimens annealed at both temperatures. There were also some larger particles present in the specimens annealed at 1050°C, and this specimen contained a distribution of dislocations, evidently the remnants of the prior cold work (Fig. 9). "Wavy" boundaries were observed after both heat treatments, and it appeared that the boundary had faceted [Fig. 10(b)]. In some instances, this appeared to be associated with precipitates [Fig. 10(b)].

Vanadium in combination with Ti, B, and P (MnCrCTiVBP) resulted in a large increase in the amount of fine precipitates that formed in the steel annealed at 1050°C (compared to the steel without B and P). Many of these precipitates appeared in bands (Fig. 11), which must be associated with moving boundaries during recrystallization of the cold-worked structure. There was some grain boundary precipitation. After the 1150°C anneal, the grains contained a few precipitates, although most of the precipitation was on the boundaries — much more than for the specimen annealed at 1050°C. Grain boundary faceting was observed after both annealing treatments.

Finally, for the MnCrCTiWVBP, a relatively high density of precipitates was again present in the steel annealed at 1050°C, many of them in bands, as observed in the MnCrCTiVBP. A much lower density of precipitates was present in the steel annealed at 1150°C. In this specimen, many of the precipitates were surrounded by dislocations. A discontinuous layer of precipitates was observed on the grain boundaries. and grain boundary faceting was again evident (Fig. 12).

ORNL-PHOTO 4970-89

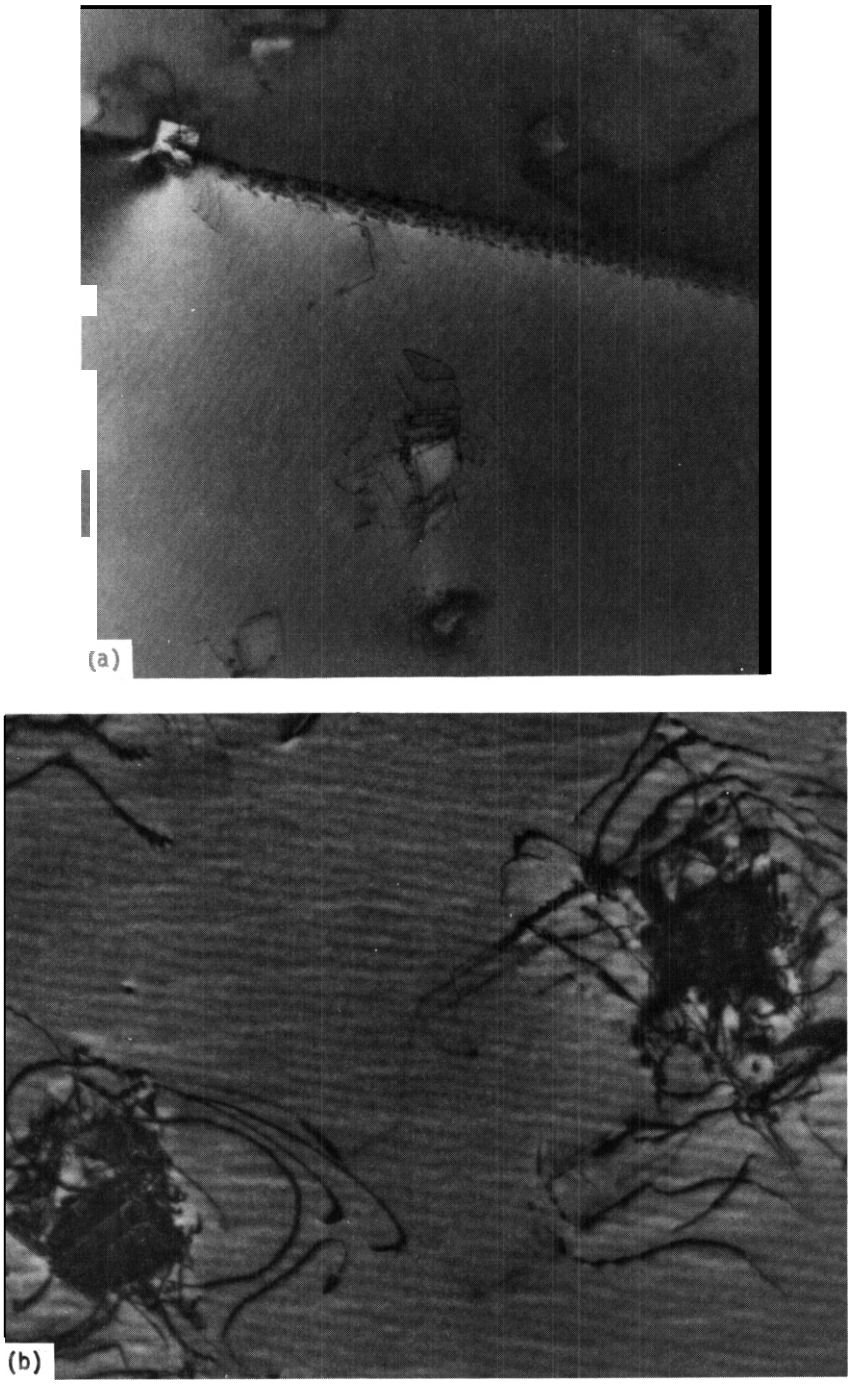

Fig. 6. (a) Grain boundary and matrix precipitates in MnCrCTi and (b) the matrix precipitates at higher magnification after annealing 2 h at 1150°C.

YE-13929

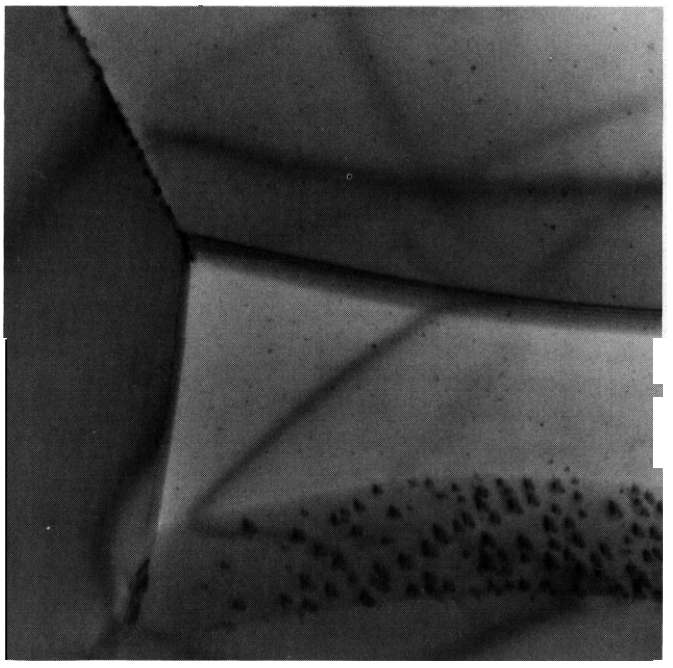

Fig. 7. Grain boundary precipitates in MnCrCW annealed 2 h at 1150°C.

Only two types of precipitate were identified: MC, generally present in fine distributions, and $M_{23}C_6$, which was generally observed as coarse particles, often on grain boundaries.

Because the small specimens from which the TEM specimens were taken were cooled rapidly after the anneal, precipitates must have formed during the anneal (or failed to dissolve). Thus, these heat treatments are not a true solution anneal. A finer distribution of precipitates is expected at the lower temperature, as observed. The distribution of precipitates in bands after the 1050°C anneal indicates that the precipitation process is intimately connected with the recrystallization process at this temperature. Precipitates present in these steels prior to the anneal were those formed by an anneal at 1150°C prior to the final cold-working treatment.

Tensile Behavior — Figures 13 and 14 show a comparison of the tensile properties of type 316 stainless steel (316 SS) with the MnCrC after annealing 1 h at 1050°C and after being cold worked 20% (common conditions for using such a steel). The 0.2% yield stress (YS) of the manganese-stabilized steel in both conditions was equivalent to that of the type 316

ORNL-PHOTO 4971-89

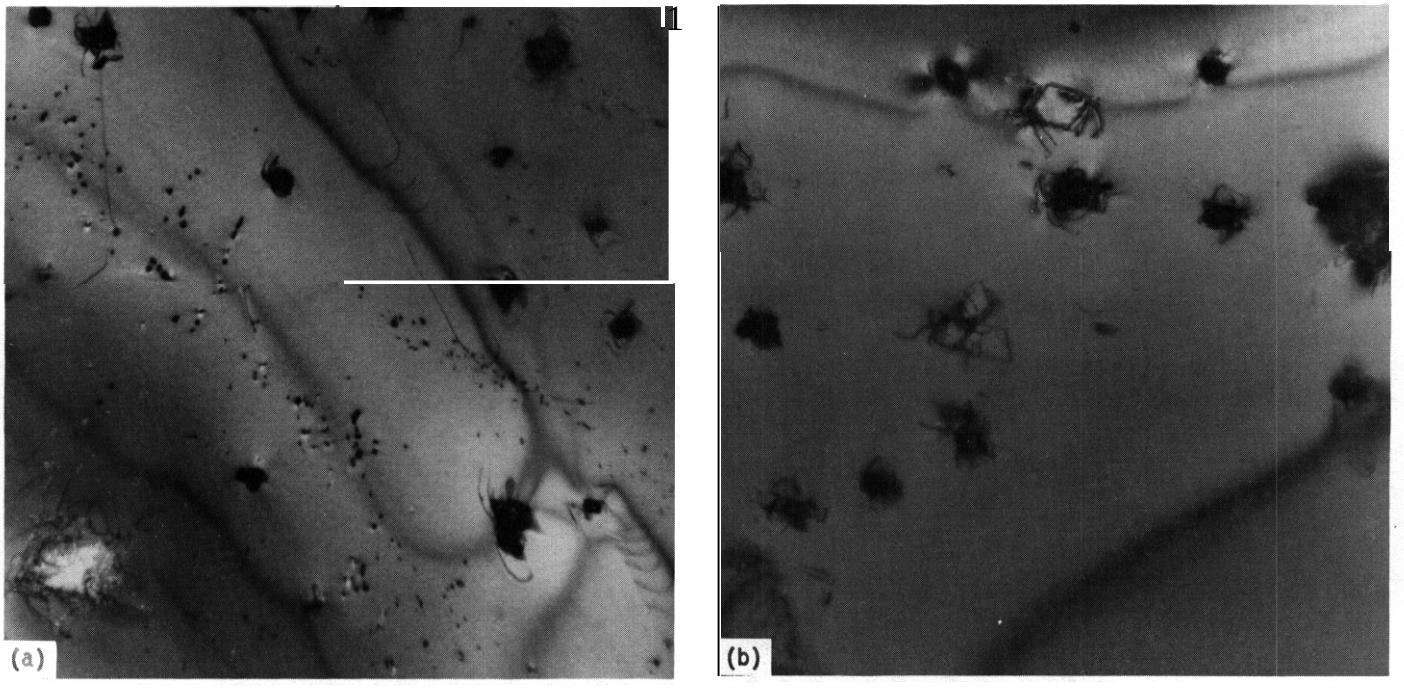

Fig. 8. Examples of matrix precipitation observed in the MnCrCTiW after annealing (a) 1 h at 1050°C and (b) 2 h at 1150°C.

YE-13934

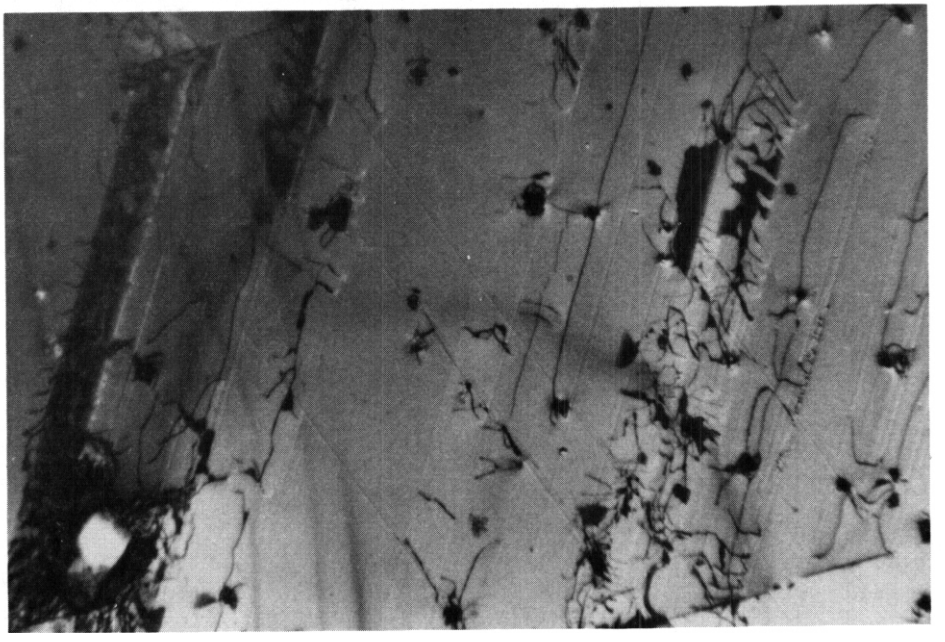

Fig. 9. Microstructure of MnCrCTiBP annealed 1 h at 1050°Cr showing matrix precipitate and dislocation structure.

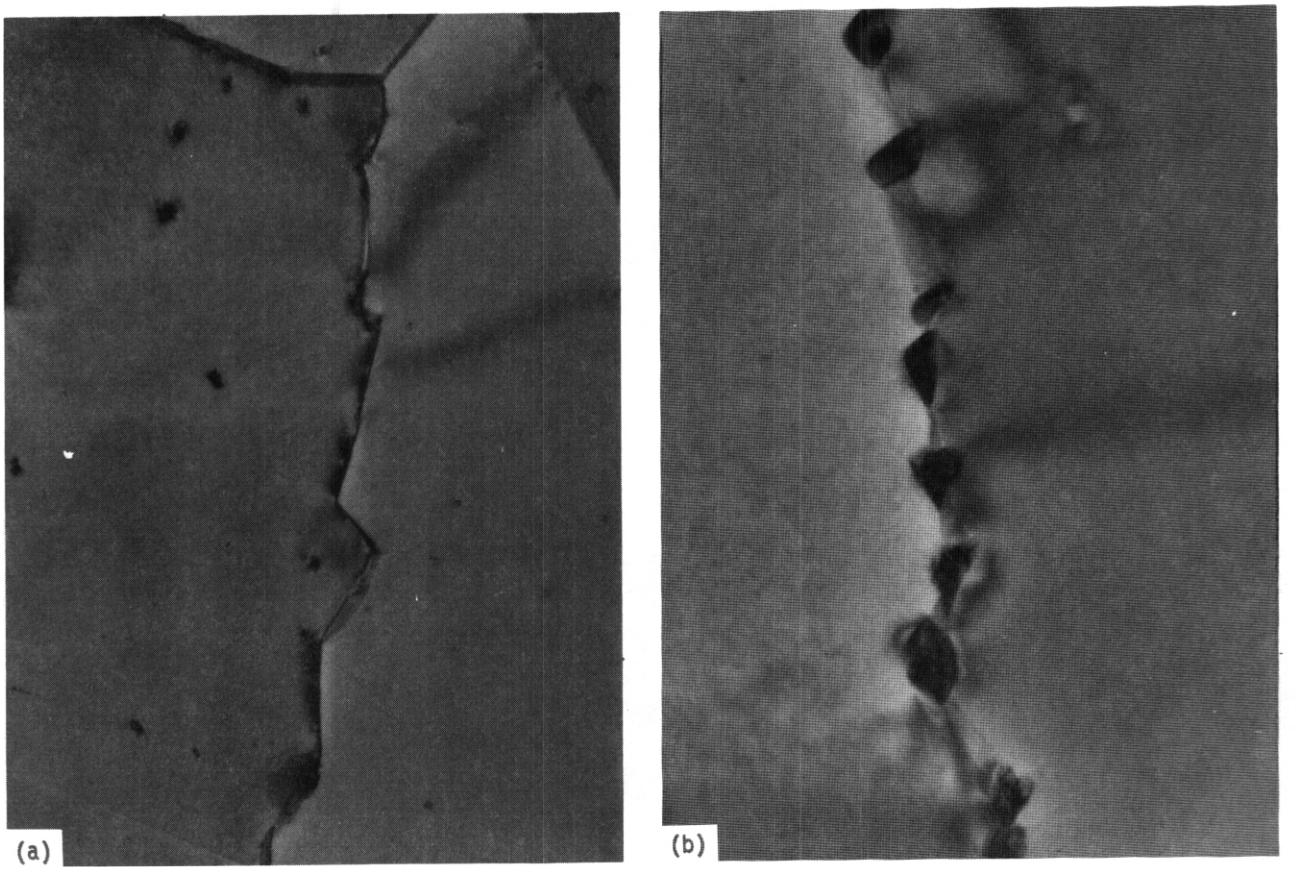

Fig. 10. Microstructure of MnCrCTiBP annealed 2 h at 1150°C showing (a) "wavy" or faceted grain boundary and (b) higher magnification photomicrograph of the precipitates observed in association with wavy boundaries.

YE-13935



Fig. 11. Microstructure of MnCrCTiVBP annealed 1 h at 1050°C.

YE-13821

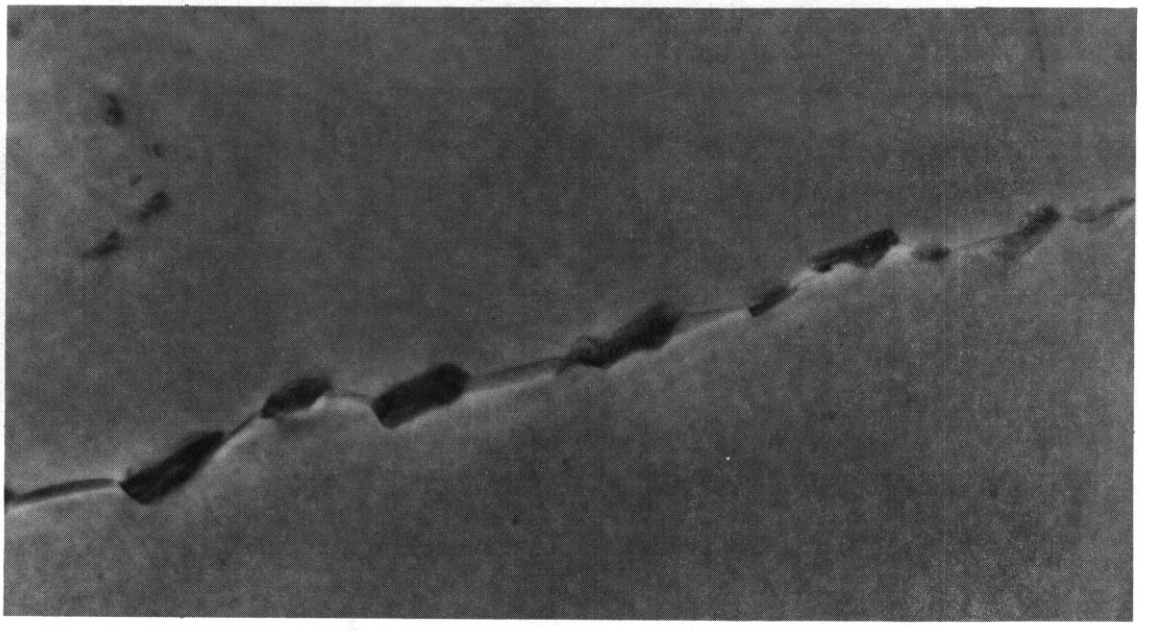

Fig. 12. Grain boundary and matrix precipitation in the MnCrCTiWVBP annealed 2 h at 1150°C.

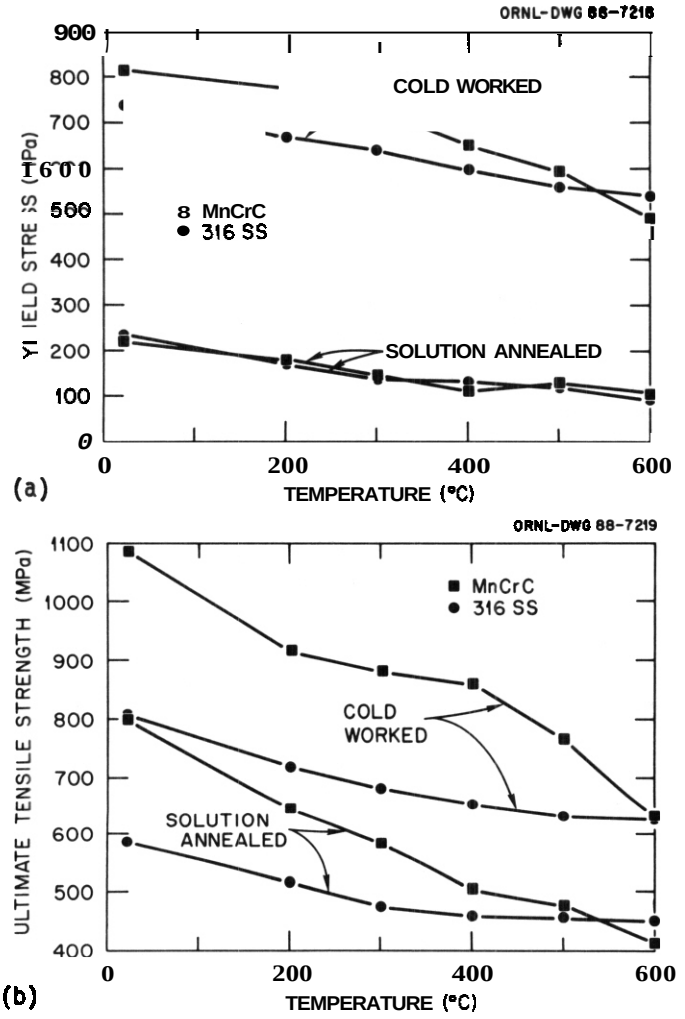

Fig. 13. (a) 0.2% yield stress and (b) ultimate tensile strength plotted against test temperature for the Fe-Mn-Cr-C alloy and type 316 stainless steel in the 20% cold-worked condition and annealed 1 h at 1050°C.

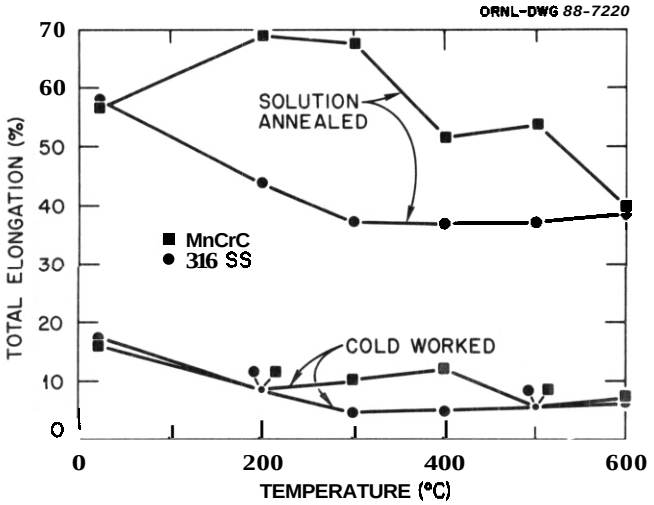

Fig. 14. Total elongation plotted against test temperature for the Fe-Mn-Cr-C (MnCrC) alloy and type 316 stainless steel in the 20% cold-worked condition and annealed 1 h at 1050°C.

SS [Fig. 13(a)]. Because manganese additions cause an increased work-hardening rate, the MnCrC steel achieved a higher ultimate tensile strength (UTS) for both thermo-mechanical conditions [Fig. 13(b)]. Despite this higher work-hardening capability, the high-manganese steel still had equivalent or better ductility (as measured by total elongation) in the solution-annealed and cold-worked conditions (Fig. 14).

These results indicated that an austenitic base alloy with substantial strength and ductility can be obtained using the information developed in the modified Schaeffler diagram.[1] The next objective was an improvement in the strength of the new alloys by making further minor element additions. This was accomplished by adding Ti, W, V, P, and B to the Fe-20Mn-12Cr-0.25C base composition (Table 1).

Table 3 gives the room-temperature tensile properties for seven alloys, which includes the MnCrC steel, along with similar results for type 316 stainless steel. The manganese-stabilized steels were tested in two annealed conditions and in the 20% cold-worked condition. The 316 SS was tested after the 1050°C anneal and after cold working 20%.

Table 3. Room-temperature tensile properties of manganese-stabilized stainless steels

Alloy Designation	Strength, MPa		Elongation, %	
	YS	UTS	Uniform	Total
Annealed 1 h 1050°C				
MnCrCTi	279	927	49.7	53.0
MnCrCW	267	803	57.1	59.9
MnCrCTiW	302	918	53.8	56.9
MnCrCTiPB	288	935	52.2	55.6
MnCrCTiVPB	275	935	51.0	53.9
MnCrCTiWVPB	304	915	54.9	57.5
316 SS	236	586	54.3	58.2
Annealed 2 h 1150°C				
MnCrC	233	766	53.4	55.1
MnCrCTi	258	891	53.5	56.4
MnCrCW	247	761	55.4	57.0
MnCrCTiW	258	882	54.5	57.2
MnCrCTiPB	271	891	52.8	54.2
MnCrCTiVPB	221	859	49.6	50.4
MnCrCTiWVPB	264	869	59.9	61.7
20% Cold Worked				
MnCrC	815	1086	14.1	16.0
MnCrCTi	954	1160	10.7	13.0
MnCrCW	784	1057	17.6	20.0
MnCrCTiW	980	1168	6.6	9.5
MnCrCTiPB	946	1158	10.4	12.1
MnCrCTiVPB	862	1126	11.4	13.1
MnCrCTiWVPB	915	1114	11.3	13.6
316 SS	739	807	11.5	17.4

The room-temperature results indicated that for the high-manganese steels the strength after annealing 1 h at 1050°C generally exceeded that of the same steel annealed 2 h at 1150°C. With one exception, the YS and UTS of the manganese-stabilized stainless steels annealed at 1050°C exceeded those of 316 SS annealed at this temperature. The exception was that the YS for the MnCrC steel annealed at 1050°C was slightly lower than the YS of 316 SS. (Note also that only two of the YS values for the manganese-stabilized steels annealed at 1150°C were less than that of the 316 SS annealed at 1050°C.) Similarly, the YS and UTS of the manganese-stabilized steels in the 20% cold-worked condition exceeded those for 316 SS in that condition.

In the annealed condition, the uniform and total elongations of the manganese-stabilized steels at room temperature were equivalent to those for 316 SS (Table 3). Equivalent ductility was also observed for most of the alloys in the cold-worked condition. The only exception was the MnCrCTiW alloy, which had the lowest uniform and total elongations, although these values still indicate adequate ductility.

The addition of tungsten (MnCrCW) to the base composition had the least effect on the strength of the annealed steels. An addition of titanium by itself (MnCrCTi) had only a slightly greater effect. A combination of Ti, B, and P (MnCrCTiBP) and these three elements plus vanadium (MnCrCTiVBP) gave rise to strengths similar to those for MnCrCTi. However, the combination of titanium and tungsten (MnCrCTiW) resulted in a substantial strength increase over the base composition. Adding V, P, and B to this last combination had little effect on the room-temperature strength of the annealed steel over that for MnCrCTiW.

In the cold-worked condition tested at room temperature, an approximately similar relative strength behavior was observed for the various combination of elements as observed for the annealed steels. For this condition, the MnCrCTiW had higher YS and UTS values than the MnCTiWVPB. However, this greater strength was accompanied by a lower uniform and total elongation.

Tensile tests were conducted over the range of room temperature to 600°C. In Figs. 15 to 20, the tensile properties for the five strongest manganese-stabilized steels (MnCrC and MnCrCW are not shown) are compared with type 316 SS. Results clearly indicated the superiority of the manganese-stabilized steels after an anneal of 1 h at 1050°C (Figs. 16 and 18), 2 h at 1150°C (Figs. 17 and 18), and after cold working (Figs. 19 and 20). Despite this strength superiority, ductility was equivalent or better than that for 316 SS in the annealed condition (Figs. 14 and 16). In the cold-worked condition, 316 SS had a higher total elongation below ~200°C, but at the higher temperatures, the manganese-stabilized steels had equivalent or better ductility (Fig. 20). These observations on ductility are important,

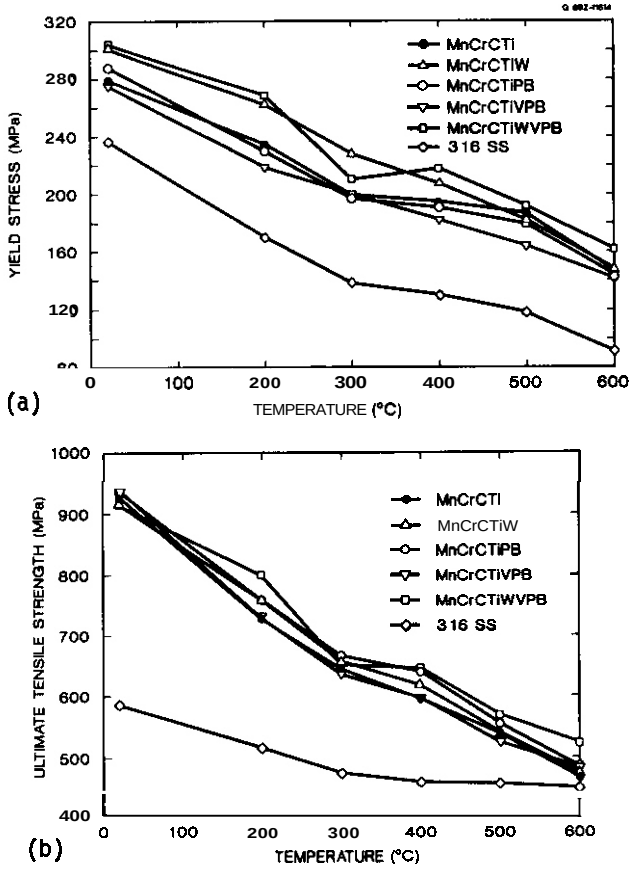

Fig. 15. (a) 0.2% yield stress and (b) ultimate tensile strength plotted against test temperature for five heats of manganese-stabilized stainless steels and type 316 stainless steel. All steels were annealed 1 h at 1050°C.

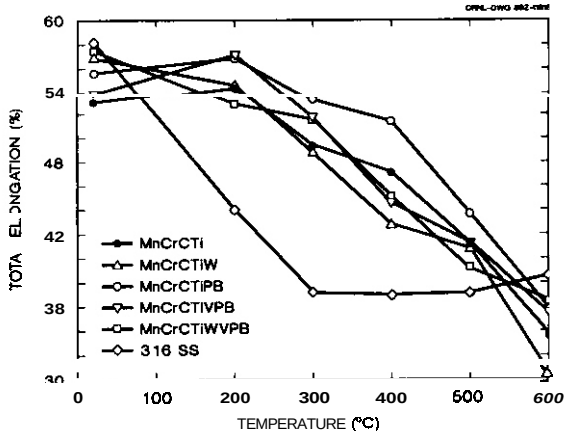

Fig. 16. Total elongation plotted against test temperature for five heats of manganese-stabilized stainless steels and type 316 stainless steel as a function of test temperature. All steels were annealed 1 h at 1050°C.

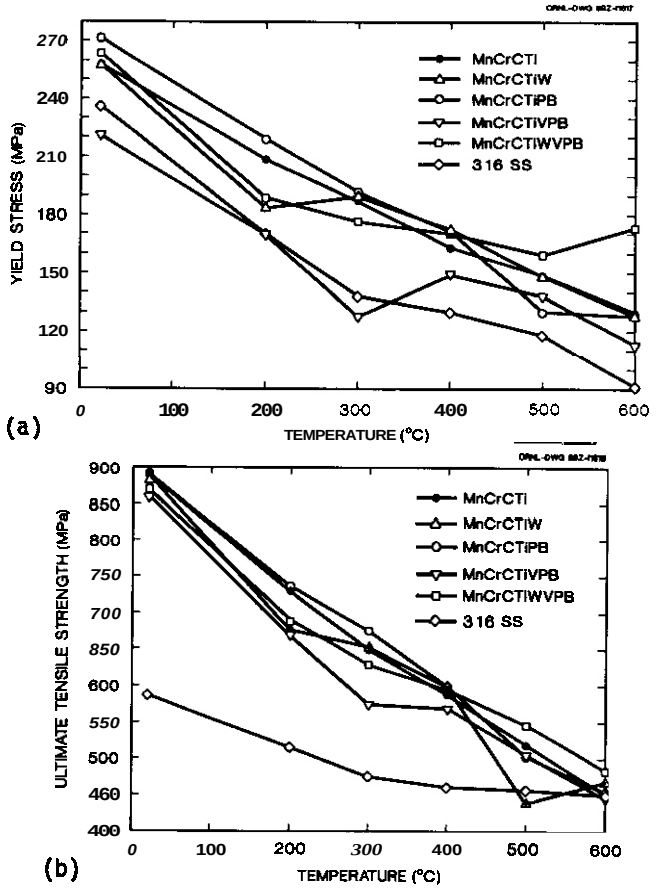

Fig. 17. (a) 0.2% yield stress and (b) ultimate tensile strength plotted against test temperature for five heats of manganese-stabilized stainless steels and type 316 stainless steel. The manganese steels were annealed 2 h at 1150°C and the type 316 stainless steel was annealed 1 h at 1050°C.

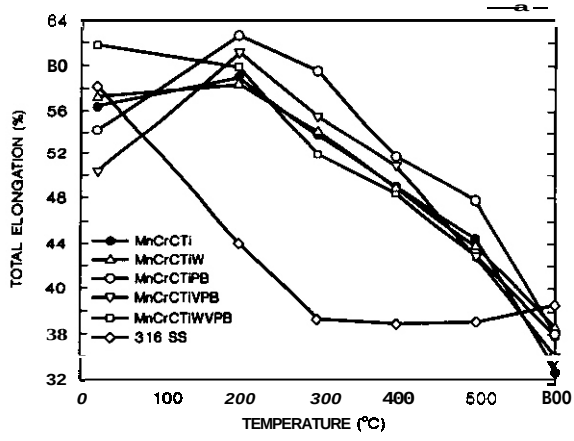

Fig. 18. Total elongation as a function of test temperature for five heats of manganese-stabilized stainless steels and type 316 stainless steel. The manganese steels were annealed 2 h at 1150°C and type 316 stainless steel was annealed 1 h at 1050°C.

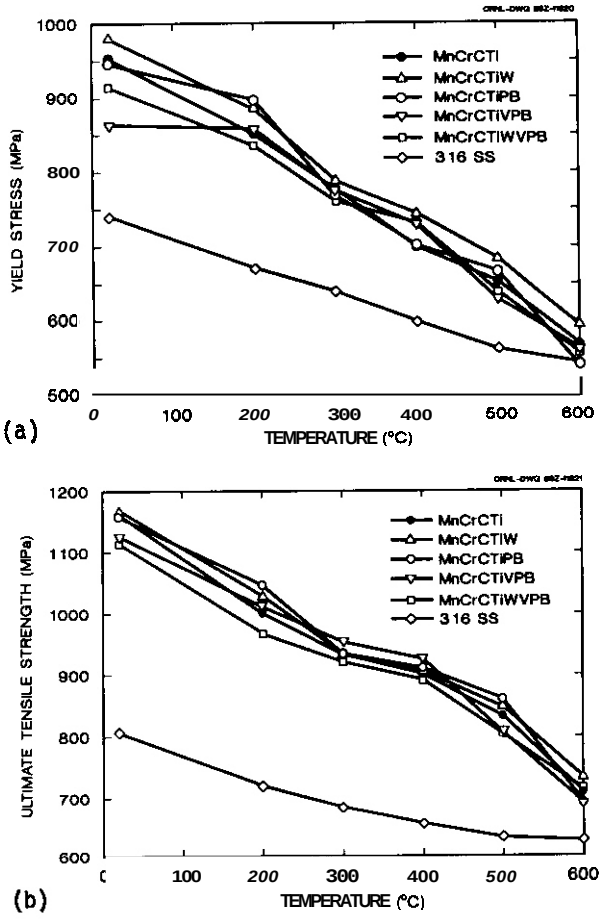

Fig. 19. (a) 0.2% yield stress and (b) ultimate tensile strength plotted against test temperature for five heats of manganese-stabilized stainless steels and type 316 stainless steel. All steels were in the 20% cold-worked condition.

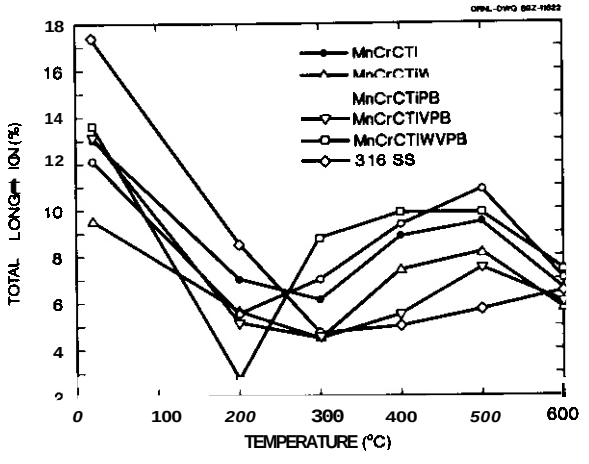

Fig. 20. Total elongation plotted against test temperature for five heats of manganese-stabilized stainless steels and type 316 stainless steel. The manganese steels were annealed 2 h at 1150°C and type 316 stainless steel was annealed 1 h at 1050°C

because normally strength and ductility are trade-offs. These new steels, therefore, represent a significant gain in strength that does not come at the expense of ductility.

For the steels annealed 1 h at 1050°C, the MnCrCTiW and the MnCrCTiWVBP clearly had the highest YS [Fig. 15(a)]. Further, at the highest test temperatures, the MnCrCTiWVBP is the strongest. A somewhat similar behavior was observed for the UTS behavior [Fig. 15(b)], where the MnCrCTiWVBP is essentially the strongest over most of the temperature range. Ductilities of all the manganese-stabilized steels annealed at 1050°C were excellent over the entire temperature range (Fig. 16).

Tensile data for the steels annealed *2* h at 1150°C (Figs. 17 and 18) displayed the same general behavior as those annealed 1 h at 1050°C. The MnCrCTiWVBP again had the best strength properties at the highest test temperatures. This steel also had good ductility.

In the cold-worked condition, the YS of the MnCrCTiW was highest over most of the temperature range [Fig. 19(a)]. There was much less difference in the UTS behavior of the five manganese-stabilized steels over this temperature range [Fig. 19(b)]. The ductility (Fig. 20) of the MnCrCTiW was lowest and the MnCrCTiWVBP was highest for much of the temperature range, although the MnCrCTiWVBP had the lowest ductility at 200°C.

These results indicate that it is possible to develop a FIRD steel free of Ni, Mo, N, and Cu, with tensile properties better than those of type 316 stainless steel. In fact, the room-temperature YS of the 20% cold-worked MnCrCTiWVBP exceeded that of the fusion prime candidate alloy (PCA), a 16Ni-14Cr-2.5Mo-08C austenitic alloy which contains small amounts of Ti, Nb, V, N, and P (ref. 10). However, the rate at which the YS of the MnCrCTiWVBP decreases with temperature is greater than for the PCA, and above about 450°C, the PCA becomes stronger. The PCA has been under development for several years to optimize its properties for strength and irradiation resistance. Further optimization of the manganese steels should also be possible.

Although the experimental steels discussed in this report appear to have good strength, for the steel to be of use, it must be weldable and have compatibility with the coolant that it will be subjected to during service. Corrosion and weldability studies are to be conducted. The steels are also being irradiated in fission reactors to determine their irradiation resistance.

The tensile results generally indicate the importance of titanium on strength, along with the importance of the combination of titanium and tungsten (Table 3 and Figs. 15–20). Steels containing titanium were generally among the strongest; these were basically the steels that contained the fine MC matrix precipitates observed by TEM, especially for the steels annealed at 1050°C. Of interest is the steel with the combination of vanadium and titanium without any tungsten (MnCrCTiVBP). This steel contained little precipitation, even though vanadium would be expected to appear in MC; it was generally the weakest of the steels displayed in Figs. 15 to *20.* However, when tungsten was added to this combination of elements, the steel became one of the strongest.

SUMMARY AND CONCLUSIONS

A series of experimental high-manganese austenitic stainless steels were produced. An Fe-20Mn-12Cr-0.25C steel was used as a base composition that was alloyed for strength by adding small amounts of Ti, W, V, B, and P. Austenite stabilization was achieved with manganese and carbon alone, without the use of high-nickel and/or high-nitrogen concentrations, as is the case in most high-manganese austenitic steels. In tensile tests over the range room temperature to 600°C, the manganese-stabilized steels had 0.2% yield stress and ultimate tensile strength values that were superior to those of type 316 stainless steel, a typical nickel-stabilized austenitic stainless steel. It was superior in both the solution-annealed and cold-worked conditions. The ductility of the manganese steel was as good or better than that of the 316 stainless steel for most test conditions.

REFERENCES

1. R. L. Klueh and E. E. Bloom, Optimizing Materials for Nuclear Applications, F. A. Garner, D. S. Gelles, and F. W. Wiffen, Eds., The Metallurgical Society, Inc., Warrendale, PA, 1985, pp. 73-85.

2. E. Ruedl, D. Rickerby, and T. Sasaki, Fusion Technology, Vol. 2, p. 1029, Pergamon Press, London, 1984.

3. E. Ruedl and T. Sasaki, J. Nucl. Mater. 122 & 123 (1984) 794-798.

4. H. R. Brager, F. A. Garner, 0. S. Gelles, and M. L. Hamilton, J. Nucl. Mater. 1336134 (1985) 907-911.

5. A. H. Bott, F. B. Pickering, and G. J. Butterworth, J. Nucl. Mater. 141-143 (1986) 1088-1096.

6. M. Tamura, H. Hayakawa, M. Tanimura, A. Hishinuma, and T. Kondo, J. Nucl. Mater. 141-143 (1986) 1067-1073.

7. R. L. Klueh, P. J. Maziasz, and E. A. Lee, Mater. Sci. Eng. 102 (1988) 115-124.

8. P. J. Maziasz and T. K. Roche, J. Nucl. Mater. 103&104 (1981) 797-802.

9. P. J. Maziasz et al., J. Nucl. Mater. 1088109 (1982) 296-298.

10. P. J. Maziasz, Optimization of Processing, Properties, and Service Performance Through Microstructural Control, B. L. Bramfitt, R. L. Benn, C. R. Brinkman, and G. F. Vander Voort, Eds., American Society for Testing and Materials, Philadelphia, 1988, pp. 116-161.

DEVELOPMENT OF TENSILE PROPERTY RELATIONS FOR ITER DATA BASE -- M L. Grossbeck (Oak Ridge National Laboratory)

OBJECTIVE

This research is directed toward developing equations that express tensile properties of irradiated austenitic stainless steels, especially at low temperatures. The equations are to be used by designers of the International Thermonuclear Experimental Reactor (ITER).

SUMMARY

Tensile data from the Oak Ridge Matrix (Fusion Implementing Agreement Annex II), the U.S. Japan collaboration, and from the available literature were reviewed. Type 316 stainless steel, in both cold-worked and annealed conditions and PCA (both U.S. and Japanese heats) were included. Equations were developed for yield strength, uniform elongation, and total elongation. In many cases, one expression could be used for alloys and conditions, in others, separate equations had to be used. In all cases an attempt was made to provide a conservative expression rather than to have the best fit to the data. Especially in the case of strength, the value was rather insensitive to alloy composition.

PROGRESS AND STATUS

Introduction

In order to provide design data for the ITER project, data from irradiations in mixed-spectrum reactors, where helium is produced simultaneously with displacement damage, were considered. Data from the U.S. Fusion Program ORR (Oak Ridge Research Reactor) Spectral Tailoring Experiment was considered especially relevant since the fusion reactor He:dpa level was maintained. Fast reactor data from type 316 stainless steel (316 SS) irradiated in the EBR-II have been included in an effort to determine the importance of high levels of helium on tensile properties.

In most cases, the curve was fit by eye rather than by a regression program. Since the data were often very limited, were from different sources, and had to be treated subjectively in relative importance, a statistical fit was not considered meaningful. In some cases, however, a regression analysis program was used for ease of determining parameters. Polynomial expressions were avoided when possible since they are often ill-conditioned, necessitating the carrying of several significant figures in the coefficients. In a few cases, however, a quadratic or cubic fit was the obvious choice.

Although very elegant models for predicting tensile behavior of irradiated stainless steels are available,[1,2] they were found either to not extend to low temperatures or to not fit the recent data. In dismissing these models, the opportunity to have a single equation to express tensile properties as functions of both damage level and temperature is missed. As a result, expressions for each property as a function of temperature were developed for 10, 20, 30, and 50 dpa.

Data Sources

Both published and unpublished data were used for the analysis. A major source was the U.S. Japan Collaborative Fusion Materials Program.[3-5] The data from this program, which appear in Table 1, were used for several reasons: Both annealed and cold-worked type 316 stainless steel and PCA were included in the program, irradiation temperatures ranged from 50 to 600°C, and damage levels as high as 50 dpa were attained. Since most of the specimens were irradiated in the HFIR (High Flux Isotope Reactor), they contain high concentrations of helium. In cases of 50 dpa, the helium levels were as high as 3000 appm. As a result, high temperature ductility must be considered a lower limit to the behavior expected in a fusion reactor.

Data from the ORR Spectral Tailoring Experiment, ORR-MFE-4, were available for 316 SS and PCA at irradiation and test temperatures from 330 to 600°C (ref. 6) (Table 2). Since these data were for specimens having a He:dpa level of about 12, characteristic of a fusion reactor with a lithium-cooled stainless steel blanket, they were particularly relevant. A disadvantage is that they were irradiated to a maximum damage level of only 15 dpa. These data were grouped with the 10 dpa data.

The European Community/U.S./Japan program under the auspices of the IEA Implementing Agreement, Annex II, was another important source of data. In this program, EC (European Community), U.S., and Japanese alloys were all irradiated in several research reactors. Data are now available from the HFIR, HFR (Petten), and the BR-2 (Mol). Data from the HFIR and HFR at 10 dpa at temperatures of 250°C for the HFR (Table 3) and 250 to 400°C for the HFIR (Table 4) were used in the development.[7,8] Data from the

Table 1. Tensile properties of austenitic stainless steels irradiated in HFIR from U.S./Japan program

Sample[a]	Temp. (°C)	dpa	Strength, MPa		Elongation, %	
			Yield	UTS	Uniform	Total
10 to 15 dpa						
EC 36	600	15	585	643	3.1	3.8
EL 15	300	14	933	933	0.21	5.1
EL 30	300	14	945	947	0.19	5.3
EL 24	600	15	567	643	4.2	6.0
TB 9	300	14	876	889	0.39	8.0
TE 1	300	14	878	889	0.53	1.9
TE 12	300	15	889	903	0.63	7.2
20 dpa						
EL 21	400	21	993	1000	0.31	4.4
EL 29	600	21	417	528	5.9	7.4
TE 11	400	21	952	972	0.42	5.5
TE 19	400	21	859	914	1.4	6.3
TB 2	400	21	878	888	0.38	6.4
TB 8	400		896	910	0.44	6.0
AA 42	500	26	681	807	8.7	10.6
CL 1	55	26	823	833	0.7	15.8
CL 2	55	26	821	833	0.6	17.7
DL 1	55	26	847	859	0.6	8.9
DL 2	55	26	847	a67	0.9	10.2
EC 34	300		803	813	0.97	5.9
EL 26	600	25	507	507	0.18	0.18
EL 28	500	26	695	792	5.1	7.1
EL 31	500	26	658	756	5.5	8.4
EL 36	300	25	933	947	0.69	4.5
TB 6	300	25	770	789	2.4	9.9
TB 1	500	26	650	732	4.7	8.2
TB 7	500	26	631	724	7.2	11.7
TE 9	300	25	775	798	1.0	6.5
TE 24	300	25	741	780	1.7	7.2
TE 10	500	26	678	765	7.1	11.4
TE 16	600	32	519	582	3.7	5.2
TE 17	600	30	432	621	6.3	8.1
TE 18	500	26	624	713	6.3	10.2
40 to 50 dpa						
O 1	55	37	690	706	16.2	20.8
O 2	55	37	694	710	10.8	15.3
O 31	55	37	739	772	11.6	15.9
D 32	55	37	726	742	4.9	7.7
EC 32	500	44	450	450	0.0	0.0
EL 25	500	44	660	701	0.83	1.22
EL 35	600	36	369	452	1.33	1.46
EC 31	400	36	907	988	1.04	5.14
EL 37	400	36	976	979	0.41	4.0
EL 39	500	44	706	769	4.4	6.6
TB 4	500	44	620	682	5.8	7.8
TB 5	400	36	858	872	0.55	5.7
TB 12	430	44	742	781	1.8	5.0
TE 8	400	36	914	946	0.49	5.0
TE 7	500	44	663	738	4.5	5.8
TE 22	500	50	640	675	1.04	1.47
TE 21	600	54	501	508	0.28	0.46

[a] AA 42 — US 316 20% cold worked.
CL — JPCA solution annealed.
CL — JPCA 15% cold worked.
D1–2 — J316 solution annealed.
031–32 — J316 20% cold worked.
EC — USPCA solution annealed at 1100°C plus 25% cold work.
EL — USPCA solution annealed at 1100°C plus 8 h at 800°C plus 25% cold work.
TB — JPCA solution annealed at 1100°C.
TE — JPCA solution annealed at 1100°C plus 15% cold work.

BR-2, shown in Table 5, have not yet been published but were made available.[9] These data are especially important since the He:dpa level is also characteristic of the fusion environment.

Since many of the mixed-spectrum data, especially from the HFIR, are from specimens with high concentrations of helium, data from fast reactor-irradiated specimens were also examined. Many of the recently obtained data in the U.S. are on a heat known as the FFTF First Core Heat. This heat is known to have a low strength level, in unirradiated and irradiated conditions, compared with other heats in the U.S. Breeder Reactor Program and with the fusion program heats used for this analysis. As a result, a more typical heat of 316 SS was sought. Heats identified in the U.S. Breeder Reactor Program as N and T lots were found to correlate better with the other heats of 316 SS, and tensile properties from these heats[10] are given in Table 6. Tensile properties were also found for annealed irradiated 316 SS on a heat of material that pre-dates the U.S. Breeder Reactor Program but has similar properties to the two previously discussed heats.[11] Data for this heat appear in Table 7. Data from these fast reactor-irradiated specimens were used for guidance in predicting the equations for properties in a fusion reactor in the present study. Since they have very small concentrations of He, data from these specimens can be used as a lower limit to helium effects.

Because of the scarcity of data at irradiation temperatures below 100°C, little attention was paid to obtaining data from a standard heat of material. A few data points on ORNL 00 heat of 316 SS were found for an irradiation temperature of 60°C at a displacement level of 10 dpa in the HFIR. These data are shown in Table 8.

Table 2. Tensile properties of austenitic stainless steels irradiated in ORR in a spectrally tailored flux (ORR-MFE-4) (sheet specimens with 20.3 mm gauge length)

Sample	Temp. (°C)	dpa	He (appm)	Strength (MPa)		Elongation, %	
				Yield	UTS	Uniform	Total
316 — 20% Cold Worked							
AC 9	330	13	240	996	996	0.2	1.3
AC 29	330	13	240	996	996	0.2	1.3
AC 46	330	13	240	973	973	0.3	2.5
AC 53	400	13	240	908	908	0.2	2.4
AC 57	400	13	240	988	1004	0.4	2.3
AC 71	400	13	240	973	988	0.5	2.4
AC 226	500	17	220	747	797	1.8	3.8
AC 201	500	12	220	793	843	2.0	4.0
AC 189	500	12	220	785	835	2.5	4.5
AC 244	600	12	220	410	529	5.1	6.3
AC 246	600	12	220	402	525	5.9	7.3
AC 239	600	12	220	406	525	5.0	6.5
PCA — 25% Cold Worked							
EC 58	330	13	320	942	942	0.2	2.2
EC 15	330	13	320	866	866	0.3	3.1
EC 47	330	13	320	820	820	0.2	3.1
EC 13	400	13	320	927	927	0.2	2.1
EC 41	400	13	320	915	915	0.2	2.4
EC 53	400	13	320	984	1000	0.3	2.4
EC 201	500	12	280	774	785	0.6	2.3
EC 190	500	12	280	789	808	0.6	2.3
EC 244	500	12	280	766	785	0.8	2.5
EC 215	600	12	280	486	536	1.9	2.0
EC 200	600	12	280	475	525	1.5	1.6
EC 230	600	12	280	410	536	5.8	6.5

Table 3. Tensile properties of austenitic stainless steels irradiated in the HFR (Petten)[a] as part of the U.S./EC/Japan program under IEA Annex II (rod tensile specimens, 18.3 mm gauge length)

Temp. (°C)	dpa	Strength, MPa		Elongation, %	
		Yield	UTS	Uniform	Total
EC 316 — Annealed					
250	10	812	815	0.29	8.0
U.S. 316 — 20% Cold Worked					
250	10	1057	1059	0.18	4.6
U.S. PCA — 25% Cold Worked					
250	10	1061	1064	0.23	4.2
JPCA — Annealed					
250	10	830	834	0.33	8.4

[a]Data based on average of 10 specimens.

Correlation of Data

Difficulty arises in correlating data from different types and sizes of specimens. In evaluating strength, the size of the specimen should have little effect as long as the specimens are not so thin that surface effects such as damage from machining and corrosion are not significant. For reactive metals, the latter might be a consideration, especially for materials from long reactor irradiations, perhaps in liquid metals. Since all of the specimens used are of one of the types shown in Fig. 1, and the alloys were all stainless steels neither Consideration is believed to be important.

Ductility is more difficult to evaluate. Fracture is complicated by the stress conditions which can be plane stress or plane strain for the size specimens used depending upon the fracture touahness and strength of the material. However, the fracture mode and mechanism of fracture need not be completely understood to obtain valid strenath and ductilitv. The issue of correiation of result; between specimens of different geometry is important in determining ductility. This issue has been addressed and is reviewed by Dieter.[10] Until necking occurs, there is good correlation between specimen types. The uniform deformation over the entire gauge length results in a valid measure of tensile elongation. Therefore, no corrections were applied to the uniform elongations of any specimens. However, when necking occurs and deformation becomes restricted to a limited region of the specimen gauge length, the measured elongation becomes a strong function of specimen geometry. Experimental evidence suggests that geometrically similar specimens give similar results for ductility. More generally, results are similar if the value of $A^{1/2}/\ell$ is constant, where A is the gauge area and ℓ is the gauge length.

The specimens used to obtain the data reviewed vary significantly, but all are considered miniature in that they are smaller than ASTM standard specimens. Figure 1 shows the specimen types used. The specimens irradiated in the HFIR are either sheet specimens with a gauge 0.76 mm x 1.52 mn and 20.3 mm in length or rod specimens with a gauge 2.03 mm in diameter and 18.3 mn in length. Since the first wall of a fusion reactor will probably be a sheet structure (even though the thickness could be rather large), the sheet specimen was used as the standard and the total elongation values for other specimens normalized to this specimen

Table 4. Tensile properties of austenitic stainless steels irradiated in HFIR as part of the U.S./EC/Japan program under IEA Annex II (rod tensile specimens, 18.3 mm gauge length)

Sample	Temp. (°C)	dpa	Strength (MPa)		Elongation, %	
			Yield	UTS	Uniform	Total
U.S. 316 — 20% Cold Worked						
AA 100	250	5.1	972	972	0.28	6.4
AA 41	270	6.8	979	986	0.32	6.2
AA 31	400	9.7	1000	1007	0.35	4.7
EC 316 — Annealed						
135	250	5.1	724	724	0.31	20.4
139	270	6.8	807	807	0.31	14.6
142	290	8.2	827	827	0.23	9.4
147	340	9.9	821	821	0.33	9.3
143	400	9.7	765	772	0.95	7.0
USPCA — 25% Cold Worked						
EK 11	270	7.0	924	924	0.21	5.5
EK 12	290	8.4	1062	1069	0.34	5.7
EK 14	400	9.9	945	952	0.31	4.8
JPCA — Annealed						
544	250	5.3	703	724	8.6	15.6
545	340	10.2	807	807	0.38	8.3
546	400	10.0	800	807	1.4	7.2

Table 5. Tensile properties of austenitic stainless steels irradiated in the BR-2, Mol, as part of the U.S./EC/Japan program under IEA Annex II (rod tensile specimens, 18.3 mm gauge length)

Sample	Temp. (°C)	dpa	Strength (MPa)		Elongation, %	
			Yield	UTS	Uniform	Total
U.S. 316 — 20% Cold Worked						
U006	250	10	1010	1010	0.1	4.8
U007	250	10	978	978	0.1	5.5
U008	250	10	1040	1040	0.1	5.9
USPCA — 25% Cold Worked						
U106	250	10	1100	1100	0.3	5.8
U107	250	10	1010	1010	0.3	5.5
U108	250	10	1030	1030	0.2	5.2
EC 316L — Annealed						
109	250	10	757	757	0.2	17.4
113	250	10	803	803	0.2	10.9

using the value $A^{1/2}/\ell$. The specimen dimensions and correlation factors are given in Table 9. In the case of the two HFIR specimens, the correction factor on total elongation appears to make the data more consistent.

The specimen with the most uncertainty is the tube specimen used in determining the properties of the EBR-II irradiated cold-worked 316 SS. The specimens consisted of tubes 5.84 mm in outside diameter with 0.38 mm wall thickness. The tubes were 44.5 mm long but were tested by placing mandrel type plugs in the ends and attaching swage lock grips.[10] The gauge length was taken as the distance between contact points of the mandrels which was 19.1 mm.[13] Using the correction previously described, the total elongation values are divided by 2.6. Since the tubular geometry was not used in development of the correlation, this correlation factor might lead to a large uncertainty. However, keeping this in mind, the values may be used as a guide in assessing ductility.

Results and Discussion

The data are plotted in Figs. 2 through 13; the first four graphs are yield strength at the damage levels of 10, 20, 30, and 50 dpa followed by uniform and total elongations at the same damage levels. The mathematical relations for the data are given in Table 10. In many cases, such as yield stress, the behavior of all alloys was so similar that only one curve was drawn. In other cases, separate curves were drawn for annealed and cold-worked material, and in still other cases, a separate curve was drawn for a particular alloy or heat treatment as in Figs. 7 and 10. This is easily seen in Table 10. Although ultimate tensile strength has not been plotted, for exposures above 10 dpa, uniform elongation is usually sufficiently low that ultimate tensile and yield strengths are nearly equal. The curves for yield stress are drawn monotonically, decreasing between 60 and 300°C, but more recent data not considered in this review indicate a maximum in this region.[11]

Both 316 SS and PCA in annealed and cold-worked conditions are plotted on the same graphs. The difference between annealed and cold-worked material is very apparent at 10 dpa and discernible at 20 dpa but insignificant at 30 and 50 dpa. This trend is known from fast reactor irradiations as shown in Fig. 14 from Garner et al.[2] Annealed material hardens and cold-worked material softens as irradiation proceeds. This latter trend is also apparent in Figs. 2 through 5 where yield stress of 20% cold-worked material falls approximately 30% from 10 to 50 dpa. There appears to be little difference in strength between heats of 316 SS and heats and cold-worked conditions of PCA perhaps with the exception of the 316 SS irradiated in EBR-II. However, the lower strength

Table 6. Tensile properties of 20% cold-worked type 316 stainless steel irradiated in the EBR-II (after Fish)'
(tube specimens N and T lots)

Temp. (°C)	Strength (MPa) Yield	UTS	Elongation, % Uniform	Total	Temp. (°C)	Stren th Yield	UTS	Elongation, % Uniform	Total
	10 dpa (2 × 10^{26} n/m^2)					30 dpa (5.7 × 10^{26} n/m^2)			
371	810	890	4.5	7.3	371	870	920	1.2	2.6
427	710	800	4.7	11.0	538	400	500	4.4	6.4
483	610	720			593	350	440	5.0	6.9
538	400	500	4.5	6.6	649	290	350	2.8	3.8
593	350	440	8.9	12.0					
649	290	350	4.5	9.5		50 dpa (9.6 × 10^{26} n/m^2)			
704	225	260	2.0	2.8					
					371	870	920	1.0	2.5
	20 dpa (3.8 × 10^{26} n/m^2)				649	290	350	2.0	2.9
371	860	910	2.0	3.3					
427	760	830	4.0	5.2					
483	640	730	2.5	3.0					
538	400	500	4.5	6.5					
593	350	440	6.4	8.2					
649	290	350	3.8	5.9					
704	225	260	1.4	1.5					

Table 7. Tensile properties of annealed type 316 stainless steel irradiated in the EBR-II (Heat 332990)
(after Fish and Holmes)"
(rod tensile specimen with 28.6 mm gauge length)

Sample	Temperature, °C Test	Irradiation	dpa	Strength (MPa) Yield	UTS	Elongation, % Uniform	Total
		10 to 15 dpa					
A32-7T	430	410	13	679	707	1.7	5.0
6E16-1	430	430	9.1	605	661	4.8	8.0
6E26-1	430	430	13	641	696	3.1	6.3
7E16-2	430	400	12	605	681	6.9	9.1
6E16-2	480	430	9.7	605	656	4.9	8.0
6E26-2	480	430	13	607	640	2.2	5.1
6F26-2	540	480	13	308	493	12.8	14.0
21B76-1	700	710	8.4	145	235	6.5	7.7
21B56-5	700	710	12	130	235	6.0	6.8
		20 dpa					
A32-8T	430	400	17	758	773	1.1	4.2
A32-9T	430	390	18	748	756	0.9	3.9
33-3-5	650	670	23	288	341	1.9	2.1
33-3-1	650	670	19	269	331	2.8	3.1

ORNL-DWG 78-7701R

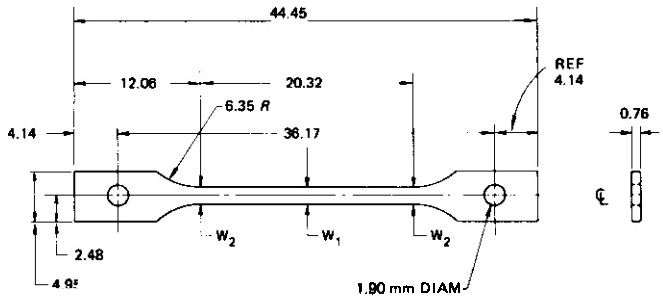

W_1 = 1.52 mm
W_2 = 0.025 TO 0.038 mm
GREATER THAN W_1

(a) DIMENSIONS IN MILLIMETERS

ORNL-DUG 89-13384

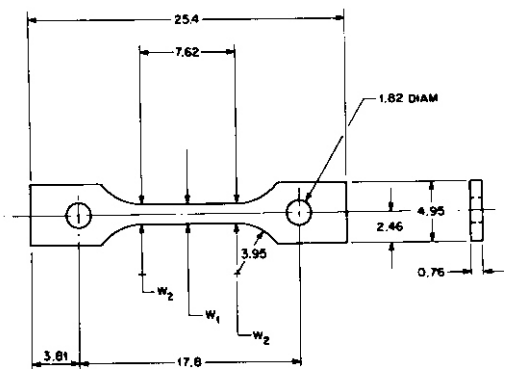

W_1 = 1.52 mm
W_2 = 0.025 TO 0.038 mm
GREATER THAN W_1

(b) DIMENSIONS IN MILLIMETERS

ORNL – DWG 76 – 11167

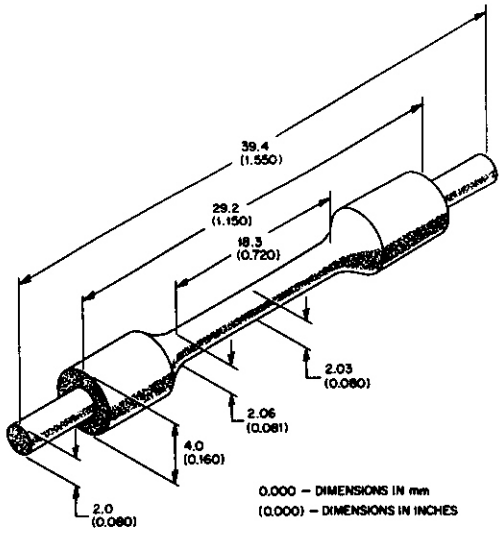

(c) HFIR – CTR TENSILE SPECIMEN

ORNL-DWG 89Z-12248

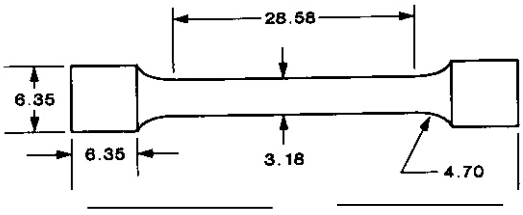

(d) Dimensions in mm

ORNL-DWG 89Z-12249

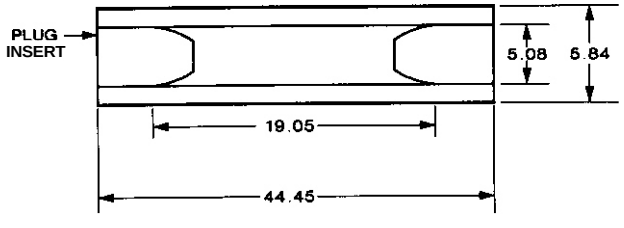

(e) Dimensions in mm

Fig. 1. Tensile specimens used in irradiation experiments reviewed. (a) sheet tensile specimen used in HFIR and ORR, (b) sheet specimen used in HFIR and ORR, (c) rod specimen used in HFIR, HFR, BR2, and ORR, (d) rod specimen used in EBR-II for annealed material, (e) tube specimen used in EBR-II for cold-worked material.

Table 8. Tensile properties of type 316 stainless steel[a] irradiated in HFIR at 55°C (ORNL heat D0) (rod tensile specimen with 28.6 mm gauge length)

Fluence (E > 0.1 MeV) (10^{26} n/m^2)	dpa	Test Temperature (°C)	Strength (MPa)		Elongation, %	
			Yield	UT	Uniform	Total
1.13	8.8	35	943	950	0.4	14.7
1.35	10.8	35	948	954	0.4	12.0

[a]($\dot{\epsilon} = 4.7 \times 10^{-5}$ s^{-1})

Table 9. Specimen dimensions and correlation factors for total elongation

Specimen Type	Gauge, mm				Tube Wall (mm)	$\sqrt{\text{Area}}$/ Length	Correction Factor[a]
	Thickness	Width	Diameter	Length			
Sheet (ORNL SS-1)	0.76	1.52		20.3		0.0529	1
Rod (ORNL)			2.03	18.3		0.0983	1.86
Tube (HEDL/EBR-II)			5.84	19.1	0.38	0.138	2.6
Rod (HEDL/EBR-II)			3.18	28.6		0.0985	1.86

[a]Measured total elongation is to be divided by the correction factor to normalize data to the sheet specimen results.

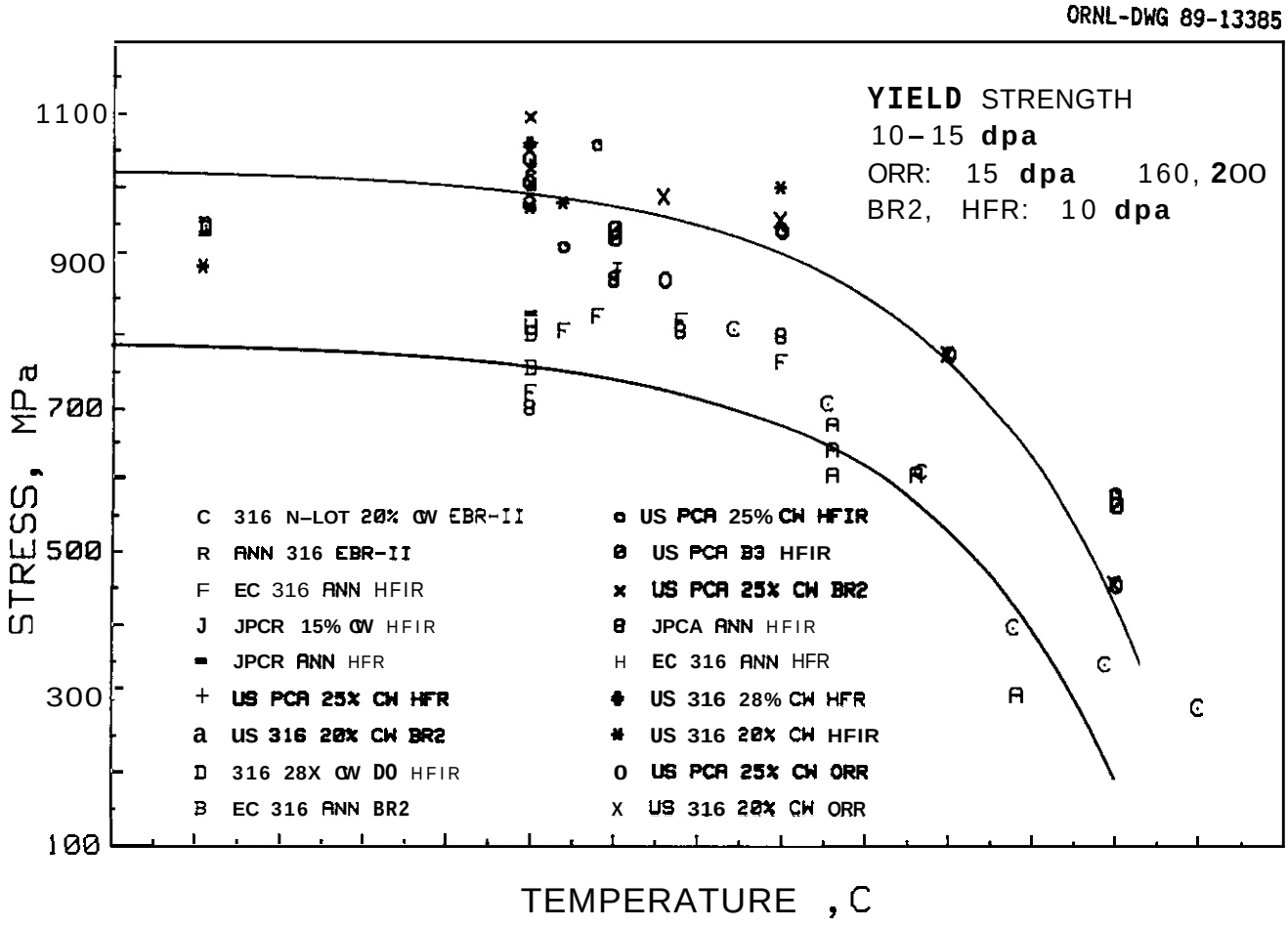

Fig. 2. Yield strength (0.2% offset) of austenitic alloys irradiated to atomic displacement levels in the range of 10 to 15 dpa. The upper curve is for cold-worked alloys and the lower curve is for annealed alloys. The curves are intended to underpredict the data.

ORNL-DWG 89-13386

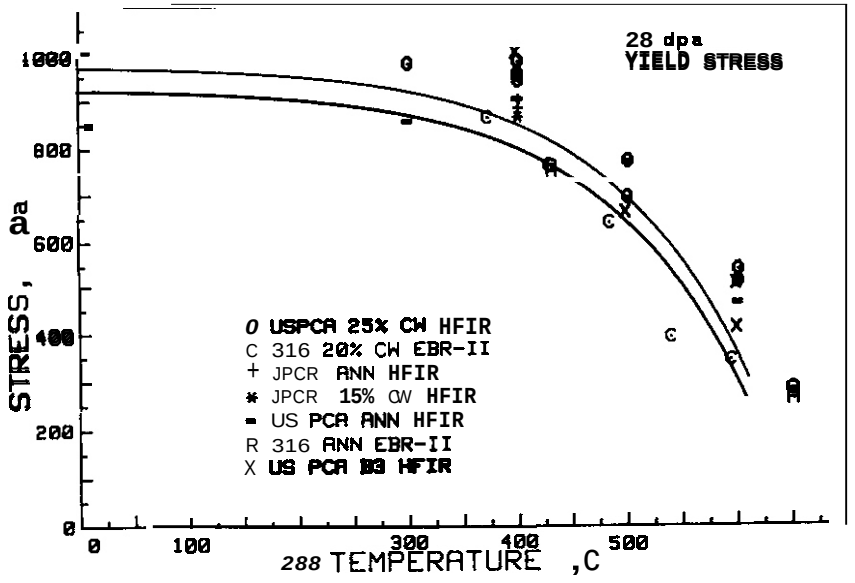

Fig. 3. Yield strength (0.2% offset) of austenitic alloys irradiated to an atomic displacement level of 20 dpa. The upper curve is for cold-worked alloys and the lower curve is for annealed alloys. The curves are intended to underpredict the data.

ORNL-DUG 89-13387

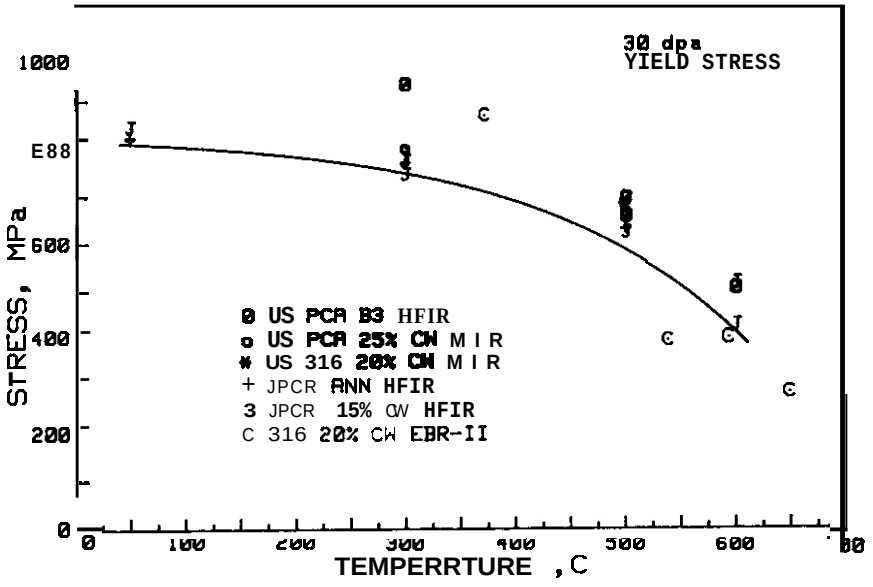

Fig. 4. Yield strength (0.2% offset) of austenitic alloys irradiated to an atomic displacement level of 30 dpa. The curve is intended to underpredict the data.

Table 10. Tensile property equations for austenitic stainless steels. The curves are conservative in that they underpredict *the* data.

Alloy	Yield Strength, MPa	Uniform Elongation, %	Total Elongation, %
		10 dpa	
Austenitic SS			
Cold worked	$YS = 102511 - \exp[-(665 - T)/120]\}$		
Annealed	$= 1025\{1 - \exp[-(665 - T)/120]\} - 235$		
316 CW *6* Ann		$UE = 3.0 \times 10^{-3}\ e^{T/80} + 0.2$	
PCA CW & Ann		$UE = 3.7 \times 10^{-3}\ e^{T/100}\ t\ 0.2$	
PCA CW			$TE = 26$
316 CW			$= 7 \times 10^{-5}(T - 325)^2 + 2$
Aust. SS Ann			$= 22\ e^{-T/80} + 3.6$
		20 dpa	
All Austenitic SS			
Cold worked	$YS = 975\{1 - \exp[-(660 - T)/130]\}$		
Annealed	$= 975\{1 - \exp[-(660 - T)/130]\} - 50$		
316 CW PCA 83		$UE = 45\ \exp[-(T - 600)^2/15{,}000] + 0.2$	
PCA-A1, 316 Ann		$= 1.2\ \exp[-(T - 500)^2/4000] + 0.2$	
PCA-A3		$= 2.5\ \exp[-(T - 525)^2/4000 + 0.2$	
PCA-B3			$TE = 14.8 - 0.122\ T + 3.62 \times 10^{-4}\ T^2 - 3.23 \times 10^{-7}\ T^3$
PCA-A1, A3			$= 12.5 - 6.7 \times 10^{-2}\ T - 1.56 \times 10^{-4}\ T^2$
316 Ann			$- 1.28 \times 10^{-7}\ T^3$
		30 dpa	
Austenitic SS			
CW *6* Ann	$YS = 975\{[1 - \exp - (760 - T)/190]\} - 140$	$UE = 0.7\{1 + \exp[(T - 450)/20]\}^{-1} + 5\ \exp[-(T - 500)^2/3000]$	
			$TE = -3.8 \times 10^{-7}\ [(T - 200)(T - 550)] + 2.5$
Ann			$= 22.9 - 0.148\ T + 4.08 \times 10^{-4}\ T^2$
316 CW			$- 3.75 \times 10^{-7}\ T^3$
		50 dpa	
Austenitic SS			
CW & Ann	$YS = 775\{[1 - \exp[-(670 - T)/80]\} - 80$		
CW *6* Ann		$UE = 8\ e^{-0.01T} + 0.3$	
CW *6* Ann			$TE = 18\ e^{-T/200} - 0.6$

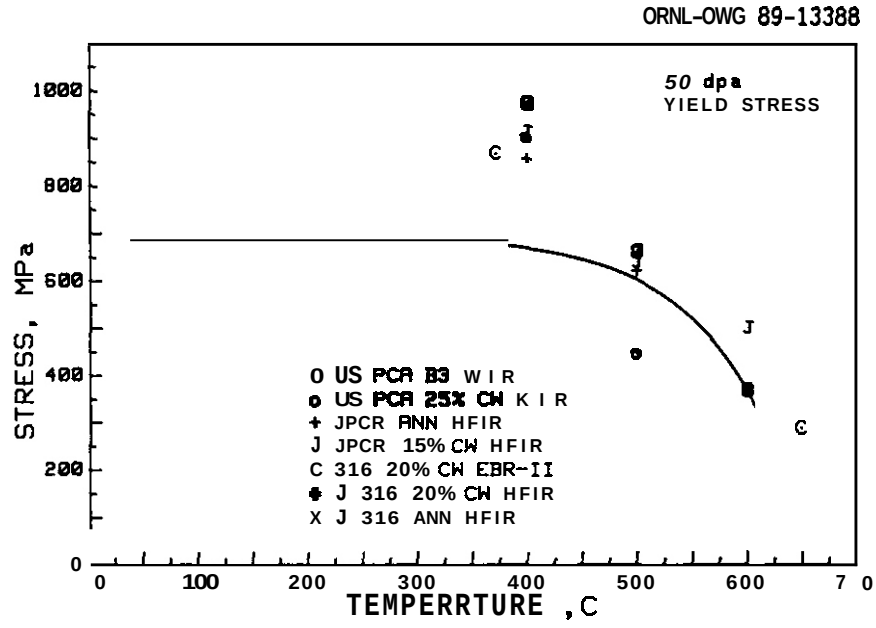

Fig. 5. Yield strength (0.2% offset) of austenitic alloys irradiated to an atomic displacement level of 50 dpa. The curve is intended to underpredict the data.

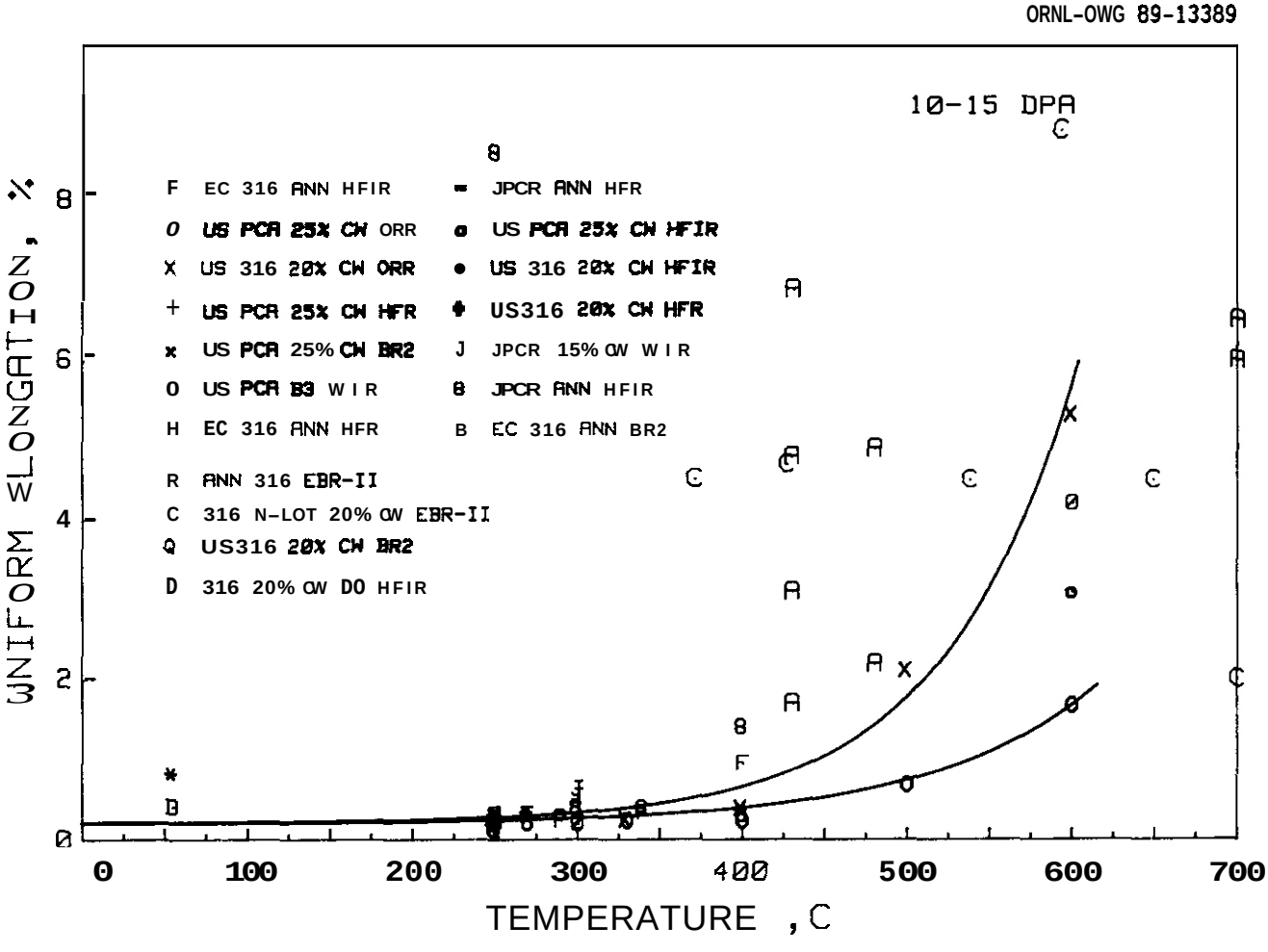

Fig. 6. Uniform elongation of austenitic allays irradiated to atomic displacement levels in the range of 10 to 15 dpa. The upper curve represents type 316 stainless steel, and the lower curve represents PCA. The curves are intended to be a conservative estimate of the property.

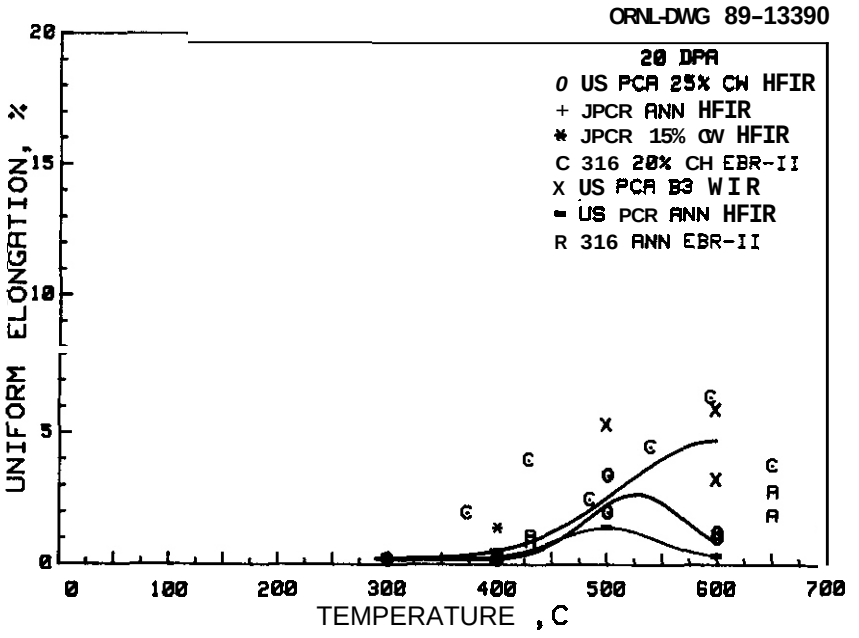

Fig. 7. Uniform elongation of austenitic alloys irradiated to an atomic displacement level of 20 dpa. The upper curve is to be used as a guide for PCA-B3 (aged and cold-worked) and cold-worked type 316 stainless steel. The middle curve is to be used for 25% cold-worked PCA, and the lower curve represents annealed PCA and type 316 stainless steel.

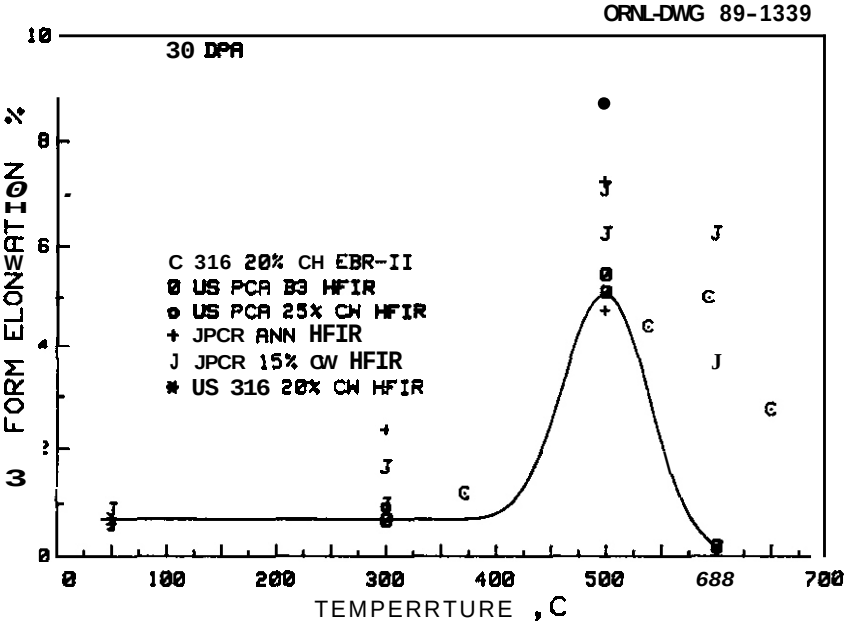

Fig. 8. Uniform elongation of austenitic alloys irradiated to an atomic displacement level of 30 dpa. The curve is to be used as a lower limit for both JPCA and type 316 stainless steel.

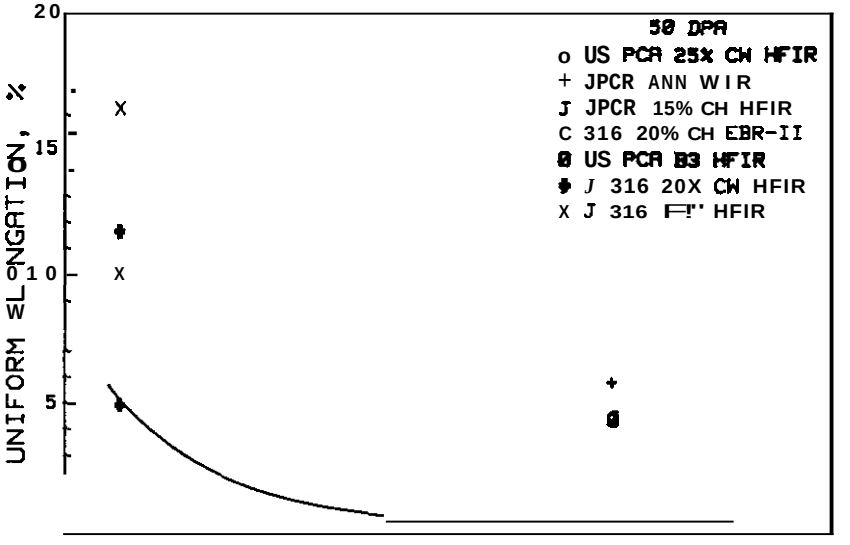

ORNL-OWG 89-13393

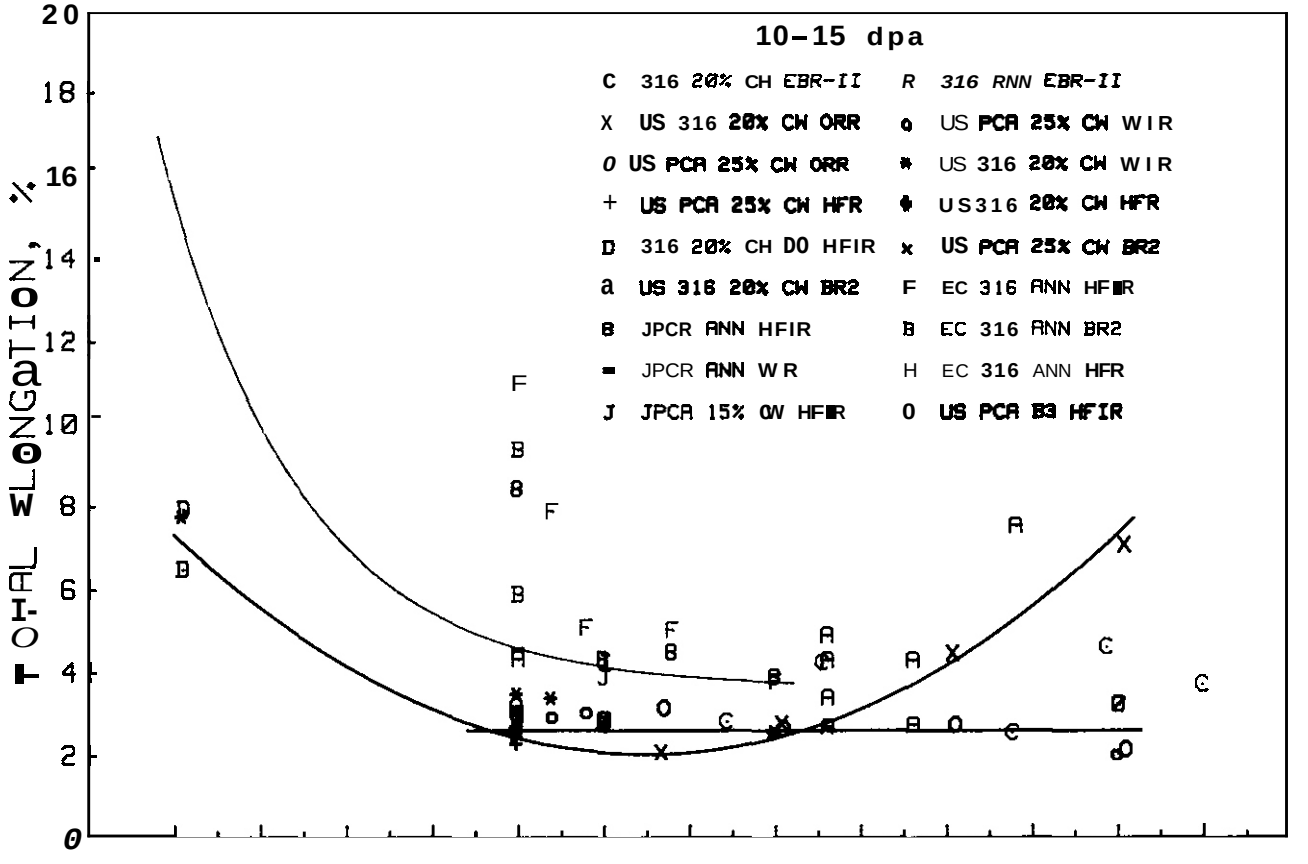

316-stainless steel'. The middle curve represents cold-worked type 316 stainless steel, and the constant value of 2.6% represents cold-worked PCA.

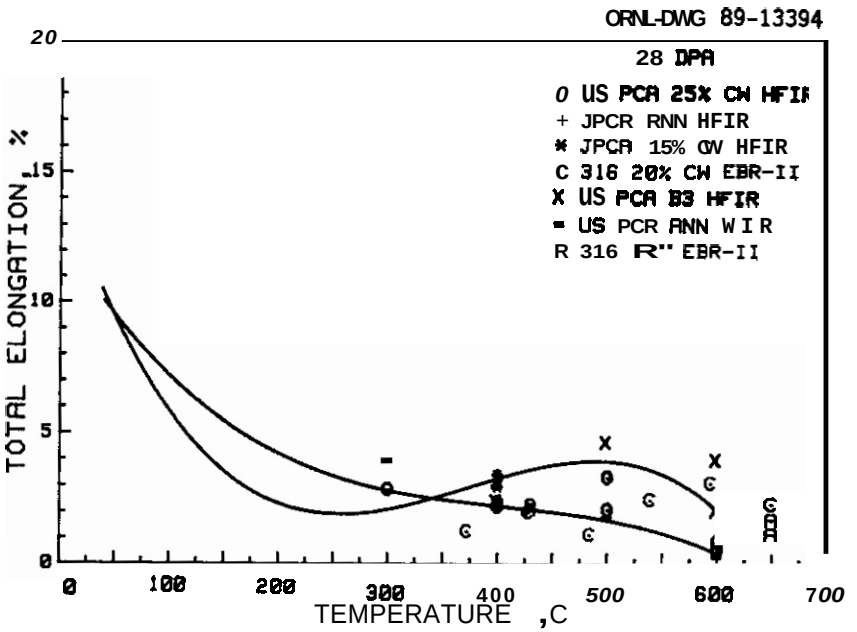

Fig. 11. Total elongation of austenitic alloys irradiated to an atomic displacement level of 20 dpa. The upper curve at 500°C is intended to be used for PCA-B3 (aged and cold-worked), and the lower curve at 500°C is intended for annealed and cold-worked PCA.

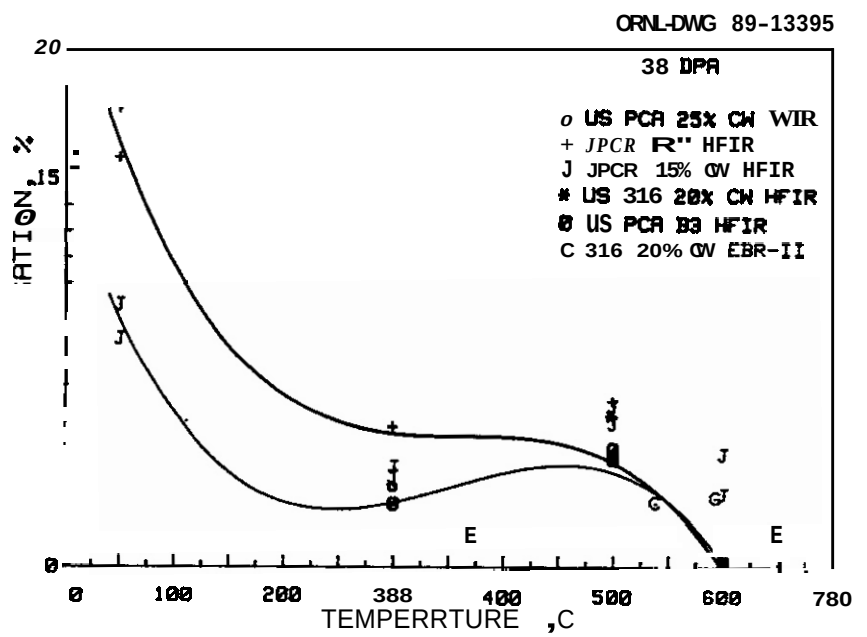

Fig. 12. Total elongation of austenitic alloys irradiated to an atomic displacement level of 30 dpa. The upper curve represents annealed alloys, and the lower curve represents cold-worked alloys.

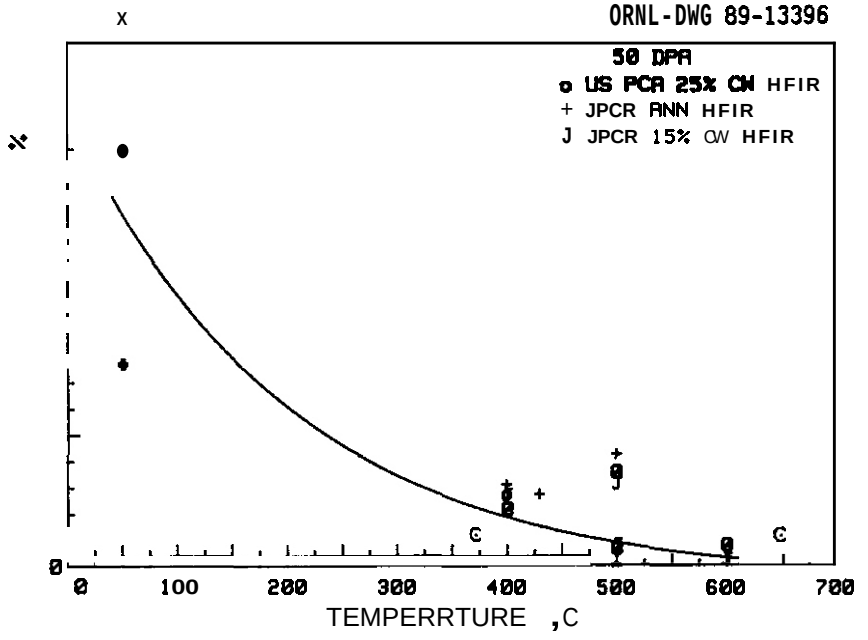

Fig. 13. Total elongation of austenitic alloys irradiated to an atomic displacement level of 50 dpa. The curve is a conservative estimate of behavior for all alloys reviewed.

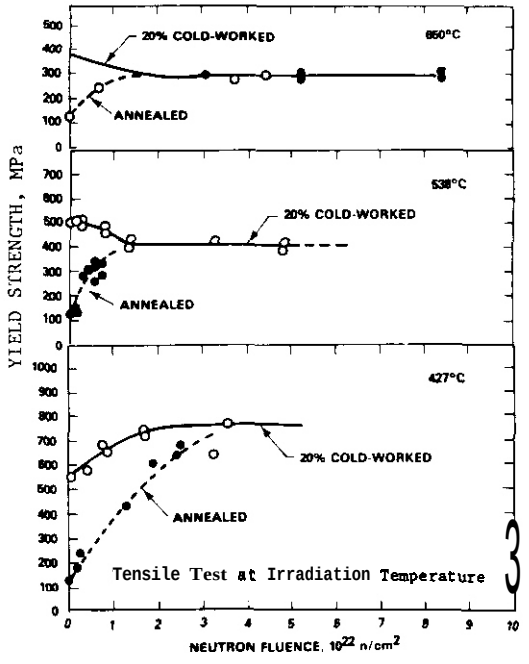

Fig. 14. Yield strength as a function of fluence for cold-worked and annealed type 316 stainless steel irradiated in the EBR-II [after Garner et al., J. Nucl. Mater. 1036104 (1981) 803–808 (ref. 2, this report)].

observed in this alloy could have resulted from the much lower concentration of helium compared with the materials irradiated in the mixed-spectrum reactors.

Uniform elongation is of the order of 0.2 to 0.3% from 50 to 400°C at 10 and 20 dpa. A slight recovery is observed at 30 dpa where values in the same temperature range are nearly 1%. Recovery appears to have progressed further by. 50 dpa where uniform elongation is several percent at 55°C. Although there are four data points at 55°C, there are no others below 400°C. This leads to a high uncertainty in the curve in this region but provides evidence for a rise in ductility at the low-temperature end.

At all damage levels but 50 dpa, uniform elongation begins to rise at about 400°C. Of particular interest in the 10 dpa graph are data from the ORR spectral tailoring experiment. These specimens have a He:dpa value characteristic of a fusion reactor. The 316 SS exhibits a significantly higher ductility than PCA. Although this may be a valid trend, it cannot be concluded from these data since the PCA has about 30% more helium than the 316 SS resultina from a higher nickel concentration. Since it is at high temperatures where the effect becomes evident, the difference in helium concentrations is a possible explanation for the observed difference. At 20 dpa the curves clearly pass through a minimum and decrease above 500°C. This is believed to be a true helium effect which persists at 30 dpa. It is also apparent at 30 dpa that USPCA in an aged and cold-worked condition, B3, has a particularly low ductility at 600°C. At 50 dpa the effect of helium is believed to still be present but to such an extent that low ductility has moved below 400°C. This must be studied further with lower temperature tests at 50 dpa. Some of the specimens contain over 3000 appm He at this exposure level. This is about five times the level expected in fusion reactor irradiation, but the curve is suggested for use as a very conservative estimate of ductility. It is also evident that the EBR-II irradiated 316 SS has high ductility at the highest temperatures investigated, further evidence that helium is the embrittling agent in this regime.

The low-temperature plastic instability evidenced by low uniform elongation is not indicated by the total elongation. As shown in Figs. 10 through 13, total elongation is as high as 10 to 17% at 55°C decreasing with increasing temperature. There is a discernible difference between annealed and cold-worked material in total elongation, more so than with the other tensile properties. The total elongation of annealed material is about 50% higher than cold-worked material at 30 dpa. Since the cold-worked structure is not expected to recover significantly between 10 and 30 dpa, the 30 dpa value for total elongation has been used for the cold-worked material at 10 dpa. The 30 dpa values have also been used as guidance in developing the curves for 20 dpa. Further research remains to confirm these assumptions, but they are expected to be conservative. A reduction in ductility is again evident above 550°C at 20 and 30 dpa, especially for the USPCA in the B3 heat treatment, With a reduction below 400°C evident at 50 dpa. This is again attributed to helium embrittlement.

CONCLUSIONS

1. Equations for post-irradiation tensile properties of the austenitic stainless steels AISI type 316 and PCA have been developed.
2. Trends in yield strength such as the convergence of annealed and cold-worked materials at dpa levels between 20 and 30 and reduction in yield strength observed at 50 dpa.
3. Low uniform elongation at temperatures below 400°C was observed at most dpa levels.
4. Reduction in ductility attributed to helium was observed at helium levels of a few thousand appm or greater at temperatures of 500°C and above.

FUTURE WORK

Rdditional tensile testing results are becoming available from irradiations in the ORR.[14] These results will be incorporated into the equations. In addition, the results of unirradiated specimens will be compared with the results for the irradiated specimens. Before these results can be used by the ITER Design Team, they must be reviewed by representatives of the fusion materials community and their suggestions incorporated.

REFERENCES

1. R. L. Fish, N. S. Cannon, and G. L. Wire, "Tensile Property Correlations for Highly Irradiated 20 Percent Cold-Worked Type 316 Stainless Steel," Effects of Radiation on Structural Materials, ASTM STP 683, ASTM, 1979, pp. 450-465.
2. F. A. Garner, M. L. Hamilton, N. F. Panayotou, and G. O. Johnson, "The Microstructural Origins of Yield Strength Changes in AISI 316 During Fission or Fusion Irradiation," J. Nucl. Mater. 103 & 104 (1981) 803-808.
3. J. L. Scott et al., "Second Annual Progress Report on United States-Japan Collaborative Testing in the High Flux Isotope Reactor and the Oak Ridge Research Reactor for the Period Ending September 30, 1985," ORNL/TM-10102, Oak Ridge National Laboratory, Oak Ridge, TN, 1986.
4. M. P. Tanaka et al., "Post Irradiation Tensile and Fatigue Behavior of Austenitic PCA Stainless Steels Irradiated in HFIR," J. Nucl. Mater. 155-157 (1988) 957-962.
5. J. L. Scott and M. P. Tanaka. "Status of U.S./Japan Collaborative Testing in HFIR and ORR," Fusion Reactor Materials Semi. Prog. Rept., September 30, 1986, DOE/ER-0313/1, USDOE Office of Fusion Energy, 1987, pp. 23-29.
6. M. L. Grossbeck and K. R. Thoms, "ORR-MFE-4: A Spectral Tailoring Experiment to Simulate the He/dpa Ratio of a Fusion Reactor in Austenitic Stainless Steel," ADIP Quart. Prog. Rept., June 30, 1980, DOE/ER-0045/3, Oak Ridge National Laboratory, Oak Ridge, TN, 1980, pp. 10-23.
7. M. L. Grossbeck, "Tensile Properties of HFIR-Irradiated Austenitic Stainless Steels at 250 to 400°C from the European Community/U.S./Japan Fusion Materials Collaboration," Fusion Reactor Materials Semi. Prog. Rept., September 30, 1986, DOE/ER-0313/1, USDOE Office of Fusion Energy, 1987, pp. 265-274.
8. B. Van der Schaaf, M. L. Grossbeck, and H. Scheurer, "Oak Ridge Test Matrix No. 5B and 5C HFR and HFIR Irradiations and Post-Irradiation Tensile Tests in Support of Fusion Reactor First Wall Material Development," EUR 10659, EN Comnission of the European Communities, Brussels-Luxembourg, 1986.
9. Private Communication, W. Van der Meulen, SCK, Mol, Belgium, 1988.
10. M. M. Paxton, "Mechanical Properties of Annealed and Cold Worked Type 316 Stainless Steel Fast Reactor Seamless Tubing," HEDL-TME 74-11, UC-79, 79b, Hanford Engineering Development Laboratory, Richland, WA, 1974.
11. R. L. Fish and J. J. Holmes, "Tensile Properties of Annealed Type 316 Stainless Steel After EBR-II Irradiation," J. Nucl. Mater. 46 (1973) 113-120.
12. G. E. Dieter, "Introduction to Ductility," Ductility, American Society for Metals, Metals Park, 1968, pp. 1-30.
13. Private Comnunication, R.L. Fish, Babcox & Wilcox, Lynchburg, VA, 1988.
14. M. L. Grossbeck, T. Sawai. S. Jitsukawa, and L. T. Gibson, "Tensile Properties of Austenitic Stainless Steels Irradiated in the ORR Spectral Tailoring Experiment ORR-MFE-6J and -7J," this report.

TENSILE PROPERTIES OF AUSTENITIC STAINLESS STEELS IRRADIATED IN THE ORR SPECTRAL TAILORING EXPERIMENT ORR-MFE-6J AND -7J

M. L. Grossbeck (Oak Ridge National Laboratory), T. Sawai, S. Jitsukawa (Japan Atomic Energy Research Institute, assigned to ORNL), and L. T. Gibson (Oak Ridge National Laboratory)

OBJECTIVE

The objective of this investigation is to determine tensile properties at low temperatures following irradiation introducing the fusion reactor value of He:dpa. The effect of irradiation on weld joints was also investigated under these conditions.

SUMMARY

Tensile properties were found to be consistent with those of previous irradiations in mixed-spectrum reactors. The yield strength at 60°C was found to be less than that at 330°C, but this can be understood in terms of hardening by dislocation loops. The properties of welds were found to resemble those of annealed base metal whether or not the weld was made in annealed or cold-worked material.

PROGRESS AND STATUS

Introduction

This experiment made contributions in three areas where there were weaknesses in the previous data base. One area is the low-temperature regime, below 400°C. In this experiment, specimens were irradiated at 60, 200, 330, and 400°C. The next area is that of welded materials. Both tungsten inert gas (TIG) welded alloys and electron beam (EB) welded alloys were irradiated. The third area was the data base of materials irradiated with a neutron spectrum producing the fusion reactor value of the ratio of helium production to atomic displacements. The combination of these features made this experiment a valuable contribution.

Experimental Procedure

Alloys investigated were AISI type 316 stainless steel in annealed, 15% cold-worked, and 20% cold-worked conditions, JPCA in annealed and 15% cold-worked conditions, and U.S. PCA in 25% cold-worked, and aged cold-worked conditions. A few JPCA specimens were cold-worked to 15%, then given a heat treatment at 800°C for 2 h in order to form uniformly distributed MC precipitates.

The specimens were irradiated in the ORR (Oak Ridge Research Reactor) to achieve an atomic displacement level of 7 to 8 dpa and helium levels of 100 appm. The irradiation temperature of 60°C was achieved by having the specimens in contact with the reactor coolant water. Temperatures of 330 and 400°C were achieved by having the specimens in a NaK-filled capsule with heat transferred across gas-filled gaps, and 200°C was achieved by having the specimens attached to an aluminum heat sink and exposed to helium. The elevated temperatures were controlled by altering the composition of the mixture of helium and argon gases in the heat transfer gaps.

Specimens were tested on an Instron universal testing machine Model 1122 equipped with a tungsten mesh furnace and a vacuum chamber capable of testing at elevated temperatures at pressures in the 10^{-4} Pa range. Strain rates of 5.6 x 10^{-4} s^{-1} were used for the U.S. alloys for which the specimens had a gauge length of 7.62 mm, and a strain rate of 4.2 x 10^{-4} s^{-1} was used for the Japanese alloys for which the specimens had a gauge length of 20.3 mm. All specimens were made from sheet with a thickness of 0.762 mm. Specimens that were irradiated at 60°C were tested at room temperature since no significant differences were expected in testing at 60 or 25°C. In addition, temperature control is difficult at temperatures as low as 60°C.

Results and Oiscussion

Results of the tensile tests are shown in Table 1. The table is self explanatory except perhaps for the footnote that indicates that for two specimens the tabulated yield stress is not the 0.2% yield stress. In these two cases, plastic instability was observed at a deformation below 0.2%. Since the stress at which this instability occurred was so close to the stress level when 0.2% strain was reached, the value at 0.2% strain was tabulated in order to give an indication of the strength of the material.

Table 1. Tensile Properties from ORR-MFE-6J and -7J

Specimen	Alloy	Temperature, °C		Stress, MPa		ϵ_u (%)	ϵ_T (%)
		Irrad.	Test	Yield	Ultimate Tensile		
FL31	J316 20 CW	60	RT	834	869	0.64	8.9
FL32	J316 20 CW	60	RT	855	883	0.63	7.5
FL13	J316 20 CW	330	330	862	876	0.44	2.3
FL14	J316 20 CW	330	330	993	1007	0.34	2.0
FL15	J316 20 CW	330	330	972	993	0.41	2.4
FL1	J316 20 CW	400	400	415	457	1.	2.8
FL3	316 20 CW	400	400	800	848	1.6	3.4
EL33	316 SA	60	RT	703	752	24.5	29.9
EL34	316 SA	60	RT	690	745	27.6	32.5
EL1	316 SA	330	330	848	855	0.29	3.1
EL2	316 SA	330	330	869	869	0.31	2.9
EL14	316 SA	400	400	595	677	4.6	7.0
EL15	316 SA	400	400	650	717	4.3	6.8
DL36	PCA 15 CW	60	RT	876	889	0.38	8.1
DL37	PCA 15 CW	60	RT	862	869	0.44	7.3
DL7	JPCA 15 CW	330	330	876	889	0.38	2.3
DL8	JPCA 15 CW	330	330	938	945	0.38	2.2
DL19	JPCA 15 CW	400	400	855	896	0.59	2.9
DL20	JPCA 15 CW	400	400	827	841	0.38	1.9
TE31	JPCA 15 CW Rod	330	330	931	945	0.42	5.3
TE30	JPCA 15 CW Rod	330	330	958	958	0.31	5.4
GL6	JPCA 25 CW	60	RT	910	924	0.44	4.5
GL7	JPCA 25 CW	60	RT	917	931	0.44	4.5
DLA6	JPCA Aged	60	RT	910	917	0.44	5.6
DLA7	JPCA Aged	60	RT	896	903	0.40	5.5
CL7	JPCA SA	330	330	821	821	0.23	2.5
CL8	JPCA SA	330	330	800	807	0.38	3.2
CL9	JPCA SA	330	330	876	883	0.25	2.7
CL19	JPCA SA	400	400	505	652	10.5	12.9
CL20	JPCA SA	400	400	549	667	2.5	10.5
AE05	316 20 CW (SS3)	60	400	647	717	3.3	11.0
AE02	316 20 CW (SS3)	60	RT	903	903	0.4	19.0
AE01	316 20 CW (SS3)	60	RT	903	917	0.5	20.1
EK20	PCA 25 CW (SS3)	60	RT	862	869	0.5	15.7
EK18	PCA 25 CW (SS3)	60	RT	848	848	0.5	13.5
EK19	PCA 25 CW (SS3)	60	RT	848	855	0.4	14.1
D58	J316 CW TIG WM	60	RT	635	675	7.2	9.4
D57	J316 CW TIG WM	60	RT	631	683	11.1	14.2
D50	J316 CW TIG WM	330	330	652[a]	655	0.03	2.2
D49	J316 CW TIG WM	330	330	687[a]	690	0.06	1.9
D53	J316 CW TIG WM	400	400	598	603	0.5	2.4
D54	J316 CW TIG WM	400	400	614	627	1.2	3.1
FLW6	J316 CW TIG WJ	60	RT	710	710	5.6	8.4
FLW1	J316 CW TIG WJ	60	RT	682	731	6.4	8.6
D29	J316 SA TIG WM	60	RT	655	675	24.2	27.1
D30	J316 SA TIG WM	60	RT	607	643	13.8	16.8
D19	J316 SA TIG WM	330	330	703	703	0.25	2.0
D17	Damaged						
D23	J316 SA TIG WM	400	400	591	611	1.3	2.8
D24	J316 SA TIG WM	400	400	587	611	1.9	4.4
ELW1	J316 SA TIG WJ	60	RT	659	687	3.9	6.8
ELW2	J316 SA TIG WJ	60	RT	678	710	3.6	5.9
JL6	J316 SA EB WJ	60	RT	637	676	2.8	5.6
JL7	J316 SA EB WJ	60	RT	660	696	2.7	6.5
JL1	J316 SA EB WJ	330	330	731	738	0.7	2.8
JL2	J316 SA EB WJ	330	330	724	731	0.7	2.7
JL3	J316 SA EB WJ	400	400	637	656	0.6	2.6
JL4	J316 SA EB WJ	400	400	610	625	0.8	3.1

WM = weld metal

WJ = weld joint

[a]Not 0.2% YS

Base Metal – The yield strengths for the base alloys are plotted in Figs. 1 and 2 for the annealed and cold worked materials, respectively. The aged PCA has been plotted with the annealed alloys although it clearly belongs neither with the annealed nor the cold-worked alloys. Several observations can be drawn from the figures: The first is that there is little difference in strength between type 316 stainless steel and PCA; the only significant difference is between cold-worked and annealed material. The curves plotted in the figures are curves based on a large amount of data from several reactors and represent lower limits to strength at a displacement level of 10 dpa (ref. 1). The present data lie very close to these curves since the strength is still increasing with irradiation at this level of exposure. Saturation is not expected until a displacement level of 15 to 20 dpa has been reached. There is also a trend for strength to increase with temperature from 60 to 330°C. This trend is also evident in previous data, although not previously clear due to the lack of a consistent data set. The present experiment makes this trend clear.

The reason for the observed increase in strength in this temperature regime can be understood in terms of strengthening from dislocation loops. Hardening results from other obstacles such as bubbles and precipitates, but an attempt is being made only to qualitatively explain the trend in the temperature dependence of hardening, not to quantitatively estimate the hardening from irradiation. Since loops are most likely to be the major strengthening agent in the low-temperature regime, the temperature dependence of strengthening due to loops will be estimated. Strengthening due to loops may be represented by the following expression[2] if the loops are assumed to be strong obstacles:

$$\Delta S = Gb(dn)^{1/2}/B \ , \qquad (1)$$

where G is the shear modulus, b is the Burgers vector, d is the loop diameter, n is the loop density, and B is a constant that has a value of about four. Since electron microscopy has not yet been done on the alloys irradiated in this experiment, measurements of d and n are not available. In order to make an estimate of the strengthening, microstructural parameters from austenitic stainles steels irradiated in the HFIR and EBR-II will be used. Such data have already been assembled and equations for loop density and loop diameter as functions of irradiation temperature have been derived.[2] Loop density is given by

$$n = 7 \times 10^{16} \exp(-T/2.6 \times 10^{7})T^{2} + 4.05 \times 10^{22} \exp(-0.037T - 1500/T) \ cm^{-3} \ , \qquad (2)$$

and

$$d = 10^{-7} \{(0.17T - 30.5)[1 - \exp(-T/350)] + 13\} \ cm \ , \qquad (3)$$

where T is the temperature in degrees centigrade. Equations (2) and (3) are substituted into Eq. (1) to calculate the increment of strength attributed to the dislocation loops. The result of the calculation is shown in Fig. 3. It can be seen that the increase in strength from 60 to 330°C can be accounted for although the magnitude of the strengthening is somewhat small. Since the uncertainty in the microstructural parameters is large, this is not a great concern.

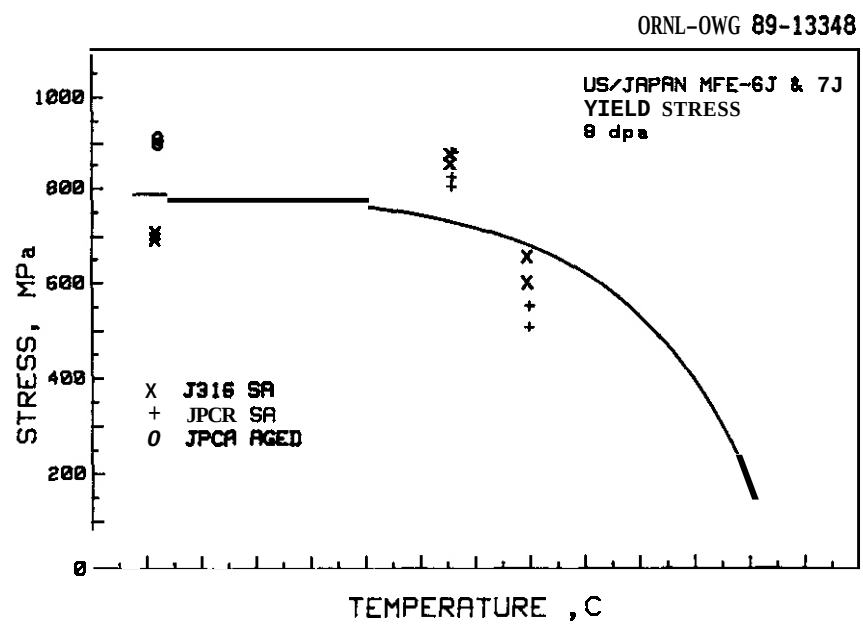

Fig. 1 Yield strength as a function of irradiation and test temperature for Japanese heats of annealed AISI type 316 stainless steel and PCA irradiated in the ORR to a displacement level of 8 dpa. The curve is a lower limit for a large base of similar materials.

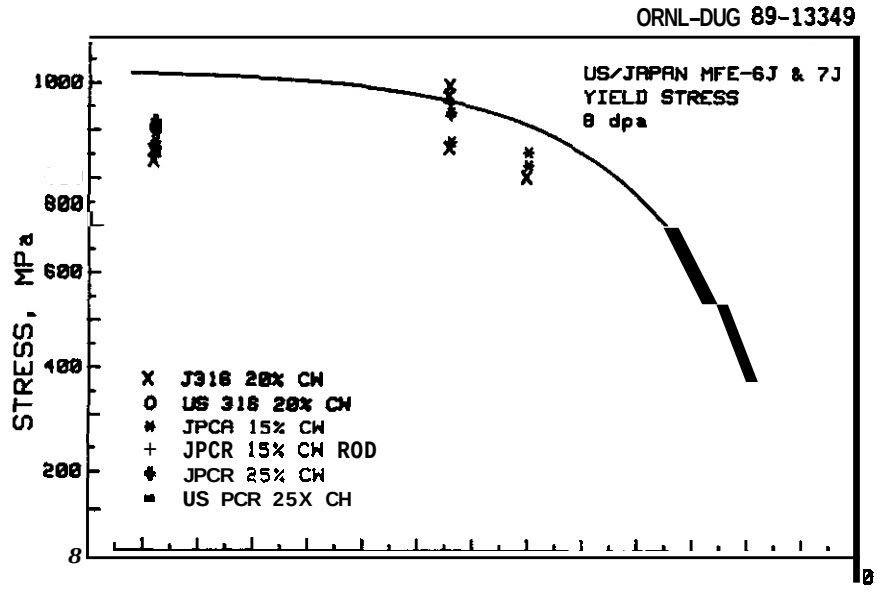

Fig. 2. Yield strength as a function of irradiation and test temperature for cold-worked type 316 stainless steel and PCA irradiated in the ORR. The curve is a lower limit for a large base of similar materials.

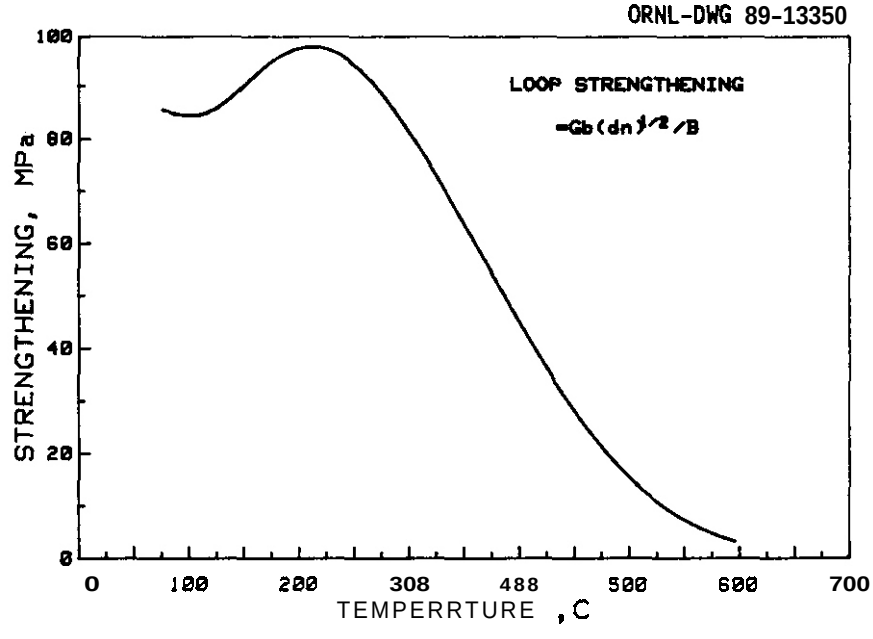

Fig. 3. Increment of strengthening due to dislocation loops as a function of temperature.

Uniform elongation is plotted in Figs. 4 and 5. As indicated by the trend curves from previous data, uniform elongation in these alloys is nearly always below 0.5% for temperatures below 400°C. In the present investigation, this holds for the cold-worked alloys and for the cold-worked and aged material, but the annealed 5316 (Japanese heat of AISI 316) demonstrated ductilities of about 25% at 60°C. This high ductility dropped to below 0.5% at 330°C. The values of total elongation, plotted in Figs. 6 and 7 for annealed and cold-worked material, respectively, reveal a trend to higher ductilities at low temperatures for all alloys and conditions. Even in the case of cold-worked material, the trend is quite clear where total elongations range from 4 to 8% at 60°C. This is encouraging for the case of deformations that relieve the stress that created them such as thermal stresses. In this case, the material will not fail when the ultimate tensile strength is reached because the resulting plastic deformation immediately relieves the stress. If, however, the total elongation were exceeded, the material would fail in any case.

ORNL-DWG 89-13351

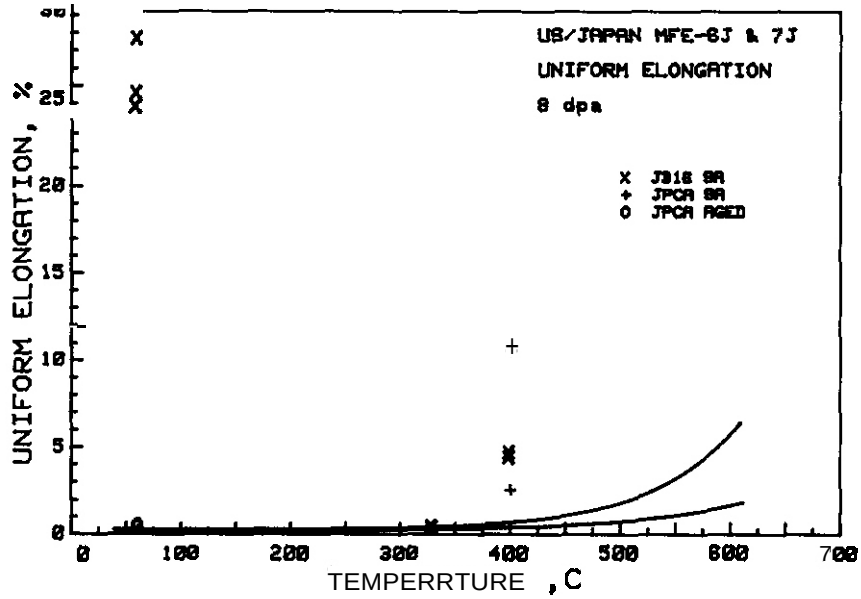

Fig. 4. Uniform elongation as a function of irradiation and test temperature for Japanese heats of annealed type 316 stainless steel and PCA. The curves are for a larger base of similar but cold-worked irradiated alloys. The upper curve is for PCA, and the lower curve is for type 316 stainless steel.

ORNL-DWG 89-13352

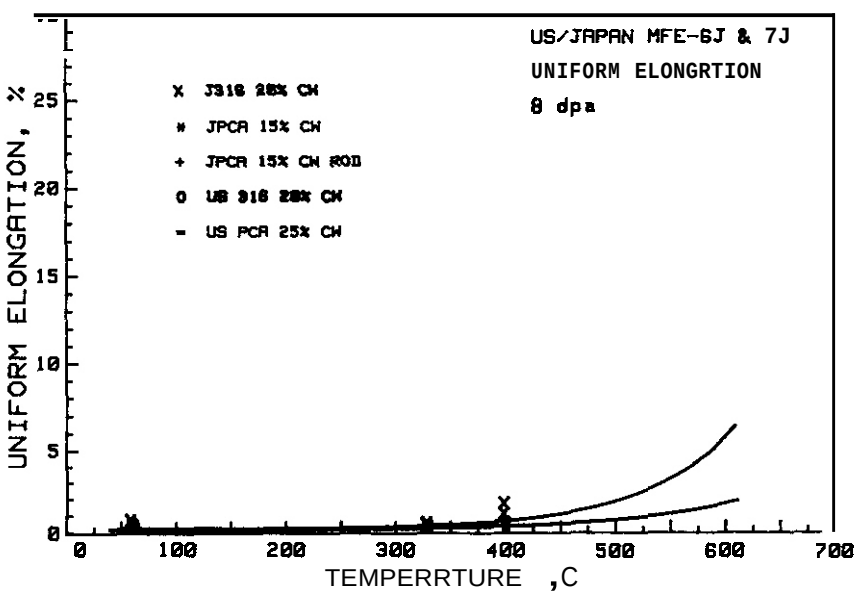

Fig. 5. Uniform elongation as a function of irradiation and test temperature for cold-worked type 316 stainless steel and PCA irradiated in the ORR. The curves are for a larger base of similar irradiated alloys. The upper curve is for PCA, and the lower curve is far type 316 stainless steel.

Welds — Weld joints were made in Japan of the Japanese heat of AISI 316 in annealed and cold-worked conditions. Both tungsten inert gas (TIG) and electron beam (EB) welding techniques were used. Specimens were prepared in two orientations. Some specimens were cut transverse to the weld so as to include the fusion and heat affected zones as well as base metal in the gauge section. Other specimens were cut longitudinally to the weld to include only the fusion zone in the specimen. The former are designated "weld joint" and the latter "weld metal" in Figs. 8 through 13.

Figure 8 is a plot of yield strength as a function of irradiation and test temperature for welds in annealed material. Yield strength does not appear to be a function of weld technique. Again a curve for 10 dpa irradiated specimens is shown, and the differences discussed with respect to base metal specimens still apply. No significant differences are seen between the longitudinal and transverse specimens.

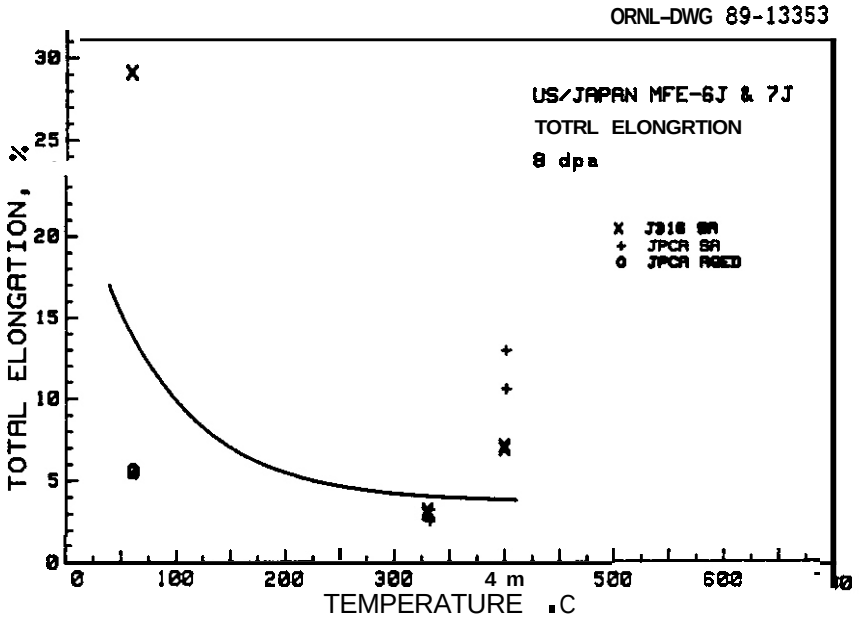

Fig. 6. Total elongation as a function of irradiation and test temperature for Japanese heats of type **316** stainless steel and PCA irradiated in the ORR. The curve is for a larger base of similar irradiated alloys.

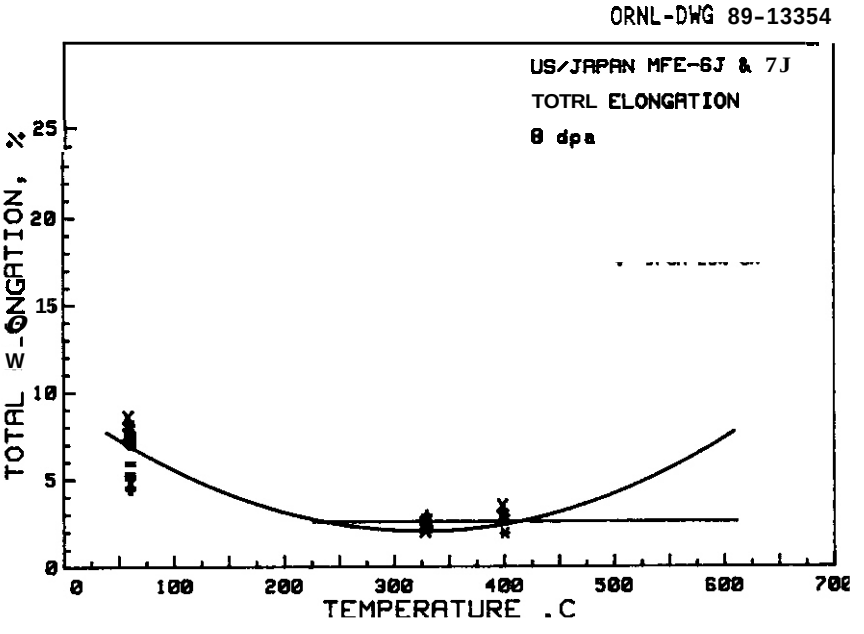

Fig. 7. Total elongation as a function of irradiation and test temperature for cold-worked type **316** stainless steel and PCA irradiated in the ORR. The curves are for a larger base of similar irradiated alloys. The concave curve is for type **316** stainless steel and the straight line is for PCA.

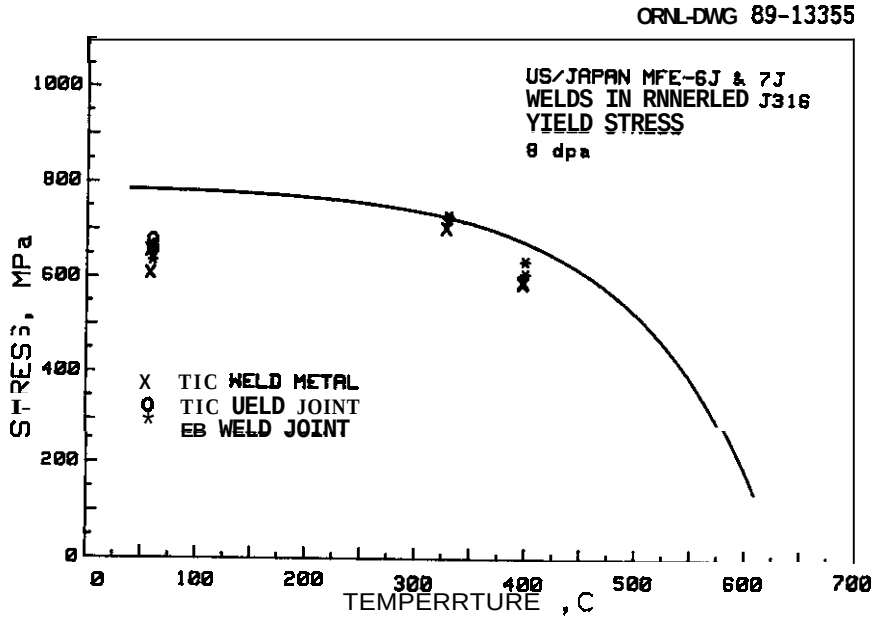

Fig. 8. Yield strength as a function of irradiation and test temperature for welded annealed type 316 stainless steel irradiated in the ORR. The curve is for a larger base of irradiated unwelded material.

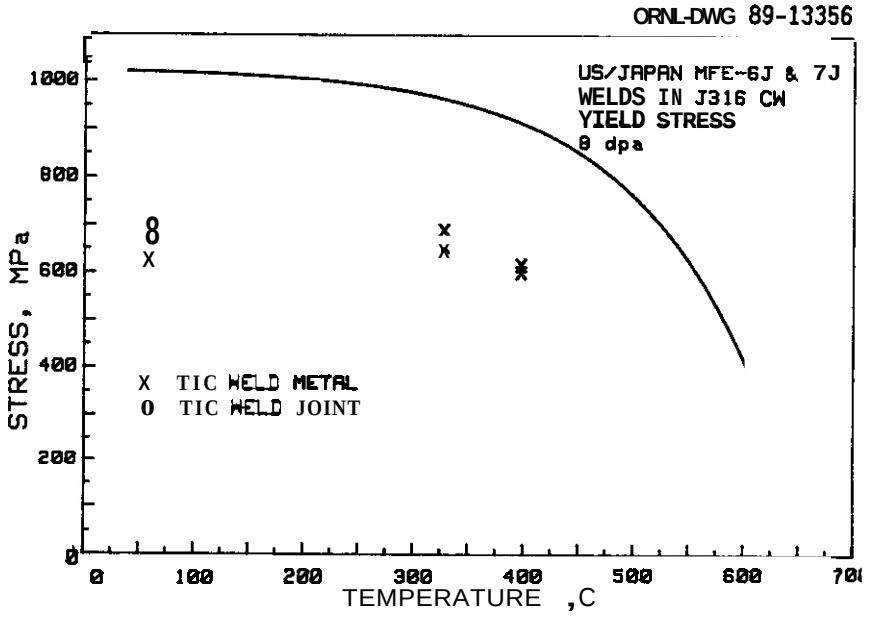

Fig. 9. Yield strength as a function of irradiation and test temperature for welded 20% cold-worked type 316 stainless steel irradiated in the ORR. The curve is for a larger base of irradiated unwelded material.

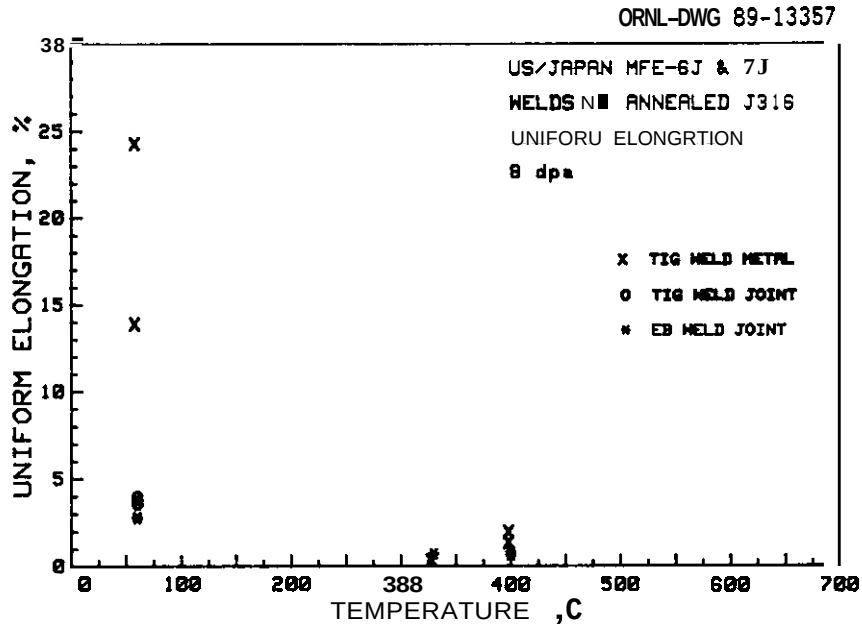

Fig. 10. Uniform elongation as a function of irradiation and test temperature for welded type 316 stainless steel irradiated in the ORR.

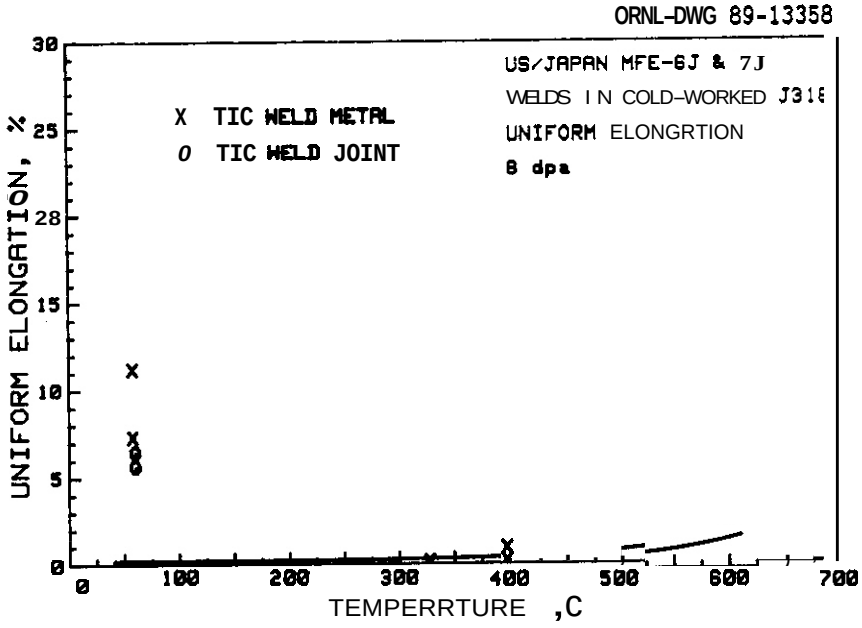

Fig. 11. Uniform elongation as a function of irradiation and test temperature for 20% cold-worked type 316 stainless steel irradiated in the ORR. The curves are for a larger base of unwelded irradiated material.

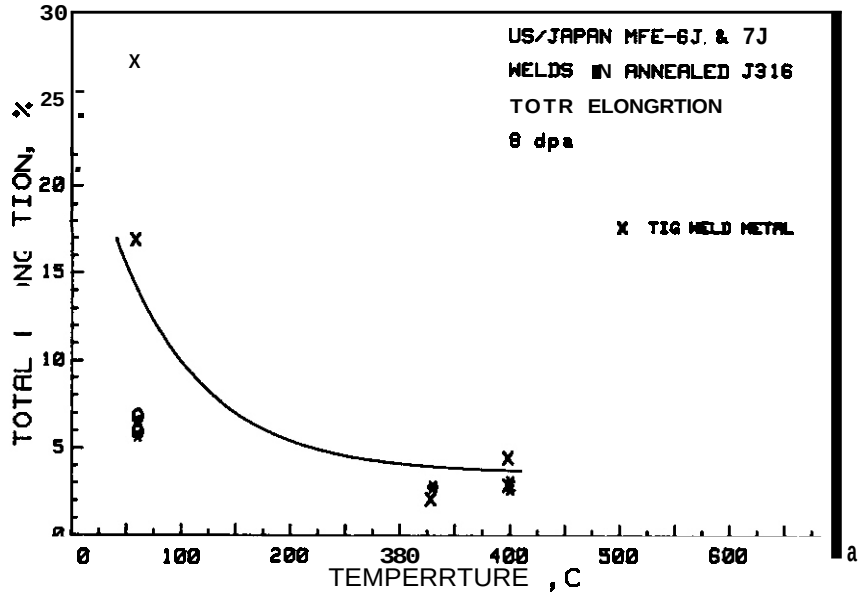

Fig. 12. Total elongation as a function of irradiation and test temperature for annealed type 316 stainless steel irradiated in the ORR. The curve is for a larger base of unwelded irradiated material.

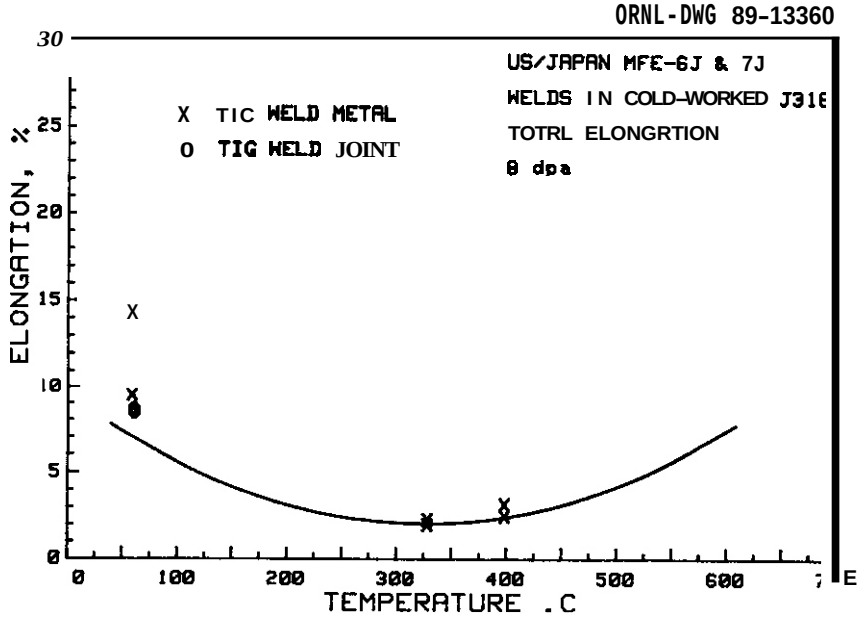

Fig. 13. Total elongation as a function of irradiation and test temperature for 20% cold-worked type 316 stainless steel irradiated in the ORR. The curve is for a larger base of unwelded irradiated material.

Since the fusion zone is usually the weakest material, and the weakest material determines the strength, this is a predicted result. In addition, the fusion zones for the annealed and cold-worked specimens are identical after welding. This is, of course, reflected in the yield strengths which are the same for both materials. The yield strength for welds in 20% cold-worked material is shown in Fig. 9. The strength levels are comparable with those of the annealed welded specimens and with the annealed base metal specimens. An exception to the similarity of the strengths of all of the welded specimens appears at 330°C where the base metal is stronger than the annealed weld metal. This is not understood at the present time, but could result because the annealed material is not as completely annealed as the fusion zone of the welds or could result from slight porosity in the welds.

Uniform and total tensile elongations are plotted as functions of temperature in Figs. 10 through 13. Figures 10 and 11 show that the welded materials also exhibit low uniform elongation at 330 and 400°C. However, at 60°C, uniform elongation is 7 to 24% for annealed and cold-worked material, reflecting the anneal during the welding process. Uniform and total elongations for the longitudinal joints, consisting entirely of fusion zone weld metal, are significantly greater than those of the transverse specimens. This is understood on the basis of effective gauge length. Since the fusion zone is weaker than the surrounding material, most of the deformation is in this region. Since this region is small compared to the gauge section of the specimen, which is used to compute elongation, the calculated value of elongation under-predicts the actual deformation which is confined largely to the fusion zone of the specimen. This effect is even more pronounced in EB welds where the fusion zone is even smaller. Since there seems to be a slight reduction in strength from welding, as seen from Figs. 1 and 8, the effect of an effectively shorter gauge section also applies to comparison of the unwelded specimens to the welded specimens. In general, the trends in behavior of the welds can be approximated by the behavior of annealed material.

CONCLUSIONS

1. Tensile properties for the fusion reactor He:dpa ratio have been obtained for temperatures of 60, 330. and 400°C. Data for specimens irraidated at 200°C are expected during the next reporting period.

2. An increase in strength between 60 and 330°C has become apparent and can be understood in terms of dislocation loop strengthening.

3. Cold-worked material exhibits uniform elongations below 0.5% from 60 to 330°C. but annealed material has uniform elongation above 20% at 60°C.

4. Tungsten inert gas and electron beam welds were successfully made in AISI type 316 stainless steel. Property trends follow those of annealed material even if the welds are made in cold-worked material.

FUTURE WORK

During the next reporting period, the 200°C specimens are expected to be tested and the data analyzed.

REFERENCES

1. M. L. Grossbeck, "Development of Tensile Property Relations for ITER Data Base," this publication.

2. A. L. Bement, Jr., "Fundamental Materials Problems in Nuclear Reactors," 2nd International Conference on the Strength of Metals and Alloys, 1970, ASM, pp. 698-728.

3. M. L. Grossbeck, L. K. Mansur, and M. P. Tanaka, "Irradiation Creep in Austenitic Stainless Steels at 60 to 400°C with a Fusion Reactor He:dpa Ratio," 14th International Symposium on the Effects of Radiation on Materials, Andover, Massachusetts, June 27-30, 1988, ASTM.

DEVELOPMENT OF LOW ACTIVATION FE-MN AND FE-MN-CR ALLOYS FOR FUSION SERVICE-

L. D. Thompson (San Diego State University) and T. A. Lechtenberg (General Atomics)

OBJECTIVE

The objectives of this communication are to disseminate some available data on the Fe-Mn and Fe-Mn-Cr alloy systems and to provide insight and guidance regarding the current alloy design and development program efforts in Neutron Irradiation Materials (NIM) and for the International Thermonuclear Experimental Reactor (ITER).

SUMMARY

Recent attention in the fusion materials research community has been focused on attempting to define compositional requirements for low-activation stainless steel alloys for first wall and blanket structures of future fusion reactors. Alloy design efforts have been initiated by the NIM. as well as in other fusion materials programs, to develop materials and microstructures inherently resistant to neutron damage. More recently, to address the concern about expected post-service neutron activation characteristics, the baseline programs focused primarily on developing neutron damage resistant materials have expanded to include the investigation and development of low-activation structural steels containing manganese. (Refs. 1-5) Iron alloys containing 25-50% Mn and ternary alloys containing 10-20% Mn with 5-20% Cr are included In the alloy classes being studied.

The former U.S. Energy Research and Development Administration (ERDA), and now the Department of Energy (DOE), was interested in developing alternative austenitic stainless steels which would rely less on strategic and expensive alloying elements for their properties. They sponsored a substantial alloy design effort during the 1970s directed at investigating the properties of Fe-Mn and Fe-Mn-Cr alloy compositions for cryogenic applications (such as liquid natural gas containment structures) which were similar to those of interest in the fusion materials program. While the database for the Fe-Mn and Fe-Mn-Cr systems is limited, the data obtained in these earlier studies are useful in understanding the alloy design capabilities of this system and for providing guidance to the current program. Many of the compositions previously investigated complement those In the NIM program and the data we will report will help establish trends in behavior. Mechanical properties and microstructural characterization data and their correlations are presented for those alloy systems of general interest to the present NIM program and ITER alloy development efforts.

PROGRESS AND STATUS

Introduction

Possibly critical to the eventual commercialization of advanced fusion reactors is the requirement that the spent structural components display radioactivity characteristics consistent with inexpensive disposal. This generally restricts the allowed amounts of long-lived radioisotopes which result from high energy neutron interaction with the structural material. Current reactor design scenarios predict. perhaps pessimistically, that first wall and blanket components will reach their expected design life limitations In about one to three years of reactor operation. Furthermore, high levels of neutron irradiation results in loss of ductility for the classes of Fe-Ni-Cr austenitic stainless steels presently considered for such applications. Thus, the periodic changeover and maintenance of these systems may result In significant structural waste disposal problems. Safety assurance will be a key consideration in the final design of a fusion power reactor facility. Because the hostile nature of the near-plasma environment severely limits the service life of any austenitic stainless material relative to components in fossil or nuclear power plants, the low-activation focus of the NIM program Is to concentrate on alloy canpositions which can be "surface-burled" as low-level waste under regulation 10CFR61 following reactor service. (Refs. 1-5)

The structural materials for the above mentioned components must be easily fabricable into tubing and other relevant shapes, weldable, and also must exhibit adequate levels of corrosion reslstance. While the Internal plasma chamber components present the most serious deslgn challenges, Fe-Mn-Cr base stainless steels may be a sound alternative for other reactor canponents as weil.

The constraint of surface burial places restrictions on the types of elements which can be considered for the developmental alloys. The control or elimination of some of the more common alloying elements for the AISI 300 series stainiesses. including, but not limited to nickel. molybdenum. niobium, etc.. complicates the task at hand. These elements would transmutate to form radioactive isotopes with either extremely long half-lives or which would emit unacceptably high energy decay products. The development and characterization of several series of Fe-Mn-Cr alloys formed the basis of research at U. C. Berkeley in the 1970s. (Refs. 6 and 7) Many of the present NIM program compositions (Ref. 8) are slmllar to those investigated durlng thls earlier program. A recent review paper summarizes the mechanical behavior and microstructural characteristics of a series of Fe-16Mn-13Cr alloys which were included in the U. C. Berkeley study. (Ref. 9) This general class of alloys would seem to have wide appeal for future fusion reactor applications based on the combinations of strength, ductility and toughness observed wlth many of the alloy formulations earlier explored.

Summary of ERDA/DOE Alloy Development Program

The objective of the ERDA/DOE Fe-Mn-Cr ai ioy development program was to develop nickel-free austenitic stainless steels wlth lower chromium concentrations than the AISI 300 series alloys. Much of thls work was performed at U. C. Berkeley under the tutelage of Parker and Zackay. (Refs. 6,7,9-18) The materials. once sufficiently developed, were to compete with the standard AISI 300 series alloys for a share of the marketplace. While the cryogenic applications being addressed dictated that the developmental steels had to display adequate low temperature strength and toughness, acceptable overall corrosion reslstance was also a major goal as it is in the NIM program.

The U. C. Berkeley program alloys most pertinent to the NIM and ITER research community are the Fe-Mn. Fe-Mn-C, Fe-Mn-Cr. and Fe-Mn-Cr base materials. (Refs. 6.7. 9-18) Much of the information generated In the Fe-Mn and Fe-Mn-C system studies (Refs. 15-18) was taken into consideration durlng the formulation of the Fe-Mn-Cr ternary and Fe-Mn-Cr base materials to be discussed in this paper.

Tensile, hardness. and impact toughness properties for many of these Fe-Mn-Cr base alloy systems were evaluated at room temperature (RT), 195K and 77K. The RT data were used to screen the alloys prior to extensive lower temperature testing. Alloy phase constituents, stabilities and transformatlon behavior were correlated with the mechanical properties. Optlcal. scanning electron and transmission microscopy. dilatometry, and x-ray diffraction were used to characterize the evolution of microstructures and to provide correlations with the mechanlcal properties obtained. Sane corrosion experlments were also conducted where the behavlor of the most promising developmental alloys was compared with that of AISI 347 stainless steel, a grade slmllar to AISI 316L, but which contains niobium to decrease susceptibility to sensitization reactions and stress corrosion cracking.

In this paper the effects of Mn and Cr concentratlons on the propertles of representative Iron-base compositions are discussed by the authors along wlth microstructural Correlations and the evolution of mlcrostructure In these materials. Details of the experimental procedures used durlng the course of these investlgatlons have been previously reported (Refs. 6,7, 9, 15 and 18) and will not be repeated beyond a level necessary to effectively convey the Information. The possible application of these or slmllar materlals for other fuslon reactor components. e.g., the superconducting magnet system reinforcement structure, may require cryogenic performance so some of the low-temperature data are Presented In conjunction wlth ambient temperature data. Information on alloys whlch are not suitable for fuslon applications Is Included In certaln Instances to clarify a point or to illustrate a particular feature representatlve to the generic class of materials.

As stated, Ref. 8 lists the nominal and, in some cases, actual chemical compositions of the materials Included in the NIM program. These alloy compositions were formulated based on the available Schaeffler diagram. (Ref. 19) There has been considerable variation between the predicted and observed phase constituents. (Refs. 8 and 20) A screening study is underway and the mechanical properties of the most promising alloy systems are being evaluated in both the unirradiated and irradiated conditions at temperatures representative of the application range. Many of the NIM materials are similar in composition to those of the previous studies which is why the present communication was believed to be valuable.

Commercially available steels, the AISI 200 series alloys. do substitute Mn for Ni: however, the substitution is generally not complete since the presence of some Ni improves the elevated temperature oxidation resistance. (Ref. 21) Also. one of the inherent limitations imposed by substantial manganese levels In austenitic iron is the high Mn vapor pressure at temperatures exceeding approximately 923-973K. Phase instabilities and microstructural changes can occur as the Mn concentration decreases at the exposed surface, thus changing the mechanical properties and probably affecting the corrosion resistance. Fortunately, fusion structural reactor component temperatures will be limited to levels where both the absence of nickel and manganese surface vaporization are not expected to result in significant component degradation during service. The vaporization rates and other vapor pressure related effects will have to be clearly understood so that reactor operating conditions can be maintained in a manner such that quenching of the plasma does not occur. Thls vaporization could poze a safety hazard as Mn exhibits a hlgh level of short term radioactivity. (Ref. 22)

Discussion

The phase consituents and their respective stabilities are extremely sensitive to alloying in Fe-Mn and Fe-Mn-Cr alloy systems. The most common phases observed in these alloys have the FCC. HCP, and BCC crystal structures with the phase proportions dependent on the alloy chemistry and thermomechanical processing history. In alloys where all three phases can form the transformation sequence is from FCC to HCP to BCC. These transformations can occur athermally if the temperature is reduced below the respective M_s temperatures or they can occur during plastic deformation via strain-induced mechanisms if the deformation temperature is below the respective M_d temperatures. Typically, these reactions are martensitic. although it is possible to have BCC delta ferrite present if the alpha Iron phase is strongly stabilized by alloylng. This has been observed in recent and earlier studies. (Refs. 6-8) The key to designing and optimizing the microstructures of these alloys lies, therefore, in (1) adjusting the chemistry to produce the desired Initial combination of phases, and (2) adjusting the phase stabilities to produce a stable microstructure during service temperature cycling and exposure to the fusion plasma environment. The methodology by which the initial phase Proportions is developed remains somewhat flexible because thermomechanical processing strongly Influences the degree of strain-induced transformatlon In these alloys. (Refs. 6,7 and 9) This implies that the microstructural optimization for fusion applications will require a thorough understanding of the final microstructure(s) most likely to perform well In fusion reactors taking into account mechanical and neutron interactive behavior. The best use of alloy chemistry and thermomechanical processing as material optimization tools in the alloy design program directly depend on this information.

Microstructural Characteristics of Fe-Mn Aiiova

Manganese additions to Iron-base alloys have been shown to stabilize the face-centered-cublc austenltlc phase. gamma, although the effect is not as strong as wlth nickel (Refs. 15 and 16) and also to significantly decrease the stacking fault energy of the resultant austenite. (Ref. 23) The decrease in stacking fault energy promotes dislocation dissociation reactlons and the formatlon of partial dislocations whlch result in alloys somewhat more difficult to mechanically process as compared wlth nickel-stabilized austenltlc alloys. Manganese concentrations In excess of about 10% decrease the stacking fault energy to an extent whereby an hexagonal-close-packed phase. epsilon, becomes metastable. (Refs. 15. 16, 23 and 24)

Figure 1 shows how the room-temperature tensile properties of Iron change wlth additions of manganese. (adapted from Ref. 16) Alpha is used to represent the

stable ferritic phase while alpha prime refers to the martensitically formed variant of the BCC phase. The stability of the ferrite decreases with increasing Mn and in binary alloys containing substantial Mn concentrations only epsilon and austenite are stable (or metastable). The yield strength decreases as these closely-packed phases stabilize related to the easier dislocation shear processes in the HCP and FCC phases. Note that at about 16% Mn a large increase in tensile strain hardening occurs as evidenced by the increase in ultimate to yield strength ratios and the marked increase in elongation.

The range of manganese concentrations (14-20 weight percent) included in the ERDWDOE Fe-Mn-Cr alloy design program (Refs. 6 and 7) were chosen to take advantage of this marked increase in ductility and toughness. Chromium levels for these experimental steels were maintained at 13 w/o, consistent with the minimum level to achieve passivity in an oxidizing environment, and 18 w/o, a level chosen to compare with many of the 300 series alloys. Nitrogen and carbon additions were made to enhance the stability of the austenitic phase while molybdenum and silicon additions were to provide improved corrosion resistance.

The FCC and HCP phases formed can transform during plastic deformation to HCP (and then to BCC) and to BCC martensites, respectively. (Refs. 6.7. 9-14) The strain hardening/toughening effect associated with metastable phase transformations during deformation was originally used by Parker, Zackay, and colleagues to enhance the properties of a class of materials known as TRIP (TRansformation Induced Plasticity) steels. (Refs. 25-29) In addition to alloy chemistry, the degree to which phase transformations occur in metastable systems such as these depends on the prior thermomechanicai processing which establishes the initial microstructure, and the test temperature, specifically the test temperature relative to the critical temperatures for the strain-induced transformations. Obviously, alloy chemistry in these cases, only provides a basis in terms of available "phase space" with thermomechanical processing history actually controlling the initial proportions and morphologies of phase constituents. Thus, this system offers interesting and flexible opportunities that the alloy designer can use to produce an optimized combination of mechanical properties for fusion service.

Figure 2 schematically illustrates an appropriate model for the FCC to HCP phase transformation in low stacking fault energy austenites. (Refs. 9, 30 and 31) Also shown is the mechanism of twinning under similar conditions. The metastable epsilon phase forms in response to the decrease in stacking fault energy. Partial dislocation mechanisms are responsible for both the twinning reaction and the formation of HCP phase from the parent austenite. Once the stacking fault energy decreases to an extent where widely separated partial dislocations occur, plastic deformation mechanisms involve the motion of that partial (in a particular pair of partial dislocations) which is aligned most favorably with respect to the applied shear stresses. Some of the mechanical energy supplied during deformation can be absorbed by the material in expanding the area of stacking faults. Inevitably, as these faults expand on parallel slip planes, fault overlapping occurs. An HCP band will evolve if the overlapping faults lie on alternating parallel slip planes whereas a twin will evolve if they lie on adjacent and consecutive planes as shown in Fig. 2.

Both of these transitions increase the strain hardening rate of the material. In addition, the planar slip deformation associated with low stacking fault energy materlais contributes to straln hardening of the austenitic phase. Twinning of the austenite results in orientation shifts at the austenitic twin boundaries which act as slip barriers. The metastable HCP phase, when present as a phase of intermediate stability between the austenite and the ferrite. increases the strain hardening capacity by further increasing the crystallographic resistance imposed to slip. Slip dislocations passing along the (111) type slip planes in the austenite repeatedly encounter bands of HCP phase which hinder an easy glide mechanism of motion. In compositions where the austenite is more stable the extent of strain hardening is reduced to a level consistent with the amount of twinning combined with the inherent austenite strain hardening contribution.

Alloy design studies were conducted to investigate these effects and to optimize conditions to enhance toughness and retain strength. (Refs. 6.7 and 9) Further discussion is provided In these references with additional useful data related to Fe-Mn and Fe-Mn-C materials. The remainder of this paper will be

used to communicate results obtained In those alloy development studies emphasizing Fe-Mn-Cr ternary alloys and Fe-Mn-Cr base alloys. Emphasis in these studies was placed on alloys having a minimum of 13% Cr to achieve passivity in oxidizing environments and to obtain generally good corrosion resistance. (Ref. 32)

Mechanical Properties and Microstructural Correlations in Fe-Mn-Cr Ternary Alloys and Fe-Mn-Cr Base Alloys

Chromium, belng body-centered-cubic, stabilizes the BCC ferritlc and martensitic phases in Iron alloys, alpha and alpha prime, respectively. As interstitiais. both nitrogen and carbon are austenlte stabilizers in these composition ranges. (Ref. 7) Carbon additions to conventional austenitic stainless steels must be carefully controlled to prevent the precipitation of grain boundary chromium carbides during component fabrication. The resultant sensitized microstructures are very susceptible to stress corrosion cracking under some environmental conditions. (Ref. 33) Nitrogen does not precipitate out as readily In Fe-Mn-Cr steels (Ref. 7) and if used to optimize austenite stability should produce steels which are more weldable and serviceable. There is also evidence that stabilization of the HCP phase Increases with interstitial element additions, undoubtedly a result of the close-packed lattice configuration.

Silicon and molybdenum are important alloying elements used to enhance corrosion reslstance. Molybdenum stabilizes the BCC phase in a manner similar to chromium. The behavior of the molybdenum-contalnlng steels will not be discussed at length since these compositions would be unsuitable for fuslon reactor components that must be surface buried following service. The effects of silicon depend on the other alloying elements in the steel, but generally silicon will slow down austenite decomposition/precipitation reactlons by affecting interstitial diffusion rates/precipitation nucleation rates and within these composition ranges can be vlewed as an austenlte stabilizer if present in small concentratlons wlth nitroge and carbon. (Refs. 6 and 7)

Work done by Schanfein (Refs. 15 and 16) and Haddick (Ref. 18) on Fe-Mn and Fe-Mn-Cr alloys and on Fe-Mn-C alloys, respectively, had established the basis for the alloy design approach employed wlth the Fe-Mn-Cr system. The ternary Fe-Mn-Cr alloys contained 14, 16, 18, or 20% Mn with either 13 or 18% Cr. The 13 Cr alloys proved to be the most promising with both adequate strength and excellent ductlllty. The ternary compositions contained small amounts of titanium and aluminum to getter interstltlal impurities. In order to investigate the interrelationships between the three primary phases in these alloys it was necessary to eliminate the confusing contributions of interstitial elements. Table I lists the alloys lnvestlgated and the transformation temperatures for the HCP to FCC transition on heating and the FCC to HCP transltion on cooling. Dilatometry was used to determine these critical temperatures. Two heat treatments (A and B) were used to produce the initial microstructures in these alloys. Following an initial austenitlzation treatment, heat treatment A Involved an air cooling to room temperature and heat treament B involved an ice brine quench and subsequent immersion in liquid nitrogen prior to air warming to RT. The latter treatment resulted in significantly greater amounts of transformation products since the LN temperature is lower than the critical temperatures for the athermal transformations Involved. The resultant phase proportions are presented in Table 11.

Table III lists the Rockweli hardnesses for all of the alloys Included In the study. Those data In the "gettered" column refer to the Fe-Mn-Cr ternary alloys. The abrupt increase in hardness associated with the Fe-20Mn-18Cr alloy Is the result of brittle sigma phase formatlon. (Ref. 6) The mechanical properties of this alloy were poor with the lntermetaillc sigma phase essentially controlling the material response resuitlng In low ductilities and little energy absorption capacity during fracture.

Table IV summarizes the mechanical property data for the ternary alloys. The tenslle data represent the average value for two or three specimens tested. A triplex microstructure consisting of roughly equal proportions of the three possible phases was especially effective In strengthening by providing a high density of crystallographic barriers to slip. Excellent toughness was also observed for alloys havlng this type of mlcrostructure. Figure 3 shows the Charpy V-notch impact energy curves obtained. The increase in Cr concentration from 13 to 18% was found to substantially increase the ductile-to-brittle transition temperature (DBTT) for 14-18% Mn materlals. This increase was

related to increased Proportions of BCC phase Initially present which has a comparatively high DBTT. Figures 4-6 show the effects of manganese concentration on mechanical properties. The room temperature tensile data show that increased levels of toughening are related to increased presence of metastable phases in the microstructure. Manganese concentrations of 16% were found to exhibit the best overall Properties regardless of which heat treatment was used.

Figure 7 shows similar data as a function of chromium concentration in an Fe-16Mn base material. The 0 and 8% Cr data from previous work (Ref. 15) are included to indicate overall trends. The Increase in Cr concentration from 13 to 18% was found to decrease tensile ductility and to produce a marked increase in DBTT. Unfortunately, a comparison similar to this for alloys which had not experienced a cooling cycle to LN temperature is not possible since those data are not currently available for the lower chromium alloys. Some of the NIM program data will be useful in improving the confidence of the property trend curves shown.

The behavior of the ternary alloys was used to establish the basis for further alloy development. It was decided to use 16 and 20% Mn alloys containing either 13 or 18% Cr as base compositions. Alloying additions were then made to address particular aspects of the original program goals. Table V shows the alloy design scheme used for these materials. (Ref. 7) Table VI shows the nominal and actual chemistries for the alloys. Table VII lists the steps involved for the four heat treatments used to produce the Initial microstructures. Heat treatment A does not involve the LN exposure while for the remaining treatments the only difference was the austenltlzation temperature. Increasing the austenltization temperature resulted In an increase in grain size and, for the most part, austenltlzation temperatures of 900 or 1000C produced microstructures with the greatest Inherent fracture resistance. The tensile and Impact properties are shown in Tables VIII and IX. respectively. The tenslle properties of only those alloys of particular relevance to fusion applications are included In Table VIII.

The microstructural phase constituents, before and after tensile testing at RT or LN temperature, are listed in Table X. In several alloy compositions it was possible to decrease the athermal transformation temperatures on cooling to below 77K. Nitrogen and nitrogen plus silicon additions were found to produce fully austenitic structures. It is difficult to estimate the amount of epsilon initially present from the optical micrographs since it appears similar geometrically to twins. In both cases bands cross austenite grains providing slip barriers as discussed above. Figures 9-11 show the mlcrostructures typical for fully austenitic. duplex and triplex phase mixtures. In Fig. 9(a) the heavy fault densltles show how austenites with low stacking fault energies result in a mlcrostructurally complex network of intersecting and overlapping faults. The lnteractlons of the partial dislocations boundlng these faults durlng slip Increase the resistance to slip and contribute to the inherent toughness of the FCC phase. Fig. 9(b) shows an example where the fault overlapping process involved in the twinning and FCC to HCP transformation Is clearly indlcated. An overlap of faults is indicated when the fringe contrast changes. It was not possible to determine which process was Involved in any of the overlap examples shown; however, this sort of analysis was performed and is discussed In an earlier paper. (Ref. 9)

The network of intersecting faults, shown in Fig. 9(a), will develop into a network of Intersecting epsilon phase bands during plastic deformation. (Refs. 6.7 and 9) The phase distributions are more easily Illustrated In alloy systems where the respective M temperatures are high enough to achieve athermal reactions during heat Treatments. The heavy dislocation densltles obtained when deformation induced transformations are involved complicates the microscopy and the interpretation of the microstructures. AS a result. athermal transformation sequences and examples of athermal transformatlon products will be used to discuss the important features of the materials In this paper.

Figure 10(a) shows the Interface between heavily faulted austenite and an HCP band. Note the faulted nature of the epsilon martensite where partial dislocations can be readily observed within the band. Figure 10(b) shows the three phases in a location near an austenite grain boundary. The HCP band terminates at the grain boundary and contalns an alpha martensitic iense crossing the field of view. The alpha martensite lenses nucleate preferentially at the intersections of either HCP bands or those of HCP bands and stacking

faults. The atomic configuration at these intersections is complicated and the atomic geometrical configurations conducive to alpha martensite nucleation and the subsequent mechanism of growth have not been studied in detail. The sequential phase transformations delayed mechanical instabilty and necking by strengthening the region being heavily deformed.

The change in orientation across the FCC/HCP interface in conjunction with the crisscrossing network of fault bands produces a periodically dispersed three dimensional array of dislocation glide obstacles resulting in the high impact toughnesses and ductilities observed in these materials. Strain hardening by multiple dislocation interactions combines with that provided by strain-induced phase transformations to produce behavior akin to that observed in the TRIP steels developed in the 1960s. (Refs. 25-29) The TRIP steels have received relatively little further attention because of the complicated thermomechanical processing necessary to achieve the extraordinary properties displayed. The primary problem associated with complicated thermomechanical processing requirements is the Inability to reproduce the characteristic properties in the weld/heat-affected-zone at a joint. The weld Joints thus become the "weak link" In an otherwise exceptionally strong and tough structural material. The Fe-Mn-Cr system alloys do not require such complicated processing, but the yield strengths developed are not as high as those observed with TRIP steels. Room temperature yield and ultimate strengths of 300-400MPa and 900-1100MPa, respectively, with elongations of 60-80% were obtained for the most promising Fe-Mn-Cr base alloy systems. These strength values, combined with the high levels of Impact toughness and fracture resistance, may translate to improved fusion component performance.

Figs. 11(a) and (b) show further examples of the morphology of epsilon and alpha martensitic phases formed athermally. The diffraction analysis was performed to supplement other information regarding the orlentation relationships present between the three phases. (Ref. 7) A more complete transmission electron microscopy and diffraction analysis of phases and orientation relationships was included in the review paper. (Ref. 9) Fig. 11(c) shows a single example of the microstructures developed after tensile testing. This particular sample was tested to failure resuitlng in a heavy dislocation density throughout the microstructure. In the middle of the photograph some alpha lenses can be seen crossing a band of strain-induced epsllon martensite. Microstructures containing high dislocation densities with multiphase dispersions may be beneficial in delaying swelling in fusion components. Residual ductility levels could be controlled, at least in principle, by manipulating the thermomechanical processing of an alloy with excellent inherent toughness.

The presence of interstitial nitrogen or carbon was found to have a negative impact on low temperature ductility in those alloys where the strain-induced FCC to HCP transformation occurred. (Refs. 6 and 7) Note the impact toughness curves presented In Figure 12. As the concentration of interstitial element increased the upper shelf impact energies tended to decrease wlth a simultaneous Increase In DBTT. Much of this low temperature reduction in ductility is related to cleavage of the HCP bands (the lattice of which is stralned by the interstitial atoms). Good ductility. even at -196C, was retained for similar compositions which were free of interstitial additions. Figure 13 shows impact curves for the Fe-Mn-Cr-Si-C alloys. The reduction in low temperature toughness is again apparent. Figure 14 shows the tensile properties of the Fe-Mn-13Cr-Si-N alloys as a function of test temperature. The increase in slip resistance and decrease in ductlllty Is apparent at 77K. Reference 7 discusses these effects in greater detail.

Fig. 15 Illustrates how the fracture modes change depending on test temperature and alloy canposition. Note the transition to cleavage crack propagation mechanisms at decreased temperatures for alloys containing substantial concentratlons of interstitial atoms. In Fig. 15(b) the cleavage of adjacent epsilon bands resulted in the formation of the layerlike fracture surface morphology present in the upper portion of the photograph. Indlvidual cleaved bands of epsilon are shown to be separated by austenite which still displays ductlllty resultlng In the cusps between the flat layerlike regions. In Figs. 15(e) and (f) the transition to a predominantly cleavage crack growth mode with decreasing temperature is clearly shown. Any ferrite which is present in the microstructure will also cleave at low temperatures.

Fig. 16 shows several graphs illustrating the improvements in mechanical

properties obtained for the Fe-16Mn base material through alloylng. (Refs. 6.7 and 9) Increases in yield and ultimate strengths wlth marked increases in uniform ductility (note the increase in elongation) were achieved. The ductilities at -196C do decrease for alloy compositions containing nitrogen for the reasons discussed above. Note that the ternary alloy elongation was actually higher at -196C, the result of Increased straln-Induced phase transformation activity in the absence of embrittling Interstitial nitrogen.

Fig. 17 shows some tenslle data obtalned over a range of strain rates for the Fe-16Mn-13Cr-SI-C alloy. Elongation data are shown for AISI 304 stainless steel over the same range in strain rate. These limited data suggest that at least this composition, and likely many others, are less susceptible to reductions in ductility and toughness as a function of increased loading rates than the commercial stainless steel. These data were obtalned as part of a paper study (Ref. 34) conducted to explore the deslgn advantages of using the Fe-Mn-Cr base alloys in nuclear fuel shipping cask applicatlons. High strain rates, even beyond the range used In the evaluation, are pertinent to account for accldents. etc.. Hlgh strain rates can also occur during plasma instabilities in fusion systems. Impulse thermal loads generate hlgh straln rate stress Impulses and It wlll be Important to malntaln structural Integrity. The present data are not sufflclent to establish modes of behavlor at higher strain rates and thls would be an area of interest for future experimentation.

Fig. 18 shows a compllatlon of RT tensile data plotted against the respective alloy DBTT. (Ref. 7) The only purpose of these curves is to illustrate the very wide range of properties attalnable in alloys where no optimization of thermomechanlcal processing directed at fusion condltlons was considered. Comments specific to fuslon reactor applications will follow In a later section.

Corrosion Behavior of Fe-Mn-Cr Alloys

A series of corrosion experlments were performed In which the experimental alloys were compared wlth the behavlor exhiblted by AISI 347 stainless steel. Thls stabilized grade contalns nlobium to reduce the carbide precipitation at graln boundaries and resultant sensitlzatlon of the microstructure. The tests encompassed a range typically used to characterize and compare the corrosion resistance of austenitic stainless steels. (Ref. 6) The results of these tests are tabulated in table XXII. Fig. 19 shows these corrosion rate data plotted for visual comparison. The experimental alloys were found to be adequately corrosion reslstant over a range of testing environments and frequently displayed better corrosion resistance than the control material. Sensitlzatlon exposures dld not generally have a negatlve effect on the reslstance exhiblted. although in some cases there did appear to be some decrease in corrosion resistance. Interestingly, the 18 Cr alloys dld not seem to display significantly better corrosion resistance than 13 Cr alloys of simllar composltion. Thls is encouraging and system development can probably be concentrated on alloys wlth lower chromium concentrations. particularly since the current operating temperatures envisioned for the plasma chamber components are at moderate levels.

Fe-Mn-Cr Base Alloys for Fusion Reactor Structurai Applications

It would be useful, prior to closing. to discuss some of the features observed in Fe-Hn-Cr base alloy systems whlch warrant further development of thls class of materials for future fuslon reactor appllcatlons. Inltlally, it is important to realize that the Properties obtained and the data provided are for laboratory-generated heats of roughly 40-45 kllograms each. Some reduction in ductlllty would be expected If the materlals were produced commercially in larger amounta. Discussions were held several years ago wlth a representative at ESCO Steel Company In Portland. Oregon regarding the commercial vlabllity of melting large heats wlth compositions simllar to those Included in this Paper. (Ref. 35) The chemlstrles of the experimental alloys were not expected to cause significant problems during melting and casting. The energy absorptlon capacity of the alloys wlll influence the manner by whlch they are forged and formed Into product geometries. It was felt that these problems would be manageable given some experience base wlth which to work. Also, the effects of trace impurities have not been evaluated nor the effects of structural instabilities and preclpltatlon reactions during long term exposures. A complete program to address these issues must be conducted to ensure commercial feasibility of these materials.

The elevated temperature data being collected in the NIM program, on both unirradiated and irradiated materials, will help establish service limitations and ultimately be useful in guiding further optimization research. The longterm stability of these materials has not been systematically studied and documented. The effects of such exposures on phase stabilities and subsequent deformation characteristics would be an issue that should be addressed prior to service application. It has become clear from the preliminary elevated temperature data collected in the NIM program that precipitation of various phases will occur in certaln alloy chemistries. Signa and chi phases have been detected following elevated temperature exposures in the NIM program (Ref. 20) and signa phase was found to form in the Fe-20Mn-18Cr alloy previously studied. (Ref. 6) These intermetallic phases will cause embrittlement so the conditions under which they form must be well understood. Nonetheless, the low austenite stacking fault energies in these materials should increase the creep resistance by making cross slip more difficult in a manner slmllar to that observed in other austenitic stainless steels. (Ref. 36)

It will be important to define as exactly as possible the upper limit in acceptable nitrogen content, as well as other alloying elements, which will still result in a structure which can be surface buried. While detailed evaluation is still needed, preliminary estimates of the maximum concentration limits of pertinent elements for some of the alloys studied are shown below:

Element	weight %
Iron	100
Manganese	100
Chromium	100
Molybdenum	5×10^{-6} (5 ppm)
Nitrogen	50
Silicon	25
Carbon	100

These estimates for fusion materials were prepared (Ref. 22) based on data included in the Paper by Fetter. Cheng and Mann (Ref. 37) and are consistent with fusion interpretation of regulation 10CFR61 for low level waste disposal. There are also stringent limits on some Impurities (e.g., niobium and silver) where maximum allowable concentrations are about 1 ppm. These estimates show that the chemistries of the Fe-Mn-Cr, Fe-Mn-Cr-N. Fe-Mn-Cr-Si-N and Fe-Mn-Cr-Si-C alloys discussed above should produce materials whlch can be surface buried after service in fusion applications provided that impurity limitations are carefully controlled. This latter requirement would apply to any structural material considered for these applications. Other possible alloying elements and their respective allowable levels will influence both the initial phases present and the stabllitles/transformation characteristics during processing or deformation.

The large amounts of energy absorbed during tensile fracture, even at liquid nitrogen temperatures. are indicative of the extreme toughness of the microstructures. If an initial high toughness results in a relatively higher toughness after service, then the high initial ductility could be useful in reactor design for components expected to experience radiation embrittlement. It may be possible to obtain enhanced service lifetimes by delaying the time required to reach a critical level of residual ductility. The microstructures and phase mixtures can be controlled through the alloy chemistry and thermomechanical treatments with the additional benefit that deformatlon treatments can be used to obtain work hardening combined with specific phase morphologies. The heavily dislocated martensitic structure of the martensitic 12 Cr steels has demonstrated improved resistance to swelling (Refs. 38-40) as compared to ferritic steels. whereas the austenitic structure of the present PCA alloy has advantages related to initial ductility and fabricability. (Ref. 41) There is reason to expect that an optimized microstructure could be developed for the Fe-Mn-Cr alloys which would have the inherent benefits of both of these materials.

The synergistic effects of thermomechanical processins have not been extensively studied and documented. Tailoring the dislocation density and substructure with a phase morphology to accomodate the fusion plasma environment has interesting possibilities. The three phase distribution could be designed to provide ductility and toughness with inherent swelling resistance. Alloy design efforts for fusion applications should be directed at optimizing the

relative stabilities of the three phases and obtaining transformation characteristics to produce mechanical behavlor consistent with particular component design goals. Combinations of these varlables with additional alloylng elements to promote other Strengthening mechanisms, e.g., precipitation hardening, provides another avenue open to enhance fusion reactor performance. The preclpltatlon of a fine dispersion of tltanium carbides has been shown to enhance swelling reslstance in AISI 316 stainless steel. (Ref. 42)

Joining, and other fabrication-related Issues. related to these materials wlll be an important design Issue for the flrst wall and blanket structures. The air cooling heat treatment included In these experiments did not lead to the precipitation of deleterious phases in the majority of the promising formulations. This does not, of course, simulate a welding procedure; however. the observatlon certainly is encouraging.

KEY ISSUES FOR Fe-Mn-Cr ALLOY STRUCTURAL APPLICATIONS IN FUSION REACTORS

1. Phase stabllitles and transformation characteristics of Fe-Mn-Cr Alloys are likely to be affected by the neutron environment. The maintenance of adequate fracture reslstance depends on the strain-Induced phase transformatlon behavlor and heavlly faulted mlcrostructure that can be generated prior to service and durlng deformation in the event of an accident.
2. Optimlzation of initial mlcrostructure through the control of thermomechanical processing and alloy chemistry will ensure that the component initially has the maximum toughness and crack growth resistance. An understanding of how these properties decrease with neutron exposure is needed.
3. Studies should be initiated to investigate the inclusion of alloylng elements to promote additional strengthening mechanisms in the microstructures of Fe-Mn-Cr alloys and to evaluate the influence of the required chemistry adjustments on phase and microstructural stabilities.
Sliicon and *nltrogen* have been used effectively as alloying elements in Fe-Mn-Cr steels to manipulate Initial microstructural constituents and phase stabilities. Further attention should be focused on Fe-16Mn-13Cr base alloys containing these and other alloylng elements to further enhance properties.
4. A methodology must be developed to malntain and service the inner reactor chamber components and to perlodically test and examine structural components during operation to ensure adequate strength and toughness until a substantial database can be established. The transformatlon to the alpha phase can be detected uslng a magnemometer since this phase is ferromagnetic.
Development of a remote sensing apparatus for phase transformation detection would aid in the periodic evaluation of phase proportions present during service.
5. Fabrication issues particular to this class of high energy-absorbing materials must be evaluated. Joining is one key aspect which has not been addressed. As the NIM program matures and results are obtalned further deflnitlon of appropriate direction for such an evaluation should become apparent. Also, design concepts continue to fluctuate and may change substantially prior to actual reactor fabrication. The promise of improved structural materlals wlll alleviate at least some of the concern that designers must have regardlng the current status of materlals for these critical components.
6. Post-service disposal of these materials must be investigated in detail. Alloying elements and even impurities can impact neutron activation and affect disposal requirements. These considerations will have a strong effect on the choice of alloys for further development.

ACKNOWLEDGEMENTS

The authors appreciate the timely review, editorlal comments and technical input and discussion obtalned from Dr. K. Schultz of General Atomics.

REFERENCES

1. H.R. Brager. F.A. Garner, D.S. Gelles and M.L. Hamilton. J. Nucl. Mat., 133 and 134. 1965. p. 907.
2. F.A. Garner and H.R. Brager. in Radiation-Induced Changes in Microstructure, ASTM STP 955. Edited by F.A. Garner. N.H. Packan. and A.S. Kumar. American Society for Testing and Materials. Phlla., PA, 1986. P. 195.

3. R.L. Kleuh and E.E. Bloom, in Optimizing Materiala for Nuclear Applications, Edited by F.A. Garner, D.S. Gelles and F.W. Wiffen, The Metallurgical Society of AIME. Warrendale. PA, 1985. p. 73.
4. A.H. Bott. F.B. Pickerins and G.J. Butterworth. J. Nucl. Mat., 141-143, 1986, p. 294.
5. M. Snykers and E. Ruedl, J. Nucl. Mat., 103 and 104, 1981, p. 1075.
6. L.D. Thompson, " The Mechanical Properties and Microstructural Relationships in Iron-Manganese-Chromium Alloys." LBL-6234, M.S. Thesis. U. of California. Lawrence Berkeley Laboratory. Berkeley, CA. Jan. 1977.
7. L.D. Thompson, "An Investigation of New Nickel-Free Austenitic Stainless Steels." Ph.D. Thesis, U. of Callfornla. Lawrence Berkeley Laboratory, Berkeley, CA. May 1978.
8. R.L. Klueh and P.J. Mazlasz, ADIP Semiann, Pro. Report, DOE/ER-0313/2, March 1987. USDOE Office of Fusion Energy. P. 173.
9. L.D. Thompson, "The FCC to HCP to BCC Phase Transformation Sequence in Metastable Fe-Mn-Cr Alloys." In Mechanical Properties and Phase Transformations in Engineering Materials. Proceedings of Earl R. Parker Symposium on Structure Property Relationships. AIME Winter Annual Meeting, New Orleans. LA, March, 1986, p. 391.
10. L.D. Thompson, "New Nickel-Free Stainless Steels for AISI 300 Series Stainless Applications," presented at the 1976 Westec Technology Conference, Los Angeles, CA, Oct., 1976.
11. L.D. Thompson, V.F. Zackay and E.R. Parker, "An Investigation of New Fe-Mn-Cr Alloys." ASME Winter Annual Meeting. Chicago, IL, Feb., 1976.
12. G.T. Haddick. L.D. Thompson, V.F. Zackay and E.R. Parker, "The Development of Nickel-Free Austenitic Stainless Steels for Ambient and Cryogenic Applications," presented at the ASM/OTA/FMS Conference: Availabllity. Energy and Environmental Factors, Chi., Il, Sept.. 1977.
13. G.T. Haddick. L.D. Thompson, V.F. Zackay and E.R. Parker, "The Development of Nickel Free Austenitic Stainless Steels for Ambient and Cryogenic Applications," DOE Report LBL-7397, Feb. 1978.
14. G.T. Haddick, L.D. Thompson, V.F. Zackay and E.R. Parker, " New Nickel-Free Austenitlc Stainlesses for Ambient and Cryogenic Service," Metal Progress, Nov., 1978.
15. M.J. Schanfeln, "The Cryogenic Properties of Fe-Mn and Fe-Mn-Cr Alloys." LBL-2749, M.S. thesis. U. of California, Berkeley. CA. Aug.. 1974.
16. M.J. Schanfein, M.J. Yokota, V.F. Zackay, E.R. Parker and J.W. Morris, Jr., "The Cryogenic Properties of Fe-Mn and Fe-Mn-Cr Alloys." DOE Report LBL-2764, May, 1974. presented at the ASTM Symposium on Properties of Materials for Liquid Natural Gas Tankage, Boston, MA, 1974.
17. D.G. Atteridge, "An Investigation of the Structure and Properties of Iron-Manganese-Carbon Alloys," LBL-3574. D. Eng. thesis, U. of California. Berkeley, CA. May. 1975.
18. G.T. Haddick. "Optimization of Strength and Ductility in Fe-Mn TRIP Steels." LBL-3986, M.S. thesis, U. of California, Berkeley. CA, June, 1976.
19. H. Schnelder, Foundary Trade Journal. 108, 1960, pp. 563-564.
20. J.M. McCarthy and F.A. Garner, ADIP Semiann. Pro. Report, DOE/ER-0313/3, Sept.. 1987. pp.115-122.
21. H.H. Uhlig, Corrosion and Corrosion Control, Second Edition. John Wiley a Sons. NY.NY. 1971.
22. K. Schuitz, General Atomics. private communication, 1989.
23. V.H. Schumann. Arch. Eisenh.. 38, Aug. 1967. pp. 647-656.
24. A. Holden, J.D. Bolten and E.R. Petty, "Structure and Properties of Iron-Manganese Alloys," JISI. 1971. pp. 721-728.
25. V. F. Zackay. E.R. Parker, D. Fahr and R. Busch. ASM Trans. Quart., 60, 2, 1967. pp. 252-259.
26. D. Bhandarkar. V.F. Zackay and E.R. Parker, DOE Report LBL-2775. August, 1974.
27. E.R. Parker and V.F. Zackay, "Strong and Ductile Steels," Scl. Am., 219, 1968, pp. 36-45.
28. W.W. Gerberich, P.L. Hemmings and V.F. Zackay, Met. Trans., 2, 1971, pp. 2243-2253.
29. D. Fahr. Met. Trans., 2, 1971, pp. 1883-1892.
30. J.P. Hirthe and J. Lothe, Theory of Dislocations, McGraw-Hill, NY,NY, 1968. pp. 228-233.
31. J. Friedel, Dislocations, Addlson-Wesley. 1967. pp. 134-145.
32. Source Book on Stainless Steels American Society for Metals. Metals Park. Ohio, 1976. pp. 1-25.
33. R.M. Brick, R.B. Gordon and A. Phillips, Structure and Properties of Alloys. Third Edition. McGraw-Hill Book Co.. 1965. pp. 339-358.
34. V. Armbrust, Senior Project Design Stud;.: "Applicatlon of Fe-Mn-Cr TRIP

Steel in the Design of an Improved Nuclear Shipping Cask," San Diego State University, San Diego, California. 92182-0191, May. 1983.
35. L. Venne. former technical director, ESCO Steel Co.. Portland, OR, private communication, 1985.
36. R.W. Hertzberg, Deformation and Fracture of Engineering Materials, Second Edition, John Wiley & Sons. NY. NY, 1983, p. 81.
37. S. Fetter, E.T. Cheng and F.M. Mann. "Long-Term Radioactivity in Fusion Reactors," Fuslon Engineering and Design. 6, 1988. pp. 123-130.
38. D.S. Gelles and R.J. Pulgh, "Effects of Radiation on Materials." in ASTM STP-870, ASTM. Phila., PA, 1985. p.19.
39. G. Ayrault. J. Nuci. Mat., 114, 1983. p. 34.
40. P.J. Mazlasz, R.L. Klueh and J.M. Vitek. J. Nucl. Mat., 141-143, 1986. p. 929.
41. R.E. Gold, E.E. Bloom. F.W. Clinard, Jr.. F.W. Smith, D.L. Stevenson and W.G. Wolfer. "Materials Technology for Fusion: Current Status and Future Requirements.' Nuclear Technology/Fusion], 1981. pp. 169-237.
42. P.J. Maziasz, J. Nucl. Mat., 122 and 123. 1984, p. 514.

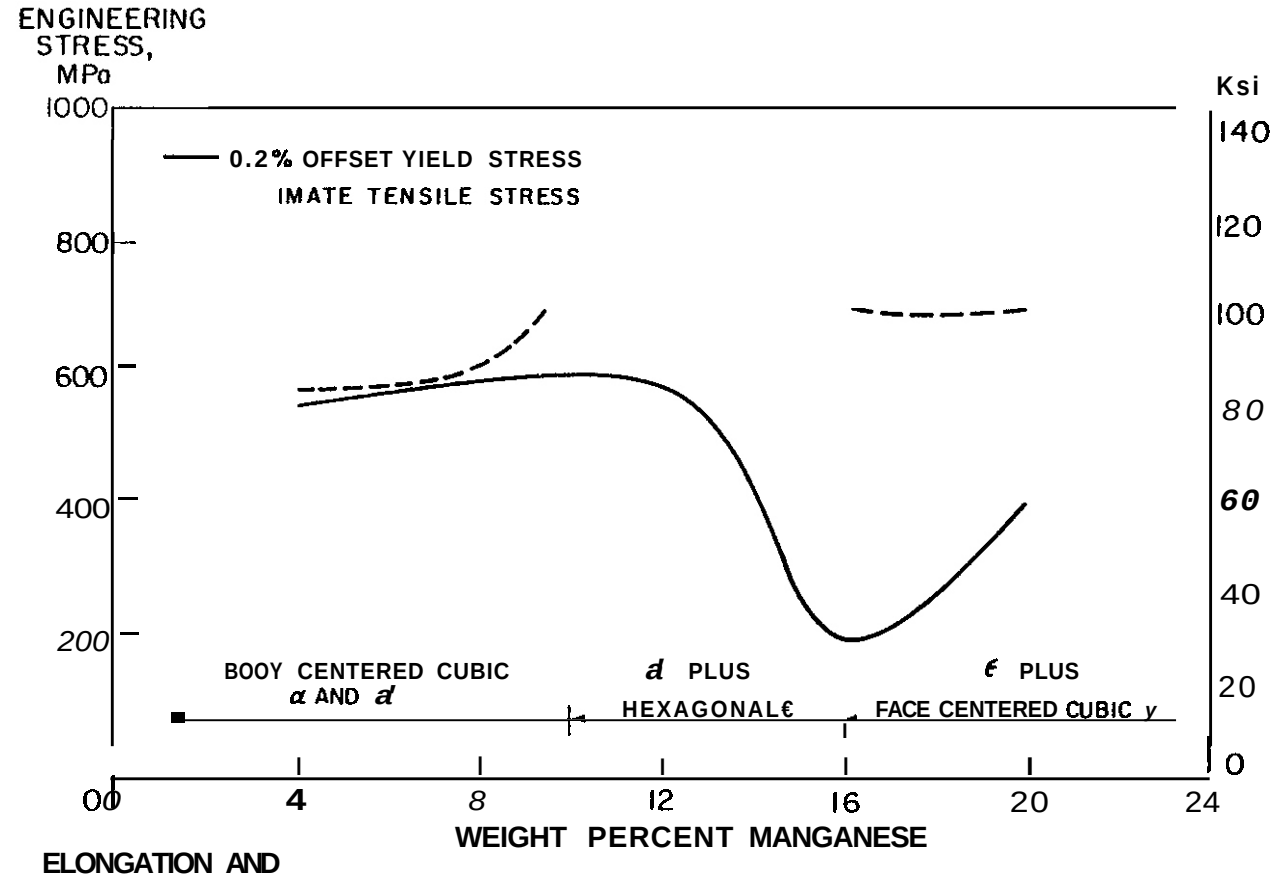

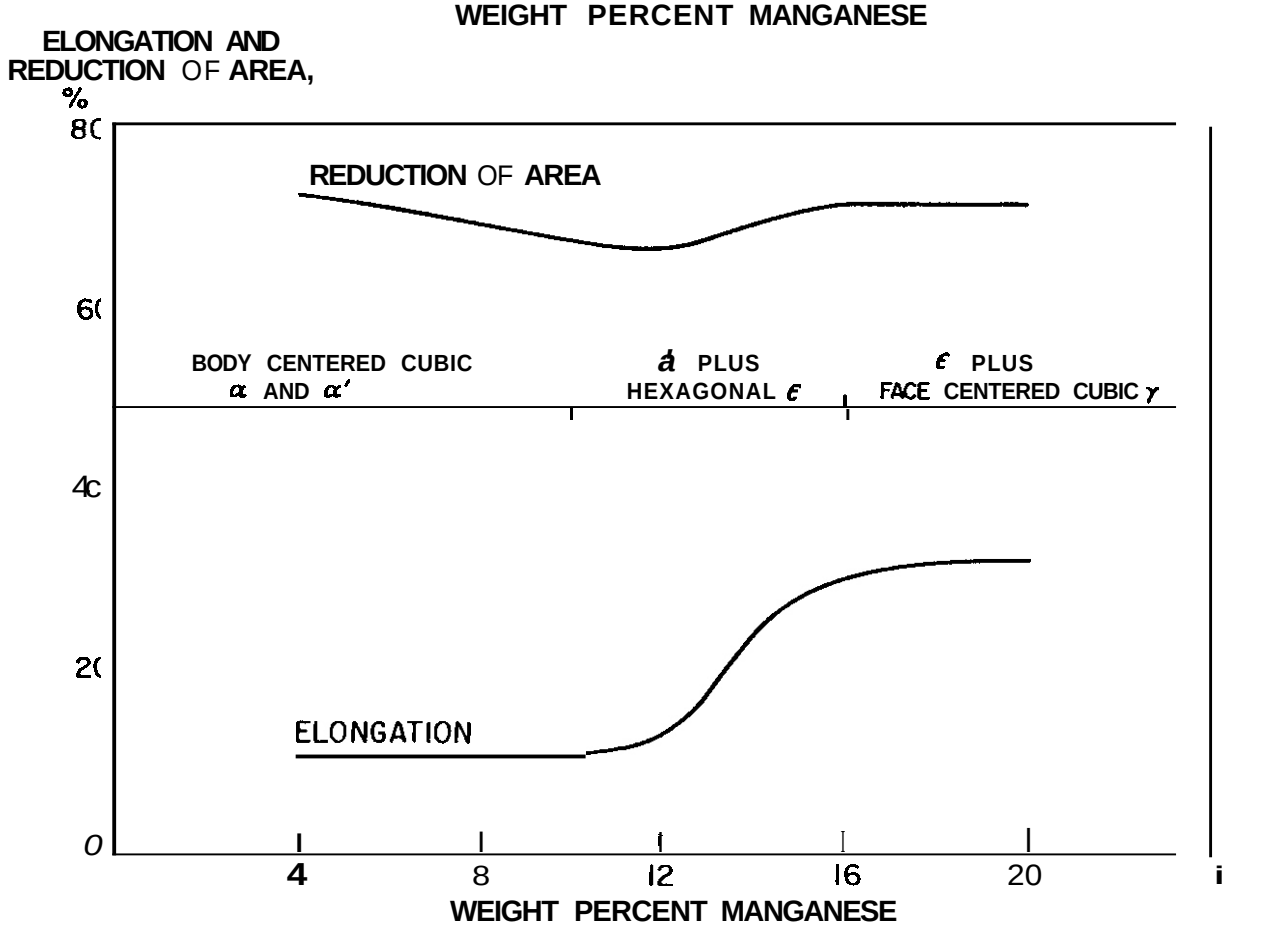

Fig. 1. Changes In Microstructure and Room Temperature Tenslle Propertlea of Iron as a Functlon of Increasing Manganese Concentration. (Ref. 15)

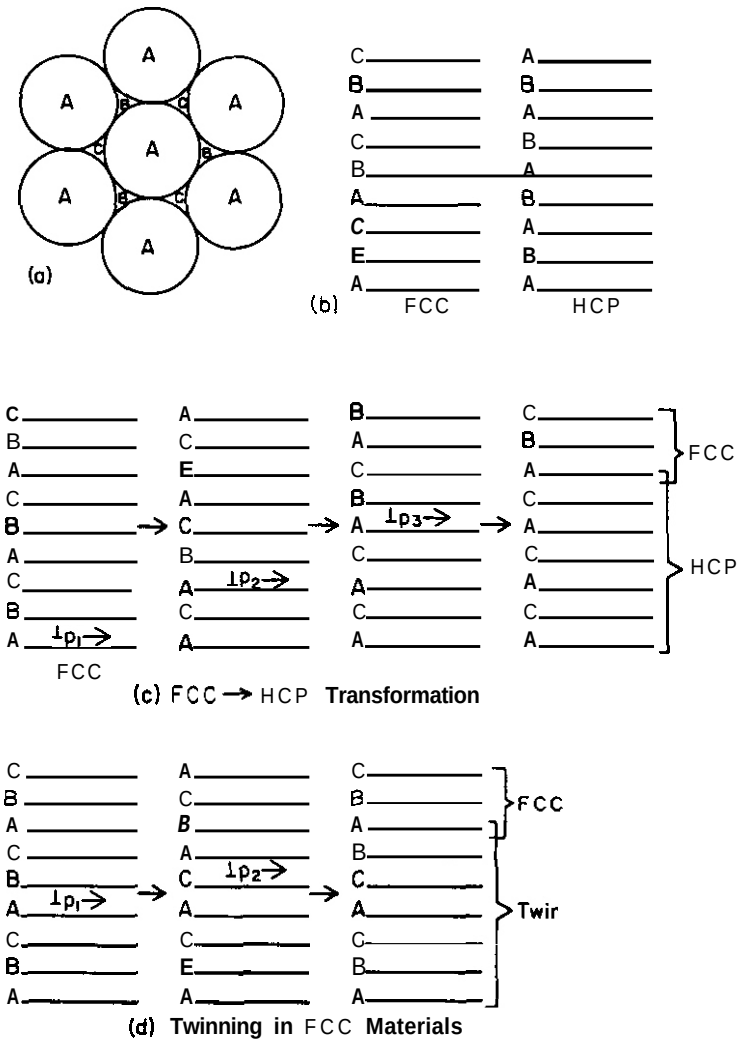

Fig. 2. An Appropriate Model to Illustrate Similarities Between Twinning and FCC to HCP Transformation in Low Stacking Fault Energy Austenite. (Ref. 9)

Table I. Phase Transformation Temperatures for FCC/HCP Transformations in Fe-Mn-Cr Ternary Alloys as Determined by Dilatometry. (Ref. 6)

Alloy Designation	On Heating	On Cooling
14Mn-13Cr	ε → γ @ 150 °C	γ → ε @ 140 °C
14Mn-18Cr	ε → γ @ 145 °C	γ → ε @ 60 °C
16Mn-13Cr	ε → γ @ 170 °C	γ → ε @ 100 °C
16Mn-18Cr	ε → γ @ 170 °C	γ → ε @ 55 °C
18Mn-13Cr	ε → γ @ 165 °C	γ → ε @ 100 °C
18Mn-18Cr	ε → γ @ 160 °C	γ → ε @ 85 °C
20Mn-13Cr	ε → γ @ 150 °C	γ → ε @ 80 °C
20Mn-18Cr	No phase transitions observed	

Table 11. Phases Observed Using X-Ray Diffraction Before and After Tensile Testing of Fe-Mn-Cr Ternary Alloys. (Ref. 6)

Alloy Designation	Heat Treatment	All Heat Treated			After Tensile Testing at 23 °C			After Tensile Testing at -196 °C		
		γ	ε	α	γ	ε	α	γ		α
14Mn-13Cr	B	24	22	54	0	0	100	0	0	100
14Mn-18Cr	B	16	5	79	0	5	95	0	3	91
16Mn-13Cr	A	31	33	36	8	40	52	4	42	54
16Mn-13Cr	0	18	33	49	6	43	51	-		
16Mn-18Cr	A	22	46	32	12	24	64	7	26	67
16Mn-18Cr	B	21	33	46	10	20	70	-		
18Mn-13Cr	A	47	46	7	16	33	51	9	24	67
18Mn-13Cr	B	51	39	10	7	28	65	5	26	69
18Mn-18Cr	B	18	30	52	5	19	76	4	13	83
20Mn-13Cr	A	23	60	17	14	60	26	13	61	26
20Mn-13Cr	B	37	48	15	26	51	23	-		

Table III. Rockwell "C" Hardness and Heat Treatments of Experimental Alloys (Ref. 7)

Alloy	Cettered[4]	+N	+Mo	+Mo+N	+Si+N	+Si+C
16Mn-13Cr	(A)6.6 (8)23.0	(A)8.2 (C)11.0	(D)6.0	(B)15.3 (D)8.7	(A)15.2 (C)15.5	(C)13.2
16Mn-18Cr	(A)11.4 (B)11.0	(C)7.5	(D)6.5	(8)15.8 (D)10.0	(C)14.0	(C)15.5
20Mn-13Cr	(A)19.4 (8)18.0	(C)13.0	(D)7.5	(D)17.2	(A)10.5 (C)6.0	(C)12.7
20Mn-18Cr	(A)42.8 (8)45.0	(C)9.8	-	(D)28.5	(C)10.3	-

Note: letters adjacent to hardness values are indicative of the heat treatment.

Table IV. Tenslle and Charpy V-Notch Impact Propertles of Fe-Hn-Cr Ternary Alloys. (Ref. 6)

Alloy Designation	Heat Treatment	Testing Temperature (°C)	Y.S. (KSI)	Y.S. (MPa)	U.T.S. (KSI)	U.T.S. (MPa)	Elongation (%)	Reduction In area (%)	Strain hardening exponent. n	Energy Absorbed (ft-lb)	Energy Absorbed (joules)
14Mn-13Cr	E	23	53.3	360	116.8	805	32	66	0.132	104	141
		-78	63.4	437	148.9	1027	30	71	0.183	156	212
		-196	75.6	521	196.1	1352	31	62	0.115	215	292
14Mn-18Cr	8	23	46.1	310	86.6	597	31	70	0.130	85	115
		-78	56.1	387	108.2	746	27	64	0.134	107	145
		-196	77.5	534	124.0	855	3	3	0.036	18	24
16Mn-13Cr	B	23	55.9	385	117.0	807	27	62	0.096	88	119
	A	23	44.9	310	100.2	691	43	EO	0.238	149	202
		-78	43.1	297	125.5	865	42	69	0.229	162	220
		-196	45.6	314	161.4	1113	53	67	0.264	250	339
16Mn-18Cr	B	23	56.4	389	89.4	616	35	68	0.174	102	138
	A	23	52.9	365	89.2	615	33	69	0.179	103	140
		-78	54.3	374	107.0	718	37	74	0.220	146	198
		-196	65.5	452	120.3	829	7	E	0.062	36	49
18Mn-13Cr	E	21	45.0	310	92.4	637	52	82	0.283	160	217
		-78	39.0	269	113.9	185	53	82	0.259	198	269
		-196	43.4	299	163.1	1126	50	70	0.305	250	340
	A	23	41.7	301	92.1	635	58	82	0.326	176	238
		-78	48.2	332	114.6	790	57	81	0.341	212	287
		-196	53.4	368	161.2	IIII	60	71	0.360	270	366
18Mn-18Cr	8	23	61.2	422	84.3	581	39	65	0.186	113	153
		-78	70.0	483	106.0	731	38	69	0.224	152	206
		-196	87.8	605	131.3	905	11	11	0.102	57	77
20Mn-13Cr	B	23	58.3	402	97.0	669	42	91	0.233	117	159
	A	23	65.6	452	98.7	681	36	69	0.228	139	188
		-78	66.0	455	116.9	806	35	70	0.286	197	267
		-196	70.7	543	164.2	1132	34	34	0.318	265	359
20Mn-18Cr	8	23	93.0	641	123.0	848	5	4	0.049	38	52
	A	23	122.2	843	146.4	1009	4	4	0.023	25	34

Alloy Designation	Heat Treatment	Impact Energy at 23°C (ft-lb)	Impact Energy at 23°C (joules)	DBTT* (°C)	Impact Energy at -196°C (ft-lb)	Impact Energy at -196°C (joules)
14Mn-13Cr	E	130	176	-113	56	76
14Mn-18Cr	8	115	156	-15	4	5
16Mn-13Cr	E	88	119	-148	14	19
	A	140	190	<-196(=-220)	85	115
16Mn-18Cr	B	108	146	-56	4	5
	A	148	201	-40	8	11
18Mn-13Cr	0	168	228	<-196(-230)	112	152
	A	168	228	<-196(-245)	122	165
18Mn-18Cr	8	130	176	-48	4	5
20Mn-13Cr	E	28	38	-0-	28	38
	A	32	43	-0-	32	43
20Mn-18Cr	B	4	5	-0-	4	5
	A	4	5	-0-	4	5

DBTT = that temperature at which the Charpy absorbed was equal to one-half the value of the Charpy v-notch energy at mom temperature.

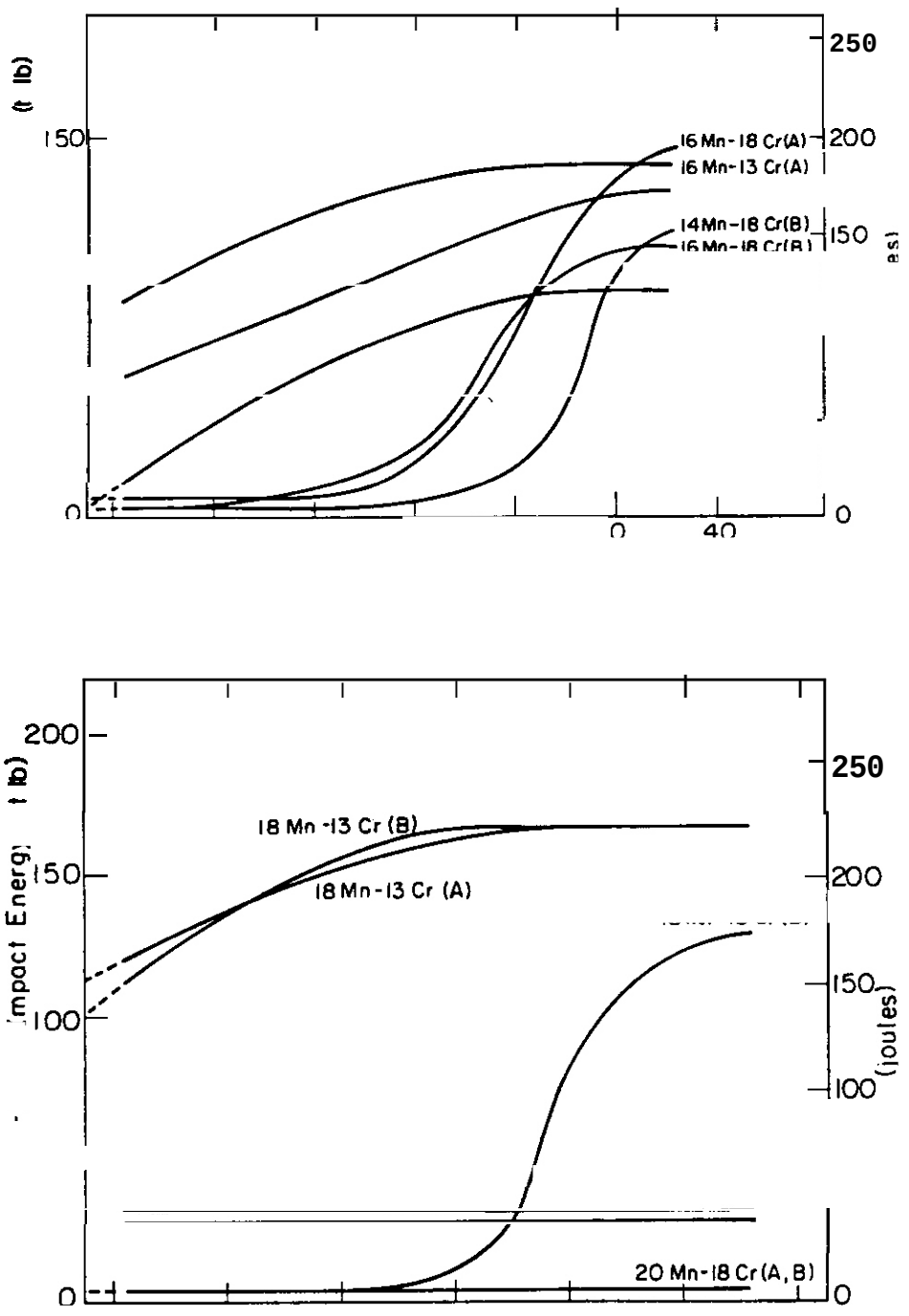

Fig. 3. Charpy V-Notch Impact Energy Curves for Fe-Mn-Cr Ternary Alloys. (Ref. 6)

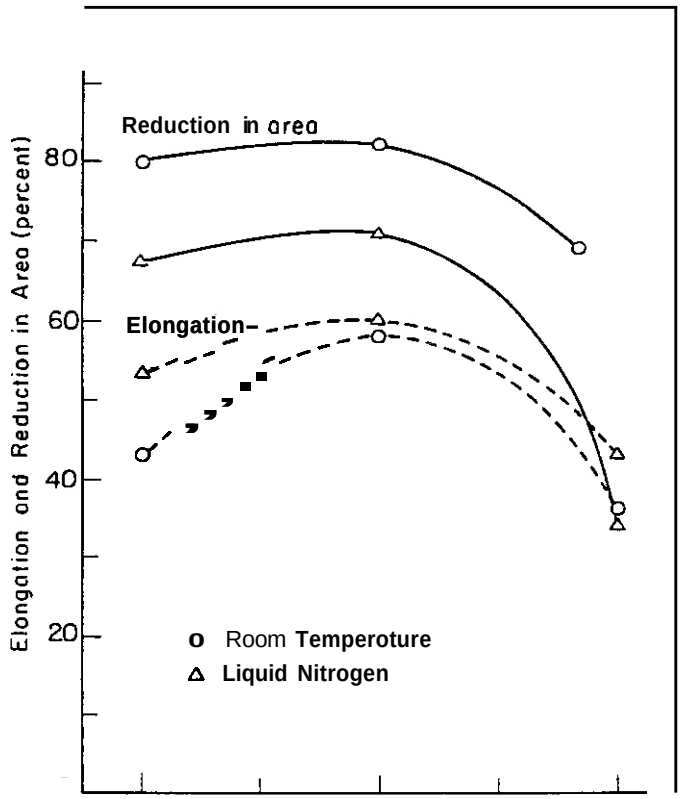
Reduction in area
Elongation
Elongation and Reduction in Area (percent)
80
60
40
20
o Room Temperoture
Δ Liquid Nitrogen

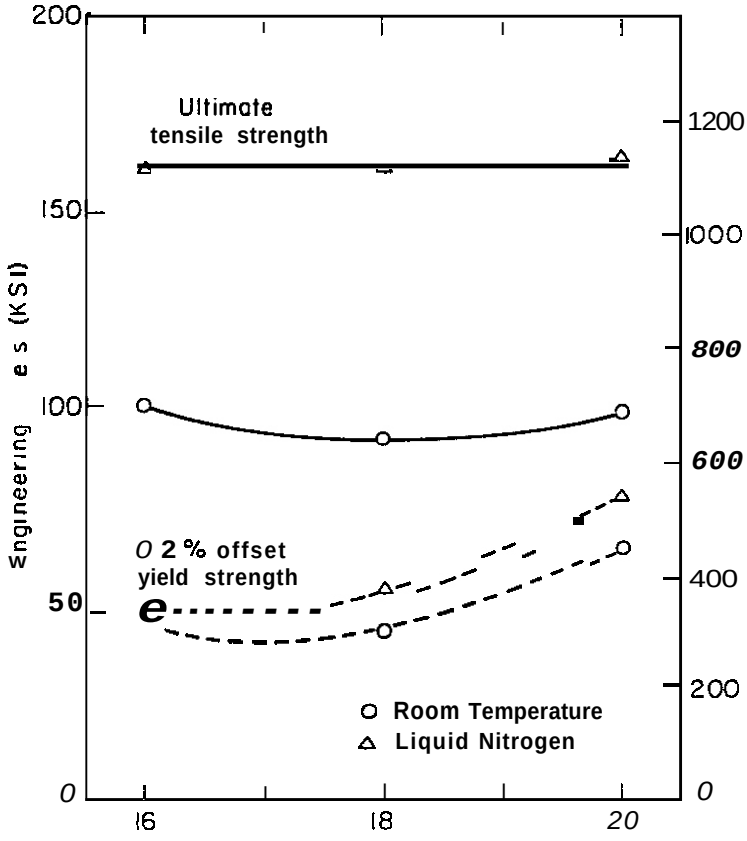
Ultimate
tensile strength
0 2 % offset
yield strength
Engineering e s (KSI)
200
150
100
50
0
1200
1000
800
600
400
200
0
16
18
20
o Room Temperature
Δ Liquid Nitrogen

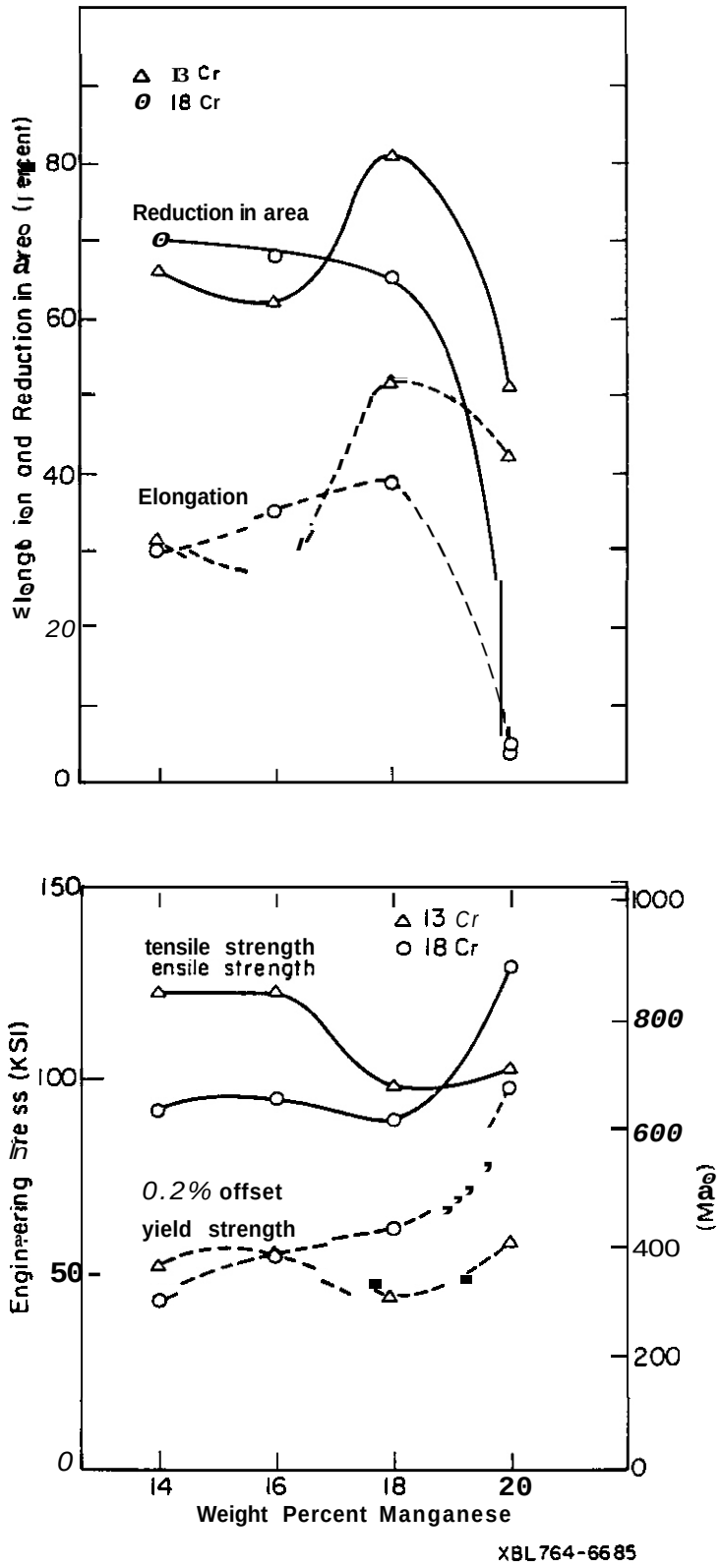

Fig. 5. Tenslle Properties of Fe-Mn-Cr(B) Alloys as a Functlon of Manganese Concentration. (Ref. 6)

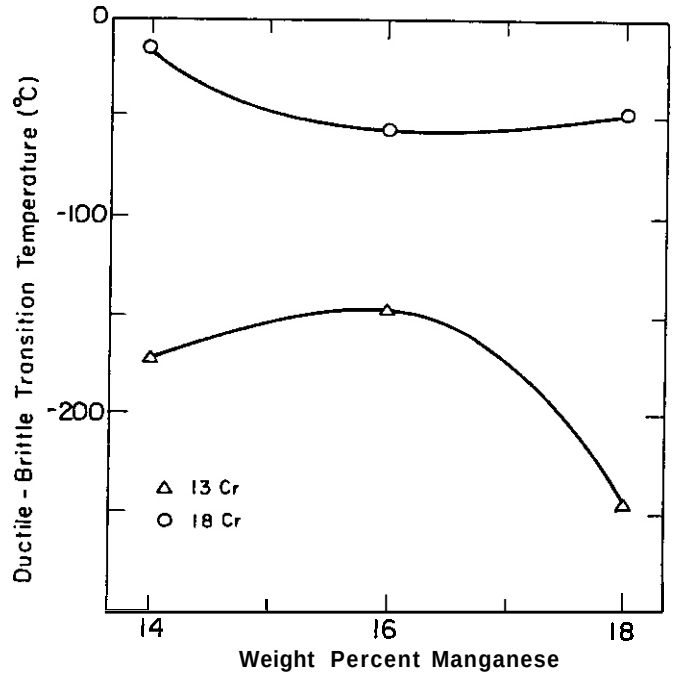

Fig. 6. DBTT of Fe-Mn-Cr(B) Alloys as a Function of Manganese Concentration. (Ref. 6)

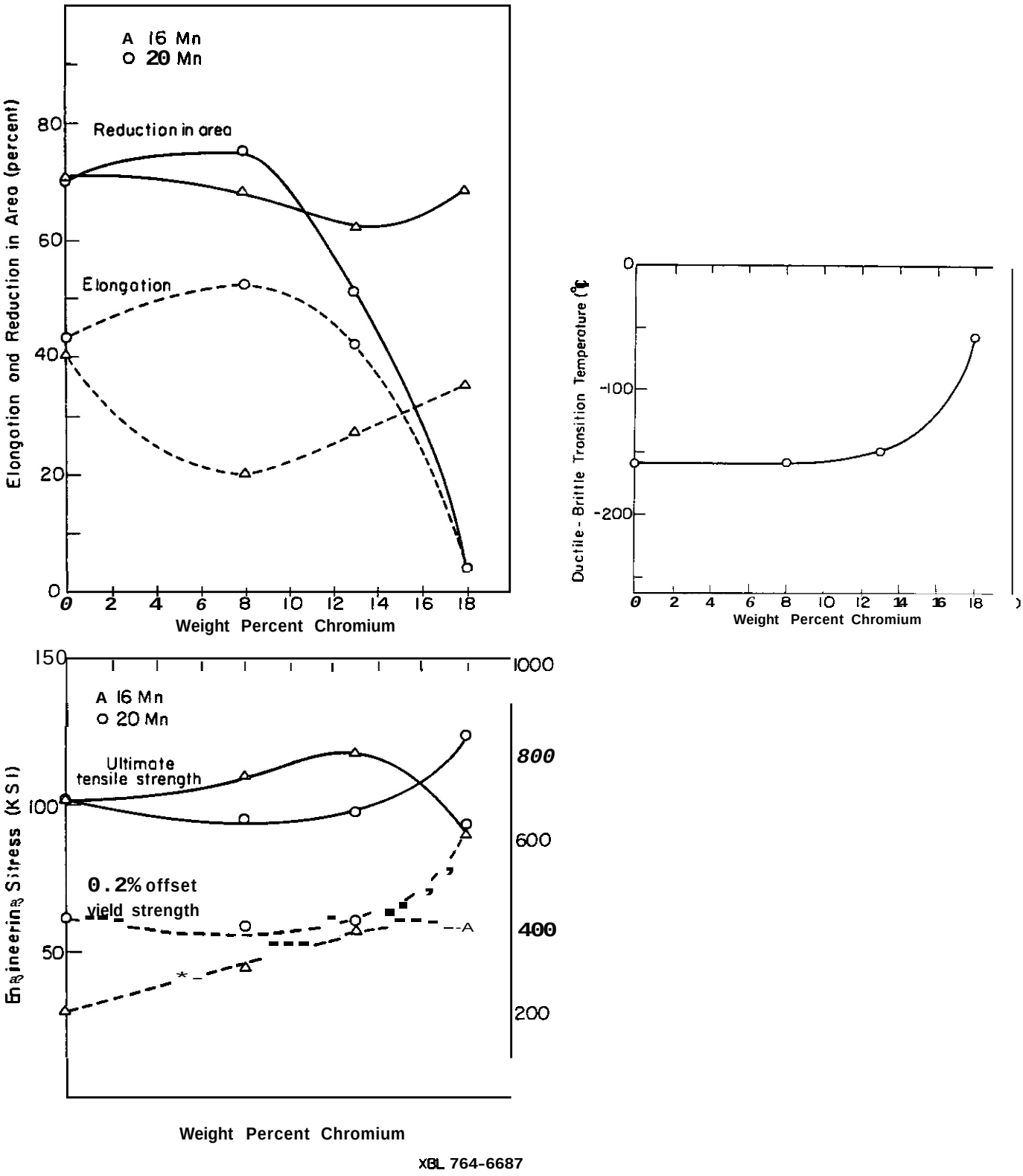

Fig. 7. Effects of Chromium Concentration on Tenalle Propertlea of Fe-16/20Mn(B) Alloys and on Charpy Impact DBTT of Fe-16Mn(B) Alloys. (Ref. 6)

Table 7 Alloy Design Scheme (Ref. 7)

Base Systems	Alloying Additions				
Base 1 16Mn-13Cr	Base 1 + N	Base 1 + Mo	Base 1 + (N + Mo)	Base 1 + (N + Si)	Base 1 + (C + Si)
Base 2 16Mn-18Cr	Base 2 + N	Base 2 + Mo	Base 2 + (N + Mo)	Base 2 + (N + Si)	Base 2 + (C + Si)
Base 3 20Mn-13Cr	Base 3 + N	Base 3 + Mo	Base 3 + (N + Mo)	Base 3 + (N + Si)	Base 3 + (C + Si)
Base 4 20Mn-18Cr	Base 4 + N	-	Base 4 + (N + Mo)	Base 4 + (N + Si)	-

Table VI. Fe-Mn-Cr Base Alloy Designations and Compositions, (wt. %) (Ref. 7)

Alloy Designation	Fe	Mn	Cr	N	C	Mo	Si
N Series							
16Mn-13Cr-0.1N	bal	15.91	12.94	0.134	-	-	-
16Mn-18Cr-0.1N	bal	15.86	17.95	0.130	-	-	-
20Mn-13Cr-0.2N	bal	19.92	12.98	0.259	-	-	-
20Mn-18Cr-0.2N	bal	19.72	17.96	0.195	-	-	-
Mo Series							
16Mn-13Cr-2Mo	bal	15.82	12.81	-	-	1.99	-
16Mn-18Cr-2Mo	bal	15.96	17.93	-	-	2.02	-
20Mn-13Cr-2Mo	bal	19.75	12.92	-	-	2.00	-
N+Mo Series							
16Mn-13Cr-0.2N-2Mo	bal	15.81	12.88	0.204	-	1.98	-
16Mn-18Cr-0.2N-2Mo	bal	15.87	17.79	0.180	-	1.99	-
20Mn-13Cr-0.2N-2Mo	bal	19.98	12.98	0.162	-	2.01	-
20Mn-18Cr-0.2N-2Mo	bal	19.91	17.99	0.179	-	2.00	-
N+Si Series							
16Mn-13Cr-0.2N-1.5Si	bal	15.91	13.01	0.227	-	-	1.22
16Mn-18Cr-0.2N-1.5Si	bal	15.93	17.95	0.216	-	-	1.40
20Mn-13Cr-0.1N-1.5Si	bal	19.81	12.94	0.130	-	-	1.42
20Mn-18Cr-0.1N-1.5Si	bal	19.71	17.81	0.130	-	-	1.42
Si+C Series							
16Mn-13Cr-0.2C-1.5Si	bal	15.90	12.93	-	0.20	-	1.44
16Mn-18Cr-0.2C-1.5Si	bal	15.91	17.91	-	0.20	-	1.42
20Mn-13Cr-0.2C-1.5Si	bal	19.84	12.99	-	0.22	-	1.46

Table VII. Heat Treatment Sequences Used With Fe-Mn-Cr Experimental Alloys. (Ref. 7)

Ingots → Homogenized (1200 °C for 24 hours) → Upset and Cross Forged → Heat Treatment

(A) 900 °C (2 hr) → air cooled to R.T.

(B) 900 °C (2 hr) → ice brine quenched → liquid nitrogen refrigeration → air warm to R.T.

(C) 1000 °C (2 hr) → ice brine quenched → liquid nitrogen refrigeration → air warm to R.T.

(D) 1200 °C (2 hr) → ice brine quenched → liquid nitrogen refrigeration → air warm to R.T.

Note: Ice brine quench (10% salt solution)

Table VIII. Tenslle Properties of Pe-Mn-Cr Base Alloys. (Ref. 7)

Alloy Designation	Heat Treatment	Testing Temperature (°C)	Y.S. (KSI)	Y.S. (MPa)	U.T.S. (KSI)	U.T.S. (MPa)	Elongation (%)	Reduction in area (%)	Strain Hardening Exponent, n	Energy Absorbed (ft-lbs)	Energy Absorbed (joules)
16Mn-13Cr-0.134N	C	21	46.6	321	121.7	839	67	70	0.416	269	365
		-78	49.1	340	149.8	1033	66	67	0.368	282	382
		-196	76.6	528	143.2	987	16	16	0.124	57	77
	A	23	45.7	315	121.2	836	68	77	0.431	263	351
		-78	48.7	336	148.8	1026	69	71	0.400	276	374
		-196	93.8	647	152.0	1048	20	18	0.176	115	156
16Mn-18Cr-0.130N	C	23	54.7	377	112.4	77s	74	68	0.462	291	395
		-78	79.6	549	148.5	1024	70	68	0.479	370	507
		-196	140.1	967	200.5	1382	21	22	0.209	190	258
20Mn-13Cr-0.259N	C	23	51.7	370	105.1	725	69	76	0.452	256	347
		-78	65.5	452	135.7	936	60	62	0.488	284	384
		-196	107.5	741	153.0	1055	20	20	0.180	128	174
20Mn-18Cr-0.195N	C	23	58.5	403	99.2	686	66	67	0.368	233	316
		-78	81.4	561	129.0	895	50	69	0.408	313	424
		-196	138.9	958	490.0	1310	30	29	0.259	245	332
16Mn-13Cr-0.227N-1.5Si	C	23	60.6	418	126.3	857	76	76	0.481	331	449
		-78	69.7	481	160.3	1105	71	70	0.442	354	480
		-196	121.3	836	169.9	1171	15	15	0.157	94	127
	A	23	63.3	436	124.9	861	77	78	0.476	318	445
		-78	71.2	491	166.2	1146	70	71	0.443	361	490
		-196	142.7	984	182.5	1258	17	17	0.136	107	145
16Mn-18Cr-0.216N-1.5Si	C	21	65.0	448	110.8	164	64	64	0.390	259	351
		-78	93.0	641	153.9	1061	63	62	0.440	367	498
		-196	144.4	996	183.9	1268	8	9	0.074	74	100
20Mn-13Cr-0.130N-1.5Si	C	23	45.4	313	105.6	728	77	79	0.481	280	380
		-18	47.8	330	132.8	916	71	77	0.486	348	472
		-196	81.7	563	160.6	1107	27	28	0.212	150	203
	A	23	49.8	343	108.6	749	72	79	0.442	260	353
		-78	50.4	348	138.5	955	73	76	0.481	369	500
		-196	98.1	676	180.5	1245	47	49	0.226	239	324
20Mn-18Cr-0.130N-1.5Si	C	23	61.6	425	96.7	667	60	78	0.338	208	282
		-18	83.9	578	124.3	857	52	70	0.314	247	335
		-196	132.6	914	175.1	1207	20	18	0.196	158	214
16Mn-13Cr-0.2C-1.5Si	C	23	48.3	331	161.6	1114	65	67	0.501	371	503
		-78	51.4	354	184.5	1272	54	52	0.392	368	499
		-196	61.4	423	136.2	939	11	12	0.108	69	93
16Mn-18Cr-0.2C-1.5Si	C	23	59.2	408	122.4	844	59	60	0.421	265	359
		-78	61.6	425	155.4	1071	51	51	0.365	350	474
		-196	89.6	618	139.6	963	8	7	0.079	45	61
20Mn-13Cr-0.2C-1.5Si	C	23	47.7	329	125.3	864	64	65	0.442	287	389
		-78	45.9	310	157.6	1087	12	72	0.505	444	602
		-196	69.11	476	171.8	1185	21	21	0.222	153	207

Table IX. Charpy Impact Toughness Data for Fe-Mn-Cr Base Alloys. (Ref. 7)

Alloy	Heat Treatment	Upper Shelf Energy (ft-lb)	DBTT* (°C)	Impact Energy at -196 °C (ft-lb)
16Mn-13Cr-0.134N	A	184	-166	30
16Mn-13Cr-0.134N	C	145	-174	8
16Mn-18Cr-0.130N	C	122	-159	26
20Mn-13Cr-0.259N	C	108	-150	30
20Mn-18Cr-0.195N	C	106	-138	10
16Mn-13Cr-0.204N-2.0Mo	B	158	-104	16
16Mn-13Cr-0.204N-2.0Mo	D	184	-144	14
16Mn-18Cr-0.180N-2.0Mo	B	42	-130	14
16Mn-18Cr-0.180N-2.0Mo	D	177	-168	48
20Mn-13Cr-0.162N-2.0Mo	D	60	+6	3
20Mn-18Cr-0.179N-2.0Mo	D	67	-3	3
16Mn-13Cr-0.10Al-0.15Ti-2.0Mo	D	134	-8	2
16Mn-18Cr-0.10Al-0.15Ti-2.0Mo	D	63	-4	2
20Mn-13Cr-0.10Al-0.15Ti-2.0Mo	D	113	-7	2
16Mn-13Cr-0.10Al-0.2C-1.5Si	C	135	-78	18
16Mn-18Cr-0.10Al-0.2C-1.5Si	C	52	-90	12
20Mn-13Cr-0.10Al-0.2C-1.5Si	C	127	-130	40
16Mn-13Cr-0.227N-1.5Si	A	165	-118	10
16Mn-13Cr-0.227N-1.5Si	C	165	-162	10
16Mn-18Cr-0.216N-1.5Si	C	154	-78	15
20Mn-13Cr-0.130N-1.5Si	A	194	-184	74
20Mn-13Cr-0.130N-1.5Si	C	210	-194	80
20Mn-18Cr-0.130N-1.5Si	C	180	-86	8

*DBTT = that temperature at which the energy absorbed in the Charpy V-Notch impact test was equal to half the upper shelf value.

Table X. Phases Detected Using X-Ray Diffraction In Fe-Mn-Cr Base Alloys. (Ref. 7)

Alloy	Before Tensile Testing			After Tensile Testing at 23 °C			After Tensile Testing at -196 °C		
	γ	ε	α	γ	ε	α	γ	ε	α
16Mn-13Cr-0.134N(A)	83	17	0	52	40	8	26	55	19
16Mn-13Cr-0.134N(C)	50	46	4	40	48	12	31	43	26
16Mn-18Cr-0.130N(C)	58	6	36	40	22	38	36	20	44
20Mn-13Cr-0.259N(C)	98	2	0	63	32	5	46	37	17
20Mn-18Cr-0.195N(C)	80	0	20	75	5	20	41	39	20
16Mn-13Cr-0.227N-1.5Si(A)	100	0	0	87	9	4	75	18	7
16Mn-13Cr-0.227N-1.5Si(C)	100	0	0	81	11	8	69	21	10
16Mn-18Cr-0.216N-1.5Si(C)	100	0	0	61	21	18	59	17	24
20Mn-13Cr-0.130N-1.5Si(A)	100	0	0	80	15	5	66	28	6
20Mn-13Cr-0.130N-1.5Si(C)	100	0	0	77	16	7	59	31	in
20Mn-18Cr-0.130N-1.5Si(C)	100	0	0	78	13	9	47	40	13
16Mn-13Cr-0.2C-1.5Si(C)	75	25	0	41	55	4	30	60	10
20Mn-13Cr-0.2C-1.5Si(C)	85	15	0	48	49	3	31	58	11
16Mn-18Cr-0.2C-1.5Si(C)	56	20	24	30	28	42	15	15	70

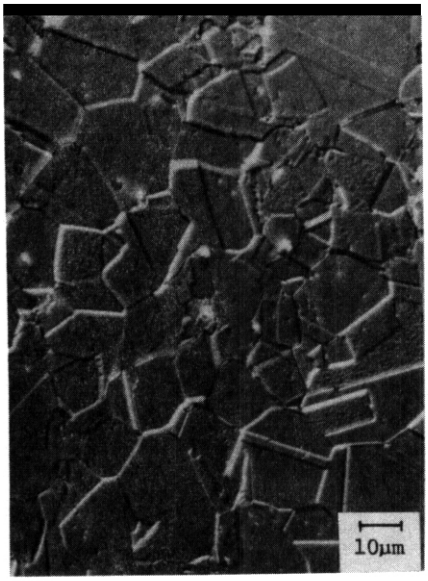

(a)



(b)



(c)

Fig. 8. Optical Micrographs Illustrating (a) Fully Austenitic Microstructure for Fe-16Mn-13Cr-0.2N-2Mo(B) Alloy. (b) Duplex Austenite/Epsilon Microstructure for Fe-20Mn-13Cr-0.26N(C) Alloy, and (c) Triplex Austenite/Epsilon/Alpha Hlcrwtructure Fe-20Mn-13Cr-0.26N(A) Alloy.

(Refs. 6 and 7)

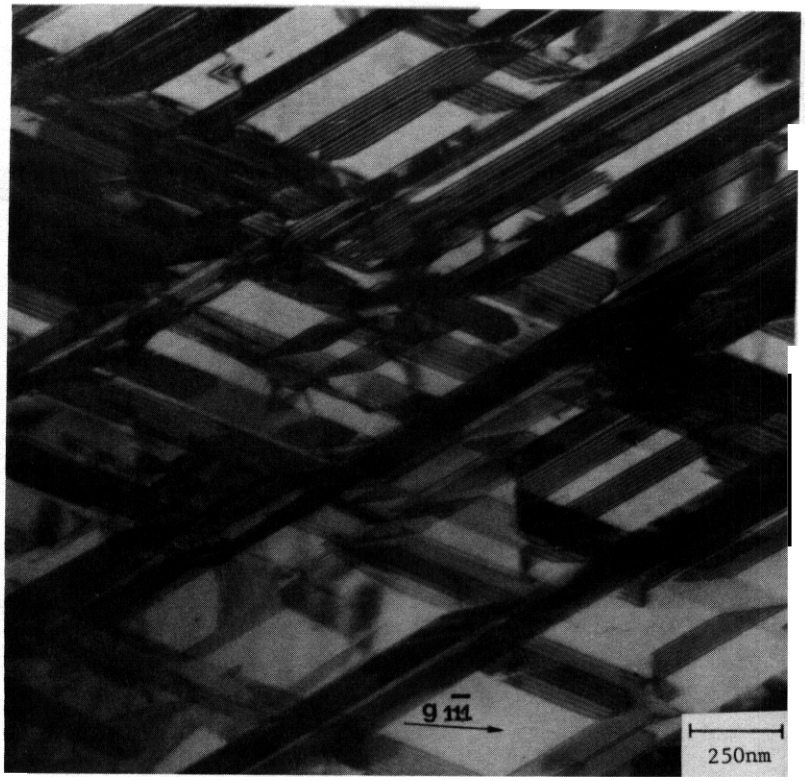

Fig. 9(a)

Heavily Faulted Austenlte In Fe-16Mn-13Cr-0.13N(A) Alloy.

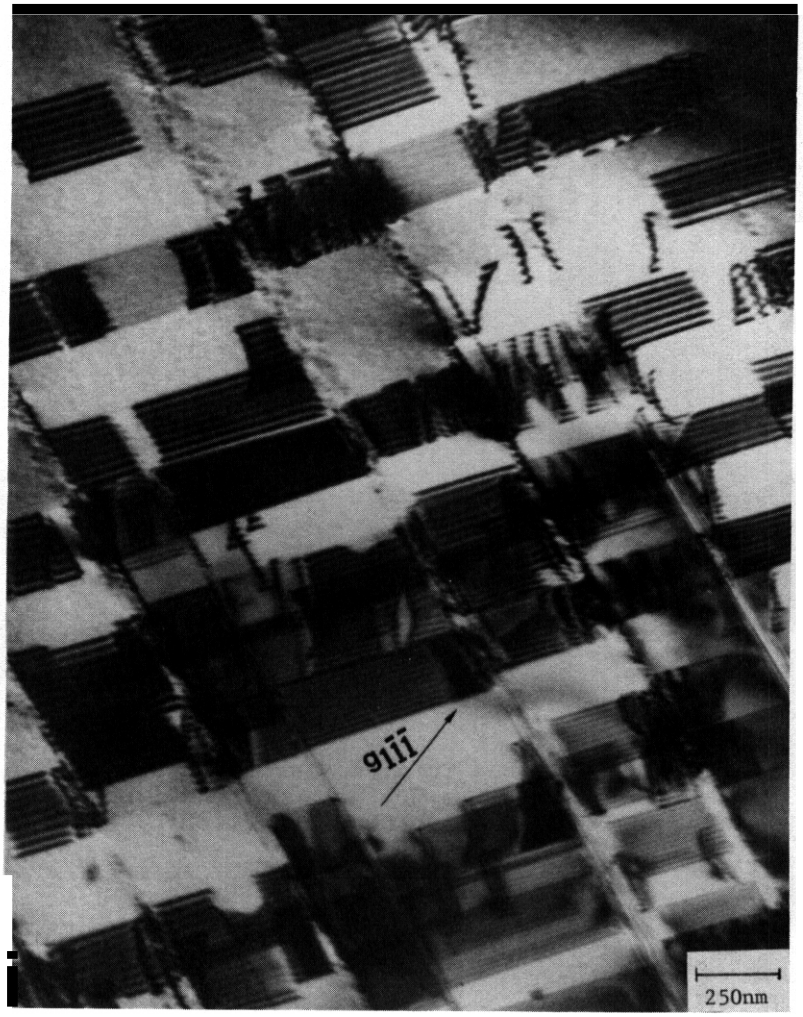

(b)

Initiation of FCC to HCP Phase Transformatlon Or FCC Twinning Reactlon In Fe-20Mn-13Cr-0.13N(A) Alloy. Note Overlapping Stacklng Faults on Parallel (111) Planes In the Austenlte.

(Ref. 7)

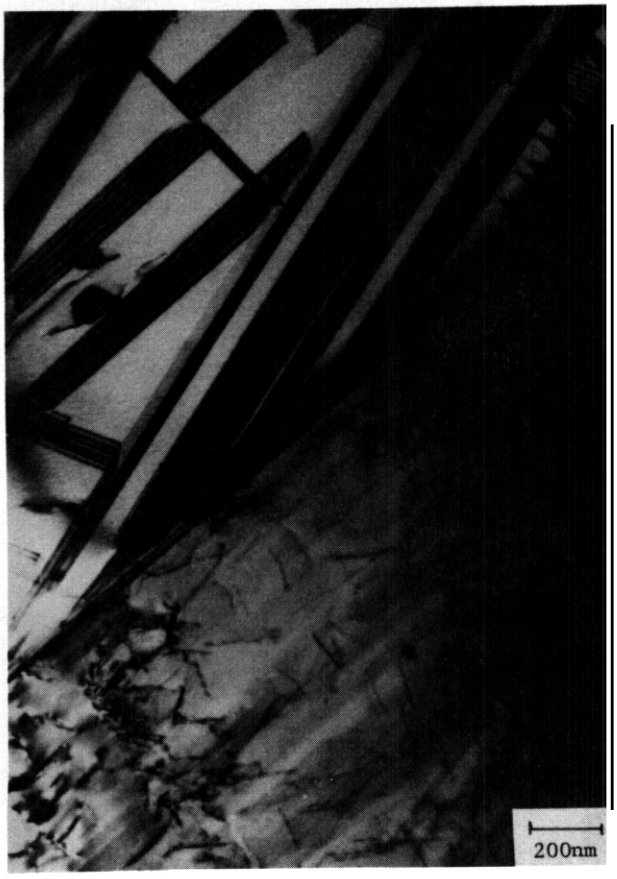

Fig. 10(a) Interface Between Heavily Faulted FCC and HCP Phases in Fe-16Mn-13Cr-0.13N(A) Alloy.

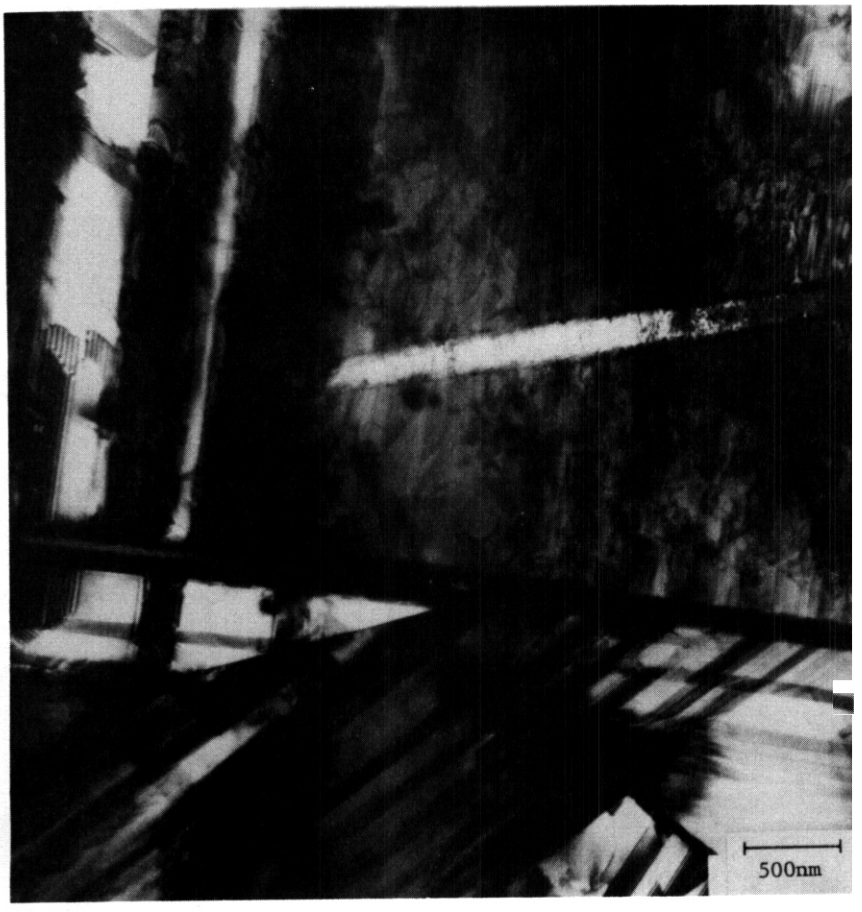

(b) Trlplex Microstructure Near a Grain Boundary Region in Fe-16Mn-13Cr-0.13N(C) Alloy.

(Ref. 7)

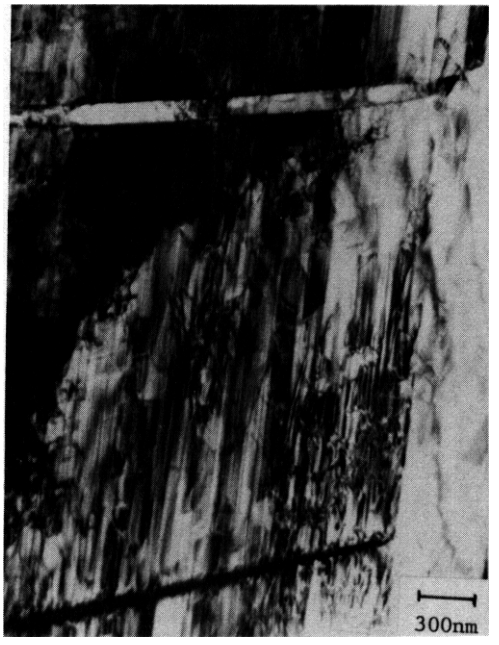

Fig. 11(a) Athermal Alpha Martenslte Lenses Crossing an Athermally Formed Epsllon Martenalto Band.

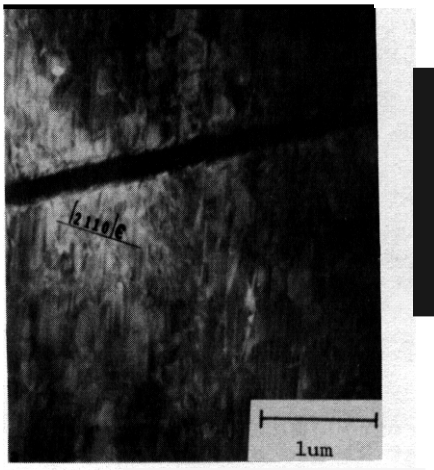

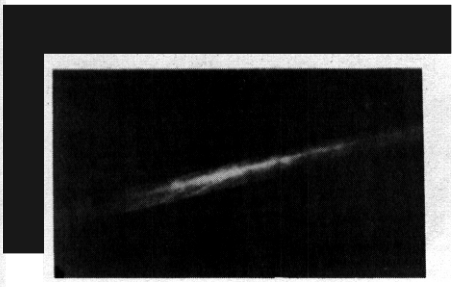

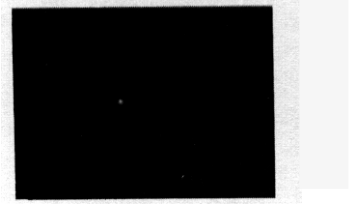

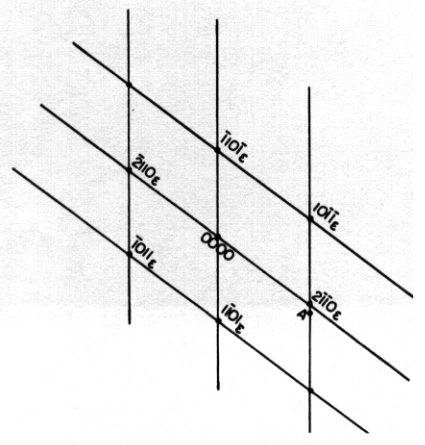

(b) Bright and Dark Field Transmlesion Electron Micrographs of Alpha Martenslte Lense in an Athermally Formed Epsllon Martenslte Band Wlth Assoclated Indexed Dlffractlon Pattern.

(Ref. 7)



Fig. 11(c) An Example of the Post-Tensile Testing Microstructure Developed In Fe-16Mn-13Cr-1.5Si-0.23N. Testing was at RT and Strain-Induced Epsilon and Alpha Martensites Are Present in This Area.

(Ref. 7)

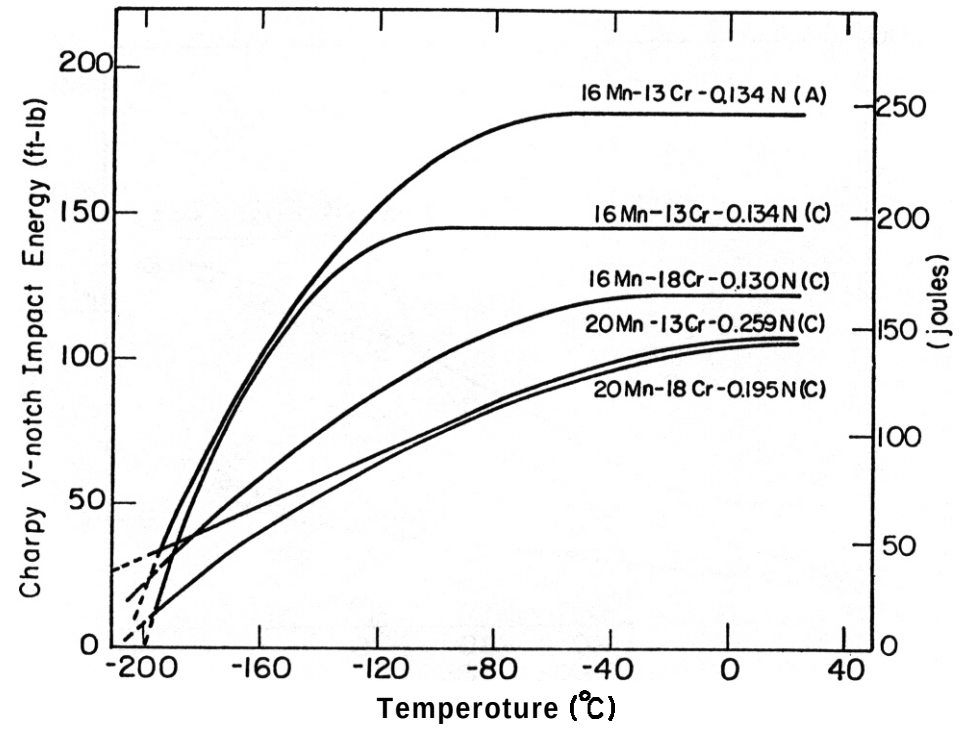

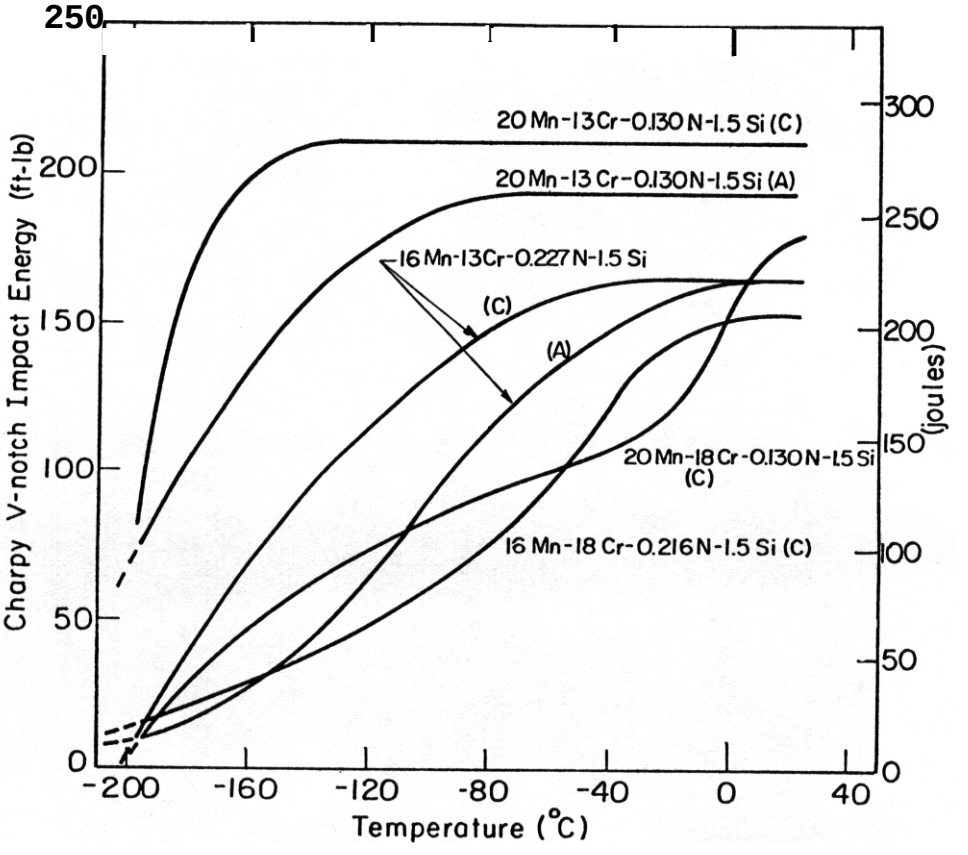

Fig. 12. Charpy V-Notch Impact Energy Curves for Fe-Mn-Cr-N Alloys. (Ref. 7)

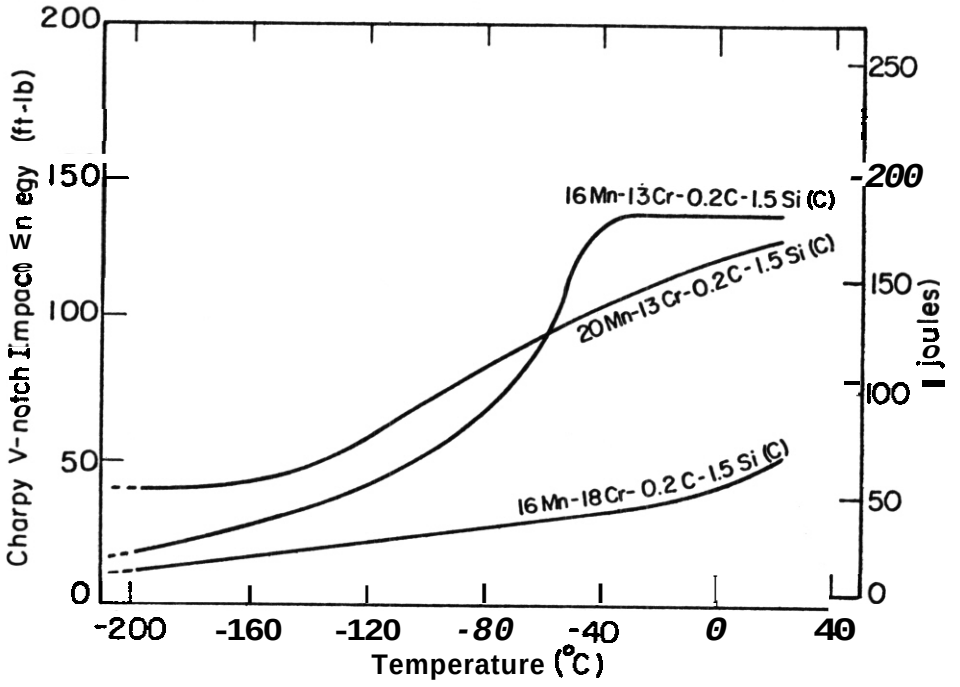

Fig. 13. Charpy V-Notch Impact Energy Curves for Fe-Mn-Cr-Si-C Alloys. (Ref. 7)

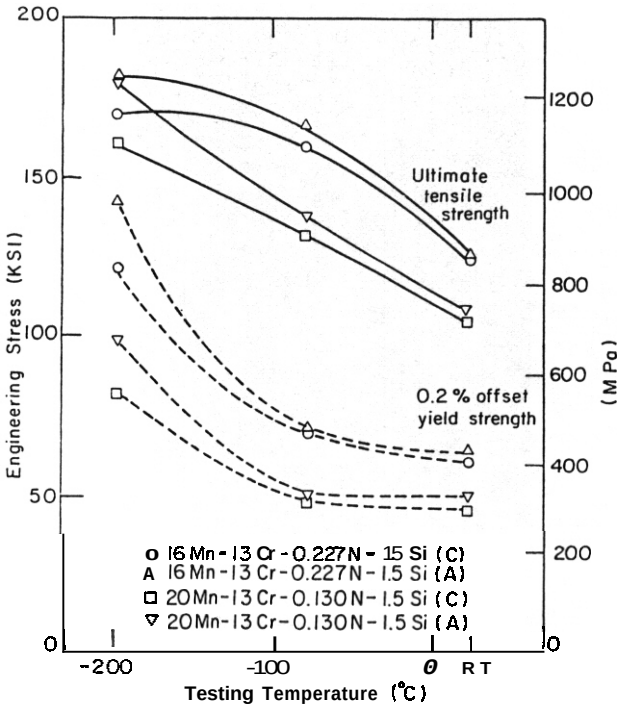

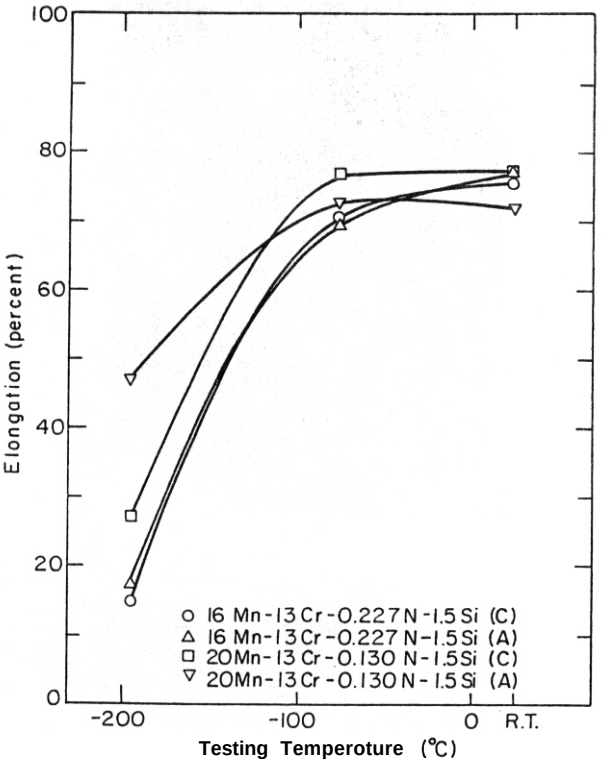

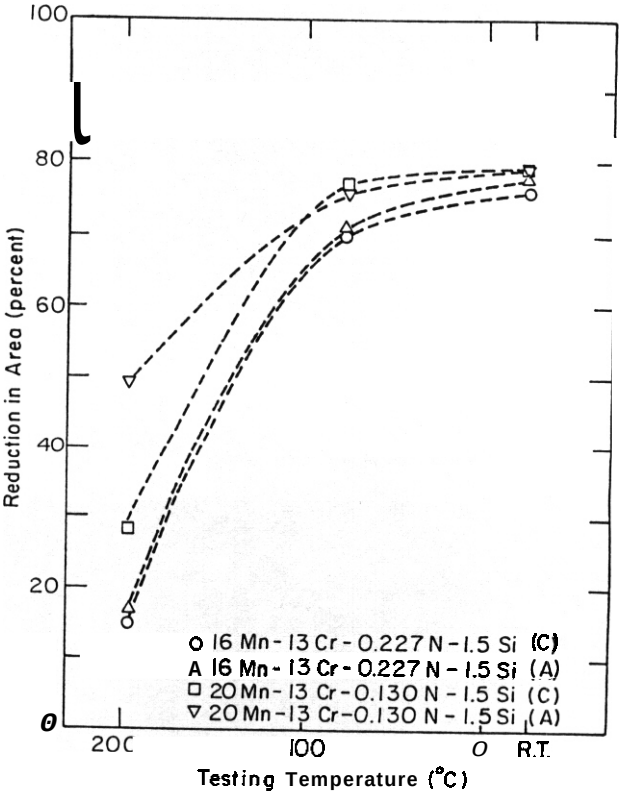

Fig. 14. Effects of Test Temperature on Tenslle Properties of Fe-Mn-Cr-Si-N Alloys. (Ref. 7)

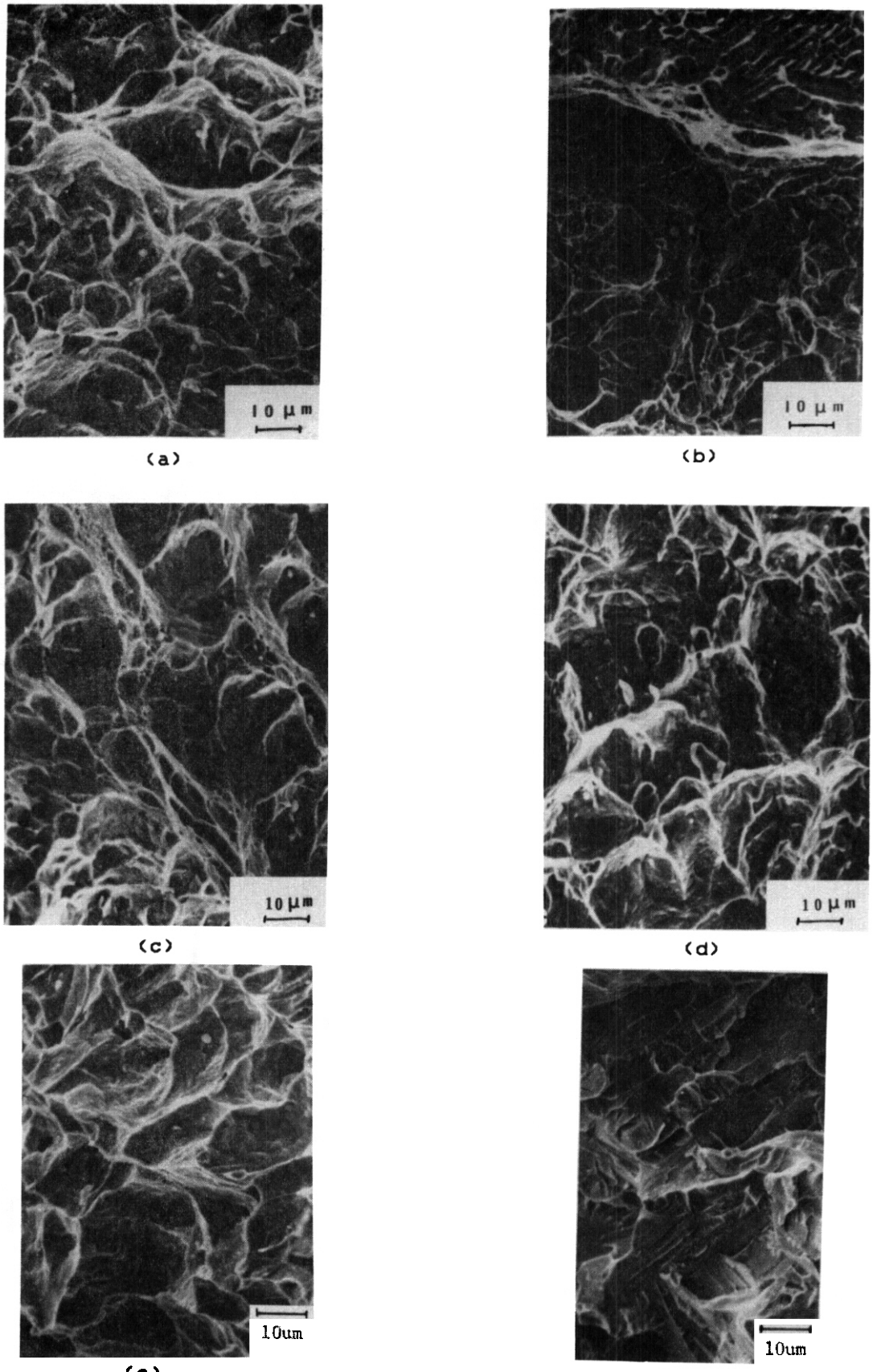

Fig. 15. Scanning Electron Fractographs for Various Fe-Mn-Cr Alloys Illustrating Effects of Alloy Composition and Temperature on Impact Fracture Mode and Toughness. (Ref. 7)

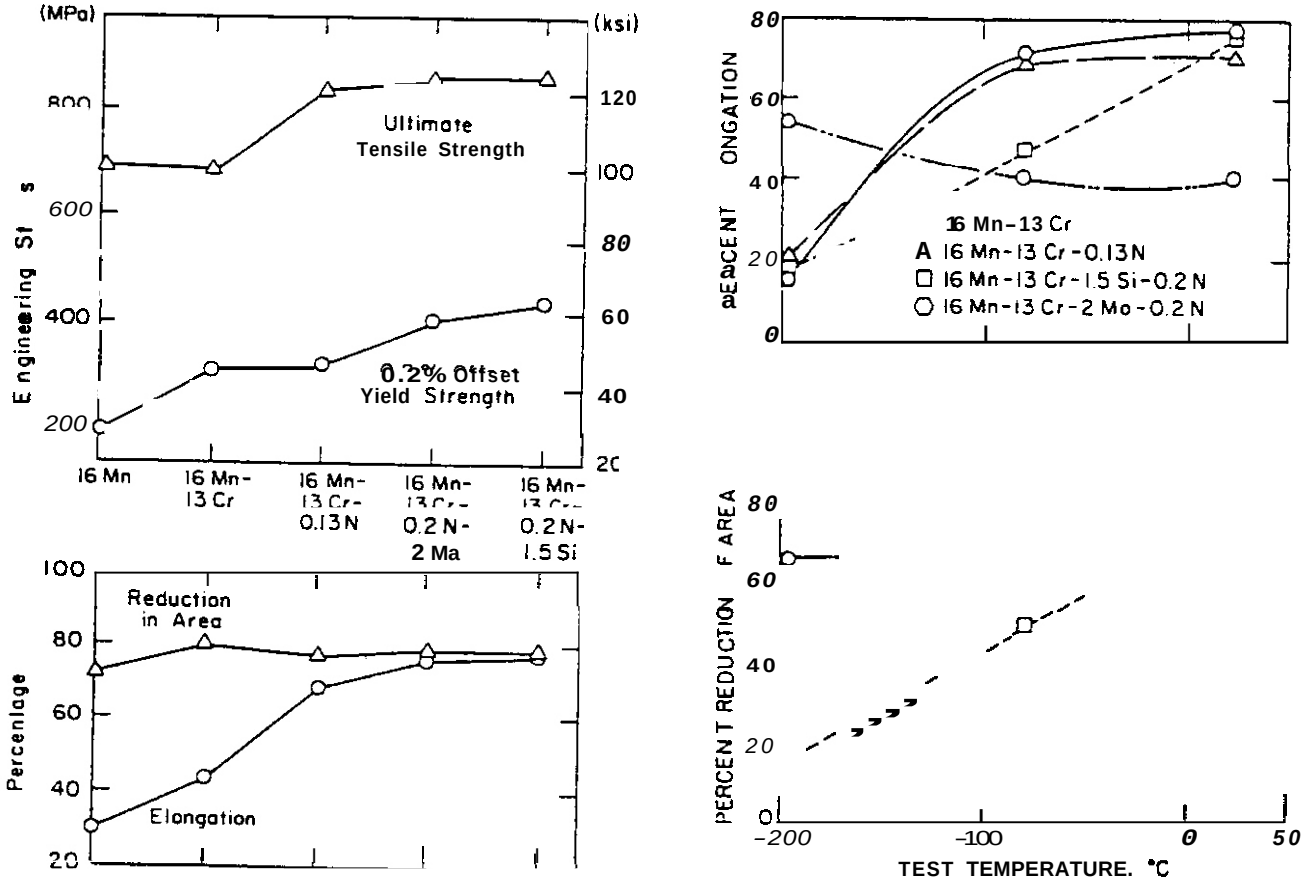

Fig. 16. Illustration of Property Improvements Obtained With Fe-16Mn Base Base Alloys by Modifying Alloy Chemistry. (Ref. 9)

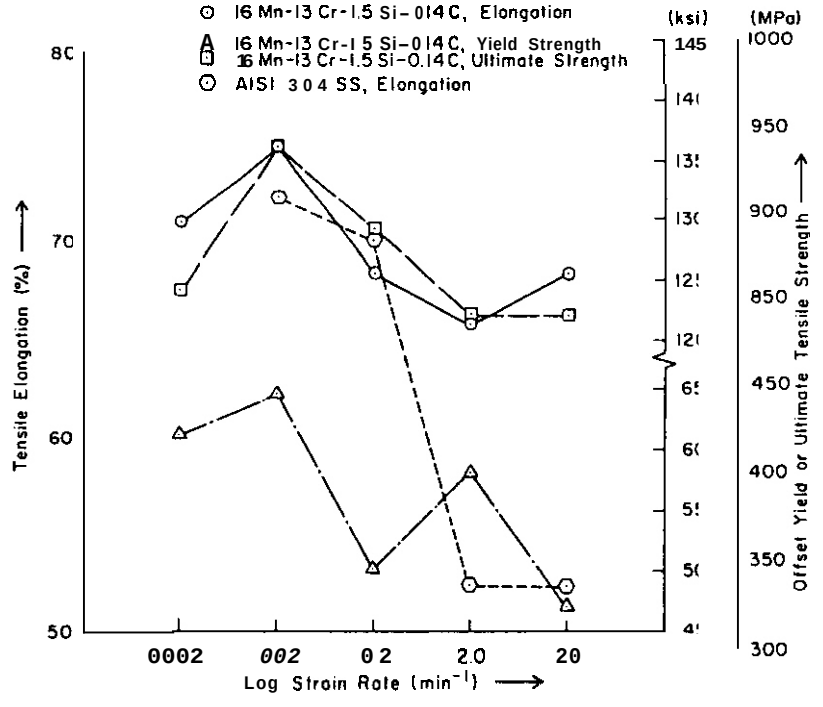

Fig. 17. Tenslle Data for a Fe-16Mn-13Cr-Si-C Alloy as a Functlon of Straln Rate Wlth Simllar Elongation Data for AISI 304 Stainless Steel. (Ref. 9)

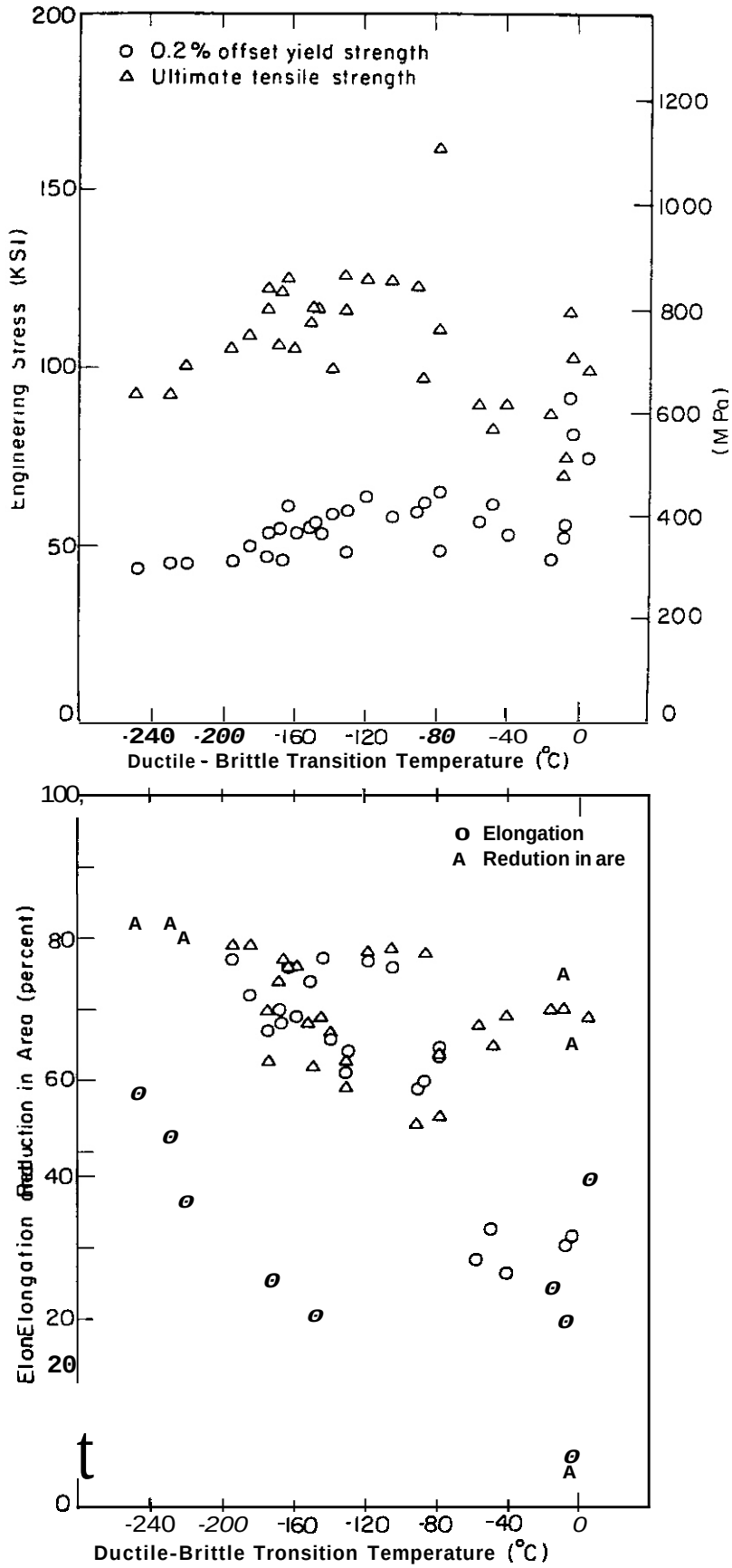

Fig. 18. Compilation of Tensile Data aa a Functlon of Respective Alloy DBTT Showing Wide Range of Combinations Obtained Prom Experimental Alloys. (Ref. 7)

Table XI. General Immersion Corrosion Tests Used to Evaluate Experimental Pe-Mn-Cr Alloys. (Ref. 7)

Test I - 0.1 M $FeCl_3$

1. Test temperature = 25 °C
2. Test duration = 24 hours

Test II Boiling 6 M HNO_3 - 0.01M CO_3

1. Test duration = 48 hours
2. Sensitization = same as Test III

Test III Huey Test

1. Boiling 65 /wo Nitric Acid
2. Test duration = 48 hours
3. Five test specimens were averaged far each composition in each condition
4. Sensitization = one-hour exposure of annealed specimens at 675 °C followed by a water quench

Test IV Boiling 6M NH_4F - 0.5M WH_4NO_3

1. Test duration = 24 hours
2. This solution is used to declnd zircalloy fuel rods

Test V Deaerated Water

1. Test temperature = 300 °C
2. Test duration = 336 hours

Test VI High Temperature Air-Oxidation Test

1. Test temperature = 1100 °C
2. Test duration = 136 hours
3. Specimens were descaled in alkaline permanganate-citric acid

Table XII. Corrosion Rate Data and Teat Results for Experimental Fe-Mn-Cr Alloys. (Ref. 7)

Alloy	0.1 M $FeCl_3$ 25°C[5]	Boiling 6 M HNO -0.01 M CrO_3 mils/mo[4]	Huey Rate mils/mo[1]	Boiling 6 M NH_4I -0.5 M NH_4NO_3 mils/mo[3]	Generated Water 300°C mils/mo[6]	Oxidation Rate in air at 1100°C mils/mo[2]
16Mn-13Cr, Annealed*	Pitting & Crevice Attack	1.2	12.6	27.5		24.1
16Mn-13Cr,Sensitized*		0.5	21.5			
16Mn-18Cr, Annealed*	Pitting	4.1	11.8	15.9		11.9
16Mn-18Cr, Sensitized*		0.4	18.7			
18Mn-13Cr, Annealed*	Pitting	1.5	14.4	24.6		21.8
18Mn-13Cr, Sensitized*		1.1	18.4			
20Mn-13Cr, Annealed*	Pitting	4.4	15.6	21.7		11.9
20Mn-13Cr, Sensitized*		1.9	19.1			
16Mn-13Cr-0.134N, Annealed	Pitting	4.7	12.2	19.4	0.12	12.6
16Mn-13Cr-0.134N, Sensitized			13.3			
16Mn-13Cr-0.204N-2Mo, Annealed	Pitting	2.1	22.5	26.8		5.9
16Mn-13Cr-0.204N-2Mo, Sensitized		2.9	19.1			
16Mn-18Cr-0.180N-2Mo, Annealed	Pitting	4.9	22.1	22.6		6.7
16Mn-18Cr-0.180N-2Mo, Sensitized		4.8	17.0			
16Mn-13Cr-0.227N-1.5Si, Annealed	Pitting	8.8	14.1	11.0	0.04	138.0
16Mn-13Cr-0.227N-1.5Si, Sensitized			21.8			
20Mn-13Cr-0.130N-1.5Si, Annealed	No Pitting	8.1	9.1	10.8	0.16	111.0
20Mn-13Cr-0.130N-1.5Si, Sensitized			8.7			
347SS, Annealed	Crevice Attack	4.3	0.5-1.0	41.2	0.06	29.6
347SS, Sensitized		11.1	1.0-2.0			

Notes: (1) Average of five 48-hour exposures to boiling 65 w/o HNO_3
(2) 136-hour exposures, specimens descaled in alkaline permanganate-citric acid
(3) 24-hour exposure
(4) 48-hour exposure
(5) 24-hour exposure

*See ref. 4.

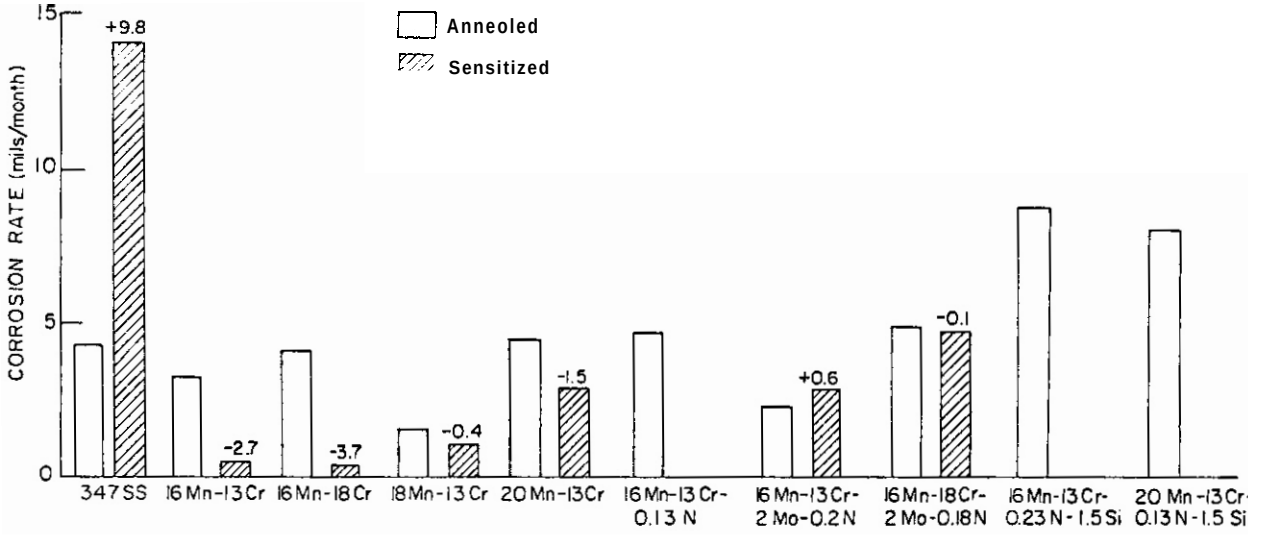

(a) Boiling Nitric Acid/Chromate Test

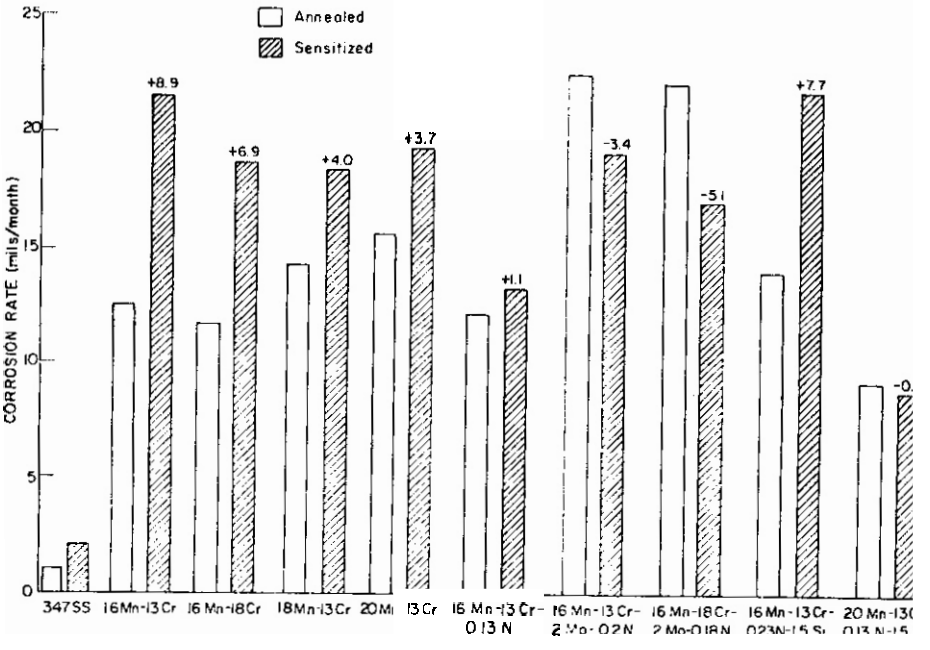

(b) Huey Test (Boiling Nitric Acid)

Fig. 19. Comparison of Corrosion Properties of AISI 347 Stainless Steel With Those of Experimental Fe-Mn-Cr Alloys. (Ref. 7)

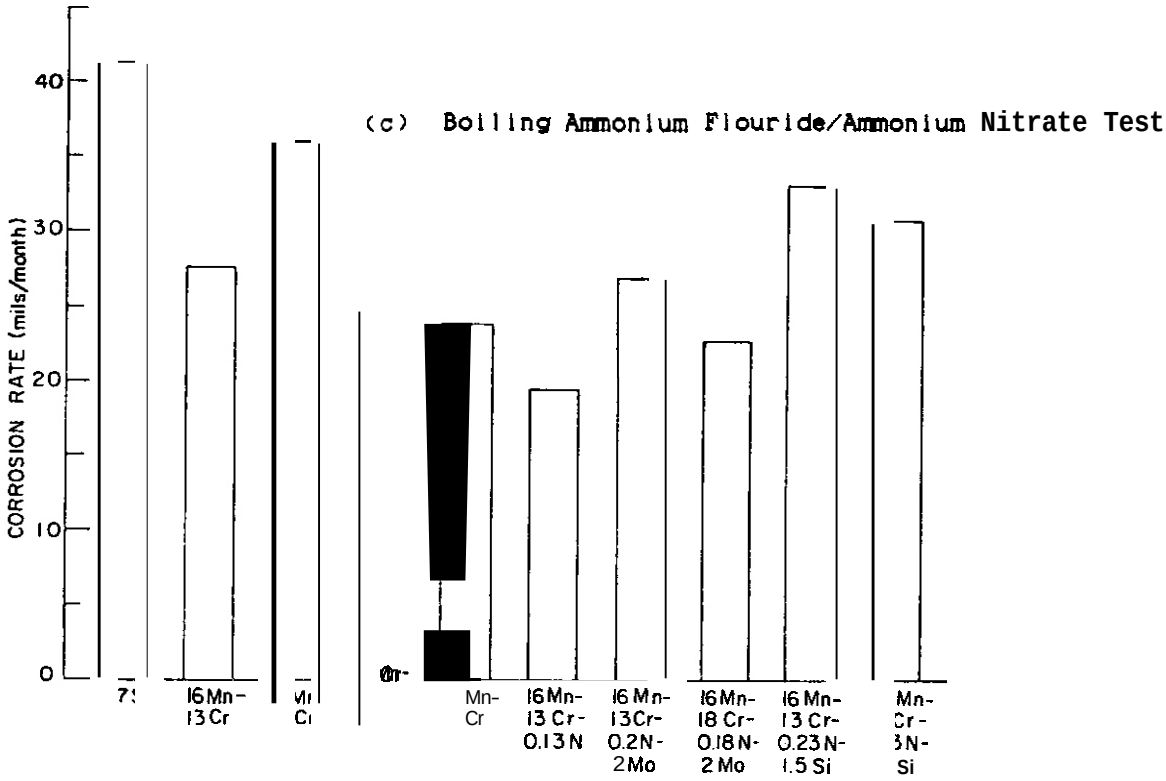

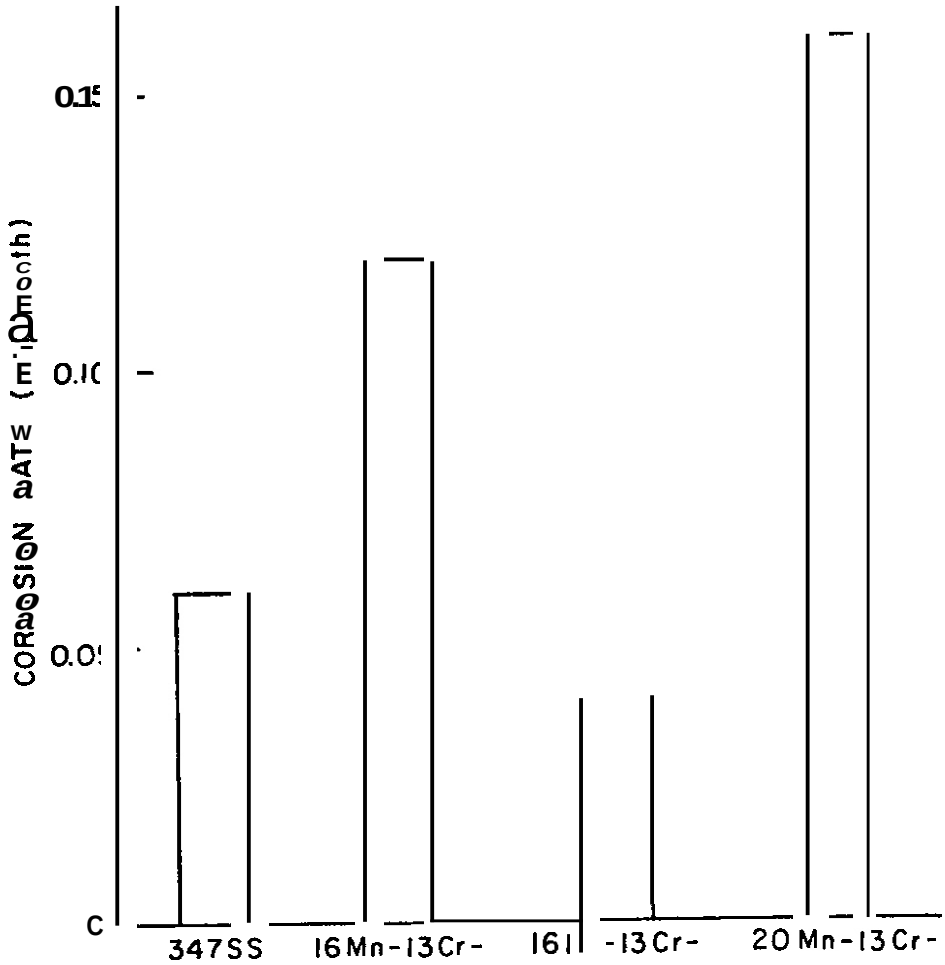

(d)

Deaerated Water Test

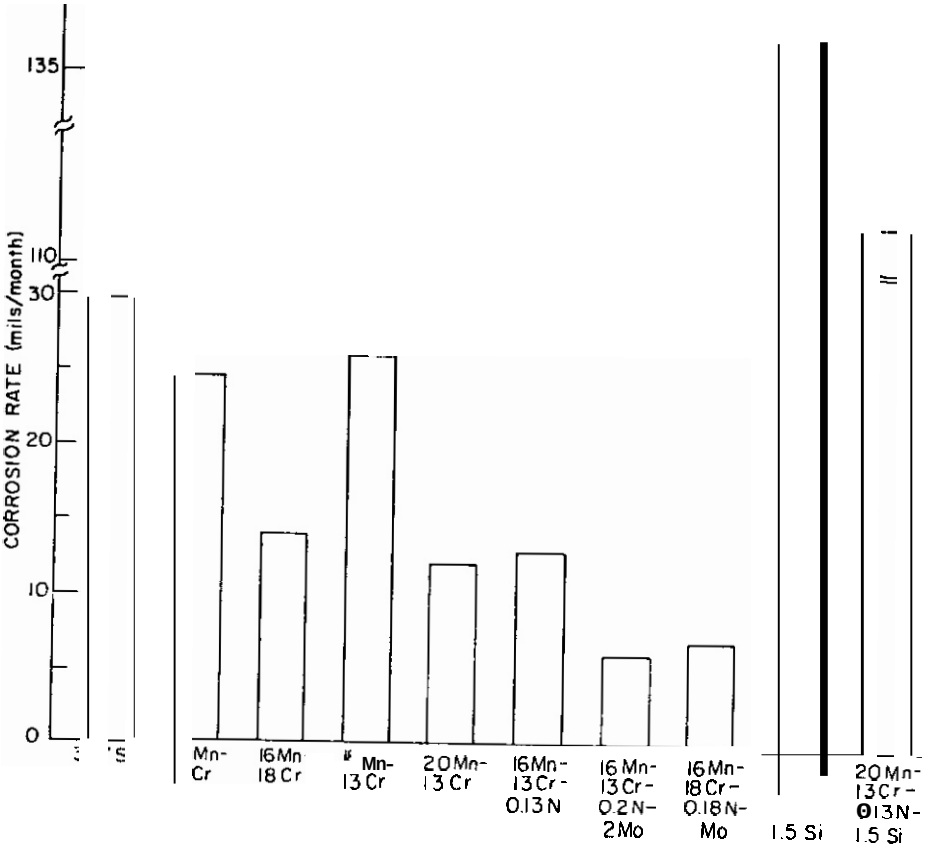

(e) 1100C Air Oxidation Test

EFFECTS OF LOW TEMPERATURE NEUTRON IRRADIATION ON THE PROPERTIES OF 300 SERIES STAINLESS STEELS -
G. R. Odette and G. E. Lucas (University of California, Santa Barbara)

OBJECTIVE

To summarize the effects of neutron irradiation at intermediate temperatures (~300°C) on the microstructure and mechanical properties of austenitic stainless steels.

SUMMARY

Neutron irradiation of austenitic stainless steels can result in significant property changes. Property degradation appears to be greatest for irradiation temperatures (and comparable test temperatures) near 300°C. Here, hardening and loss of ductility may reduce fracture toughness values to as low as 45 MPa$\sqrt{m}$ by exposure levels of 5 dpa. These data suggest an experimental test program designed to evaluate critical microstructural and mechanical property changes in austenitic stainless steels at low irradiation temperatures.

PROGRESS AND STATUS

Introduction

While it is well known that neutron irradiation results in significant mechanical property changes and dimensional instability in materials in general, quantification of these changes is a costly but necessary part of materials development and qualification for reactor application. Much of the structural materials research to date in support of fusion technology development has focussed on the effects of irradiation at relatively high temperature (400-600°C) anticipated for long term fusion structures. However, designs of interim and near term machines have suggested utilization of low operating temperatures (100-300°C), and austenitic stainless steels have been identified as possible candidate materials for these structures.[1]

Consequently, we have reviewed the literature for the effects of irradiation at or near 300°C on austenitic stainless steels. We describe the results of this below. This is divided into a description of microstructural evolution, a description of mechanical property changes, and a suggested experimental program to augment the existing data.

Microstructural Evolution

There are only a few quantitative and reliable data in the older literature on microstructural evolution in austenitic stainless steels irradiated at around 300°C. This is largely due to earlier resolution limitations in transmission electron microscopy (TEM). In general, irradiation-induced microstructures were reported as being composed of black dot damage with some indications of Interstitial loops and bubbles at higher exposures. No void swelling or precipitation was observed (e.g. swelling was found to begin at about 350°C with high Incubation exposures and low swelling rates). Maziasz[2] has reviewed this literature. More recently, however, several higher exposure (5-60 dpa) irradiations near 300°C have been carried out in the mixed spectrum HFIR[5-10] reactor and one in the ORR reactor.[11] High resolution analytical TEM techniques were used to characterize the microstructures. The alloys studied included both 316 and Ti-modified 316 type stainless steels in both cold-worked (CW) and solution annealed (SA) conditions. Further, a relevant data set for a 33 dpa irradiation in the mixed spectrum Advanced Test Reactor (ATR) of a 348 stainless steel has been reported.[12] The data from these studies are tabulated in Table 1.

These results show that the low temperature irradiation-induced microstructures are highly consistent for various alloys and a range of irradiation conditions. The microstructures are dominated by interstitial-type. Frank dislocation loops and small cavities. Table 2 summarizes average loop and cavity number density and diameter data for irradiations of the SA alloys near 300°C. The density of loops appears to decline above 5-10 dpa at an approximately constant diameter. The cavities are probably subvisible at 5 dpa but have an approximately constant number density above 10 dpa. The cavity diameter increases with exposure from about 1.1 nm at 10 dpa to 2.2 nm at 35 dpa. This can be attributed to the increased helium content (from about 400 to 2500 appm). The number density of cavities is about 10 times higher than for loops at 35 dpa. Irradiations of one alloy to 58 dpa showed a continued decline in the number of loops and a small decrease in their size. Surprisingly. the size and number density of bubbles also declined slightly. Some of these differences may be due to

TABLE 1
MICROSTRUCTURAL DATA

ALLOY	COND	T_i (°C)	dpa	He (appm)	N_l 10^{22} (m^{-3})	d_l (nm)	ρ_N 10^{14} (m^{-2})	ρ_T 10^{14} (m^{-2})	N_c 10^{23} (m^{-3})	d_c (nm)	$\frac{\Delta V}{V}$ (%)	ρ_o 10^{14}	Comments	Ref (m^{-2})
316	SA	55	7.3	290	3 3.6	3.7 1 4	<.01	1.6	0	0	0	<.01		3
316	20%CW	55	10.8	520	0.1 7.7	23 3.5	5	15	0	0	0	40	$30<\rho_o<50$	3
347	SA	55	5.4	2500	5	30	.35 3.5	50 4	0	0	0	.35	$.3<\rho_o<49$	
316	SA	300	33	2116	1.3	10.3	iow		3	2.7	29	low		5
316	20%CW	300	33	2116	1.5	10.4	40		3.5	2.5	.28	40		5
JPCA	SA	300	34	2501	1.2	11.5			1.9	2.9	.23		R=0.6[a]	6
JPCA	10%CW	300	34	2501	1.6	10			2.1	3.0	.31		R=0.8	6
JPCA	20%CW	300	34	2501	2.5	10.6			2.3	2.6	2 1		R=0.5, TiC	6
JPCA	SA1	340	10.2	550	9	10.4			1.9	1.2	.01		R=.15	7
JPCA	SA2	300	33.6	2471	4.7	11.5			2.9	1.9	.19		R=.53 3.1/1.9[b] -TiC	7
JPCA	20%CW	300	33.6	2471	9.8	10.6			2.3	2.6	.19		R=.48 3.1/2.4-TiC	
PCA	SA	300	10.5	580	8.5	10.5			3.3	1.0	.01		R=.21	7
PCA	25%CW	300	33.7	2527	4.7	10.8			2.3	2.7	.24		R=.53 4.9/2.1x10^{22},TiC	
348	SA	354	36	ATR	4.0	6.4			3.0	1.3	.13		9/6.3-G phase 1.2/140-Strain centers	1 2
PCA	SA	300	9.7	450					0	0	0			4
316 (MFE)	20%CW	290	5	39	high	3-5 8 - 2 5			0	0	0		ORR T_{ind}=250-450 No recovery	1 1
316DO	20%CW	335	7.7	390	0.1	23	5	6	.04	12	.46	40	voids	8
316Ti	20%CW	335	7.7	390	4.2	13	15	32	2.7	2.9	0.4	70	TiC	8
316Ti	20%CW	55	10.5	490	35	3.5	27	66	0	0	0	7 0		
31600	SA	335	5.3	180	9.1	10	low	29	0	0	0	<.01		2
316N	20%CW	300	10	375					0	0	0			5
316N	20%CW	300	4 4	2613					1.6	2.3				5
316	CW/SA	300	34.5	2300					35	2	.15			9
JPCA	S	300	58	4620	1	9.9	2.1	2.5			.18		TiC lower	1 0

[a] R = Estimated Helium in Bubbles / Total Helium
[b] diameter (nm) / number density (10^{22} / m^3)

T_i = irradiation temperature
N_ℓ = loop density
d_ℓ = loop diameter
ρ_v = network dislocation density
ρ_o = initial dislocation density
ρ_T = total dislocation density
N_c = cavity density
d_c = cavity d i m —
AVN = swelling

TABLE 2
SA 316 ALLOYS

Approximate Exposure (dpa)	5	10	35	60
N_l (x10^{22} m^{-3})	9.1(1)	8.75±3 (2)	2.8±1.6(4)	
d_l (nm)	10	10.5±0.1	10.4±0.6	
N_c (x$10^{23}m^{-3}$)	No	2.6±0.7(2)	2.9±0.5(5)	2.1(1)
d_c (nm)	No	1.1±0.1(2)	2.2±0.5	2.5

specimen-to-specimen variations. Where direct comparisons are possible, the only apparent effect of cold work (≈ 10-25%) appears to be an increase in the number density of loops. The loop size and cavity characteristics are not influenced by cold work. Other observations include the following:

1) In the case of a 5 dpa irradiation in ORR and a 35 dpa irradiation in HFiR there was little recovery of the dislocation structure in cold worked material. However, another cold worked 316 heat (DO) shows a factor of 10 reduction in the dislocation density in a HFiR irradiation to about 8 dpa. A Similar reduction is observed in a iow temperature (55°C) irradiation in HFIR. In this case. the cold work also increases the number of small. black dot type loops.

2) The cavities are helium bubbles except in one case (the 20% CW DO heat with a recovered dislocation structure), where a much iower density ($4x10^{20}/m^3$) of larger (12 nm) voids are Observed.

3) Precipitation is not observed in the 316 aiioys. However, TiC precipitates are found in some Ti-modified steels at intermediate exposures; the TIC is a thermodynamically stable phase. An irradiation induced Ni-Si-Nb rich G-phase is observed in the 348 alloy.

4) A very high density (≈ $1.4x10^{24}/m^3$) of Smaii (≈ 1.1 nm) unresoivabie strain centers are observed in the 348 aiioy.

5) The total dislocation density in SA alloys was observed to increase between 55 and 300°C irradiations for one heat of steel and decrease for another.

6) Expected increases in network dislocation density associated with loop disappearance (unfauiting) have not been reported. It is not known if this is a real discrepancy or simply the resuit of incomplete measurements.

7) Generally Only a fraction of the total helium inventory resides in the observed bubbles. The rest must be in solution or in smaii, submicroscopic ciusters.

These results suggest the mechanical properties wiii be primarily mediated by loops. bubbles (visible and subvisible) and, possibly, network dislocations. The character of the observed features is relatively constant for a range of metallurgical variables. However, it is important to recognize that only a limited data set has been reviewed. Hence, it is not possible to draw reliable general conclusions about the extended defect and precipitate microstructures in low temperature irradiated austenitics without further experimental verification. For example, 304 stainless steels appear to have a iower swelling temperature range than 316 alloys. Hence, they may contain voids at high exposures, and may manifest other irradiation (and deformation) instabilities due to their iower nickel contents.

Microstructural evolution which takes piace at higher temperatures (> 425°C) is reasonably consistent with theoretical models.[2,13,14] in general, the behavior at around 300°C is also qualitatively consistent with theory and represents a continuation of trends extrapolated from higher temperatures. However, the resistance to void formation is not consistent with simple models, which would predict bubble-to-void conversions at sizes less than the observed bubble diameter. The exact source of this swelling resistance is not known. In part it is due to the very high sink density (>>$10^{15}/m^2$) of the bubble and loop microstructures. Further, a high steady state (i.e. when formation and recovery rates balance) population of smaii cascade defects (e.g. vacancy loops and stacking fault tetrahedra) and subvisible bubbles may be present and retard swelling.

Solute segregation due to irradiation is a well established phenomenon which has very important implications to microstructural evolution and phase stability for high temperatures and exposures characteristic of fast reactor and fusion environments. in general, due to the fine scale of the extended detect sink structure, bulk segregation c! alloy constituents is expected to be less significant at lower temperatures.[2,13-15] However. it has been established experimentally that significant irradiation-induced solute segregation takes piace at grain boundaries down to temperatures of about 350°C or lower due to the same mechanisms operating at higher temperatures.[16] The major effects are depletion of Cr and Fe and enhancement of Ni, Si, and, possibly. other significant elements such as P. Irradiation-induced chromium depletion can sensitize steeis, in a similar way to that induced by Cr rich carbide precipitation. The resuit is enhanced vulnerability to intergranular stress corrosion cracking (IGSCC) or irradiation-assisted stress corrosion cracking (IASCC).

We will not attempt to review the rapidly evolving literature on this subject, but will briefly summarize the conclusions of some recently reported modeling[16,17] and experimental[17] studies with emphasis on the behavior of Cr. it is noted that

grain boundary chemistry can be characterized by a variety of advanced microchemical techniques, including high resolution scanning TEM, the technique used in the study reviewed here:

1) The magnitude of Cr depletion is relatively constant in the range of 200 to 400°C; minimum Cr levels are about 0.35 to 0.4 bulk concentrations.

2) Depleted zone widths decrease with decreasing temperature in the range of 300 to 500°C. Extrapolations suggest widths of about 2±1 nm at 300°C.

3) Peak (steady-state) depletions can take piace in the range of 10 dpa.

4) Depleted zone widths increase and exposures to peak depletion decrease with decreasing displacement rate (or flux).

5) it is believed that Cr depletes because it exchanges more rapidly with the flux of vacancies going to the boundary than Fe or Ni. Conversely, Ni increases at the boundary because it exchanges less rapidly than Fe or Cr. This phenomenon has been called the inverse Kirkendaii effect. The rate differences are attributed to variations in the activation energy for vacancy-atom exchange for the aiioy constituents (rather than differences in the pre-exponential factor).

6) The widths of Cr depleted zones have been found to correlate with the Strauss accelerated corrosion test.[16]

7) Rate theory model predictions are in good semiquantitative agreement with observation. However, better independent evaluations of critical thermodynamic and diffusion parameters are needed. In addition, many complications in applying simple models exist, including microstructural evolution in the matrix and near boundary region, precipitation of nickel silicide and possibly other phases at the boundary, and boundary motion. In addition, other radiation induced or enhanced mechanisms may be important for segregation, particularly for elements such as Si and P.

Mechanical Properties

Tensile Properties

There is a large amount of data in the literature on the tensile properties of 300 Series Stainless steels irradiated in both mixed and fast spectrum reactors at low to intermediate temperatures and exposures. We have examined these data to try to extract systematic trends. However. as discussed below. there is evidence that the condition which results in the maximum property degradation is at irradiation and test temperatures around 300°C. Hence. the data tabulations given here will be restricted to experiments carried out near these conditions for SA 300 series stainless steels and welds.

Table 3 lists the data obtained at approximately 300°C. While there are exceptions, the overall trends discussed below are fairly consistent. The irradiated yield stress (YS) data are plotted in Figure 1 as a function of the square root of dpa. The YS rapidly increases at low exposures below about 5 dpa and saturates above this value. There is little apparent difference between fast and mixed spectrum behavior at high exposures or between various alloys. The YS saturates at a value of about 850±100 MPa. Comparisons based on changes in YS are slightly more consistent, with values saturating at an average of about 650±75 MPa.

The ultimate tensile strength (UTS) also increases with exposure, but at exposures above about 3 dpa the yield and ultimate stress values nearly coincide. as shown in Figure 2. This and subsequent tensile data plots do not distinguish among the various aiioys and irradiation spectra, since little systematic difference could be discerned from the data available. Figure 3 shows the UTSNS behavior is also reflected in the trends in the uniform elongation (UE) which approaches very low values (<1%) at high exposures. in this condition, the aiioys exhibit essentially no macroscopic strain hardening (i.e. for $\sigma \propto \varepsilon^n$, $n \approx 0$). The total elongation (TE) also decreases as shown in Figure 4. Note that the definition of the ductility parameters varies in some cases. Fewer data have been reported on reduction-in-area (RA), but this is also observed to decrease with irradiation.

TABLE 3
TENSILE DATA

DATA	ALLOY	TI (°C)	Ti (°C)	S[a]	dpa	s_y^u (MPa)	s_y^I (MPa)	s_u^u (MPa)	s_u^i (MPa)	e_t^u (%)	e_t^I (%)	e_u^u (%)	e_u^i (%)	Ref
Mixed	348	343	290	M	48	186	931	504	931	25	0.2	20	0.1	18
Spec-	348	343	290	M	8.9	186	993	504	993	25	0.3	20	0.1	18
trum	348	343	290	M	11.9	186	1048	504	1048	25	0.3	20	0.1	18
	316	300	290	M	36(18)		124	862	448	862	45	10		18
	316	300	290	M	38(19)	128	710	445	814	45	12			18
	348	316	305	M	46		846		850				0.9	19
	304	204	200	M	1.05	112	645	427	718	52	14.8	38	9.4	20
	316	290	290	M	5	157	830	479	830	39	7.5	37	0.2	21
	316	290	290	M	5	160	777	475	777	35	6.1	34	3.9	21
	316	290	290	M	5	171	806	479	812	30	5.7	30	0.2	21
	JPCA	300	300	M	16	200	887	450	887	36	7.9	28	0.4	22
	JPCA	300	300	M	10	200	800	450	800	36	10	28	4	22
	EC316	300	300	M	10	240	825	525	825	33	10	25	0.4	23
	316.W	300	290	M	6.5	241	771	333	775	13	4.9	10	1.0	24
	316,W	300	290	M	5.3	238	675	443	694	16	5.4	11	1.6	25
	316-Ti	300	300	M	22		851		851		7.3		0.3	26
	304	300	290	M	0.22	156	400	413	547	other data presented				27
	304	300	290	M	0.51	156	484	473	633	as Interpolated curves				27
	304	300	290	M	1.05	156	578	473		at several fluences				27
	304	300	290	M	8.9	158	834	473		43	2.7	40	0.9	27
	348	300	290	M	0.15	196	363	430	501	other data presented				27
	348	300	290	M	0.57	196	544	430	563	as Interpolated curves				27
	348	300	290	M	0.82	196	531	430	566	at several fluences				27
	348	300	290	M	2.7	196	713	430	575					27
	348	300	290	M	12	196	822	430	822	38	1.8	30	0.5	27
	316	280	290	M	1	198	535	460	604					28
	316.W	260	290	M	0.08		306		506					28
	304	290	280	M	0.8	116	448	375	572					29
Fast	316M	300	290	F	38	160	890	490	890	38	10	21	0.8	30
Spec-	316	300	300	F	18	124	862	448	862	45	10			18
trum	318	300	240	F	19	128	710	445	814	45	12			18
	1.4988	230	230	F	10	225	925					>30	1.3	31
	1.4988	230	230	F	20	225	900					>30	0.8	31
	1.4988	230	230	F	30	225	850					>30	0.7	31
	1.4988	230	230	F	5	225	800					>30	3	31
	304	370	232	F	38		867		892		1.4		0.8	32
	304	370	232	F	18		788		800		3.6		0.7	32
	304	388	232	F	48		880		906		1.8		0.7	32

[a] M=mixed spectrum reactor; F=fast spectrum

T_I = irradiation temperature

T_t = test temperature

s_U^U = unirradiated YS

s_U^I = irradiated YS

s_U^u = unirradiated UTS

s_U^i = irradiated UTS

e_t^u = unirradiated TE

e_t^I = irradiated TE

e_U^u = unirradiated UE

e_U^i = Irradiated UE

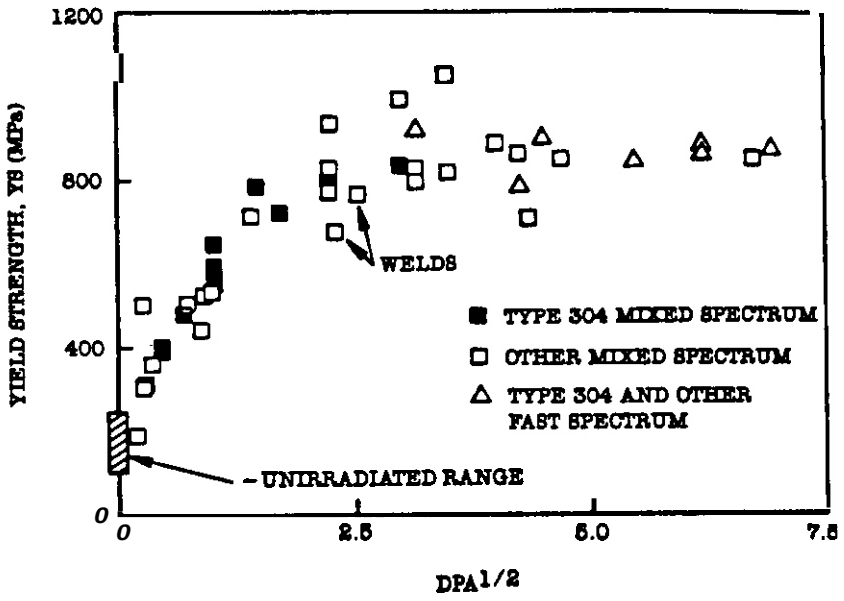

Figure 1. Variation of yield Stress with $\sqrt{dpa}$ for 300 series stainless steels irradiated and tested at approximately 300' at approximately 300°C.

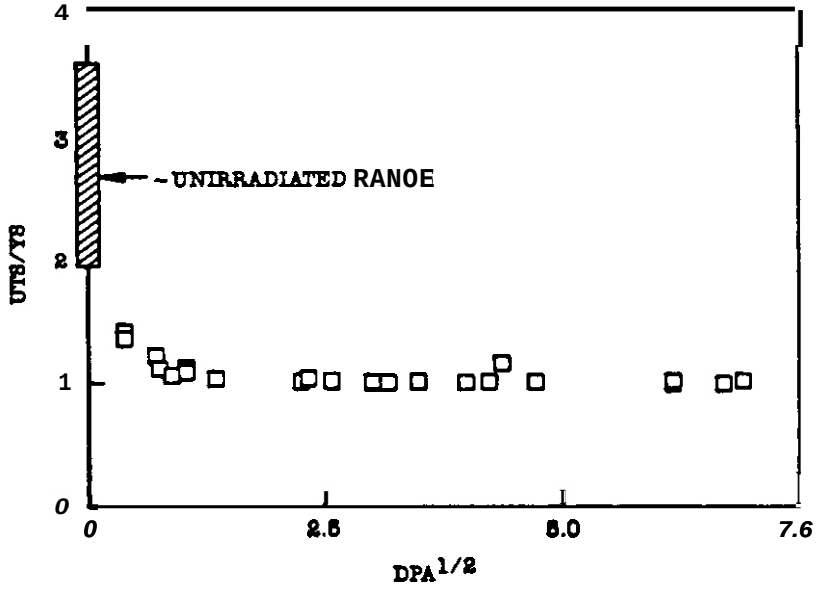

Figure 2. Variation of ultimate tensile strength with $\sqrt{dpa}$ for 300 series stainless steels irradiated and tested at approximately 300' at approximately 300°C.

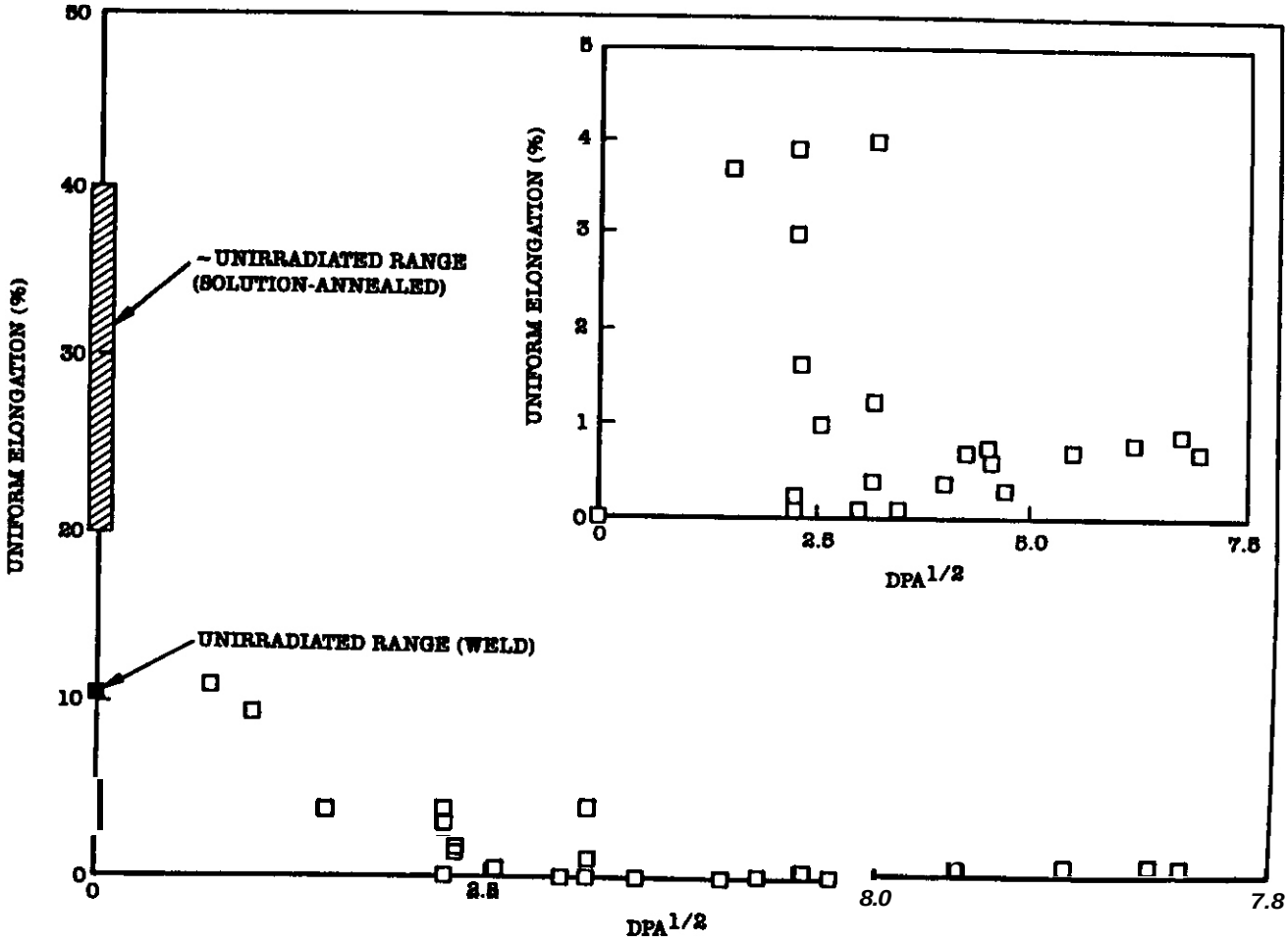

Figure 3. Variation of uniform elongation with $\sqrt{dpa}$ lor 300 series stainless steels irradiated and tested at approximately 300' at approximately 300°C.

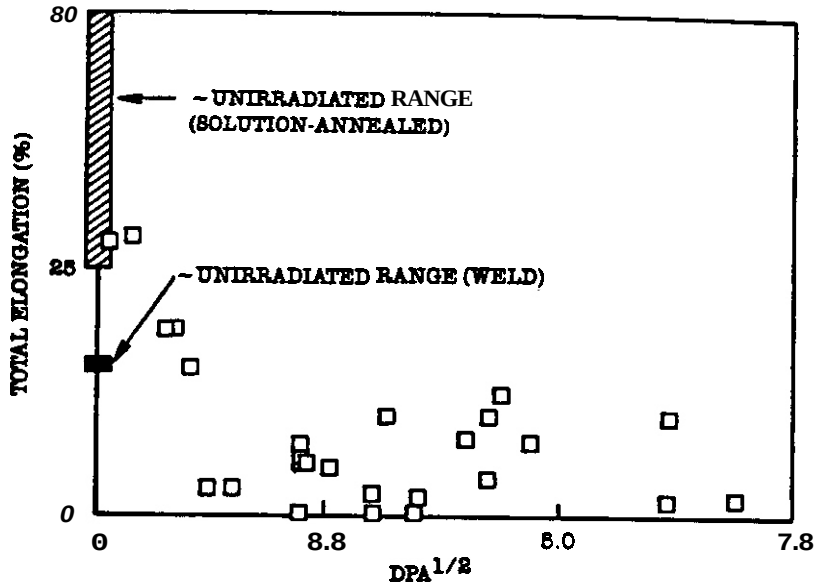

Figure 4. Variation of total elongation with $\sqrt{dpa}$ for 300 series stainless steels irradiated and tested at approximately 300°C. at approximately 300'

Other trends established in a preliminary analysis of both this and other (untabulated) data sets are as follows:*

1) irradiated yield stress values are higher in room temperature (RT) tests.

2) However, at RT the UTS stays above the YS to higher exposures, and ductility -- particularly uniform elongation – is higher than near 300°C. A broad ductility minimum occurs at test temperatures between 200 and 400°C in both irradiated and unirradiated alloys.

3) At high exposures the increases in YS and decreases in ductility are larger at irradiation temperatures between 200 to 400°C than for 55°C irradiations. Above 400°C irradiation-induced changes in the tensile properties decrease with increasing temperature.

4) The combination of observations 2 and 3 suggest that irradiation effects will be maximum for austenitic stainless steel components operated near 300°C.

5) Most data on SA steels suggest relative insensitivity to metallurgical variables. Cold worked alloys have systematically smaller increases in YS. However, the absolute values of the YS are larger after irradiation. Ductility, which is much lower in CW alloys initially. is further reduced by irradiation. in contrast. very limited data on welds indicate slightly smaller increases in the YS and decreases in ductility.

6) There is some indication that while the tensile properties in mixed and fast spectrum reactors are similar at high (saturation) exposures, the changes occur at lower dpa in mixed spectrum irradiations.[33] However, it is noted that classical high temperature helium embrittlement (associated with low ductility intergranular fracture) is not expected to be operative at temperatures below 500 to 600°C.

7) There are no systematic studies of damage rate (flux) effects. Limited comparisons (uncontrolled) do not indicate a large systematic difference between behavior in the high flux HFiR reactor versus other lower flux test reactors.

Simple models of dislocation-defect interactions can be used to estimate the strengthening associated with the void and loop structures described above. The YS change can be calculated from the relation[34]

$$\Delta\sigma_{ys} \approx 2.5Gb[N_l d_l/9 + N_b d_b/25]^{1/2} \qquad (1)$$

where G is the shear modulus (≈ 70 MPa), and b the dislocation Burgers vector (≈ .25 nm). The factor of 2.5 is to convert critical resolved shear stresses to uniaxial YS. The computed yield stress changes are about 440, 465 and 330 MPa at 5, 10 and 35 dpa respectively for the microstructural parameters given in Table 2. At lower exposures the calculations predict about 70% of the observed yield stress changes (≈ 650 MPa). At higher exposures softening is predicted but has, with one exception,[31] not been observed. These differences may be due to the inadequacy of the simple models (e.g. the strengths assigned to the loops and voids) or unresolved and/or otherwise unaccounted for microstructural features. As noted earlier, these features may include subvisible bubbles (i.e. the missing helium) and fine scale residual cascade damage. Network dislocations from unfaulted loop may be important at high exposures. For example, a network dislocation density of 40% of the line length of loops which disappeared between 10 and 35 dpa would result in predicted yield stress increases of 650 MPa. Such network dislocation densities are consistent with trends extrapolated from higher temperatures, but have not been specifically reported in the studies reviewed. Applied stresses leading to irradiation creep might also affect the dislocation as well as other microstructural components, producing a form of creep embrittlement.

in addition to the large changes in macroscopic tensile properties. irradiation also affects the basic characteristics of the tensile deformation process. in the unirradiated state deformation is homogeneous. The microstructure is characterized by dense dislocation tangles; and at higher deformation temperatures, a dislocation cell subgrain structure.[35] in contrast after irradiation deformation becomes very heterogeneous, and is localized to submicron regions of intense shear, surrounded by relatively undeformed matrix.[35-37] These regions, known as dislocation channels. are believed to form due to strain softening mechanisms.[38,39] it is postulated that the passage of the early slip dislocations progressively destroys

* See reference 32 for examples of observations 1-5 also seen in other studies.

the loop and cavity hardening microstructure. Dislocation sources subsequently operate on the set of slip planes which are partially cleared of obstacles but not in the surrounding harder matrix. The surrounding defect structure also retards cross slip, and adiabatic heating in the channels may also contribute to strain softening. In alloys containing voids, dislocations appear to cut through and elongate them. This also reduces the ligament area between holes. The overall internal deformation pattern is a series of intersecting channels oriented favorably for slip to the tensile axis. Necking occurs at very low strains and macroscopic strain hardening is negligible.

At low-to-intermediate exposures final fracture is by a hole coalescence mechanism in the necked region, producing a ductile-dimpled fracture surface which is qualitatively similar to that found in unirradiated alloys. In this mode of fracture, large holes nucleate at Inclusions and precipitates and grow as a result of dilational deformation. This continues to a point of necking instability on the interhoie ligaments. The subsequent linking of holes gives rise to a dimpled fracture surface. In irradiated alloys there are indications that the dimples tend to be shallower and that post-necking fracture strains are reduced by irradiation.

At higher exposures there is a transition to a new and unique fracture mode known as channel fracture.[35-37] The channel fracture surface is characterized by flat, crystallographic type facets inclined at about 45' to the tensile axis. The facets contain evidence of very fine scale dimpling. Channel fracture is clearly associated with the highly localized flow discussed above; however, it occurs at exposures beyond the level needed for saturation of the YS and into the regime of void swelling. However, it is not known if irradiation-induced voids are a prerequisite to this fracture mode. Irradiation-induced voids would enhance the flow. instabilities (localization), reduce tensile ligaments in sheared regions, and lower the strains needed to link deformation-induced holes. Further, it has been proposed that the segregation of nickel to growing voids results in loss of stability in the nickel poor austenite matrix.[37] In extreme cases this could lead to the formation of an interconnected ferritic phase, which is brittle at low temperatures and high strain rates. Under less severe conditions of segregation, deformation-induced formation of e−martensite could also promote brittle type fracture. This type of transformation is consistent with gradual increases in the ultimate tensile strength of steels with increasing dpa at very high exposures.37

In summary, the effect of inadiation on the tensile properlies of austenitic stainless steels near 300°C and at exposures greater than a few dpa can be anticipated to be as follows: large increases (on the order of 650 MPa) in the YS and smaller increases in the UTS; nearly equal values of YS and UTS and very low values of UE of (< 1%) and strain hardening exponents; reduced TE (< 5-10%) and RA (< 30-40%). Deformation would tend to be localized in dislocation channels. The fracture mode will probably be (deformation) hole coalescence leading to a dimpled fracture surface. However, the strains to final fracture would be reduced and the dimple morphology modified. If void swelling occurs at high exposures, channel fracture may occur.

Fracture Toughness

Available data show that irradiation also results in reductions in fracture initiation toughness and crack growth resistance (tearing modulus) in austenitic stainless steels. Unfortunately, the data base is limited and there are few controlled studies of the effects of irradiation and metallurgical variables. Further, there are few valid toughness data for either unirradiated (generally due to low strength/high toughness properties) or irradiated alloys (generally due to the limited amount of material and the use of small specimens and/or nonstandard test techniques).

Toughness is generally lower for tests above room temperature in both the irradiated and unirradiated states, following trends in tensile ductility. Hence, we will focus here on elevated temperature tests from 230 to 430°C where toughness is at a minimum. The data are given in Table 4. Some other data for stainless steels in the cold-worked condition and other alloys (Inconel 600 and PE-16) have been examined but are not tabulated here. It is also noted that Lucas and Gelles have recently reviewed the effects of higher temperature irradiation on fracture.[46]

We have attempted to determine data trends by grouping the data according to the irradiation type and conditions (mixed versus fast spectrum, dpa and temperature), material condition (weld versus solution annealed) and test condition (static/dynamic and temperature).

There are 5 high exposure (> 29 dpa) data points for SA type alloys irradiated in mixed spectrum reactors between 275°C and 375°C and at test temperatures below 430°C. The average toughness for this data subset is 55±11 MPa$\sqrt{m}$. A 316 alloy irradiated in a mixed spectrum to about 1 dpa had a high toughness of about 200 MPa$\sqrt{m}$ when tested at the irradiation

TABLE 4
FRACTURE TOUGHNESS DATA

DATA	ALLOY	T_t	Ti (°C)	S[a]	dpa	K^u_{Ic} MPa$\sqrt{m}$	T^u	K^i_{Ic} MPa$\sqrt{m}$	T^i	Ref.
Mixed	SA316	260	280	M	1	346		200		28
Static	316,W	260	260	M	0.08	145		100		28
	347	427	275	M	69			48		40
	348	427	327	M	35			55		40
	348	427	353	M	47			48		40
	304	268	280	M	0.8	265		59		49
	348	427	364	M	37			54		19
	346	427	364	M	29			75		19
	316H	350	350	M	0.09			232		41
	316H	350	350	M	0.24			226		41
	316H.W	350	350	M	0.15			96		41
	316H,W	350	350	M	0.25			107		41
Fast	316	427	427	F	19	299	353	79	8	42
static	304	427	427	F	25	462	917	75	5	42
	308,W	427	427	F	25	133	295	47	8	42
	304	400	425	F	2.4	220		164		43
	304,W	400	425	F	2.4	185		47		43
	316L	400	425	F	2.2	194		132		43
	316L,W	400	425	F	2.3	173		55		43
Fast	308,W5[b]	427	427	F	7.5	250		85		44
Dyna-	308,W10	427	427	F	7.5	250		67		44
mic	308,W19	427	427	F	7.5	250		55		44
	321	230	230	F	14	249		119		45
	321	230	400	F	14	224		120		45
	321	400	400	F	14	224		105		45
	321	400	390	F	21	224		110		45
	321	400	250	F	21	224		100		45
	321	400	390	F	32	224		110		45
	321	400	230	F	32	224		110		45

[a] M–mixed spectrum reactor; F=fast spectrum
[b] numbers refer to ferrite number

T_t = test temperature
T_i = irradiation temperature
K^u_{Ic} = unirradiated fracture toughness
K^i_{Ic} = irradiated fracture toughness
T^u = unirradiated tearing modulus
T^i = irradiated tearing modulus

temperature of about 270°C. Tests and irradiation of another 316 alloy to about 0.17 dpa at 350°C resulted in a toughness of about 228 MPa$\sqrt{m}$. In contrast, mixed spectrum irradiation of a 304 alloy to about 0.8 dpa resulted in a low toughness of 59 MPa$\sqrt{m}$ when tested at the irradiation temperature of about 270°C.

Fast reactor irradiations of SA 304 and 316L to about 2.3 dpa at 425°C reduced toughness to about 148±16 MPa$\sqrt{m}$ for tests at the irradiation temperature. Higher exposure (= 22 dpa) fast reactor irradiations of SA 304 and 316 resulted in lower toughness levels of about 77±2 MPa$\sqrt{m}$ at similar temperatures.

A SA 316 weld irradiated in a mixed spectrum and tested at about 270°C had a toughness level of about 100 MPa$\sqrt{m}$ at only about 0.08 dpa. Mixed spectrum reactor irradiation to about 0.7 dpa of a 316 MIG weld resulted in a toughness of about 102 MPa$\sqrt{m}$ for tests at the irradiation temperature of 350°C. Fast reactor irradiations of 304, 316L and weids at 427°C to 2.3 dpa resulted in low toughness levels of about 52±4 MPa$\sqrt{m}$ for tests at 400°C. Testing and fast reactor irradiations of a 308 SMA weld at 427°C resulted in a toughness of 47 MPa$\sqrt{m}$ at 25 dpa.

A SA 321 alloy tested and irradiated in a fast reactor at about 240-400°C to 14 to 32 dpa gave dynamic toughness values of 110±10 MPa$\sqrt{m}$. Fast reactor irradiations and tests at 427°C to 7.5 dpa for a 308 SMA weld resulted in dynamic toughness levels which decreased with ferrite number (FN) as follows: 85 MPa$\sqrt{m}$ for FN = 5.2; 67 MPa$\sqrt{m}$ for FN = 0.4; 55 MPa$\sqrt{m}$ for FN = 19.

The data are plotted against the square root of dpa in Figure 5a and for weids in Figure 5b. it is difficult to reach reliable conclusions from these data since the experiments are not controlled and the toughness values subject to considerable uncertainty. Nevertheless, it appears that:

1) Static toughness of SA alloys decreases and approaches a value in the range of 50 MPa$\sqrt{m}$ at high exposures. There is little apparent difference between fast and mixed spectrum irradiations at high exposures. The lowest toughness levels in SA aiioys is for conditions where the tensile ductility parameters are low and YS increases have saturated near values of the UTS.

2) Static toughness values are less at low exposures for welds than for alloys in the SA condition. The toughness of weids approaches a value of about 50 MPa$\sqrt{m}$ at exposures above a few dpa in fast reactor irradiations (there are no data from mixed spectrum irradiations in this exposure regime). Low values of toughness can occur in welds prior to exposure levels corresponding to very low ductility and saturated yield stress. This raises the possibility of additional decreases in toughness levels at higher exposures. Notably, data at higher irradiation temperatures indicate that the saturation value of toughness in weids is lower than for wrought material.[46]

3) Dynamic toughness tends to be somewhat higher than static values. This may be due to the assumption that initiation takes place at the maximum load in a dynamic test; this would be invalid if there is significant stable crack growth. Dynamic toughness of welds decreases with increasing delta ferrite content.

The above discussion has focussed on initiation toughness. However, it is well-established that irradiation has a greater embrinling effect on crack growth resistance as quantified by the tearing modulus (T_R)

$$T_R = [dJ/da][E/\sigma_0^2) \qquad (2)$$

where E is Youngs modulus and σ_0 is the flow stress σ_0 = (YS + UTS)/2. Unirradiated austenitic alloys have values of T_R of several hundred; high exposure fast reactor irradiations reduces this to values of 5-10.[42]

Mechanistic analysis and modeling is useful for data interpretation, extrapolation of conclusions to conditions where data are not available and guiding additional research. Loading of structures or specimens containing sharp cracks (produced by fatigue or intergranular corrosion processes) results in concentrated (localized) stress and strain fields near the tip (i.e. a plastic zone).[47] When a sufficient volume of material is strained beyond a critical value, the crack extends or initiates growth. Depending on the loading conditions, the crack may arrest or continue to grow stably. Final fracture occurs when unstable crack growth occurs. The deformation and fracture processes vary in tundamental ways from those taking piace during tensile deformation to fracture. Significant differences include the stress-strain and stress-state histories and the presence of strong field gradients in the vicinity of crack tips.

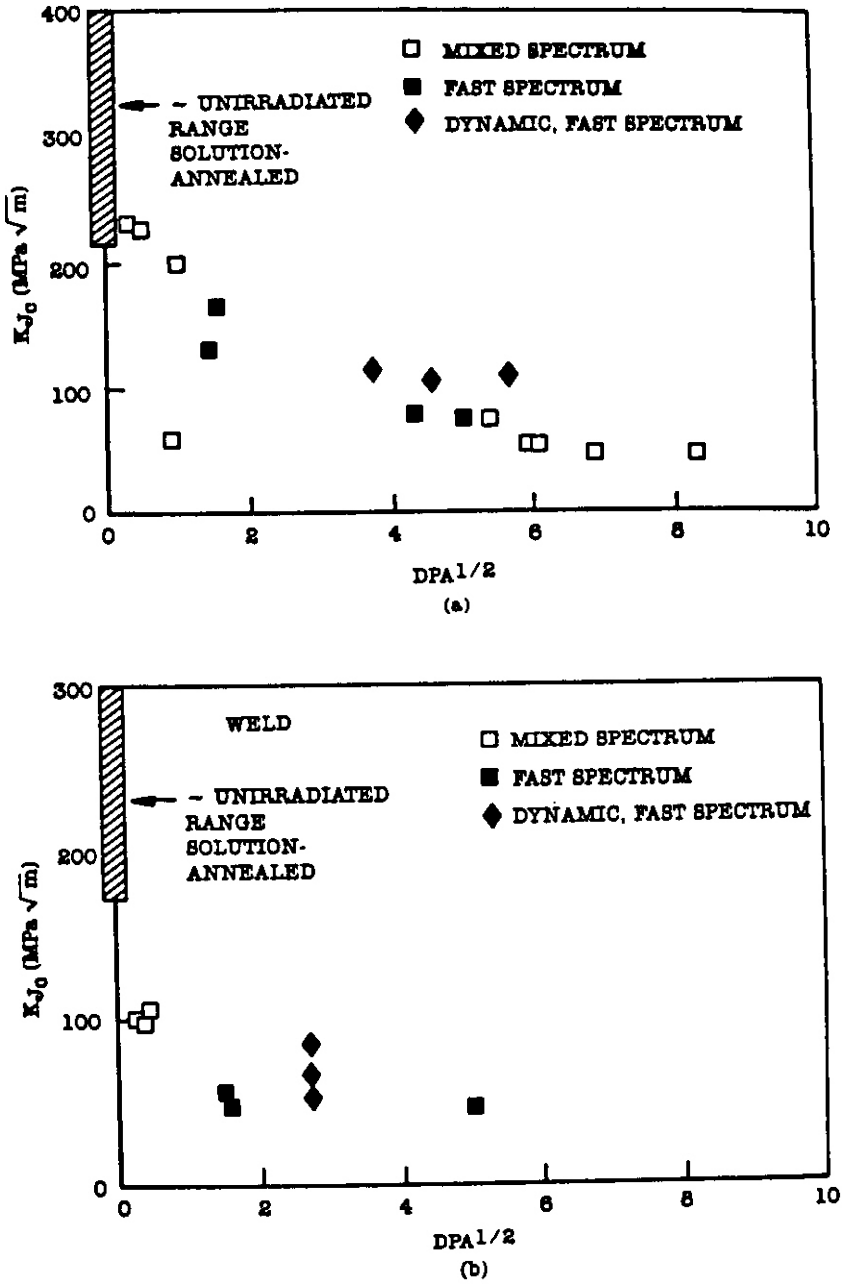

Figure 5. Variation of K_{Ic} with $\sqrt{dpa}$ for a) wrought material and b) welds.

In general the loads and displacements needed to initiate crack growth depend in a complex way on the material properties and the crack-structure/specimen size and geometry. However, for well-defined conditions of plane strain (or stress) and well contained plasticity, or small scale yielding, the stress and strain fields of a blunting crack can be characterized by a single proportional loading parameter, namely the stress intensity parameter K, which can be computed from elasticity theory. It follows that fracture initiation takes place at a critical value of this parameter; for Mode I loading under plane strain conditions this is K_{Ic}. The size requirement for the application of linear elastic fracture mechanics (LEFM) depends on material properties; in general, the plastic zone size ($r_z \approx K_I^2/2\pi\sigma_o^2$) must be less than about 1/50 the crack and ligament dimension. Plane strain conditions also place Similar size requirements on the specimen thickness. Experimentally, K_{Ic} can be determined by measuring fracture loads on fatigue precracked specimens, subject to the size requirements noted above and evidence that stable crack growth is negligible, as determined from the linearity of the load-displacement curve.[48]

Even when the requirements of LEFM are violated by larger scale plasticity and crack growth, the crack tip fields can be characterized. within relaxed size requirements, by another singularity parameter, J.[47] Fracture initiation takes place at a critical value of $J = J_{Ic}$. In the small scale yielding limit $K_{Ic} \rightarrow K_{Jc} = \sqrt{J_{Ic}E/(1-\nu^2)}$, where E is Young's modulus and v Poisson's ratio. Experimentally. J can be determined from load, load-line displacement data, coupled with crack growth (Δa) measurements to generate J-Aa curves. This curve is extrapolated to a crack blunting line to estimate J_{Ic}. The size requirements for J-controlled initiation depend on the geometry, or deformation pattern. as well as material properties. For loading conditions dominated by bending moments -- hence, a Prandtl type flow field -- the criteria is that all relevant specimen dimensions (unbroken ligament. crack length and specimen thickness) must be larger than $25\text{-}50J_Q/\sigma_o$, where J_Q is the apparent value of J_{Ic}.[49]

The crack growth reslstance can be determined from the slope of the J-Δa curve (dJ/da) and is usually characterized in terms of the T_R. However, there are very severe size requirements for unique measurements of T_R due to the loss of proportional loading conditions, and crack growth is usually limited to small values.[50,51]

The concept of unique singularity fields is important to understanding the micromechanics of fracture, since it permits relating microscopic processes of deformation and damage accumulation to macroscopic toughness. Models of ductile fracture toughness postulate that crack growth initiates when the the strains near the tip of a crack exceed a critical value over a critical distance.[50,55] Most models are based on the strain induced growth of holes in front of the crack, which link to cause crack extension. The critical distance (*l*) often interpreted as the spacing between the large inclusions which are the nuclei of significant deformation-induced holes; experimentally this is often associated with the dimple size or spacing on a fracture surface. Alternately the distance has been characterized as the width or length of intense shear bands formed at the crack tip at high angles to the crack tip.[50,51] The failure process in this case is then associated with a shear decohesion in the deformation band.

In unirradiated austenitic alloys, holes nucleate at hard particles and grow to a size of about R = l/2 where *l* is the inclusion spacing. Subsequent necking on the remaining ligament results in crack extension. The crack opening displacement (COD) δ reaches a critical value of δ_{Ic} at initiation. Theory indicates that the dimensionless parameter δ_{Ic}/l is an increasing function of l/R_o where R_o is the inclusion radius.[52] The ratio δ_{Ic}/l varies from about 0.5 to 2-3 and is a weak function of the strain hardening exponent and the degree of plasticity. in small scale yielding the toughness is given by the expression

$$K = \sqrt{C\delta_{Ic}\sigma_o E/(1-\nu^2)} \qquad (3)$$

where C is a parameter which depends on the strain hardening exponent and yield Stress. but typically has values of about 2.[53]

Data trends for tough ductile alloys with high strain hardening exponents are reasonably consistent with this model. The critical strain (ε_f^*) is the tensile strain required to nucleate the hole at the particle (nucleation may require combined conditions of both critical local stress and strain) and to grow it to final instability by internal necking and rupture of the ligament between the void and crack tip. For hole growth mechanisms ε_f^* is very sensitive to the stress state as determined by the ratio of the hydrostatic to effective shear stress. Specifically, triaxial stresses lower ε_f^* by increasing the rate of hole growth per unit strain and, also, probably, by lowering nucleation strains. Decreased strain hardening exponents also lower ε_f^*.

Indeed, hgh strength alloys with lower work hardening exponents deviate from this behavlor as illustrated in Figure 6. In this case the flow localizes prematurely along slip lines (Figure 6a) or in intense shear bands (Figure 6b), before the holes have grown to a size of l/2.

The maximum shear strains are on a plane at high angles from the crack plane giving rise to a characteristic zig-zag fracture path. The mechanism leading to localization varies for different microstructures.[54] For instance, in pressure between the larger Inclusion-nucleated holes. In precipitation-strengthened alloys the localization may be due to destruction of dislocation obstacles or attainment of a critical stress due to dislocation pileups capable of causing a subsequent avalanche of dislocations from source operation and glide in the slip channel. In this case ε_f^* is mediated by a complicated combination of void or other shear accommodation strains and rupture strains in the shear bands. The local rupture mechanisms during shear decohesion are not well-understood. Clearly the microstructures of Irradiated austenitic alloys will promote such rapid shear fracture processes as demonstrated by the tenslle behavior.

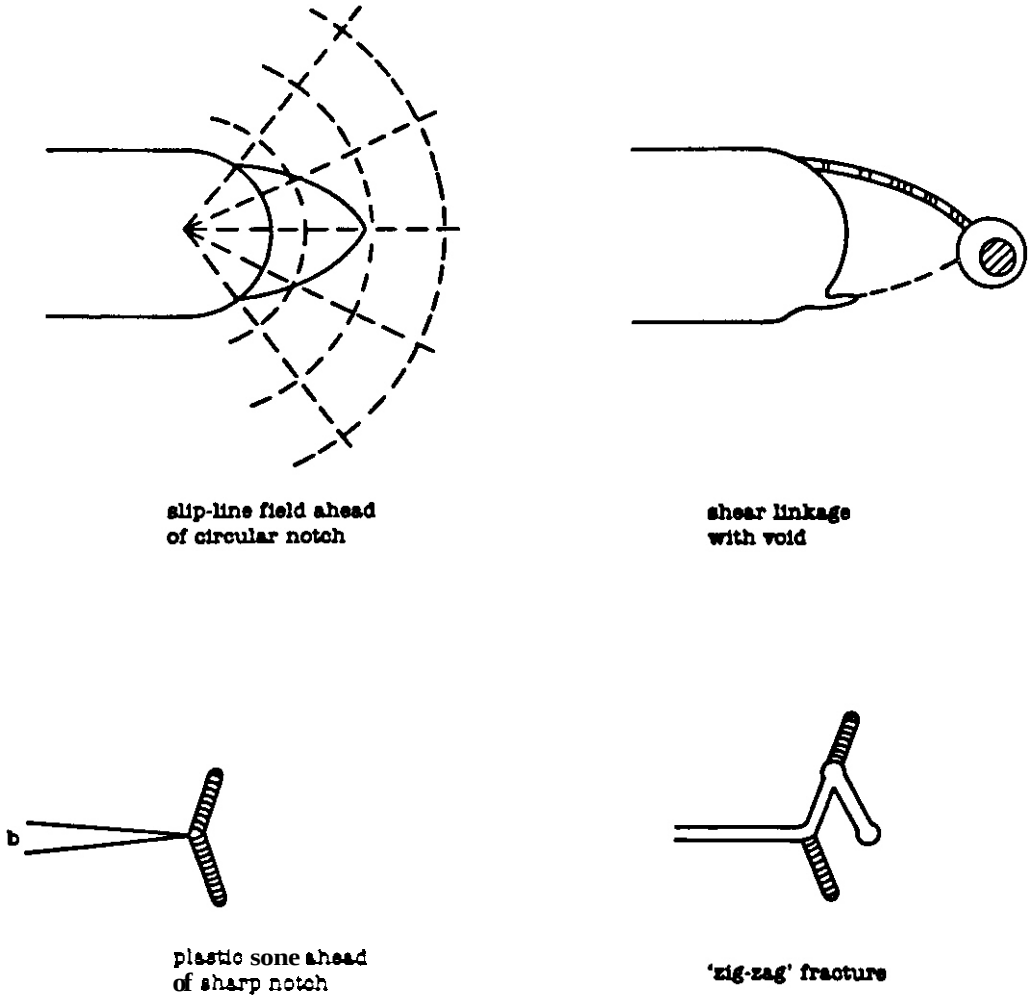

Figure 6. Illustration of flow localization effects on fracture in high strength Steels. Flow localized along a) slip bands or b) intense shear bands.

Toughness can be generally expressed by an equation of the form

$$K_{Ic} = C[El^{*}\sigma_o\varepsilon_f^{*}]^{1/2} \quad (4)$$

where C is a numerical parameter that depends on the fracture mechanisms and material parameters (e.g. the strain hardening exponent).

Various models propose different ways to define and/or measure ε_f^{*} and l^{*}. The proper choice is not trivial and, as noted above, depends very much on the microscopic characteristics of the deformation and void nucleation- growth-linking process near the crack Up. A number of efforts have been made to relate the parameters in Eq. 4 to simple tensile properties, or more sophisticated measurements such as notch tensile tests. One of the earliest such models was proposed by Krafft[55] which results in the expression

$$K_{Ic} = [\sigma_y/(1-\nu)][\pi(1+n)l(\varepsilon_f E/\sigma_y)^{(1+n)}]^{1/2} \quad (5)$$

where l is the dimple spacing and ε_f is the true fracture strain. Hamilton et. al.[56] have applied the Krafft model to irradiated stainless steels using tensile properties, as suggested by Schwalbe and Backfish.[57] Hamilton et. al. assumed that the true fracture strain is the total elongation, n was derived from the ultimate tensile stress and uniform elongation, and l set equal the grain diameter. The calculations were compared to data for a 20% CW 316 alloy tested and irradiated to about 50 dpa at 379°C in a fast reactor. The predicted toughness was 76 MPa$\sqrt{m}$ consistent with observed value of about 60 MPa$\sqrt{m}$. Wolfer and Jones showed that this model was also reasonably consistent with unirradiated toughness trends.[58]

Ritchie. Knott and Rice (RKR) used a more rigorous approach to relating critical parameters to singular crack fields. resulting in an expression similar to Eq. 4 with C approximately unity.[59] Subsequently, Ritchie et. al.[60] used the RKR model to predict upper-sheif toughness changes in unirradiated pressure vessel steel, determining ε_f^{*} from notched tensile tests and using l^{*} as an adjustable fit parameter equal to a small multiple of the prior austenitic grain size. Similar tests could be carried out for irradiated specimens but such data were not available at the time of this work. The advantage of using notch tensile data is that the stress state more closely resembles that found at a crack tip,The disadvantage of this approach is the fact that the stress and strain and stress-state histories will be different in the notched tenslle and crack tip cases, the rather ambiguous definition of l^{*}, and statistical effects related to alloy homogeneity.

More recently, Thompson and Ashby[61] have proposed using the ratio of the dimple height (h) to width (W) ratio (M = h/W) to define local fracture strains. This geometry is illustrated in Figure 7. The true fracture strain can be computed from h and the void-nucleating particle diameter (D_p) as

$$\varepsilon_f^{*} = \ln(h/D_p). \quad (6)$$

Toughness can then be computed from the RKR model laking l^{*} as the dimple spacing. Expressed in terms of the volume fraction (f_p) of the particles

$$K_{Ic} \approx [0.33\sigma_o \ln(M^2/3f_p)E/(1-\nu^2)]^{1/2}. \quad (7)$$

The fields in these models are for homogeneous deformation and the effect of volds and flow localization is not explicitly treated. Hahn and Rosenfield[50] have proposed a model which contains some elements of localization phenomena by treating shea; zones emanating from the crack with an inclination of 75' with finite widths of w. Taking the fracture strain as 1/3 of the uniaxial fracture RA (to account for stress-state effects) , toughness is given by the expression

$$K_{Ic} \approx [2/3E\sigma_y wRA]^{1/2} \quad (8)$$

Further, they noted that there was an empirical relation between the strain hardening exponent and the width of the shear band as $w \approx c_1 + c_2 n^2$. For typical unirradiated stainless steel parameters (RA ≈ 0.8, σ_y ≈ 150, n≈0.3) toughness values of about 180 MPa$\sqrt{m}$ are predicted. For irradiated alloys with very low values of strain hardening or uniform elongation ($n \approx \varepsilon_u \approx 0$) the shear zone width is a minimum of $w \approx c_1$ (≈13 pm). In spite of the relatively large minimum shear band width compared to measured values of dislocation channels (<1 μm) this model predicts very low toughness levels of about 22 MPa$\sqrt{m}$ for irradiated alloys (e.g. RA ≈0.4, σ_y ≈ 850 MPa).

Wolfer and Jones[58] have modified a localization model of Smith et. al.[62] and derive a toughness relation

$$K_{Ic} \approx 8.3\sqrt{\mu\tau_o w_f (d/b)} \qquad (9)$$

where τ_o is the critical resolved shear stress. d is the critical shear displacement for failure by decohesion in a channel, w_f is the channel width and b the Burgers vector. Using measured properties and channel widths and shear displacements prior to fracture as marked by void elongation they estimate a lower toughness bound for highly irradiated 304L to be 30 $MPa\sqrt{m}$.

Finally. Ritchie and Thompson[47] have shown that dJ/da varies approximately proportionately to J_{Ic}/l^*. Thus the tearing modulus is

$$T_R \approx J_{Ic}(E/l^*\sigma_o^2) \qquad (10)$$

H e m , irradiation, which decreases J_{Ic} and increases σ_o, can be expected to have a very large effect on T_R. For example. reductions in toughness and increases in flow stress by factors of 2.5 would decrease T_R by a factor of 2.5^4 or 39. This could be further decreased by higher values of l^*.

There are clearly a number of defkiencies in all these models, some of which already have been noted (e.g. statistical effects, effect of holes and flow localization of the crack tip fieids, mechanisms of localization and shear decohesion processes). Further, J-dominated fields require finite strain hardening, and at low values of n size requirements for singularity fields become very large. Other unresolved issues are mechanisms for hole nucleation. treatment of fields and fracture processes in three dimensions, the effect of localization on hole nucleation and growth (as well as ligament instability), and failure processes controlled by more than one feature and or event (e.g. multiple hole interactions).

However, when coupled with the fractographic and microstructural observations the models provide considerable insight into the mechanisms leading to embrittlement. The models suggest that the reductions in toughness in irradiated Stainless steels are primarily due to the large reduction in crack tip ductility (note that the increased yield strength. in itself, would increase the toughness). The high matrix strength levels and strain concentrations in deformation channels in irradiated alloys may promote void nucleation at small macroscopic strains. However. the low ductility is probably primarily the result of flow localization on the deformation voidcrack tip (or void-void) ligaments as a consequence of the low strain hardening of irradiated alloys. The flow localization and low strain hardening can be related to the irradiation induced microstructure. Further. the degradation of toughness should be qualitatively related to observed changes in the tensile properties.

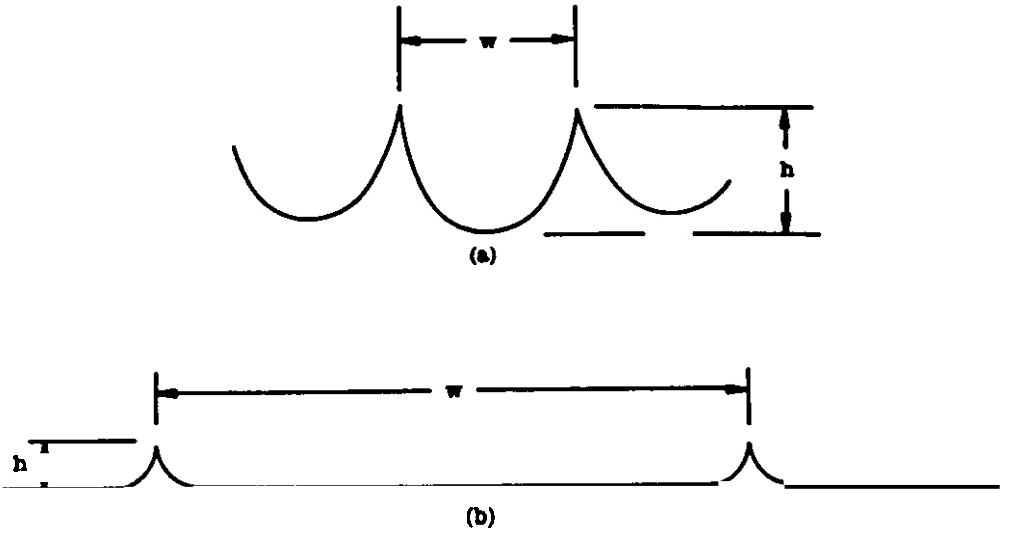

Figure 7. illustration of dimple geometry.

Based on these concepts it may be possible to correlate changes in toughness with changes in the tensile properties as

$$K^{i}_{Ic}/K_{Ic}{}^{u} \approx \sqrt{P_e} \qquad (11a)$$

where the embrittlement parameter P_e is defined as

$$P_e \approx (UE^{i}/UE^{u})(\sigma_0{}^{i}/\sigma_0{}^{u}) \qquad (11b)$$

Figure 8 compares the K^{i}_{Jc} data for plates and welds to the calculated values from Eq. 11. The parameter P_e was constructed from mean trend lines in the tensile data shown in Figures 1 to 3. The property changes were assumed to saturate above 6 dpa. Nominal unirradiated toughness values were taken as 300 MPa$\sqrt{m}$ for SA alloys and 220 MPa$\sqrt{m}$ for the welds. The simple correlation clearly predicts the correct trends.

The qualitative agreement between the simple model based evaluations and experimental observations of irradiation effects on toughness is encouraging. In particular, the model permits use of a variety of microstructural and mechanical property information to supplement the direct evaluation of toughness.

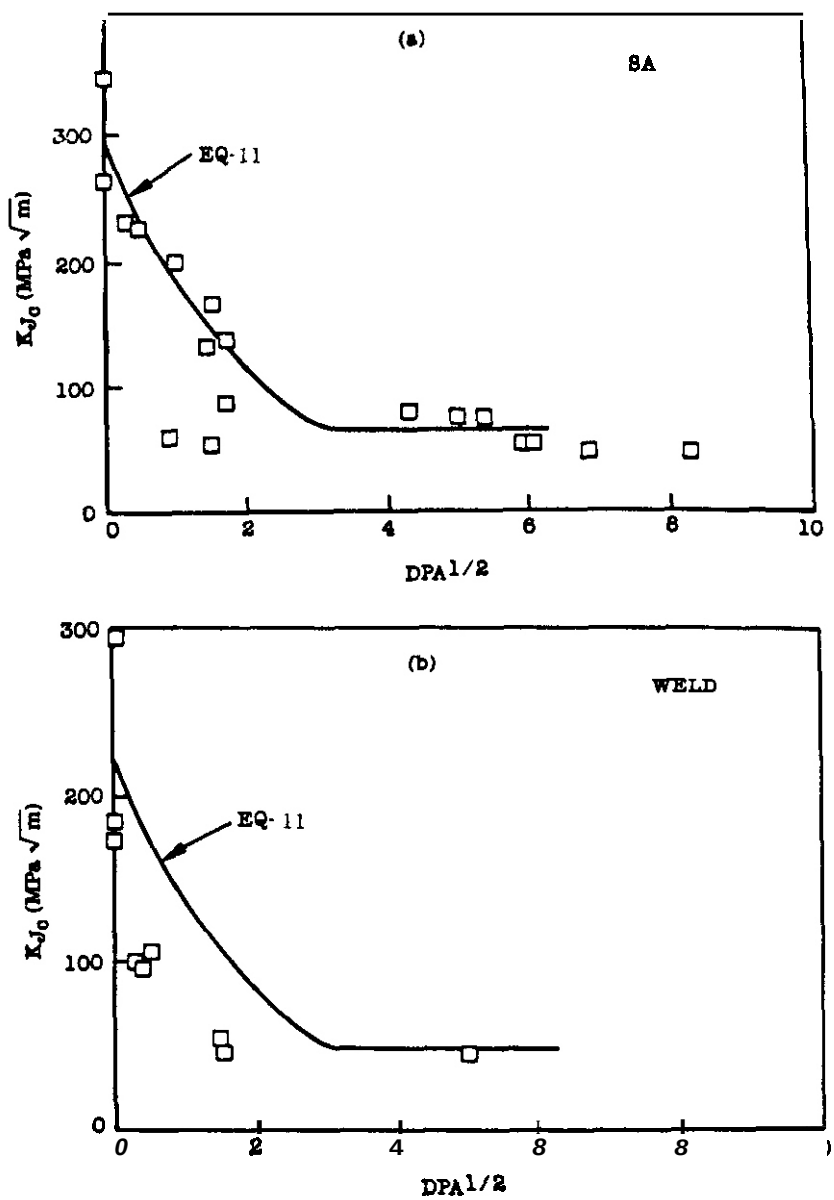

Fig. 8. Comparison of predictions of a simple fracture toughness change model with data for a) SA and b) weld material.

Irradiation Creep

Based on a brief survey of the literature, significant rates of irradiation creep (IC) can be anticipated for austenitic alloys for irradiations at or near 300°C.[12,63-69] Some trends in the IC behavior of CW alloys (note more data are available for CW than SA alloys) were also evaluated but are not tabulated here. These data support the following conclusions:

1) At low stresses the IC strain can be approximated as

$$\varepsilon = \sigma B(dpa) \qquad (12)$$

where B is creep compliance. The average value for B found in fast and mixed spectrum irradiations of 300 series austenitics (304, 316 and 348) in the SA condition is around 0.5 to $2x10^{-6}$/(MPa-dpa). For comparison, representative compliances for some SA alloys are given in Table 5; these average approximately $1.35\pm0.5x10^{-6}$/(MPa-dpa) for irradiation temperatures between 230 and 425°C in both mixed and fast spectrum reactors. In general the creep compliance of CW alloys is similar to that found for the SA condition.[64-67] Coupled with the fairly narrow range of compliances in SA material, this suggests composition and microstructure have a fairly small effect on IC. However. one study on CW 316 indicated minor solute additions had a large effect on IC.[71]

2) Compliances tend to decrease with increasing irradiation temperature in the range of 250-400°C. However, differences are expected to be less than a factor of 2.

3) Compliances increase with decreasing damage rates below about $5x10^{-7}$ dpa/s. The effect is particularly strong and systematic in CW alloys, where B increases by about a factor of 4 at 10^{-8} dpa/s.[70] Effects are less pronounced in SA alloys.[65]

4) The average B for SA alloys given above excludes one data point for a 348 steel irradiated in a mixed spectrum reactor at about 350°C, which had a much higher value [$B \approx 5.4x10^{-6}$/(MPa-dpa)].[12] Other irradiations of CW alloys in mixed spectrum reactors have also produced higher creep rates compared to fast reactor irradiations of the same alloys by factors of 3 to 10.[72] However, flux and alloy-to-alloy variations confound reaching any firm conclusion about the effect of irradiation spectrum on IC.

5) The creep behavior outlined above is for cases without void swelling. There appears to be coupling between IC and swelling. Swelling directly contributes to permanent deformations as well.

TABLE 5
CREEP COMPLIANCES OF SA 300 SERIES STEELS

ALLOY	T_i (°C)	S	B ($x10^6$/MPa-dpa)	Ref
348	305	M	1.9	12
316	428	F	1	12
304	425	F	1	63
316	230	F	1.8	64
304	297	M	1.1	65
316	400	F	1	66

Various mechanisms and models have been proposed to explain IC.[12,64,73,74] The magnitudes of compliances, the linear stress dependence and the relative insensitivity to irradiation temperature are generally consistent with a stress-induced preferred absorption (SIPA) model.[73] The SIPA mechanism postulates that interstitials are preferentially absorbed by edge dislocations with a Burgers vector in the direction of the applied stress. It has been noted that SIPA models are not consistent with the lack of sensitivity to dislocation density. Hence, a large number of alternate mechanisms have been proposed such as irradiation assisted climb-glide[64] and enhanced diffusional relaxation of grain boundary creep accommodation strains.[12] No model is fully satisfactory and it is not possible to select a single best mechanism appropriate to low to intermediate irradiation temperatures based on available information.

CONCLUSIONS

Austenitic stainless steels inadiated at or near 300°C can be embrittled in service and may approach a saturated or slowly changing property state at exposures above about 5 dpa. The estimated properties in this condition are summarized in Table 6.

The fracture resistance of large components will probably be amenable to an elastic-piastic type fracture analysis if they contain long cracks which are loaded primarily with bending Stresses. Other components with smaller characteristic size scales (e.g. first wall) with primarily tensile loaded part-through or center-crack flaws, will generally have a higher effective toughness. Evaluation procedures, such as the failure assessment diagram,[75] could be used to estimate fracture loads. It is possible that the fracture loads will actually increase due to irradiation,[76] due to the large elevation of the YS. However, in all cases the structures will have very little ductility, and can be expected to fail if there are significant displacements imposed. Further, due to the markedly increased propensity to fast shear deformation and fracture in the inadiated state there may be some flaw geometries (e.g. asymmetric edge cracks" and Mode II or III cracks) which will have particularly low fracture ductilities. Hence, realistic failure assessment of Irradiated first wall structures will require a thorough mechanics assessment of structural response for the range of imposed loads which are anticipated.

High loading rates may also be an issue. Dynamic toughness estimates based on Charpy-V-notch (CVN) maximum load type measurements may provide unconservative values of K_{Jd}. Indeed, actual toughness values may decrease with increasing loading rates. For example, we understand that austenitic components irradiated above 370°C to high exposures, have shattered when dropped,[78] in spite of the fact that their measured toughness levels were relatively high (>70 MPa$\sqrt{m}$).

Finally, we note that in practice there may be significant synergisms which were not considered in this analysis. For example, interactions between IASCC. hydrogen and creep embrittlement, fatigue crack growth (da/dN) and degraded toughness may be significant.[58] Other interactive phenomena may be IC (e.g. relaxed crack tip stresses and added damage component) and void swelling (deformations/stresses, metallurgical instabilities and modified fracture modes).

TABLE 6
IRRADIATEDPROPERTY SUMMARY

Condition	YS(MPa)	UTS(MPa)	UE(%)	TE(%)	K_{Jc}(MPa$\sqrt{m}$)	TR	B(MPa$\sqrt{m}$)
BASE	850	850	0.5	5	50	< 10	1.5×10^{-6}
WELD	850	850	0.5	5	< 50	< 10	1.5×10^{-6}

FUTURE WORK

The following areas of research are suggested for an irradiation program to assess the response of austenitic steels in the low temperature regime.

1) Microstructural Characterization

a) Comprehensive TEM evaluation of irradiation-induced microstructures including loops. bubbles and network dislocations (and voids and precipitates if needed) should be used to characterize the key components of the hardening microstructures.

b) High resolution analytical TEM (AEM) should be used to characterize grain boundary segregation; other techniques such as Auger electron spectroscopy (AES) could also be used to complement the AEM.

c) TEM techniques (including replication studies) should be applied to evaluate deformation patterns (localization) in deformed tensile and other special specimen configurations.

d) Scanning electron microscopy (SEM) should be used to characterize fracture surface morphology (dimple size and height and the inclusion content) and crack tip field-microstructure interactions (in sectioned specimens).

e) Measurement of magnetic phases (ferrite and martensite) and gross density changes should be carried Out.

f) Similar characterizations of unirradiated (archival) materials is necessary to interpret the effects of irradiation. Ideally thermally aged materials (or those with low exposures subject to a similar thermal history) should also be examined as controls. Further, measurements at several exposure levels would better detennine the evolution of the microstructure.

2. Mechanical Properties - Tensile

a) Tensile tests using small specimens should give reliable measures of the YS and UTS. However, consideration should be given to using some round specimens of adequate size to provlde reliable measures of the ductility parameters of TE. UE and RA.

b) Evaluation of the strength and ductility parameters of notched (round with varying notch radii or plane Strain configurations) specimens would be very useful and could provide an alternative approach to evaluating toughness.

c) Tensile evaluations should attempt to include archival and thermally aged controls where possible as well as multiple exposures.

3. Mechanical Properties - Toughness

a) Fracture toughness and tearing modulus data should be obtained at pertinent irradiation and test temperature

b) Fracture evaluations should attempt to include archival and thermally aged controls where possible as well as multiple exposures.

4. Modeling and Analysis

a) A thorough examination of relevant approaches to applying the mechanical property data to integrity analysis of first wall should be carried out.

b) Data from the program should be analyzed and modeled in the context of the evolving experimental and theoretical understanding of irradiation effects on austenitic stainless steels. In particular developments in other irradiation effects programs should be tracked and used to complement the results of this program.

REFERENCES

1. S. Amelinckx, J. Nucl. Mater., 155-157 (1988) 3
2. P. Maziasz, Effects of Helium on Microstructural Development In Type 316 Stainless Steel Under Neutron Irradiation, ORNL-6121 (1985).
3. P. Maziasz, Alloy Dev. for Irrad. Perform. Prog. Rep. 14, DOE/ER-0045/8, (1982),250
4. P. Maziasz and D. Braski, Alloy Dev. for Irrad. Perform. Prog. Rep. 16, DOE/ER-0045/9 (1983) 44.
5. S. Hamada, M. Tanaka and P.Maziasz, Alloy Dev. for Irrad. Perform. Prog. Rep. 22, DOE/ER-0045/15 (1985) 61.
6. S. Hamada. M. Tanaka and P.Maziasz, ibid. 15, 65.
7. M. Tanaka, S. Hamada and P.Maziasz, Alloy Dev. for Irrad. Perform. Prog. Rep. 23, DOE/ER-0045/16 (1986) 26.
8. P. Maziasz, Alloy Dev. for Irrad. Perform. Prog. Rep. 14, DOE/ER-0045/7 (1966) 54.
9. S. Hamada. M. Tanaka and P.Maziasz, Fusion Reactor Materials Prog. Rep.-1, DOE/ER-0313/1 (1987) 269.
10. M. Suzuki. S. Hamada and M. Tanaka, Fusion Reactor Materials Prog. Rep.-2, DOE/ER-0313/2 (1987) 213.
11. P. Maziasz, ibid 19, 78.
12. J. Beeston and L. Thomas, Effects of Irradiation on Materials-11, ASTM-STP 782 (1982) 71.
13. G. Odette, P. Maziasz and J. Spitznagel. Journ. Nucl. Mat. 85&86 (1979) 1289.
14. G. Odette. ibid 6, 127.
15. G. Odette. Journ. Nucl. Mat. 85886 (1979) 533.
16. D. Norris. C. Baker and J. Titchmarsh, Materials for Nuclear Reactor Core Applications-I, British Nuclear Energy Society (1987) 277.
17. J. Perks and S. Murphy, ibid 26, 165.
18. M. Kangilaski. Effects of Neutron Radiation on Materials. Mattelle Memorial Institute REIC Report No. 45 (1967).
19. J. M. Beeston, Effects of Irradiation on Materials-10, ASTM-STP 725 (1961) 303.
20. W. Martin and J. Weir, Flow and Fracture of Metals and Alloys in Nuclear Environments, ASTM-STP 380 (1964) 251.
21. R. Klueh, Alloy Dev. for Irrad. Perform. Prog. Rep.19, DOE/ER-0045/12 (1986) 45.
22. M. Tanaka. S. Hamada, P. Maziasz and M. Grossbeck, ibid 17, 33.
23. M. Grossbeck, ibid 22, 254.
24. F. Wiffen, Alloy Dev. for Irrad. Perform. Prog. Rep. 7, DOE/ER-0058/7 (1980) 128.
25. F. Wiffen, Alloy Dev. for Irrad. Perform. Prog. Rep. 8, DOE/ER-0045/1 (1986) 28.
26. D. Braski and P. Maziasz, ibid 31, 61.
27. J. Irvin and A. Bement. Effects of Radiation on Structural Metals, ASTM-STP 428 (1967) 278.
28. F. Loss and R. Gray, Toughness of Irradiated Type 316 Forging and Weld Metal Using the J-Integral, NRL Report 2875 (1974).
29. F. Loss and R. Gray, J-Integral Charcaterization of Irradiated Stainless Steels, NRL Report 7565 (1973).

30. J. Bamaby, P. Barton, R. Boothby, A. Fraser. G. Slattery, Radiation Effects in Breeder Reactor Structural Materials. TMS-AIME (1977) 159.

31. K. Erlich, ibid 6, 127.

32. R. Fish and C. Hunter, Irradiation Effects on the Microstructure and Properties of Metals, ASTP-STP 611 (1976) 119.

33. M. Grossbeck and P. Maziasz, Alloy Dev. for Irrad. Perform. Prog. Rep. 3, DOE/ER-0058/3 (1979) 32.

34. G. Odette and M. Frey. ibid (85), 817.

35. E. Bloom. Radiation Damage in Metals, ASM (1975) 295.

36. R. Fish, J. Straalsund, C. Hunter and J. Holmes, Effects of Irradiation of ther Substructure and Properties of Metals and Alloys, ASTM-STP 529 (1973) 149.

37. M. Hamilton, F. Huang and F. Gamer, Ibid 23 (22), 217.

38. M. Makin and J. Sharp, Phys. Stat. Solidi, 9 (1965) 109.

39. Mod and Mura, Matls. Science and Eng., 26 (1976) 89.

40. F. Haggag, W. Server, W. Reuter and J. Beeston, Effects of Irradiation on Materials-12, ASTM-STP 870 (1984) 548.

41 J. Bernard and G. Verzeletti, Proc. Syp. on Users Experience with Elastic-Plastic Fracture Toughness, April 20-22, 1983. Lousville. KY (preprint).

42. W. Mills, Fractur Toughness of Irradiated Stainless Steel Alloys, HEDL-SA-3471 (1986)

43. J. Dufrense. B. Henery. H. Larsson. Effects of Irradiation on Materials-9, ASTM-STP 683 (1979) 511

44. J. Hawthorne, Fatigue and Fracture Resitnace of Stainless Steel Weld Deposits After Elevated Temperature Irradiation. NRL Report-6451 (1980).

45. E. Little, Ibid (870), 563.

46. G. Lucas and D. **Gelles,** The Influence of Irradiation on Fracture and Impact Properties of Fusion Reactor Materials. to be published Joum. Nucl. Mat.

47. R. Ritchie and A. Thompson, Met. Trans. A, 16A (1985) 233.

48. ASTM E399-83, "Standard Test Methods for Plane Strain Fracture Toughness of Metallic Materials', 1983 Annual Book of ASTM STandards, Section 3, ASTM (1983) 170.

49. ASTM E813-81, "Standard Test Method for J_{Ic}, a Measure of Fracture Toughness', ibid. 762.

50. G. Hahn and A. Rosenfield. Applications Related Phenomena in Titanium Alloys, ASTM-STP 432 (1968) 5.

51. M. Stout and W. Gerberich. Closed Loop, 12-1, MTS Systems Corporation (1962) 12.

52. J. Rice and M. Johnson, Inelastic Behavior of Solids, McGraw Hill (1970) 641.

53. R. McMeeking, J. Mech. Phys. Solids, 25 (1977) 357.

54. J. Knott. Met. Science, (1980) 327.

55. J. Krafft, Appl. Matls. Res.,3 (1964) 88.

56. M. Hamilton, F. Garner and W. Wolfer. Journ. Nucl. Mat. 122/123 (1984) 106.

57. K. Schwalbe and W. Backfish, Fracture 1977, ICF4, Vol. 2 (1977) 77.

58. W. Wolfer and R. Jones, Journ. Nucl. Mats. 103/104 (1981) 1305.

59. R. Ritchie, J. Knott and J. Rice, J. **Mech** Phys. Sol., 21 (1973) 395.

60. R. Ritchie, W. Server and W. Wullaert, Met. Trans., A10 (1979) 1557,

61. A. Thompson and M. Ashby, Scripta Met., 18 (1984) 127.

62. E. Smith, T. Cook and C. Rau, ibid 64, **Vol.** 1, 215.

63. K. Eriich. Journ. Nucl. Mat., 100 (1961) 149.

64. J. Boutard, Y. Carteret, R. Cauvin, Y. Gueron and A. Maillard, Dimen. Stabil. and Mech. Prop. of Irrad. **Mets.** and Alloys, BNES (1983) 109.

65. G. Lewthwaite and D. Mosedale. ibid 75. 129.

66. J. L Straalsund, ibid 40, 191.

67. D. Mosedale. D. Harries, J. Hudson, G. Lewthwaite and R. McElroy, ibid **40,** 209.

68. D. Causey, G. Carpenter and S. MacEwen, Journ. Nucl. Mat., 90 (1980) 223.

69. J. Lehmann. J. Dupouy, R. Brouder, J. Boutard ans A. Maillard. Proc. Conf. on Irrad. Behav. of Metall. Mat. for Fast teact. Core Compts., Corsica, France (1979).

70. G. Lewthwaite and D. Mosedale, Journ. Nucl. Mat. 90 (1980) 205.

71. J. Bates, R. Powell and E. Gilbert, ibid 29, 713.

72. M. Grossbeck and J. Horak, Irradiation Creep in Type 316 Stainless Steel and U.S. PCA with Fusion He/dpa Levels, to be published Journ. Nucl. Mater.

73. W. Wolfer, ibid 79, 175.

74. R. Bullough., M. Finnis, J. Matthews and M. Wood, ibid 75, 125.

75. **I.** Milne. Mat. **Sci** and Engr., 39 (1979) 65.

76. R. **Odette,** R. Ritchie, P. McConnell and W. Server, Journ. Nucl. Mat. 103/104 (1981) 149.

77. J. Hancock and M. Cowling, Met. Sci., Aug-Sept. (1980) 293.

78. Private communication, M. Hamilton.

6.3 Vanadium Alloys

SWELLING OF NEUTRON-IRRADIATED VANADIUM ALLOYS - B. A. Loomis and D. L. Smith (Argonne National Laboratory) and F. A. Garner (Pacific Northwest Laboratory)

OBJECTIVE

The objective of this research is to provide guidance on the applicability of vanadium–base alloys for structural components in a fusion reactor.

SUMMARY

The swelling of V-10.0Cr-0.1Al, V-14.1Cr-0.3Al, V-3.1Ti-0.3Si, V-4.9Ti, V-9.8Ti, V-14.4Ti, V-17.7Ti, V-20.0Ti, V-14.4Cr-0.3Ti-0.3Al, V-14.1Cr-1.0Ti-0.3Al, V-13.7Cr-4.8Ti, V-9.0Cr-3.3Fe-1.2Zr (Vanstar-7). V-14.5Ti-7.2Cr, V-8.6W, V-4.0Mo, and V-12.3Ni alloys and unalloyed V was determined after neutron irradiation at 420°C and 600°C to irradiation damage levels ranging from 17 to 77 dpa in the FFTF-MOTA reactor facility. The swelling of these alloys was obtained from a determination of the density for the unirradiated and irradiated alloys on immersion in CCl_4. The swelling of unalloyed V at 600°C was substantially increased by the addition of Cr. The addition of either Ni, W, or Mo to V had a relatively minor effect on the swelling of V. The swelling of the V-Cr-Ti alloys was strongly dependent on the Ti concentration. The swelling of the V-3.1Ti-0.3Si and V-14.4Ti alloys at 600°C was greater than that exhibited by the other binary V-TI alloys. The Vanstar-7 alloy underwent larger swelling than the V–Ti and V–Cr–Ti alloys. For the binary V-Ti alloys and the ternary V-Cr-Ti alloys, the dependence of swelling on the amount of irradiation damage was <0.1% swelling per dpa.

PROGRESS AND STATUS

Introduction

The swelling of V-15Cr-5Ti, Vanstar-7, V-3Ti-1Si, V-20Ti, and V-15Ti-7.5Cr alloys on neutron irradiation at temperatures ranging from 420 to 600°C and irradiation damage levels ranging up to 40 atom displacements per atom (dpa) have been reported by several investigators.[1-7] The results obtained from these investigations have shown that the V-15Cr-5Ti, V-3Ti-1Si, V-20Ti, and V-15Ti-7.5Cr alloys are resistant to swelling and typically exhibit swelling values of <0.3%. The results obtained from these investigations also show that the Vanstar-7 alloy can exhibit swelling values ranging up to 6%.

Ohnuki et al. have determined the swelling of V-3Cr, V-15Ti, and V-3Mo alloys after neutron irradiation at 500-600°C to approximately 1 dpa.[8] The swelling values reported for these neutron-irradiated alloys suggest that (1) Ti strongly suppresses swelling of V, (2) Cr exacerbates swelling of V, and (3) Mo has a relatively minor effect on the swelling of V.

A dimensional change (sweliing) of materials on neutron irradiation can occur as a resuit of wid formation, cavity formation, thermal- and irradiation-induced precipitate formation and dissolution, thermal- and irradiation-induced phase change, thermal- and irradiation-induced solute segregation, and anisotropic dislocation glide and climb. The swelling values that have been previously reported for neutron-irradiated V alloys have been obtained from transmission electron microscopy (TEM) observations. Therefore, these TEM welling evaluations have only taken Into account the dimensional change (swelling) that can be attributed to the presence of voids and cavities. The TEM observations of irradiated V alloys have shown the presence of copious irradiation- and/or thermal-induced precipitates.[1-8] In this report, we present for neutron-irradiated V alloys and unalloyed V swelling values that have been derived from the determination of the density of specimens on immersion in CCl_4.

Materials and procedures

Specimens with approximate dimensions of 0.3-cm-diameter and 0.03-cm- thickness were obtained from 50% cold-worked sheets of the materials listed in Table 1. The chemical analyses of these materials were performed by the Analytical Department of the Teledyne Wah Chang Albany Company. The cold-worked specimens were annealed at 1125°C for 1 h in an ion-pumped vacuum system with a typical pressure of 8×10^{-9} mm Hg.

Table 1. Materials composition

ANL I.D.	Material	Melt Number	Concentration (wt ppm) O	N	C	Si	Fe
EL–1	V–4.0Mo	ANL 1	230	73	90	110	<100
EL–2	V–8.6W[1]	ANL 2	300	150	120	59	<100
EL–3	V–12.3Ni	ANL 3	490	280	500	405	175
E L 4	V–10.0Cr–0.1Al	ANL 4	530	76	240	<50	530
EL–5	V–14.1Cr–0.3Al	ANL 5	330	69	200	<50	570
EL–10	V–7.2Cr–14.5Ti	ANL 94	1110	250	400	400	910
EL–11	V–4.9Ti	ANL 11	1820	530	470	220	7800
EL–12	V–9.8Ti	ANL 12	1670	390	450	245	6300
EL–13	V–14.4Ti	ANL 13	1580	370	440	205	6300
EL–15	V–17.7Ti	CAM 832	830	160	380	480	390
EL–16	V–20.0Ti	CAM 833	390	530	210	480	390
EL–20	V	ANL 20	570	110	120	325	<100
EL–21	V–13.7Cr–4.8Ti	CAM 835	340	510	180	1150	300
EL–22	V–13.4Cr–5.1Ti	ANL 114	300	52	150	56	140
EL–23	V–12.9Cr–5.9Ti	CAM 834	400	490	280	1230	420
EL–24	V–13.5Cr–5.2Ti	ANL 101	1190	360	500	390	520
EL–25	V–14.4Cr–0.3Ti–0.3Al	ANL 25	390	64	120	<50	680
EL–26	V–14.1Cr–1.0Ti–0.3Al	ANL 26	560	86	140	<50	650
EL–27	V–3.1Ti–0.3Si[2]	ORNL 10837	210	310	310	2500	380
BL–28	V–9.0Cr–3.3Fe–1.2Zr[3]	CAM 837	275	540	740	–	–
EL–34	V–8.6Ti	ANL 34	990	180	420	290	150
EL–35	V–9.5Cr–0.2Al	ANL 35	340	45	120	<50	410
EL-35	V	ANL 36	810	86	250	<50	<100
BL–48	EL-23 + 20% CW	CAM 834	400	490	280	1230	420

[1]Alloy EL–2 contained 365 ppm Nb; all other alloys contained <100 ppm Nb.
[2]Alloy EL–27 contained 250 ppm Ta.
[3]Vanstar–7 alloy.

The annealed specimens were irradiated at 420°C and 600°C in lithium-filled TZM capsules during cycles 7, 8, and 9 of the FFTF-MOTA reactor facility to neutron fluences (E > 0.1 eV) ranging from 2.8 x 10^{22} n/cm^2 (17 dpa) to 13.1 x 10^{22} n/cm^2 (77 dpa). The specimens that were irradiated at 600°C experienced a temperature excursion of 249°C for 50 min during cycle 7 of the FFTF-MOTA. The irradiated specimens were removed from the lithium-filled TZM capsules by immersion of the opened capsules in liquid NH_3 and subsequent immersion in a 50/50 mixture of ethanol and methanol.

The swelling (S) of an irradiated specimen was obtained from a determination of the density of an annealed, unirradiated (D_{ann}) specimen and an irradiated (D_{in}) specimen on immersion in CCl_4, i.e.,

$$S = (D_{ann} - D_{in}) / D_{ann} .$$

The reported density for a specimen was determined with a precision of 0.2% from 6-10 separate determinations on a specimen. In the case of specimens irradiated at 600°C, some specimens of an alloy (with ostensibly the same irradiation conditions) had significantly different (2-3%) welling values. and these values are listed separately in Table 2.

Experimental results

The welling values for neutron-irradiated specimens of the V alloys and unalloyed V (Table 1) are presented in Table 2. The density (D_{ann}) values for the annealed alloys and unalloyed V are also listed in Table 2. The data in Table 2 suggest that the addition of either Ni, W, or Mo to V had a relatively minor effect on the swelling of V.

Table 2. Swelling of neutron–irradiated V alloys and unalloyed V

ANL I.D.	Material	D_{ann} (g/cc)	Irradiation Temperature 420°C DPA	420°C S (%)	600°C DPA	600°C S (%)
EL–1	V–4.0Mo	6.227	36	1.12	17	0.60
EL–2	V–8.6W	6.448	36	2.30	17	0.51
BL-3	V–12.3Ni	6.336	36	1.06	17	0.60
BL–4	V–10.0Cr–0.1Al	6.204	36	2.39	17	1.64
BL–4	V–IO.OCr-0.I Al	6.204	77	0.53	77	41.60
EL–5	V–14.1 Cr–0.3Al	6.277	36	3.76	17	1.16
EL–5	V–14.1 Cr–0.3Al	6.277	–	–	77	36.65
BL–10	V–7.2Cr–14.5Ti	6.687	36	0.61	21	0.76
EL–10	V–7.2Cr–14.5Ti	5.867	46	0.97	–	–
EL–10	V–7.2Cr–14.5Ti	5.887	77	0.18	–	–
EL–11	V–4.9Ti	6.007	36	0.03	17	–0.33
BL–11	V–4.9Ti	6.007	77	0.01	77	1.39
BL–11	V–4.9Ti	6.007	–	–	77	3.47
EL–12	V–9.8Ti	5.912	36	0.74	17	–0.10
EL–12	V–9.8Ti	5.912	77	0.22	77	1.41
EL–13	V–14.4Ti	5.835	36	0.63	21	0.60
BL–13	V–14.4Ti	5.835	77	0.39	77	2.66
EL–13	V–14.4Ti	5.835	–	–	77	7.71
EL–15	V–17.7Ti	5.704	36	0.12	21	–0.04
EL–15	V–17.7Ti	5.704	46	–	77	0.96
EL–15	V–17.7Ti	5.704	77	0.20	77	3.42
EL–16	V–20.0Ti	5.711	36	0.29	17	0.09
BL–16	V–20.0Ti	5.711	77	0.15	77	0.96
BL–20	V	6.099	36	1.67	21	0.26
EL–20	V	6.099	73	5.75	77	1.53
BL–21	V–13.7Cr–4.8Ti	6.173	36	0.44	21	0.42
EL–21	V–13.7Cr–4.8Ti	6.173	73	1.99	77	4.46
BL–21	V–13.7Cr–4.8Ti	6.173	–	–	77	6.12
EL–22	V–13.4Cr–5.1Ti	6.151	36	1.44	17	0.33
BL–22	V–13.4Cr–5.1Ti	6.151	73	0.89	77	5.37
BL–22	V–13.4Cr–5.1Ti	6.151	–	–	77	6.67
EL–23	V–12.9Cr–5.9Ti	6.145	36	1.26	21	0.26
EL–23	V–12.9Cr–5.9Ti	6.145	73	1.95	77	3.63
EL–23	V–12.9Cr–5.9Ti	6.145	–	–	77	4.26
BL–24	V–13.5Cr–5.2Ti	6.151	36	0.08	17	0.11
EL–24	V–13.5Cr–5.2Ti	6.151	46	1.17	77	3.63
BL–24	V–13.5Cr–5.2Ti	6.151	73	3.11	77	6.32
BL–25	V–14.4Cr–0.3Ti–0.3Al	6.226	36	0.46	17	0.26
BL–25	V–14.4Cr–0.3Ti–0.3Al	6.226	–	–	77	14.88
EL–26	V–14.1 Cr–1.0Ti–0.3Al	6.235	36	0.85	17	0.77
EL–28	V–14.1 Cr–1.0Ti–0.3Al	6.236	73	3.40	77	5.76
BL–27	V–3.1Ti–0.3Si	6.039	36	1.97	17	1.79
EL–27	V–3.1Ti–0.3Si	6.039	73	2.59	77	8.12
EL–27	V–3.1Ti–0.3Si	6.039	73	3.11	77	2.42
BL–28	V–9.0Cr–3.3Fe–1.2Zr	6.261	36	1.18	17	1.24
BL–28	V–9.0Cr–3.3Fe–1.2Zr	6.261	73	2.75	77	6.81
EL–28	V–9.0Cr–3.3Fe–1.2Zr	6.261	–	–	77	9.67
EL–34	V–8.6Ti	5.933	36	1.24	17	0.72
BL–34	V–8.6Ti	5.933	73	1.06	77	3.63
BL–34	V–8.6Ti	5.933	–	–	77	5.42
BL–35	V–9.5Cr–0.2Al	6.214	36	0.45	17	2.72
EL–35	V–9.5Cr–0.2Al	6.214	73	0.94	77	42.40
BL–36	V	6.110	36	1.21	17	0.10
BL–36	V	6.110	73	5.94	77	2.73
EL48	EL–23 + 20% CW	6.126	36	0.88	17	1.47

The dependence of swelling on Ti concentration for the binary V-Ti alloys on neutron irradiation at 420°C to 36 dpa and 73-77 dpa is shown in Fig. 1. For the purpose of Fig. 1, we consider that the Si content in the V-3Ti-0.3Si alloy (BL-27) did not significantly affect the swelling of binary V-Ti alloys. The swelling of V decreased with the addition of Ti to a concentration of approximately 5 wt %, and was nearly independent of Ti concentration in the range of 5 to 20 wt % Ti.

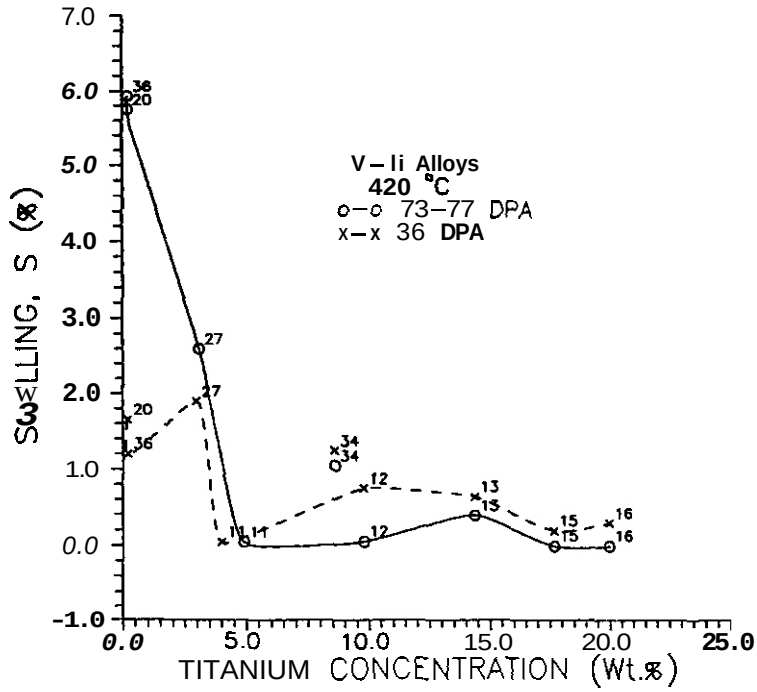

Fig. 1. Swelling of V–Ti alloys on neutron irradiation at 420°C to 36 dpa and 73–77 dpa (data point numbers refer to ANL I.D. in Table 1).

The dependence of swelling on Ti concentration for the binary V-Ti alloys on neutron irradiation at 600°C to 17 dpa and 77 dpa is shown in Fig. 2. The swelling of V was substantially increased for Ti concentrations of 3.1 and 14.4 wt % and was nearly independent of Ti concentration in the range of 5 1 0 and >17.7 wt % Ti. The V-8.6Ti (BL-34) alloy exhibited significantly higher swelling than the V-9.8Ti (EL-12) alloy (Figs. 1 and 2). The higher swelling of the V-8.6Ti alloy may be attributed to the lower oxygen concentration (990 ppm versus 1620 ppm, Table 1) in the V-8.6Ti alloy.

The dependence of swelling on Ti concentration for the V-(10-15)Cr-Ti alloys on neutron irradiation at 420°C to 73 dpa and 600°C to 77 dpa is shown in Fig. 3. For the purpose of Fig. 3, we consider that the presence of Al in the alloys did not have a significant impact on the swelling of the alloys. These swelling results suggest that the presence of 1.0 wt % Ti in the V-(10-15)Cr alloys caused a significant increase (2-3%) in swelling of the V-(10-15)Cr alloy on irradiation at 420°C to 73 dpa, but higher Ti concentrations did not result in an additional change of swelling. However, the presence of 0.3-1.0 wt % Ti in the V-(10-15)Cr alloys caused a substantial (25-40%) decrease of swelling for these alloys on irradiation at 600°C to 77 dpa. with no significant change of swelling for higher concentrations of Ti.

The dependence of swelling at 600°C on neutron irradiation damage (dpa) for the V-4.9Ti, V-17.7Ti, V-20.0Ti, V-3.1Ti-0.3Si, V-14.5Ti-7.2Cr, Vanstar-7, V-13.7Cr-4.8Ti, V-13.4Cr-5.1Ti, V-12.9Cr-5.9Ti, and V-13.5Cr-5.2Ti alloys is shown in Fig. 4. The swelling of these alloys ranged from 0.02 to 0.14% per dpa. The binary V-Ti alloys tended to undergo the lowest swelling (0.02- 0.05% per dpa). These data suggest that the Vanstar-7 alloy is the least swelling resistant of the alloys. These data also suggest that the addition of Cr to binary V-Ti alloys resulted in an increase of swelling for the V-Ti alloys by a factor of approximately 2.

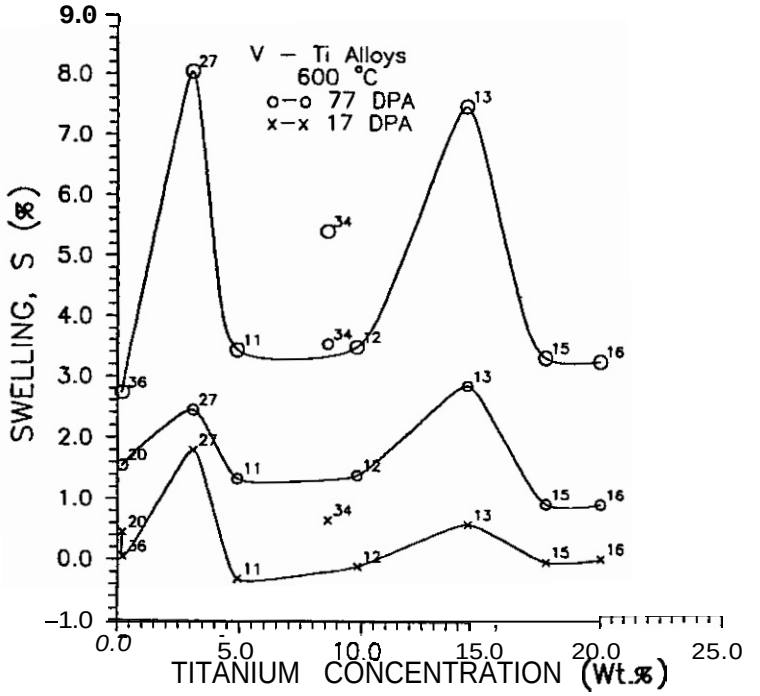

Fig. 2. Swelling of V–Ti alloys on neutron irradiation at 600°C to 17 dpa and 77 dpa (data point numbers refer to ANL I.D. in Table 1).

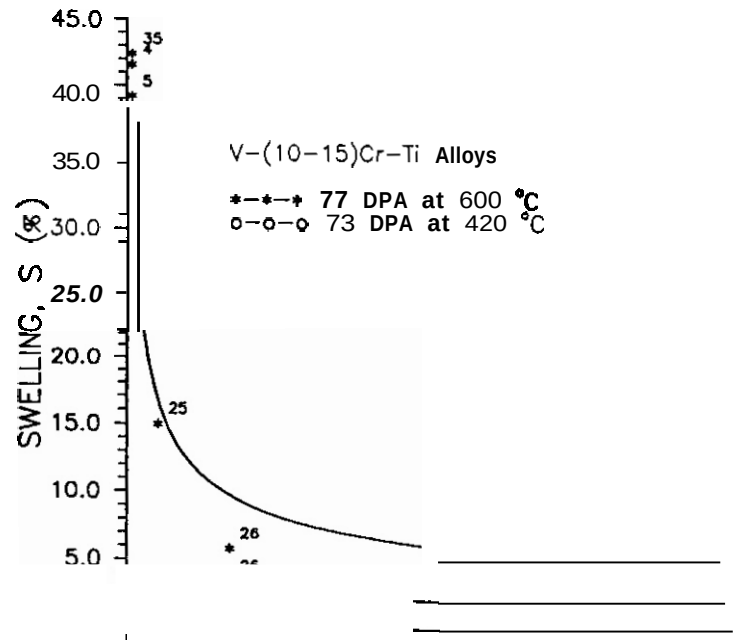

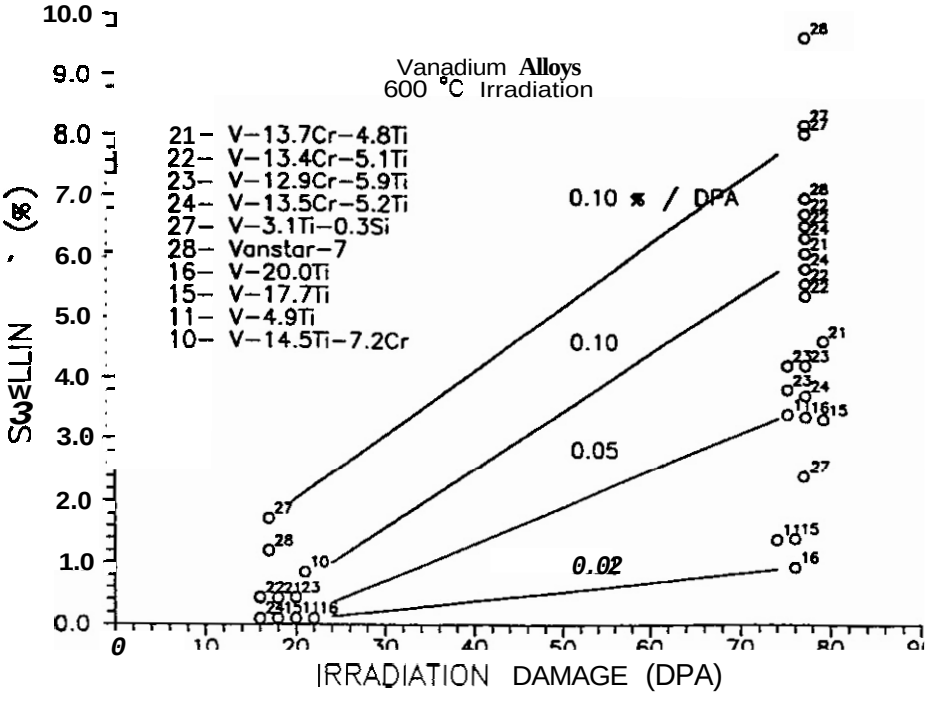

Fig. 4. Swelling of vanadium alloys on neutron irradiation at 600°C to 17–77 dpa.

Discussion of results

The swelling values presented in this report were obtained from density determinations on annealed specimens of unirradiated and irradiated alloys. It has been previously reported that V-(1.5-10.0)Ti alloys containing 1400-5000 ppm oxygen undergo aging on annealing at 550-750°C for 4-7 h.[9] Since the FFTF-MOTA reactor facility did not achieve full power within 10 h, the irradiated alloy specimens may have undergone significant aging. Therefore, the reference density for the swelling evaluations should have been the density for aged (unirradiated) specimens rather than the density for annealed (unirradiated) specimens. In addition to the aging effects that may have occurred for the specimens that were irradiated at 420 and 600°C, the specimens irradiated at 600°C underwent a temperature excursion of 249°C for 50 min. At the present time, we have no information on the impact of the aging and temperature excursion effects on the swelling of the irradiated alloys. Either or both of these effects may have contributed to the wide range (2-3%) of swelling that was determined for the alloys irradiated at 600°C.

The swelling for V-Ti alloys on irradiation at 600°C showed swelling maxima for alloys containing 3.1 and 14.4 wt % Ti (Fig. 2). The swelling maxima may have been due to the separate and/or combined effects of (1) the temperature excursion, (2) aging of the alloys, (3) phase changes, and (4) phases initially present in the alloys.[9,10]

CONCLUSIONS

1. The swelling of V-4.9Ti, V-9.8Ti, V-14.4Ti, V-17.7Ti, V-20.0Ti, V-3.1Ti-0.3Si, Vanstar-7, V-14.5Ti-7.2Cr, and V-13.5Cr-5.2Ti alloys is in the range of 0.01-0.14% per dpa on neutron irradiation at 420°C and 600°C to 77 dpa.

2. The swelling of V at 600°C is increased substantially by the addition of Cr.

3. The swelling of V–Cr alloys at 600°C is significantly reduced by the addition of Ti

FUTURE WORK

1. The density of V-base alloys will be determined after receiving an aging treatment that is similar to the time-temperature schedule for the start-upof the FFTF-MOTA reactor facility.

2. The swelling of V-base alloys that were irradiated during cycle 10 of the FFTF-MOTA will be determined for the purpose of evaluating the effect of the temperature excursion during cycles 7 and 8 on the swelling of V-base alloys.

REFERENCES

1. D. N. Braski, "influence of Radiation on Material Properties: 13th International Symposium," ASTM STP 956, F. A. Garner, C. H. Henager. Jr.. and N. Igata, Eds., American Society for Testing Materials, Philadelphia, 1986. pp. 271-290.

2. J. Bentley and F. W. Wiffen, Nucl. Technol. 30, 376-384 (1976).

3. H. Bohm, "Proceedings: International Conference on Defects and Defect Clusters in B.C.C. Metals and Their Alloys," Gaithersburg, MD, R. J. Arsenault, Ed., M. P. Graphics Inc., Washington, D. C., 1973, pp. 163-175.

4. M. L. Grossbeck and J. A. Horak, "Influence of Radiation on Material Properties: 13th International Symposium," ASTM STP 956, F. A. Garner, C. H. Henager, Jr., and N. Igata. Eds., American Society for Testing Materials, Philadelphia, 1986, pp. 291-309.

5. R. Carlander, S. D. Harkness, and A.T. Santhanum, "Effects of Radiation on Substructure and Mechanical Properties of Metals and Alloys," ASTM STP 529, American Society for Testing Materials, Philadelphia, 1973, pp. 399-414.

6. M. P. Tanaka, E. E. Bloom, and J. A. Horak, J. Nucl. Mater. 103 & 104,895-900 (1981).

7. D. N. Braski, J. Nucl. Mater. 141 & 143, 11251131 (1986).

8. S. Ohnuki, H. Takahashi, H. Kinoshita, and R. Nagasaki, J. Nucl. Mater. 155-157, 936939 (1988)

9. S. Komjathy, J. less-Common Met. 3, 468-488 (1951).

10. J. L. Murray, Phase Diagrams of Binary Titanium Alloys, ASM Monograph Series on Alloy Phase Diagrams, 1987, pp. 319-327.

LITERATURE REVIEW OF RESEARCH ON VANADIUM AND VANADIUM RASE *ALLOYS* FOR USE IN FUSION REACTOR FIRST WALL/BLANKET APPLICATIONS

- C. A Marsh and A B. Hull (Argonne National Laboratory)

OBJECTIVE

The objective of this review is to consolidate research information on vanadium and vanadium base alloys that pertains to their **use** as a reactor first-wall material.

SUMMARY

The literature was reviewed for research on **the** fabrication of vanadium base alloys and the **effects** of chemical environment. helium implantation, and neutron irradiation on the mechanical properties, microstructure. and corrosion behavior of vanadium and vanadium base alloys. ***The*** relevant material was compiled into an annotated bibliography of more than 100 representative references. These references address the topics highlighted in this report.

PROGRESS AND STATUS

Introduction

Research on the applicability of vanadium base alloys for structural components in a fusion reactor has intensified over the past 10 years in the hope of developing alloys that exhibit low induced radioactivity amenable to simplified disposal techniques. Vanadium alloy development has progressed to the point when? these materials appear to offer an excellent option as a fusion energy **source.**

Since the research on vanadium and vanadium base alloys has been extensive and far ranging, a review of the existing literature and its presentation in the form of an annotated bibliography was deemed necessary.' Research topics reviewed include the effects of helium implantation and irradiation on **the** mechanical properties and microstructure of vanadium and vanadium base alloys, and the corrosion behavior of these materials in flowing lithium and in high-pressure water. A summary of each reference in the annotated bibliography provides information that is most pertinent to determining the composition of a vanadium base alloy with the optimum combination of swelling, corrosion resistance, and mechanical properties for use in fusion reactor first-wall/blanket applications.

Results and Analysis

The dominant feasibility issue for the **use** of vanadium alloys in a fusion environment. as for **all** other alloy systems, is excessive embrittlement that can lead to failure. Thus the central theme of the vanadium alloy development effort has been to understand the dominant mechanisms that cause this embrittlement and to develop alloys that are least sensitive. Many of the results from the types of investigations mentioned above have profound implications for this issue. Table 1 summarizes the types of vanadium alloys that have been produced and tested for these various characteristics.

CONCLUSION

The existing information on vanadium and vanadium base alloys, as it pertains to their use in fusion reactors, has been compiled into an annotated bibliography of more than 100 references. The bibliography emphasizes fabrication history, chemical composition, and experimental investigations.

FUTURE WORK

Because the completed work is the subject of an ANL Technical Memorandum[1] that contains more than 100 publications dealing with the topics highlighted above, no additional compilation of references is planned at this date.

Table 1. Types of Vanadium Alloys that have been Produced and Tested

Alloy	Number of Investigations				
	Fabrication History	Chemical Environment	Helium Implantation	Mechanical Properties	Neutron Irradiation
V	1	4	1	6	5
V-20Ti		5		8	3
V-12Cr-5Ti		1		2	1
V-5Ti		2			
V-15Cr-5Ti	8	12	7	12	4
V-7.5Cr-15Ti		1			
V-15Ti-7.5Cr	1			4	1
V-10Cr-5Ti	2			2	
V-10Ti				1	
V-15Cr		2		1	
V-9Cr-3Fe-1Zr		3		4	1
V-10Cr	1				
V-10Cr-3Fe-Zr		1			
V-3Ti-0.5Si		2			
V-3Ti-1Si		3		2	1

REFERENCES

1. C.A. Marsh and A. B. Hull, in preparation.

6.4 Copper Alloys

OVERVIEW OF COPPER IRRADIATION PROGRAMS - F. A. Garner, M. L. Hamilton (Pacific Northwest Laboratory), K. R. Anderson, J. F. Stubbins (University of Illinois), B. N. Singh, A. Horsewell (RISØ National Laboratory), W. F. Sommer (Los Alamos National Laboratory)

OBJECTIVE

The objective of this effort is to provide data on the radiation response of copper alloys intended for both near-term and long-term applications in fusion systems.

SUMMARY

Researchers at Pacific Northwest Laboratory[a] are collaborating with scientists from RISØ National Laboratory, Los Alamos National Laboratory and the University of Illinois to generate data on the response to radiation of copper alloys intended for use in ITER, NET and long-term fusion devices. An overview of these experiments is presented.

PROGRESS AND STATUS

Introduction

For ITER applications, relatively pure copper and oxide dispersion strengthened (ODS) copper have been selected to serve as the high heat flux materials employed in the diverter assembly. CuBeNi has also been mentioned as a possible backup material. The choice of these alloys was strongly influenced by irradiation data generated at Westinghouse Hanford Company and Pacific Northwest Laboratory (PNL).

Although there is some uncertainty in the possible range of design parameters, the current maximum temperature anticipated for ITER applications is 475°C and the anticipated target displacement levels are relatively low (≤10 dpa). Data are therefore required for mechanical properties, thermal conductivity and dimensional stability of these alloys during irradiation in the range of 25°C to about 500°C. This report outlines the status of a series of irradiation experiments on copper alloys conducted jointly by Pacific Northwest Laboratory with the RISØ National Laboratory in Denmark and the LASREF (Los Alamos Spallation Radiation Effects Facility) group in New Mexico. The University of Illinois is also participating under the sponsorship of the NORCUS (Northwest College and University Association For Science) program. The RISØ group not only participates in the ITER effort but is also the lead laboratory for copper studies in the Next European Torus (NET) program.

Since thermal conductivity values are not easily obtained with small radioactive specimens, electrical resistivity is measured and used to calculate an estimate of the thermal conductivity. Both properties change due to transmutation and radiation-induced microstructural components, particularly voids.

Previous Experiments in Fast Reactors

There were several studies conducted in the EBR-II reactor on copper alloys to ≤15 dpa at temperatures of ~400°C, one of which was subsequently investigated at Los Alamos National Laboratory[1-3] and another at Massachusetts Institute of Technology.[4-5] Where there was overlap in the specimen matrix, these EBR-II studies agreed fairly well with a "first generation" exploratory experiment conducted in FFTF/MOTA by Pacific Northwest Laboratory and Westinghouse Hanford Company at roughly the same temperature to four dose levels ranging from 16 *to* 98 dpa.[6-9] The latter study was directed toward both near-term (ITER) and long-term, high-fluence concerns.

Each of these fast reactor studies demonstrated the potential of various ODS copper alloys to resist void swelling. In all three of the earlier experiments, however, no data were generated at temperatures below 385°C or above 425°C, leaving much of the ITER-relevant temperature range unexplored.

Ongoing Experiments in FFTF/MOTA

Based on the results of the "Generation 1" experiment, two successively more focussed experiments were designed. The "Generation 1.5" experiment contained many of the original Generation 1 alloys plus a variety of alloys strengthened by dispersoids, precipitates or spinodal decomposition. These alloys are listed in Table 1. Irradiation of TEM disks and miniature tensile specimens proceeded at 414°C to 34 dpa and at 529°C to 32 dpa in MOTA-ID. Whereas the Generation 1 specimens at higher fluence levels experienced increasing levels of self-welding and interaction with the aluminum foils used as spacers, the Generation 1.5 specimens were separated with tantalum spacers and did not interact.

(a) Operated for the U.S. Department of Energy by Battelle Memorial Institute under Contract DE-AC06-76RLO 1830.

TABLE 1

Generation 1.5 Copper Alloy Specimens in MOTA-1D

Alloy[a]	Condition	Specimen Engraving Code	34 dpa 414°C		32 dpa 529°C	
			Tensile	TEM Disks	Tensile	TEM Disks
MARZ	Annealed	RO	3	3	-	3
AL20	Annealed	UV	3	3	-	3
AL20	20% cold-worked	UX	6	6	3	6
AL20	80% cold-worked	UZ	3	3	-	3
CuBeNi	Solutionized and Aged	U1	3	3	-	3
CuBeNi	Solutionized, 20% cold-worked and aged	U3	2	6	3	6
CuBeNi	Solutionized, 20% cold-worked and aged	U4	3	3	-	3
MZC	Solutionized, 90% cold-worked and aged	U6	3	6	3	6
MZC	Solutionized, 90% cold-worked and aged	U7	3	3	-	3
MZC (MIT#2)	Solutionized and aged	U9	3	3	3	3
Cu-5Ni	Annealed	VP	3	6	-	6
MZC (MIT#3)	Solutionized and aged	VB	3	6	3	6
Cu-4Ni-4Sn (LANL)	Solutionized and aged	VN	3	3	-	3
Cu-3.5Ti (LANL)	Solutionized and aged	VT	3	6	-	6
A115+B (LANL)	Annealed	VO	3	3	-	3
Cu-5Ni-2.5Ti (MIT#6)	Solutionized and aged	VK	3	6	3	6
Cu-5Ni-2.5TI (LANL)	Solutionized and aged	VL	3	6	-	6

(a) Source of new alloys shown in parentheses, all other alloys were included in the Generation 1 experiment.

Researchers at PNL retained half of these specimens for room temperature tensile measurements and measurements of density change, resistivity and microstructural evolution. The other half of the specimens were forwarded to RISØ laboratory for a variety of measurements, especially high-temperature tensile tests and activation analysis directed toward benchmarking of transmutation calculations.

Another experiment, designated "Generation 2," employed a more extensive matrix concentrating heavily on ODS alloys (Table 2). This matrix also contained the European candidate copper alloy for NET, designated CuCrZr, supplied by the Joint Research Center (JRC) at Ispra. In this experiment the copper specimens were separated with molybdenum foils to reduce the overall radioactivity of the foil packets. Two identical sets of alloys were inserted into MOTA-1E to be irradiated at 411°C. One set was discharged after 50 dpa and the other set continued irradiation in MOTA-IF to a target dose of ~100 dpa. This latter set was recently discharged from FFTF. A large subset of the Generation 2 MOTA-1E specimens (concentrating primarily on ODS alloys) are now being examined at PNL. The current results of electrical resistivity measurements of the 1.5 and 2 generations are presented in reference 10. The contents of the Generation 2 MOTA-1F subset at 100 dpa will not be examined for at least a year, depending on the results of the MOTA-1E experiment.

The RISØ research group is particularly interested in the relatively lower displacement levels that are relevant to NET applications. They are also interested in both technologically and fundamentally oriented alloys. Therefore, another set of copper alloys (Table 3) was prepared for insertion into MOTA-IG for irradiation outside the core at 373 and 418°C to damage levels of ~3 and ~10 dpa, respectively. These alloys will be sent directly to RISØ for examination after discharge in 1990. The response of these alloys will be compared with that of other specimens irradiated in various European experiments. The fundamental alloys in the MOTA-IG experiment will also be compared with a number of similar alloys irradiated in a joint PNL/RISØ pure metals experiment (Table 4) and recently discharged from MOTA-1F.

Neutron Experiments in Other Irradiation Facilities

The MOTA experiments are limited by their inability to go very far below 400°C, while the ITER design range extends to room temperature. There are very few data at design-relevant displacement levels in this lower temperature range. The most relevant experiment was recently conducted in the Oak Ridge Research Reactor (ORR) to ~1.3 dpa at a relatively low damage rate of $\sim 2 \times 10^{-7}$ dpa/sec.[11] This microstructurally oriented experiment showed that at this dose level, the temperature regime of swelling is from ~200°C to ≤450°C. No swelling was found at 500°C and it was concluded that 500°C represents the upper temperature limit of the swelling regime. This conclusion will be tested in the higher fluence Generation 1.5 experiment conducted at 529°C in FFTF/MOTA. Unfortunately, the ORR data set contains no information concerning the fluence dependence of swelling, which is also needed for ITER applications.

Generation 2 Copper Alloy Specimens Irradiated at 411°C in MOTA-1E and 1F

Alloy	Condition	Specimen Engraving Code	Displacement Dose: 50 dpa (ET)[a] Tensile	50 dpa (ET)[a] TEM	50 dpa (IV)[a] Tensile	50 dpa (IV)[a] TEM	~100 dpa (E9)[a] Tensile	~100 dpa (E9)[a] TEM	~100 dpa (17)[a] Tensile	~100 dpa (17)[a] TEM
MARZ	Annealed	RO	1	4	1	4		4		4
AL25	50% cold-worked	R4	1	4	1	4	1	4	1	4
AL25	50% cold-worked 6 weld	3N	1	4	1	4	1	4	1	4
CuBe	Solutionized, 20% cold-worked and aged	R1		4		4		4		4
CuBe	Solutionized and aged	R3	1	4	1	4	1	4	1	4
A120	20% cold-worked	UX	1	4	1	4	1	4	1	4
MZC	Solutionired. 90% cold-worked and aged	U6		4		4		4		4
MZC	Solutionized, 90% cold-worked and aged	U7	-	4	-	4	-	4	-	4
MZC (MIT#2)	Solutionized and aged	U9	1	4	1	4	1	4	1	4
MZC (MIT#3)	Solutionized and aged	VB	1	4	1	4	1	4	1	4
Cu-5Ni-2.5Ti (MIT#6)	Solutionized and aged	VK	-	4	-	4	-	4	-	4
Cu-5Ni-2.5Ti (LANL)	Solutionized and aged	VL		4		4		4		4
A115+B (LANL)	Annealed	VO	-	4	-	4	-	4	-	4
CuCr (MIT)	20% cold-worked, stress relieved	3A	1	4	1	4	1	4	1	4
CuHf (MIT)	20% cold-worked, stress relieved	38	1	4	1	4	1	4	1	4
CuCrZr (JRC)	Solutionized and aged	3E	-	4	-	4	-	4	-	4
ODS-1 (TRAA)	40% cold-worked	3F	1	4	1	4	1	4	1	4
ODS-1 (TRAA)	40% cold-worked and weld	3H	1	4	1	4	1	4	1	4
ODS-2 (TRAB)	40% cold-worked	3K		4		4		4		4
ODS-3 (TRAC)	40% cold-worked	3L		4		4	1	4	1	4
ODS-4 (TRAD)	40% cold-worked	3M	1	4	1	4	1	4	1	4
			12	84	12	84	12	84	12	84

(a) Location codes engraved on specimens are shown in parentheses.

Copper Alloy Specimens to be Placed in MOTA-1G

Alloy	Condition	Specimen Engraving Code[a]	3 dpa 373°C (OE01/OE03)[b]	10 dpa 418°C (OE02/OE0U)[b]
MarzCu	Annealed	1	3/3[c]	3/3
Cu-5Ni	Annealed	2	3/3	3/3
Cu-5Ni	40% CW	3	3/3	3/3
Cu-5Mn	Annealed	4	3/3	3/3
Cu-5Mn	40% CW	5	3/3	3/3
CuBe	Solutionized	6	3/3	3/3
CuBe	Solutionized and Aged	7	3/3	3/3
CuBeNi	Solutionized	8	3/3	3/3
CuBeNi	Solutionized and Aged	9	3/3	3/3
CuAl20	20% CW	10	3/3	3/3
CuAl25	50% CW	11	3/3	3/3
CuAl20	Stress Relieved	12	3/3	3/3
CuAl25	Stress Relieved	13	3/3	3/3

(a) This simple code is not a standard MOTA code. These specimens will be de-encapsulated and examined in RISØ.
(b) These designations are packet codes. There are two identical packets at each temperature, allowing for the possibility of not only reaching 3 and 10 dpa, but 6 and 20 dpa as well.
(c) This code means 3 TEM disks in each of two identical packets.

TABLE 4

Copper Alloys Irradiated in RISØ/PNL on Pure Metals and Model Alloys in MOTA-1F

Alloy[b]	Packet LM2 385°C	Packet LN3 410°C
Cu (OFHC)	1[c]	1
cu (99.999%)	1	1
Cu (100 appm He implanted)	–	1
Cu (100-150 appm He produced by irradiation in LAMPF)	–	1
Cu-5Ni	2	1
Cu-5Al	2	1
Cu-5Mn	2	1

(a) Other specimens are pure metals (Ni, W, Mo, Pt, Au, Ag), some with helium preinjection.
(b) All copper alloys are in the annealed condition.
(c) Number of TEM disk specimens in each packet.

In an effort to obtain data at lower temperatures, irradiations are also proceeding in other facilities. Some of these irradiations are also designed to explore the possibility that neutron spectral differences have a significant impact on the microstructural and microchemical evolution of copper alloys.

The first of these experiments involves the irradiation of OFHC and MARZ grades of copper in the DR-3 fission reactor at RISØ to fluences of 0.38, 2.5 and 5 x 10^{20} n/cm^2 (~0.5 dpa maximum) at 400°C and to 0.5 and 5.0 x 10^{20} n/cm^2 at 250°C. Irradiation is continuing to higher fluence levels. These data will be compared with the ORR data of Zinkle and Farrell[11] and with that of the MOTA-IF and MOTA-IG irradiations.

These data will also be compared with the results of an irradiation to 0.5-1.0 dpa just completed in the LASREF facility using spallation neutrons at 330 and 400°C (Table 5). These specimens are currently in Europe awaiting examination and dosimetry measurement. Another set of specimens irradiated with spallation neutrons at 90-100°C is currently in Los Alamos awaiting removal from the irradiation capsule prior to shipping and examination at PNL. This is the first use of spallation neutrons as a possible surrogate for fusion neutrons. The "high energy tail" of the neutron spectra extends to ~300 MeV and may involve special problems in the interpretation of the data. If the spallation neutron experiment appears to be successful, a more comprehensive ITER-relevant irradiation experiment in LASREF will be designed to cover the entire temperature range of interest, focusing on the alloys exhibiting the best behavior in Generation 2 of the FFTF/MOTA experiments.

An extension of the spectral effects studies of H. L. Heinisch[12] from the Omega West Reactor and RTNS-II device to that of LASREF and OR-3 is now being planned.

Charsed Particle Facilities

Some of the alloys described previously have been or will soon be irradiated with high-energy protons in the LAMPF (Los Alamos) and PIREX (Switzerland) facilities. This effort is primarily of interest only to European researchers, although PNL has supplied some alloys used in the U.S. program for comparison purposes. Additional comparison efforts between the effects of high-energy protons and spallation neutrons are under way at Los Alamos National Laboratory. PNL is not currently a participant in these studies, but may become involved later.

The European program is also interested in studying high-temperature, low-cycle fatigue of copper alloys during proton irradiation in PIREX. The development of these tests is proceeding at RISØ and also involves the participation of J. F. Stubbins of the University of Illinois. The possibility exists that similar studies will be conducted in the future using neutron-irradiated specimens.

FUTURE WORK

O. S. Gelles of PNL will serve a two-month assignment at RISØ and will examine by microscopy the OR-3, LAMPF spallation neutron and MOTA-10 specimens, roughly in that order of priority. He will also become involved in the high-temperature mechanical property studies on MOTA specimens. K. R. Anderson, F. A. Garner and M. L. Hamilton will continue to examine the Generation 1.5 and 2 specimens at PNL. Examination of proton-irradiated specimens from LAMPF will be conducted by RISØ personnel as soon as specimens are removed from their irradiation capsules and shipped to RISØ. F. A. Garner will explore the possibility that more data at lower temperatures can be generated in European reactors in Petten and Mol. J. F. Stubbins, who recently completed an assignment at RISØ, will assist F. A. Garner in developing a program to provide additional property data needed for ITER purposes. The RISØ researchers, along with J. F. Stubbins, will continue to develop high-temperature, low-cycle fatigue tests for copper alloys.

TABLE 5

Copper Alloys Irradiated in PNL/RISØ/LANL Joint Experiment in LASREF Spallation Neutron Facility[a]

		90-100°C	330°C	400°C
Cu (OFHC)	Annealed	2[b]	4	4
Cu (MARZ)	Annealed		2	2
Cu-5Mn	Annealed	2	2	2
Cu-5Ni	Annealed	2	2	2
Cu-5Al	Annealed	2	2	2
MZC	HTA		2	2
MZC	HTB		2	2
CuCrZr (JRC)	20% Cold-Worked		2	2
CuAl25	20% Cold-Worked		2	2

(a) Displacement dose is approximately 2 to 3 dpa, the final value awaiting completion of dosimetry analysis.
(b) Number of TEM disk specimens in each packet.

REFERENCES

1. R. J. Livak, H. M. Frost, T. G. Zocco, J. C. Kennedy and L. W. Hobbs, Journal of Nuclear Materials, 141-143 (1986) 160-192.

2. H. M. Frost and J. C. Kennedy, ibid, 169-173.

3. R. J. Livak, T.-G. Zocco and L. W. Hobbs, Journal of Nuclear Materials, 144 (1987) 121-127.

4. M. Ames, G. Kohse, T.-S. Lee, N. J. Grant and O. K. Harling, Journal of Nuclear Materials, 141-143 (1986) 174-178.

5. T.-S. Lee, L. W. Hobbs, G. Kohse, M. Ames, O. K. Harling and N. J. Grant, ibid, 179-183.

6. H. R. Brager, H. L. Heinisch and F. A. Garner, Journal of Nuclear Materials, 133-134 (1985) 676-679.

7. H. R. Brager, Journal of Nuclear Materials, 141-143 (1986) 79-86.

8. H. R. Brager, ibid, 163-168.

9. H. R. Brager and F. A. Garner "Effects of Neutron Irradiation to 98 dpa on the Swelling of Various Copper Alloys," HEDI-SA-3714 FP, accepted for publication in ASTM-STP series on Radiation Effects on Materials: 14th Symposium.

10. K. R. Anderson, F. A. Garner, M. L. Hamilton and J. F. Stubbins, this report

11. S. J. Zinkle and K. Farrell, "Void Swelling and Defect Cluster Formation in Reactor-Irradiated Copper," accepted for publication in the Journal of Nuclear Materials.

12. H. L. Heinisch, Journal of Nuclear Materials, 155-157 (1988) 121-129.

ELECTRICAL RESISTIVITY CHANGES INDUCED IN COPPER ALLOYS BY FAST NEUTRON IRRADIATION - K. R. Anderson (NORLUS Program, University of Illinois), F. A. Garner, M. L. Hamilton (Pacific Northwest Laboratory) and J. F. Stubbins (University of Illinois)

OBJECTIVE

The objective of this effort is to identify suitable copper alloys for high heat flux applications in fusion reactors.

SUMMARY

Thirteen copper-base alloys were irradiated in FFTF/MOTA to determine the response of various alloy classes to neutron irradiation. This effort is directed towards the selection of copper alloys to serve as high heat flux components in both near-term and long-term fusion devices. Post irradiation measurements showed that a wide variety of responses was observed in the neutron-induced changes in electrical resistivity. Tensile tests are in progress and microscopy examination will be initiated soon.

PROGRESS AND STATUS

Introduction

Various copper alloys have been proposed for high heat flux applications for both near-term and long-term fusion goals.[1] In response to these proposals, an early exploratory experiment was conducted in FFTF/MOTA at ~420°C to 98 dpa. On the basis of the results of this earlier experiment [2-5], several more focussed experiments were designed and placed into FFTF/MOTA.[1] Irradiation of these experiments is now complete and a subset of this "second generation" alloy matrix is currently being examined. This subset contains thirteen commercial and experimental alloys, spanning a variety of strengthening mechanisms and fabrication technology.

Three categories of alloys were selected for this study. Alloys in the first category rely solely on an oxide dispersion for strengthening and present the design engineer with several problems regarding fabrication and welding. Alloys in the second category are spinodally strengthened and exhibit excellent formability, joinability and ease of heat treatment. The third category of alloys utilizes multiple strengthening mechanisms. The major combinations employed are oxide and spinodal strengthening, and oxide and precipitation strengthening.

In addition to the three categories of alloys mentioned above, zone refined copper from Materials Research Corporation was also included to serve as a control material for comparison with previous irradiation experiments.

Allovs Investiaated

The internally oxidized alloys designated CuAl25, CuAl20 and CuAl15+B were obtained from SCM Metal Products. One of these, CuAl25, was also included in a laser welded condition in order to determine whether laser welding is a viable fabrication technique for this alloy class in nuclear service. The CuCr and CuHf alloys are also oxide strengthened alloys and were provided by Dr. N. Grant of Massachusetts Institute of Technology (MIT). The spinodally strengthened alloy Cu-4Ni-4Sn was produced by AT&T Bell Laboratories.

The developmental alloys designated ODS-1, ODS-2, ODs-3 and ODS-4 are castable and potentially weldable alloys provided by Technical Research Association in Salt Lake City. These alloys rely on strengthening by both oxides and precipitates. One of these alloys, ODS-1, was also included in the laser welded condition. There were also two different alloys which utilized both oxide and spinodal strengthening. These alloys were both of nominal composition Cu-5Ni-2.5Ti, one supplied by Or. N. Grant of MIT and one by Or. R. Livak of Los Alamos National Laboratory (LANL).

The compositions and final processing conditions of these alloys are summarized in Table 1.

ExDerimental Techniaues

These alloys were irradiated in the Materials Open Test Assembly (MOTA) of Fast Flux Test Facility (FFTF). In most cases, both miniature tensile specimens and 3 mm microscopy (TEM) disks were irradiated at 411°C to 50 dpa in FFTF cycle 9. Some, but not all, of these alloys were also irradiated in cycles 7 and 8 at 414°C to 34 dpa and at 529°C to 32 dpa. The test matrix for these irradiations is shown in Table 2.

Thermal conductivity and its influence on thermal fatigue are important properties for fusion applications, but thermal conductivity is difficult to measure using the small specimens employed in this test. At temperatures above ~0.2 of the Debye temperature (Θ_D = 340K for copper[6]) the electrical conductivity is

TABLE 1.

Composition and Final Processing Conditions of Copper Alloys

Alloy	Material Code	Composition (wt%)	Final Processing Condition[a]
Marz Cu	RO	99.999% Cu	Annealed
CuAl25	R4	0.25% Al as Alumina, bal. Cu	50% CW[b]
CuAl25	3N	0.25% Al as Alumina. bal. Cu	50% CW t Welded
CuAl20	UX	0.20% Al as Alumina, bal. Cu	20% CW
CuAl15+B	VO	0.15% Al as Alumina, <200 ppm Boron, bal. Cu	Annealed
CuCr	3A	3.5% Cr as Cr Oxide, bal. Cu	20% CW, 1/2 hr 450°C
CuHf	38	1.1% Hf as Hf Oxide, bal. Cu	20% CW, 1/2 hr 450°C
ODS-1	3F	0.25% Mg, 1% Alumina, bal. Cu	40% CW
ODS-1	3H	0.25% Mg, 1% Alumina, bal. Cu	40% CW t Welded
ODs-2	3K	0.25% Mg, 1% Alumina, bal. Cu	40% CW
ODS-3	3L	0.5% Mg, 1% Zr Oxide, bal. Cu	40% CW
ODS-4	3M	0.5% Mg, 1% Alumina, bal. Cu	40% CW
Cu-5Ni-2.5Ti	VK	5.09% Ni, 2.10% Ti, 0.8% Titanium Oxide. 0.22% Zr. bal. Cu	Solutionize (1 hr, 950°C), Water Quench, Age (1 hr, 500°C), Air Cooled
Cu-5Ni-2.5Ti	VL	5% Ni, 2.5% Ti (some as Titanium Oxide), bal. Cu	Solutionize (20 min, 900°C), Water Quench, Age (1 hr., 525°C), Air Cooled
Cu-4Ni-4Sn	VN	4% Ni, 4% Sn, bal. Cu	Solutionize (30 min, 750°C), Water Quench, Age (1 hr, 450°C), Air Cooled

(a) All heat treatments in Argon.
(b) CW = cold worked.

Irradiation Conditions

Alloy	Material Code	411°C 50 dpa	414°C 34 dpa	529°C[a] 32 dpa
Marz Cu	RO	d/t[b]	d/t	d[c]
CuAl25	R4	d/t	--	--
CuAl25 (welded)	3N	d/t	--	--
CuAl20	UX	d/t	d/t	d/t
CuAl15 (boron deoxidized)	VO	d d/t	d	
ODS-1	3H	d/t	--	--
ODS-1 (welded)		d/t	--	--
ODS-2	3K	d --	--	
ODS-3	3L	d --	--	
ODs-4	3M	d/t	--	--
CuCr	3A	d/t	--	--
CuHf	3B	d/t	--	--
Cu-5Ni-2.5Ti (MIT)	VK	d d/t	d/t	
Cu-5Ni-2.5Ti (LANL)	VL	d d/t	d	
Cu-4Ni-4Sn (LANL)	VN	--	d/t	d

(a) Overtemperature of 201°C for 50 minutes.
(b) d/t = TEM disks t tensiles.
(c) d = TEM disks.

known to be proportional to the thermal conductivity. Since electrical conductivity is easy to measure, and can be related to the thermal conductivity, the electrical resistivity was measured at room temperature on both types of specimens using a four point probe and a dc potential drop technique. An Alessi probe was used with a probe spacing of 0.025 in. Electrical current was passed between the outer probes while the potential drop between the inner probes at steady state was measured (*see* Figure 1). The potential drop was then converted to electrical conductivity (%IACS) at room temperature.

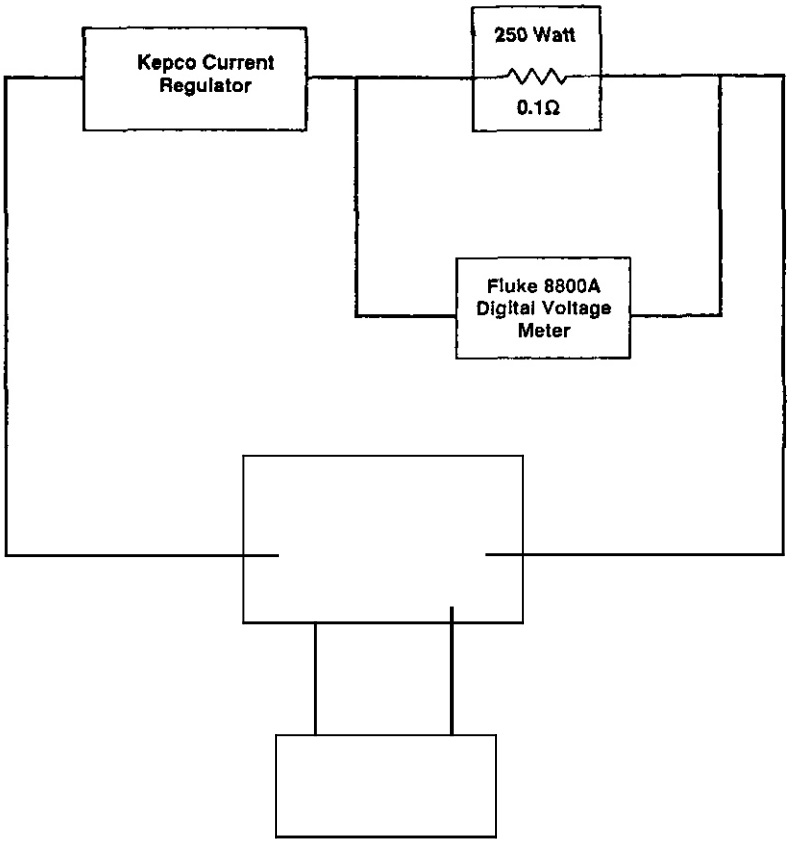

Figure 1. Schematic Drawing of Resistivity Testing Fixture Used in This Experiment

Results and Discussion

The electrical conductivity data are tabulated in Table 3. Measurements were made for some alloys on multiple specimens. In general, measurements on miniature tensile specimens were found to be more reproducible than those on disks.

Many previous irradiation studies have shown that radiation-induced microstructural evolution is often very sensitive to the time-dependent details of the radiation environment, particularly temperature and displacement rate. When comparing the relative performance of various alloys it is therefore better to make initial comparisons within each irradiation canister and secondly make comparisons between various canisters to ascertain the impact of other variables on the evolution of the microstructure. Figures 2a,b, and c show a comparison of the average values of conductivity for the various alloys irradiated together at 411°C to 50 dpa. Figure 3a shows the data for alloys irradiated at 414°C to 34 dpa and Figure 3b shows the results of the 529°C irradiation to 32 dpa.

Since some of the alloys were irradiated in more than one canister it is also instructive to plot the data as a function of neutron fluence. Figure 4 shows that the data generated in this study on MARZ copper at 411-414°C is in very good agreement with those data derived from two previous studies at 385°C(EBR-II)[7] and 420°C(FFTF).[2-4] The transmutation at 529°C and 32 dpa should not be significantly different from that at 414°C and 34 dpa, so the smaller drop in electrical conductivity at 529°C probably represents a much lower level of void swelling. This is in agreement with the results of a recent irradiation study conducted

TABLE 3

Electrical Conductivities (% IACS)[a] of Copper Alloys Irradiated in FFTF/MOTA

Alloy	Material Code	0 dpa	414°C 34 dpa	411°C 50 dpa	529°C 32 dpa
MARZ Cu	RO	100.9 100.9	70.4 70.1	58.1 58.1	82.7[b] 90.8[b]
CuAl25	R4	85.7 85.2		83.2 81.6	
CuAl25(welded)	3N	77.7 73.9		59.6 57.7	
CuAl20	UX	88.5 88.4	81.6 85.4	72.7[b] 76.3[b]	84.0 86.4
CuAl15+B	VO	91.6	80.0 83.6	74.7[b] 73.8[b]	85.8[b] 88.6[b]
ODS-1	3F	80.6		63.7 59.3	
ODS-1(welded)	3H	88.4 88.5		67.9 64.9	
ODS-2	3K	85.7[b] 88.7[b] 91.3[b]		67.2[b] 73.6[b] 68.0[b]	
ODS-3	3L	86.0 89.0		59.0[b] 57.0[b]	
ODS-4	3M	79.8 78.5		67.4 72.0	
CuCr	3A	89.4 90.2		77.9 79.4	
CuHf	3B	88.8		77.6	
CuNiTi	VK	40.4[b] 40.9[b] 37.5[b] 42.0 40.5 40.8	52.3 52.9	48.7[b] 47.3[b] 46.2[b]	68.7[b] 65.0[b]
CuNiTi	VL	31.4 32.9 31.0	56 59	48.6[b] 49.8[b]	67.2[b] 68.9[b]
CuNiSn	VN	15.8 16.5 16.5 18.0[b] 18.2[b] 18.6[b]	40.8		27.9[b] 25.3[b] 27.7[b]

(a) Multiple values represent measurements from separate specimens.
(b) Indicates TEM disks; no notation denotes measurements made on gage section of miniature tensile specimen.

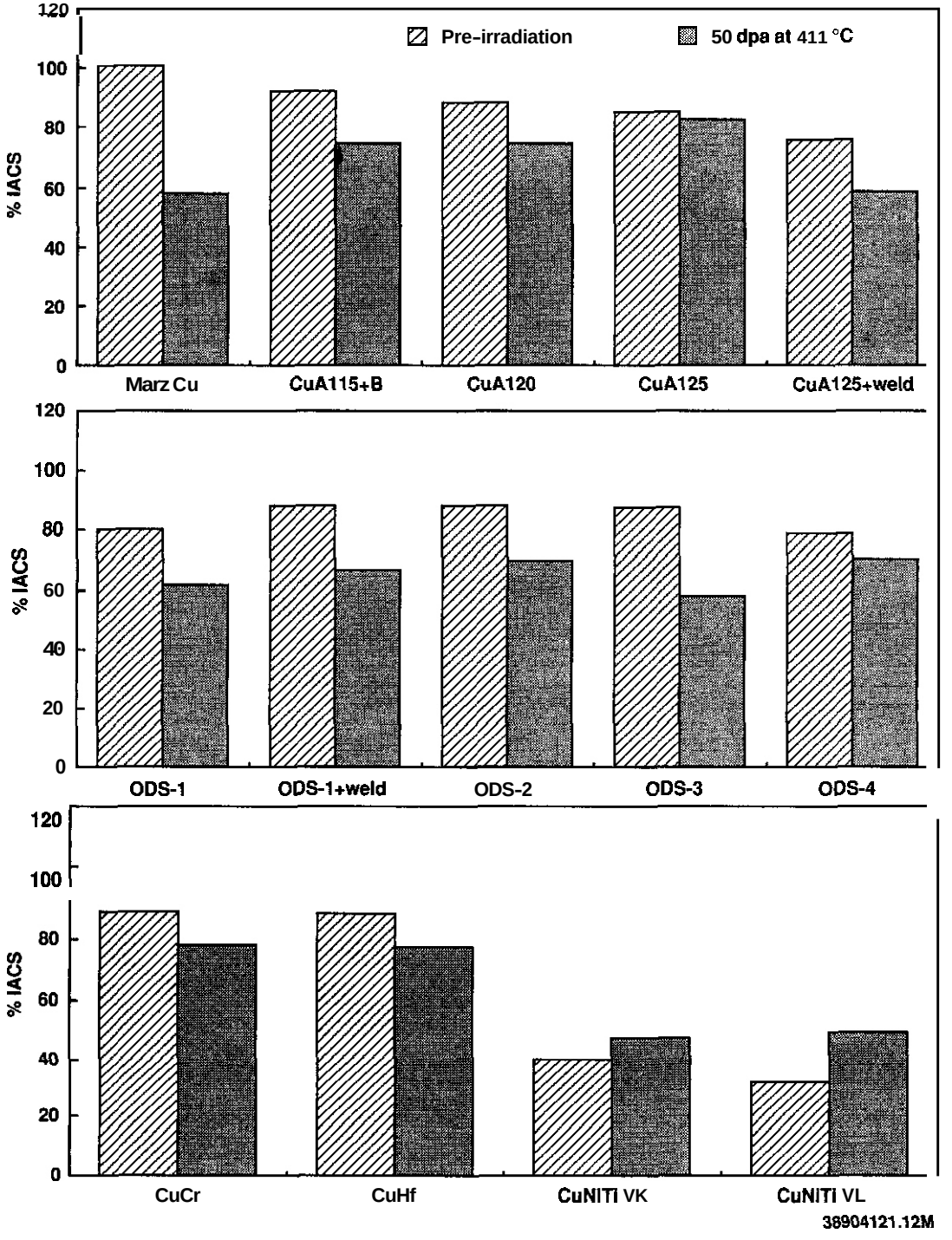

Figure 2. Average Measurements of Electrical Conductivity of Both Unirradiated and Irradiated Copper Alloys

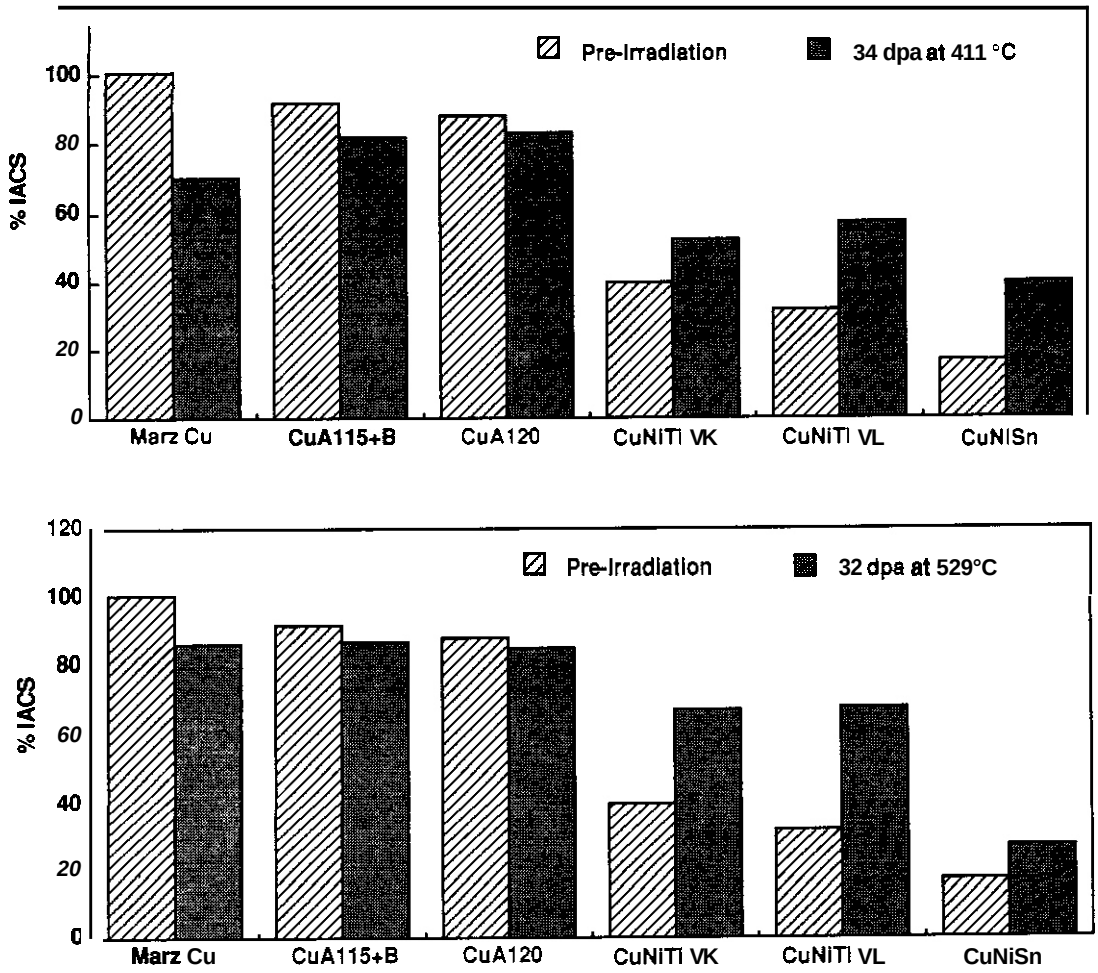

Figure 3. Average Measurements of Electrical Conductivity of Both Unirradiated and Irradiated Copper Alloys

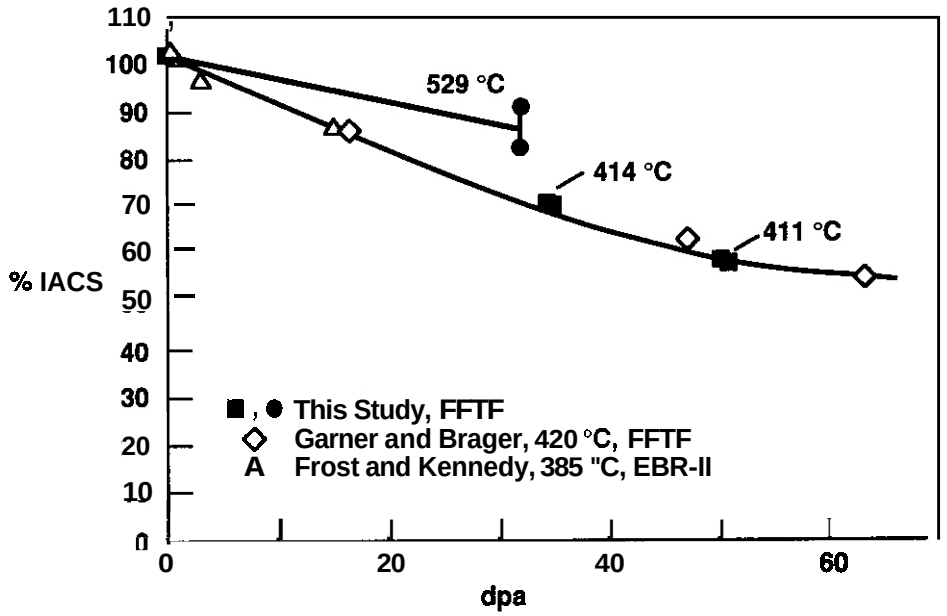

Figure 4. Changes Induced in the Conductivity of MARZ Copper During Fast Neutron Irradiation

in ORR that shows swelling in copper falls quickly with increasing temperature in the vicinity of 500°C.[8] The rather large variation seen in conductivity at 529°C between the two disks available represents the largest observed deviation between nominally identical specimens in the study.

Previous studies of the oxide dispersion strengthened alloy CuAl25 did not show any swelling at ~420°C and displacement levels of ≤63 dpa and it is anticipated that CuAl20 will behave in a similar manner. Thus we would expect the drop in conductivity of CuAl20 (in the absence of swelling) to be independent of irradiation temperature in the range 400-529°C. As shown in Figure 5, such behavior was indeed observed. Figure 6 shows, however, that welding of CuAl25 caused first a decrease in preirradiation conductivity and second a larger drop during irradiation than was observed in unwelded material. This suggests that the microstructural changes induced by welding may have caused swelling to occur, possibly in the heat affected zone.

Figure 7 shows that at the lower oxide level of CuAl15, some difference in behavior may be developing between 414 and 529°C. The small apparent difference may reflect measurement uncertainties, however, and no conclusions can be drawn until microscopy data are available. Comparison of the behavior of CuAl25, CuAl20 and CuAl15 show that the oxide level has some small influence on both the preirradiation and postirradiation conductivity. We can see in Figure 8, however, that the alloys CuCr and CuHf exhibit very little difference in behavior as a function of composition.

Alloys ODS-1 and ODS-2 are very similar alloys but the former has a finer dispersion of oxide. Although the preirradiation conductivity reflects this difference, both alloys respond to irradiation at 411°C in much the same manner, as shown in Figure 9. Upon welding, however, the ODS-1 alloy increases in conductivity and retains this relative increase during irradiation (Figure 10). The ODs-3 and ODS-4 alloys are different in composition and exhibit different rates of change in conductivity during irradiation (see Figure 11). The reasons for these different behaviors will be sought during microscopy examination.

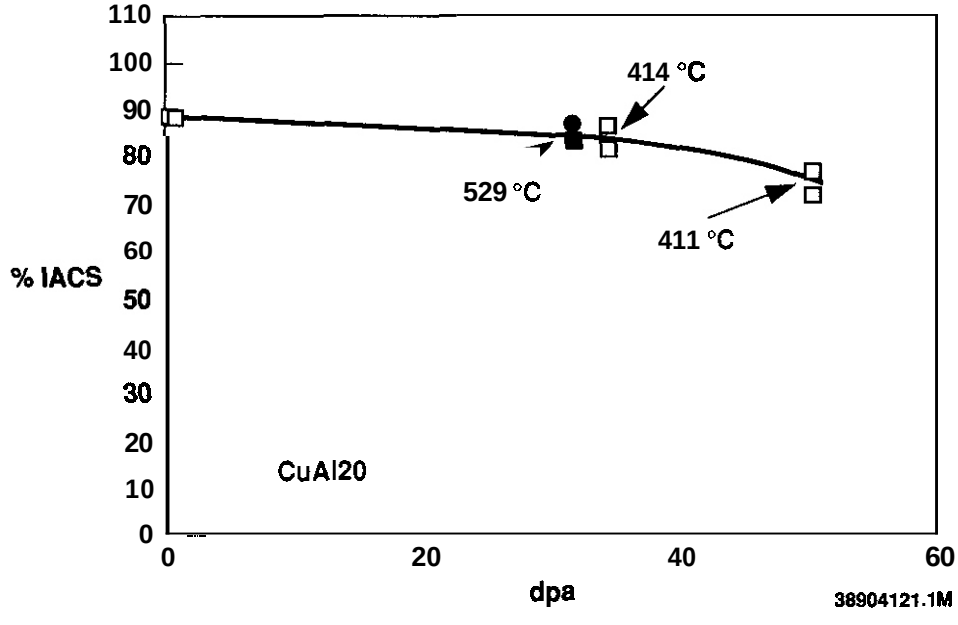

Figure 5. Electrical Conductivity of CuAl20

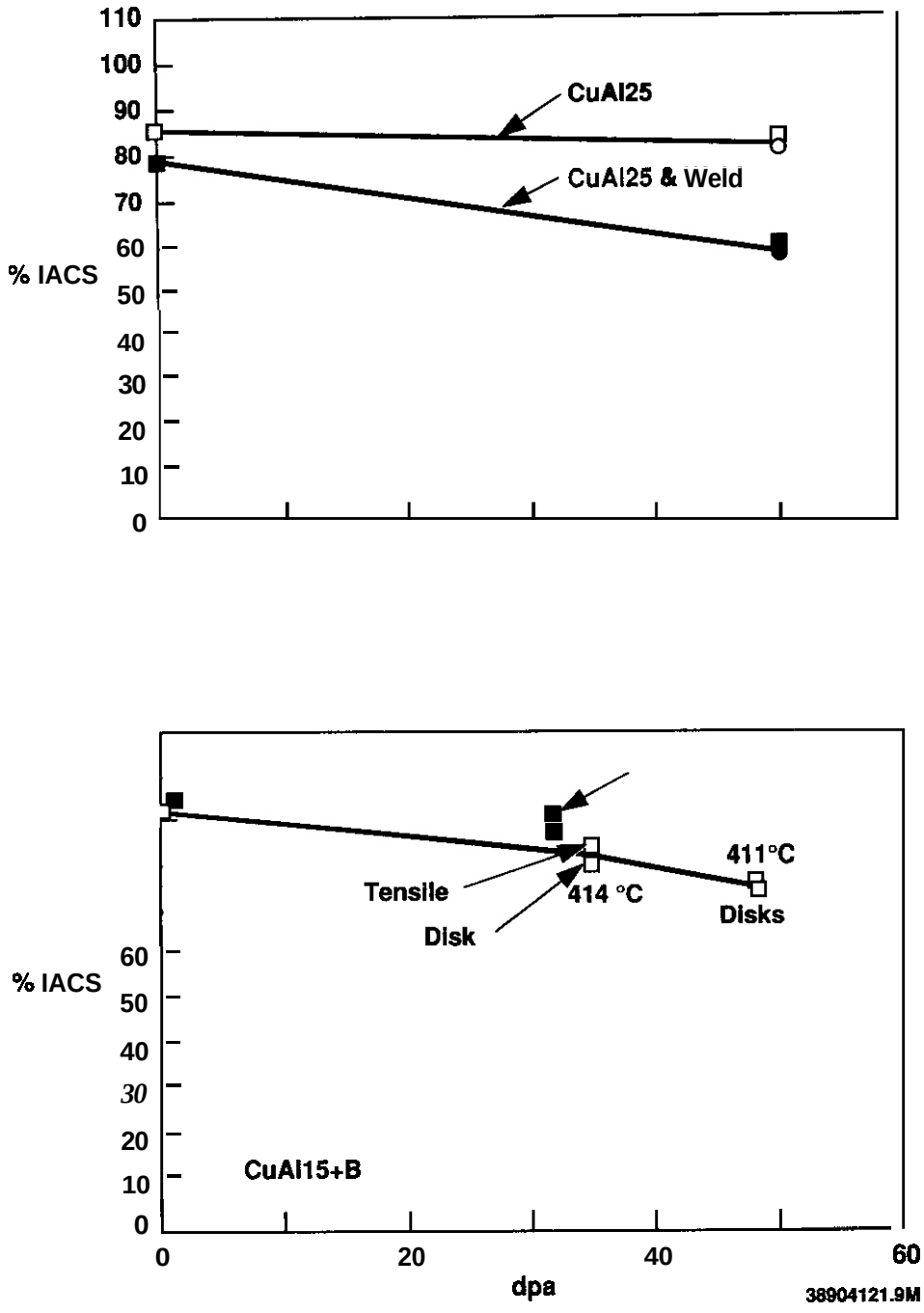

Figure 7. Electrical Conductivity of CuAl15+B

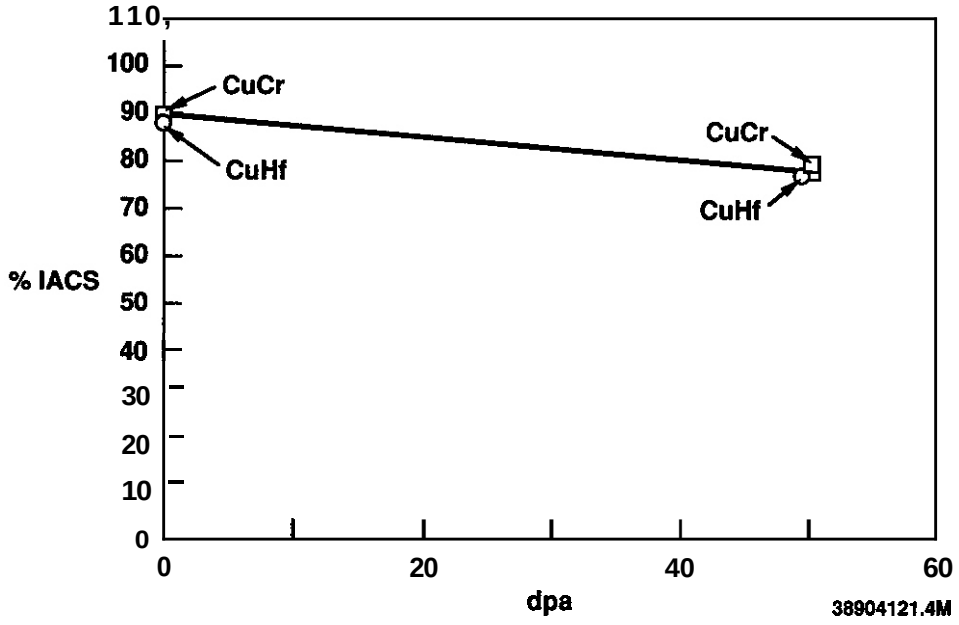

Figure 8. Electrical Conductivity of CuHf and CuCr Irradiated at 411°C

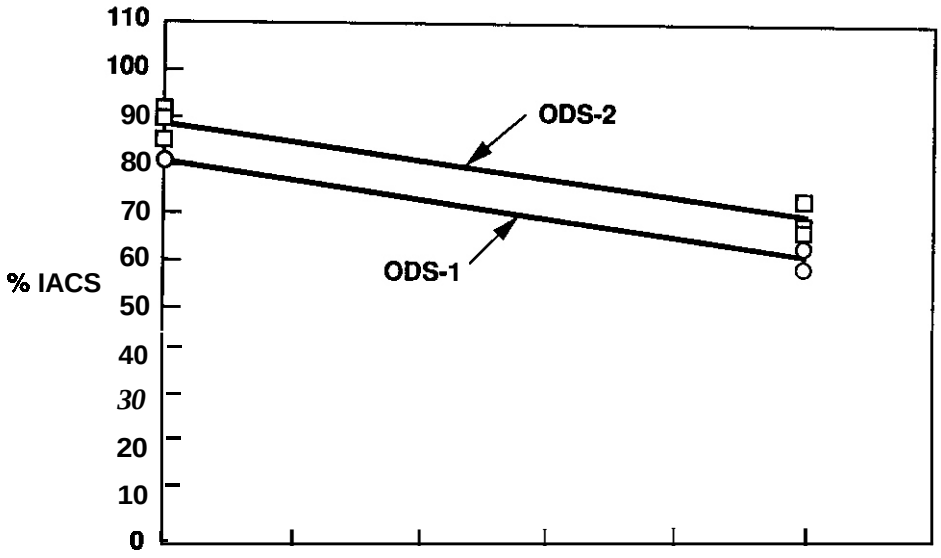

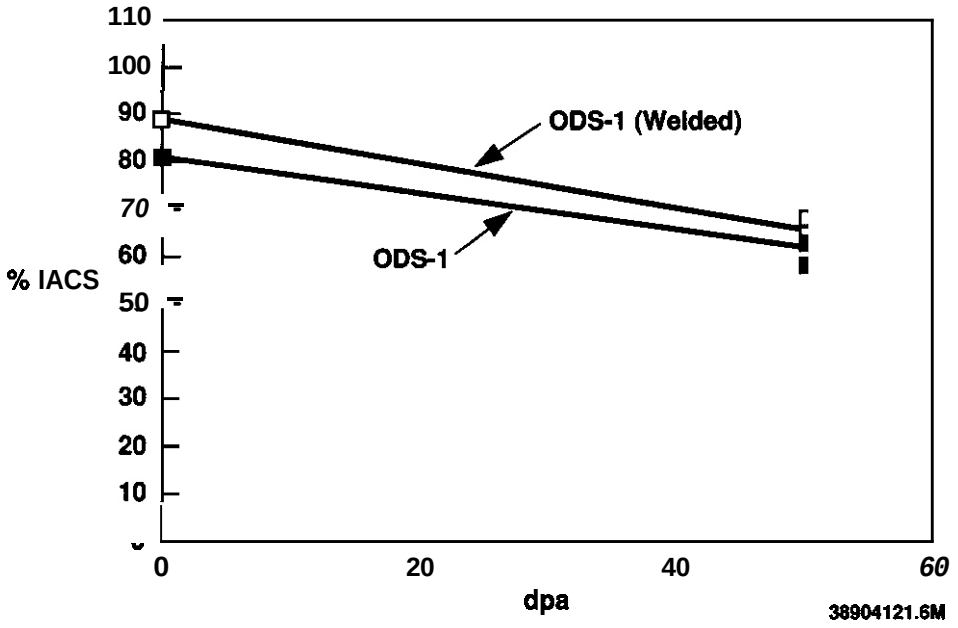

Figure 10. Electrical Conductivity of ODS-1 Irradiated at 411°C

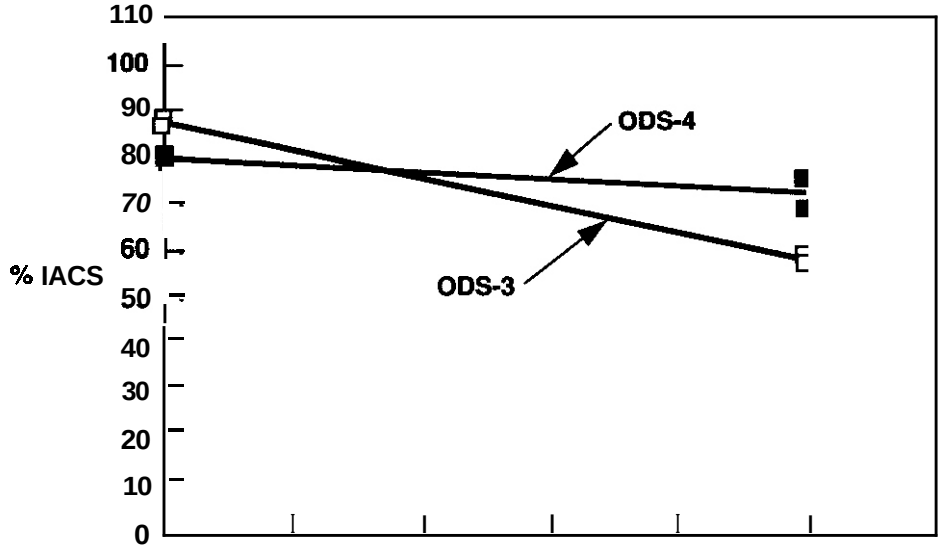

Figure 11. Electrical Conductivity of ODS-3 and ODS-4 Irradiated at 411°C

When more than one strengthening method is employed it is possible that a non-monotonic behavior may arise as is illustrated in Figures 12 and 13. The initial increase in conductivity of CuNiTi is probably related to changes in the spinodally-hardened microstructure, while the eventual decrease is similar to that of other alloys, arising from transmutation and possibly void swelling. In cases where only one neutron fluence level was reached, it is not certain that such non-monotonic behavior occurred. This is the case for CuNiTi at 529°C and for CuNiSn at both 414 and 529°C, as shown in Figure 14.

Conclusion

Depending on the alloy class, composition, starting condition and temperature, copper alloys exhibit a variety of changes in electrical conductivity during irradiation in FFTF-MOTA. At this point no microscopy has been performed and no clear statement can be made concerning the microstructural origins of these changes.

Future Work

Measurements of tensile properties are in progress and electron microscopy will be performed.

Acknowledgments

The participation of K. R. Anderson and J. E. Stubbins is supported by the Northwest College and University Association for Science.

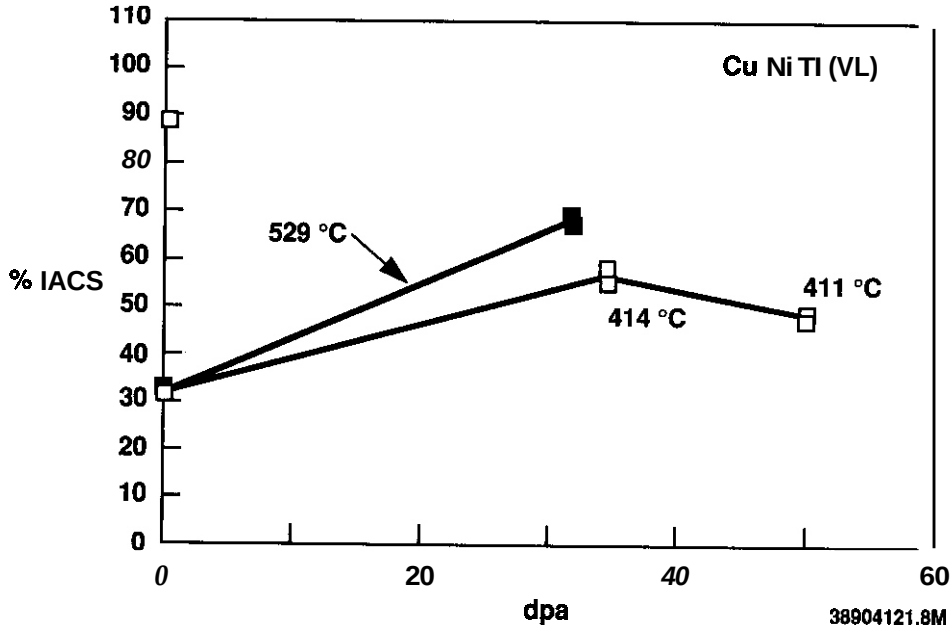

Figure 12. Electrical Conductivity of CuNiTi (VL)

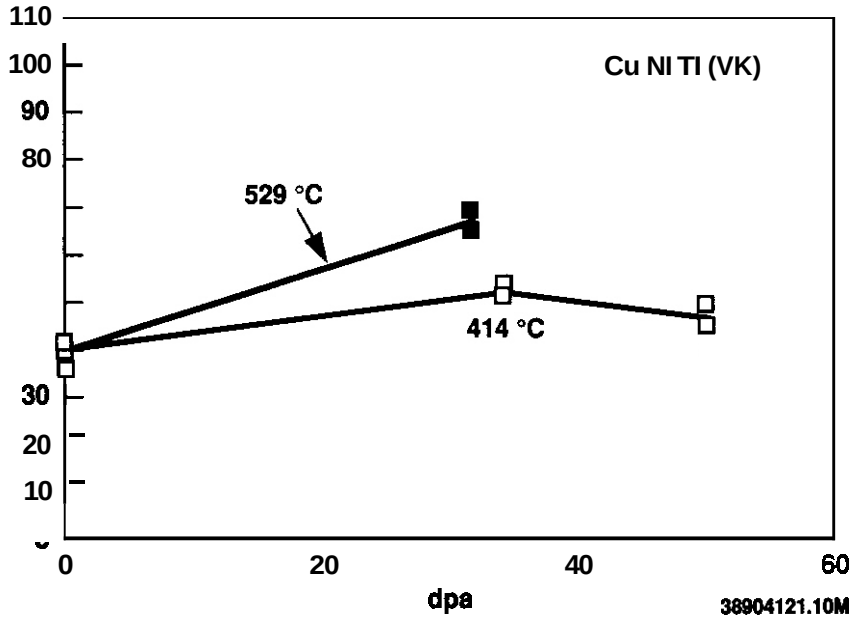

Figure 13. Electrical Conductivity of CuNiTi (VK)

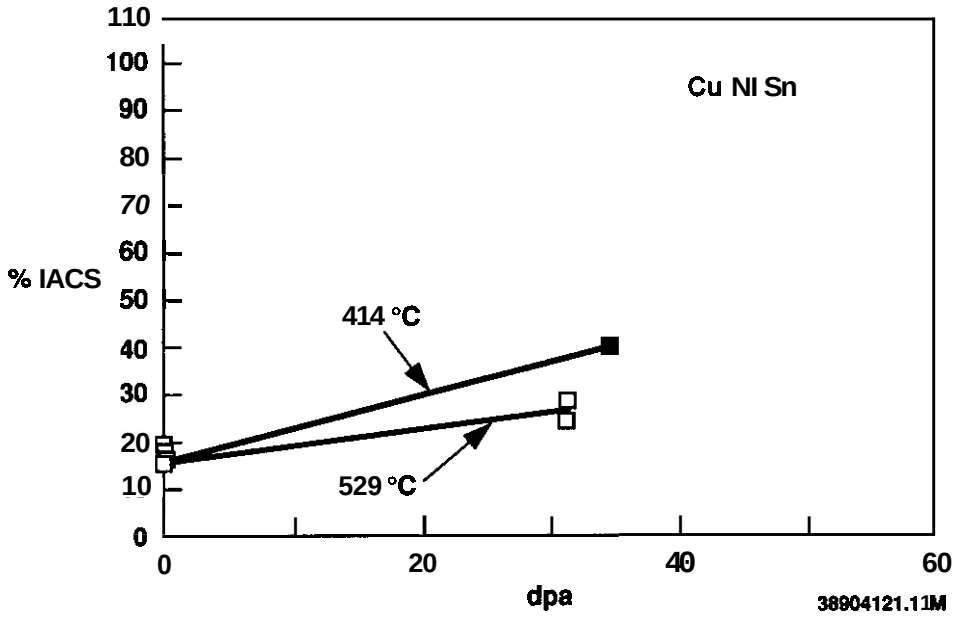

Figure 14. Electrical Conductivity of CuNiSn

References

1. F. A. Garner, M. L. Hamilton, K. R. Anderson, J. F. Stubbins, 8. N. Singh, A. Horsewell and W. F. Sommer, "Overview of Copper Irradiation Programs," this report.

2. H. R. Brager, H. L. Heinisch and F. A. Garner, Journal of Nuclear Materials, 133-134 (1985) 676-679.

3. H. R. Brager, Journal of Nuclear Materials, 141-143 (1986) 79-86.

4. H. R. Brager, ibid, 163-168.

5. H. R. Brager and F. A. Garner, "Effects of Neutron Irradiation to 98 dpa on the Swelling *of* Various Copper Alloys," HEDI-SA-3714 FP, accepted for publication in ASTM-STP series on Radiation Effects on Materials: 14th Symposium.

6. C. A. Wert and R. M. Thompson, Physics of Solids (Second Edition), McGraw-Hill, Inc., New York, 1970

7. H. M. Frost and J. C. Kennedy, Journal of Nuclear Materials, 141-143 (1986) 169-173.

8. S. J. Zinkle and K. Farrell, "Void Swelling and Defect Cluster Formation in Reactor-Irradiated Copper," accepted for publication in the Journal of Nuclear Materials.

6.5 Environmental Effects On Structural Alloys

DESIGN OF AN BLECTROCHENICAL TESTING SYSTEM TO EVALUATE SENSITIZATION OF AUSTENITIC STAINLESS STEELS USING MINIATURIZED SPECIMENS - T. Inazumi (Japan Atomic Energy Research Institute, assigned to ORNL) and G.E.C. Bell (Oak Ridge Associated Universities)

OBJECTIVE

The objective of this work is to evaluate the propensity for sensitization in neutron-irradiated austenitic stainless steels by electrochemical testing of miniaturized specimens.

SUMMARY

An electrochemical testing system was developed to evaluate the sensitization of austenitic stainless steels using miniaturized disk-type specimens, 3 mm diam by 0.25 mm thick. The specimens are also suitable for examination using transmission electron microscopy (TEM) after electrochemical testing. The apparatus consists of a specimen holder in which a miniaturized specimen is mounted as the working electrode, a test cell designed to handle radioactive materials and waste, and a potentiostat/galvanostat. Sensitization of thermally-aged austenitic stainless steel specimens was successfully detected by the single-loop electrochemical potentiokinetic reactivation (SL-EPR) method.

PROGRESS AND STATUS

Introduction

Irradiation assisted stress corrosion cracking (IASCC) is a form of intergranular stress corrosion cracking (IGSCC) that has been considered one of the major environmental degradation processes of stainless steels in water-cooled nuclear power systems.[1-3] IASCC occurs above a fast neutron ($E > 1$ MeV) fluence level above ~5×10^{20} n/cm^2 (ref. 1). It has been suggested that enrichment of impurities, such as phosphorus, sulfur, and silicon, to grain boundaries by radiation induced segregation (RIS) plays an important role in increasing susceptibility of stainless steels to IASCC.[3-10] Lower susceptibility of high-purity stainless steels to IASCC supports such a mechanism.[7,8] However, chromium is depleted along grain boundaries as a result of RIS[4,10-13] and has been suggested as a contributing factor for sensitization.[14] The chromium concentration at grain boundaries can be reduced by RIS to below 12 wt %, the minimum level to form protective films an austenitic steel surfaces.[12,13] In the case of water-cooled stainless steel components for fusion reactors, IASCC may again be a degradation process. In this case, RIS characteristics will be different from those in Sight water reactors because of the harder neutron spectrum and higher neutron flux (viz. higher damage rate and higher helium production).

In assessing the effects of RIS on corrosion resistance, it is necessary to develop miniaturized experimental techniques because of limited space in irradiation facilities (thus, requiring a small specimen size) and the need for low personnel radiation exposure from specimen handling and testing. For successful application of the miniaturized experimental techniques, it is essential that the corrosion test methods to be used have sufficient sensitivity to quantify results with small tested area of specimens. Furthermore, nondestructive corrosion testing techniques are preferable because corrosion properties can be directly related to the microstructure of the specimen by microstructural analysis of the same specimens.

The SL-EPR is a nondestructive, quantitative test method to evaluate the degree of sensitization of austenitic Stainless steels associated with chromium depletion near grain boundaries.[15-21] The principle of SL-EPR is to detect the dissolution current caused by the breakdown of passive films on the chromium depleted areas during a controlled potential sweep from the passive to active regions (electrochemical reactivation).[16,18] Previous studies have shown that the SL-EPR method was more sensitive than the conventional wet chemical tests (e.g., Practices A, B, and E of ASTM A262) particularly for the level of sensitization of practical importance for industrial application.[16,17,20,21] Therefore, for the detection of chromium depletion caused by RIS, the SL-EPR method seems to be an appropriate corrosion test technique to which miniaturized experimental techniques are applicable. In the present study, the electrochemical testing system using miniaturized specimens was developed to evaluate degree of sensitization associated with chromium depletion in neutron irradiated austenitic stainless steels by the SL-EPR method.

System description

The schematic diagram of the electrochemical testing system is shown in Fig. 1. The system consists of the potential/current measurement system, the polarization cell, and the specimen holder. The measurement System, EG&G PARC MODEL *342*, is a computer controlled potentiostat/galvanostat with Current resolution of 100 pA. The polarization cell was constructed as specified in ASTM G5-87 and was modified to have an exterior cooling jacket to control temperatures with circulating water. The remotely operated electric drain systems, salt bridge/calomel reference electrode adjusting system, and test solution supply/cell rinsing system were installed to minimize personnel exposure during handling of radioactive specimens and Waste.

Pig. 1. Schematic diagram of electrochemical testing system.

The disk specimens, 3 mm diam by 0.25 mm thick, were chosen for the convenience of microstructural examination by TEM after SL-EPR testing and because appropriately irradiated specimens were available in this form. The specimens are mounted on the specimen holder and serve as a working electrode with a platinum counter electrode. The method for mounting the specimens on the holder is shown in Pig. 2. The specimen holder is made of acrylic and silicon rubber for resistance to the sulfuric acid electrolyte, which is recommended for the SL-EPR test. Specimens are set on a platinum lead wire and pressurized by silicon rubber to promote good contact and avoid exposure of the platinum lead wire to the solution.

The assembled test cell, Specimen holder. and specimen loading stand are shown in Pigs. 3 and 4.

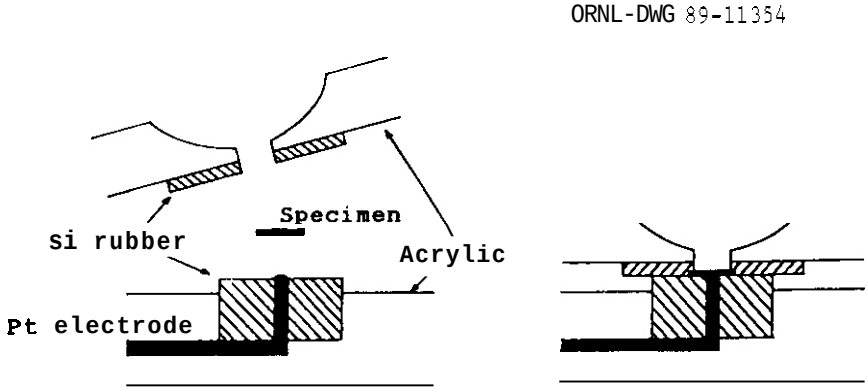

Fig. 2. Method for mounting specimens.

Detection of thermal sensitization of type 316 stainless steel

Experiments were conducted using thermally-aged disk specimens of type 316 stainless steel. The chemical composition of the steel is shown in Table 1. The specimens were aged at 675°C for 1 h, where the steel was expected to be sensitized according to the normalized parameter proposed by Bruemmer.[22]

For the SL-EPR tests. the test conditions of W. L. Clarke et al.[17] were followed. The specimens were polished to 0.05 μm alumina slurry and then immersed in 0.5 M H_2SO_4 + 0.01 M KSCN at a temperature of 30°C. The passivation was accomplished by setting the potential to +200 mV versus the saturated calomel electrode and holding far 2 min. The reactivation scan proceeded at the rate of 6 V/h and the dissolution current was recorded.

The reactivation curves of the solution annealed and thermally-aged specimens are shown in Pig. 5. The sensitization in the aged specimen was successfully detected as evidenced by the large peak in current density while no sensitization (no peak) was detected in the solution-annealed specimen.

YP 8010

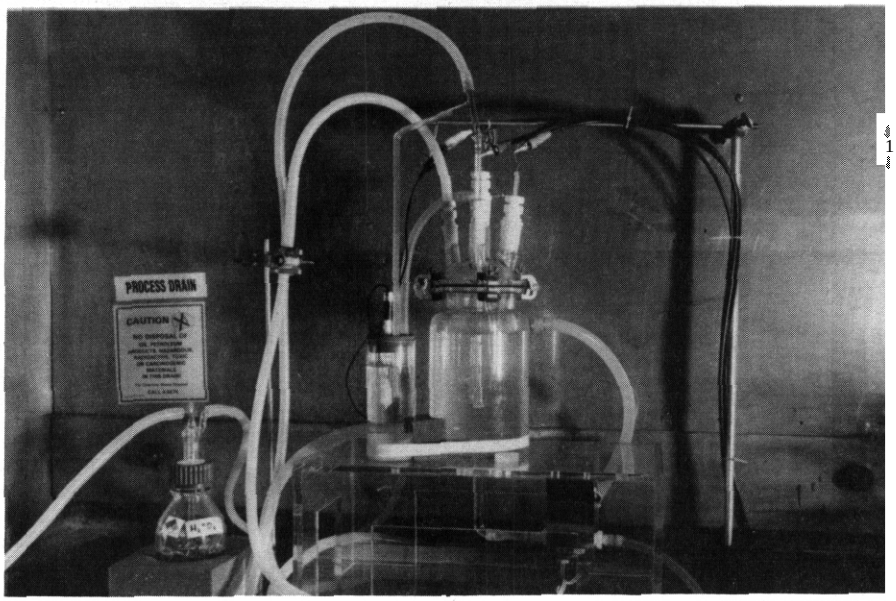

Fig. 3. Polarization cell assembled in hood.

YP 8002

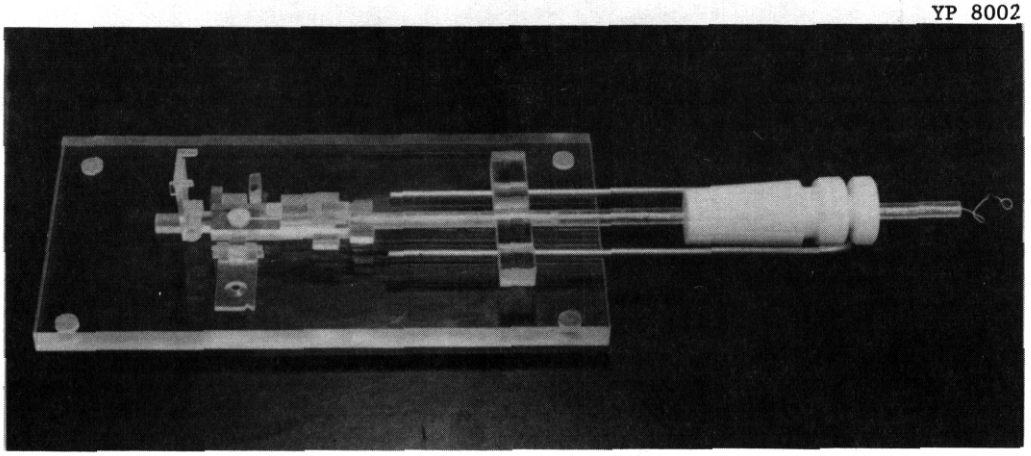

Fig. 4. Specimen holder and loading stand.

FUTURE WORK

Surface preparation technique

The results of the SL-EPR tests are significantly affected by surface condition of the specimens. The tarnished surface films formed on the specimens during irradiation must be removed before testing. Furthermore, the surface must be polished to a mirror finish with 1 μm diamond paste or 0.05 μm alumina slurry to get the maximum sensitivity.[16,20] Because of the difficulty in applying these mechanical polishing techniques to the miniaturized and radioactive specimens, electropolishing techniques are being considered. The effects of electropolishing techniques on SL-EPR are being investigated before testing irradiated materials.

The degree of sensitization in neutron irradiated stainless steels. including the prime candidate alloy (PCA) and type 316 stainless steel, will be evaluated relative to control data of thermally aged specimens.

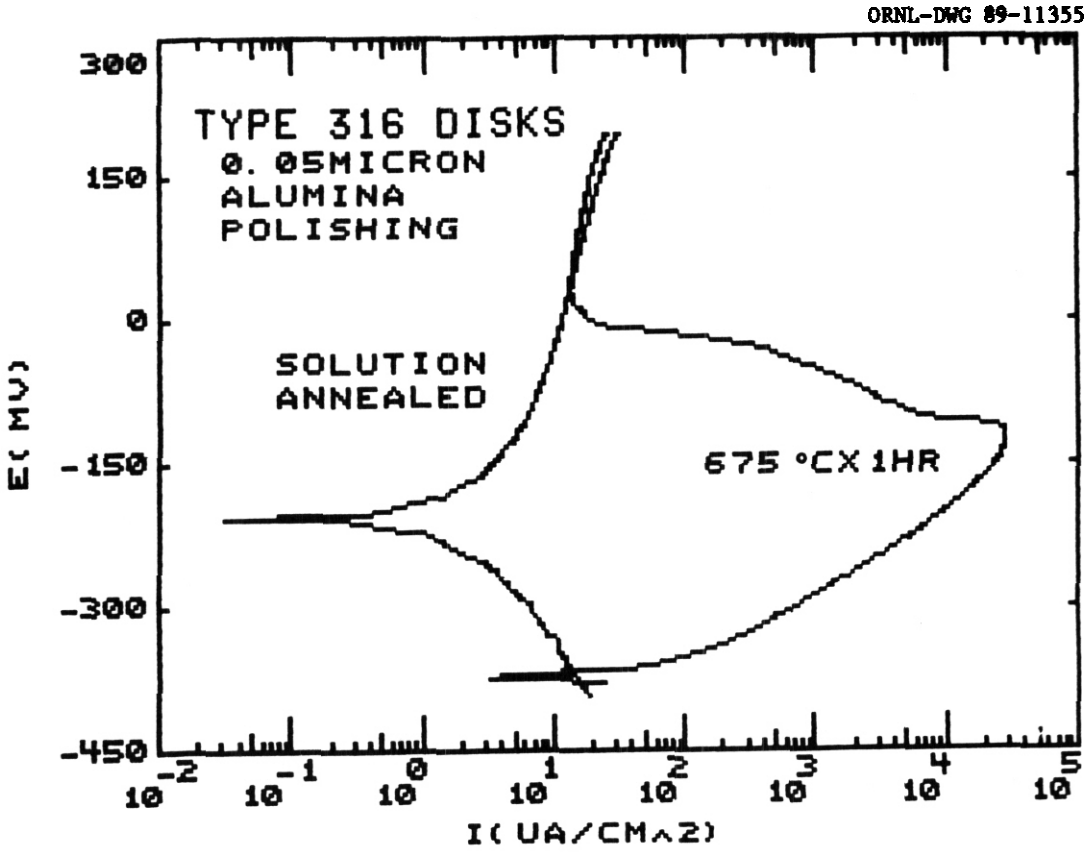

Fig. 5. Reactivation curves of type 316 stainless steel.

Table 1. Chemical composition of type 316 stainless steel (wt %)

C	Si	Mn	Ni	Cr	Mo	Ti	Fe
0.08	1.06	2.06	13.7	16.4	1.7	0.15	bal

REFERENCES

1. A. J. Jacobs and G. P. Wozadlo, "Irradiation-Assisted Stress Corrosion Cracking as a Factor in Nuclear Power Plant Aging," pp. 173-80 in Proceedings of *International Conference* on *Nuclear* Power *Plant Aging, Availability* Factor *and* Reliability *Analysis,* ASM, ed. V. S. Goel, 1985.

2. W. L. Clarke and A. J. Jacobs, "Stress Corrosion Teat Facility for Studying Irradiated Materials," pp. 153–60 in *Materials in* Nuclear *Energy* (Proc. Intern. Conf.). ASM, 1982.

3. R. N. Duncan, Stainless *Steel Failure* Investigation *Program, Final* Report, GEAP-5530, 1968.

4. K. Fukuya et al., "Grain Boundary Segregation of Impurity Atoms in Irradiated Austenitic Stainless Steels," pp. 665–71 in Proceedings of the *Third International Symposium* on *Environmental Degradation* of *Materials in* Nuclear Power *System* — Water *Reactors,* The Metallurgical Society, ed. G. J. Theus, 1987.

5. A. J. Jacobs et al., "Radiation Effects on the Stress Corrosion and Other Selected Properties of Type 304 and Type 316 Stainless Steels." pp. 673–81 in *Proceedings* of the *Third International Symposium on Environmental Degradation* of *Materials in Nuclear Power System* — Water Reactors, The Metallurgical Society, ed. G. J. Theus, 1987.

6. E. P. Simonen and R. H. Jones, "Calculated Solute Segregation Kinetics Related to Irradiation Assisted Stress Corrosion Cracking," pp. 683-90 in *Proceedings of* the *Third International Symposium* on Environmental Degradation of Materials in Nuclear Power System — Water Reactors, *ed. G. J. Theus,* The Metallurgical *Society, 1987.*

7. H. Hanninen and Aho-Mantila, "Environment-Sensitive Cracking of Reactor Internals," pp. 77-92 in *Proceedings of the* Third *International Symposium* on *Environmental Degradation of Materials* in *Nuclear Power System — Water Reactors,* The Metallurgical Society, ed. G. J. Theus, 1987.

8. P. Garzarolli et al., "Deformability of Austenitic Stainless Steels and Ni-Base Alloys in the Core of a Boiling and a Pressurized Water Reactor," pp. 657—64 in *Pmceedings of the* Third *International Symposium* on *Environmental Degradation of Materials in Nuclear Power System — Water Reactors,* The Metallurgical Society, ed. G. J. Theus, 1987.

9. Aho-Mantila and H. Hanninen, "Electrochemical Methods to Estimate IASCC Susceptibility of Stainless Steels," pp. 349—56 in *Materials for Nuclear* Reactor *Core Applications* (Proc. of Intern. Conf.), Vol. 1, BNES, 1987.

10. A. J. Jacobs et al., *Irradiation-Assisted* Stress Corrosion *Cracking and Grain Boundary Segregation* in *Heat Treated Type 304SS,* CONP-880613-3, 1988.

11. E. A. Kenik, "Measurement of Equilibrium and Nonequilibrium Segregation by X-Ray Microanalysis," pp. 209—16 in *Proceedings of Material Research Society Symposium,* Vol. 62, 1986.

12. D.R.I. Norris, C. Baker, and J. M. Titchmarsh, "Compositional Profiles at Grain Boundaries in 20%Cr/25%Ni/Nb Stainless Steel," pp. 86-98 in *Radiation-Induced Sensitization* of *Stainless Steels* (Proc. of the Symposium held at Berkeley Nuclear Laboratories, Sept. 23, 1986), CEGB, ed. D.I.R. Norris, 1987.

13. J. M. Perks, A. D. Marwick, and C. A. English. "Fundamental Aspects of Radiation-Induced Segregation in Pe-Cr-Ni Alloys," pp. 15-34 in *Radiation-Induoed Sensitization of* stainless *Steels* (Proc. of the Symposium held at Berkeley Nuclear Laboratories, Sept. 23, 1986), CEGB, ed. D.I.R. Norris, 1987.

14. C. Taylor, "The Formation of Sensitized Microstructures During the Irradiation of CAGR Fuel Pon Cladding," pp. 60-73 in Radiation-Induced Sensitization of Stainless Steels *(Proc. of the Symposium held at Berkeley Nuclear Laboratories on Sept. 23, 1986), CEGB, ed. D.I.R. Norris, 1987.*

15. P. Novak, R. Stefec, and P. Franz, "Testing the Susceptibility of Stainless Steel to Intergranular Corrosion by a Reactivation Method," *Cormswn* 31(10), 344—47 (1975).

16. W. L. Clarke, V. M. Romero, and J. C. Danko, *Detection of Sensitization in Stainless Steel Using Electrochemical Techniques,* GEAP-21382, 1976.

17. W. L. Clarke, R. L. Cowan, and W. L. Walker, "Comparative Methods for Measuring Degree of Sensitization in Stainless Steel," pp. 99—132 in *Intergranular* Corrosion *of Stainless* Alloys, ASTM STP 656, ed. J. B. Wheeler et al., 1978.

18. V. Cihal, "A Potentiokinetic Reactivation Method for Predicting the I.C.C. and I.G.S.C.C. Sensitivity of Stainless Steels and Alloys," *Cormsion Science* 20, 737—44 (1980).

19. W. L. Clarke and D. C. Carlson, "Nondestructive Measurement of Sensitization of Stainless Steel: Relation to High Temperature stress Corrosion Behavior," *Material Performance* 19, 16—23 (1980).

20. A. P. Majidi and H. A. Stretcher, "Potentiodynamic Reactivation Method for Detecting Sensitization in AISI 304 and 304L Stainless Steels," *Cormswn* 40(8), 393—408 (1984).

21. A. P. Majidi and M. A. Streicher, "The Double Loop Reactivation Method for Detecting Sensitization in AISI 304 Stainless Steels," Corrosion 40(11), 584—93 (1984).

22. S. M. Bruemmer, "Composition-Based Correlations to Predict Sensitization Resistance of Austenitic Stainless Steels," *Corrosion* 42(1), 27-35 (1986).

AQUEOUS STRESS CORROSION OF AUSTENITIC STEELS - H. Khalak, A B. Hull. and T. F. Kassner (Argonne National Laboratory)

OBJECTIVE

The objective of this study, which is part of the ITER validating R&D, is to provide baseline information on the stress corrosion cracking (SCC) susceptibility of candidate austenitic **steels** under conditions of interest for **the** ITER design. The initial focus here was to develop a computer model for radiolysis of fusion reactor water and assess the relevance of coolant chemistry to SCC of reactor structural components.

SUMMARY

Stress corrosion cracking (SCC) of austenitic stainless **steel** in water is considered a key unresolved issue for the **U.S.** ITER shield and blanket design activities.' A computer code has been developed to determine the concentration of radiolytic species produced in the aqueous environment in various subsystems of a fusion reactor in order to estimate the subsequent likelihood of stress corrosion cracking. This code also serves as a valuable precursor to slow-strain-rate tests to determine the SCC susceptibility of austenitic stainless **steels.** The code is being benchmarked with the concentrations of radiolytic molecular species in boiling water reactors. Samples of candidate **steels,** primarily Type 318 NGSS, are being prepared to initiate low-strain-rate tests.

PROGRESS AND STATUS

Introduction and Background

Blanket cooling by means of circulating pressurized water is being considered in a fusion reactor configuration.1 **A** water coolant offers excellent heat transfer characteristics, and has a well-developed technology from commercial fission reactor experience. However, the susceptibility of austenitic steels to SCC under the anticipated conditions for a water-cooled fusion reactor has not been previously addressed in detail. The SCC of these **steels** in nuclear systems is thought to **be** caused by tensile stress, sensitization, and the environment,?in which radiolysis of coolant is a major factor in promoting the SCC. Irradiation-assisted stress corrosion cracking (WCC) may also occur under conditions in which fusion reactors are designed to operate.[3] Radiolytically produced chemical species increase the open-circuit electrochemical corrosion potential (ECP) of the steel. The ECP is the major environmental parameter affecting IASCC. The influence of this factor, coupled with ionic impurities in the coolant, on IASCC is not always easily ascertained from the reactor design. Consequently, both computer and laboratory simulations will be addressed in this project and in other projects.4

Experience with fission reactors has led to various measures[5] to mitigate SCC. However. such is not the case with fusion reactors. A simulation that can quantify the equilibrium speciation according to gamma and neutron fluxes and temperatures expected in a fusion reactor is of great utility.

Computer Simulation Procedures

The radiolytic chemisty in a low-temperature (~45°C) coolant system of a fusion reactor has been evaluated by means of a computer simulation. The computer program generates concentration values of certain chemical species, such as H_2O_2, O_2, and H_2, in the irradiated environment at various points throughout each pertinent subsystem, e.g., the firstwail, breeding blankets, and supports.

To ascertain the levels of dissolved O_2 , H_2O_2, and other water species, a number of chemical reactions with rate constants, activation energies, and G-values for gamma and neutron radiation were incorporated into a system of chemical kinetics equations. Tables I and II contain the chemical equations and radiolysis G-values, respectively, derived from the earlier radiolysis studies of Burns and Moore[6] and Willis et al.[7]

The WR87 computer code, used for reactor physics and design, was substantially modified for our radiolysis code. This computer code operates efficiently on DEC VAX 8700, running the VMS version **4.5** Fortran operating system. Existing numerical routines[8] were incorporated to solve a system of differential equations in order to calculate time-dependent concentrations of the chemical species.

Table 1. Chemical Reactions, Rate Constants, and Activation Energies **Used** for Predicting Concentrations **of** Radiolytically Produced Species in Reactor Coolant

Reactions	K at 25°C (L/mol-sec)	Actlvation Energy (Kcal/mol)
$e^- + e^- \rightarrow H_2 + OH^-$	1.700E+06	3.0
$e^- + H^+ \rightarrow H$	2.400E+10	3.0
$e^- + OH \rightarrow OH^-$	3.000E+10	3.0
$e^- + H_2O_2 \rightarrow OH + OH^-$	1.300E+10	3.0
$e^- + H_2O \rightarrow H + OH^-$	1.600E+01	3.0
$H^+ + OH^- \rightarrow H_2O$	1.438E+11	3.0
$H + H \rightarrow H_2$	1.000E+10	3.0
$H + OH \rightarrow H_2O$	2.000E+10	3.0
$OH + OH \rightarrow H_2O_2$	4.500E+07	3.0
$OH + H_2 \rightarrow H_2O + H$	4.500E+07	7.0
$OH + H_2O_2 \rightarrow H_2O + H$	4.500E+07	4.5
$H + H_2O_2 \rightarrow H_2O + OH$	9.000E+07	4.5
$e^- + O_2 \rightarrow O_2^-$	1.900E+10	3.0
$H + OH^- \rightarrow e^- + H_2O$	2.000E+07	3.0
$H + O_2 \rightarrow HO_2$	2.000E+10	3.0
$HO_2 + * \rightarrow H^+ + O_2^-$	8.000E+05	3.0
$H+ + O_2^- \rightarrow HO_2$	5.000E+10	3.0
$HO_2 + HO_2 \rightarrow H_2O_2 + O_2$	2.700E+06	4.5
$HO_2 + O_2^- \rightarrow H_2O_2 + O_2 - H^+$	1.500E+07	3.0
$OH + HO_2 \rightarrow H_2O + O_2$	1.200E+10	3.0
$OH + O_2^- \rightarrow OH^- + O_2$	1.200E+10	3.0
$H + HO_2 \rightarrow H_2O_2$	2.000E+10	3.0
$e^- + HO_2 \rightarrow H_2O_2 - H^+$	2.000E+10	3.0
$H + O_2^- \rightarrow H_2O_2 - H^+$	2.000E+10	3.0
$H_2O + * \rightarrow H+ + OH^-$	2.600E-05	3.0
$e^- + HO_2 \rightarrow HO_2^-$	2.000E+10	3.0
$HO_2 + O_2^- \rightarrow O_2 + HO_2^-$	1.500E+07	4.5
$OH- + H_2O_2 \rightarrow HO_2^- + H_2O$	1.000E+08	4.5
$HO_2^- + H_2O \rightarrow OH^- + H_2O_2$	1.022E+04	3.0

Table 2. Radiolysis G-Values Used for Predicting Concentrations of Radiolytically Produced Species in Reactor Coolant

Species	H	H^+	H_2	H_2O	H_2O_2	HO_2	O_2	OH	OH^-	e^-
G-values										
γ-ray	0.6	**2.7**	**0.45**	0.4	0.6	0.02	0.225	**2.6**	1.0	2.6
neutron	0.5	0.93	**0.88**	0.66	0.99	-	0.44	1.09	*1.0*	0.93
at 280°C	0.3	0.4		2.0	-			4.7		0.4

Input consists of the reactor loop configuration, dose rate and type of radiation, specified chemical reactions, their rate constants, and the initial reactant concentrations. The code then calculates. as a function of time, the concentration of all chemical species (such as H_2O, H_2, O_2, H_2O_2, OH, H, e^-, HO_2, O_2^-, HO_2^-, OH-, H^+) from a ***set*** of radiation–induced chemical reactions with homogeneous kinetics. The coolant **is** pure water (conductance of < 10 mmho/cm).[9] Further details about the simulation logic can **be** observed in Figure 1.

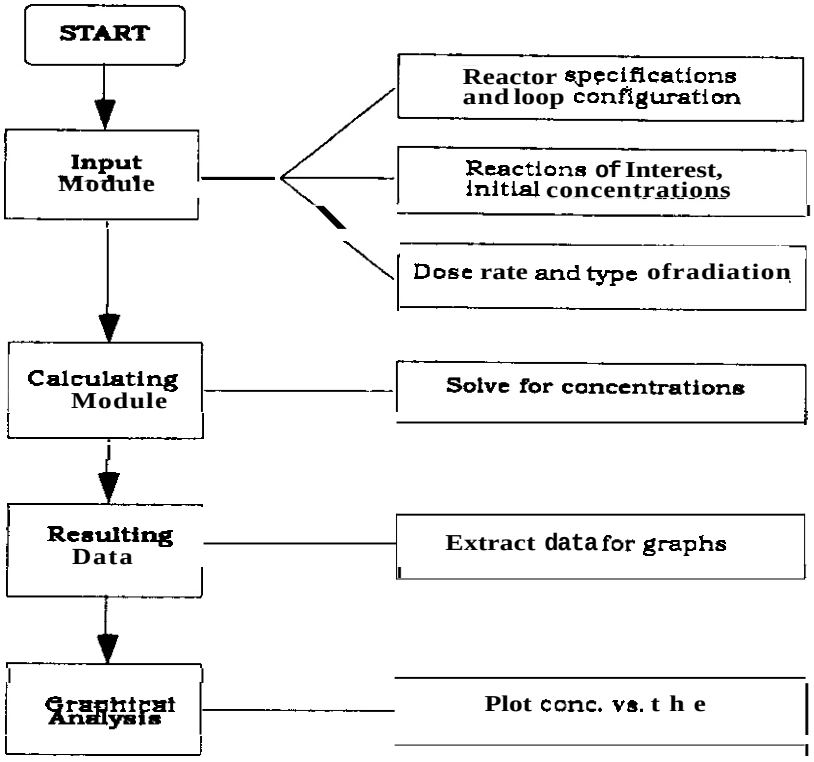

Figure 1. Simulation Flowchart Diagram

Results and Analysis

Code Benchmarking

The effect of gamma and neutron radiation levels on the concentrations of several radiolytic species at 75°C and an irradiation time of five seconds, when most species are approaching steady-state concentrations, is shown in Figure 2. The concentration of steady-state radiolytic species increases somewhat at higher energy loads. The *effect* of neutron radiation on equilibrium concentrations was greater than that of gamma radiation. For an energy loading of 1 W/cm^3, the concentration of H_2O_2 was 0.02 ppb under both gamma and neutron radiation. However, for 10 W/cm^3, the concentrations were 0.1 and 0.2 ppb, respectively. The concentrations of radiolytic species showed very little dependence on temperature (Figure 3).

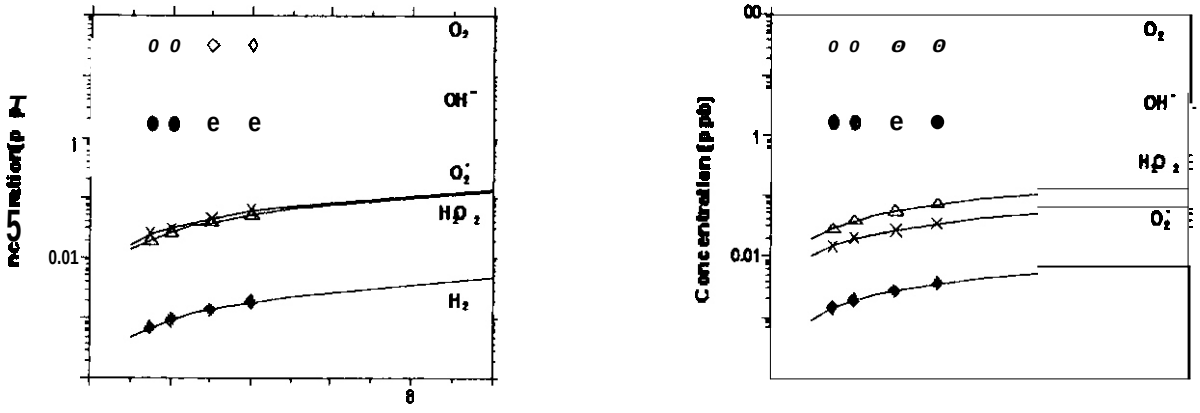

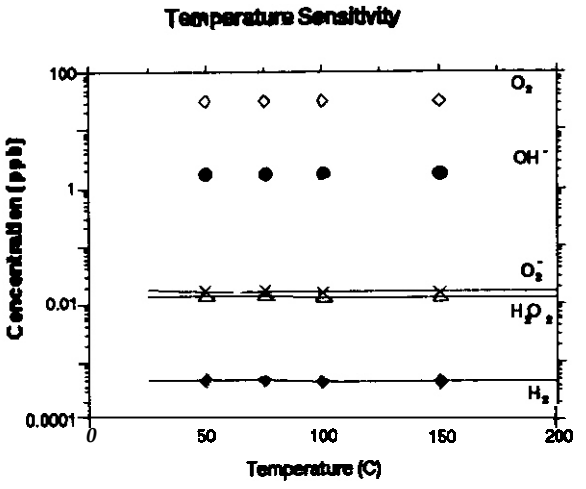

Flg. 3. Effect of Temperature on the Concentrations of Selected Radiolytic Species

Simulation of an ITER S

A computer simulation was made for the U.S. ITER design ot a fusion reactor breeding-blanket coolant system.[10] This design was for a low-temperature water coolant (45%) and for gamma radiation of 0.8 W/cm³ and neutron load of 3 2W/cm³.[11] The concentrations of molecular species versus time of irradiation (0–so00 seconds) are shown in Flgures 4 and 5. For gamma radiation, the O_2 concentration achieved a value of 32 ppb. Under neutron radiation, however, it rose to 50 ppb after so00 seconds and had not yet reached equilibrium at ~5000s. Peroxide levels under gamma radiation stayed under 10 ppb (max. ~8 ppb), but reached concentrations similar to those of O_2 under neutron nux.

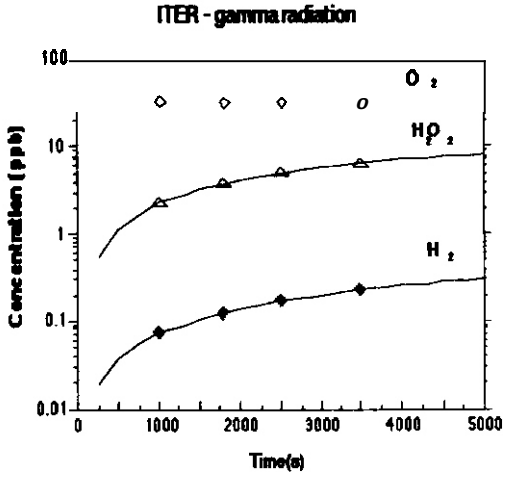

Figure 4. Molecular Concentrations Produced in ITER Configuration Under 0.8 W/cm³ y-radiation

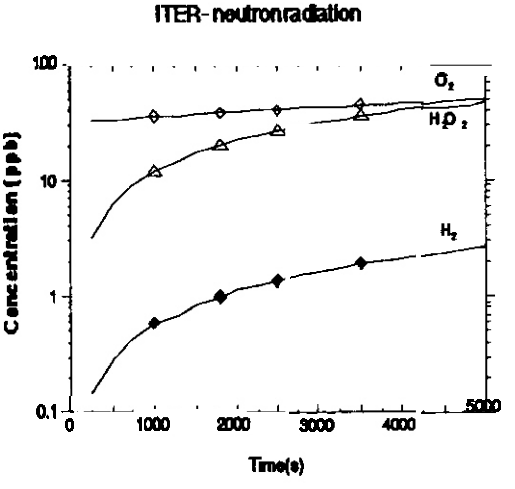

Figure 5. Molecular Concentrations Produced in ITER Configuration Under a 3.2 W/cm³ Neutron Load

Discussion

Although the results from this computer simulation are still somewhat preliminary, they do provide insight into the contribution of radiolysis to the chemical environment that may be found in a water-cooled fusion reactor. Until such time that field data are available from operating fusion reactors. such a model is necessary to obtain parameters relevant to fusion reactor materials.

CONCLUSIONS

Preliminary results for the concentrations of radiolytically produced species have been obtained from a *new* computer code that was developed to simulate the radiolysis of fusion reactor water coolant. The modeling work provides a useful precursor to laboratory studies of SCC of candidate alloys in the simulated coolant environments.

FUTURE WORK

The SCC susceptibility of several candidate stainless steels, including weldment specimens, will be determined in high-purity water containing low concentrations of radiolysis products (O_2, H_2, and H_2O_2) obtained from computer simulations on fusion reactor coolant systems.

REFERENCES

1. C. Baker, "U.S. ITER Shield and Blanket Design Activities," Fusion Technol. 15, 849-57 (1989).
2. F. Farfaletti-Casali, "Systems Integration, Maintenance, Containment and Shielding." Nucl. Eng. Des./Fusion 3, 383-98 (1986).
3. R. H. Jones, "Assessment of Stress-Corrosion Cracking for Near-Term Fusion Reactors," pp. 184-188 in Fusion Reactor Materials Semiannual Progress Report, DOE/ER-0313/4, March 31, 1988.
4. E. P. Simonen and R. H. Jones. "Modeling Grain Boundary Microchemistry Related to IASCC", NACE preprint 560, Corrosion 89, New Orleans, LA, April 17-21, 1989.
5. J. C. Danko, organizer, Proceedinas: Second Seminar on Countermeasures for Pipe Crackina in BWRs, Vols. 1-3, EPRI NP-3684-SR, (1984).
6. W. G. Burns and P. B. Moore, "Water Radiolysis and Its Effect Upon In-Reactor Zircaloy Corrosion," Radiat. Eff., 30, 233-42 (1976).
7. C. Willis, A. W. Boyd, A. E. Rothwell, and O. A. Miller, "Experimental and Calculated Yields in the Radiolysis of Water at Very High Dose Rates," Int. J. Radiat. Phys. Chsm. 1, 373-81 (1969).
8. K.H. Schmidt, "A Computer Program for the Kinetic Treatment of Radiation-Induced Simultaneous Chemical Reactions: A Revised Version in Fortran IV", ANL-7693 (1970).
9. P.A. Finn and D. K. Sze, "Impact of Radiolysis on the Design of Breeder Blanket Systems for ITER," ANL Fusion Power Program Research report, October 1988.
10. Y. Gohar, "Solid Breeder Blanket," Argonne National Laboratory, U.S. Contributions to the Homework for ITER, February/March 1989.
11. P.A. Finn and A. Lide, "Water Coolant Conditions," Argonne National Laboratory, U.S. Contributions to the Homework for ITER, February/March 1989.

CORROSION AND COMPATIBILITY STUDIES IN FLOWING LITHIUM ENVIRONMENTS – A. B. Hull and O. K. Chopra (Argonne National Laboratory)

OBJECTIVE

The objective of this research is to provide experimental data for the development of an analytical model that will predict the effect of flow velocity and nonmetallic elements on the corrosion behavior of vanadium–base alloys in lithium. Measurements of chemical and metallurgical changes are used to establish the mechanisms and kinetics of rate–controlling processes.

SUMMARY

The Argonne Lithium Corrosion Experiment (ALICE), a high–flow-velocity ferritic steel forced circulation test facility, is now fully operational and is being used to address the effects of fluid flow velocity and nonmetallic elements on corrosion, mass transfer, and deposition in liquid metal systems. Hydrogen distribution data were obtained from the austenitic steel Fatigue and Failure Testing in Lithium (FFTL–3) facility in which the low circulation velocity provided only for impurity control of the liquid metal; analysis of these data indicates that hydrogen fractionates between lithium and vanadium alloys in accordance with the thermodynamic distribution coefficients.

PROGRESS AND STATUS

Introduction

When structural materials are exposed to liquid lithium systems. local corrosion phenomena and mass and interstitial–element transfer rates depend on the difference between the chemical activities of the alloy constituents in lithium and in the structural material. Thus, chemical interactions have been shown to play a dominant role in both the corrosion behavior of vandium–base alloys[1] and in the solubility, diffusivity, and resultant distribution of hydrogen.[2,3]

These earlier studies emphasized the effects of time, temperature, and liquid metal purity: however, the influence of additional system parameters on corrosion needs more attention. In particular, the effects of lithium flow velocity on corrosion and deposition in experimental test facilities has not been well established.

This report presents information about the start-up and steady–state operation of the ALICE[4] facility and data from further hydrogen distribution studies.

Operation of new high–flow–velocity lithium corrosion test facility

ALICE, a unique ferritic/martensitic (Fe–9Cr–1 Mo, ASTM P9 A355) facility for studies of fusion materials and systems, has been successfully filled and as of March 31, 1989. had acumulated > 3000 h of running time. This facility[4] (see Fig. 1) employs five electromagnetic pumps circulating 26 liters of lithium through two counterflow primary loops and a secondary purification loop linked by a common mixing vessel. Magnetic flowmeters are emplaced in–line on the cold end piping of each of the three loops. The cylindrical specimens are depicted in the cutaway portion of test section A, and the flat corrosion coupons can be visualized in the cutaway portion of the isothermal test vessel.

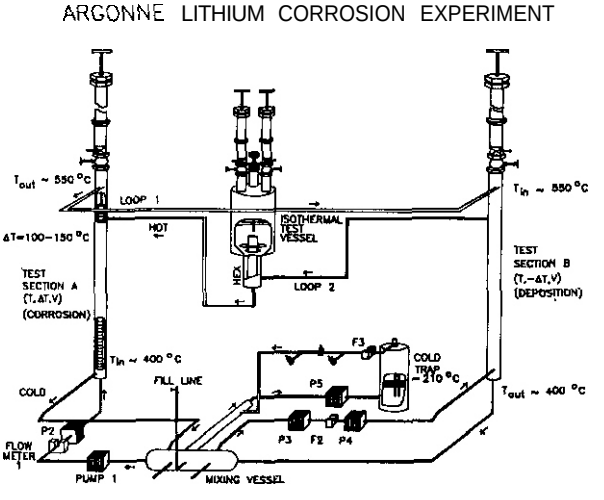

FIG. 1. Schematic of high–flow–velocity ferritic steel Argonne Lithium Corrosion Experiment.

Reactor grade lithium was transferred into the loop from a supply tank filled at the Lithium Corporation. During the initial stages of lilling. the loop was kept under vacuum until the secondary cold-trap loop was completely filled. This procedure prevented the trapping of argon gas in the system and insured against vanability of flow through different sections of the loop because of poor lithium wetting properties. The remainder of the test sections A and B and the isothermal vessel were filled with differential argon pressure (a slightly higher pressure, i.e., 0.5 to 1 psi. in the supply tank) until lithium reacnea the specimen holding ledge in the three vessels. This differential pressure provided a slow and Controllea transfer of lithium.

Temperature measurements are continuously obtained from 60 chromel-alumel thermocouples located on the outside surfaces of the system piping. Three instrumentation cabinets house the temperature controllers. two 30-channel process recorders, timers. ana alarms for overheat, lithium flow, and cover gas pressure. There are three programmable microprocessor heater controllers. one each for the test sections and isothermal tank: and two controllers for the cold trap and mixing vessel. Twenty-two manual controllers are available for the line heaters. The electrical heaters are either a clamshell type used on the vessels or GE wire or a heating tape for the piping. The test sections. isothermal test vessei. ana mixing vessel are insulated witn 1-1/2 in.-thick rigid hydrous calcium silicate insulation. Additionally, the loop has been insulated with a 1000°C ceramic blanket-type insulation.

An automated argon blanketing system was designed and deployed to function as a reaction suppression system. Two independent argon blanketing systems are employed. One is focused on the lower level of the test facility (Fig. 1) and the otner system traces along the lithium-containing piping and test vessels. In each system, two cylinders of argon with separate solenoids are connected in parallel so that when there is a leak (causing a temperature excursion) or when preset temperature limits are exceeded. the main power supply will be tripped and the system will be flooded with an inert argon blanket. displacing air lrom the space around the loop piping, floor, and test vessels. Air for cooling the induction pumps is vented to the outside of the stainless steel enclosure. Temperature detectors rather than smoke detectors are employed as blanketing triggers immediately above the enclosure because of the quicker response.

Checkout of all operational systems on the loop is continuing. The slightly higher carbon in the ferritic (compared to austenitic) steel structural material of the loop creates a aecarbunzation effect with resultant high carbon content in the lithium. Additional chemical analyses will be performed to ensure that the lithium chemistry in the loop has stabilized before actual corrosion/mass-transfer tests are initiated.

Partitioning of hydrogen between vanadium alloys and lithium

The hyarogen distnbution tests were conaucted in the FFTL-3 forced-circulation lithium loop. This facility. constructed of Type 304 stainless steel. consists of a pnrnary loop equipped with three test vessels and with cold- and hot-trapping purification capaoilities to control the concentration of nonmetallic elements. Various vanadium alloys were immersed in the flowing lithium in two separate isothermal test vessels maintained at different temperatures. Following exposure, the specimens were gently cleaned in chilled ethanol/methanol to avoid the introduction of hydrogen. For ail tests, Li was c rculated at ~ 1 liter/min in the primary loop, and the concentration of hydrogen in the Li was maintainea at ~120 wppm.

Specimens of V, V-20Ti, V-15Cr-5Ti, and V-3Ti-0.5Si were immersed in the flowing lithium in two separate isothermal test vessels maintained at different temperatures. The specimens had approximate dimensions of 1.9 x 1.0 x 0.09 cm and were mechanically polished before exposure to lithiurn. Total hydrogen in the specimens after lithium immersion was determined from both residual gas analysis and inert gas and vacuum fusion procedures. The concentrations of hydrogen in tne vanadium-base alloy specimens after exposure were all well under 5 wppm. Further details on these procedures and aetermination of hydrogen in the lithium are provided elsewhere.[2,3]

Hydrogen will fractionate between Li and various refractory metals as a function of temperature. A distribution coefficient, K_w, can be defined as the ratio of the H concentration in the V alloy to that in the liquid Li:

$$K_w = C_V / C_{Li}$$

where C_V and C_{Li} are concentrations (wt%) of H in the V alloy and Li. respectively, at constant hydrogen partial pressure. The theoretical temperature-dependent distributions[3] of H between Li and several refractory metals are shown graphically in Fig. 2 as a function of temperalure. At a temperature of 500°C, a hydrogen concentration of 100 wppm in lithium will establish a calculated hydrogen concentration of ~3000 wppm in yttrium, 10 wppm in titanium, 0.3 wppm in vanadium, and <0.0001 wppm in chromium.

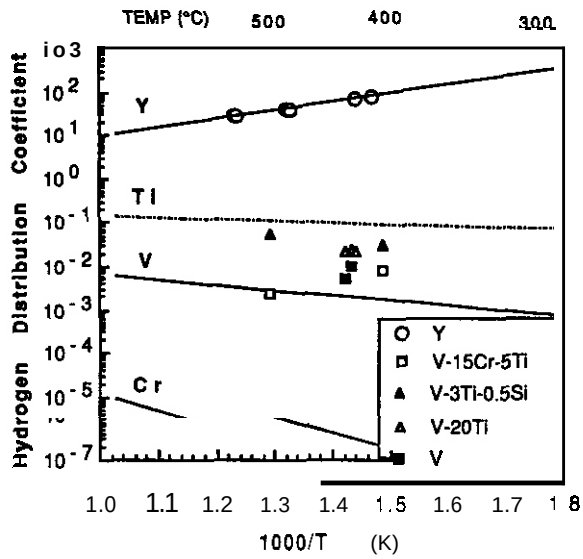

FIG. 2. Temperature dependence of equilibrium distribution coefficients for hydrogen between lithium and selected vanadium alloys or yttrium.

Experimental results from these hydrogen distribution studies (Fig. 2) were compared with thermodynamic distribution coefficients for hydrogen in the vanadium/lithium system. Both experimental and theoretical results concurred in demonstrating that K_w was very low; i.e., hydrogen in lithium did not increase the hydrogen content in vanadium alloys. This suggests that hydrogen concentrations in vanadium alloys will be extremely low under reactor conditions, where the hydrogen (tritium) concentration in lithium is anticipated to be < 1 wppm.

CONCLUSIONS

Results obtained in this study indicate that tritium pickup by vanadium alloys in the reactor structure will not be significant. ALICE is fully operational and the flow rate regimes are such that the effect of the flow velocity parameter on corrosion and deposition can be fruitfully explored during the next year.

FUTURE WORK

Experiments are continuing to better define temperature-dependent hydrogen distribution coefficients between V alloys and Li as a function of substitutional alloying elements. Future studies will utilize ALICE to examine the effects of flow velocity on mass transfer and corrosion; and any trends that are observed will be compared with those reported by other researchers.

REFERENCES

1. O. K. Chopra and A.B. Hull, "Influence of Carbon and Nitrogen Impurities on the Corrosion of Structural Materials in a Flowing–Lithium Environment," Fusion *Technol.* 15, 309–314 (1989).
2. B. A. Loomis, A.B. Hull, O. K. Chopra, and D. L. Smith, "Hydrogen Concentration Distribution in Vanadium-Base Alloys After Surface Preparation and Exposure to Liquid Lithium," pp.160–167 in Fusion Reactor Materials Semiannual Progress Report for the *Period* Ending March ***31, 1988.*** DOE/ER–0313/4, Oak Ridge National Laboratory, Oak Ridge, Tenn.
3. A. B. Hull, O. K. Chopra, B. Loomis, and D. L. Smith, 'Partitioning of Hydrogen in the Vanadium–Lithium–Hydrogen System at Elevated Temperatures," Fusion *Technol.* 15, 303–308 (1989).
4. D. L. Smith, O. K. Chopra. and A. B. Hull, 'Corrosion and Compatibility Studies in Flowing Lithium Environments," pp.189–192 in Fusion Reactor Materials Semiannual Progress Report for the Period Ending March ***31, 1988,*** DOE/ER–0313/4, Oak Ridge National Laboratory. Oak Ridge, Tenn.

ASSESSMENT OF STRESS-CORROSION CRACKING IN A WATER-COOLED ITER--R. H. Jones and S. M Bruemmer, Pacific Northwest Laboratory[a]

OBJECTIVE

The objective of this evaluation was to assess the effects of material chemistry and processing and water temperature and chemistry on the stress-corrosion cracking (SCC) of austenitic stainless steels in high-purity water. The emphasis of this evaluation is non-irradiation effects on SCC. Recommendations regarding material chemistry and processing temperatures and water chemistry limits are also objectives of this study.

SUMMARY

Water-cooled. near-term reactors will operate under conditions at which SCC is possible; however, control of material purity and processing and coolant chemistry can either eliminate or greatly reduce the probability of this type of structural failure. This evaluation has focused on an assessment of water impurity effects on SCC of austenitic stainless steel at temperatures below 100 C and on the conditions controlling sensitization in the fusion heat of Type 316 SS and the fusion materials heat of modified Type 316 SS designated as PCA. This assessment identifies the dominant effect of small concentrations of impurities in high-purity water on SCC such that crack growth rates at 25-75 C in water with as little as 5-15 ppm Cl^- are equal to the crack growth rates at 200-300 C in high-purity water. These effects are primarily for Sensitized Type 304 SS, so analysis of sensitization behavior of fusion austenitic alloys was also undertaken. An SSDOS model developed at PNL was used to make these assessments, and correlation to experimental results for Type 316 SS was very good. Both the fusion heat of Type 316 SS and PCA can be severely sensitized but with proper thermal treatment it should be possible to avoid sensitization.

PROGRESS AND STATUS

Water Purity Effects on Stress-Corrosion Cracking

Stress-corrosion cracking (SCC) of austenitic stainless steel has been studied extensively at temperatures exceeding 100 C and especially at 288 C, because of impetus from the light-water reactor industry. At temperatures lower than 100 C there have been relatively few studies. However. conclusions from these studies indicate that 1) neither transgranular nor intergranular stress-corrosion cracking has been reported in deionized (DI) high-purity water; 2) impurities such as Cl^-, F^-, $S_2O_3^=$, can cause intergranular SCC at temperatures as low as 25 C with crack growth rates equal to or exceeding those observed at 288 C; 3) there has been a report that impurities can cause transgranular SCC at 98 C, but not below; and 4) rack initiation is a very slow process at low temperatures even though the crack growth rate may be equal to or greater than those observed at 288 C.

Stress-corrosion cracking occurs with selected combinations of materlal microchemistry and mlcrostructure. environment. and mechanical stress. In austenitic stainless steels. the most severe material condition coincides with the precipitation of chranium-rich carbides at the grain boundaries, producing a condition known as sensitization; however, transgranular stress-corrosion cracking (TGSCC) which is unrelated to this grain boundary condition, has also been observed. Important environmental variables include oxygen. chloride. fluoride and sulfur ions, temperature, and pH. Mechanical stress from external loads. or residual stresses fran welding or cold working, can cause SCC. A threshold stress or stress intensity below which SCC does not occur has been measured for most materlals which exhibit SCC. Available data on SCC of austenitic stainless steel at temperatures lower than 100 C indicate that the controlling parameters are the same at low and elevated temperatures, so experience at elevated temperatures can be extrapolated to low-temperature water.

An assessment of intergranular stress-corrosion cracking (IGSCC) in a spent fuel pool component. which was in contact with water at temperatures ranging from 7 C to 33 C, was reported by Jones et al. (1,2). Cracks propagated through the 0.6-an-thick wall of the piplng in this fuel pool in less than 5 yrs of service. It was concluded that crack growth was by IGSCC of a high-carbon (0.07 wt%) 304 SS, which was sensitized by welding. Cracks propagated in the heat-affected zone (HAZ) with the probable assistance of either Cl^- or sulfur compounds in the water. Surface defects produced by grinding during weld preparation may also have contributed to the relatively fast SCC observed in this component.

Laboratory SCC tests conducted by Bruemmer et al. (3) and by Bruemmer and Johnson. Jr. (4) corroborated most of the conclusions reached by Jones and Johnson. Jr. regarding the role of C concentration of the steel and Cl^- or $S_2O_3^-$ effects in the water on SCC at 30 C. These tests were conducted using constant load samples. which were loaded to 1.8 to 2.4 of their yield strengths for 640 hrs. Using compact tension samples, Jones

---

a) Operated for the U.S. Department of Energy by Battelle Memorial Institute under Contract DE-AC06-76RLO 1830.

et al. (5) observed crack grath rates approaching 10^{-4} mm/s at 90 C. and using constant load samples loaded to 1.2 of their yield strength. a crack growth rate of 3 x 10^{-5} mm/s at 25 C in DI water with 15 ppm $S_2O_3^=$ (6). Ford and Povich (7) observed IGSCC in sensitized Type 304 SS at 100 C in DI water using a constant extension rate test (CERT); Ford (8) also reported IGSCC results at 98 C in 0.01 M Na_2SO_4. Other reports on the effect of specific impurities on IGSCC include those by Shoji et al. (9) on IGSCC during cyclic loading in water with 15 ppm O_2 at 83 C, and Ward et al. (10), Sharfstein and Brindley (11), and Sieradzki et al. (12) on the effects of F^-, Cl^- and $S_2O_3^=$ ions. respectively. Using U-bend samples. Sharfstein and Brindley (11) observed TGSCC in both Type 304 and 347 SS at temperatures of 75 C and 98 C and 200 and 25 ppm Cl^-, respectively.

Crack growth rate data for austenitic stainless steels are shown as a function of temperature in Figure 1. The results of Ford and Povich (7) and Ford (8) for SCC of sensitized Type 304 SS in DI water (solid circles and squares), indicates that the crack growth rate decreases substantially at temperatures below 100 C. The conductivity of the DI water used by Ford and Povich was 0.4 mho/cm, while the addition of 0.01 M Na_2SO_4 increased the conductivity to 2400 mho/cm and the Crack growth rate by a factor of 100 at 100 C. At tenp-eratures above 200 C, a decrease in the O_2 concentration from 8 to 0.2 ppm produced TGSCC in a sensitized Type 304 SS with 0.07 wt% C. Transgranular SCC was also observed in a Type 347 SS tested at 98 C in water with 25 ppm Cl^-. The TGSCC velocity is about a factor of 10 slower than the IGSCC velocity at 288 C, but at temperatures below 100 C. the crack velocities are primarily a function of the Cl^- concentration. Figure 2. Stress corrosion data on other austenitic stainless steels such as 316 SS are not as plentiful as for Type 304 SS; however, in general the 300 series stainless steels behave similarly. given equal grain boundary Cr microchemistries. The SCC behavior of a low-C Type 304 SS and Type 316 SS are similar: the Type 316 SS exhibits more resistance to TGSCC. Thus, so the data presented in Figures 2 and 3 are expected to apply to Type 316 SS, even though there are no data on low-temperature SCC of Type 316 SS.

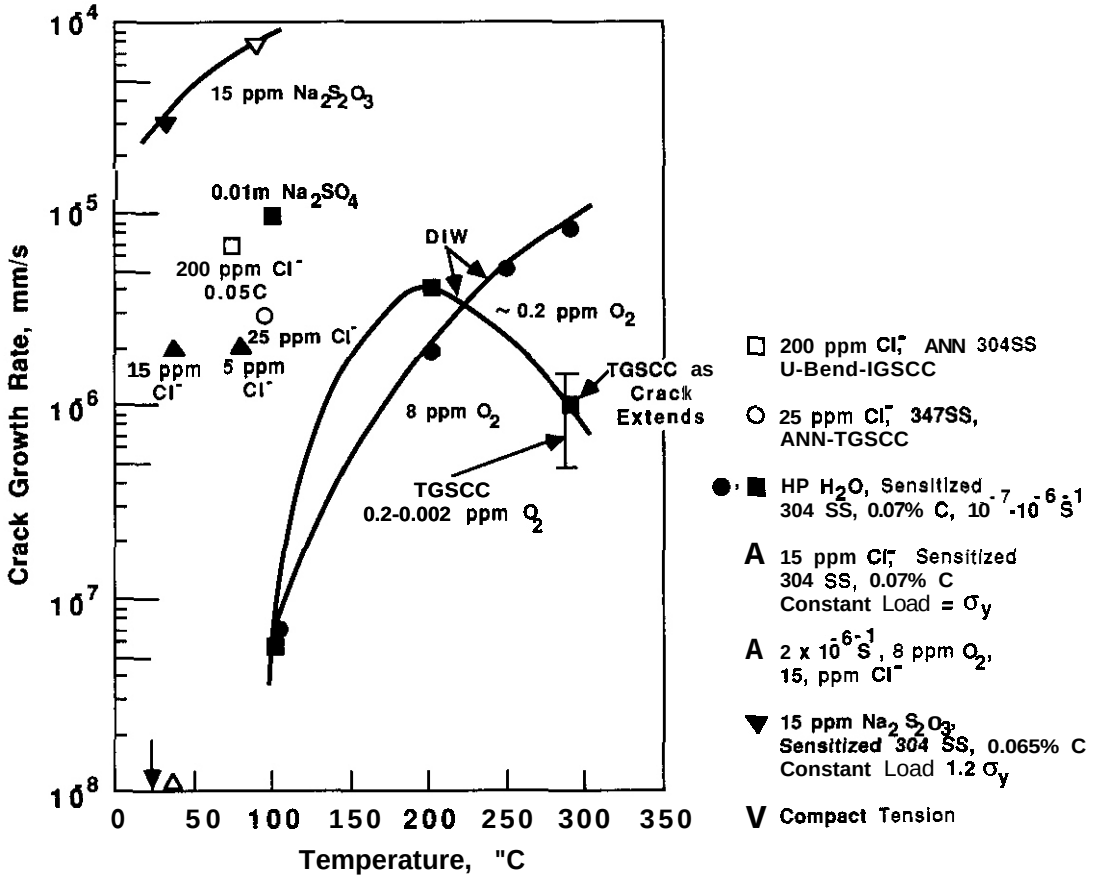

Figure 1. Stress-Corrosion Crack Growth Rate Versus Water Temperature for Austenitic Stainless Steel Showing the Effect of Impurities in the Water.

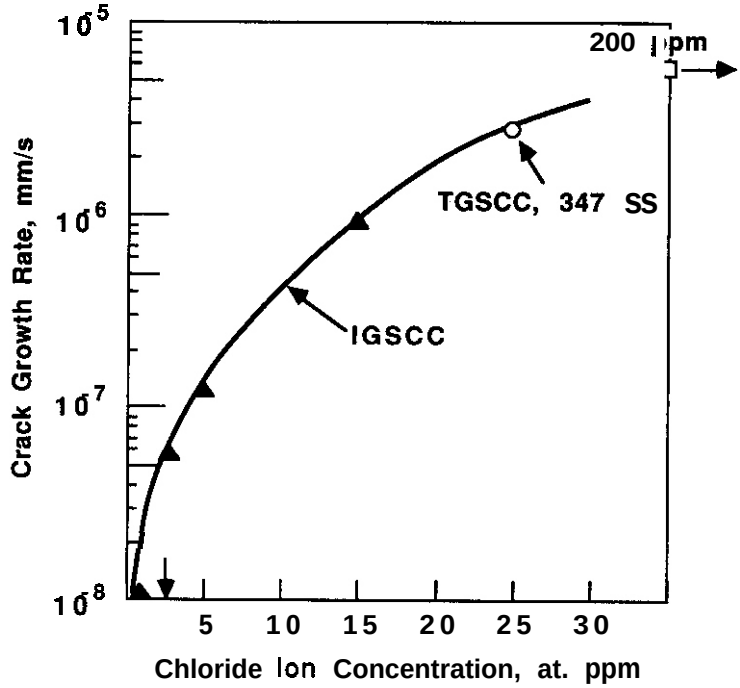

Figure 2. Stress-Corrosion Crack Growth Rate Versus Chloride Ion Concentration in Water for Austenitic Stainless Steel.

A key parameter that correlates the grain boundary microchemistries of austenitic stainless steels with their resistance to IGSCC is degree of sensitization (DOS). This electrochemically derived parameter has been shown to correlate with IGSCC resistance. A high DOS corresponds to low IGSCC resistance or high susceptibility to IGSCC. Bruemmer et al. (13) have evaluated the DOS of Types 304L, 304, 316L, 316 and 316LN SS with C concentration ranging from 0.013 to 0.072. Their results indicate that Type 316L SS with 0.014 wt% C could not be sensitized much above 1 or 2 C/cm^2, while a Type 316L with 0.02 wt% C was sensitized to 10 at 600 C and 25 C/cm^2 at 700 C. A DOS value of 10 C/cm^2 is sufficient to produce IGSCC. Also, a Type 316 SS with 0.035 wt% C was sensitized to 20 and 50 C/cm^2 at 600 C and 700 C. The specification for C concentration in Type 316L SS is 0.035 wt%. Clearly, C concentrations within the specification for Type 316L SS are sufficient to produce a sensitized material that can undergo IGSCC.

The detrimental effect of impurities in water is clearly shown by the data in Figures 1 and 2. In Figure 1 the effect of concentrations, as *low* as 15 ppm of Cl^- and $S_2O_3^=$ on the crack growth rate. is apparent fran the reversal of the tmperature dependence shown for DI water. Impurities such as Cl^- and $S_2O_3^-$ clearly modify the rate-limiting step for crack growth in DI water so that velocities equal to or exceeding those at 288 C result. The smooth increase in the crack velocity with increasing Cl^- concentration shown in Figure 2 also illustrates the detrimental effect of water impurities. Their effect is sufficient also to override the dominance of Cr depletion on crack growth rate so that both TGSCC and IGSCC data fit the same curve. Fluoride ions are clearly more detrimental than Cl^- ions. and may be even more detrimental than S_2O_3 ions. Fluoride ion concentrations as low as 0.5 ppm produced IGSCC at stresses above 350 MPa. Residual stresses usually do not substantially exceed the yield strength of a material (200-250 MPa for Type 304 SS), so stresses equal to or exceeding 350 MPa generally require an external load.

Stress thresholds for SCC are generally equal to or exceed the yield strength of the material. Again, for low-temperature SCC there is a scarcity of data to evaluate the stress dependence of SCC, but the data given in Figure 3 give sane indication of their magnitude. These results suggest that the stress must be equal to or exceed the yield strength of the material for IGSCC in low-temperature water. The $MgCl_2$ data fran results of Jones and Wang (14) are shown only for canparison purposes. as this test is conducted at 155 C in a concentrated Cl^- environment, and are not considered typical for aqueous SCC. The crack morphology is transgranular and the threshold is considerably less than the yield strength. Crack advance is probably due to a hydrogen-induced process, unlike aqueous environments. which is primarily an anodic dissolution process. Stress intensity thresholds are another method for describing the limiting mechanical loading condition for SCC. The stress intensity is a function of both the stress and the square root of the crack length. In DI water at 97 C Ford (8) measured a stress intensity threshold of about 12 MPa-m for sensitized Type 304 SS, while in DI water with 15 ppm $S_2O_3^=$, Jones et al. (5) measured a threshold of about 25 MPa-m . These are relatively low values, as the fracture toughness of Type 304 SS exceeds 100 MPa-m .

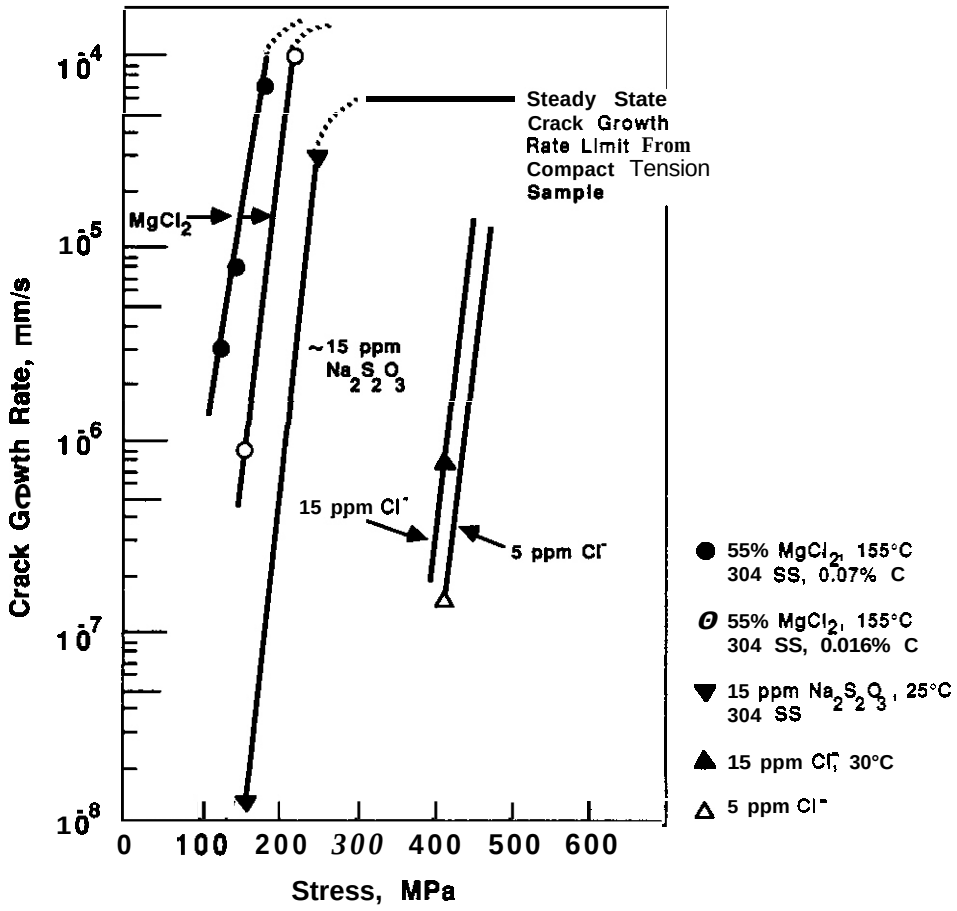

Figure 3. Stress-Corrosion Crack Growth Rate Versus Applied Stress for Austenitic Stainless Steel in Various Environments.

Sensitization Development in Fusion Reactor Materials

Quantitative sensitization development in two austenitic SS heats from the fusion materials stockpile was predicted using the model SSOOS (15,16). Compositions for the heats. X-15893 (316 SS) and K-280 (PCA), are listed below. SSDOS enables prediction of chromium depletion and degree of sensitization (DOS) as measured by the electrochemical potentlokinetic reactivation (EPR) test fran material composition and initial condition. The model has been shown to accurately predict sensitization development in a large number of 304 and 316 SS heats (16,17).

Table 1. Compositions of Fusion Heats of Austenitic Stainless Steels

Heat	C	Cr	Ni	Mo	Mn	Si	Ti	N
316	0.056	16.7	12.0	2.4	1.7	0.7	-	-
PCA	0.046	14.0	15.9	1.9	1.7	0.5	0.3	0.01

Isothermal sensitization behavior for both heats was assessed for heat treatment temperatures between 500 and 1000 C. Predictions for the 316 heat showed rapid sensitization at temperatures fran 700 to 850 C. Sensitization is thermodynamically limited at higher temperatures and kinetically limited at lower temperatures. Time-temperature-sensitization (TTS) behavior is illustrated in Figure 4 using a critical EPR-DOS value of 5 C/cm^2 to indicate the onset of sensitization.

A direct comparison can be made between measured and predicted EPR-COS for this heat, as shown in Figure 5. Limited sensitization measurements were performed previously (17) after solution annealing at 1100 C. The quantitative nature of the predictive capability is documented by canparing data at 600, 700, and 800 C. Although predictions are not exact, EPR-DOS is reasonably estimated at most temperatures and times.

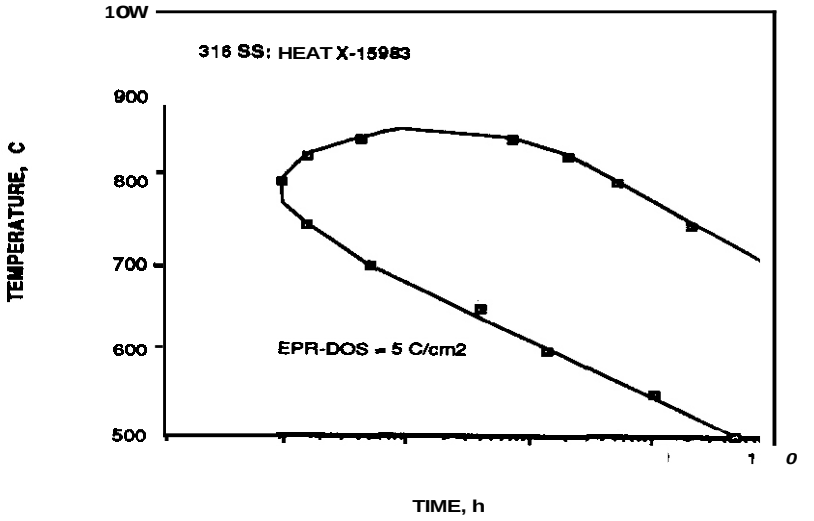

Figure 4. Time-Temperature-Sensitization Curve for 316 Heat X-15893.

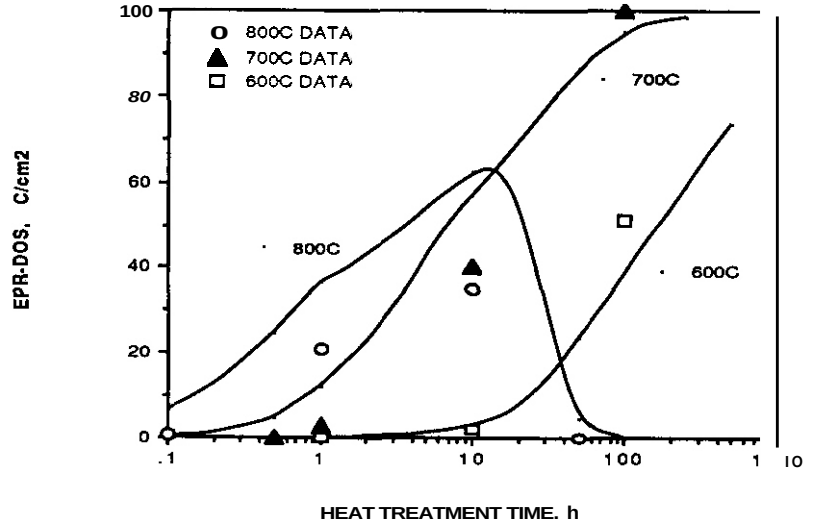

Figure 5. Comparison of Measured and Predicted Sensitization Development in 316 SS Heat X-15893.

Isothermal sensitization behavior for the PCA material was also evaluated using the SSDOS model. However. the presence of a stabilizing alloying element. titanium. in this alloy will impact the carbon in solution available to form chranium carbides and. thereby. prompt sensitization. The amount of soluble before heat treatment is critical to making realistic DOS predictions. A relationship for carbon solubility in titanium-modified SS was developed based on literature data(4,5). This relationship is shown in Figure 6 along with measured solubilities as a function of temperature. It is important to note that this information is for an 18-8 alloy which may be different than that for the PCA canposition. As expected, carbon solubility drops with decreasing temperature, reaching values below 0.01 wt% at temperatures of 950 C. The PCA bulk level of 0.046 wt% carbon corresponds to a temperature of about 1130 C. Since mill-annealing temperatures were reported to be 1050 C, the available carbon should be about 0.021 wt%.

The TTS curves for the PCA heat are presented in Figure 7. Three initial conditions are evaluated: (1) all carbon in solution (0.046%). (2) after annealing at 1050 C (~0.021% in solution), and (3) 0.01% in solution. Sensitization is predicted to occur after very short treatments (<0.1 h) at temperatures between 700 and 900 C. Times to sensitize are less than 30 s at 800 to 850 C. This rapid sensitization over a rather large range of temperatures is due to the extremely low chromium content in the PCA material. Intergranular attack and SCC of 304 and 316 SS have been shown to occur when grain boundary chranium levels drop below 13 to 13.5 wt% (20.21). The initial chromium concentration in PCA is only slightly above this critical amount and 2 to 4 wt% below typical SS. As a result. any chranium carbide precipitation tends to promote sufficient localized chranium depletion to cause susceptibility. Titanium additions will reduce this susceptibility by

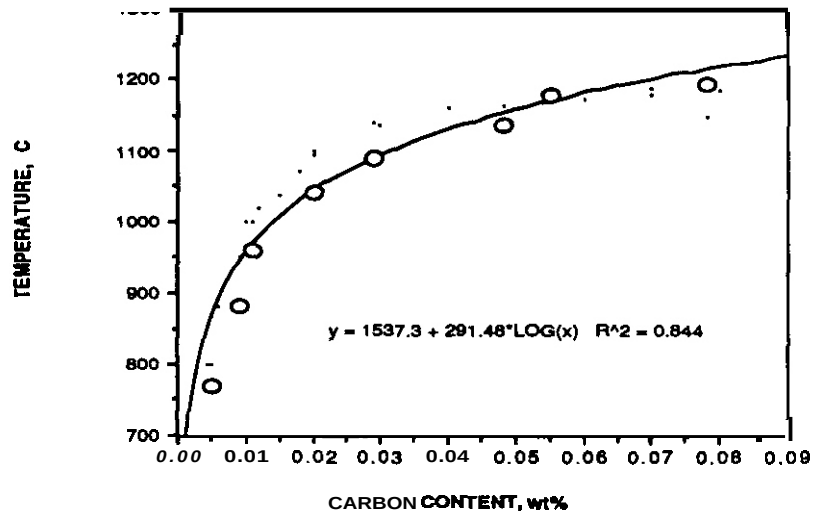

Figure 6. Carbon Solubility for a Ti-Modiffed 18-8 Stainless Steel.

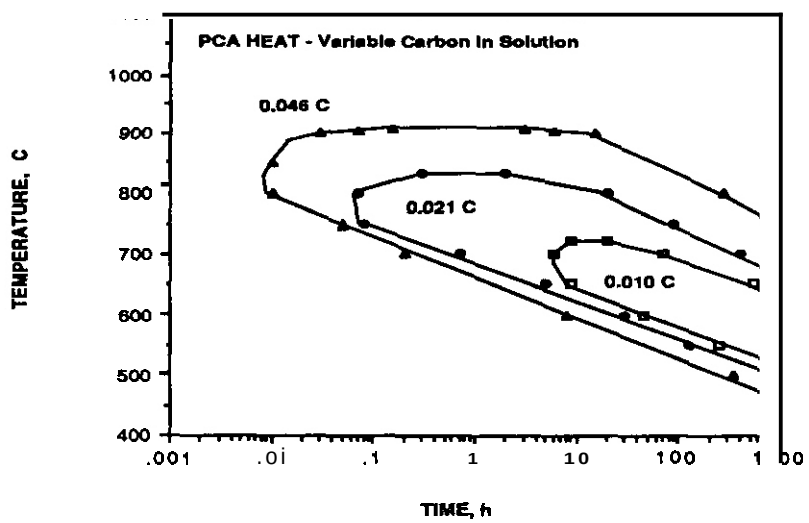

Figure 7. Time-Temperature-Sensitization Curves for PCA Heat K-280.

limiting the carbon available for precipitation. However, dropping the soluble carbon to 0.021% still produces a predicted sensitization response canparable to the high-carbon 316 heat (Figure 4). A further reduction to 0.01% carbon in solution (950 C heat treatment) significantly reduces the tendency for sensitiration.

These results suggest that effectively tying up carbon may be critical to ensure SCC resistance in service. The worst case would be a high-temperature treatment followed by a low-temperature exposure where chranium carbide precipitation is favored over titanium carbide precipitation. If service construction requires welding. high-temperature exposures which could put significant carbon back into solution are possible. Sensitization that might develop during cooling will depend on the specific thermomechanical history in the weld HAZ. In order to indicate potential welding-induced sensitization. SSDOS was used to predict continuous-cooling sensitization. Cooling rate effects on sensitization development for the 316 and PCA heats are shown in Figure 8. Critical cooling rates to cause sensitization are on the order of 0.1 C/s for the 316 heat, 0.3 C/s for PCA with all carbon in solution. and 0.03 C/s for PCA with 0.021% C in solution. Once again the high sensitivity of the PCA heat is predicted, along with the importance of carbon in solution.

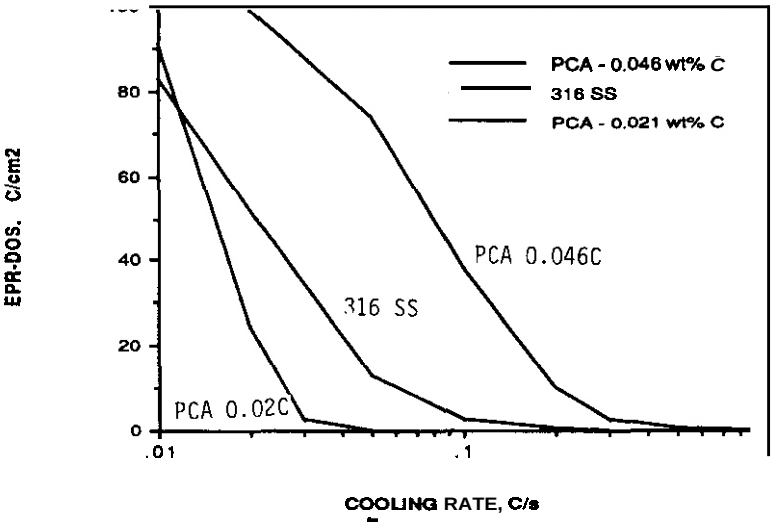

Figure 8. Continuous-Cooling Sensitization of 316 and PCA Heats.

Both sensitization and water impurity conditions can be eliminated in an ITER machine. Water treatment capabilities can maintain high-purity water conditions while proper material treatment during processing and fabrication can minimize the DOS. Use of a low-carbon Type 316 SS is recommended, while a thermal treatment is desirable for PCA that precipitates the maximum volume fraction of TiC and therefore minimizes the amount of dissolved carbon. However, welding can redissolve the TiC and thereby cause sensitization. Specific fabrication and joining information relative to the ITER will be needed before a detailed sensitization analysis can be completed for ITER applications.

FUTURE DIRECTIONS

The calculated DOS for PCA will be compared to experimental values for material given variable solution and intermediate annealing treatments. These data and the data for the Type 316 SS will be used to give guidelines for fabrication of the ITER vessel using these materials. Also. sensitization analyses of FeCrMn low-activation alloys will be conducted using both the SSDOS and experimental EPR measurements. Stress-corrosion cracking measurements of Type 316 SS and PCA in the solution-annealed and sensitized conditions will be conducted in a gamma irradiation facility to measure the effects of radiolysis on SCC of these materials.

References

1. R. H. Jones, A. B. Johnson. Jr., and F. S. Giacobbe, National Association of Corrosion Engineers. Paper No. 165 Corrosion/81, Toronto, Ontario. 1981.

2. R. H. Jones, A. B. Johnson, Jr.. and S. M. Bruemmer, Proc. Conf. Environment Degradation of Engineering Materials. VPI, 1981, p. 321.

3. S. M. Bruemmer, R. H. Jones, J. R. Divine. and A. B. Johnson. Jr., ASTM Symp. on Environment-Sensitive Fracture: Evaluation and Comparison of Test Methods. National Bureau of Standards. April. 1982.

4. S. M. Bruemmer and A. B. Johnson. Jr., Effect of Chloride. Thiosulfate and F IGSCC Resistance of Type 304 SS in Low Temperature Water, PNL-SA-11140. Pacific Northwest Laboratory, Richland. Washington, 1983.

5. R. H. Jones, M. A. Friesel, and W. W. Gerberich, Metall. Trans. A, Vol. 204 (1989) P. 6.

6. R. H. Jones. unpublished research.

7. F. P. Ford and M. J. Povich, Corrosion, 35, 1979, p. 569.

8. F. P. Ford, Mechanisms of Environmental Cracking in Systems Peculiar to the Power Generation Industry, EPRI Report NP-2589. Electric Power Research Institute. Palo Alto. California. 1982.

9. T. Shoiji. T. Ise, H. Takanashi, and M. Suzuki. Corrosion 34, (10) 1978, pp. 366-367.

References (cont'd.)

10. C. T. Ward. D. L. Mathis, and R. W. Staehle, Corrosion, 25 (9), 1969, pp. 394-396.

11. L. R. Sharfstein and W. F. Brindley. Corrosion, 14 (12), 1958, pp. 5881-5922.

12. K. Sieradzki, H. S. Isaacs, and R. C. Newman, Preprint 224, Corrosion-82. National Association of Corrosion Engineers. Houston. 1982.

13. S. M. Bruemmer, L. A. Charlot, and D. G. Atteridge, Corrosion. in press.

14. R. H. Jones and R. W. Wang. Corrosion. 40 (6), 1984, p. 272.

7. SOLID BREEDING MATERIALS

A FAST NEUTRON IN SIN TRITIUM RECOVERY EXPERIMENT ON SOLID BREEDER MATERIALS - G. W. Hollenberg (Pacific Northwest Laboratory)[a], T. Kurasawa and H. Watanabe (Japan Atanic Energy Research Institute), S. E. Berk (U.S. D.O.E./OFE), J. Hastings and J. Miller (Atanic Energy of Canada Research Canpany), D. E. Baker. R. E Bauer and R. J. Puigh (Westinghouse Hanford Co.)

OBJECTIVE

The overall objective of the BEATRIX-II experiment is to determine the in situ tritium recovery characteristics of Li_2O under fast neutron irradiation to extended burnups under both isothermal and thermal gradient conditions.

SUMMARY

An in situ tritium recovery experiment has been designed and is being fabricated for the irradiation of Li_2O in the Fast Flux Test Facility (FFTF). Two in situ tritium recovery canisters will be irradiated with lithium atan burnups to 4%. One canister will provide fundamental data on tritium release as a function of temperature. gas composition. and flow rate. The other canister will contain solid pellet specimens with large (430°C) radial temperature gradients in order to provide integrated performance data.

PROGRESS AND STATUS

Introduction

In the last decade considerable progress has been made on the development of solid breeder materials for tritium production in fusion blankets. Experimental efforts in fabrication, in property measurements, in irradiation damage[1], and in tritium recovery [2-8], have continually yielded positive results. The in situ tritium recovery experiments thus far have been on relatively small samples with modest lithium atom burnup. Japan, Canada and the U.S. have initiated an in situ tritium recovery experiment in the FFTF reactor as administered by the International Energy Agency's BEATRIX-II program. BEATRIX-II will achieve high damage and tritium production rates in two fully instrumented. larger volume canisters with in situ recovery in 1989. This paper describes those two tests.

TEST DESIGN

The objectives of the Cycle 11 experiment are to quantify tritium release characteristics and to measure the thermal stability of Li_2O as a function of neutron exposure. tenperature, gas composition, and sweep gas flow rate. To accomplish these objectives one in situ recovery canister will contain a thin walled (1.5mm) ring specimen capable of incremental temperature change steps and another canister will contain solid pellets with blanket-relevant tenperature gradients. Tritium release characteristics of solid breeder materials are important to fusion blanket designs in order to assure rapid replenishment of tritium for DT-fueled plasmas. Thermal stability is important in order to assure the maintenance of beginning-of-life blanket operating temperatures. The unique experimental parameters associated with the BEATRIX-II Cycle 11 testing are:

1. High lithium atom burnup. Essentially homogeneous lithium atom burnups of 4% will be achieved in the Li_2O samples irradiated in 1989. Higher burnups (>8%) are planned in subsequent irradiations.

2. High total tritium production. Over 7000 curies of tritium will be produced. measured and recovered during the 300 equivalent full power days (EFPD) irradiation.

3. Reactor relevant tritium partial pressures. The reference steady state tritium partial pressure will be 50 ppm which is much higher than most experiments (1 ppm). To increase the efficiency of tritium recovery fran sweep gas streams. high tritium partial pressures are projected for solid breeder blanket designs. Higher tritium partial pressures should minimize experimental uncertainties, i.e. initial sweep gas contaminants and surface adsorption/desorption fran downstream tube walls.

4. Engineering-oriented testing. The solid pellet canister will generate temperature and tritium production gradients typical of Li_2O prototypic conditions to relatively high lithium atan burnup.

The FFTF reactor possesses several desirable features for testing candidate solid breeder materials. The FFTF is noted for its high, fast neutron flux (4.8 x 10^{15} n/cm^{2}s [E>0.1 MeV]) and its ability to easily

(a) Operated for the U.S. Department of Energy by Battelle Memorial Institute under Contract DE-AC06-76RLO 1830.

accommodate instrumented experiments. The neutron spectrum in FFTF results in a relatively la cross section for neutron reactions with lithium-6 (1-2 barns) which is similar to several solid breeder blanket designs. With essentially no self-shielding, larger sample volumes and high lithium atom burnup levels cdn be achieved in a simple test. Two canisters are contained within the Materials Open Test Assanbly (MOTA)[9], a standard FFTF instrumented irradiation vehicle, which was modified by the addition of sweep gas lines.

The temperature change canister (Figure 1) will allow temperature changes between 460°C and 650°C on a thin ring of Li_2O in a manner similar to earlier experiments[2-8]. Temperature control is obtained by computer controlled helium/argon gas mixtures in the gas gap between the specimen subcapsule and the reactor coolant. After an instantaneous increase/decrease in temperature, tritium will be released/ retained in the ceramic until the tritium release rate returns to steady stdte. The exact shape and time constant associated with this transient data can then be canpared with theoretical models for analysis of mechanism. Similar parametric increments are planned for flow rate (10 - 1000 cm^3/m) and sweep gas canpositton (helium plus 0-1% hydrogen). A Self-Powered-Neutron-Detector (SPND) will measure the local neutron flux and allow normalization of the tritium production rate. Thermocouples will measure the temperature gradient across the ring specimen to indicate the effective thermal conductivity.

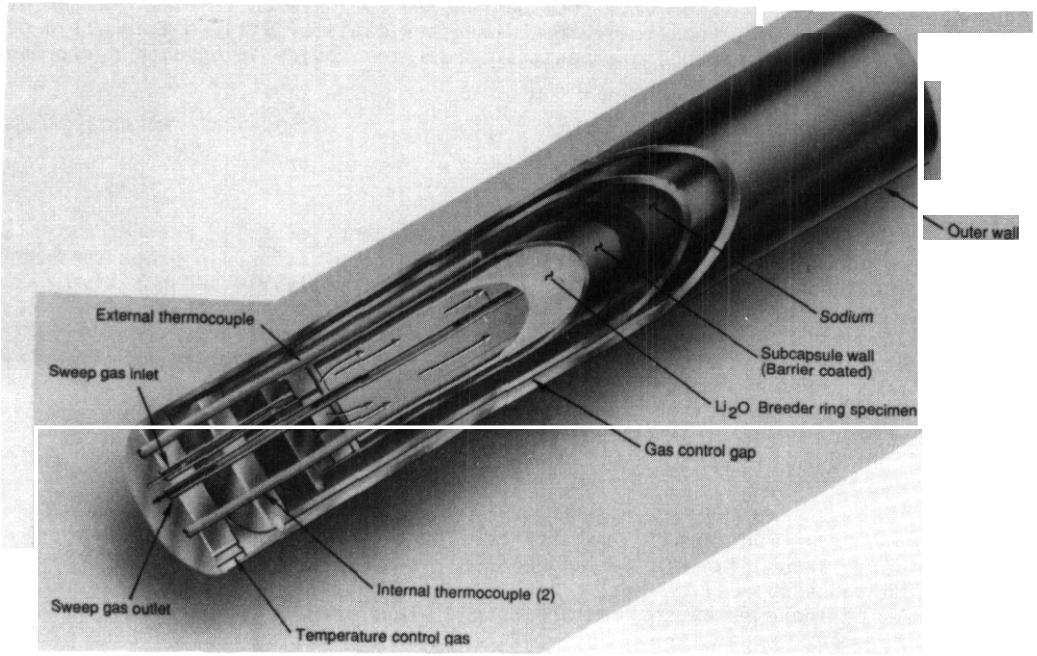

Figure 1. Schematic of Temperature Change Canister Containing Ring Specimen

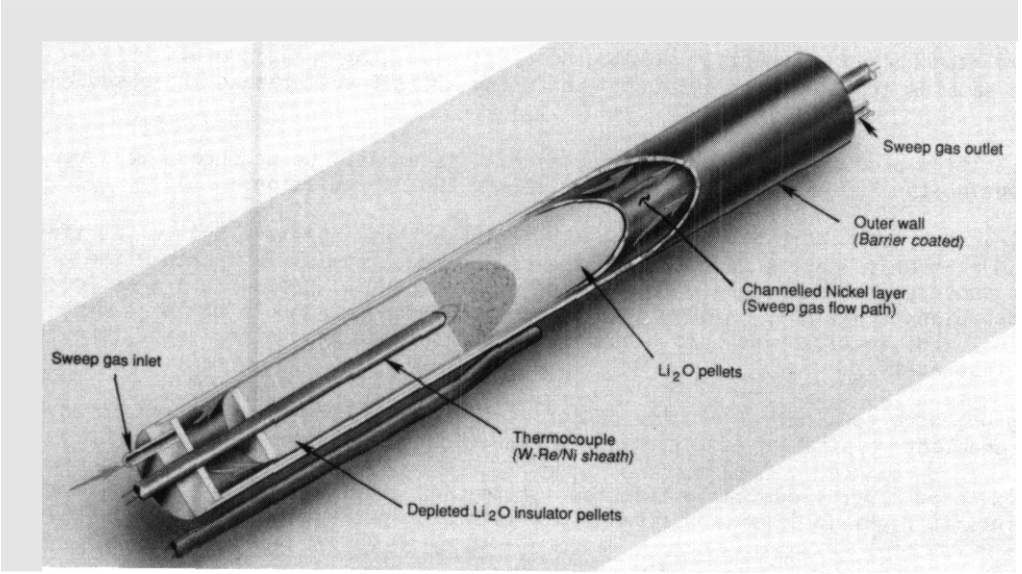

Figure 2. Schematic of Solid Pellet Canister

In the other canister, a column (Figure 2) of solld Li_2O pellets will be irradiated. The specimen is predicted to have an initial centerline temperature of 900°C and outer circumference temperature of 450°C. The purpose of the solld pellet canister is to monitor the tritium release from Li_2O under thermal gradient conditions typical of a blanket. The temperature gradient across the solid pellet will be continuously measured with thermocouples. In particular. the large temperature gradient provides an opportunity to evaluate the upper temperature limiting phenmenon of Li_2O, i.e. lithium transport from high temperature to colder temperature regions.

The major characteristics of the Li_2O specimens and their anticipated environment are summarized in Table 1. The lithium-6 enrichment for both specimens was chosen to obtain a lithium atm burnup of 4% at 300 equivalent full parer days (EFPD). Monte Carlo calculations were used to optimize the position for maximum lithium atan burnup and the lowest practical irradiation temperatures.

Table 1. Characterization of the Li_2O Specimens and Anticipated Envlronment

Specimen	Ring Specimen	Solid Pellet Specimen
Physical Dimensions		
Outside Diameter (mm)	18.57	17.02
Wall Thickness (mm)	1.50	--
Length (mm)	88.9	88.9
Lithium-6 Enrichment (%)	61.0	61.0
Density (%TD)	a5	89
Graln Size (μm)	5	5
Irradiation Temperature		
Inner Radius (°C)	500 - 685	863
Outer Radius (°C)	460 - 651	430
Maximum Gradient (°C)	28	433
Total Tritium Production (Ci)	2025	5300
Sweep Gas System		
Gas Composition	helium+(0-1%H_2)	helium+(0-1%H_2)
Flow Rates (cm^3.min)	10-1000	10-1000

Dimensions of the ring geometry specimen minimize the radial temperature gradient and the Irradiation temperature while maintaining a temperature-control capability and high tritium production levels. The dimensions of the solld pellet specimen were chosen to obtain an initial centerline temperature of 900°C. The calculated radial temperature gradients in the two specimen types are compared in Figure 3.

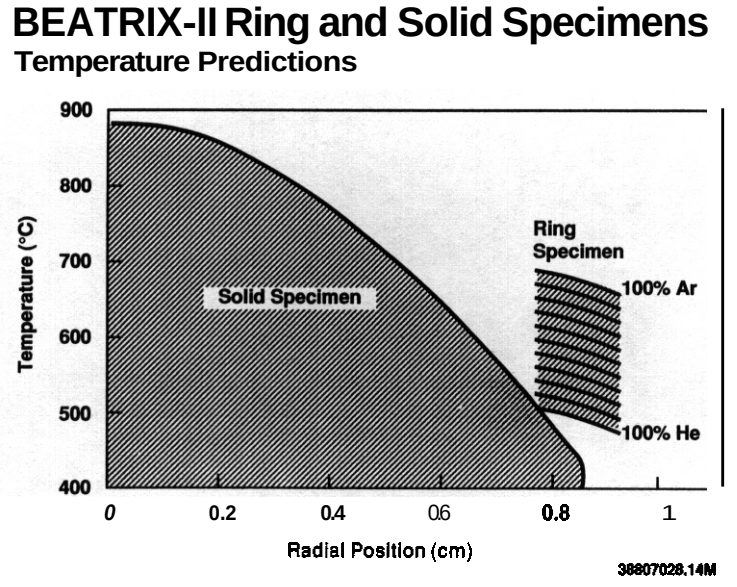

Figure 3. Temperature Predictions for the Ring and Solid Pellet Li_2O Specimens.

TEST FABRICATION

The environment and test conditions of BEATRIX-II have mandated the following unique fabrication features:

1. Tritium barriers. Tritium loss due to permeation is an issue. not only in this experiment but in actual fusion blankets due to the high temperature of the coolants (300 to 450°C). To reduce tritium losses, a permeation barrier[10] (nickel aluminide) was applied to the canister walls for each Li_2O specimen and to the exiting sweep gas lines (see Figure 4). Because the centerline temperature for the solid pellet will be 900°C, tritium losses through the thermocouple penetrations were reduced by a W-22%Re sheathed chromel-alumel thermocouple. Permeation calculations indicated that less than 0.3% of the tritium will be lost to the coolant.

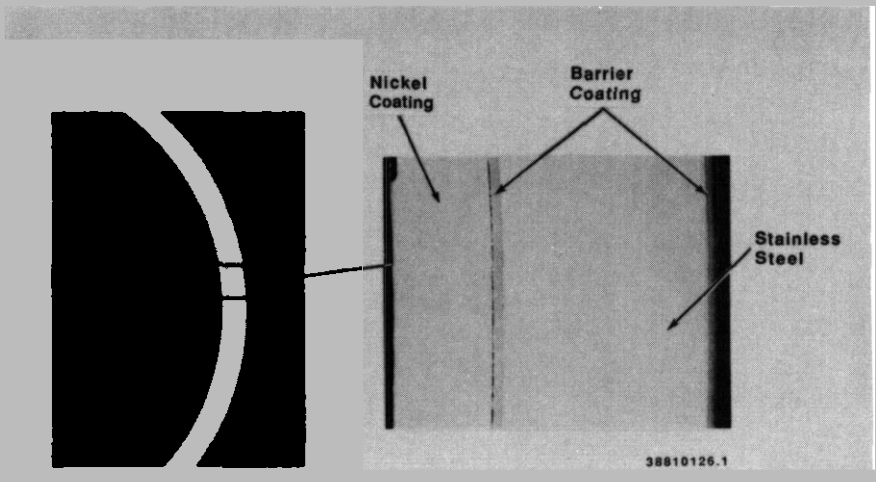

Figure 4. Tritium Barrier Coating Applied to Ring Specimen Canister

2. A Channelled Nickel Layer. The solid pellet canister was designed to direct the sweep gas fla away fran the high temperature regions in order to avoid unidirectional. gas phase transport of LiOT, the temperature limiting phenomena for Li_2O. A la density channeled nickel layer (50% TD) was formed by pressing and sintering coarse nickel pader to the inside diameter or the stainless steel cladding (see Figure 5). The open porosity in the nickel forms the preferred sweep gas fla path around the circumference of the solid pellet column.

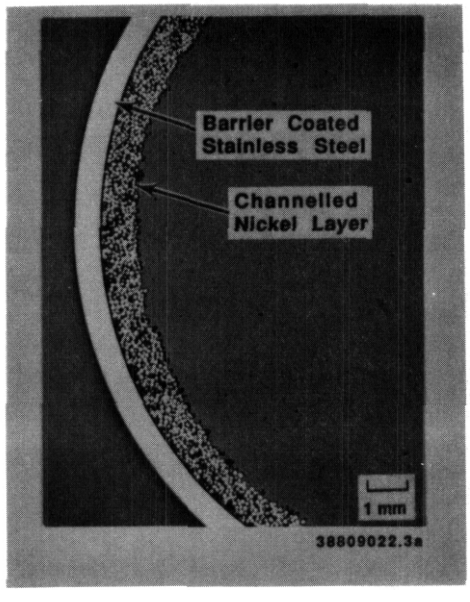

Figure 5. Channeled Nickel Layer on Cladding of Solid Specimen

3. Thin-Walled Li_2O. Fabrication of a thin-walled ring specimen (Table 1) wlth tight dimensional tolerances was necessary to examine the temperature range of interest (460 to 650°C). Fabrication of this fraglle specimen was accomplished by isostatically pressing to precise outside dimensions and slntering to net shape.

GAS ANALYSIS SYSTEM

The sweep gas flow for the in situ tritium recovery tests is shown in Figure 6. The Gas Inlet System will provide the sweep gas to the in situ tritium recovery canisters. The reference sweep gas composition will be helium plus 0.1% hydrogen with non-reference compositions ranging fran pure helium to 1% hydrogen. The sweep gas is routed into the canisters which are mounted on the MOTA stalk. The sweep gas lines are routed out of the reactor and to the tritium measurement system which is located within a glovebox. The sweep gas line fran each canister is then split into a total tritium measurement path as seen in Figure 6. The elemental tritium analysis path incorporates a molecular sieve bed prior to an ionization chamber so as to prevent decalibration of the ionization chamber by surface adsorption of tritiated water.

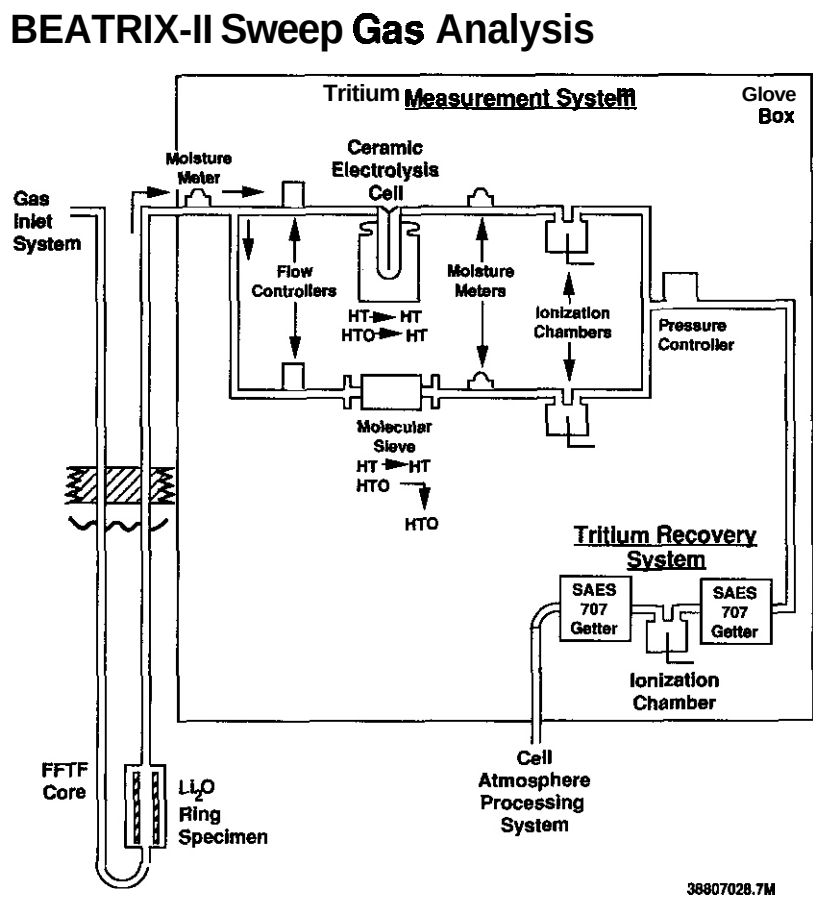

Figure 6. Schematic for the BEATRIX-II Sweep Gas Flow.

Similarly. the total tritium measurement path possesses a ceramic cell[11] for electrolytically reducing any tritiated water in the gas stream. The small ionization chamber volumes (100 cm^3 active volume) were specifically selected for their short time constants which permit the measurement of short transients. High precision is possible with these small ion chambers due to the high sweep gas concentrations of tritium (50 ppm).

To reduce tritium releases in the exhaust stream below established limits, tritium will be recovered fran the flow streams with a metal getter (SAES 707). Other experiments have used ethylene glycol or catalytic oxidation/molecular sieve beds, but the metal beds appear to be better suited to a non-oxidizing operation and the demonstration of tritium recovery techniques consistent with actual blanket operation. In Figure 7 the experimentally-determined performance of the SAES 707 getter is shown. Detritiation factors of 2500 are required under normal operating conditions. Detritiation factors as great as 50.000 have been measured for the SAES 707 getter in preparation for this experiment. The detritiation factor degrades as the getter bed becomes saturated with the hydrogen in the sweep gas and will be replaced at periodic intervals. The hydrogen in the sweep gas improves the detritiation factor by an isotopic dilution effect but shortens its useful life.

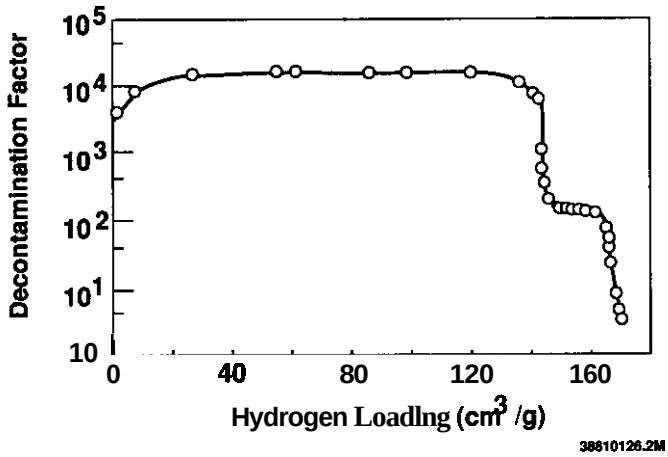

Figure 7. Tritium decontamination performance for 30 gm of SAES 707 getter under laboratory conditions with tritium. The getter was at 350°C with a flow rate of 1.45 cm^3/sec transit time) of 6.2% H_2 in helium.

CONCLUSIONS

Two in situ tritium recovery tests are scheduled to begin irradiation in FFTF in Cycle 11 in the spring of 1989. The experiment is desianed to provide tritium release and Irradiation performance data on the candidate solid breeder material. Li_2O, to high lithium atom burnups. Subsequent in situ tritium recovery experiments are currently being planned for irradiation in 1990.

FUTURE WORK

The BEATRIX-II experiment is to begin irradiation in July 1989. In 1990, a follow on in situ experiment will be conducted on Li_2O to even higher burnup levels and on the ternary lithium ceramic adopted by ITER. i.e. Li_2ZrO_3 or Li_4SiO_4.

ACKNOWLEDGEMENTS

The inspiration and guidance of IEA leaders such as T. C. Reuther (US DOE). T. Kondo (Japan's JAERI) and G. Phillips (Canada's AECL) is gratefully acknowledged. Tritium permeation calculations by Dr. R. Causey are appreciated.

REFERENCES

1. D. L. Baldwin and G. W. Hollenberg. "Measurements of Tritium and Helium in Fast Neutron Irradiated Lithium Ceramics Using High Temperature Vacuum Extraction", J. Nucl. Mat. 141-143, 305 (1986).

2. R. G. Clemmer, et al., "The TRIO-1 Experiment: In Situ Tritium Recovery Results". J. Nucl. Mat. 122-123, 80 (1984).

3. T. Kurasawa et al.. "The Time Dependence of In Situ Tritium Release fran Lithium Oxide and Lithium Aluminate (VOM-22H Experiment)". J. Nucl. Mat. 141-143, 265 (1986).

4. R. A Verrall. et al., "CRITIC-1 Irradiation of Lithium Oxide". presented at the Third International Conference on Fusion Reactor Materials. Karlsruhe, FRG, October 1987 (to be published J. Nucl. Mat.).

5. H. Werle et al.. "The LISA1 Experiment: In Situ Tritium Release Investigations", J. Nucl. Mat. 141-143, 321 (1986).

6. E. Roth. et al., "Tritium Recovery from a Breeder Material: Gamma Lithium Aluminate". J. Nucl. Mat. 141-143, 275 (1986).

7. M. Briec. et al., "In and Out-of-Pile Tritium Extraction fran Samples of Lithium Aluminates". J. Nucl. Mat. 141-143, 357 (1986).

8. H. Kwast, et al.. "In-Pile Tritium Release from $LiAlO_2$, Li_2SiO_3 and Li_2O in EXOTIC Experiments 1 and 2", J. Nucl. Mat. 141-143, 300 (1986).

9. O. L. Greenslade, et al.. "FFTF as an Irradiation Test Bed for Fusion Materials and Components". J. Nucl. Mat. 141-143 1032 (1985).

10. J. C. McGuire, "Hydrogen Permeation Resistant Layers for Liquid Metal Reactors", Conference on Tritium Technology in Fission, Fusion, and Isotopic Applications, Dayton. OH. April 29, 1980.

11. A. Nishimura, et al., "Operation of a Ceramic Electrolyte Cell (CEC) for Reduction of Tritiated Water at Low Moisture Levels". JAERI-MEMO 61-105, Japan Atanic Energy Research Institute. Tokai-Mura, Ibaraki-Ken, Japan.

INTERFACIAL ROUGHNESS AND THE THERMAL CONDUCTIVITY OF A SPHERE-PAC BED - S. W. Tam and C. E. Johnson (Argonne National Laboratory)

OBJECTIVE

SUMMARY

Various configurations for the solid breeder (e.g., Li_2O) plus neutron multiplier (i.e., Be) component has been considered for blanket application in fusion reactor technology.[1] One possible option is the sphere-pac configuration. This consists of the solid component in the form of small particles (ideally as spheres) put together in a bed in a close-packed manner. In order to achieve high packing density, particles of several different sizes need to be used. The interstitial spaces between particles of a given size are packed with particles of the next smaller size and so on in a heirachical manner. The packing process can be achieved by vibratory compaction.2 Much experience has been gained on this configuration in fission reactor related technology.2 In particular extensive data has been gathered via fission-related research as well as from high thermal insulation technology work3 on the thermal conductivities K_{sp} of such systems. The heat conduction properties of these systems possess unusual characteristics due to the convoluted interweaving bicontinuous nature of the solid component and the porosity phase. For example, when sphere-pac beds immersed in a gas (e.g., He, Ar) the thermal conductivities K_{sp} are found to be dependent on the gas pressure P. Typically, K_{sp} increases rapidly by 50-100%, when P is raised by as little as a MPa and then changes much more slowly thereafter[2-6] (see Fig. 1 and discussion in the following section). It may be thought that such subtle behavior may he exploited to the advantage of blanket technology if a sphere pac configuration is utilized in the breeder-plus-multiplier component. However, straightforward extrapolation from fission and thermal insulation technological experience to a fusion blanket environment should be treated with care since quite different materials characteristic are involved. It turns out that a careful analysis of the physics of the situation reveals that a gas pressure-sensitive thermal conductivity is a much less prominent effect than would have been suggested from other technology experiences alone. In order to understand this one needs to first appreciate the reasons why such pressure effects are so dramatic in fission and thermal insulation materials.

PROGRESS AND STATUS

Physical Basis

The Pressure dependence of thermal conductivity, K_{sp} of a sphere-pac bed arises from a dependence of K_{sp} on K_g, the gas conductivity. In fact, the materials utilized for the solid component in fission and thermal insulation-related experiments all have low solid conductivities K_{sp}, as low as only 5-10 times larger than K_g[2-3] For these systems the heat flux density is expected to be reasonably uniform and a substantial fraction of the flux lines passes through the gas phase. This gives rise to a critical dependence of K_{sp} on K_g. In fact, several of the theories[4-6] that have been successfully applied to describe K_{sp} and related systems have been able to exploit the simplification resulting from this uniform flux approximation.

Although K_g for the gas phase in the bulk is well known to be pressure-independent under ordinary conditions this is no longer true when the gas is confined to a bounded region whose linear dimension is comparable or smaller than l_g, the mean free path of the gas.[7] In that case, heat transfer is not via intermolecular collision as in the bulk but rather is accomplished through gas molecule-solid surface scattering. The relative inefficiency of the latter heat conduction process gives rise to a temperature difference between the solid surface and the gas phase region imnediately above the surface. It is this factor which leads to the unusual pressure dependence of K_g (in a confined region) and ultimately that of K_{sp}, the sphere-pac bed thermal conductivity.

Note that the critical parameters here are the ratio K_s/K_g the solid to gas thermal conductivities and the smoothness of the contact surfaces between solid particles. To maximize the influence of K_g on K_{sp} one needs a small ratio of K_s/K_g to, in part, ensure a high flux density through the gas. Smooth spherical surfaces for the solid particles would lead to only point contacts between particles and thus, minimize direct heat conduction between solid microspheres. The low conductivity solids (e.g., UO_2, ThO_2) utilized in fission technology[2] satisfy such criteria and one should not be surprised to see the gas pressure dependence of K_{sp} observed in both experiments[2,3] and theoretical calculations.[4-6]

Sphere-Pac Bed with Be Particles

However, when one starts considering a sphere-pac system whose major solid component is a metal one needs to proceed with care. Previous experience from fission and thermal insulation technologies may well be misleading. This is the case for a bed with mainly Be particles as neutron multiplier for fusion blanket application. In this case the ratio K_s/K_g is easily of the order of 500 or more.[8] The heat flux lines are far from uniform with most of them trying to pass directly from one solid particle to the next through the limited area of contact between the particles (thus bypassing the gas phase).

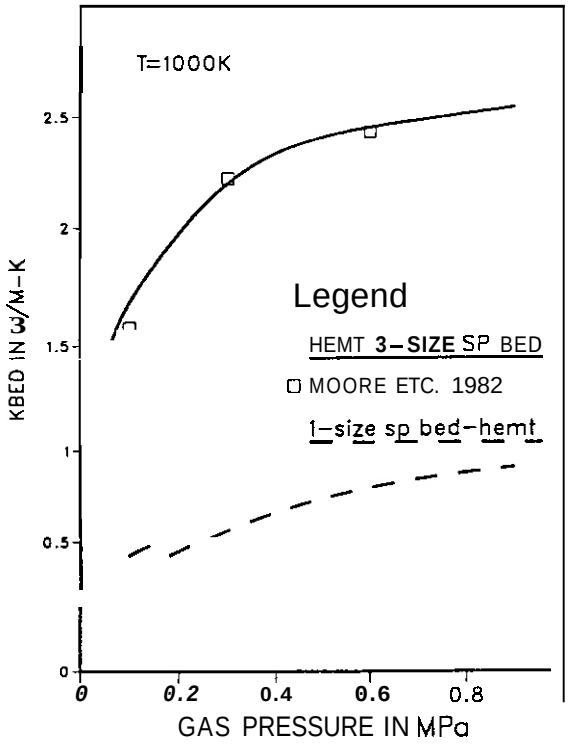

Fig. 1. Thermal conductivity of UO_2/He Sp Bed.

Now in practice an inevitable degree of roughness of the particle surfaces must give rise to finite contact areas and not the point contacts in ideal systems. These factors serve to enhance direct heat conduction between solid particle and thereby reduce the effect of K_g (and, hence, the gas pressure) on K_{sp}. Such decreased sensitivity to gas pressure would arise mainly from flux constriction and interfacial roughness effects acting in concert to complement each other.

To verify such physical consideration we have constructed simple models to include the effect of flux constriction and interfacial roughness on K_{sp}. In particular, we have used the models to estimate the effects of gas pressure P on K_{sp} once these two factors are taken into account.

A conplete theory of K_{sp} including the effect of interfacial roughness would require a detailed microstructural informations in the vicinity of the contact region. However, an upper and lower bound to the effect of gas pressure on K_p due to roughness can be estimated using two simple models with sound physical basis. The first modef assumes that within a typical unit cell the effective solid component (conductivity K_s) acts as an effective series resistance with both the contact resistance due to roughness (conductivity K_c) and the effective gas phase resistance (conductivity K_g). The last two components are in parallel with each other. Thus, one has

$$1/K_{sp} = 1/K_s + 1/(K_c + K_g) \tag{1}$$

Note that both K_s and P include geometrical factors but one expects them to have similar order of magnitude as that of the pure solid and gas phases. According to equation 1 only K_g depends on the gas pressure P. We have estimated the contact conductivity K_c using[8]

$$K_c = h_{contact}\,\pi\delta \tag{2}$$

where

$$h_{contact} = k_s\,1/R_1\,\frac{(R_1/R_2)^2}{\mathrm{Tan}^{-1}[R_2/R_1 - 1]} \tag{3}$$

Here the interfacial roughness is modeled as a group of cylindrical protrusions with height 6, base radius R_1 and the centers of adjacent cylinders spaced R_2 apart. K_s is the solid component conductivity. Thus, $(R_1/R_2)^2$ measures the fractional surface area of the solid particles covered 6 by the protrusions. Small values of S/R_1 (e.g., <1) describe pill-box-like structures. Larger values of δ/R_1 (e.g., >1) would give a more elongated cylindrical protrusions. We have evaluated K_c (for Be) at 500°K for S/R_1=1,4 for various protrusion density (i.e., degree of roughness). The results are shown in Table 1. One can see that in general $K_c >> K_g$ (which for He would be in the range of 0.1-0.2 W/(M-K).[9] In this case the pressure

Table 1. Interfacial Contact Conductivity K_c

S/R_1	$(R_1/R_2)^2$	T=400 K	K_c (W/(M-K)
1	0.04	15.3	13.2
	0.02	7.3	6.3
	0.01	3.5	3.0
4	0.04	61	52.7
	0.02	29.4	25.3
	0.01	13.8	12.0

dependent effect which comes from K_g is completely overwhelmed by K_c. Thus, within this mdel one would expect to see very little pressure effect. Due to flux constriction the whole system conducts heat between solid particles via the contact resistance while bypassing most of the gas phase.

The second mdel adopts a different approach. It seeks to give an upper bound to the effect of the gas phase. The system is assumed to conduct heat by two parallel pathways. One is via the bulk solid in series with the gas phase. The other is via the bulk solid in series with the interfacial contact resistance. In the second pathway the conductance is essentially controlled by the contact resistance K_c. Thus, for this model

$$K_{sp} = K_c + K_{sp}^{o} \tag{4}$$

Here K_{sp} is the sphere-pack bed conductivity when the assumptions of uniform heat flux and interparticle point-contact both hold. Figure 2 shows the result for Be/He system. The vertical axis represents the percent change in K_{sp} for T = 500 K and pressure change of 0.5 to 2 atmosphere. (10) The horizontal axis represents the fractional surface area covered by the protrusions. For point contact the percent change is about 86%, a significant increase. However, with the inclusion of the contact resistance the change in K_{sp} becomes significantly less for as little as 2-3% of particle surface area covered with protrusions. This illustrates the drastic effect of interfacial roughness on the gas pressure dependence of K_{sp}. Note that the present estimate already give an upper bound on the pressure effect of K_{sp} for the conditions considered. The first model lead to practically null pressure effect as a lower bound. The actual behavior is likely to be somewhere in between. Thus, one would expect that for a sphere-pac bed with high conductivity solid component with roughness at a few percent surface coverage the sensitivity of K_{sp} to gas pressure variation is significantly less than those bed with thermal insulator as the solid component.

FUTURE WORK

In considering sphere-bed configuration for blanket component in fusion technology applications care must be exercised in extrapolating experience from previous technologies. The high thermal conductivity of the metallic component (i.e., Be as neutron multiplier) gives rise to serious heat flux constriction and indirectly enhances the importance of interfacial roughness in the solid contact region. Both factors complement each other to reduce significantly the sensitivity of the thermal conductivity of a sphere-pac bed to variations in the gas pressure.

REFERENCES

1. D. L. Smith et al., "Blanket Comparison and Selection Study," ANL-FPP-84-1, Argonne National Laboratory, 1984.

2. J. P. Moore, R. J. Oippenaar, R. O. A. Hall, and D. L. McElroy, "Thermal Conductivity of Powders with UO_2 or ThO_2 Microspheres in Various Gases from 300-1300 K, ORNL/TM-8196, June 1982.

3. L. Binkele, "High Temperature-High Pressure, 15 (1983) 131.

4. R. O. A. Hall and D. G. Martin, J. Nucl. Mater. 101 (1981) 172.

5. S. W. Tam and C. E. Johnson, "Fractal Aspects of Materials Proceedings," D. Schaifer, S. Liu, and E. Mandelbrot, Materials Research Society (1986)

6. S. W. Tam and C. E. Johnson, J. Nucl. Mater. 141-143 (1986) 348.

7. E. H. Kennard, "Kinetic Theory of Gases," McGraw-Hill, NY 1953, p. 291.

8. J. N. Cetinkale and M. Fishenden, Proc. of the General Discussion on Heat Transfer, P. 271, The Institution of Mechanical Engineers, London, 1951.

9. "Thermophysical Properties of Matter, The TPRC Data Series, Vol. 2 and 3," Y. S. Touloukian, series editor: C. Y. Ho, series technical editor (IFI/Plenum Press, NY. Washington, 1970).

10. A. R. Raffray, UCLA, private comunication. Oct. 1988.

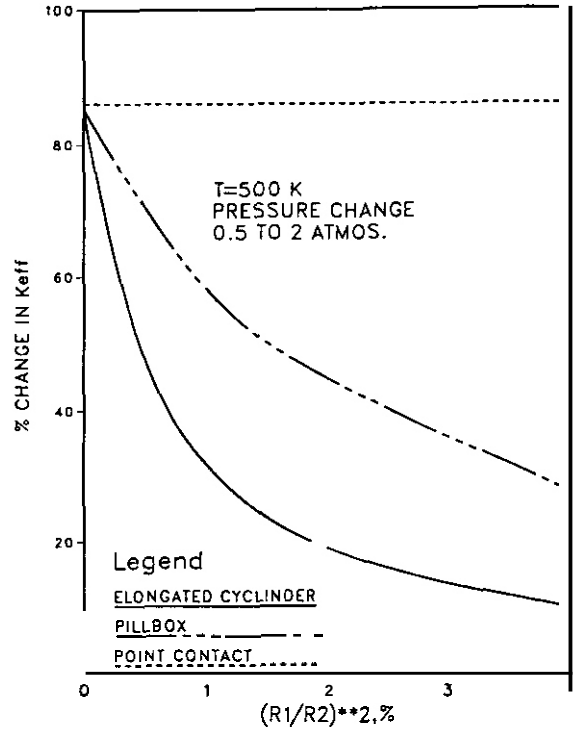

Fig. 2. Effect of roughness on Keff.

TRITIUM TRANSPORT MODELING - J. P. Kopasz and C. E. Johnson (Argonne National Laboratory)

OBJECTIVE

The objective of this work is to develop a comprehensive model of tritium transport in a ceramic breeder blanket. The model will enable one to calculate the transient tritium inventory in the blanket for changes in blanket operating conditions.

SUMMARY

The modeling effort for this period was focused on the desorption process. The desorption process consists of a surface reaction and desorption of surface bound tritium in the form of HTO, T_2O, HT, or T_2. Of concern are the order of the surface reaction and the energetics of the surface reaction and desorption step. In most of our previous work, desorption of tritium was considered to be first order in tritium due to the expected excess of hydrogen in the system. Equations for desorption which are second order in tritium were derived for situations where the hydrogen concentration on the breeder surface would be low and comparable to the expected tritium concentration. Expressions for tritium inventory were derived and calculations were performed to determine the grain radius regimes where desorption would be expected to be the rate controlling release process. In our previous work we have found evidence that the desorption energetics change as a function of surface coverage. We believe that this is due to the presence of multiple sites for desorption of tritium from the ceramic. To support this view we have analyzed constant rate heating tritium release experiments from the literature to determine the number of desorption sites and to obtain estimates of the desorption activation energies. Estimates of activation energies for desorption of tritium from Li_2O and Li_4SiO_4 were obtained.

PROGRESS AND STATUS

The tritium transport modeling effort for the last period has been focused on the tritium desorption process. The desorption process is considered to be the combination of surface reactions leading to a surface bound molecule and desorption of the surface bound molecule into the gas phase. These processes are not handled separately due to the difficulties in separating the processes experimentally. Our current modeling efforts are related to (1) the kinetic order of the surface reactions leading to desorption under various conditions, and (2) the energetics of the surface reactions and the desorption step.

The reactions which we consider as likely candidates for those which lead to desorption of tritium from the surface are:

$$OH_{surf} + OT_{surf} \rightarrow HTO_{surf} \qquad OT_{surf} + OT_{surf} \rightarrow T_2O_{surf}$$

and

$$H_{surf} + OT_{surf} \bullet HT_{surf} \qquad T_{surf} + T_{surf} \rightarrow T_{2surf}$$

Of these, the reactions on the left are first order in tritium while those on the right are second order in tritium. Previously, our models were based on a desorption which was first order in tritium since we believe that, due to the presence of hydrogen and water in the purge stream, the hydrogenic species on the surface will be present at a much higher concentration than the tritium soecies at the surface. We have now performed some calculations to determine the release equations and inventory under conditions where release would be second order in tritium or a combination of first and second order.

Steady State Tritium Inventory

Case 1: Pure Desorption (instantaneous diffusion)

A) First order desorption
$I=(4/3)\pi a^3\ Ga/(3K_d1)$

B) Second order desorption (hydrogen<<Tritium)
$I-(4/3)\pi a^3\ (Ga/(3K_d))^{1/2}$

C) mixed first and second order (hydrogen ≃ tritium)
$I=(4/3)\pi a^3\ [-C_H+/-dsqrt(C_H{}^2+4Ga/(3K_d))]1/2$
limiting cases of this are"

1) $C_H=0$
then $I=(4/3)\pi a^3\ (Ga/(3K_d))^{1/2}$
2) $C_H>>C_T$
then $I=(4/3)\pi a^3\ Ga/(3K_d\ C_H)$
this is the same as case B with $K_d1=K_d\ C_H$

Case 2: Diffusion-desorption

A) psuedo-first order ($C_H \gg C_T$)

$$I=(4/3)\pi a^3 G\{a^2/(15D)+a/(3K_d C_H)\}$$

B) second order ($C_I \gg C_H$)

$$I=(4/3)\pi a^3 G\{a^2/(15D)+[a/(3K_d)]^{1/2}\}$$

In order to determine the phase space where diffusion is the dominant release mechanism, plots of the fraction of the total inventory which is due to diffusion versus the factor aK_d/D were calculated. For first order release, for values of aK_d/D of less than 0.5, diffusion accounts for less than 10% of the inventory while for values of aK_d/D of greater than 20 diffusion accounts for 90% of the inventory. For second order release, the term aK_d/D is of little value in determining the rate controlling mechanism. One must use the value of $(a^3K_d)^{1/2}/D$ to obtain the same type of relationship. For values of $(a^3K_d)^{1/2}$ of less than 0.5 diffusion accounts for less than 10% of the inventory, while for values above 50 diffusion accounts for over 90% of the inventory.

In most cases, we believe the hydrogen surface concentration on the ceramic, (due to hydrogenic inpurities present as a result of ceramic fabrication and from adsorption of hydrogenic impurities or added hydrogen from the purge gas), will be much larger than the tritium surface concentration. This will result in psuedo-first-order kinetics and tritium release will be first order in tritium. This belief stems from the difficulties in obtaining an oxidic ceramic free of hydroxide impurities and in obtaining a purge flow with water contamination near the ppm range. Even for experiments employing ultra high purity helium as a purge gas desorption is likely to be first order in tritium. Commercially available ultra high purity helium contains from 1 to 10 ppm of water. In addition to this amount of water, in the purge stream there will be water present from desorption of water adsorbed on the transport lines. Finally, hydroxides will be present in the ceramics as a result of their preparation in concentrations expected to be around the order of 0.01 weight percent. One would expect the combination of these effects to result in concentrations of hydrogen at the surface greater than the tritium concentration.

We have also investigated the energetics of desorption from ceramic breeder materials. Desorption has been determined to be the rate-limiting process in some tritium release experiments. Despite the importance of tritium desorption in determining the merits of candidate breeder materials, little is known about the tritium desorption process. Tritium desorption has been treated as occurring from one site with one desorption activation energy in most cases. Recent experiments suggest that there are several sites for desorption, each with a corresponding activation energy.[4-6]

Evidence for Multiple Desorption Sites

In some of the experiments on the adsorption-solubility relationships for $LiAlO_2$ performed by A. Fischer[7], after uptake of $H_2O(g)$ was complete, the sample was heated to a hlgher temperature in a helium stream and the evolution of water vapor was recorded. During the temperature ramp, the rate of evolution of $H_2O(g)$ was observed to go through several maxima. This was interpreted as showing that evolution proceeded from several types of sites. Isotherms and isobars derived from Fischer's adsorption data revealed two adsorption processes with different activation energies for adsorption.7 Furthermore, the heats of adsorption were found to depend on the degree of surface coverage. Due to the fact that the activation energy for desorption is equal to the sum of the heat of adsorption and the activation energy of adsorption, the desorption activation energy will exhibit the same trend as observed for the heat of adsorption. The observed range of values for the heat of adsorption indicates a range of activation energies for desorption. Earlier work on alumina also indicated several types of adsorption/desorption sites.[8]

Supporting evidence for multiple desorption sites on $LiAlO_2$ was obtained in the tritium release from the LILA-1 experiment. For several runs an increase in temperature resulted in a small decrease in tritium release followed by an increase to a maximum then a decay to steady state.9 Similar tritium release curves were observed for release from Li_2O in the CRITIC experiment.[10] This type of tritium release behavior could not be explained using a diffusion-desorption release model with one desorption activation energy, but could be modeled with a desorption activation energy which varies with surface coverage.[11]

A constant-rate heating experiment was performed by Tanifuji et al. on irradiated Li_2O.[4] This experiment is, in essence, a TPO study. In TPO, a sample with adsorbed material on it is heated at a specified rate, and the quantity of desorbed species is measured as a function of temperature. For a constant heating rate, a peak will be observed in a plot of the amount desorbed versus temperature. The position of the peak is

indicative of the desorption activation energy. The presence of more than one peak indicates multiple desorption processes. Tanifuji et al. interpreted their results based on the presence of one broad desorption peak for each sample;[4] however, if the data are examined more closely, one can recognize several overlapping peaks. An analysis of these peaks indicates five types of sites for desorption of tritium from Li_2O.

Supporting evidence for the presence of multiple desorption sites in Li_2O was also observed in the CRITIC in-pile tritium release experiment. In this experiment, an increase in sample temperature resulted in a sharp decrease in tritium release followed first by an increase to maximum release and then decay to steady state.[10] This behavior was successfully modeled using a desorption activation energy which varied with surface coverage: it could not be modeled by a diffusion-desorption model with a single desorption activation energy.[11]

Evidence for multiple types of desorption sites in Li_4SiO has been observed in several out-of-pile tritium release experiments.[3,5,6] The first suggestion of multiple desorption site types in this material came from attempts to fit tritium release data from out-of-pile annealing studies. Breitung et al. found that the best fit to their data was obtained for a desorption model with two types of desorption sites.3 More conclusive data have recently been reported. Two separate studies describing tritium release and water release from TPD experiments indicate multiple desorption activation energies.[5,6] In the first of these experiments, pre-irradiated samples of doped and undoped Li_4SiO_4 were heated at a rate of 4.8°C/min, and the amount of tritium released was measured as a function of temperature.[5] Multiple desorption peaks were observed in the TPD curve for all the samples, with six desorption peaks present for the pure silicate. The second study investigated the desorption of water from Li_4SiO_4.[6] The TPD curve for water desorbed from Li_4SiO_4 powder stored in air showed what appear to be six overlapping peaks, indicating six types of desorption sites. Both of these studies on Li_4SiO_4 are consistent with the presence of up to six different desorption activation energies.

CALCULATIONS

The mathematics governing desorption in TPD or constant-rate heating experiments have been covered in detail elsewhere[12,13] and are beyond the scope of this report. A brief description of the relevant equations follows.

For first-order desorption into a vacuum (or into a rapidly flowing purge stream), the pressure of the desorbing species in the purge stream from one site with desorption activation energy E_a can be calculated as follows[12]:

$$P = (\nu/C)\exp\{-\nu\beta\ (E_a/R)I - E_a/RT\} \quad (1)$$

where

$$I = \exp(-\epsilon)\ [1 - (2!/\epsilon) + (3!/\epsilon^2) - (4!/\epsilon^3) + \ldots]/\epsilon^2 \quad (2)$$

and ν = desorption preexponential term
β = heating rate
E_a = desorption activation energy
C = the initial concentration
T = the temperature
R = the gas constant
$\epsilon = E_a/RT$

Second-order desorption gives the pressure as[12]

$$P = \frac{\nu \exp(-E_a/RT)\ I\ E_a/R}{C(E_a/R)\ (1 + \nu\beta\ I\ E_a/R)^2} \quad (3)$$

The total release at any time would be the sum of the release over all the active desorption sites. Using these equations, one can calculate the tritium release profile as a function of tine or temperature given the desorption activation energies, preexponential terms, and the heating rate.

Using the data from constant-rate heating experiments, one can estimate the desorptlon activation energies from the temperatures at which the maxima in plots of tritium release versus temperature occur. For experiments where the flow rate and heating rate are such that readsorption does not interfere, if the desorption is first order, then an estimate of the activation energy can be obtained by the following:[13]

$$E_a = RT[\ln(\nu\ T/\beta) - 3.46] \quad (4)$$

Using an estimate of 1×10^8 for the desorption preexponential, (a value in agreement with tritium release measurenents from Li_2O and kinetic studies of the decomposition of LiOT + LiOH[14]), we obtained estimates for the activation energies of desorption of tritium from Li_2O from the Tanifuji et al. data4 and for desorption from Li_4SiO_4 using $\nu = 1 \times 10^8$ and the Skokan et al.[5] and Schauer and Schumacher data.6 These estimates were then used as input to a program calculating the tritium release as a function of temperature using equation (1) or (3). The initial concentrations and activation energies for each site were then varied to optimize the fit to the data.

Estimates of Activation Enemies of Desorption

Li_2O

Our analysis of the data obtained by Tanifuji et al. for their constant heating rate experiment suggests that there are six different sites for desorption of tritium from Li_2O. The estimates of the activation energies from the first-order desorption equation are 140.6±0.4, 149.4±1.7, 162.8±1.7, 178.2±3.8 and 186.2±1.7 kJ/mol (33.6±0.1, 35.7±0.4, 38.9±0.4, 42.6±0.9 and 44.5±0.4 kcal/mol). The desorption peak corresponding to the highest activation energy, 186.2 kJ/mol (44.5 kcallmol), was of low intensity and was not always seen. Exanples of the calculated tritium release curves are illustrated in Fig. 1. The relative populations of the sites responsible for the different desorption peaks were dependent on the history of the sanple and the heating rate. For experinents with a heating rate of 1 K/min the major desorption peak was due to the process with an activation energy of 149.4 kJ/mol (35.7 kcallmol), while the peak corresponding to an activation energy of 140.6 kJ/mol (33.6 kcallmol) was dominant when the heating rate was 10 K/min. This suggests that there is a redistribution in the population of the sites as the sample is heated. In part, a low heating rate allows the most active sites to remain filled longer.

The tritium released from Li_2O and collected as HT was also determined as a function of temperature by Tanifuji et al.4 These curves were analyzed using our model with multiple desorption activation energies. Estimates of desorption activation energies of 139.7, 148.5, 159.4, 175.7, and 187 kJ/mol (33.4, 35.5, 38.1, 42.0, and 44.7 kcal/mol) were obtained. These energies are in good agreement with those determined from the curves of total tritium released. The amount of released tritium detected as HT was found to be of the order of 1%of the total tritium released.4 The agreement between the desorption activation energies for the tritium detected as HT and the total tritium released (detected as mostly HTO) suggests that tritium collected as HT and that collected as HTO are released by the same mechanisms. Thus, the form of tritium detected downstream is probably not determined by the form in which it is released from the solid, but by the gas phase chemistry.

It is of interest to compare our estimates of desorption activation energies with some reported in the literature. The first in the sequence of desorption processes, with an estimated activation energy of 140.6 kJ/mol (33.6 kcallmol), is expected to be for desorption from a surface with a relatively high surface coverage. This value is in good agreement with the desorption activation energy reported by Kudo and Okuno of 129.7 kJ/mol (31 kcal/mol)[14] and the activation energies reported by Quanci. (for tritium release into a helium purge stream containing 0.1 to 1.0% added hydrogen), of 130.6 kJ/mol (31.2 kcal/mol).[15] The second energy (149.4 kJ/mol, 35.7 kcallmol) is expected to correspond to desorption from a slightly more energetic type of sight. Desorption from this site would begin to dominate when the population of a previously active site is diminishing. This activation energy is in excellent agreement with that reported by Quand (for desorption into a pure helium purge) of 152.2 kJ/mol (36.4 kcal/mol),[15] Bertone has reported lower activation energies than our estimates,(118.8 kj/mol, 28.4 kcal/mol)[2] as has Quanci (102.0 kJ/mol, 24.4 kcal/mol, for a purge gas of He +4.82% H_2).[15] There may be sites for desorption from Li_2O with even lower activation energies than those we estimated, but these are expected to correspond to samples with a higher surface coverage than the samples studied by Tanifuji et al. As a possible limiting case for high surface coverage, we note that Kudo and Okuno reported the activation energy for thermal decomposition of LiOH as 123.4 kJ/mol (29.5 kcal/mol).[14] However, additional depression of the activation energy might result from radiation effects or reaction of the surface with H_2 in the purge.

The degree of surface coverage present at any particular time determines which activation energy will control the desorption process at that tine. Unfortunately, we could not obtain estimates of surface coverage from the Tanifuji et al. data so we can not determine what surface coverages our estimated activation energies relate to. However, because these experiments were performed with pure helium purge gas, the results should be comparable with and relevant to tritium release experiments that were also performed with pure helium purge streams. A detailed experimental study is needed to quantitatively relate the hydrogen/tritium surface coverage to the desorption activation energies.

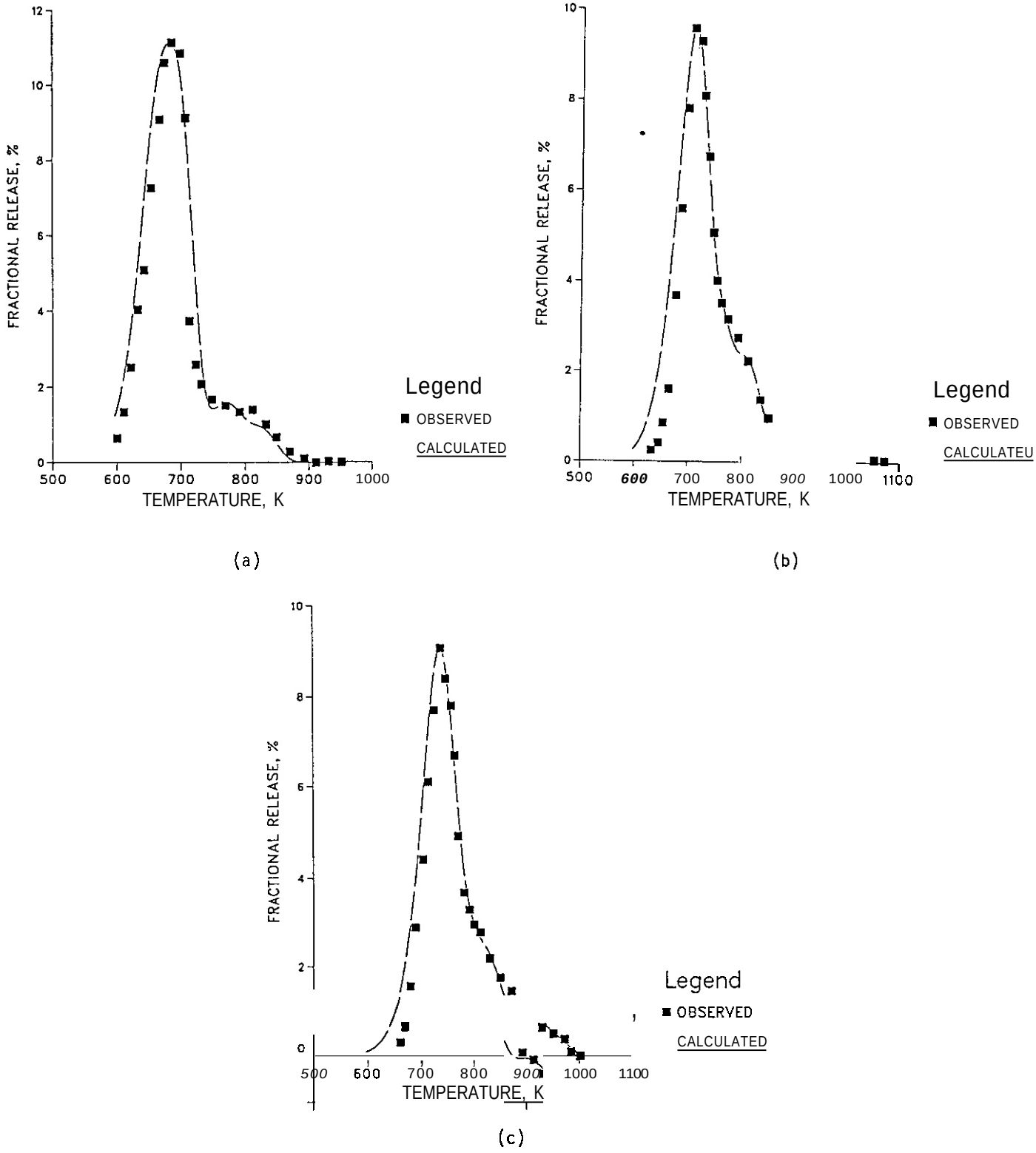

Fig. 1. Tritium released from Li_2O observed from Tanifuji et al. Calculated from multiple desorption site model. (a) Heating rate = 1K/min, (b) Heating rate = 5K/min, and (c) Heating rate = 10K/min.

Li_4SiO_4

We derived approximations for desorption activation energies for Li_4SiO_4 obtained from the data of Skokan et al.5 and Schauer and Schumacher[6] using equation 4 and an estimated value of the desorption preexponential tern of 1×10^8. Activation energies of 73.6, 96.7, 110.9, 143.1, 178.2, and 215.9 kJ/mol (17.6, 23.1, 26.5, 34.2, 42.6, and 51.6 kcal/mol) were obtained from Skokan et al. Values of 83.3, 97.9, 112.1, 146.9, 171.1, 193.3 and 218.8 kJ/mol (19.9, 23.4, 26.8, 35.1, 40.9, 46.2 and 52.3 kcal/mol) were obtained from Schauer and Schumacher. The expected first-order release was calculated and compared to the observed release of H O in the Schauer and Schumacher experiment.[6] The positions of the calculated peaks were found to agree wel? with the experimental data: however, the peak widths for the calculated curves were narrower than the observed peak widths. Calculations based on second-order desorption using activation energies of 83.3, 97.9, 112.1, 144.3, 171.5, and 194.1 kJ/mol (19.9,23.4,26.8,34.5 ,41.0, and 46.4 Kcal/mol) provided a much better fit to the observed data. The agreement between the activation energies calculated from the Skokan et al.[5] and Schauer and Schumacher[6] data is quite good, with a maximum deviation of less than 10 kJ/mol. One additional peak was observed in the tritium release curve from the Schauer paper. This peak may be masked by other more intense peaks in the curves of Skokan et al.

Our estimates of these desorption activation energies can be compared with values calculated by Breitung et al. from a fit of LISA data to a two-site desorption mdel of 53.6 and 90.9 kJ/mol (12.8 and 21.7 kcal/mol).[3] The energy we calculated of 97.9 kJ/mol is in good agreement with the second of their energies, suggesting that we have made a reasonable choice for the preexponential term. Again, it is not possible to determine the surface coverage from the data given in the Schauer and Schumacher paper: thus, the surface coverages which correspond to our estimates of desorption activation energies are unknown.

Skokan et. al. also studied the tritium release from several doped samples of Li_4SiO_4. These doped samples showed different release characteristics than the pure silicate. The materials studied had the compositions $Li_{4.05}Si_{0.95}Al_{0.05}O_4$, $Li_{3.7}Al_{0.1}SiO_4$, $Li_{3.9}Si_{0.9}P_{0.1}O_4$, and $Li_{3.3}P_{0.7}Si_{0.3}O_4$.[5]

The material creating Li vacancies by doping with aluminum, $(Li_{3.7}Al_{0.1}SiO_4)$, exhibited better tritium release than pure $Li SiO_4$.[5] The TPO release curve showed a new desorption peak at low temperature (near room temperature) a d the peak at 73.6 kJ/mol increased in intensity relative to that for the pure silicate while the peak at 96.7 kJ/mol in the pure silicate is no longer observed. The other peaks appear to be the same as for the pure silicate. The overall result is to introduce a new low activation desorption mechanism, improving the tritium release.

The material doped with P to form $Li_{3.9}Si_{0.9}P_{0.1}O_4$ showed poorer tritium release than the pure silicate.[5] The low temperature peak observed in the Al doped Li deficient material is also present for this material: however, the peak at 73.6 kJ/mol is decreased in intensity relative to the pure silicate and the peaks at 96.7 and 110.9 kJ/mol are no longer visible. The peak at 178.2 kJ/mol is increased in amplitude relative to the pure silicate and has a long tail to the high energy side of the peak. The overall result is to shift the tritium release to processes with higher activation energies. A similar effect was seen for $Li_{3.3}P_{0.7}Si_{0.3}O_4$ and $Li_{4.05}Si_{0.95}Al_{0.05}O_4$.[5] For the P doped material three desorption peaks were observed at 73.6, 110.9 and 143.1 kJ/mol. The peak at 143.1 kJ/mol was the most intense peak and had a long trailing tail. Again, the tritium release is shifted to higher activation processes. For the aluminum doped material the peaks at energies of 73.6 and 96.7 kJ/mol are decreased in intensity relative to the pure silicate while the peaks at energies of 178.2 and 215.9 kJ/mol are increased in intensity.

The effects of doping based on the most likely defects formed are as follows:

1) Creating a Li vacancy leads to the availabilty of a new low activation tritium desorption process and improves tritium release.

2) Creating Si vacancies decreases the availabilty of low activation desorption mechanisms and leads to poorer tritium release.

3) Creating Li interstitials decreases the availability of low energy desorption mechanisms and leads to poorer tritium release.

FUTURE WORK

The current estimates of desorption activation energies will be used to try to calculate the observed tritium release from in-pile release experiments. Relationships between purge gas chemistry, surface coverage, and desorption activation energies will be derived from laboratory experiments, in-pile experiments, and modeling efforts.

REFERENCES

1) M. Briec, F. Botter, J. J. Abassin, R. Benoit, P. Chenebault, M. Masson, B. Rausner, P Sciers, H. Werle. and E. Roth, "In and Out-of-Pile Tritium Extraction From Samples of Lithium Aluminates" J. Nucl. Mater. 141-143 (1986) 357-363.

2) P. C. Bertone, "The Kinetics that Govern The Releaseof Tritium from Neutron-Irradiated Lithium Oxide," J. Nucl. Mater. 151 (1988)281-292.

3) W. Breitung, H. Elbel, J. Lebkucher, G. Schumacher, and H. Werle. "Out-of-pile Tritium Extraction From Lithium Silicate,' J. Nucl. Mater. 155-157 (1988) 507-512.

4) T. Tanifuji, K. Noda, S. Nasu, and K. Uchida, "Tritium Release from Neutron-Irradiated Li_2O; Constant Rate Heating Measurements," J. Nucl. Mater. 95 (1980) 108-118.

5) A. Skokan. D. Vollath, H. Wedemeyer. E. Gunther, H. Werle "Preparation, Phase Relationships and First Irradiation Results of Lithium Orthosilicate Doped with Al^{3+} and P^{5+} Ions," 15th Symp. on Fusion Technology, Utrecht, The Netherlands, Sept. 1988.

6) V. Schauer and G. Schumacher, "Study of Adsorption and Desorption of Water on Li_4SiO_4," presented at STNM-7, Chicago, IL, Sept. 1988 (to be published in J. of Nucl. Mater.).

7) A. K. Fischer and C. E. Johnson, "Measurements of Adsorption in the $LiAlO_2$-$H_2O(g)$ System," Fusion Technology 15 (1989) 1212-1216.

8) J. B. Peri,"A Model for the Surface of 7-Alumina.' J. Phys. Chem. 69 (1965) 220.

9) M. Briec and E. Roth, "Tritium Extraction Mchanisms from Lithium Aluminates During In-Pile Irradiation Experiments," Proc. of Specialists' Workshop on Modelling Tritium Behavior in Fusion Blanket Ceramics, Chalk River, Canada, pp 28-57 (1987).

10) J. M. Miller, R. A. Verrall, D. S. MacDonald, and S. R. Bokwa, "The CRITIC Irradiation of Li_2O-Tritium Release and Measurement," presented at the Third Topical Meeting on Tritium Technology in Fission, Fusion and Isotopic Applications, Toronto, Canada, May 1988.

11) J. P. Kopasz, S. W. Tam, and R. A. Verrall, "Modeling Unusual Tritium Release Behavior from Li_2O," Fusion Technology 15 (1989) 1217-1222.

12) A. W. Smith and S. Aranoff. "Thermodesorption of Gases from Solids," J. Phys. Chem. 62 (1958) 684-686.

13) O. A. King, "Thermal Desorption From Metal Surfaces: a Review," Surf. Sci. 47 (1975) 384-402.

14) H. Kudo and K. Okuno, "Kinetic Studies of the Tritium Release Process in Neutron-Irradiated Li_2O and LiOH," J. Nucl. Mater. 101 (1981) 38-43.

15) J. Quanci, "Tritium Breeding and Release-Rate Kinetics from Neutron- Irradiated Lithium Oxide," Phd. Thesis, Dept. of Chemical Engineering, Princeton University, January 1989.

ADSORPTION, DISSOLUTION, AND DESORPTION CHARACTERISTICS OF THE $LiAlO_2$-$H_2O(g)$ SYSTEM - Albert K. Fischer and Carl E. Johnson (Argonne National Laboratory)

OBJECTIVE

Adsorption of $H_2O(g)$, dissolution of OH-, and rates of evolution of $H_2O(g)$ are being measured for the $LiAlO_2$-$H_2O(g)$ system. These thermodynamic and kinetic data for these processes relate to the issues of tritium retention and release, and, hence, to concerns about tritium inventory in ceramic tritium breeder materials. The information will enable (1) comparison of candidate breeder materials, (2) calculation of operating conditions, and (3) elucidation of the principles underlying the behavior of tritium in breeder materials.

SUMMARY

Analysis of adsorption isotherms for the $LiAlO_2$-$H_2O(g)$ system has defined a range of heats of adsorption from 80 to 360 kJ/mol in the region of 873 K; these heats are dependent on the fraction of surface coverage which ranges from 0.1 to 0.001, respectively. Desorption activation energies follow these values closely and are also dependent on coverage. Adsorption activation energies were estimated (the values are small) and confirm the earlier report of two differently activated adsorption processes, depending on temperature. Modelling tritium release from irradiation tests requires accurate values for desorption activation energies. Though such information can be derived from the adsorption isotherm measurements, a technique specifically suited for desorption activation energy measurements is available: temperature programed desorption. Apparatus for such measurements has been constructed and the first measurements will continue with the $LiAlO_2$-$H_2O(g)$-H_2 system. The participation of H_2 is important to evaluate because it has been found that H_2 enhances tritium release in irradiation tests.

PROGRESS AND STATUS

Data Analysis

Further analysis of the adsorption isotherms presented in the last report provided estimates of the heats of adsorption of $H_2O(g)$ on $LiAlO_2$ in the region of 873 K. As discussed in that report, the data indicate that two adsorption processes with different activation energies operate in this system. In most of the 573 to 873 K range of measurement, they contribute together to the adsorption process. Only at the ends of this range can one isotherm apparently be clearly identified with each process (the 573 and the 873 K isotherms). Consequently, calculation of heats of adsorption by the Clausius-Clapeyron equation cannot be pursued rigorously. However, the shapes of the isosteres (plots, at constant coverage, of the partial pressure of $H_2O(g)$ as a function of temperature) suggest minimum values for the heat of adsorption in the region of 873 K. The values are 80, 150, 220, 290, and 360 kJ/mol, respectively, for values of $\log(\theta)$ of -1, -1.5, -2, -2.5, and -3. (θ is the fraction of surface covered by adsorbate.) The values follow the trend, that is generally true, for the heat of adsorption to increase as the surface coverage decreases.

Unfortunately, a similar range of estimates is not possible at the lower temperature end of the range; measurements would be needed for temperatures below 573 K. However, one isostere, the one for relatively high coverage at $\theta = 0.1$, does suggest that the heat of adsorption is about 40 kJ/mol for these conditions.

For the conditions where heats of adsorption may be estimated, values of the activation energies of desorption may also be estimated. This is possible because the activation energy of desorption is equal to the sum of the heat of adsorption and the activation energy of adsorption. Because the activation energy of adsorption is usually small, even nearly zero, it is a useful approximation to take the activation energy of desorption as about equal to the heat of adsorption. It follows that the desorption activation energy is also dependent on the degree of surface coverage.

Though not designed as kinetic experiments, the adsorption measurements were analyzed further to extract information on the rates of adsorption. Figure 1 shows the rate of adsorption as a function of temperature for a selected value of $pH_2O(g)$ of 15 Pa. In the regions where this rate increases with temperature, the slopes allow an estimate to be made of the activation energy of adsorption. Confirming the earlier deduction that two different adsorption processes with different adsorption activation energies are involved in different temperature ranges, these curves suggest a 3 kJ/mol adsorption activation energy in the 573 to 623 K range and a 15 kJ/mol adsorption activation energy in the 673 to 773 K range. The high temperature adsorption process is probably dissociative chemisorption and the low temperature process is perhaps low activation energy chemisorption or unimolecular physisorption. This figure also illustrates the possibility that observed net rates of adsorption decrease with increasing temperature when different processes coexist which have different activation energies and different dependencies on coverage.

The coverage-dependent values of the desorption activation energy indicated in this work are the result of surface heterogeneity in respect to chemical differences between adsorption sites, crystallographic differences for exposed crystal planes, and defects on the surface. Multiple types of sites are involved in

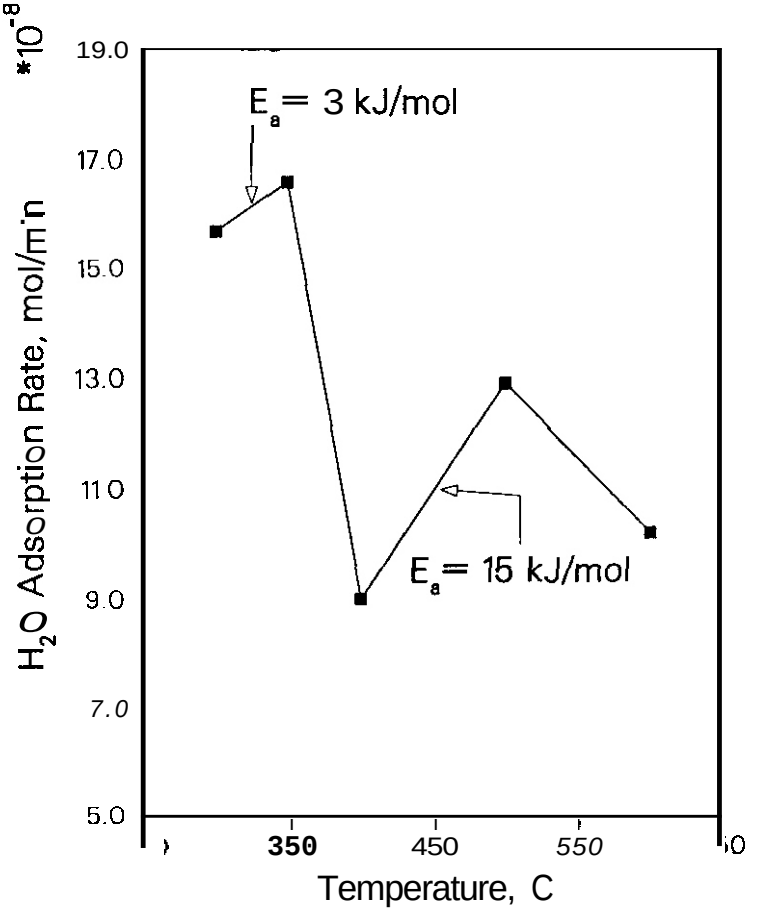

Fig. 1. Rates of adsorption of $H_2O(g)$ at a partial pressure of 15 Pa on $LiAlO_2$.

adsorption and desorption. This is consistent with our own earlier evidence for site dependent evolution (desorption) of $H_2O(g)$ from $LiAlO_2$ obtained from a rough temperature programed (TPD) experiment (see below for further discussion).[1] It is also consistent with other reports on other materials that revealed the same complexity. For example, a theoretical analysis of the types of OH- sites possible on the surface of alumina, characterized in terms of the number of O^{2} nearest neighbors, showed five types to be present. These were related to experimentally measured infrared spectra.[2]

The above material is part of a paper for the April meeting of the American Ceramic Society, under the title, "Oesorption Activation Energies for Tritium Release from Ceramic Breeders," by J. P. Kopasz, A. K. Fischer, and C. E. Johnson.

Implementation of Temperature Proqramned Desorption Measurements

Recent work on modelling tritium release observations from irradiation tests has emphasized the need for data on surface properties to analyze dynamic inventory; for this the activation energies of desorption are of primary importance. These activation energies can be supplied directly by the temperature programned desorption (TPD) technique which is now being imlemented. TPD can also give information on quantities of adsorption, though not as well as the frontal analysis technique that was used for the adsorption isotherms discussed above. TPD and frontal analysis are complementary approaches to studying surface processes.

In essence, the TPD technique consists of measuring the rate of desorption of a given species (i.e., in the form of the evolved species, not necessarily the surface species) into a sweep gas during an upward ramp of the sample temperature. The evolution rate goes through a maximum, giving a peak in the curve. A number of theoretical treatments for analyzing the data exist and require either single or multiple TPD curves, at fixed or variable initial coverages, and for single or multiple heating rates. Depending on treatment, the various outputs provide values for various combinations of the preexponential factor, the activation energy for desorption, and the order of the evolution reaction.

A schematic diagram of the TPD apparatus that has been constructed is shown in Fig. 2. The valves F, K, and L are high tenperature gas chromatographic switching valves so that all gas trains carrying $H_2O(g)$ can be maintained at 473 K to eliminate holdup of this species. Not shown is a quadrupole mass spectrometer that samples effluent gas between valves K and L. This instrument is an important feature because data are needed not only for $H_2O(g)$ evolution but also for $H_2(g)$ adsorption and evolution. This is because it has been found that H in the purge stream of irradiation tests facilitates release of tritium. It is believed that adsorbed H_2 hocks energetic sites that would otherwise retain OH- and impede evolution of $H_2O(g)$. Data are needed for a quantitative evaluation of this process.

FUTURE WORK

Following proof-testing and calibration of the TPD apparatus, measurements will be made to obtain activation energies for desorption of $H_2O(g)H_2(g)$ from $LiAlO_2$. Substrates to be studied after that include Li_4SiO_4, Li_2O, and Li_2ZrO_3.

REFERENCES

1. A. K. Fischer and C. E. Johnson, "Adsorption, Dissolution, and Desorption Characteristics of the $LiAlO_2$-H_2O System," DOE/ER--0313/1, Fusion Reactor Materials Semiannual Progress Report for Period Ending September 30, 1986, p. 362.

2. J. B. Peri, "A Model for the Surface of 7-Alumina," J. Phys. Chem., 69 (1965) 220.

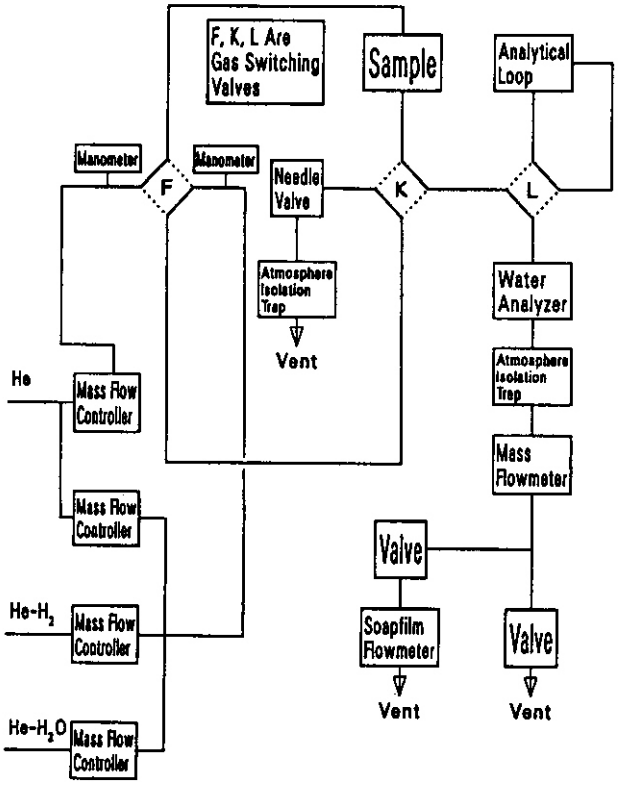

Fig. 2. Schematic diagram for temperature programed desorption measurements.

8. CERAMICS

No contributions.

DOE/ER-0313/6
Distribution
categories
UC-423, 424

DISTRIBUTION

1-18. Argonne National Laboratory. 9700 South Cass Avenue, Argonne, IL 60439

M. C. Billone
O. K. Chopra
R. G. Clemmer
D. R. Diercks
P. A. Finn
A. K. Fischer
L. R. Greenwood
C. E. Johnson
Y. Y. Liu
B. A. Loomis
R. F. Mattas
L. A. Niemark
D. L. Smith
S. W. Tam
E. R. Van Deventer
H. Wiedersich

17. Argonne National Laboratory, EBR-II Division. Reactor Materials Section, P.O. Box 2528, Idaho Falls. ID 83403-2528

D. L. Porter

18. Arizona State University. Department of Mechanical and Aerospace Engineering, Tempe, AZ 85281

W. A. Coghlan

19. Auburn University. Department of Mechanical Engineering, Auburn, AL 38849

B. A. Chin

20-34. Battelle-Pacific Northwest Laboratory, P.O. Box 999, Richland, WA 99352

M. D. Freshley
F. A. Garner (5)
D. S. Gelles
M. L. Hamilton
H. L. Heinisch
G. W. Hollenberg
R. H. Jones
J. M. McCarthy
8. D. Shipp
O. D. Slagle
J. L. Straalsund

35-38. Carnegie Institute of Technndogy. Carnegie-Mellon University, Schenley Park, Pittsburgh, PA 15213

W. M. Garrison, Jr.
J. C. Williams

37. Department of Energy, Richland Operations Office, Federal Building, MS A590, Richland, WA 99352

Paul Pak

38. Department of Materials Science. University of Tokyo. 3-1, Hongo 7-Chome Bunkyo-Ku
Tokyo 113, Japan

Professor Akira Kohyama

39. Department of Nuclear Engineering, Nagoya University. Furo-Cho, Chikusa-Ku, Nagoya 464-01, Japan

Professor Michio Kiritani

40. Department of Nuclear Engineering. Tohoku University. Aoba, Aramaki, Sendai 980, Japan

Professor Katsunori Abe

41-42. Department of Nuclear Engineering. University of Tokyo. 3-1, Hongo 7-Chome, Bunkyo-Ku
Tokyo 113, Japan

Professor Shiori Ishino (2)

43. EG&G Idaho. Inc., Fusion Safety Program. P.O. Box 1825, Idaho Falls. ID 83415-3523

D. F. Holland

44. Faculty of Engineering. Hokkaido University, Kita 13, Nishi 8, Kita-Ku, Sapporo 060, Japan

Professor Heishichiro Takahashi

45-47. General Atomics, P.O. Box **85608,** San Diego, **CA 92138**
J. Baur
D. I. **Roberts**
T. A. Lechtenberg

48. General Dynamics Corporation, **5001 Kearny** Villa **Road,** San **Diego. CA 92138**
T. L. Cookson

49. Georgia Institute *of* Technology, School *of* Textile Engineering, Atlanta, GA **30332**
D. **S.** Tucker

50. Grumman Aerospace Corporation, c/o TFTR Project. Princeton Plasma Physics Laboratory. Princeton University, A. Site, Building 1-E, Princeton, NJ **08540**
R. G. Micich

51. Institute for Materials Research, Tohoku University, Katahira **2-1-1,** Sendai **980.** Japan
Professor **Hideki Matsui**

52. Institute for Materials Research, Oarai Branch, Tohoku University, Oarai, **Higashi-Ibaraki-Gun,** Ibaraki-Ken **311-13,** Japan
Professor **Hideo** Kayano

53-54. Institute *of* Plasma Physics, **Nagoya** University, **Furo-Cho, Chikusa-Ku,** Nagoya **464-01,** Japan
Professor Akira Miyahara
Dr. **Chusei** Namba

55-57. Lawrence Livermore National Laboratory, P.O. Box **808,** Livermore, CA **94550**
E.N.C. **Dalder**
J. **Perkins**
M. Guinan

58-66. Los Alamos National Laboratory, P.O. **Box 1663, Los** Alamos, NM **87545**
J. L. Andersen
L. D. **Caudill**
D. J. **Dudziak**
H. M. Frost
F. W. Clinard
G. **Hurley**
C. D. Kise
R. Liepens
T. Zocco

87. Manlabs, **Inc., 231** Erie Street, Cambridge, MA **02139**
D. **Tognarelli**

68. Massachusetts Institute of Technology, Department of Metallurgy and Materials Science. Cambridge, MA **02139**
L. W. Hobbs

89. Massachusetts Institute of Technology, **138** Albany Street, Cambridge, MA **02139**
O. K. Harling

70-71. Massachusetts Institute of Technology, **77** Massachusetts Avenue, **Cambridge, MA 02139**
I-Wei Chen
N. J. Grant

72-73. Massachusetts Institute of Technology. Plasma Fusion Center Headquarters, **Cambridge,** MA **02139**
H. D. Becker
D. B. Montgomery

74. McDonnell-Douglas Astronautics Company, East, P.O. **Box 518,** Bldg. **92,** St. Louis. **MO 83186**
J. W. Davis

75-78. National Institute *of* Standards and Techndogy. Boulder, **CO 80302**
F. R. Fickett
M. B. Kasen

77. National Materials **Advisory** Board, **2101 Constitution** Avenue, Washington, **DC 20418**
K. M. **Zwilsky**

78-79. National Research Institute for Metals. **Tsukuba** Branch, Sengen, **Tsukuba-Shi,** Ibaraki-Ken 305, Japan
Dr. **Masatoshi** Okada
Dr. Haruki Shiraishi

80. Naval Research Laboratory, Washington, DC **20375**
J. A. Sprague

81-118. Oak Riie National Laboratory, P.O. Box 2008, Oak Rii, TN 37831

Central Research Library
Document Reference Section
Laboratory Records Department (2)
Laboratory Records—RC
Patent Section
D. J. Alexander
C. W. Baker
J. Bentley
E. E. Bloom
D. N. Braski
T. D. Burchell
M. L. Grossbeck
T. Inazumi
R. L. Klueh
Eal Lee
A. W. Longest
L. K. Mansur
P. J. Maziasz
T. K. Roche
A. F. Rowcliffe (10)
J. Sheffield
T. Sawai
R. L. Senn
R. E. Stoller
K. R. Thoms
P. F. Tortorelli
F. W. Wiffen
S. J. Zinkle

119-120. Princeton Plasma Physics Laboratory, Princeton University, P.O. Box 451, Princeton, NJ 08540

H. Furth
Long-Poe Ku

121. Research Institute for Applied Mechanics, Kyushu University, 6-1, Kasuga-Koen, Kasuga-Shi, Fukuoka-Ken 816, Japan

Professor Takeo Muroga

122. Rensselaer Polytechnic Institute, Troy, NY 12181

D. Steiner

123. Rockwell International Corporation, NA02, Rocketdyne Division, 6633 Canoga Avenue, Canoga Park, CA 91304

D. W. Kneff

124-125. Sandia National Laboratories, P.O. Box 5800, Albuquerque, NM 87185

M. J. Davis
W. B. Gauster

126-127. Sandia National Laboratories, Livermore Division 8316, Livermore, CA 94550

W. Bauer
W. G. Wolfer

128. San Diego State Univ., Mechanical Engineering Dept., San Diego, CA 92182-0191

L. D. Thompson

129-132. Tokai Research Establishment, Japan Atomic Energy Research Institute, Tokai-mura, Naka-gun, ibaraki-Ken 319-11, Japan

Dr. Tatsuo Kondo
Dr. Akimichi Hishinuma (3)

133-134. University of California, Department of Chemical and Nuclear Engineering, Santa Barbara, CA 93106

G. E. Lucas
G. R. Odette

135-137. University of California, Department of Chemical, Nuclear and Thermal Engineering, Loa Angeles, CA 90024

M. A. Abdou
R. W. Conn
N. M. Ghoniem

138. University of California. Los Alamos National Laboratory, P.O. Box 1663, Loa Alamos, NM 87545

T. Zocco

139. University of Michigan, Department of Nuclear Engineering, Ann Arbor, MI 48109

T. Kammash

140. University of Missouri, Department of Nuclear Engineering, Rolla, MO 65401

A. Kumar

141. University of Wisconsin, Nuclear Engineering Dept., 1600 Johnson Drive, Madison, WI 53706
G. L. Kulcinski

142-147. Westinghouse Hanford Company, P.O. Box 1970, Richland, WA 99352
H. R. Brager
A. M. Ermi
G. D. Johnson
F. M. Mann
R. J. Puigh
R. L. Simons

148. Department of Energy, Oak Ri e Operations Office, P.O. Box 2001, Oak Ridge, TN 37831
Assistant Manager for Energy Research and Development

149-152. Department of Energy. Office of Fusion Energy. Washington. DC 20545
S. E. Berk
A. Davies
M. M. Cohen
T. C. Reuther

153-202. Department of Energy, Office of Scientific and Technical Information, Office of Information Services, P.O. Box 62, Oak Ridge, TN 37831

For distribution as shown in DOE/TIC-4500, Distribution Categories UC423 (Magnetic Fusion Reactor Materials) and UC424 (Magnetic Fusion Energy Systems)